Sleep and navigation in *Drosophila*

Kumulative Dissertation
zur
Erlangung des Doktorgrades (Dr. rer. nat.)
der
Mathematisch-Naturwissenschaftlichen Fakultät
der
Rheinischen Friedrich-Wilhelms-Universität Bonn

vorgelegt von
Andres Flores-Valle
aus
Toledo, Spanien

Bonn, November 28, 2023

Angefertigt mit Genehmigung der Mathematisch-Naturwissenschaftlichen Fakultät der
Rheinischen Friedrich-Wilhelms-Universität Bonn

1. Gutachter: Prof. Dr. Michael J. Pankratz
2. Gutachter: Prof. Dr. Jason Kerr

Tag der Promotion: 6. November 2023
Erscheinungsjahr: 2023

Abstract

Sleep plays an essential role in life and is critical for the optimal functioning of the brain, for example in learning and memory. *Drosophila* displays many of the signatures of sleep observed in mammals or humans, including sleep homeostasis. Sleep homeostasis tracks the accumulating need to sleep during wakefulness, thus investigating sleep homeostasis will provide insights into why sleep is necessary for optimal brain function.

In the fly brain, a neural control circuit for sleep homeostasis has been located in the central complex, a brain region important for navigation and spatial or visual learning. Since the same brain area is involved in sleep, navigation, and learning, it provides the opportunity to investigate the connection between sleep and navigation, as well as the influence of sleep on spatial and visual learning, at the level of well-characterized, genetically identified neural circuits.

To investigate this relation between sleep, navigation, and memory, this thesis first implements theoretical and computational models, which predict autonomous activity in the head direction system of the fly during sleep. Then, methods for improved imaging in behaving flies are developed. These methods include a setup for (semi-) automated dissection of flies, feeding, and imaging over multiple days during behavior; a method for volumetric imaging at high frame rates; a method for correction of brain motion during imaging; a novel virtual reality setup for learning in head-fixed walking flies; and finally a setup for combined two-photon imaging and learning behavior.

The developed techniques are applied for the investigation of sleep homeostasis in neurons and glia. In particular, it is found that ensheathing glia, a type of glia in the fly brain, encode sleep need through their calcium dynamics with the dynamics expected of a sleep homeostat. Additionally, the dynamics of a neural population in the central complex that is modulated by feeding are reported. Finally, a neural population that encodes the traveling direction of the fly navigating in virtual reality is investigated. This neural population is found to exhibit autonomous activity when the fly is resting or sleeping, similar to activity observed in the head direction system in mammals.

Overall, the methods developed here have a range of potential applications in monitoring brain dynamics in flies over long timescales or during learning. By applying these methods, this thesis contributes to an understanding of sleep regulation and navigation in the central

complex by clarifying the role of previously studied neurons important for sleep, by discovering a sleep homeostat in ensheathing glia, and by describing the autonomous dynamics of neurons in the head direction system during rest and sleep.

Acknowledgments

I want to express my sincere gratitude to many people that taught me and supported me so much along this journey. All of them have contributed to the work presented here in one way or another. First of all, I would like to thank Prof. Dr. Michael Pankratz, Prof. Dr. Jason Kerr, Prof. Dr. Ruben Portugues, and Prof. Dr. Ilona Grunwald Kadow for agreeing to be part of the examination committee for this thesis.

I want to thank Prof. Dr. Michael Pankratz and Dr. Kevin Briggman, who as part of my thesis advisory committee offered guidance, advice, and feedback. I would also like to thank Prof. Dr. Raoul-Martin Memmesheimer and Prof. Dr. Julijana Gjorgjieva, who introduced me to computational neuroscience early on in my Ph.D. studies.

I am very grateful to my supervisor Dr. Johannes Seelig, who not only provided fantastic supervision, expertise, and support, but also contributed to the work in this thesis with insightful ideas, by building optical setups and by performing experiments. I also want to thank Rolf Honnef of the mechanical workshop, who worked very closed with me to design and build some of the setups used for experiments. I am grateful to my colleagues in the lab, Dr. Ivan Vishniakou and Joel Valdivia for the fun journal clubs and interesting discussions in lab meetings, as well as to previous lab members, Dr. Stephanie Miceli for helpful discussions, and Dr. Alex Turpin for providing motivation and feedback.

I would like to thank our collaborator Dr. Pedro Gonçalves, from whom I learned so much about computational analysis. I further want to thank Prof. Dr. Jason Kerr for providing us with vital lab equipment that was used in experiments in this thesis, as well as feedback on our manuscripts.

I am very grateful to the Max Planck Institute for Neurobiology of Behavior (MPINB) and the IMPRS for Brain and Behavior graduate program, which have provided a great scientific environment and many of the resources that made this work possible. In particular, I want to thank the mechanical workshop, the scientific computing team for their support in the cluster usage for data analysis, the IMPRS coordinator Ezgi Bulca, for her care and dedication to the students, as well as Bettina Bosse for her administrative support.

Last but not least, I have been supported during my PhD at a personal level by many people I love. I am grateful beyond words to my partner Ezgi Bulca for always being there for me in the good and bad moments, for being loving, supporting, and understanding, and

for creating a home with me in a foreign country. I also would like to thank my friends at the MPINB for the wonderful experiences and moments we have shared together.

In spanish: Quiero agradecer a la gente de España a la que quiero. Gracias a mi madre María de los Ángeles, a mi padre Andrés y a mi hermano Jorge, por motivar y estimular mi curiosidad desde niño, por educarme, por garantizar que siempre tuviera todo lo que necesitaba, y por contribuir a formar la persona que soy hoy. Los tres sois un ejemplo de fuerza, perseverancia y superación. Quiero agradecer al resto de mi familia Toledana: a mis abuelos y abuelas; a mis tíos y tías; y a mis primos y primas. Nunca se olvidan las raíces. Por último quiero agradecir a mis amigos y amigas, con quien mantengo una profunda amistad a pesar de la distancia.

To all of you, thank you!

x

Contents

Abstract **v**

Acknowledgments **vii**

Contents **xi**

List of Figures **xix**

List of Tables **xxv**

1 Introduction **1**

1.1 Sleep . . . 3
1.1.1 Sleep in humans and mammals . . . 3
1.1.2 Sleep in other animals . . . 5
1.2 Sleep behavior in *Drosophila* . . . 6
1.2.1 Monitoring sleep behavior . . . 6
1.2.2 Circadian behavior . . . 8
1.2.3 Behavior under sleep deprivation . . . 9
1.2.4 Visual and spatial learning . . . 9
1.2.5 Impact of sleep on learning and memory . . . 11
1.3 The brain of *Drosophila* during sleep . . . 12
1.3.1 Neural circuit dynamics . . . 13
1.3.2 Synaptic changes . . . 13
1.3.3 Accumulation and clearance of sleep substances . . . 15
1.3.4 Glia . . . 16
1.4 Hypotheses for the function of sleep . . . 19
1.4.0.1 Energy restoration . . . 19
1.4.0.2 Synaptic homeostasis hypothesis . . . 19
1.4.0.3 Clearance of metabolites . . . 20
1.5 The regulation of sleep . . . 20
1.5.1 Circadian clocks and rhythms . . . 21

1.5.2 Sleep homeostasis . . . 22
1.6 Interaction of sleep and navigation in the central complex . . . 23
1.6.1 Sleep regulation in the central complex . . . 23
1.6.2 Navigation in the central complex . . . 25
1.6.3 Visual and spatial learning in the central complex . . . 26
1.7 Experimental Tools for investigating sleep and navigation in *Drosophila* . . . 27
1.7.1 Genetic tools . . . 27
1.7.2 The connectome . . . 28
1.7.3 *In vivo* functional imaging . . . 29
1.7.3.1 Fly preparations for *in vivo* experiments . . . 29
1.7.3.2 Fast volumetric imaging . . . 30
1.7.3.3 Brain motion correction . . . 32
1.7.3.4 Long-term imaging during behavior . . . 33
1.7.4 Place learning . . . 33
1.8 Theoretical and computational models for sleep and navigation . . . 35
1.8.1 Models for sleep and wake regulation . . . 35
1.8.2 Sleep for training neural networks . . . 36
1.8.3 Models for navigation: ring attractor networks . . . 36
1.9 Aims of this thesis . . . 38

2 Integration of sleep and navigation in Drosophila 41
2.1 Abstract . . . 43
2.2 Introduction . . . 43
2.3 Results . . . 45
2.3.1 Sleep homeostasis model . . . 45
2.3.2 Connectivity between head direction and sleep circuits . . . 46
2.3.3 Integration of sleep homeostasis and navigation circuits with fixed connections . . . 48
2.3.4 Integration of sleep homeostasis and navigation circuits with plasticity 48
2.3.5 Two-population model with plasticity . . . 49
2.3.6 Dynamics of the two-population model with plasticity . . . 51
2.3.7 Ring attractor model with plasticity . . . 52
2.3.8 Autonomous dynamics in the ring attractor model . . . 58
2.4 Discussion . . . 59
2.5 Methods . . . 62
2.5.1 Anatomy based on the fly connectome . . . 62
2.5.2 Numerical simulation of models . . . 62
2.5.3 Sleep homeostasis circuit . . . 63
2.5.4 Sleep homeostasis and ring attractor with fixed connections . . . 64

2.5.5 Two-population model with plasticity for R5 and wedge neurons . . . 65
2.5.5.1 Plasticity rules . . . 65
2.5.5.2 Stability of the two-population model . . . 67
2.5.5.2.1 Fast-timescale limit . . . 67
2.5.5.2.2 Slow-timescale limit . . . 68
2.5.5.3 Two-population dynamics during wakefulness . . . 69
2.5.5.4 Two-population model dynamics during sleep . . . 70
2.5.6 Ring attractor network with plasticity . . . 72
2.5.7 Ring attractor network: bump stability analysis . . . 73
2.5.8 Ring attractor network: autonomous bump path analysis . . . 75
2.5.9 Ring attractor network: bump drift during wake phase . . . 77
2.6 Supplementary information . . . 78
2.6.1 Ring attractor network: resetting the weights during sleep without autonomous activity . . . 78

3 Automated long-term two-photon imaging in head-fixed walking *Drosophila* 89
3.1 abstract . . . 91
3.2 Introduction . . . 91
3.3 Results . . . 94
3.3.1 Laser surgery . . . 94
3.3.2 Microrobotic arm for surgery assistance . . . 94
3.3.3 Volumetric two-photon imaging . . . 96
3.3.4 Feeding robot . . . 97
3.3.5 Calcium imaging over multiple days . . . 97
3.4 Discussion . . . 102
3.5 Methods . . . 103
3.5.1 Motorized micromanipulators for fly feeding and laser surgery . . . 103
3.5.2 Laser surgery setup . . . 105
3.5.3 Microrobotic arm . . . 105
3.5.4 Fly stocks and preparation . . . 106
3.5.5 Temperature control . . . 107
3.5.6 Virtual Reality setup . . . 108
3.5.7 Hardware and software synchronization . . . 108
3.5.8 Data storage and preprocessing . . . 110
3.5.9 Imaging data analysis from EPG neurons . . . 111
3.5.10 Behavioral data analysis for each fly . . . 115
3.5.11 Statistical analysis of behavior and imaging data . . . 116

4 Techniques for improving imaging using temporal multiplexing 125
4.1 Two-photon Bessel beam tomography for fast volume imaging 127
4.1.1 abstract 127
4.1.2 Introduction 127
4.1.3 Results 128
4.1.3.1 Setup 128
4.1.3.2 Tomographic volume reconstruction 136
4.1.3.2.1 Radon transform for Bessel beam scanning 136
4.1.3.2.2 Calibration of Bessel beam projections 137
4.1.3.2.3 Back projection 138
4.1.3.2.4 Neural networks for distortion correction 139
4.1.4 Discussion 140
4.1.5 Supplementary information 142
4.2 Axial motion estimation and correction for simultaneous multi-plane two-photon calcium imaging 145
4.2.1 abstract 145
4.2.2 Introduction 145
4.2.3 Results 147
4.2.3.1 Outline of motion correction approach 147
4.2.3.2 Motion estimation and correction algorithm 148
4.2.3.3 Motion correction in simulated data for a single voxel 150
4.2.3.4 Motion correction in simulated data for multiple voxels . . . 151
4.2.3.5 Estimation and correction of controlled sample motion *in vivo* 158
4.2.3.6 Estimation and correction of controlled sample motion and intensity variations 159
4.2.3.7 Estimation and correction of controlled motion for *in vivo* two-photon calcium imaging 160
4.2.3.8 Estimation and correction of brain motion for *in vivo* two-photon calcium imaging in behaving animals 160
4.2.3.9 Algorithm for imaging with four simultaneously recorded focal planes 161
4.2.4 Discussion 161
4.2.5 Supplementary information: Methods 162
4.2.5.1 Microscope setup 162
4.2.5.2 *Drosophila* preparation 163
4.2.5.3 Extracting head direction from calcium signals 163
4.2.5.4 Analytical approximation of motion correction algorithm for a single ROI 163
4.2.5.5 Simulation of a moving single ROI 167

4.2.5.6 Algorithm for motion estimation and correction for several ROIs with noise . . . 169
4.2.5.7 Simulation of several moving ROIs . . . 171
4.2.5.8 Simulation for motion estimation and correction with four simultaneously recorded focal planes . . . 173

5 Calcium dynamics of sleep homeostasis in *Drosophila* during walking and feeding behavior 179
5.1 abstract . . . 182
5.2 Introduction . . . 183
5.3 Results . . . 184
5.3.1 Expected time constants of sleep homeostasis . . . 184
5.3.2 Glia activity varies across the day . . . 184
5.3.3 Glia activity monitors active and rest states . . . 188
5.3.4 Glia monitor behavioral effort . . . 188
5.3.5 Flies sleep during imaging . . . 189
5.3.6 Sleep deprivation saturates glia activity . . . 189
5.3.7 Glutamate changes faster than calcium . . . 191
5.3.8 Homeostat model describes glia activity . . . 192
5.3.9 Homeostat integrates multiple behaviors . . . 194
5.3.10 Glia and neuron dynamics . . . 195
5.3.11 Hunger state encoded in dFB neurons . . . 198
5.4 Discussion . . . 201
5.5 Methods . . . 203
5.5.1 *Drosophila* preparation . . . 203
5.5.2 Setup for experiments with freely walking flies . . . 203
5.5.3 Imaging setup . . . 204
5.5.4 Data acquisition . . . 205
5.5.5 Data post-processing . . . 206
5.5.6 Behavior classification . . . 207
5.5.7 Probing of arousal threshold . . . 207
5.5.8 Fitting of fluorescence traces during 'active' and 'rest' states . . . 209
5.5.9 Sleep deprivation . . . 210
5.5.10 Homeostat model . . . 211
5.5.11 Three-state homeostat model . . . 212
5.5.12 Seven-state homeostat model . . . 213
5.5.13 Hunger-walk model . . . 214
5.5.14 Model fitting . . . 215
5.5.15 Comparison between models . . . 216

5.5.16 Velocity modulation of glia activity . . . 217
5.5.17 Comparison between activity of ensheathing glia and neurons . . . 218
5.5.18 Fitting of fluorescence traces during 'hungry' and 'fed' states . . . 220
5.5.19 Change in body size before and after feeding . . . 220

6 Autonomous activity in the head direction system of *Drosophila* during learning 261
6.1 A place learning assay for tethered walking *Drosophila* . . . 264
6.1.1 abstract . . . 264
6.1.2 Introduction . . . 264
6.1.3 Materials and Methods . . . 265
6.1.3.1 Mechanical VR . . . 265
6.1.3.1.1 Rotation . . . 266
6.1.3.1.2 Translation . . . 267
6.1.3.2 Ball tracking . . . 267
6.1.3.3 Cylindrical arena and visual stimuli . . . 268
6.1.3.4 Aversive heat stimulus . . . 268
6.1.3.5 Hardware and software control . . . 268
6.1.3.6 Kinematics and collision avoidance . . . 269
6.1.3.7 *Drosophila* preparation . . . 271
6.1.4 Results . . . 271
6.1.4.1 Setup . . . 271
6.1.4.2 Place learning with respect to a visual landmark . . . 273
6.1.4.3 Place memory is preserved also after learning in a fraction of flies . . . 277
6.1.5 Discussion . . . 279
6.2 Autonomous activity in PFR neurons during place learning . . . 287
6.2.1 abstract . . . 287
6.2.2 Introduction . . . 287
6.2.3 Results . . . 289
6.2.3.1 PFR neurons . . . 289
6.2.3.2 Imaging in mechanical virtual reality setup . . . 289
6.2.3.3 Learning behavior . . . 290
6.2.3.4 Drift activity while the fly is standing still . . . 293
6.2.3.5 Drift during sleep . . . 299
6.2.4 Discussion . . . 299
6.2.5 Methods . . . 302
6.2.5.1 Drosophila preparation . . . 302
6.2.5.2 Setup . . . 302

6.2.5.2.1 Mechanical virtual reality . . . 302
6.2.5.2.2 Aversive stimulus . . . 303
6.2.5.2.3 Two-photon microscope . . . 303
6.2.5.3 Experimental design . . . 304
6.2.5.4 Data acquisition . . . 305
6.2.5.5 Behavior data analysis . . . 305
6.2.5.6 Imaging data analysis . . . 305
6.2.5.6.1 Dimensionality reduction . . . 306
6.2.5.6.2 Analysis of PFR phase velocity . . . 308
6.2.5.6.3 Analysis of the PFR phase during sleep . . . 308

7 Conclusions **317**
7.1 Methods for studying sleep in behaving flies . . . 317
7.1.1 Theoretical approaches . . . 317
7.1.2 Long-term imaging . . . 318
7.1.3 Development of imaging techniques . . . 319
7.1.4 Place learning assay . . . 320
7.2 Sleep regulation in *Drosophila* . . . 321
7.2.1 Ensheathing glia . . . 321
7.2.2 dFB and R5 neurons for sleep homeostasis . . . 323
7.3 Sleep and navigation . . . 325

Bibliography **371**

List of Figures

1.1 EEG recordings of brain activity from a laboratory mouse during sleep and wakefulness . . . 4
1.2 DAM and video-based methods for monitoring sleep . . . 7
1.3 Circadian behavior of flies under laboratory conditions . . . 8
1.4 Flight simulator setup for visual learning . . . 10
1.5 SWA activity in mammals and flies . . . 14
1.6 Synaptic changes in the fly brain after sleep deprivation . . . 15
1.7 Extraceullar adenosine concentration in the mouse basal forebrain . . . 16
1.8 Types of glia cells in *Drosophila* . . . 17
1.10 The central complex of the *Drosophila* brain . . . 24
1.11 Two-photon temporal multiplexing . . . 31
1.12 Visual place learning assay for freely moving flies . . . 34
1.13 Ring attractor network . . . 37
1.14 Organization of chapters in this thesis . . . 39

2.1 Sleep homeostasis and navigation circuits in the central complex . . . 45
2.2 Integration of the sleep homeostasis circuit with a ring attractor network . . . 47
2.3 Two-population model . . . 50
2.4 Dynamics of ring attractor network during wake phase . . . 54
2.5 Simulation of ring attractor combined with sleep homeostasis model . . . 56
2.6 Relation between wake and sleep dynamics in the ring attractor network . . . 57
S2.1 Connectivity between the navigation-related and sleep-related populations . . . 79
S2.2 Analysis of the two-population model in the fast and slow-timescale limits . . . 80
S2.3 Bump profile in the ring attractor network in response to different inputs . . . 81
S2.4 Ring attractor network with no plasticity . . . 82
S2.5 Stability analysis of the bump in the ring attractor network . . . 83
S2.6 Values of the synaptic weights $w_{EE}^{(ij)}$ in the simulation of Fig. 2.4 . . . 84
S2.7 Simulation of the ring attractor network with flashing input (details in Methods(2.5.9)) . . . 85

S2.8 Simulation of the ring attractor network with flashing input (details in Methods(2.5.9)) . . . 86
S2.9 Simulation of the ring attractor network with flashing input (details in Methods(2.5.9)) . . . 87
S2.10 Simulation of ring attractor combined with sleep homeostasis model using an exponentially decaying plasticity rule during sleep . . . 88

3.1 Long-term imaging preparation . . . 93
3.2 Microrobotic arm for dissection assistance . . . 95
3.3 Optical setups . . . 96
3.4 Imaging and behavior experiment for fly 1 . . . 99
3.5 Statistical analysis of experiments . . . 101
S3.1 Motorization of micromanipulator . . . 104
S3.2 Different views of holder for microscope cover slide with glued fly . . . 109
S3.3 Schematic of setup control . . . 111
S3.4 Analysis of imaging data . . . 116
S3.5 Imaging and behavior experiment for fly 2 . . . 119
S3.6 Imaging and behavior experiment for fly 3, first part . . . 120
S3.7 Imaging and behavior experiment for fly 3, second part . . . 121
S3.8 Imaging and behavior experiment for fly 4 . . . 122
S3.9 PVA-VR correlation and bump drift in fly 3 . . . 123

4.1 Schematic of the experimental tomography setup . . . 129
4.2 Calibration procedure for a single Bessel beam . . . 130
4.3 . . . 131
4.3 Directional vector fields of each Bessel beam . . . 132
4.4 Tomographic reconstruction of $1\mu m$ diameter beads . . . 133
4.5 U-net architecture and simulated data . . . 134
4.6 Tomography reconstruction on pollen grain sample . . . 135
4.7 Simulated reconstruction error of 3D tomography depends on number of projections . . . 140
S4.1.1 2D normalized distribution of the elevation and azimuth angles for each Bessel beam . . . 143
S4.1.2 Pictures of the setup . . . 144
4.2.1 Approach and setup for motion estimation and correction . . . 148
4.2.2 Motion correction in a simulated single ROI . . . 152
4.2.3 Motion correction in a simulated ring attractor . . . 153
4.2.4 Axial motion estimation and correction in GFP labeled neurons . . . 154

4.2.5 Axial motion estimation and correction in GFP labeled neurons at different laser powers . . . 155
4.2.6 Motion estimation and correction in wedge neurons labeled with jGCaMP8f during controlled axial motion . . . 156
4.2.7 Motion estimation and correction in wedge neurons labeled with jGCaMP8f . 157
S4.2.1 Example of two different ROI functions . . . 175
S4.2.2 Distributions of fluorescence changes for ROI 1 in the experiment shown in Fig. 4.2.4 . . . 176
S4.2.3 Simulation of a single moving voxel stacks which have a flat axial profile . . . 177
S4.2.4 Simulation of a single moving voxel for a configuration with four temporally mulitplexed beams . . . 178

5.1 Sleep and feeding behavior in freely moving flies and long-term calcium imaging in ensheathing glia . . . 185
5.2 . . . 186
5.2 Calcium dynamics in ensheathing glia increases due to effortful behavior and decreases during rest . . . 187
5.3 . . . 190
5.3 Glia activity due to sleep deprivation . . . 191
5.4 . . . 192
5.4 Glia glutamate dynamics and two-state model for calcium dynamics . . . 193
5.5 . . . 196
5.5 Calcium dynamics in sleep-related neurons and comparison with ensheathing glia . . . 197
5.6 . . . 198
5.6 Feeding-related modulation in dFB neurons. **a** Long-term imaging in dFB neurons . . . 199
S5.1 Behavioral activity of freely moving flies . . . 222
S5.2 Four different recordings in ensheathing glia where flies are fed every 26 minutes 223
S5.3 Three different long-term imaging recordings in ensheathing glia where flies are fed every 16 minutes . . . 224
S5.4 Five different recordings in ensheathing glia where flies are fed every 4 hours 225
S5.5 Calcium dynamics from ensheathing glia in the LAL . . . 226
S5.6 Normalized fluorescence traces during active and rest epochs for 5 flies . . . 227
S5.7 Trials where the ball was blocked during recordings in glia . . . 228
S5.8 Trials where the ball was blocked after feeding while activity in glia was recorded 229
S5.9 Experiments for arousal threshold probing during imaging . . . 230
S5.10 Glia activity during mechanical sleep deprivation and food deprivation . . . 231
S5.11 Four different recordings using glutamate sensor expressed in ensheathing glia 232

S5.12 Normalized fluorescence traces recorded with glutamate sensor during active and rest epochs for 4 flies . . . 233
S5.13 Fitting glia activity with homeostat 2-state model . . . 234
S5.14 Stop time distributions during imaging experiments . . . 235
S5.15 Fitting glia activity with the 3-state homeostat model, where sleep defined as immobility epochs longer than 5 minutes . . . 236
S5.16 Fitting glia activity with the 3-state homeostat model, where sleep defined after 5 minutes of immobility . . . 237
S5.17 Fitting calcium activity with 7 behavioral states (seven-state homeostat model) 238
S5.18 Significance levels for behaviors in 7-state homeostat model . . . 239
S5.19 Correlation of ensheathing glia activity and fly velocity between trials . . . 239
S5.20 Classification of the behavior of the fly on the ball during long-term imaging 240
S5.21 Regions of interests (ROIs) for recordings of R5 and dFB neurons . . . 241
S5.22 Four different long-term imaging recordings of calcium activity in R5 neurons labeled by 58H05-GAL4 . . . 242
S5.23 Normalized fluorescence traces during active and rest epochs for four flies in R5 neurons (labeled by 58H05-GAL4) . . . 243
S5.24 Fitting calcium activity from R5 neurons (labeled by 58H05-GAL4) with the 2-state homeostat model . . . 244
S5.25 Four different recordings of calcium activity in R5 neurons labeled by 88F06-GAL4 . . . 245
S5.26 Four more recordings of calcium activity in R5 neurons labeled by 88F06-GAL4 246
S5.27 Normalized fluorescence traces during active and rest epochs for eight flies in R5 neurons (labeled by 88F06-GAL4) . . . 247
S5.28 Fitting calcium activity of R5 neurons (labeled by 88F06-GAL4) with 2-state homeostat model . . . 248
S5.29 Four more recordings and fits of 2-state homeostat model with calcium activity of R5 neurons (labeled by 88F06-GAL4) . . . 249
S5.30 Four different recordings of calcium activity in dFB neurons labeled by 23E10-GAL4 . . . 250
S5.31 Three recordings of calcium activity in R5 neurons labeled by 23E10-GAL4 . 251
S5.32 Normalized fluorescence traces during active and rest epochs for seven flies in dFB neurons (labeled by 23E10-GAL4) . . . 252
S5.33 Normalized fluorescence traces during hungry and fed epochs for seven flies in dFB neurons (labeled by 23E10-GAL4) . . . 253
S5.34 Trials where the ball was blocked after feeding while activity in dFB neurons was recorded . . . 254
S5.35 Trials where air supply of the ball was intermittently interrupted to promote walking after feeding . . . 255

S5.36 Fitting calcium activity of dFB neurons (labeled by 23E10-GAL4) with 2-state homeostat model . . . 256
S5.37 Four more experiments and fits of the 2-state homeostat model with calcium activity of dFB neurons (labeled by 23E10-GAL4) . . . 257
S5.38 Fitting calcium activity of dFB neurons (labeled by 23E10-GAL4) with hunger-walk model . . . 258
S5.39 Another four experiments with dFB neurons and fits of hunger-walk model to calcium activity (labeled by 23E10-GAL4) . . . 259
S5.40 Slope of linear fit between active and rest epochs in glia and neurons . . . 260

6.1 Mechanical VR . . . 272
6.2 Control of the mechanical VR . . . 273
6.3 Ball tracking, conditioning IR laser, and arena . . . 274
6.4 Overview of hardware and software components of the mechanical VR . . . 275
6.5 Difference in walking direction during either only rotation control (R) or rotation together with translation (R + T) . . . 277
6.6 Place learning experiment with a single bright stripe . . . 278
6.7 Training performance . . . 279
6.8 Fly behavior during the exploring phase and during the testing phase . . . 280
S6.1.1 Isolation of the mechanical VR with respect to the optical table . . . 282
S6.1.2 Comparison between green and blue stripes during rotation and translation control . . . 283
S6.1.3 Difference in walking direction during rotation and translation (R+T) control before and after learning . . . 283
S6.1.4 Trajectories of flies 1 to 8 across all trials during learning . . . 284
S6.1.5 Trajectories of flies 9 to 16 across all trials during learning . . . 285
S6.1.6 Performance of each fly during the training phase . . . 286
6.2.1 . . . 290
6.2.1 PFR neurons and experimental setup . . . 291
6.2.2 . . . 292
6.2.2 Learning assay and performance of flies during learning . . . 293
6.2.3 Activity of PFR neurons . . . 294
6.2.4 . . . 295
6.2.4 Dimensionality reduction for analysis of PFR neuron activity . . . 296
6.2.5 Normalized distributions of the PFR phase during walk and rest . . . 297
6.2.6 . . . 298
6.2.6 Velocity analysis for the phase of PFR neurons . . . 299
6.2.7 PFR displacement during rest and walking, and during sleep . . . 300
S6.2.1 Learning during imaging for fly 1 . . . 309

S6.2.2 Learning during imaging for fly 2 310
S6.2.3 Learning during imaging for fly 3 310
S6.2.4 Learning during imaging for fly 4 311
S6.2.5 Learning during imaging for fly 5 311
S6.2.6 Learning during imaging for fly 6 312
S6.2.7 Learning during imaging for fly 7 312
S6.2.8 Learning during imaging for fly 8 313
S6.2.9 Learning during imaging for fly 9 313
S6.2.10 Dimensionality reduction analysis for PFR neurons during rest and walking for flies 2-5 314
S6.2.11 Dimensionality reduction analysis for PFR neurons during rest and walking for flies 5-9 315

List of Tables

1.1 List of publications that this thesis is based on, in the order of their appearance. 2

2.1 Model hypothesis and predictions 59
S2.1 Parameter values used in the two-population model 78
S2.2 Parameter values used in the ring attractor network. 78

S3.1 Trials, timings and temperatures of the long-term imaging experiments for each recorded fly 108
S3.2 Parameter values used in each experiment for data analysis 112
S3.3 Sample size used for the statistical analysis shown in Fig. 3.5 118

S4.1.1 Variation of elevation and azimuth angle of Bessel beam vector fields 143

S5.1 Percentage of time sleeping per hour for each fly according to the different definitions used in the paper. 210
S5.2 Comparison between 2-state and 7-state models in the EB 217
S5.3 Comparison between the 2-state and 7-state models in the FB 217
S5.4 Comparison between the homeostat model and hunger-walk model for dFB neurons 218
S5.5 Pearson's correlation between the changes in high frequency fluorescence fluctuations (change in $\Delta F/F$) and changes in velocity. 218
S5.6 Pearson correlation and p-values for the relative body size changes and changes in activity of dFB neurons before and after feeding events. 221

Chapter 1

Introduction

The brain is a highly complex organ with extraordinary computational powers. It is responsible for processing sensory information, storing and recalling memories, generating new ideas, or coordinating movements. The brain, which contains neurons and glia that communicate with each other, is self-assembled during development, trained through experience, and maintained through homeostatic processes, yet many of the principles governing these properties are still unknown. It is therefore a goal of neuroscience to reveal how animals and ultimately humans perceive, learn, and remember by understanding the emergent properties of neurons and glia interacting in circuits [1].

One of the processes that is essential for the proper functioning of the human brain is sleep. However, the reasons for why we sleep are still insufficiently understood [2, 3, 4]. Sleep has been observed throughout the animal kingdom, but with differences between species [5]. The diversity of the observed temporal sleep patterns and rhythms is thought to be a result of evolutionary adaptation to specific environments. This additionally raises the question of whether the function of sleep is conserved across species or has also diverged during evolution [6, 7]. However, a common feature of sleep is reduced vigilance, which at first sight appears to be an evolutionary disadvantage that puts animals at risk from predators or quick environmental changes [7, 8]. The fact that sleep developed and did not disappear throughout evolution suggests that the benefits of sleep outweigh its disadvantages [9].

Sleep produces changes at the molecular and cellular level, as well as at the level of neural circuits. Many of these changes take place at the same time and can additionally depend on the previous waking history [10]. Disentangling these interdependent processes requires overcoming a variety of technical challenges. To meet these challenges scientists have turned, as in other areas of neuroscience, to the different (genetic) model organisms, with their advanced tools for investigating neural circuits. These organisms include rats, mice, zebrafish, and nematodes, as well as the fruit fly, which is the focus of this thesis.

The fruit fly *Drosophila melanogaster* has served as a model organism since the early 1900s and has made important contributions to several fields of biology [11]. With a brain

[27] **Flores-Valle, A., Gonçalves, P.J. and Seelig, J.D.** Integration of sleep homeostasis and navigation in Drosophila. PLoS Computational Biology 17.7 (2021): e1009088.
[28] **Flores-Valle, A., Honnef, R. and Seelig, J.D.** Automated long-term two-photon imaging in head-fixed walking Drosophila. Journal of Neuroscience Methods 368 (2022): 109432.
[29] **Flores-Valle, A. and Seelig, J.D.** Two-photon Bessel beam tomography for fast volume imaging. Optics express 27.9 (2019): 12147-12162.
[30] **Flores-Valle, A. and Seelig, J.D.** Axial motion estimation and correction for simultaneous multi-plane two-photon calcium imaging. Biomedical Optics Express 13.4 (2022): 2035.
[31] **Flores-Valle, A. and Seelig, J.D.** Dynamics of a sleep homeostat observed in glia during behavior. bioRxiv (2022): 2022-07.
[32] **Flores-Valle, A. and Seelig, J.D.** A place learning assay for tethered walking Drosophila. Journal of Neuroscience Methods 378 (2022): 109657.

Table 1.1: List of publications that this thesis is based on, in the order of their appearance.

size of about 200,000 neurons [12], fruit flies are used in neuroscience for investigating the neural basis of behavior [13, 14]. A wide spectrum of genetic tools [15, 16] allows labeling and manipulating neural circuits, and since 2020, the fly connectome [17] provides a map of the connectivity of neurons in a substantial portion of the fly brain.

Since the discovery that fruit flies have a sleep-like state [18, 19], *Drosophila* has become a valuable model organism for sleep research. Sleep in *Drosophila* is impacted by different classes of neurons, as well as different brain areas such as the mushroom bodies (MB) or central complex (CX) [20, 21]. Glia cells such as astrocytes and ensheathing glia are also important for sleep [21, 22].

In recent years, much work has been dedicated to establishing a circuit for sleep control in the central complex [21, 23], a neuropil in the center of the fly brain. The central complex also contains neural circuits for navigation [24, 25, 26]. This brain area therefore provides a unique opportunity to investigate the close interplay between navigation circuits and sleep control circuits in genetically identified cells.

This thesis investigates how sleep is regulated in the central complex and how sleep impacts navigation (and *vice versa*). For this purpose, this thesis introduces novel theoretical models as well as newly developed experimental methods for improved imaging and behavior experiments in flies. The developed techniques are applied for characterizing the dynamics

and function of neurons and glia important for sleep for the first time during behavior. Motivated by the importance of the connection between sleep and memory, a novel learning paradigm for fruit flies is developed. Finally, this paradigm is used together with functional imaging for the characterization of circuits in the head direction system during learning and sleep. The present thesis is based on the list of publications shown in Table 1.1, and additionally contains preliminary experiments and results that are not published at the time of submission (several experiments and results in chapter 5, and section 6.2).

This introductory chapter provides an overview of the current state of research relevant to this thesis with an emphasis on *Drosophila*, including how sleep is characterized and studied in the fruit fly, the neurophysiological changes associated with sleep, the different hypotheses proposed for the function of sleep, and how sleep is regulated. Next, the role of the central complex in sleep regulation and navigation is introduced, followed by the different methods that allow investigating sleep and navigation in fruit flies. Finally, the end of the chapter describes the aims and organization of this thesis.

1.1 Sleep

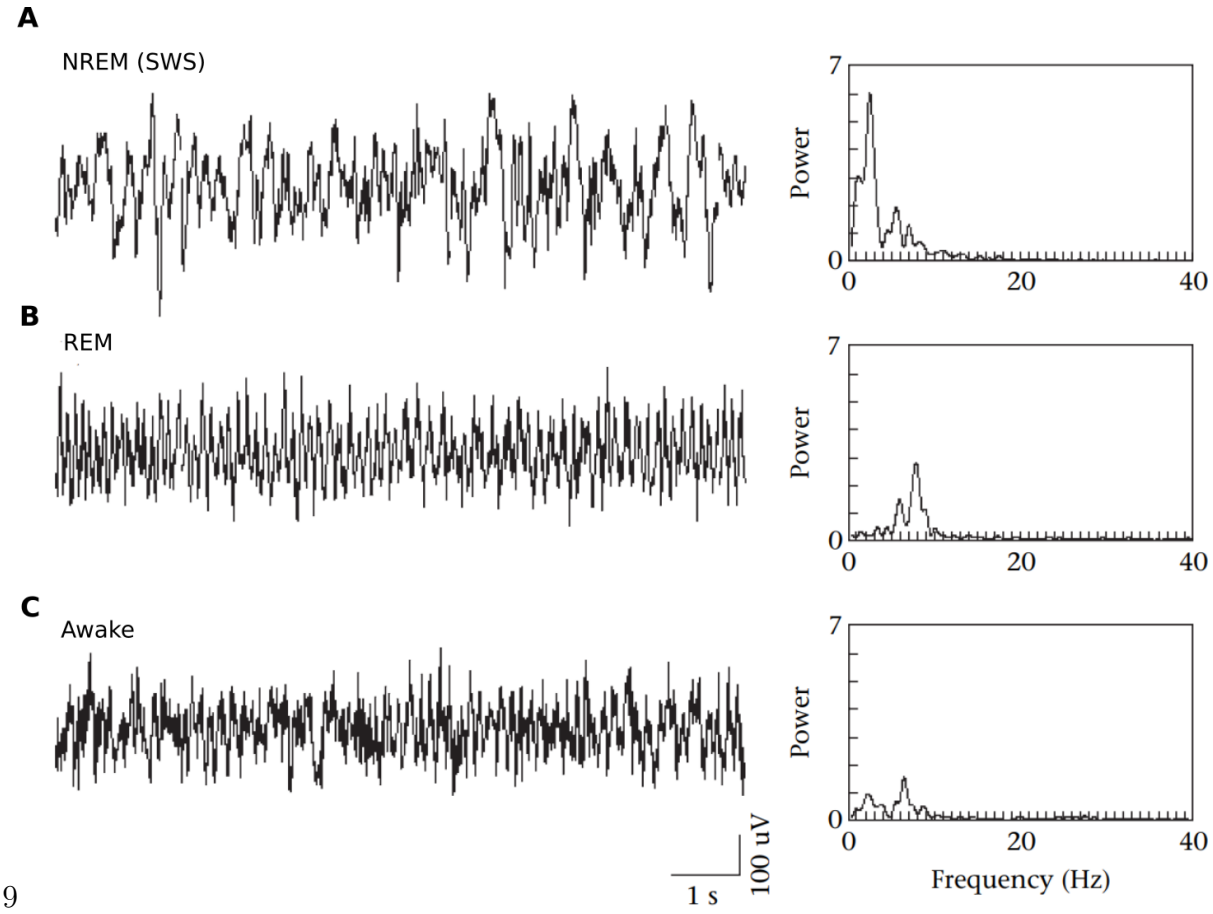
1.1.1 Sleep in humans and mammals

Sleep is an important part of our lives: we spend approximately one-third of our life sleeping, experiencing a loss of consciousness, decreased response to environmental stimuli, and inhibition of voluntary movements [33, 34]. Sleep is involved in many critical biological processes, including waste clearance in the brain[35], metabolic regulation [36], DNA repair [37], immune function [38], endocrine function [39], or development [5, 40].

Sleep in particular impacts brain function [41, 42]. Insufficient sleep impairs perception, attention, concentration, vision, and reaction times, which leads to a decrease in the efficiency of task performance [43, 44, 45, 46, 47]. Lack of sleep further affects memory, learning, decision-making, mood, or motivation [41, 45, 48, 49]. Moreover, abnormal sleep is associated with many neurological and psychiatric disorders [42, 50]. Severe brain disorders that produce an inability to sleep, such as familial or sporadic fatal insomnia, lead to dementia and death [51].

The function of sleep for all these processes remains only partially understood, but sleep is crucial for maintaining the health and function of brain cells [52, 53]. Sleep has not been observed in individual cells [3], but it is assumed to emerge from interacting populations of neurons [54, 55, 56, 57] as well as glia [58, 59]. The combined activity of these interacting cell populations can be measured by electroencephalograms (EEG) [60], and such recordings show that sleep is not just a quiescent state for the brain with inhibited perception but a dynamic state.

Different patterns of neural activity observed during sleep led to the classification of



0.9

Figure 1.1: EEG recordings of brain activity from a mouse during sleep and wakefulness. **A** EEG recording during NREM sleep on the left, and power spectrum of the signal on the right. **B** and **C** Same as A but for the REM phase and during wakefulness. Reprinted from [61] with permission from Elsevier.

different sleep phases [62]. In humans and mammals, sleep is subdivided into two different phases, rapid eye movement (REM) sleep and non-rapid eye movement (NREM) sleep [63]. REM and NREM sleep have different functions and properties: for example NREM sleep is mostly characterized by slow waves (0.5-4 Hz, Fig. 1.1A), while REM sleep contains beta waves (13-30 Hz, Fig. 1.1B) that look similar to activity during wakefulness [64] (Fig. 1.1C). Dreaming is more common during REM sleep [65], while NREM sleep is considered to be the deepest and most restorative sleep phase [63].

1.1.2 Sleep in other animals

Sleep-like states are observed in many other animals, suggesting that from an evolutionary point of view, sleep fulfills a common purpose that benefits animal survival [9]. It is still not known if all animals sleep [6], but sleep has been observed through EEG recordings in mammals [66], some birds [67], some reptiles [68], and some amphibians [69]. Whales, dolphins [70], fur seals [71], or migratory birds [72] have evolved unihemispheric sleep, where one hemisphere sleeps at a time, suggesting that sleep can occur locally in the brain [59, 73].

While in these animals EEG recordings allow identifying sleep from patterns of brain activity that differ from those observed during wakefulness, small animals, such as flies or worms, make EEG recordings challenging or unfeasible. Different criteria that are not based on EEG have therefore been proposed to identify sleep-like states in these animals [74, 75]. These criteria include: quiescence with loss of locomotion, rapid reversibility to a wakeful state, preferred environment or locations for sleep, characteristic postures that are maintained during the sleep episode, increased arousal threshold to stimuli, and a homeostatic regulation of sleep, which monitors the sleep duration and produces sleep rebound after sleep deprivation.

By applying the above criteria, sleep-like states have been identified in fish [76] such as the zebrafish *Danio rerio* [77, 78, 79, 80], in insects [81] such as the fruit fly *Drosophila melanogaster* [18, 19], in the nematode *Caenorhabditis elegans* [82], and in two cnidaria species, the jellyfish *Cassiopea* [83] or the *Hydra* [84].

It is unclear whether sleep in simpler organisms is homologous to mammalian sleep given the differences in neuroanatomy as well as sleep quality, intensity, duration, and temporal patterns [4, 6, 75]. Nevertheless, all animals share a reduction of vigilance and responsiveness to external stimuli during sleep [7, 75]. The study of sleep in simpler organisms also revealed genetic components involved in sleep that are shared across species, such as the epidermal growth factor signaling pathway, involved in growth, healing processes and regulation of sleep [85, 86, 87, 88, 89], or the dopaminergic pathway, which modulates sleep and wakefulness [90, 91, 92]. These examples of sleep-related processes that are conserved across species support the idea of studying sleep in simpler organisms such as flies. At the same these simpler animals offer the advantages of reduced numerical complexity of the nervous system,

genetic tractability, or a known connectome [15, 16, 73, 93].

1.2 Sleep behavior in *Drosophila*

Drosophila has become a widely used model organism for studying sleep [94]. Sleep in flies was first described using video recordings [18] or an ultra-sound monitoring system [19] for detecting fine movements. These experiments resulted in the observation of a preferred location, increased arousal threshold, and a preferred posture for sleep. These studies also led to a widely used definition of sleep as a period of immobility lasting at least 5 minutes, after which flies showed a significant increase in their threshold for arousal resulting from sensory stimulation [18, 19]. While defining sleep as a state of immobility is convenient for behavior classification, due to the absence of any clearly visible signatures of sleep, the reliable distinction between sleep and resting requires additional measurements, such as probing of an arousal threshold [18, 19].

Sleep in flies shares multiple features with sleep in humans: flies for example are also diurnal animals that follow a circadian rhythm, experience sleep rebound after sleep deprivation, and the amount of sleep is decreased and fragmented as flies age [20, 21]. Further, some neurotransmitters and neuromodulators involved in sleep regulation are also shared between mammals and flies, such as dopamine, octopamine (homolog to noradrenaline in mammals), and histamine, which all promote wakefulness, or GABA, which promotes sleep [95, 96, 97]. Serotonin also promotes sleep in flies, but its role in mammalian sleep is more complicated [96, 98]. Additionally, adenosine antagonists such as caffeine decrease sleep in a dose-dependent manner in flies [18, 99, 100], although the mechanism of action seems to be different from that in mammals [99]. Drugs that potentiate $GABA_A$ receptor signaling also share a sleep-promoting effect in both flies and mammals [101]. Molecules involved in immune response and sleep regulation, such as the transcription nuclear factor κB (NF-κB) and cytokines, are also common between mammals and flies [102]. Thus, *Drosophila* has the potential of contributing to an understanding of the many conserved features of sleep with its usual advantages of low cost, genetic tractability, and fast life cycle [94].

1.2.1 Monitoring sleep behavior

Analysis of sleep behavior in *Drosophila* has heavily relied on the *Drosophila* Activity Monitor (DAM) [94, 104], which measures a fly's walking activity by counting the number of times the animal crosses an infrared beam at the center of an elongated tube in which the fly walks [104] (Fig. 1.2A). A fly is assumed to be sleeping when it stops crossing the infrared beam for at least 5 minutes. Although the DAM overestimates sleep [105, 106], for example by assuming that flies are sleeping when in reality they might be awake without crossing the infrared beam (see Fig. 1.2C), it allows efficient screening of flies in search of

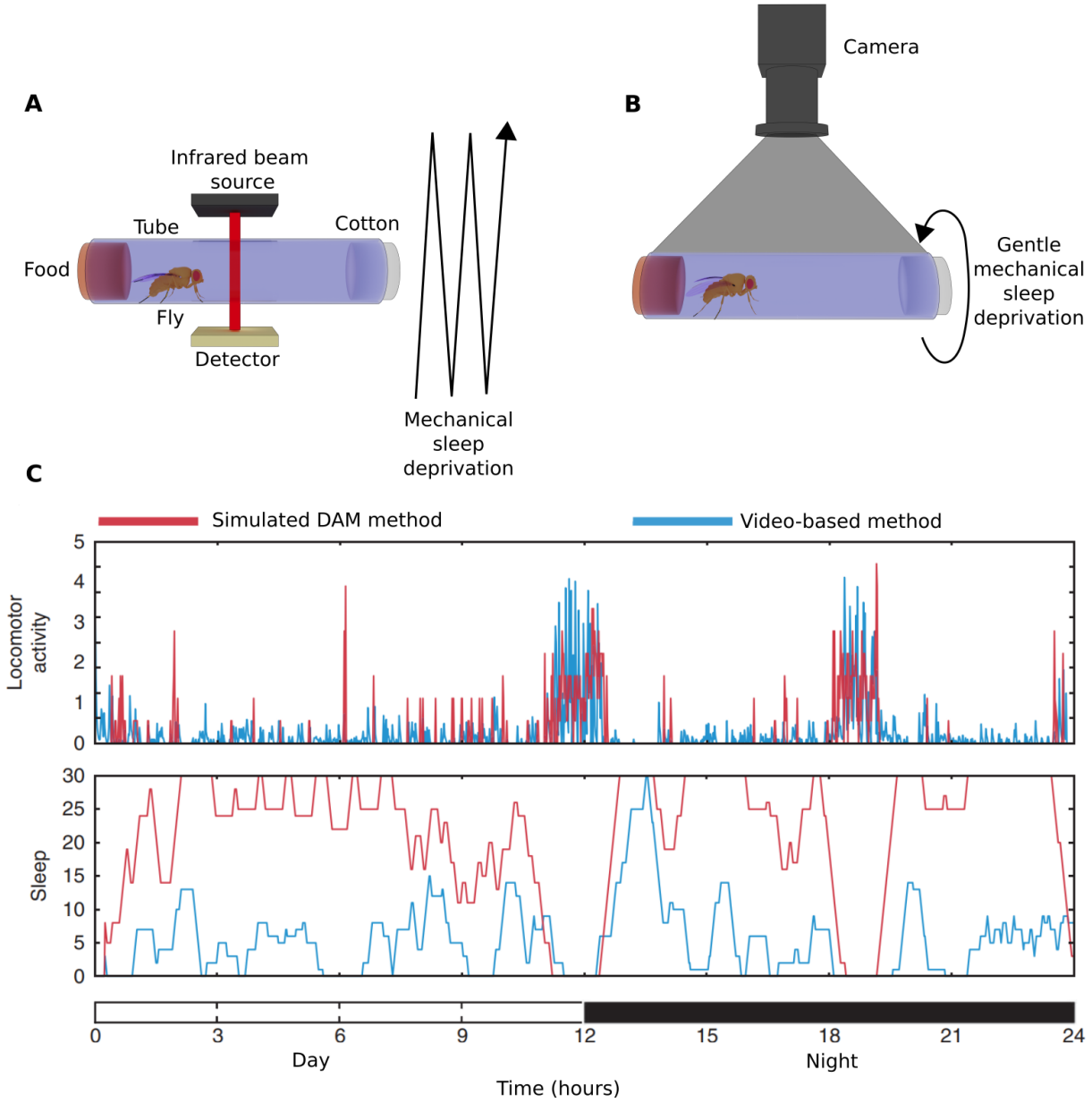


Figure 1.2: DAM and video-based methods for monitoring sleep. **A** DAM method, where the locomotor activity of a fly confined in a tube with food is measured when the fly crosses an infrared beam in the middle of the tube. Traditional mechanical sleep deprivation methods shake the tube. **B** Video-based method where the position of the fly in the tube is tracked using a camera and computer vision algorithms. Newer and more gently mechanical sleep deprivation methods rotate the tube. **C** Comparison between the DAM and video-based methods. The first row shows the locomotor activity of a single fly recorded with a camera over 24 hours. The DAM system here is simulated for comparison by defining a virtual line in the middle of the tube and measuring the locomotor activity only when the fly crosses the virtual line (red line). The video-based method shows the distance that the fly walks in the tube (blue line). The second row shows the amount of sleep of the fly in bins of 30 minutes from the obtained locomotor activity using each method. Panel C is reproduced from [103] with permission from Springer Nature

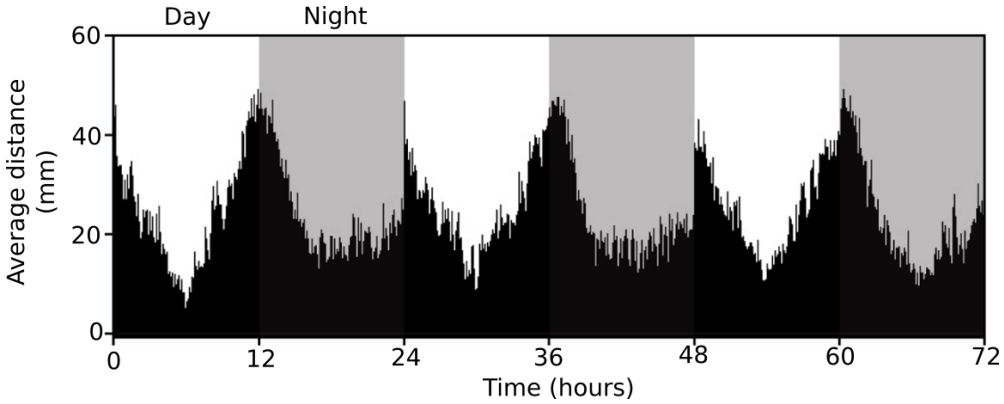


Figure 1.3: Circadian behavior of flies under laboratory conditions monitored using a video-based method. The y-axis shows the average distance of 29 flies (binned in one minute bins) over 72 hours with a 12-hour light/dark cycle and constant temperature. From [106] used under Creative Commons CC-BY license.

sleep phenotypes [20]. Different populations of neurons involved in the regulation of sleep have been identified with this method, for example by thermogenetically manipulating their activity (see section 1.7.1) and observing concomitant or subsequent changes in the amount of sleep [107]. The DAM was also improved by using multiple infrared beams for increased resolution [108]. Nevertheless, DAM methods are increasingly being replaced with video recordings, thanks to the easy availability of systems for recording and processing large amounts of video data which can be used for tracking the position of flies at much higher spatial and temporal resolution [103, 105, 106, 108, 109] (Fig. 1.2B).

1.2.2 Circadian behavior

Under laboratory conditions, which typically include a 12-hour light/dark cycle for simulating day and night, the locomotor activity of isolated flies can be observed with the DAM or camera-based tracking systems over multiple days [94]. Under these conditions, flies display a characteristic activity pattern with a 24-hour period, also known as circadian rhythm, where higher locomotor activity precedes light transitions, *i.e.* at dusk and dawn, also known as morning and evening activity peaks (Fig. 1.3). Most sleep occurs in the middle of the day and during the night [18, 19, 94]. The circadian rhythm in *Drosophila* is highly sensitive to environmental stimuli such as temperature, which strongly affects sleep in flies as opposed to mammals, since insects have only limited body temperature regulation [21, 94, 110].

Internal states such as sexual arousal, aggression, mating status, or hunger also affect circadian rhythms and sleep; for example starvation suppresses sleep while satiation promotes sleep [21, 94, 111, 112].

1.2.3 Behavior under sleep deprivation

In flies, similar to mammals, sleep deprivation is widely used to study how the lack of sleep affects the brain [4, 21]. Sleep deprivation in flies can be produced by starvation [113, 114], sexual arousal [115, 116], or caffeine intake [19, 100, 100]. However, sleep deprivation is most typically achieved by mechanical stimulation in the DAM, where different protocols are used for shaking the tubes containing individual flies (see Fig. 1.2A), for example for 12 hours during the night [18, 19, 117, 118, 119, 120, 121, 122, 123, 124, 125, 126, 127]. This method forces flies to move inside the monitoring tubes, leading to longer sleep time and increased arousal threshold after sleep deprivation compared to unperturbed flies, an effect which is known as sleep rebound [18, 19, 119].

Mechanical sleep deprivation has allowed identifying neural and glial populations involved in sleep regulation [123, 125, 128, 129], brain-wide changes in synaptic connectivity that correlate with sleep loss [120], and learning deficits resulting from lack of sleep [130, 131]. However, the effects observed following mechanical sleep deprivation might not only be a consequence of sleep loss, but also due to other physiological effects such as stress [132, 133]. In fact, prolonged mechanical sleep deprivation leads to premature death in flies [118], which is not observed when flies are sleep deprived using another method (see below) [134].

Compared with mechanical sleep deprivation, starvation or sexual arousal-induced sleep deprivation produces little or no noticeable sleep rebound in the DAM [113, 114, 115, 116]. This suggests that either these forms of sleep deprivation abolish sleep homeostasis [21] or that other factors such as stress significantly contribute to the observed sleep rebound under mechanical sleep deprivation. Additionally, given the limited time-resolution of the DAM system, video-based methods could lead to a reassessment of some of these results.

Methods for more gentle mechanical sleep deprivation have been developed, where individual flies are prevented from sleeping by slowly rotating the tubes in which they walk, as shown in Fig. 1.2B, depending on how much time they have been immobile [109, 134]. This method, which instead of the DAM additionally uses camera-based tracking to better characterize sleep [109], finds little sleep rebound, only in the order of a few minutes compared to hours of sleep rebound observed using traditional mechanical sleep deprivation methods [134, 135]. Taken together, this suggests that the method used for sleep deprivation has to be carefully considered, and possible confounds between sleep loss and other physiological effects resulting from the respective methods, such as stress, need to be taken into account [133].

1.2.4 Visual and spatial learning

Drosophila has been successfully used as a model for studying how memories are created, encoded, and retrieved [136, 137, 138] and how sleep affects learning and memory consoli-

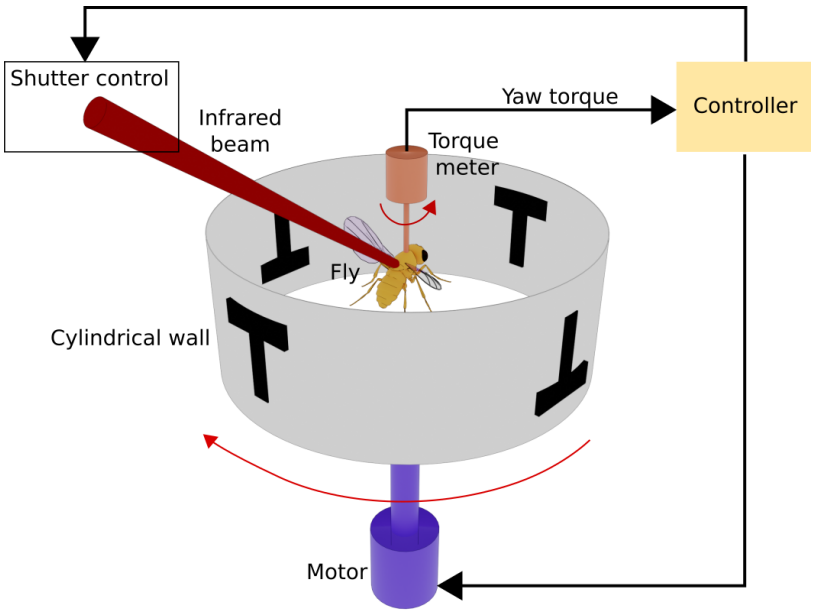


Figure 1.4: Flight simulator setup for visual learning. A torque meter measures yaw torque of a tethered flying fly. A controller then controls a motor for rotating a cylindrical wall with visual patterns around the fly in closed loop. Additionally, the controller controls a shutter of an infrared beam focused on the fly, which acts as an aversive stimulus. Reproduced from [148] with permission from Springer Nature.

dation [20, 131, 139]. Learning in *Drosophila* can be achieved through operant conditioning [140], where an animal engages in a behavior that is either rewarded or punished during a training phase. After training, a test phase that does not contain reward or punishment is used to evaluate memory of the conditioned behavior [140]. Learning can be accomplished using different modalities, including olfaction [141], [136] courtship [142], vision, or spatial perception [143]. Visual and spatial learning are important for navigation, and neural populations involved in these types of learning have been identified in the central complex [144, 145, 146], anatomically close to neurons that regulate sleep [21, 147]. For this reason, this section focuses only on visual and spatial learning. For a review on olfactory or courtship learning see [141, 142].

Visual learning experiments in the early 1990s made use of the flight simulator, shown in Fig. 1.4, where the flight maneuvers of a tethered flying fly were measured with a torque sensor to control the rotation of a surrounding cylindrical arena in closed loop [149]. In this experiment, the arena contained two different visual patterns. During training, one of the patterns was paired with an aversive stimulus such as heat [148]. Flies learned to avoid facing the aversively conditioned visual pattern during the training phase as well as during the subsequent test phase (in the absence of the aversive stimulus), indicating that a memory

had been formed [148]. This paradigm allowed probing how flies remember visual patterns by varying the two visual features with respect to size, shape, or color [148, 150, 151]. Flies learned such features independent of the elevation of the visual cues in the cylindrical arena, or the distance between them, and thus in a translationally invariant manner [152].

More recent experiments used digital virtual reality setups, where a screen in front of the fly displays visual patterns that move depending on tethered flying [153, 154] or walking [155, 156, 157] activity. Using such virtual reality setups, visual learning in flying flies similar to the one mentioned above can be observed [158]. Another type of learning with tethered flies flying in a virtual reality environment, which also combined learning with calcium imaging, is delay and trace conditioning [159]. During training, flies were presented with a visual pattern for a fixed duration, which was paired with an aversive stimulus right before the pattern disappeared (delay), or at a certain time interval after the disappearance (trace). During the test phase after delay or trace conditioning, flies avoided facing the previously conditioned visual pattern in closed-loop [159]. Finally, walking flies could learn the geometry of visual objects encountered in a three-dimensional virtual reality using optogenetically induces aversive or rewarding stimuli [160].

Learning with spatial or visual components has been studied in freely moving flies using a number of different paradigms. In Aversive Phototaxic Suppression (APS), flies are placed in a T-maze that contains a bright and dark channel; flies are then trained to avoid the bright side of the maze by pairing it with an aversive stimulus [161]. In another paradigm, flies learn to remember an invisible location in a rectangular arena after training through stimulation of reward-mediating dopaminergic neurons, without requiring vision, likely through path integration [162]. In the heat-box assay flies learn to avoid one side of a small rectangular chamber paired with heat as an aversive stimulus, only applied during the training phase [163]. Finally, in visual place learning flies are trained to learn the position of a cool spot in an otherwise hot circular arena [146, 164], similar to the Morris Water Maze assay for rats [165]. In this experiment, flies learn to locate the (invisible) cool spot from visual cues around the arena, and to optimize both time and distance for reaching the cool spot [146, 164]. The implementation of this assay is described in more detail in section 1.7.4 and Fig. 1.12.

1.2.5 Impact of sleep on learning and memory

The impact of sleep on learning in flies can be studied using sleep deprivation by comparing the performance of sleep-deprived flies to that of unperturbed control flies [131]. Mechanical sleep deprivation impairs spatial learning in the Aversive Phototaxic Suppression (APS) paradigm [121], visual place learning [166], as well as in olfactory [121, 167, 168, 169] and courtship learning [170]. Artificial activation of wake-promoting neurons before an olfactory learning task also impaired performance [171]. However, spatial learning through APS was

not impaired after sleep deprivation by starvation [114]. In another paradigm for spatial learning, called Y-track, where a fly walks in a Y-shaped maze and is rewarded with sucrose if it chooses the same turning direction repeatedly, learning is only achieved in flies that rest between trials. This suggests that resting periods, which might be short sleep episodes, support learning and memory consolidation [172].

Deficits in learning and memory have also been associated with abnormal sleep patterns in mutant flies. For example, short-sleeping *hyperkinetic* and *crossveinless-c* mutants showed impairments in spatial learning in the heat-box paradigm [173] and in olfactory learning [169], respectively. Other short-sleeping phenotypes resulting from different manipulations of the expression of immune factors showed learning deficits in the APS paradigm [174], as did insomnia-like flies that were selected over 60 generations from short-sleeping phenotypes [175].

Another way of studying the impact of sleep on memory consolidation is by artificially inducing sleep after learning in flies, for example by activating sleep-promoting neurons in the central complex [122, 176, 177] or by feeding flies with the GABA-A agonist gaboxadol (Gab) [122, 166, 178]. Activation of sleep-promoting neurons induced long-term courtship memory after courtship behavior [176, 177]. Induction of sleep was also applied in classic learning mutant flies that show cognitive and memory deficits, such as the *rutabaga (rut)* or *dunce (dnc)* mutants. Spatial memory acquired in either the APS, heat-box, or visual place learning paradigm, as well as courtship memory, was restored in both *rut* and *dnc* mutants after sleep was induced through Gab feeding [122, 166, 178] or through the activation of sleep-promoting neurons [122].

The effects of sleep on learning can also be age dependent. Impairments in APS and courtship learning behaviors were observed for up to 6 days when mechanical sleep deprivation was applied during the first day of the adult life of flies, suggesting an impact on development [179]. Flies also showed a decrease in performance in the visual place learning paradigm as they aged, which could be corrected by inducing sleep through Gab feeding [166]. Moreover, inducing sleep through Gab feeding in *Drosophila* models of Alzheimer's disease restored learning in APS as well as courtship learning [180]. Taken together, these experiments suggest that sleep plays an important role in learning and memory formation in *Drosophila* [130, 131, 181].

1.3 The brain of *Drosophila* during sleep

Sleep across species is linked to structural and dynamic changes in the brain [182, 183, 184]. This section reviews signatures of sleep in the *Drosophila* brain at the level of populations of neurons and glia, at the synaptic level, as well as at the molecular level, and draws comparisons with similar processes in mammals.

1.3.1 Neural circuit dynamics

The mammalian brain shows different neural activity patterns across different phases of sleep. Some of these patterns can be measured with EEG (Fig. 1.1) and include fast oscillations during REM sleep, and a combination of slow oscillations and events such as spindles and sharp wave-ripples during NREM sleep [187, 188].

In *Drosophila*, local field potentials (LFPs) have been recorded during sleep by inserting two electrodes into the brain [189]. These experiments showed a decrease in LFP amplitude during sleep, which was linked to a general decrease of neural activity and increased arousal threshold during sleep [189, 190, 191, 192, 193]. Different phases of sleep, such as REM or NREM sleep, have not been observed in flies using neural recordings [20]. However, behavioral measurements show a dynamic change of the arousal threshold over time spent sleeping, suggesting that different sleep phases exist also in flies [20, 190]. It was also proposed that during natural sleep brain activity in flies transitions from an active, wake-like state, reminiscent of REM sleep in mammals, to an inactive state, named deep sleep, where waste clearance is increased, reminiscent of NREM sleep [194, 195].

In mammals, the amplitude of slow wave activity (SWA), which comprises EEG oscillations between 0.5 and 4.5 Hz, is an indicator of sleep homeostasis during NREM sleep. SWA is highest at the beginning of the sleep episode, decreases throughout the episode, and increases with the amount of prior wake time [185, 196, 197], as shown for example in Fig. 1.5A. Experiments on fly brain explants have reported a potentially related effect in a population of ring neurons in the ellipsoid body of the central complex, R5 neurons. These neurons show a lower spike rate in the morning than in the evening, and the spike rate increases after mechanical sleep deprivation (Fig. 1.5B). Additionally, R5 neurons display slow oscillations of the membrane potential (0.5-4 Hz), and the amplitude of these oscillations increases after flies are mechanically sleep deprived for several hours [186] (Fig. 1.5C, see section 1.6.1 for more details).

In mammals, the reactivation during sleep or rest of spatio-temporal patterns of neural activity observed during active behavior, and in particular learning, is known as replay [10, 198, 199, 200, 201]. In flies, replay during sleep has not been directly observed. However, dopaminergic neurons that participate in courtship learning are also active during sleep and are required for memory consolidation, suggesting the neural reactivation of previous experiences [177].

1.3.2 Synaptic changes

Memory consolidation during sleep involves reorganization of neural connectivity [202, 203]. In mammals, synaptic plasticity has been observed during sleep across the brain, including synaptic downscaling and potentiation [202, 204, 204, 205].

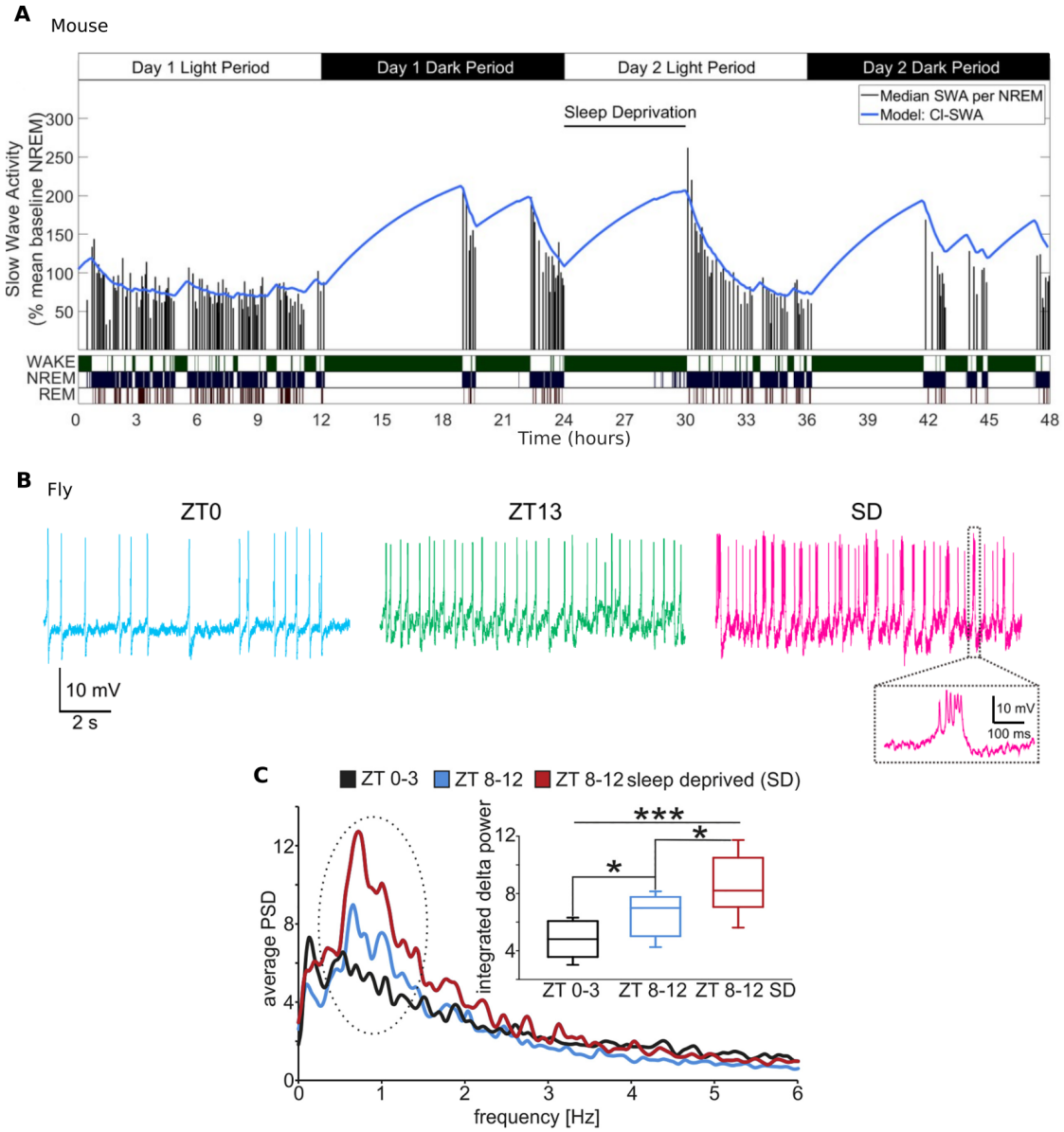


Figure 1.5: SWA activity in mammals and flies. **A** Average EEG spectral power of SWA (0.5-4 Hz) measured in the primary motor cortex of a mouse over 48 hours (day and night indicated in the first row). Each vertical black bar represents the median SWA spectral power over an entire NREM episode (wake, REM, and NREM episodes shown in the bottom row), while the blue line represents a fitted homeostatic process (see section 1.5 and Fig. 1.9). From [185] used under Creative Commons CC-BY license. **B** Electrophysiology recordings from R5 neurons in explant fly brains right after dissection, at the beginning of the day (left, zeitgeber time or ZT 0), at the beginning of the night (center, ZT 13) or after 12 hours of mechanical sleep deprivation in the DAM system (right, SD). Reprinted from [123] with permission from Elsevier. **C** Average of the power spectrum density (PSD) from several R5 neurons, recorded through voltage imaging in explant brains after dissection, at the beginning of the day, end of the day, and after 12 hours of sleep deprivation (ZT 0-3 black line, ZT 8-12 blue line, and SD red line, respectively). From [186] used under Creative Commons CC-BY license.

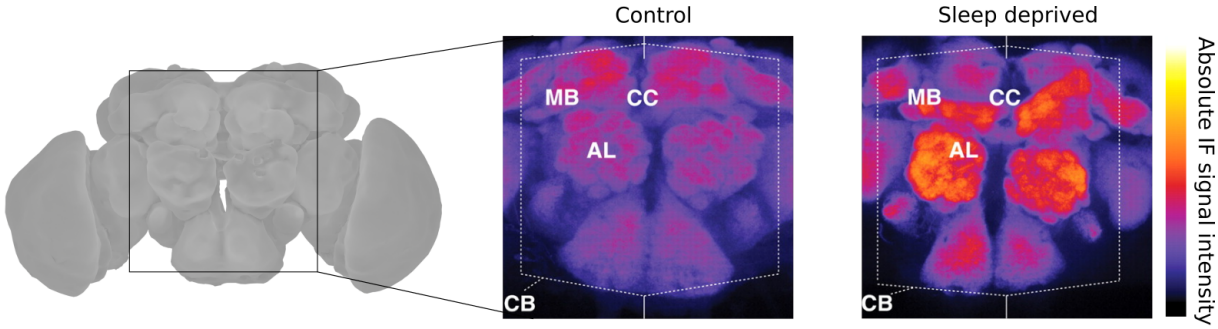


Figure 1.6: Synaptic changes in the fly brain after sleep deprivation. The fly brain is shown on the left. The center and right panel show a zoom-in on the central cerebrum (CB, which does not include the optic lobes), where color represents BRP immunofluorescence (IF) measured in explant brains from unperturbed flies and sleep deprived flies, respectively. Different brain regions are highlighted, including the mushroom bodies (MB), the central complex (CC) and the antennal lobes (AL). Center and right panels are from [120]/ Reprinted with permission from AAAS.

In *Drosophila*, protein levels that are involved in synaptic plasticity, as well as the density or size of synaptic structures change depending on sleep or sleep deprivation [111, 120, 123, 127, 206, 207]. Changes in bruchpilot protein (BPR) levels promote changes in the size and number of presynaptic active zones [207, 208], which are associated with synaptic plasticity [209, 210]. Mechanical sleep deprivation produces increased BPR levels across the fly brain, which was associated with synaptic potentiation, compared to BPR levels in rested flies [120] (Fig. 1.6). Synaptic plasticity has also been linked to sleep homeostasis and sleep need, as increased BRP levels promote sleep and modulate the arousal threshold [207]. In the mushroom bodies (MB), a pair of neuropils known for their role in olfactory learning and memory [211], mechanical sleep deprivation increases both terminal axon size [206] as well as BPR levels [127]. In the central complex, R5 ring neurons increase BPR levels after mechanical sleep deprivation [123]. Olfactory learning impairment was linked to increased BRP levels in the same neurons [207].

1.3.3 Accumulation and clearance of sleep substances

In mammals, different molecules that accumulate in the brain during wakefulness and are depleted during sleep, are considered indicators of sleep homeostasis [53, 213, 214]. For example adenosine, which is linked to energy metabolism in the brain, and in mammals acts as a neuromodulator, accumulates in the extracellular space of most brain areas during wakefulness [8, 215] (Fig. 1.7). Adenosine also plays a role in the regulation of sleep, and for example caffeine promotes wakefulness by antagonizing adenosine receptors [214, 215].

The role of adenosine in flies is less clear since accumulation of extracellular adenosine in the fly brain has not been reported, although recent evidence suggests that for example fly

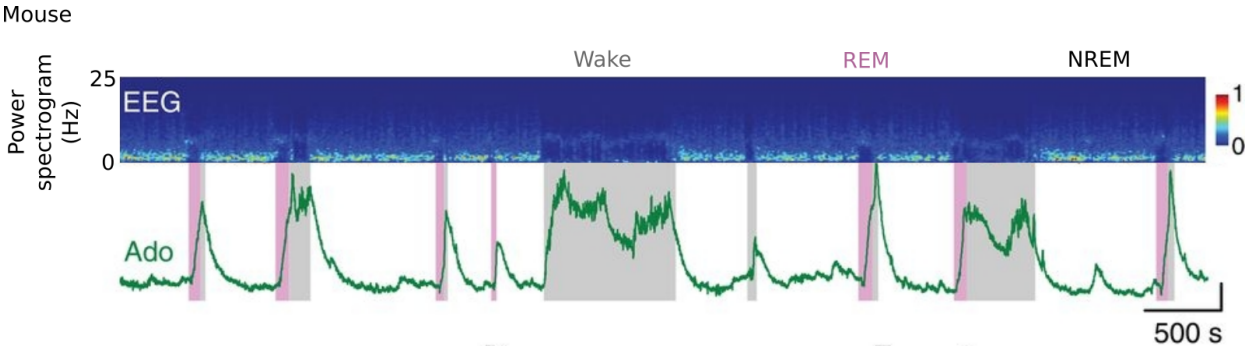


Figure 1.7: Extraceullar adenosine concentration in the mouse basal forebrain. Top row: power spectrogram from EEG recordings to classify wake, REM sleep, and NREM sleep episodes. Bottom row: fluorescence intensity recorded from a genetically encoded sensor for extracellular adenosine, where the vertical scale indicates z-score. From [212] / Reprinted with permission from AAAS.

glia, which are important for sleep (see section 1.3.4), release adenosine [216]. Caffeine was shown to promote wakefulness also in flies [18, 99, 100]. However, mutants lacking the only adenosine receptor known in flies (dAdoR) not only showed similar sleep patterns to normal flies, but also responded normally to caffeine, suggesting that, different from mammals, caffeine promotes wakefulness without antagonizing adenosine receptors [99].

The glymphatic system in the mammalian brain plays a crucial role in maintaining brain health by clearing metabolic waste and toxic biomolecules [217]. This system becomes particularly active during sleep by increasing the interstitial space of the brain by 60 %. This leads to an increase of cerebrospinal fluid flow around the brain and enhances the transport and removal of waste products [217, 218, 219]. Increased waste clearance during sleep was also investigated in *Drosophila*: the flux of xenobiotics across the *Drosophila* blood-brain barrier (BBB, see Fig. 1.8A and B, and the section below) depends on the time of day [220] and trafficking across the BBB increased during sleep [221]. Additionally, periodic extension and retraction of the proboscis during sleep was proposed to facilitate waste clearance [195].

1.3.4 Glia

Not only neurons but also glial cells are important for the function and regulation of sleep [22, 227, 228, 229]. The most abundant type of glia in the mammalian brain are astrocytes, which protect and metabolically support neurons as well as regulate plasticity and synaptic transmission [229, 230]. Moreover, endfeet of astrocytes are part of the mammalian BBB, enclosing the cerebral vasculature, and regulating the flow of solutes including interstitial waste products along the glymphatic system [218, 231, 232].

Astrocytes play an important role in wake and sleep regulation [229, 233, 234], for example by releasing different sleep promoting substances [229, 234]. Some evidence suggests that astrocytes regulate sleep through adenosine release [22, 229, 234], but astrocytes can also

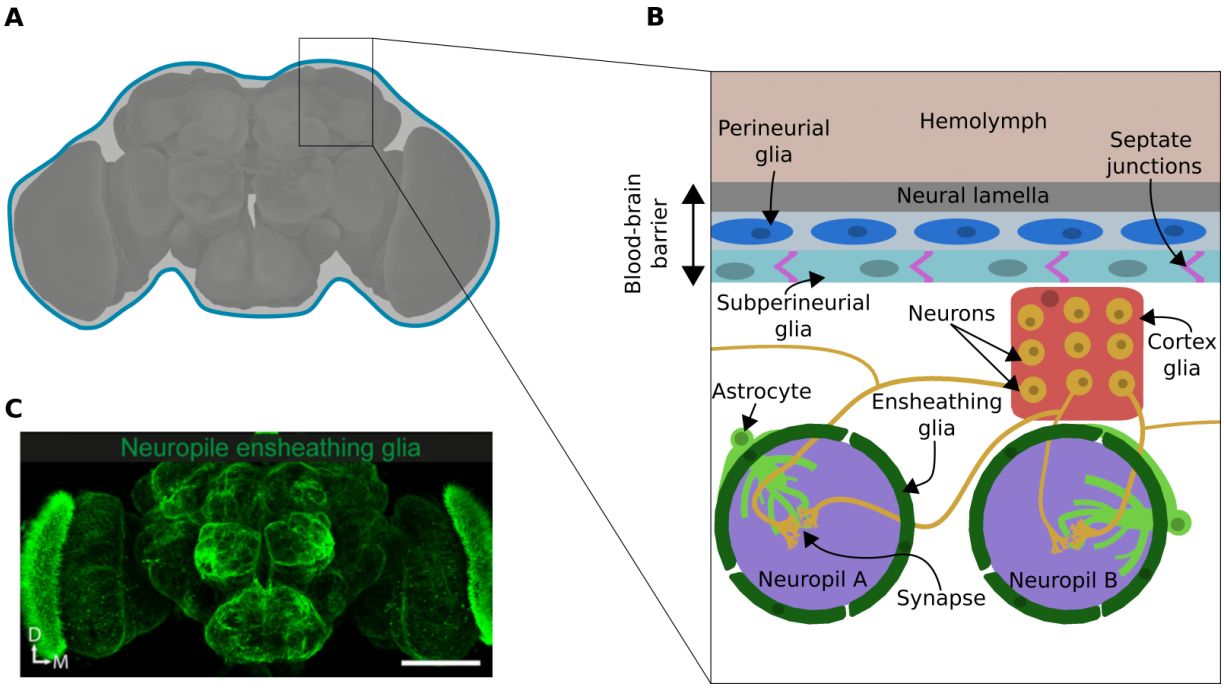


Figure 1.8: Types of glia cells in *Drosophila*. **A** Fly brain surrounded by the blood-brain barrier (blue line). **B** Schematic zoom-in of the blood-brain barrier that separates the hemolymph from the brain, composed of an extracellular matrix called neural lamella as well as perineurial and subperineurial glia. Subperineurial glia create a barrier that blocks paracellular diffusion through septate junctions [222, 223]. Inside the brain, cortex glia encapsulate the neural cell bodies [224], which send projections to different compartments, called neuropils, for synapse formation. Ensheathing glia wrap around the different neuropils to create a diffusion barrier [225], while astrocytes invade the neuropils to support synaptic transmission among other functions [226]. **C** Ensheathing glia in the *Drosophila* brain, where the scale bar indicates 100 μm. Panel C is from [224] used under Creative Commons CC-BY license.

regulate sleep independently of adenosine [235]. Intracellular calcium activity in astrocytes changes across sleep and wake states, being lower during sleep and higher during wakefulness [229, 235, 236]. Furthermore, recent evidence shows that astrocytic calcium peaks upon awakening, and was proposed to regulate and maintain slow wave activity (SWA) during sleep [235].

In the fly brain, approximately 10 % of cells are glia [224] and, as in mammals, glia are also involved in sleep regulation [22, 237]. Different types of glia cells in the fly brain have been identified with a role in sleep regulation [22], including astrocytes, ensheathing glia, cortex glia, and (sub-)perineural glia [224, 237, 238]. Fly mutants with different modifications in these glial cell types show abnormal sleep patterns [239, 240, 241, 242, 243].

Subperineural and perineural glia in the fly brain form the blood-brain barrier (BBB) and are in that sense similar to astrocytes which contribute to forming the BBB in the mammalian brain [244] (Fig. 1.8A and B). Subperineural and perineural glia increase endocytosis during sleep, and have been hypothesized to encode sleep need [221]. Cortex glia, which encapsulate neuronal cell bodies and are in contact with the BBB as well as glia that surround neuropils (ensheathing glia and astrocytes, Fig. 1.8B) [238], are involved in glutamate recycling, a process that is also linked sleep modulation [242]. In addition, a major steroid hormone in insects called ecdysone has been recently reported to act on cortex glia to stimulate lipid metabolism and modulate sleep [245].

Calcium activity in astrocytes was proposed to encode sleep need, as mechanical sleep deprivation increases calcium fluctuations in astrocytes, and artificially activating astrocytes, which supposedly increase intracellular calcium, promotes sleep [129]. Mechanical sleep deprivation also affects the interaction between neurons and astrocytes in the MB, suggesting that neuron-glia interaction is modulated by sleep [246].

Ensheathing glia in the fly brain, which do not directly correspond to any mammalian cell type, are also involved in sleep [224, 237]. Ensheathing glia create a diffusion barrier by wrapping around and partially innervating the different compartments of the fly brain [22, 225, 247], as shown in Fig. 1.8B and C. They also engulf neuronal debris similar to astrocytes in mammals [224, 237, 248]: neural injury resulting from antennal removal increased sleep in flies, and sleep promoted clearance of damaged neurites through ensheathing glia[249, 250]. In ensheathing glia, the excitatory amino acid transporter 2 (Eaat2), which is responsible for glutamate uptake after neurotransmission[251], regulates sleep in flies as Eaat2 knockdown increases sleep [252]. Control flies ingesting taurine, a GABA receptor agonist, showed increased sleep [100], which was not observed in Eaat2 mutants. This suggests that ensheathing glia might control sleep through a taurine-dependent mechanism. The role of ensheathing glia in sleep control is discussed in detail in Chapter 5.

1.4 Hypotheses for the function of sleep

The function of sleep is not fully understood but several hypotheses and theories have been proposed [3, 253]. These include that sleep is important for enhancing the immune system, for changes in brain connectivity, for tissue regeneration, or for energy restoration [3, 254, 255]. Many aspects of these theories are not understood in detail, and it is likely that sleep accounts for many or all of these functions simultaneously [256]. The current section reviews the most important theories that were proposed for explaining the role of sleep for brain function, focusing on evidence from *Drosophila*.

1.4.0.1 Energy restoration

This hypothesis proposes that energy progressively decreases in the brain during wakefulness and sleep is later necessary to refill energy stores [257, 258]. Different measures for energy usage during wakefulness have been proposed, including depletion of astrocytic glycogen stores, or accumulation of ATP byproducts, such as adenosine [257, 258].

Circadian changes in glycogen concentration have been observed in brain explants, with glycogen being higher at times of the day when flies usually are less active. This suggests that glycogen might be restored when flies rest [259]. Energy consumption has also been assessed by studying the coupling between metabolism and activity in neurons [260, 261]. *In vivo* experiments in flies showed how movement increased neural activity and intracellular ATP concentrations in neurons. This suggests that active behavior drives consumption and production of ATP in neurons [260, 261]. Moreover, short events of artificial neural activation produced a sustained increase in intracellular ATP, implying that energy is allocated in neurons that are soon going to be active [260]. However, similar experiments have so far not been performed in sleeping flies. Extracellular adenosine has been not been monitored across sleep and wake in the fly brain either, although adenosine could be released by ensheathing glia [216]. However, *in vivo* experiments in mice have shown how neural activity during wake and sleep, mostly from glutamatergic neurons, contributes to extracellular adenosine accumulation in the basal forebrain (Fig. 1.7), without drawing a link to energy consumption [212].

Glia cells, which have been involved in the regulation of sleep (reviewed in section 1.3.4), also support the energy demands of neurons in flies [261, 262].

1.4.0.2 Synaptic homeostasis hypothesis

This hypothesis proposes that learning during wakefulness produces a net increase of synaptic strength across connections in the brain, and subsequent sleep is therefore required for synaptic downscaling [263, 264, 265]. In *Drosophila*, different studies have reported an overall synaptic upscaling after mechanical sleep deprivation, as reviewed in section 1.3.2 and

shown in Fig. 1.6. The processes deciding which synapses are maintained or enhanced to promote memory consolidation during sleep are still being worked out. Changes in neural excitability or synaptic tagging during wakefulness provide potential mechanisms for strengthening or pruning synapses during subsequent sleep [266].

1.4.0.3 Clearance of metabolites

This hypothesis proposes that the function of sleep is to support the glymphatic system in the removal of harmful metabolites that accumulate during wakefulness in the brain [218, 219]. While flies lack a vasculatory system, the interstitial fluid in the brain is also separated from the hemolymph by the *Drosophila* blood brain barrier (BBB) [244] (Fig. 1.8A and B). Recent evidence supports such increased waste clearance during sleep across the BBB in flies, as reviewed in section 1.3.3.

1.5 The regulation of sleep

Our understanding of the processes and neural circuitry involved in the control of sleep has increased considerably over the past decades [270, 271, 272]. However, a basic phenomenological model that is still relevant today, the two-process model, was proposed more than 40 years ago for explaining the timing of human sleep [273]. Since then, many variations have been implemented [269, 274], for example to include NREM and REM cycles [275], or to describe sleep in rodents [276].

The two-process model, shown in Fig. 1.9, proposes that sleep is regulated by the interaction of two processes: a circadian process and a homeostatic process [267, 268, 269]. The circadian process or pacemaker is an internal clock that oscillates with a period of 24 hours, keeps track of the time of day, and informs about the optimal time to sleep. The homeostatic process represents sleep debt, which accumulates during wakefulness and resets during sleep. These two processes interact in such a way that the circadian pacemaker acts as a low threshold of the homeostatic process for triggering wakefulness [269].

Understanding how sleep is regulated will likely also contribute to a better understanding of the function of sleep. In particular, the homeostatic process keeps track of the prior waking duration as well as of aspects of the behavioral experience to determine how much subsequent sleep is needed [185, 277]. Therefore, a better understanding of how behavior is tracked and integrated by the homeostat might also contribute to a better understanding of why sleep is needed [278].

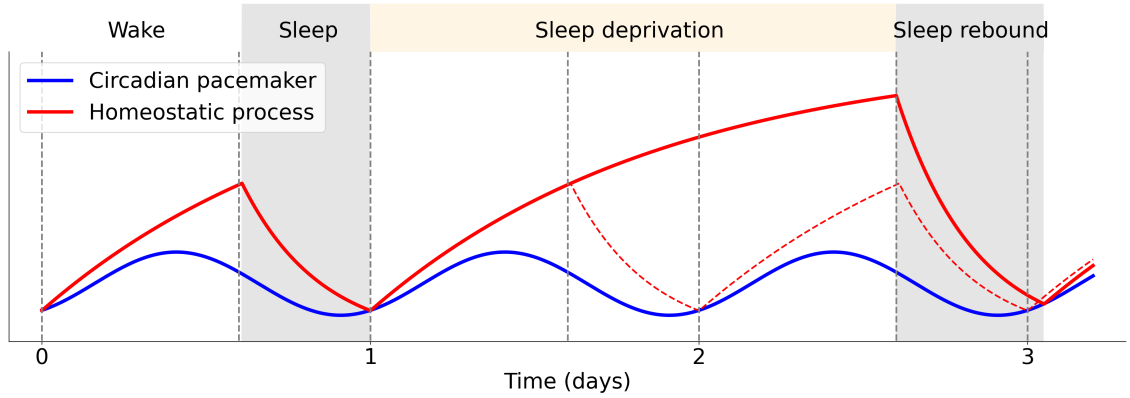


Figure 1.9: The two-process model for sleep regulation. The circadian pacemaker (blue line) oscillates with a period of 1 day. The homeostatic process (red line) increases during wakefulness and decreases during sleep. The two processes interact such that the circadian pacemaker acts as a lower threshold of the homeostatic process; a sleep-to-wake transition is triggered when the homeostatic process reaches this threshold. Sleep deprivation increases the amplitude of the homeostatic process beyond the normal range (dashed red line), producing sleep rebound in the subsequent sleep episode. This figure is created based on the original two-process model [267, 268, 269]

1.5.1 Circadian clocks and rhythms

Circadian clocks modulate different metabolic processes and behaviors, including sleep [279, 280, 281, 282]. In the mammalian brain, the main circadian pacemaker is located in the suprachiasmatic nucleus (SCN) of the hypothalamus [283, 284], which receives light cues from the retina for synchronization with the day and night cycle, and transmits that information to other brain areas and other organs [281, 282].

Drosophila has allowed disentangling various components of the molecular machinery of the circadian clock [279, 282]. The core of the clock in flies arises intracellularly from transcriptional-translational feedback loops of genes referred to as clock genes, resulting in molecular oscillations with a 24-hour period [282, 285, 286, 287]. Approximately 150 neurons in the fly brain express the clock genes, also known as clock neurons, which transform these periodic molecular oscillations into neural activity patterns that modulate the circadian rhythm [107, 279, 282, 288, 289]. These clock neurons are arranged in different clusters across the fly brain and have different functions. For example a set of these clock neurons called lateral neurons (LNs) promotes arousal and locomotor activity at dusk and dawn [107, 282]. The synchronization of the circadian rhythm of flies to the day and night cycle is mediated by a dedicated circadian photoreceptor expressed in a subset of clock neurons [290, 291] as well as the visual system [107].

Although it is still only partially understood how the network of interconnected clock neurons and their output activity regulates many of the physiological functions in flies, including sleep [107], clock neurons have been shown to convey information to the central complex and the mushroom bodies to modulate sleep and wakefulness [21, 147, 292, 293, 294, 295]. The *Drosophila* behavioral circadian rhythm is also supported by glial cells [22].

1.5.2 Sleep homeostasis

Sleep deprivation results in increased intensity and duration of subsequent sleep epochs, a phenomenon which is described as sleep homeostasis [269]. In the early theoretical work of the two-process model, sleep homeostasis was modeled as a dynamic process solely dependent on the duration of wakefulness and sleep [267]; however, sleep homeostasis also depends on the nature of behavior during wakefulness [185, 277].

Compared to the circadian process, how and where sleep homeostasis is represented in the mammalian brain is less clearly established. For example, the mechanisms of how wake behavior is integrated over time, what biological markers encode the need for sleep, or how sleep resets the sleep homeostat, are still being worked out [102, 212]. In mammals, homeostatic sleep pressure is reflected in slow wave activity (SWA) during NREM sleep, as mentioned in section 1.3.1 and shown in Fig. 1.5A. Other markers for sleep need have been proposed [185], for example the accumulation of adenosine [212] (Fig. 1.7) or the increase in synaptic strength [265] (mentioned in sections 1.3.3 and 1.4), and these two processes are thought to be mediated by astrocytes [22, 229, 234, 296].

In *Drosophila*, synaptic upscaling, as reviewed in section 1.3.2 and shown in Fig. 1.6, was suggested to be a marker for sleep pressure [265]. Glial cells, in particular astrocytes, were proposed to encode sleep need [129], as described in section 1.3.4. Further, different neural populations for sleep homeostasis were identified [21, 130]. For example, artificial activation of cholinergic, octopaminergic or dopaminergic neurons leads to sleep deprivation, but only activation of cholinergic neurons produces subsequent sleep rebound, implying that cholinergic neurons charge the sleep homeostat in flies [171]. The MB is known to regulate sleep in flies [128, 297], where a microcircuit of cholinergic sleep-promoting neurons and glutamatergic wake-promoting neurons has been described [298, 299]. Mechanical sleep deprivation increased activity in populations of sleep-promoting neurons in the MB, indicating that these neurons sense sleep loss [300]. Finally, a circuit that controls sleep homeostasis has been described in the central complex [125], as discussed in detail in section 1.6.1.

How the circadian clock could modulate sleep homeostasis, as for example proposed by the two-process model, is still not clear at the level of neural circuits. However, this modulation could partially happen in the central complex, which receives input from clock neurons (see section 1.5.1).

1.6 Interaction of sleep and navigation in the central complex

The central complex is a brain region in the center of the brain that originated in insects more than 400 million years ago [302, 303]. It is composed of different neuropils, including the ellipsoid body (EB), the fan-shaped body (FB), the protocerebral bridge (PB), and a pair of noduli (NO) [304, 305] (Fig. 1.10A). The connectivity in the central complex is highly structured: its neuropils have a shared columnar architecture and are additionally subdivided into different layers [304, 305], as shown in Fig. 1.10B.

In *Drosophila*, neurons that regulate sleep homeostasis have been found in the central complex [21, 123, 147, 176]. Additionally, the central complex is also involved in navigation as well as visual and spatial learning. This rises the question of why these different functionalities, sleep and navigation, are located in the same brain area and how they interact [305, 306]. This section reviews the role of the central complex in the regulation of sleep homeostasis, as well as in navigation and visual or spatial learning.

1.6.1 Sleep regulation in the central complex

In the central complex of *Drosophila* different neural populations that regulate sleep have been identified. In particular, a set of ring neurons called R5 neurons and shown in Fig. 1.10C, which were mislabeled in the original article as R2 neurons, take part in sleep homeostasis by integrating time spent awake [123]. These neurons were first identified in a screen of GAL4 lines (see section 1.7.1) assessing sleep behavior with the *Drosophila* Activity Monitor (DAM). Thermogenetic activation of R5 neurons increased sleep during and after activation, suggesting that these neurons promote sleep through increased activity. Furthermore, inhibiting neurotransmitter release from R5 neurons reduced sleep rebound following 12 hours of mechanical sleep deprivation in the DAM, indicating that these neurons are required for sleep homeostasis. Electrophysiology recordings in brain explants showed that the firing rate of R5 neurons was higher in the evening than in the morning, which was interpreted as an increase of activity in R5 neurons throughout the day, when flies are most active. Additionally, after 12 hours of mechanical sleep deprivation, R5 neurons in brain explants displayed a burst-firing activity pattern accompanied by increased calcium and structural changes [123, 307], which was not observed in brains from unperturbed flies. Another study using brain explants reported oscillatory activity in R5 neurons, with an increased amplitude of oscillations depending on the duration of mechanical sleep deprivation [186]. Additionally, circadian modulation of calcium activity in R5 neurons has been reported during long-term imaging in constrained flies [294]. These studies suggest that R5 neurons encode sleep need and integrate wakefulness in the fly through synaptic structural changes as well as increased calcium levels and firing rates [123, 186].

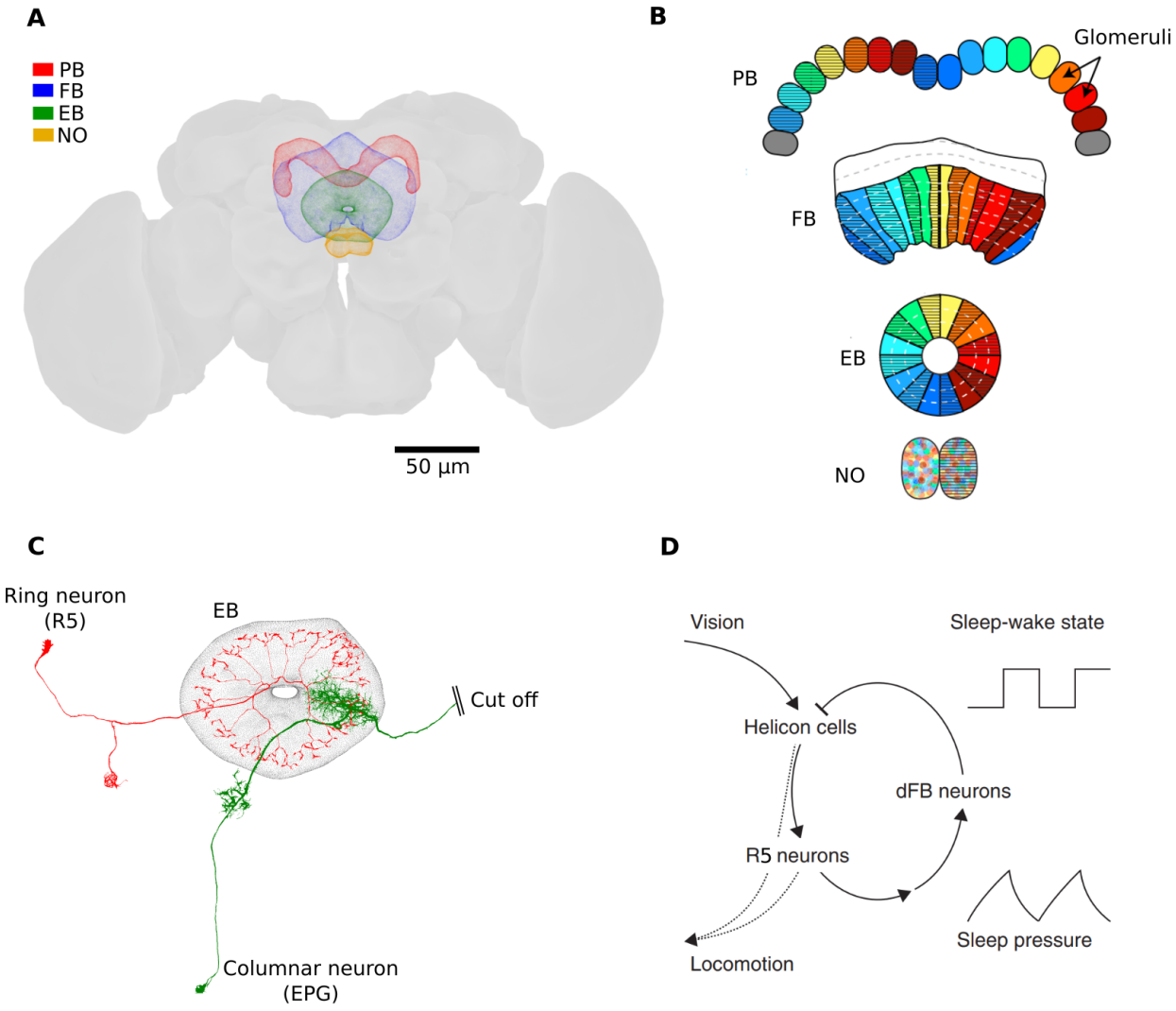


Figure 1.10: The central complex of the *Drosophila* brain. **A** The fly brain and the different neuropils that form the central complex. Panels A and C are created using the connectome [93]. **B** Columnar architecture shared among the neuropils of the central complex. Different neuronal types connect glomeruli of the same color located in different neuropils. The FB and EB are additionally divided into layers (dashed lines). Reprinted from [301] with permission from Elsevier **C** Example of a ring neuron (R5 neuron) and columnar neuron (EPG or compass neuron). Both neurons send projections that overlap in the EB. **D** Proposed recurrent circuitry for sleep homeostasis in the central complex [125]. Panel D is from [106] used under Creative Commons CC-BY license.

R5 neurons provide functional output to a population of neurons that innervate the dorsal fan-shaped body (FB), thus called dFB neurons, which have been identified as sleep promoting [123, 176]. However, since dFB and R5 neurons seem not to have a direct anatomical connection, the exact pathway of their interaction is currently unknown. dFB neurons are nevertheless assumed to sense sleep need from R5 neurons by increasing their excitability [125, 169]. dFB neurons are also viewed as a switch that triggers sleep in flies [125, 308] and to switch from low neural activity during wakefulness to high neural activity to promote sleep [125]. The proposed switching mechanism involves the wake-promoting neuromodulator dopamine, as dopamine suppresses excitability and activity of dFB neurons for a few minutes [308].

Artificial activation of dFB neurons produced immobility in flies [176], which was interpreted as sleep since this activation also consolidated courtship memory [122, 176]. However, the GAL4 line used to activate dFB neurons (see 1.7.1) contains multiple types of neurons, such as vFB neurons that innervate the ventral FB. More recent experiments have shown that activation of dFB neurons alone (with a more constrained GAL4 line) does not improve learning in the Y-track paradigm (see section 1.2.4), nor consolidate courtship memory [177]. In fact, courtship memory consolidation is attributed to the activation of vFB neurons [177].

During sleep, dFB neurons inhibit the activity of helicon cells, which are large interneurons in the central complex innervating the EB and FB. dFB neurons inhibit helicon cells through the release of the neuropeptide Allatostatin A (AstA) [125], which is involved in feeding, growth, learning, and locomotor activity, [309]. Helicon cells respond to visual stimuli and trigger locomotion when they are artificially activated. Helicon cells are anatomically connected to R5 neurons, and sustained artificial activation of helicon cells for 12 hours led to sleep deprivation as well as sleep rebound afterwards, implying that helicon cells charge R5 neurons [125].

Taken together, the proposed control circuit for sleep homeostasis contains three neural populations: R5 neurons, dFB neurons, and Helicon cells, depicted in Fig. 1.10D. In this circuit, wakefulness is characterized by activity of helicon cells, which charge R5 neurons. R5 neurons encode sleep need, and when their activity increases after prolonged wakefulness, they trigger a switch in dFB neurons from a silent to an active state. This switch then promotes sleep by inhibiting helicon cells, in turn inhibiting visual processing and locomotion. During sleep, R5 neurons do not receive input from helicon cells and reset synaptic strength and activity [125].

1.6.2 Navigation in the central complex

The central complex is a brain area important for navigation in *Drosophila* as well as in other insects [24]. Flies with mutations that affect the structure of the central complex show abnormal walking and turning patterns [310]. Additionally, multiple different sensory

modalities converge in the central complex, and motor outputs diverge, suggesting a role in decision-making during navigation [25, 26, 306, 311, 312].

The ellipsoid body (EB) of the *Drosophila* central complex has a torus-like shape and contains ring-shaped neurons (Fig. 1.10C), the ring neurons already introduced in section 1.3.1. Columnar neurons, another type of EB neurons, tile the EB torus into different wedges and additionally intersect with the ring neurons [304, 305] (Fig. 1.10C). The EB is known for its role in encoding the head direction of the fly in its environment, were a subclass of columnar neurons, known as compass neurons, act as an internal compass, with a bump of activity that moves across the EB when the fly rotates [306, 313]. The encoding of a circular variable, such as heading angle, emerges from the circular anatomical arrangement of the EB [313], suggesting that neurons in the EB form a ring attractor network [25, 306, 311, 313, 314, 315, 316]. This type of mathematical model was originally developed for the head direction system in mammals [317, 318] and is described in section 1.8.3.

Different classes of columnar neurons form a recurrent circuit between EB and PB for integrating the angular velocity of the fly in the compass neurons [314, 316]. In addition, compass neurons combine different modalities to accurately track the head direction of the fly, and different classes of ring neurons convey visual information [155] and wind direction [319] from other brain regions to compass neurons. Moreover, as in other insects [320, 321], polarized skylight information is also projected to the central complex [322] and likely also integrated by compass neurons [322].

In part thanks to the fly connectome [17], which allows dissecting network motifs in the central complex [305], the function of the FB has been linked to vector-based computations for navigation [25, 305, 323, 324]. Different types of columnar neurons in the FB perform vector computations for frame of reference transformations. For example, head direction in the EB is transformed from a body-centric to a world-centric frame or reference in the FB [305, 323]. In the world-centric frame of reference, the fly is believed to store goal direction as well as to perform path integration through the recurrent neural circuitry within the FB [25]. Finally, the FB generates steering commands that are transformed back into a body-centric frame of reference [324, 325].

Overall, our understanding of the role of the central complex in navigation has considerably increased thanks to the available genetic tools, in particular GAL4 lines [16, 326, 327, 328] and calcium indicators [15, 16], the connectome [17], as well as virtual reality experiments in behaving animals [329, 330, 331].

1.6.3 Visual and spatial learning in the central complex

Visual pattern recognition in the flight simulator, reviewed in section 1.2.4, involves populations of neurons in the central complex [144, 145]. Mutation of the *rut* gene leads to flies

that cannot remember visual patterns when conditioned with heat [144, 145]. Expressing the *rut* gene in these mutants in neurons located in neuropils of the central complex, such as the EB and FB, rescues visual memory deficits [144, 145]. In particular, *rut* expression in neurons innervating different layers of the FB made flies remember visual patterns depending on a defining parameter. For example, flies with expression of *rut* in either F5 or F1 neurons were able to only discriminate between patterns at different elevations or with different orientations, respectively. This suggests that different layers in the FB are involved in processing different visual parameters, such as elevation or orientation [144]. Additionally, *rut* expression in R2 and R4m ring neurons of the EB allowed flies to remember visual patterns independently of the visual parameter that defined them [145]. Inhibition of R2 and R4m ring neurons also impaired delay and trace associative learning of visual patterns [159] (described in section 1.2.4). Moreover, trace associative learning was supported by increased oscillations in R2 and R4m neurons as well as by sustained activity between the disappearance of the visual pattern and the following aversive stimulus [159].

In the place learning assay, described in section 1.7.4, silencing R1 ring neurons in the EB impaired learning in flies but not visual pattern discrimination, suggesting that these neurons play a role in processing, storing or retrieving visual or spatial information [146].

Further, visual working memory has been linked to neurons in the central complex. In an assay called the detour paradigm, ring neurons were required for flies to remember the location of a visual cue even after it disappeared from the arena for a few seconds [332, 333].

1.7 Experimental Tools for investigating sleep and navigation in *Drosophila*

This section reviews the experimental methods and tools that are most relevant to this thesis.

1.7.1 Genetic tools

Neurons and glia in *Drosophila* are genetically tractable, meaning that they can be genetically identified and manipulated [13]. The binary GAL4/UAS expression system [334] is widely used to target gene expression of an effector or a reporter in specific cells through genetic crosses [13]. A GAL4 line, meaning flies that express the GAL4 transcription factor in specific cells, can be crossed to another UAS line, flies with an enhancer called upstream activation sequence (UAS). The enhancer then promotes the expression of an effector or reporter gene thanks to the GAL4 transcription factor binding to UAS. Therefore, in the offspring of flies resulting from a GAL4/UAS-cross, the effector or reporter gene is expressed

only in the cells that express GAL4, for example to monitor neural activity in specific neurons with a genetically encoded calcium indicator [15].

A large collection of GAL4 lines with around 7,000 different lines, most lines driving expression in a small fraction of cells in the adult fly nervous system, was provided in [16, 326, 327]. An additional 2800 lines, called split-GAL4 [328], were developed with higher specificity with regards to cell type [335]. This was achieved by targeting neural populations resulting from the intersection of two GAL4 expression patterns.

UAS lines can be used for manipulating or visualizing cells. The most popular ones for manipulating neural activity include thermogenetic effectors, which can either inhibit or excite neurons when the temperature is raised above a threshold [15, 336, 337, 338], or optogenetic effectors, which express light-sensitive proteins such as ion channels or pumps that can either excite or inhibit neural activity under illumination with light [15]. For example CsChrimson, a light-gated cation channel, can be expressed by the GAL4/UAS system to activate neurons with pulses of red light (around 590 nm), even without dissection of the fly, with light penetrating directly through the cuticle [15, 339, 340].

For monitoring neural activity, the most commonly used UAS lines encode calcium indicators such as GCaMP [15, 341]. GCaMP is a protein that increases its fluorescence (at a peak emission wavelength around 510 nm) when bound to calcium ions and is excited with blue light (single-photon) or infrared light (two-photon). Fluorescence changes of GCaMP captured through a microscope allow measuring intracellular calcium, which can be used as a proxy for neural activity [342]. The original GCaMP version from 2001 [343] has been optimized and improved, resulting in the current GCaMP8 version [344].

Other binary expression systems such as lexA/lexAop [345] or Q [346] can be used in parallel with the GAL4/UAS system to target two or more sets of cells at the same time [13], for example to manipulate one group of cells while monitoring the activity of another group.

1.7.2 The connectome

The *Drosophila* connectome aims to provide the connectivity between all neurons in the fly brain at synaptic resolution [347, 348]. While the reconstruction of the neurons for the complete brain is still in progress at the time of writing, the hemibrain dataset released in 2020 already tracked around 25,000 neurons [93], including those in the central complex [305].

The hemibrain was assembled in a collective effort from the Janelia Research Campus and the Connectomics Group at Google. First, the brain of a single female fly was imaged using electron microscopy (EM) at synaptic resolution. Then, the obtained high-resolution images were aligned and automatically segmented to track single neurons and the location of synapses. Human proofreading was included in the process to correct for errors and to

improve tracking accuracy. This effort finally resulted in a framework for visualizing the number of synapses between two pairs of neurons, the skeleton or arborizations of each tracked neuron, and the classification of neurons based on connectivity and morphology [93].

However, a more complete understanding of the fly brain requires additional information that the connectome alone cannot provide [349, 350]. For example, gap junctions are missing, as are the relevant neurotransmitters, neuromodulators, or receptors for each neuron [350]. In addition, the current connectome reconstruction does not include glial cells. Nevertheless, since its release the hemibrain connectome has proven highly useful for obtaining a better understanding of the processing that occurs in specific neural circuits of the *Drosophila* brain [305, 351].

1.7.3 *In vivo* functional imaging

How dynamic neural activity drives behavior, including sleep, can be investigated through experiments that monitor neural activity in behaving animals [352, 353]. In *Drosophila*, the change in fluorescence from genetically encoded sensors such as GCaMP can be measured using a variety of microscope setups, including confocal [354], light sheet, two-photon [15, 353, 355], and three-photon microscopes [356, 357].

One of the most popular approaches for imaging in adult *Drosophila in vivo* is two-photon microscopy, where an infrared excitation beam (for example with a wavelength of around 900 nm for green fluorophores) is scanned across the fly brain. The energy in the beam is compressed into pulses of tens to hundreds of femtoseconds to avoid heating of the sample, and emitted fluorescence is collected by a photomultiplier tube (PMT). Two-photon microscopy allows deeper tissue penetration than single-photon fluorescence microscopy due to the longer excitation wavelength and tighter confinement of the excitation, which reduces photobleaching and increases (axial) resolution [352, 358]. An additional advantage of two-photon imaging compared with one-photon imaging is also that the excitation light is not visible to flies and therefore does not interfere with their visual system or behavior.

1.7.3.1 Fly preparations for *in vivo* experiments

In vivo imaging is severely affected by scattering tissue that surrounds the brain, such as the cuticle, air sacks, or fat tissue, which decreases the penetration of the excitation light and collection of fluorescence. The first *in vivo* physiology experiments in *Drosophila* for imaging as well as electrophysiology cut a window for accessing the brain by manually removing parts of the cuticle, as well as the underlying tissue and air sacks using forceps [342, 359, 360, 361]. The legs of the fly were constrained and, to limit brain motion during experiments, the proboscis was also fixed while muscles in the head were removed [342, 360, 361]. The

experiment started a few minutes after the dissection, under constant perfusion with saline solution [331, 342, 359, 362]. Other methods were developed without constraining the limbs, where flies were able to walk or fly during imaging or electrophysiology experiments for a few hours [330, 331]. This is still the most popular technique for *in vivo* imaging in the central complex [25, 26, 306, 312].

To simplify the dissection, reduce variability, and increase the lifetime of the preparation, a method for dissection was developed that used a pulsed UV laser for cutting the window in the head cuticle. The opening was then covered with transparent glue to keep the brain shielded but at the same time allow optical access [363]. After surgery, flies recovered while freely behaving in vials with food, and had a similar lifespan to non-dissected flies. These flies could repeatedly be positioned under the microscope for intermittent imaging sessions [363]. Finally, methods that do not require dissection of the cuticle have been developed, taking advantage of three-photon microscopy and adaptive optics [364]. In a recent variation of this idea, flies were glued to a transparent cover slide and the head of the fly was compressed to squeeze the air sacs and decrease scattering during imaging. This method allowed imaging neurons in the brain using two and three-photon microscopy at various depths, depending on the level of compression and the excitation wavelength [365].

1.7.3.2 Fast volumetric imaging

A two-photon microscope produces a 2D image by continuously scanning a focused beam across the focal plane, and each pixel value in the image is defined by the number of detected fluorescence photons. The number of images obtained per second, the frame rate, depends on the resolution of the images but usually ranges from a few Hertz to tens of Hertz. This frame rate is suitable for observing neural dynamics with genetically encoded calcium sensors, which have a time resolution in the order of tens of milliseconds [344]. Neurons however are not limited to the focal plane but arborize in three dimensions. Additionally, even a mostly two-dimensional structure can move in and out of the focal plane due to brain motion, which is common when imaging in behaving animals. Therefore, recording sample volumes is often required for monitoring activity. In scanning microscopy, a volume is obtained by recording a stack of 2D images at different positions along the optical axis, or z-axis. This however produces low volume rates in the order of Hertz which is ill-suited for resolving fast calcium changes in each focal plane of the stack [15].

Different approaches for scanning microscopy with faster volume rates have been developed [366, 367, 368]. For example, temporal multiplexing microscopy permits recording different focal planes at different z-positions at the same time [369, 370, 371, 372]. In temporal multiplexing, each scanned beam is offset in time and a single detector is used to sort the collected fluorescence by the time of arrival of photons (see Fig. 1.11 for how temporal multiplexing is achieved). This approach is however still limited by the maximum possible

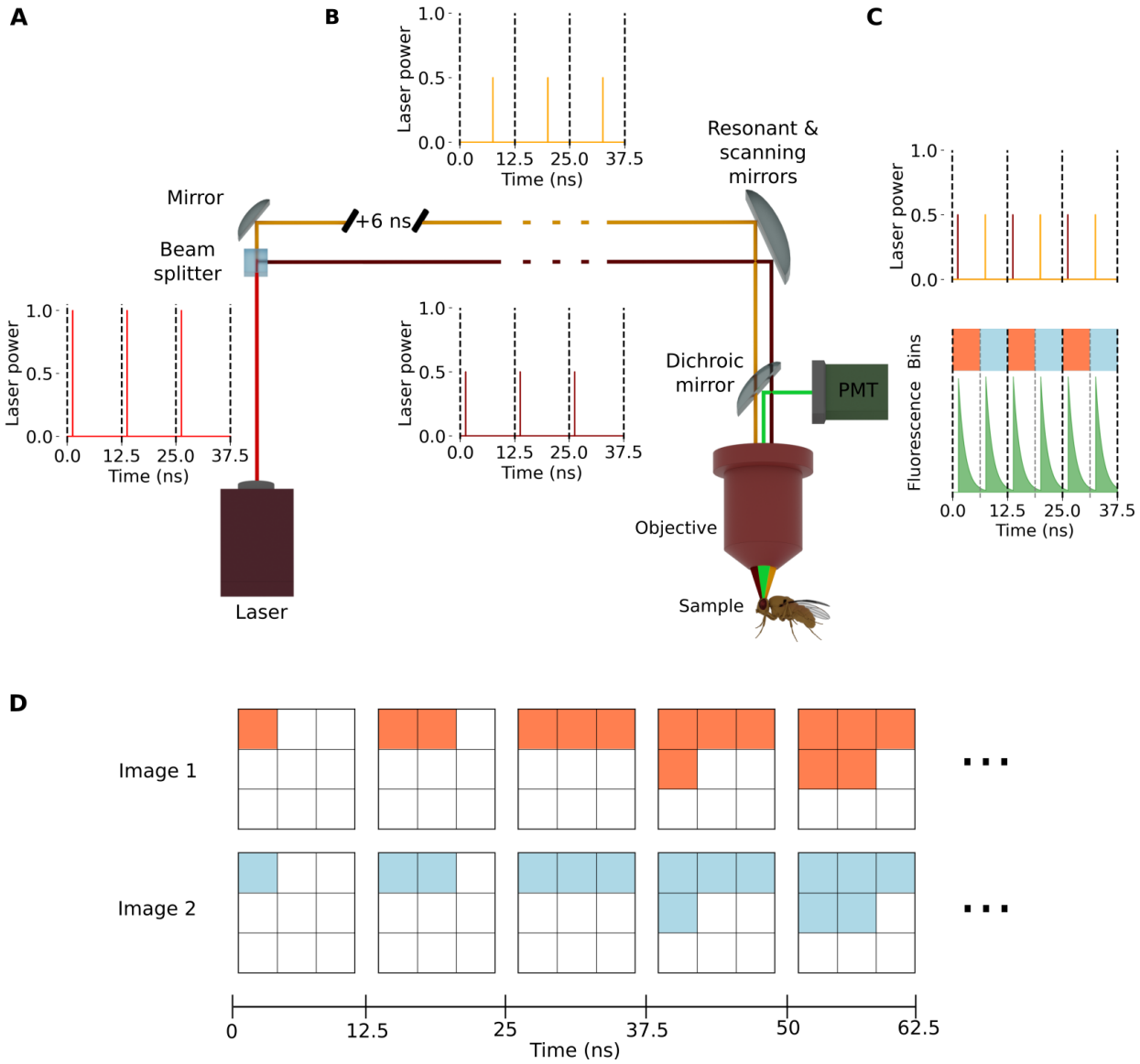


Figure 1.11: Two-photon temporal multiplexing. **A** An infrared laser produces pulses of 120 fs every 12.5 ns (80MHz repetition rate). **B** A beam splitter splits the laser beam into two beams with half of the power (orange beam and top panel, and dark red beam and bottom panel). One of the beams (orange) is delayed by 6 ns. **C** Additional optical elements (not shown) combine these two beams (top right panel) and resonant and scanning mirrors scan the beams across the sample through the objective. Fluorescence is collected through a dichroic mirror with a photomultiplier tube (PMT). The measured fluorescence (bottom right panel, second row) is binned in time (light red and light blue areas, first row). The fluorescence in each bin is then linked to the pulses from each beam (dark red and orange, respectively). **D** Two images are created by scanning the two beams across the sample. The value for each pixel is obtained every 12.5 ns, where images 1 and 2 contain the measured fluorescence from the light red and light blue bins obtained in C, respectively.

number of simultaneously scanned beams. Each beam requires approximately a time interval corresponding to the fluorescence lifetime and thus the time between subsequent laser pulses limits the number of beams.

Other approaches include using Bessel beams which produce an excitation focus extended along the z-axis and allow projecting a volume into a 2D image when the beam is scanned across the sample [373, 374, 375, 376]. This approach allows covering a larger volume fraction of the sample with only a single frame, but structures at different z positions are recorded in a single projection and therefore axial information is lost.

Axial information can be partially recovered by using two Bessel beams delivered to the sample at different angles, thus recording two different projections of the same volume [377, 378, 379]. The difference in the angles between the two Bessel beams, also known as parallax, results in an object appearing at different locations in each of the two recorded projections, which allows extracting the object position along the z-axis, similar to stereo or binocular vision. This approach requires some form of image postprocessing for identifying the related objects in the two recorded views [377, 378, 379].

1.7.3.3 Brain motion correction

Another challenge for *in vivo* imaging in behaving animals, including flies, is brain motion, where the brain moves with respect to the head due to body or muscle movements. Since these movements are in the order of micrometers, similar to the size of many neural structures, brain motion makes it difficult to reliably monitor the activity of neurons over time.

Motion of the brain in the focal plane, that is, lateral motion, can be corrected with image processing [329, 380, 381, 382, 383, 384]. However, motion perpendicular to the focal plane, or axial motion, is more difficult to correct since image features can disappear from the focal plane, or previously unseen features can appear. Such motion can be mistakenly interpreted as a changes in activity when imaging with indicators that rely on changes in intensity. In this way axial motion produces motion artifacts that cannot easily be distinguished from neural activity [329, 381, 383, 384, 385].

Different methods for correcting axial motion have been proposed for a single focal plane. For example, a reference signal can be used to track axial motion of the sample and either correct neural activity through post-processing algorithms or to reposition the focal plane along the z-axis in real-time [385, 386, 387, 388, 389]. Measuring a reference signal requires that sample structures are labeled for example with a second fluorescent dye with a different color that does not change in time [385, 389], or by inserting fiducials into the brain such as fluorescent beads [385].

1.7.3.4 Long-term imaging during behavior

Monitoring dynamics in the brain related to sleep, circadian rhythms, or memory consolidation, requires functional imaging over long timescales. However, in behaving flies immersed in virtual reality, neural activity can be reliably recorded for only a few hours, since the head of the fly is opened and the brain is exposed, limiting the lifetime of the preparation [330, 331]. Imaging in dissected flies was optimized for monitoring neural activity from clock neurons for 24 hours, however, in fully constrained flies with an exposed brain, and thus preventing behavior [294, 390]. Since observing sleep in flies requires finding epochs of immobility, methods with fully constrained animals do not allow identifying sleep bouts.

Another long-term imaging approach that created a transparent window in the cuticle above the brain (mentioned in section 1.7.3.1) allowed capturing behavior and brain activity in flies for a few minutes every day for up to 50 days [363]. Finally, three-photon imaging has also allowed recording neural activity for up to 12 hours through the cuticle [365] (also mentioned in section 1.7.3.1), although this approach seems to work best for neurons closer to the surface of the brain where scattering is low.

1.7.4 Place learning

Visual place learning allows studying how flies use visual cues to navigate and remember locations [146, 164], as mentioned in section 1.2.4. This assay was developed for flies that freely walk in a circular arena, as shown in Fig. 1.12A. The floor of the arena was tiled by Peltier modules, which maintained the floor of the arena at an aversively hot temperature, except for one square cool spot (Fig. 1.12B). Around the walking platform, a cylindrical array of green LED lights created visual patterns that flies could use for orienting themselves. Learning in this assay was tested over 10 trials. In each trial, (most) flies started from a hot position in the arena, and needed to find the cool spot. Once the majority of flies found the cool spot, another trial started by displacing both the cool spot and the visual cues simultaneously by 90 degrees around the arena (Fig. 1.12C). This rotation at the beginning of each trial is equivalent to flies being translated away from the cool spot, so that they need to locate and reach the cool spot again. Learning was measured by the reduction of both the time and walking distance required to reach the cool spot over the trials [146, 164].

In this assay, flies require visual memory and the ability to use this memory for spatial navigation. Mechanical sleep deprivation before place learning led to worse performance and impaired learning [166]. This assay, which involves neural populations in the central complex [144, 145, 146], therefore offers the possibility to investigate the effect of sleep on visual and spatial learning.

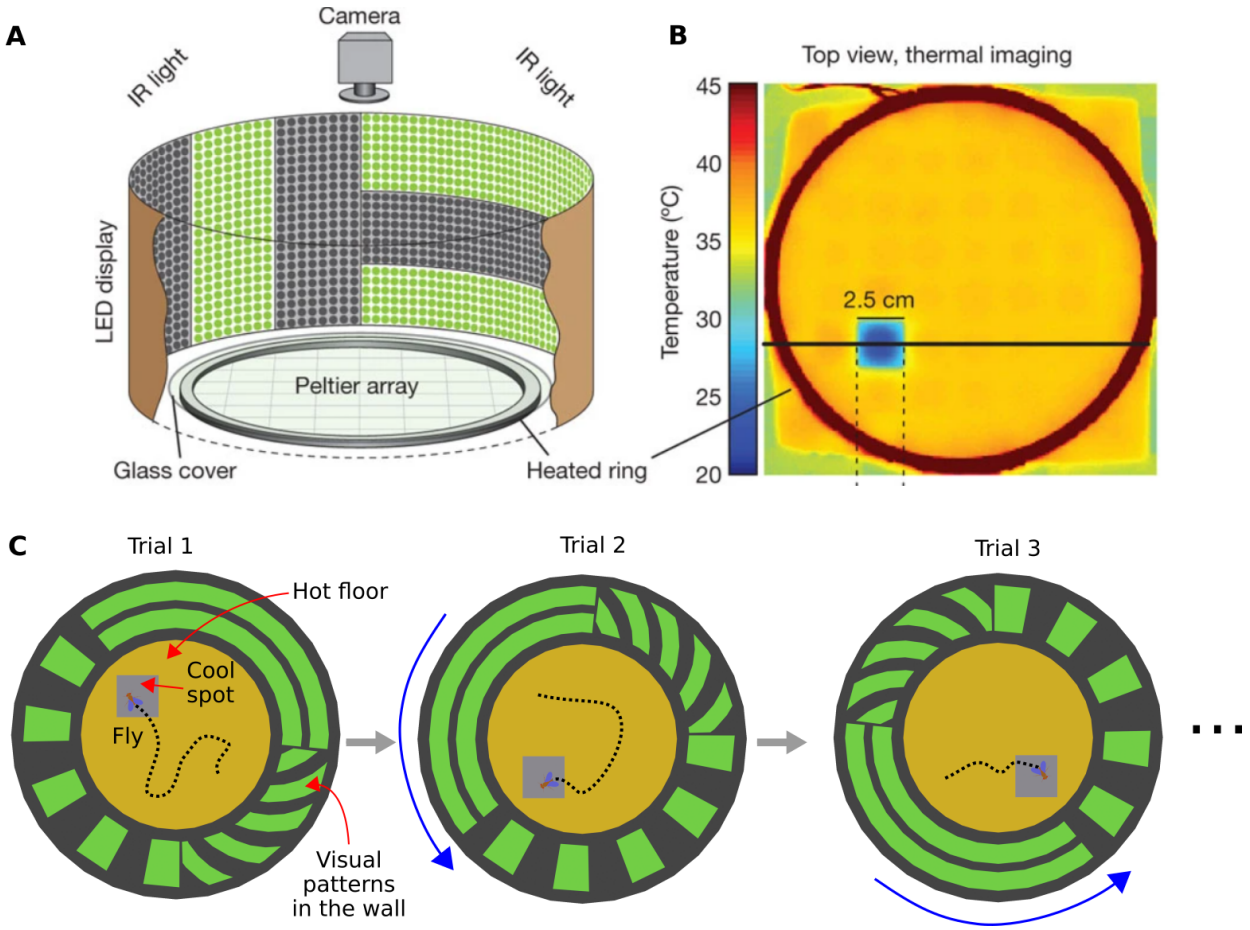


Figure 1.12: Visual place learning assay for freely moving flies. **A** Flies are placed in a circular arena and prevented from flying by a glass cover. The arena is surrounded by a heated ring to prevent flies from approaching the edge, and the floor is heated by Peltier modules. Visual patterns are displayed with an LED display around the arena, and the positions of flies are tracked with a camera from the top under infrared (IR) illumination. **B** Temperature of the setup seen from the top. The arena contains a cool spot that flies have to find. **C** In the first trial, a fly starts from a random position and finds the cool stop (left, trajectory depicted by the dashed black line). Then the cool spot and visual patterns are rotated together 90 degrees from the previous position, the next trial starts, and the flies have to find the cool spot again (center and right). Reproduced from [146] with permission from Springer Nature.

1.8 Theoretical and computational models for sleep and navigation

Theoretical and computational models in neuroscience aim to capture specific characteristics of a given biological system and ideally to provide predictions that can guide experiments [391, 392, 393]. Models in neuroscience, including those for sleep, are proposed across different scales and levels of biological detail, from modeling entire brain regions and their connectivity to neural networks or cellular compartments [274, 394, 395, 396]. Also, different machine learning algorithms, such as those for training artificial neural networks (ANN), can shed light on the impact of sleep on learning. This section reviews the models that are most important for this thesis, including networks for sleep and wake regulation, training algorithms for artificial neural networks with a sleep phase, and ring attractor networks, which are used to describe the head direction system of *Drosophila* in the central complex.

1.8.1 Models for sleep and wake regulation

At the phenomenological level, the two-process model (mentioned in section 1.5) offers a quantitative framework for investigating the regulation of sleep through the interaction of the circadian clock and sleep homeostasis [267, 268, 269], as reviewed in section 1.5. The two-process model has been adapted recently to describe the circadian rhythm in *Drosophila* [397], which also captures the locomotor activity of mutant flies with a non-functional circadian clock [397]. Other models that describe the circadian rhythm of flies have been implemented, including a parametric model which describes behavioral activity [398], or a Hidden Markov Model that predicts different sleep stages [399].

At the level of neural networks in mammals, one of the simplest sleep regulatory models is the flip-flop model, first proposed conceptually [274, 400] and later implemented mathematically [401, 402]. This model includes two hypothalamic neural populations, one that promotes wake and another one that promotes sleep, that inhibit each other [400] and can produce cycles of sleep and wakefulness [401, 402]. This model has also been extended to include neural populations that control REM and NREM sleep cycles [403, 404, 405]. The flip-flip model as well as the two-process model are also integrated into the mutual inhibition model, which includes circadian modulation and sleep homeostasis [406].

Models that consider the synaptic homeostasis hypothesis [265] have also been proposed, with net synaptic strength in neural networks increasing during wakefulness and decreasing during sleep [407, 408, 409, 410].

In *Drosophila*, a conceptual model has been proposed, describing homeostatic sleep control in flies through the interaction of three neural populations [125], as described in section 1.6.1.

1.8.2 Sleep for training neural networks

In addition to the computational approaches listed above, more abstract models, without a direct link to biological neurons, have been introduced. Dreaming during sleep has been proposed as an unlearning mechanism, enabling the brain to remove attractor states that form during wakefulness through temporal dynamics during sleep, or "dreams" [411]. This idea has been applied in the training of an artificial neural network (ANN) to improve performance [412] and it also motivated the creation of the wake-sleep algorithm, which learns patterns from data through unsupervised learning [413]. This algorithm alternates between a wake phase, where a multilayer ANN is trained to match and generate the input data from its deepest and therefore most abstract layers, and a sleep phase, where training is reversed and the network is trained to match and generate its most abstract representations without any given input [413]. Similarly, another algorithm has used a Hebbian plasticity rule during a wake phase, which produces attractor states in the ANN, and a following sleep phase to dissolve these attractors through an anti-Hebbian rule [414]. A sleep phase can also be used to avoid catastrophic forgetting in ANNs through the reactivation of previously established configurations during sleep [415].

Finally, replay dynamics observed in biological neurons during sleep can similarly be applied 'offline' in reinforcement learning [199, 416, 417]. An artificial agent driven by a neural network can for example relive old memories in an offline (sleep) period and in this way improve learning performance and generalization [416, 417].

1.8.3 Models for navigation: ring attractor networks

An attractor network is a recurrent network that gradually approaches a stable pattern as it evolves over time [418, 419]. A ring attractor network is a subtype of attractor network, which was first proposed as a model of the head direction system in rats [317]. In this network, depicted at the bottom of Fig. 1.13A and B, excitatory neurons are arranged in a circular or ring-like pattern. These neurons are connected to their neighbors and the strength of their connection decreases with the distance between two neurons along the ring. For example, two neurons that are close together are connected more strongly than two neurons that are farther away. Additionally, global inhibition is provided equally to all neurons. Such connectivity between neurons can create a sustained pattern, or bump, of activity, with the center of the bump located along one of the neurons in the network. This bump of activity can be shifted along the ring-like arrangement of the neurons when excitatory input to the network is provided. In this way, the position of the bump can track the motion of a circular variable, such as head direction. In addition, ring attractor networks can store information through a sustained bump of activity over time if no input is provided. Sustained activity in attractor networks without any input has been suggested

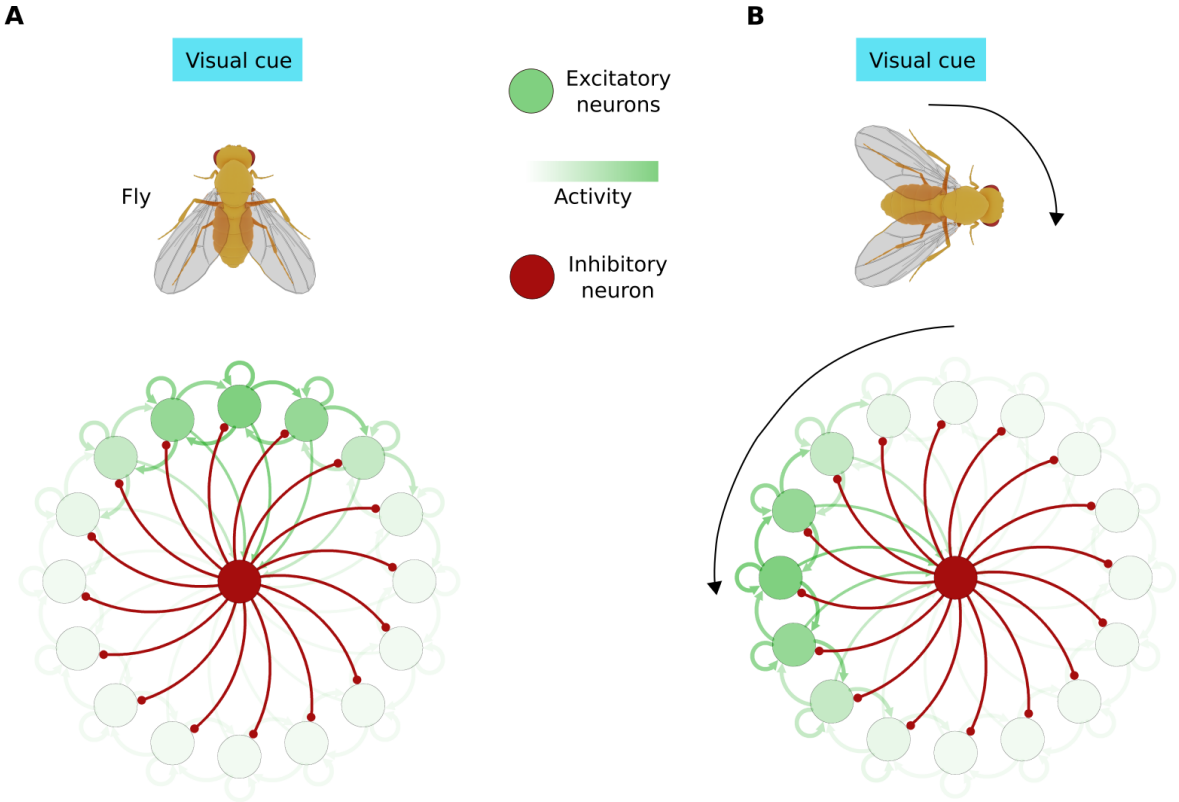


Figure 1.13: Ring attractor network. **A** Top: fly and visual cue. Bottom: a ring attractor network is composed of excitatory (green) neurons connected more strongly to their closest neighbors. An inhibitory neuron (or an inhibitory neural population) provides global inhibition to excitatory neurons. The network produces a bump of activity (green gradient color in excitatory neurons) encoding the orientation of a fly with respect to a visual cue (top). **B** When the fly rotates clockwise by 90 degrees with respect to the visual cue (top), the bump of activity in the ring attractor network rotates by 90 degrees in counter-clockwise direction, encoding the position of the visual cue with respect to the fly heading.

as a mechanism for working memory [420, 421, 422].

Ring attractor networks have been used for modeling head direction not only in mammals [423, 424], but also in zebrafish [425] and *Drosophila* [306, 311, 315]. In flies, compass neurons in the EB have been identified as the excitatory neurons in the ring attractor network, while global inhibition could be provided by ring neurons (Fig. 1.10C), as well as by other populations innervating the central complex [306, 311].

Ring attractor networks are sensitive to heterogeneities in network connectivity. Small noise in the connections between neurons, as expected in biological neural networks [419, 426], leads to drifts of the bump of activity along the ring [426, 427, 428, 429]. Such drift would compromise the function of the ring attractor for storing information. For example if an animal stops moving, the bump of activity, representing head direction, should stay stationary without drifting, otherwise the animal will lose orientation information. Different models that incorporate additional mechanisms to correct for heterogeneities in the network connectivity have been proposed, such as activity-dependent homeostasis regulation [427] or short-term plasticity [428, 429].

1.9 Aims of this thesis

Sleep in *Drosophila* exhibits many of the signatures that define sleep in mammals, including circadian rhythms and sleep homeostasis. Since sleep homeostasis monitors accumulation of the need to sleep or sleep debt in the brain, understanding sleep homeostasis could explain why sleep is necessary for maintaining optimal brain health and function. In the fly brain, a circuit for controlling sleep homeostasis has been identified in the central complex [21, 147], a brain region that has been intensely investigated in recent years for its role in navigation as well as spatial and visual learning [25, 26, 306, 311, 312].

The aim of this PhD thesis is to make progress on our understanding of the mechanisms that regulate sleep in *Drosophila*, also in particular with respect to navigation and learning in the central complex network. The central complex circuits for sleep control on the one hand, and navigation and memory on the other hand, offer the opportunity to investigate the relationship between these two different functionalities in well-defined circuits.

The organization of the thesis is shown in Fig. 1.14 based on different publications (Table 1.1). Chapter 2 [27] takes advantage of the anatomical connection between sleep homeostasis and navigation circuits for developing theoretical and computational models of these connected networks. These models offer insights into the interaction between sleep and navigation and propose several testable hypotheses and predictions, such as autonomous activity in the head direction system of the fly during sleep. Testing these hypotheses experimentally motivates the development of new methods in Chapter 3 [28] for monitoring activity in the fly brain over long timescales, which allow recording brain activity during

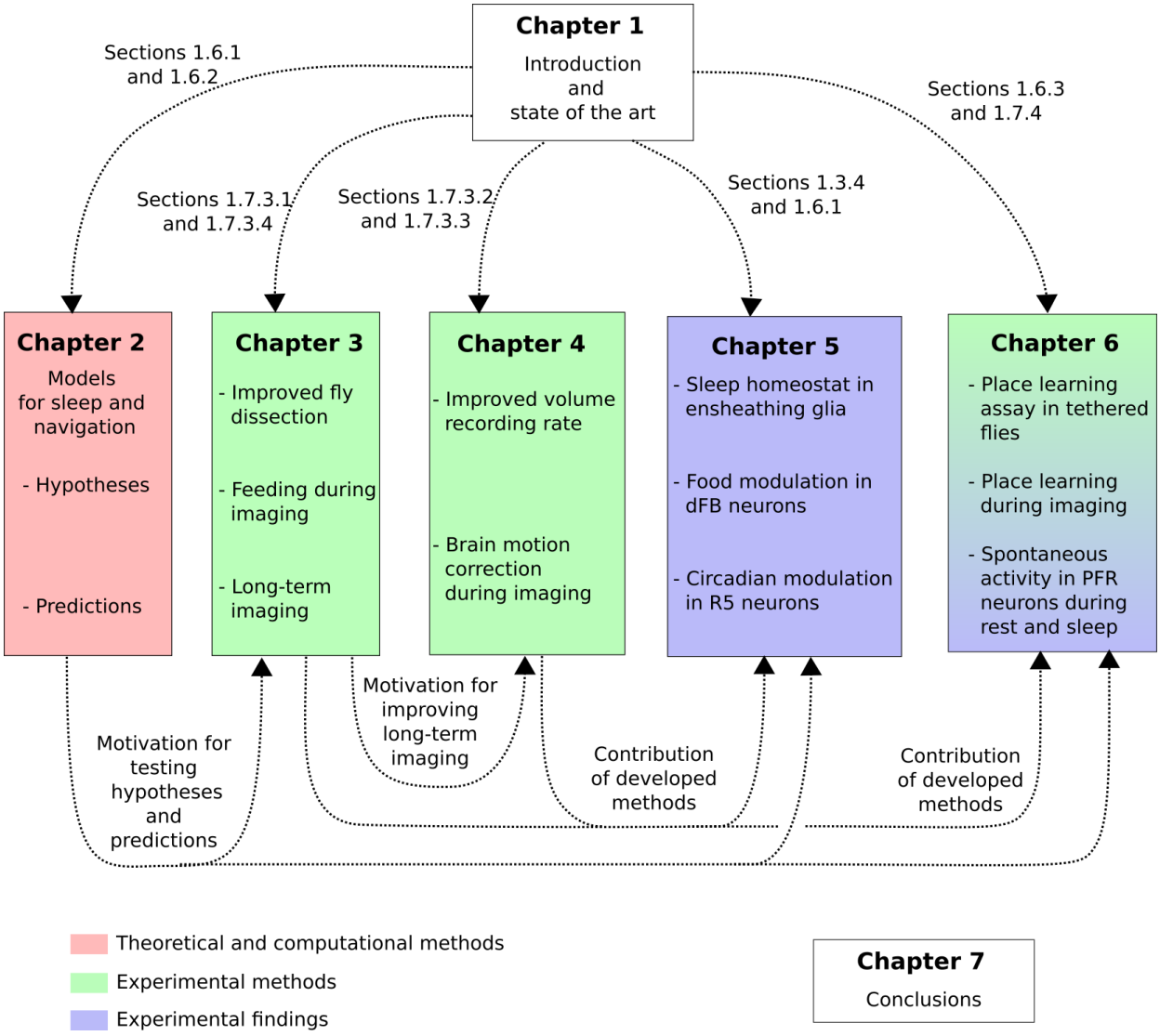


Figure 1.14: Organization of chapters in this thesis. First, Chapter 1 contains the introduction (top). Chapters 2-6 (center) contain a summary of contributions presented in each chapter and is colored depending on the content type, including theoretical and computational methods (red), newly developed experimental methods (green), and novel experimental findings (blue). The most important state-of-the-art sections for each chapter in the introduction are indicated by arrows from Chapter 1. Finally, Chapter 7 (bottom right) contains the conclusions.

naturally occurring sleep episodes in behaving flies. Additional methods for imaging are developed in sections 4.1 and 4.2, in particular for improving the temporal resolution of volumetric recordings [29] and for correcting brain motion over long timescales [30], respectively. In Chapter 5, the developed techniques are used for testing the role of the most relevant neural populations of the proposed sleep homeostasis circuit for the first time during behavior. This chapter further describes for the first time the dynamics of a cellular sleep homeostat during wakefulness and sleep [31]. To investigate the effects of sleep on learning, section 6.1 in Chapter 6 describes the development of an assay for spatial and visual learning in tethered walking flies behaving in a novel virtual reality setup [32]. Finally, section 6.2 describes the dynamics of a neural population involved in the head direction system of the fly, which shows autonomous activity when the fly is standing still or sleeping. Such activity is reminiscent of the autonomous dynamics predicted by the computational model developed in Chapter 2. Section 6.2 further characterizes the dynamics of these neurons during learning using the assay developed in section 6.1, while simultaneously recording neural activity.

Chapter 2

Integration of sleep and navigation in Drosophila

Neural circuits with different functionalities have been described in the central complex, for sleep control and for navigation, respectively. A subclass of ring neurons (R5) is important for sleep homeostasis, integrating time spent awake by increasing their activity and synaptic strength, and resetting during sleep [123, 125, 186]. R5 neurons innervate the ellipsoid body (EB), as do other types of ring neurons that convey visual information to the EB [155, 430]. This visual information is used to estimate head direction, encoded by compass or EPG neurons, with respect to visual landmarks [155, 312, 313, 431, 432]. However, compass neurons, which are an essential component of the ring attractor network in the fly [313, 315], receive not only input from visual ring neurons, but also from R5 neurons [305].

Given the anatomical connection of R5 and EPG neurons and their different functionalities, sleep homeostasis and navigation, respectively, the question arises as to how and why sleep homeostasis and the head direction system interact. From a mechanistic point of view, it needs to be addressed in particular how a wake-related increasing activity from R5 neurons can be integrated into the ring attractor network without interfering with its functionality, and in turn, how the ring attractor network could generate an increasing activity in R5 neurons that encodes sleep need.

This chapter first describes the proposed sleep homeostasis circuit in the central complex [125] with rate-based models. Then, using dynamical systems theory, both analytical and numerical models that describe the interaction between the sleep homeostat in R5 neurons and the ring attractor network are developed. This model is constrained by anatomical connectivity [93] and physiological experiments [123, 125, 186]. The model provides several hypotheses and predictions with regard to the interplay between sleep homeostasis and the head direction system. For example, the model predicts the presence of autonomous or drift activity in head direction system during sleep, which serves as a mechanism to clear attractor states that develop during wakefulness. These predictions and hypotheses motivate

the creation of new methods and imaging experiments in the following chapters.

This chapter contains the following peer-reviewed publication:
[27] **Flores-Valle, A., Gonçalves, P.J. and Seelig, J.D.** Integration of sleep homeostasis and navigation in Drosophila. PLoS Computational Biology 17.7 (2021): e1009088.

Author	**Contribution in [27]**
Flores-Valle, A.	- Conceptualization - Investigation - Methodology - Analysis - Visualization - Writing
Gonçalves, P.J.	- Conceptualization - Supervision - Writing
Seelig, J.D.	- Conceptualization - Supervision - Writing

2.1 Abstract

During sleep, the brain undergoes dynamic and structural changes. In *Drosophila*, such changes have been observed in the central complex, a brain area important for sleep control and navigation. The connectivity of the central complex raises the question about how navigation, and specifically the head direction system, can operate in the face of sleep related plasticity. To address this question, we develop a model that integrates sleep homeostasis and head direction. We show that by introducing plasticity, the head direction system can function in a stable way by balancing plasticity in connected circuits that encode sleep pressure. With increasing sleep pressure, the head direction system nevertheless becomes unstable and a sleep phase with a different plasticity mechanism is introduced to reset network connectivity. The proposed integration of sleep homeostasis and head direction circuits captures features of their neural dynamics observed in flies and mice.

2.2 Introduction

Sleep affects many different brain functions such as cognition [43] or working memory [433] and sleep dysfunction is related to a range of diseases [434]. Sleep is observed across species and different hypotheses have been put forward to explain the function of sleep [395], for example reverse learning of spurious network states (that were created as a byproduct of intended memories) [411, 412, 414] or weakening of synapses (synaptic homeostasis hypothesis) [435].

The function of sleep is linked to the dynamic and structural changes that it induces in the brain [183], which in turn are monitored by sleep control or sleep homeostasis circuits [20, 436]. The circuits that control sleep are distributed over many different brain areas and cell types [436]. Thanks to the genetic tools [15, 16] that allow dissecting neural circuits into small populations of genetically identified cell types, as well as more recently the fly connectome [437], *Drosophila* has emerged as a valuable model for sleep control [20, 23, 94, 107].

A generic sleep control circuit has been linked to specific neural populations in the brain of *Drosophila* [125]. This circuit has three components and corresponding neural populations in the central complex (Fig. 2.1A). A first component encodes sleep pressure. The corresponding neural population has been identified in the so called R5 ring neurons which arborize in concentric rings in the ellipsoid body [123], a substructure of the central complex. These R5 neurons increase both their activity and synaptic strength over waking time and are reset with sleep. A second component of the sleep control circuit executes the switch between sleep and wakefulness (depending on the amount of sleep pressure). The corresponding neural population has been associated with the dorsal fan-shaped body (dFB) neurons, which promote sleep when active [169]. A third component triggers locomotion,

processes visual input, and increases sleep pressure [125] and the corresponding neurons are so called helicon cells [125], also identified as ExR1 neurons [438]. The proposed recurrent circuit between these three neural populations[125] is illustrated in Fig. 2.1A.

The same central complex structures involved in sleep have also been shown to be important for navigation. In particular, ring neurons with similar morphology to the sleep-related R5 ring neurons, provide sensory input to the head direction system, such as visual features [146, 155] or wind direction [319]. Such input is integrated in so called wedge neurons, which arborize in different wedges of the ellipsoid body, where they intersect with ring neurons. These wedge neurons encode the head direction of the fly through a bump of activity that moves around the ellipsoid body [313].

In the context of navigation, the structure and function of circuits in the central complex are reminiscent of ring attractor networks [313]. Such networks, which are well suited to encode a circular variable, have been suggested to underlie the encoding of head direction, originally in mammals [439] and more recently in flies [313]. Several computational models for the head direction system in the insect brain have been developed (see for example [440, 441, 442]).

It is currently unknown why the circuits for sleep homeostasis and head direction converge in the central complex. The morphological similarity of the ring neurons involved in sleep and head direction and the spatial proximity of the circuits as well as the fly connectome [437], suggest that they interact. The observed activity and structural changes in R5 ring neurons after prolonged waking time and after sleep [123, 186, 207] suggests that the head direction system in the ellipsoid body needs to operate in the face of substantial synaptic and functional changes in connected circuits.

Motivated by this interaction between navigation and sleep homeostasis circuits as well as their plasticity [123, 186, 207], we here use theoretical modeling to investigate how these two circuits can be understood as a combined system. For this purpose, we first model the circuit proposed in [125] and confirm that it generates sleep homeostasis. We then extend the model by combining it with a head direction network as suggested by the connectome. In this combined model, the sleep pressure-encoding R5 neurons balance Hebbian plasticity introduced in the recurrent connections of the head direction system. In this way, R5 neurons maintain a functioning head direction system and record sleep pressure. The system is finally reset through a sleep phase.

We discuss how this model can integrate several experimental observations on the navigation and sleep homeostasis systems reported in the literature. We further discuss several predictions of the model that can be tested in experiments. This analysis contributes to an understanding of the generation and dynamics of sleep drive and links the control of sleep to sleep function.

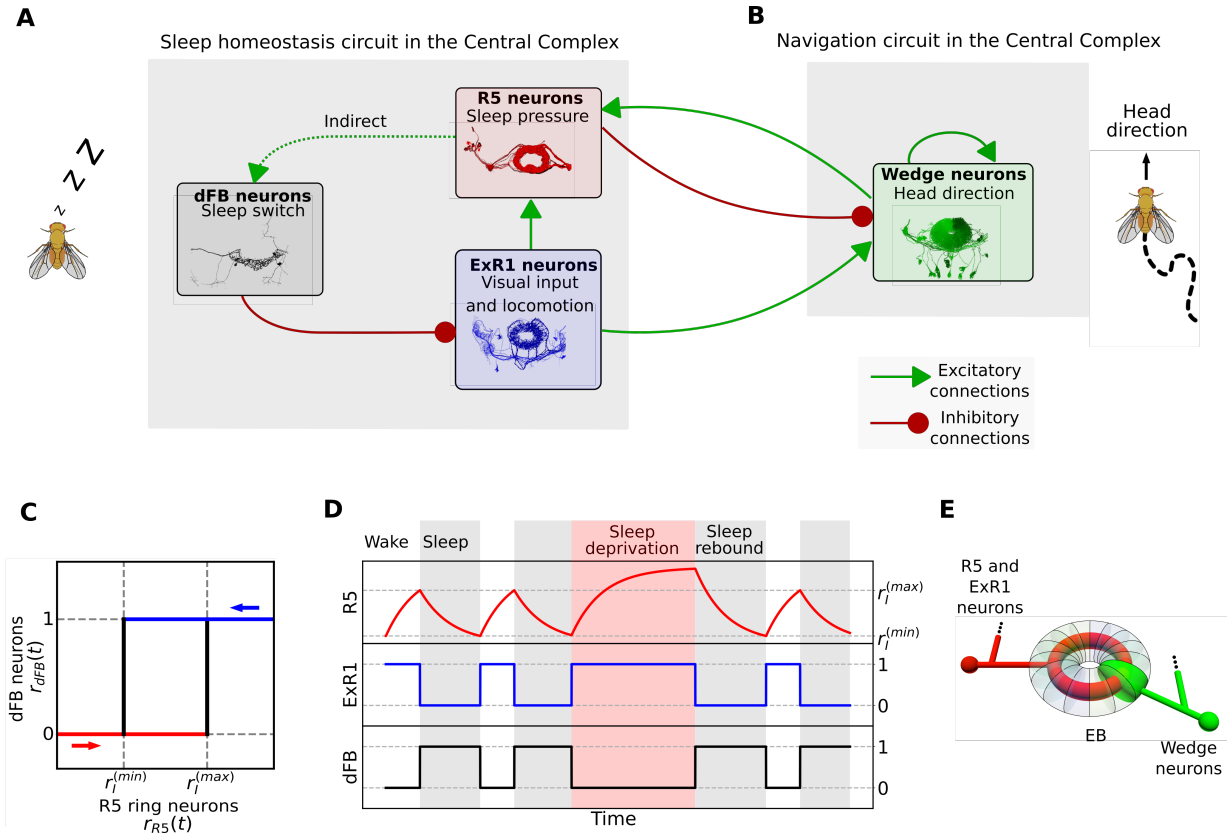


Figure 2.1: Sleep homeostasis and navigation circuits in the central complex. A: Recurrent sleep homeostasis circuit proposed in [125]. The three populations are connected via excitatory (green arrows) or inhibitory (red arrows) connections. Images are downloaded from the connectome database [437]. B: Interaction between the fly head direction circuit and populations involved in sleep homeostasis. C: Switch behavior of dFB neurons modeled with hysteresis. D: Simulation of the sleep homeostasis model illustrating the dynamics of each population over time. E: Schematic of connectivity between wedge neurons and R5 and ExR1 neurons in the ellipsoid body.

2.3 Results

2.3.1 Sleep homeostasis model

The sleep homeostasis model proposed in [125] is a variation of the two-process model [267, 269] and is illustrated in Fig. 2.1A. All connections between populations are direct [125], except the connection between R5 and dFB neurons, which is considered indirect since these neural populations are not anatomically, but functionally connected [123]. Here, we describe this circuit with a phenomenological model (Eq (2.1) in Methods).

The variables $r_{R5}(t)$, $r_{ExR1}(t)$ and $r_{dFB}(t)$ represent population firing rates of R5 neurons, ExR1 neurons and dFB neurons, respectively. R5 neurons have a time constant that accounts for the slow dynamics (on the order of hours) of their activity observed during wak-

ing time [123], whereas ExR1 and dFB neurons have an effective population time constant in the millisecond range. For simplicity, the model is defined such that population firing rates are between 0 and 1. The input to dFB neurons, e.g. representing a wake-promoting dopaminergic signal [308], takes values 0 or 1. The function which depends on the history of activity of R5 neurons and produces the observed switching behavior in dFB neurons [125], is described by a simple hysteresis (Fig. 2.1C; Eq (2.2)).

Fig. 2.1D shows a simulation of this model with the population firing rates changing over time. The sleep and wake phases are defined in terms of the activity of dFB neurons, which promote sleep while active [169]. During the wake phase, activity in R5 neurons increases, encoding sleep pressure due to sustained constant input from ExR1 neurons. After R5 neurons reach an upper threshold, $r_I^{(max)}$, dFB neurons 'switch on' and inhibit activity in ExR1 neurons, which leads to a decrease in activity of R5 neurons. Once R5 activity reaches a lower threshold, $r_I^{(min)}$, dFB neurons switch off, repeating the cycle. Sleep deprivation (by setting a longer inhibitory input to dFB neurons; red region in Fig. 2.1D) leads to an increase of the activity of R5 neurons beyond $r_I^{(max)}$. As expected for a sleep homeostasis circuit, after sleep deprivation, more time is required to reset the activity of R5 neurons back to $r_I^{(min)}$ (sleep rebound; see Methods 2.5.3).

2.3.2 Connectivity between head direction and sleep circuits

While the circuit described above can produce sleep homeostasis, the connectome [437] shows that it acts not in isolation but interacts with the head direction system. Fig. 2.1A and B show how R5 and ExR1 neurons are connected to wedge neurons that encode head direction. The anatomical organization of wedge, R5 and ExR1 neurons is shown schematically in Fig. 2.1E, where each wedge neuron arborizes in a different wedge along the ellipsoid body, and R5 and ExR1 neurons arborize in concentric rings. The wedge neurons that encode head direction have been identified as EPG neurons [313], but a similar population of wedge neurons, called EL [437, 443] or AMPG-E [444], could also potentially encode head direction. These neurons have been proposed to contribute to the persistent activity in the network by excitatory feedback to EPG neurons [444]. These neurons can mediate a connection between R5 and EPG neurons that is stronger than the direct connection between R5 and EPGs. In the following, wedge neurons refer to both EPG and EL populations without distinction. We assume that both encode head direction and are directly or indirectly connected to R5 neurons. In Supplementary Fig. S2.1, we show recurrent connections between wedge neurons (Supplementary Fig. S2.1A), between wedge and R5 neurons (Supplementary Fig. S2.1B), and between wedge and ExR1 neurons (Supplementary Fig. S2.1C) according to the connectome [437] .

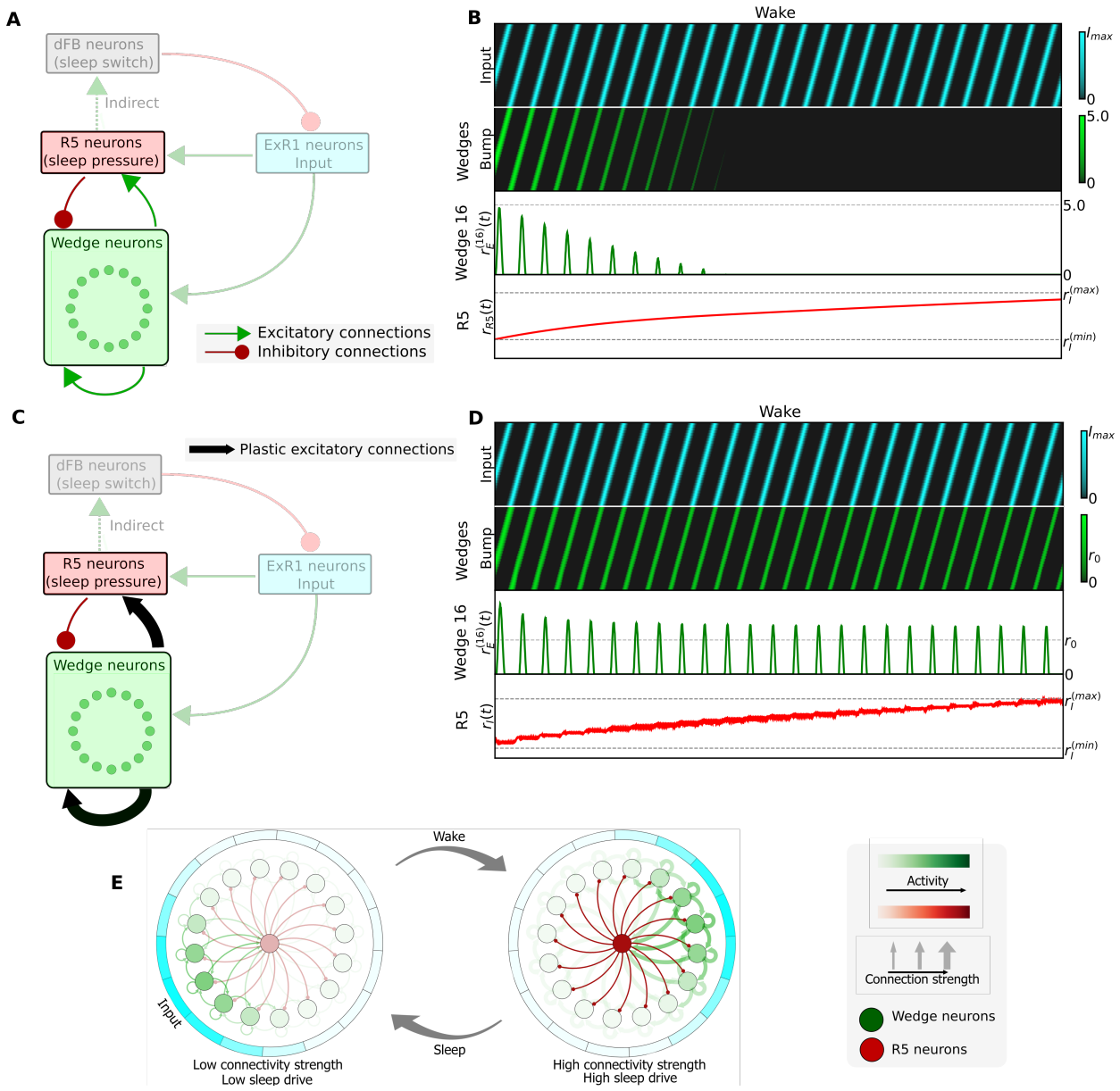


Figure 2.2: Integration of the sleep homeostasis circuit with a ring attractor network. A: Schematic of a model where wedge neurons are connected to the sleep homeostasis circuit according to the fly connectome (see Supplementary Fig. S2.1). In this model, fixed connections are assumed. B: Simulation of the model in A (dFB neurons not shown). Top row: rotating input to the ring attractor with frequency 0.5 Hz. Second row: bump of activity in wedge neurons encoding head direction. Third row: activity of the wedge neuron 16 (representative of any other wedge neuron). Fourth row: increasing activity of R5 neurons. C: Model with plastic connections indicated by black arrows. D: Simulation of the model in C (see caption in B). E: Dynamics of the model with plasticity: after a wake phase, high connectivity strength in the ring attractor leads to high sleep drive in R5 neurons, which leads to a switch to the sleep phase. After sleep, connectivity strength in the ring attractor is reset, producing low sleep drive.

2.3.3 Integration of sleep homeostasis and navigation circuits with fixed connections

The interaction of the sleep homeostasis and ring attractor circuits extracted from the fly connectome is shown schematically in Fig. 2.2A. Given that R5 neurons and wedge neurons are bidirectionally connected (see Supplementary Fig. S2.1B), we first asked how increasing activity of R5 neurons during the wake phase (see Fig. 2.1D, first row) affects the head direction network. We therefore combined a ring attractor network with the above sleep homeostasis model (section 2.3.1) according to the connectivity in Fig. 2.2A. As in previous work [315, 445], we identify wedge neurons as the excitatory component of a ring attractor network with recurrent excitation, encoding head direction with sustained bump-like activity. On the other hand, we assume that R5 neurons provide inhibition to wedge neurons [311], in agreement with the majority of ring neurons being inhibitory [446, 447]. For simplicity, we assume that ExR1 neurons, which are bidirectionally connected to wedge neurons, provide input (for example, visual input [23]) to the ring attractor similar to other ring neurons.

Fig. 2.2B shows the activity of wedge neurons and R5 neurons with a rotating input, representing any input to the ring attractor, such as visual or idiothetic cues (in blue, first row), which as expected moves the bump around the ring attractor (in green, second row). Increased activity in R5 neurons, as experimentally observed with increased sleep drive, decreases the bump amplitude in the ring attractor until it finally vanishes. Therefore, simply connecting R5 and wedge neurons as indicated by the connectome, leads to a decreasing bump of activity over time (see Methods 2.5.4 for details of this model).

2.3.4 Integration of sleep homeostasis and navigation circuits with plasticity

In Fig. 2.2C, we propose an alternative model that can sustain a stable bump amplitude. In order to overcome a decreasing bump amplitude (which has not been experimentally observed), we hypothesize that the increase of inhibition from R5 neurons, in addition to encoding sleep drive, has the role of compensating for an increase in excitation in the head direction circuit. In particular, we hypothesize that excitatory synaptic strength between wedge neurons increases during the wake phase. This could be due to Hebbian plasticity between wedge neurons, since encoding the head direction in a bump of activity requires several wedge neurons to be active at the same time, thus strengthening the recurrent connections between them. This model is additionally motivated by the experimentally observed increase of activity as well as plasticity in R5 neurons [123]. In agreement with these data, we additionally add Hebbian plasticity from wedge neurons to R5 neurons.

In this model, R5 neurons act as a closed-loop feedback controller that prevents activity

in wedge neurons from increasing due to Hebbian plasticity, by adaptively increasing inhibition. A simulation of this model is shown in Fig. 2.2D where the bump of activity (second and third row) does not decrease as the activity of R5 neurons increases (fourth row). In the context of the sleep homeostasis circuit, dFB neurons then detect synaptic growth in R5 neurons. When R5 neural activity reaches an upper threshold, dFB neurons switch on sleep. We assume that during sleep, the plastic connections are reset with long-term depression (LTD), decreasing activity in R5 neurons (as observed in [123]) and lowering sleep drive (Fig. 2.2E).

2.3.5 Two-population model with plasticity

Before we describe the full ring attractor model with plasticity (Fig. 2.2C and D), we first discuss a population model of wedge and R5 neurons based on an excitatory-inhibitory rate network [448] (Fig. 2.3A; Eq (2.7 in Methods)). As will become clear in the following sections, this simplified model shows overall similar characteristics to the extended ring attractor model. Here, $r_E(t)$ and $r_I(t)$ represent the firing rates of wedge and R5 neuron populations, respectively, at a time t. w_{AB} is the synaptic weight from population B to population A. Note that in this model, and as detailed below, the slow dynamics of R5 neurons will arise from the synaptic plasticity, and thus we do not set the time constant of R5 neurons to be on the order of hours, in contrast with the phenomenological sleep homeostasis model (section 2.3.1).

During the wake phase, we introduce plasticity rules for the excitatory weights, w_{EE} and w_{IE} (Eq (2.8) in Methods). We assume that the dynamics of the plasticity rules are much slower than the dynamics of neural populations, producing long-term plasticity. While the plasticity rule in recurrent connections w_{EE} is a linear Hebbian rule, the one in w_{IE} is a triplet rule with presynaptic threshold; its behavior is similar to the linear Hebbian rule with presynaptic threshold, but it has a quadratic dependency on the presynaptic activity while ensuring no change in w_{IE} if neural activity is zero or presynaptic activity is equal to the setpoint r_0 (see derivation in Methods 2.5.5.1 and in [449]).

The plasticity rules are motivated by our hypothesis that the observed increase in activity and synaptic strength in R5 neurons [123] balance the long-term potentiation in recurrent connections of wedge neurons, w_{EE}. The plasticity rules therefore produce the following effects: (i) The recurrent synaptic connections between wedge neurons, w_{EE}, as well as the connections between wedge and R5 neurons, w_{IE}, get stronger during the wake phase. (ii) The firing rate of R5 neurons r_I increases during the wake phase. (iii) The activity of wedge neurons (which represents head direction) evolves always towards a constant setpoint, $r_E \longrightarrow r_0$. Note that activity is not constrained to the setpoint, but evolves towards it over time, since the setpoint is a stable fixed point for wedge neurons (see Methods). Therefore, the bump amplitude will deviate from the setpoint due to any input (for example visual or

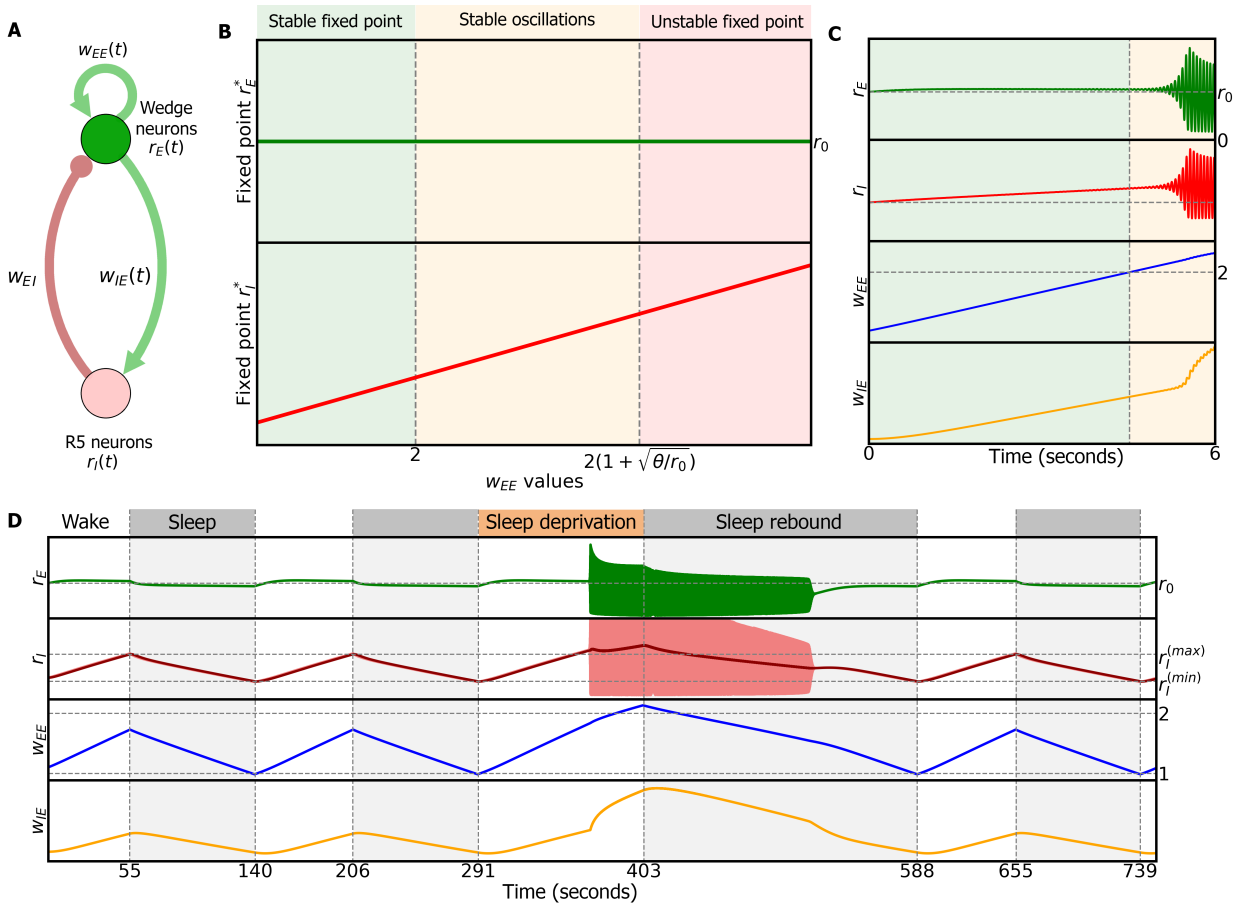


Figure 2.3: Two-population model. A: Model describing the dynamics of the activities of excitatory wedge neurons and inhibitory R5 neurons, r_E and r_I respectively, and the plasticity of the synaptic weights within the wedge population w_{EE} and from the wedge population to the ring population w_{IE}. Green connections are excitatory, red connections inhibitory. B: Stability conditions with respect to w_{EE} (fast-timescale limit, see Methods). C: Dynamics during wake phase. As w_{EE} grows, the system undergoes a Hopf bifurcation (a critical point where the system starts to oscillate) and both populations start to oscillate around a fixed point. D: Dynamics with alternating sleep and wake phases. Wake phase produces LTP in w_{EE} and w_{IE} and increases the activity of R5 neurons. Sleep produces LTD and reduces the activity of R5 neurons. Extending the wake period produces sleep deprivation and results in stable oscillations. The subsequently required sleep period for resetting is longer (sleep rebound).

self-motion related; see Supplementary Fig. S2.3), consistent with experimentally observed behavior-related changes in bump amplitude [450]. These plasticity rules avoid the problem of a vanishing bump amplitude, as observed in the model with fixed connections (compare Fig. 2.2B and D).

How plasticity can drive the observed increase in R5 neuron activity with sleep pressure [123, 186] is currently unknown. Since it is the activity of R5 neurons, and not the plasticity, which is hypothesised to trigger sleep [123, 125, 186], our models assume plasticity that directly modifies the activity of R5 neurons (Fig. 2.3C), a possibility that is consistent with the data in [123].

2.3.6 Dynamics of the two-population model with plasticity

We start by characterizing the dynamics of the two-population model in the wake phase. Since the change in w_{IE} is always coupled to the change in w_{EE}, the dynamics of the system at a given time t are completely described by w_{EE}(t) (fast-timescale limit; see Methods 2.5.5.2 for details). Therefore we can study the stability of the model as a function of w_{EE}.

Fig. 2.3B shows how the fixed point for wedge neurons r_E^* remains constant, and the fixed point for R5 neurons r_I^* increases as the connections w_{EE} (and therefore w_{IE}) get stronger. If $w_{EE} \leq 2$ (light green region), the fixed point (r_E^*, r_I^*) is stable, and both neural populations evolve towards these values. This makes wedge neurons to evolve towards a constant activity, r_0, in agreement with assumption (iii). If w_{EE} increases further, $w_{EE} \leq 2(1 + \sqrt{\theta/r_0})$, the model enters a regime of stable oscillations (light orange region). In this regime, both neural populations oscillate around the fixed point with a frequency that changes with w_{EE} (see Supplementary Fig. S2.2A and Methods 2.5.5.2). Finally, when $w_{EE} \geq 2(1 + \sqrt{\theta/r_0})$ (light red region), the fixed point is unstable and the activity of both populations diverges.

Fig. 2.3C illustrates the dynamics of the full system, i.e. the activity of wedge and R5 neurons, $r_E(t)$ and $r_I(t)$, as well as synaptic weights, $w_{EE}(t)$ and $w_{IE}(t)$. In the beginning (light green region), the fixed point of ring and wedge neurons is stable because $w_{EE} < 2$. When this boundary is crossed, the system enters the regime of stable oscillations (light orange region). Also, in the stable regime, w_{EE} increases due to Hebbian plasticity, and w_{IE} and ring neuron activity r_I increase to balance increasing excitation within wedge neurons, such that r_E remains constant and close to the setpoint r_0.

To limit synaptic growth as well as to avoid instability and oscillations (when $w_{EE} > 2$), we introduce a sleep phase, as proposed by models of sleep homeostasis [125]. In this model, dFB neurons detect the increased activity of R5 neurons and implement a switch between sleep and wake phases. dFB neurons receive as input a low-pass filter of R5 activity, motivated by the fact that R5 and dFB are not anatomically but functionally connected [123] (Eq (2.27)). Additionally, this filtering prevents uncontrollable switching between phases in the oscillatory regime.

During the sleep phase, the synaptic rule in w_{EE} is inverted producing an anti-Hebbian rule. This results in w_{EE} becoming weaker through LTD [411, 412, 414] according to the plasticity rule in Eq (2.9). The plasticity rule for w_{IE} is the same in both sleep and wake phase. The impact of LTD on the model can be understood by inspecting Fig. 2.3B from right to left: with decreasing value of synaptic strength w_{EE}, the fixed points become stable (light green) and the activity of R5 neurons decreases (see Methods 2.5.5.2).

Fig. 2.3D shows a simulation of the model combining subsequent wake and sleep phases. During wake phases (top, white region), dFB neurons are inactive ($r_{dFB}(t) = 0$, not shown), and during sleep phases (grey region) dFB neurons are active ($r_{dFB}(t) = 1$). During wakefulness, w_{EE} and w_{IE} undergo LTP and the activity of R5 neurons increases (light red line in second row in Fig. 2.3D) and r_E is constant.

When the switching signal (dark red line in second row) crosses an upper threshold, $r_I^{(max)}$, dFB neurons switch the model to sleep. During sleep, w_{EE} undergoes LTD due to the switch in plasticity, while the activity of R5 neurons decreases. Note that we do not change the plasticity rule of w_{IE}, since this rule ensures w_{IE} to always follow the trend (potentiation or depression) of w_{EE} in order to maintain the activity of wedge neurons, $r_E(t)$, at a setpoint.

Once the switching signal reaches the lower threshold, the model switches back to the wake phase. Furthermore, if we prevent dFB from switching to the sleep phase (see Methods) and thus extend the wake period (sleep deprivation, upper orange region, Fig. 2.3D), w_{EE} crosses the boundary for stability, $w_{EE} > 2$, and the model enters the regime of stable oscillations. In the subsequent sleep phase, more time is required to reset the excitatory weights, w_{EE} and to reach the lower threshold $r_I^{(max)}$, resulting in sleep rebound (Fig. 2.3D, sleep phase after sleep deprivation).

The time that the system spends in the sleep and wake phases is determined by the time constant of the plasticity rule in w_{EE}, τ_{EE} (see long-timescale limit in Methods 2.5.5.2), and the upper and lower thresholds of the switching signal, $r_I^{(min)}$ and $r_I^{(max)}$. In our simulations, we set τ_{EE} to yield dynamics on the timescale of seconds (for ease of visualization), but larger values lead to similar behavior on longer timescales (minutes or hours)

2.3.7 Ring attractor model with plasticity

We now extend the two-population model to a full ring attractor model (Eq (2.28)). The network, shown schematically in Fig. 2.2C, is implemented with $N = 32$ wedge neurons (based on anatomy [304]).

Here, $r_E^{(i)}(t)$ is the firing rate of wedge neuron i at time t (Fig. 2.4A). For simplicity, we model the population of R5 neurons with a single variable, $r_I(t)$. w_{AB} is the matrix of synaptic weights from population B to population A, and w_{EE} is initialized with a Gaussian function that depends on the distance between wedge neurons along the ring. The Gaussian

has two parameters, the maximum amplitude, $w_{EE}^{(max)}$, and the standard deviation σ (Eq (2.31)). Fig. 2.4A illustrates the connectivity from all the wedge neurons to wedge neuron 16. Additionally, each wedge neuron receives a time-varying input (for example, visual or idiothetic input). This input encompasses input from ExR1 neurons as well as from others populations. We assume that this input can be inhibited by dFB neurons, as in the sleep homeostasis model (section 2.3.1), and is defined as a Gaussian function where the peak is located at a given wedge neuron (Eq (2.32) in Methods).

The inhibition of input to wedge neurons during sleep is motivated by the fact that the fly does not move during sleep, suggesting that self-motion inputs are not present. On the other hand, ExR1 neurons, which contribute to visual processing and locomotion, are inhibited by dFB neurons during sleep [125]. We hypothesize that other neural populations providing visual input to the ring attractor [155] might require coincident activity from ExR1 neurons to reliably transmit visual information. This information might not be transmitted during sleep because of the suppressed ExR1 neural activity. This is consistent with the idea of an increased arousal threshold during sleep, where stronger stimuli are required to produce a behavioral response [451].

The plasticity rules during the wake phase in recurrent connections between wedge neurons, w_{EE}, and from wedge to R5 neurons, w_{IE} are a direct extension of the ones in the two-population model (Eq (2.29)).

Similar to the two-population model, the dynamics of the ring attractor network are determined by the recurrent excitatory weights $w_{EE}(t)$. In particular, the stability of a bump of activity centered around wedge neuron i is determined by the total excitatory connectivity towards it, $w_{EE}^{(i,sum)}(t)$, defined by Eq (2.37) (Fig. 2.4A). Here and in the following, we focus our analysis on wedge neuron $i = 16$, but the results generalize to all wedge neurons.

Fig. 2.4B shows the different dynamic regimes of the bump as a function of the parameters $w_{EE}^{(max)}$ and σ that determine the values of w_{EE} (see Methods (2.5.7) and Supplementary Fig. S2.5).

The colored lines in Fig. 2.4B are isolines of constant $w_{EE}^{(16,sum)}$, and correspond to the boundaries of distinct dynamics of the bump of activity in wedge neurons.

The boundaries are similar to the ones found in the simpler two-population model (section 2.3.5). The bump is stable around wedge neuron 16 if $1 < w_{EE}^{(16,sum)} < 2$. As the recurrent weights $w_{EE}^{(ij)}$ increase due to LTP during the wake phase, so do σ and $w_{EE}^{(max)}$. The bump starts to oscillate if recurrent connections are too strong, i.e. $w_{EE}^{(16,sum)} > 2$. When $w_{EE}^{(16,sum)} > 2(1 + \sqrt{\theta/r_0})$, the bump keeps oscillating with very low activity in wedge neurons, in contrast to the instability encountered in the two-population model (see Methods 2.5.7).

Fig. 2.4C illustrates the dynamics of the system with a bump centered in wedge neuron

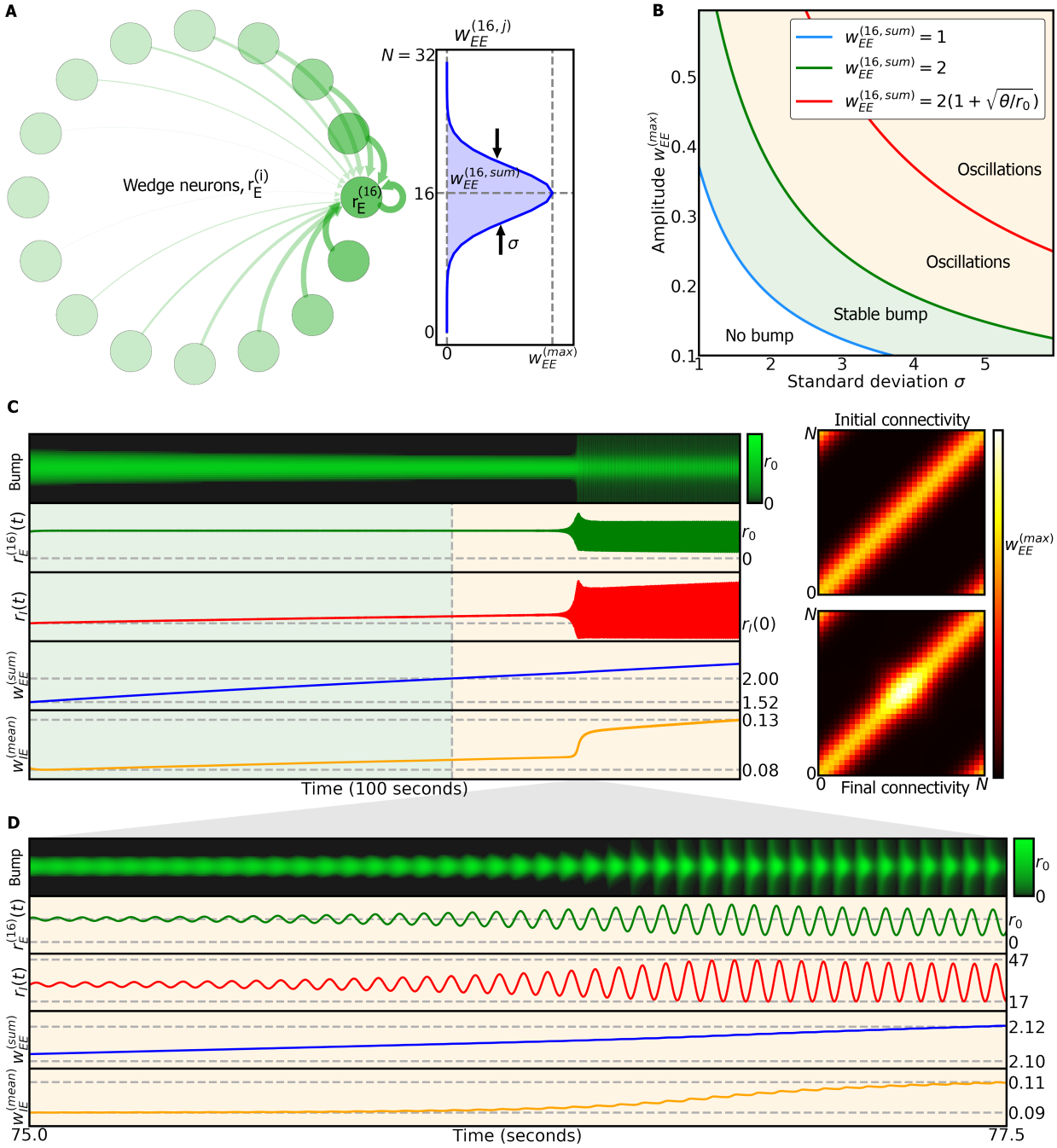


Figure 2.4: Dynamics of ring attractor network during wake phase. A Left side: representation of excitatory connections from all wedge neurons to wedge neuron $r_E^{(16)}$. Right side: Gaussian connectivity from all wedge neurons to wedge neuron 16, with maximum amplitude $w_{EE}^{(max)}$ and standard deviation σ. B Model dynamics obtained in the fast-timescale limit (see Methods(2.5.7)) depend on the parameters of the excitatory connectivity, $w_{EE}^{(max)}$ and σ. C Left side: dynamics during wake phase of the ring attractor model where the bump is located around wedge neuron 16. When the total excitatory weight, $w_{EE}^{(16,sum)}$, crosses a threshold, the bump starts to oscillate. Right side, top: initial excitatory connections between wedge neurons. Right side, bottom: final excitatory connections between wedge neurons; changes are a result of synaptic plasticity. D: Blow-up of the simulation in C, during the transition to the oscillatory regime.

16 (first row): since the active wedge neurons that form the bump have correlated activity, some entries in the recurrent connectivity matrix, w_{EE}, increase due to Hebbian plasticity. Therefore the total excitatory connectivity to wedge neuron 16, $w_{EE}^{(16,sum)}$, increases (fourth row). On the other hand, the weights $w_{IE}^{(i)}$ (represented by the mean) also increase (fifth row), leading to increased activity of R5 neurons (third row), which in turn maintains the amplitude of the bump in wedge neuron 16 constant at the setpoint r_0 (second row).

When $w_{EE}^{(16,sum)} > 2$, the bump starts to oscillate, as do R5 neurons (orange region in the last four rows) (see Fig. 2.4D for a blow-up of the transition to oscillations). In addition, the plasticity rule in the recurrent connections w_{EE} leads to an increase of the synaptic weights around the bump position (Fig. 2.4C, right side, top versus bottom).

As in the two-population model, we introduce a sleep phase to reset the connections in the ring attractor network by using the anti-Hebbian plasticity rule (Eq (2.30)). This rule produces LTD with correlated activity between neighboring wedge neurons. Fig. 2.5A shows a simulation of this model. Again, during wake phases (top, white region) dFB neurons are inactive ($r_{dFB}(t) = 0$, not shown), and during sleep phases (grey region) dFB neurons are active ($r_{dFB}(t) = 1$). In the wake phase, a rotating input with a constant frequency of $0.5Hz$ is provided; the input reverses direction between consecutive wake phases (top row). As in the two-population model, the switching is driven by a low-pass filter of R5 activity (see Eq (2.27)). During the sleep phase, the input to wedge neurons is inhibited.

During the wake phase, the bump in the ring attractor closely follows the input (second row), while the activity of R5 neurons increases (light red line in the fourth row). The second to last row shows the increasing diagonal elements of w_{EE} while the last row shows an increasing w_{IE}. During sleep, the autonomous bump movement resets synaptic connections and the activity of R5 neurons decreases. Heterogeneity in the weights w_{EE} (due to synaptic plasticity) makes the bump drift across wedge neurons. These autonomous dynamics reset the connectivity in the network[414]. The amplitude of the bump during autonomous dynamics is at setpoint level, that is, at the activity level in the absence of external input.

As in the two-population model, the time duration of wake and sleep phases depends on τ_{EE}, $r_I^{(min)}$ and $r_I^{(max)}$. This simulation shows sleep and wake phases on the order of seconds, for ease of visualization, but the simulation in Supplementary Fig. S2.7, with an increased τ_{EE}, shows slower dynamics with sleep phases of 100 minutes, which is the mean sleep time of flies during the night [452].

Wake phases without continuous input can also show drift (see Supplementary Fig. S2.8 with intermittent input). This wake drift is however different from sleep drift, since it ends once the bump reaches the location of strongest recurrent excitation, making the synaptic weights grow in this location until sleep is initiated. Such wake drift can be reduced in our model by slowing the plasticity rules and by ensuring close to homogeneous coverage of the bump movement across all wedge neurons (see Supplementary Fig. S2.9 and Methods (2.5.9)).

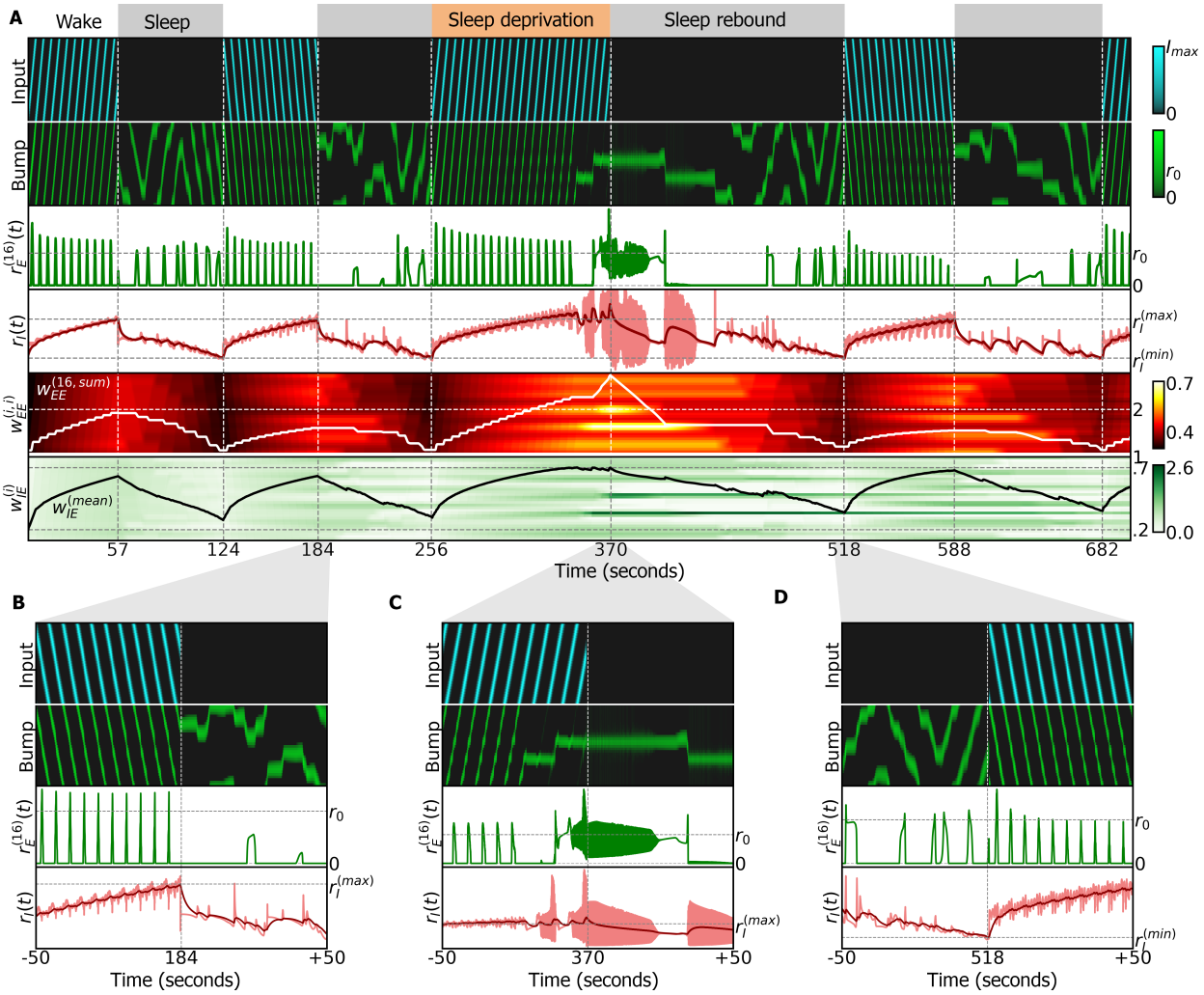


Figure 2.5: Simulation of ring attractor combined with sleep homeostasis model, using an anti-Hebbian plasticity rule during sleep. A: Entire simulation over a period of 700 seconds. White and grey regions indicate the wake and sleep phases, and correspond to dFB neurons switching off and on, respectively. Top row: input (inhibited during the sleep phase), alternating between clockwise and counter-clockwise rotations at $0.5Hz$. Second row: ring attractor bump activity. Third row: activity of wedge neuron 16. Fourth row, light red: activity of R5 neurons. Dark red: filtered activity. Switching between sleep and wake is carried out by dFB neurons that switch on and off depending on filtered activity crossing thresholds $r_I^{(min)}$ and $r_I^{(max)}$. In the third wake epoch, sleep deprivation is produced by extending the inhibition of dFB neurons ($d(t) = 1$ during the orange top layout; see Methods). Fifth row: diagonal elements of the connectivity matrix $w_{EE}^{(ij)}$. The white line is the sum of all excitatory connections to wedge neuron 16. It passes threshold 2 at around 240 seconds leading to oscillations. The full connectivity matrix $w_{EE}^{(ij)}$ at the switch times is shown in Supplementary Fig. S2.6. Sixth row: connectivity $w_{IE}^{(i)}$; black line is the mean value. B: Blow-up around 184 seconds: switch from wake to sleep phase. C: Blow-up around 370 seconds: extended wake phase leads to oscillatory behavior. Circuit switches to sleep. D: Blow-up around 518 seconds: switch from sleep to wake phase.

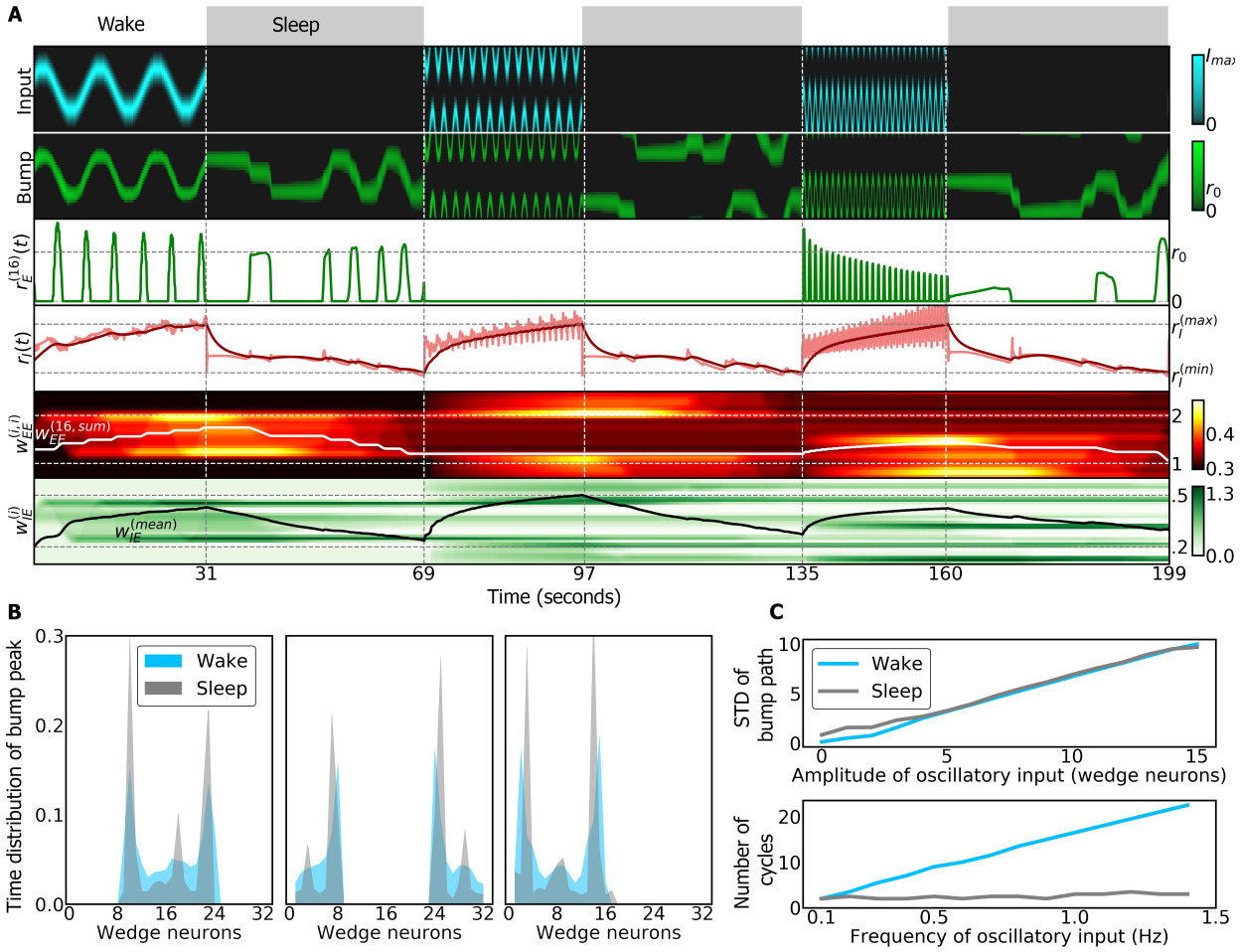


Figure 2.6: Relation between wake and sleep dynamics in the ring attractor network. A: In each wake phase, a sinusoidal input is provided to the ring attractor (top row) with increasing frequency in consecutive wake phases. During sleep, an autonomous bump of activity revisits wedge neurons active in the previous wake phase (second row). The third row shows the activity of wedge neuron 16 and the fourth row shows the activity of the ring neuron (light red) and its filtered activity (dark red) used to switch between wake and sleep phases. The last two rows represent the synaptic weights that increase during wakefulness and decrease during sleep. B: Normalized distribution of time that the bump peak is localized in each wedge neuron during wake (blue) and sleep (grey) phases. The first, second and third plots show the distribution for the first, second and third wake and sleep phases, respectively. C: Top: standard deviation (STD) of the bump path during a total of 15 simulations where different amplitudes of a sinusoidal inputs are provided during the wake phase. During the wake phase, the STD of the bump path is proportional to the input amplitude (grey). During sleep, the autonomous bump path has a correlated STD (Pearson correlation coefficient: 0.99 ($p = 1.5 \cdot 10^{-17}$). Bottom: number of cycles of the bump path during a total of 15 simulations with different frequencies of a sinusoidal input during wake phase. During the wake phase, the number of cycles is proportional to the input frequency. However, during sleep, the number of cycles does not change with the input frequency.

2.3.8 Autonomous dynamics in the ring attractor model

To investigate how the autonomous dynamics of the bump during sleep are linked to the dynamics during the preceding wake phase, we provided sinusoidal inputs in a range of amplitudes A and frequencies f. In Fig. 2.6A, we show a simulation with fixed amplitude, $A = N/4$ and different frequencies in each wake phase ($0.1, 0.5$, and 1 Hz). During sleep, the bump revisits wedge neurons that were active in the preceding wake phase, as seen in the distributions of the time spent around each wedge neuron during the first (left), second (center) and third (right) wake phase (in blue), and during the following sleep phase (in grey) (Fig. 2.6B). To further probe the amplitude dependence, we simulated a wake phase and the subsequent sleep phase, and in each simulation varied the amplitude A of a sinusoidal input in the range $[0, 16]$, with fixed frequency of $f = 1Hz$, during the wake phase. The standard deviation (STD) of the paths of the bump during the wake (blue) and sleep (grey) phases closely match (Fig. 2.6C). Similarly, we investigated the frequency dependence with a stimulus with fixed amplitude, $A = N/4$, and varying frequency in the range $[0.1, 1.5]Hz$. The number of oscillatory cycles grows linearly with the input frequency in the wake phase (blue), but remains constant during sleep. Therefore, the dynamics during sleep do not depend on the input frequency during the wake phase (Fig. 2.6C). Additionally, the frequency of oscillations of the bump around the ring can increase as the bump approaches the lower threshold of the switching signal (before waking up, Supplementary Fig. S2.9A). Overall, the autonomous dynamics of the model are reminiscent of activity observed during sleep in mice [453].

	Model hypothesis
i)	The bump amplitude in wedge neurons evolves towards a setpoint in the absence of changing input (r_E evolves towards a setpoint, r_0)
ii)	Plasticity in recurrent connections between wedge neurons (w_{EE}): - LTP during the wake phase - LTD during the sleep phase
iii)	R5 neurons keep the bump amplitude constant over long-timescales. R5 neurons balance plasticity in wedge neurons (w_{EE}) with plasticity (w_{IE}) and increasing/decreasing activity (r_I)

	Model prediction
i)	Prolonged wakefulness leads to oscillations in both wedge and R5 neurons
ii)	Prolonged wakefulness prevents wedge neurons from tracking external inputs
iii)	During sleep, wedge neurons show autonomous dynamics
iv)	The width of the bump changes over long-timescales: - decreases during the wake phase - increases during the sleep phase

Table 2.1: Model hypothesis and predictions.

2.4 Discussion

In the brain of *Drosophila*, structurally similar neurons in the center of the brain have been assigned functionally very different roles. On the one hand, navigation related ring neurons encode spatial memory or visual features [146, 155, 332]. For these ring neurons, ring attractor networks offer a compelling structure-function relationship which can provide a rationale for their ring-shaped morphology. On the other hand, sleep related ring neurons serve as homeostatic sleep integrator, encoding sleep drive through structural [123, 207] and activity changes [123, 186]. The connectome additionally shows multiple interactions between these sleep- and navigation-related circuits [437, 443].

To elucidate the relationship between these navigation and sleep functionalities of ring neurons, and to address how the head direction system can operate in the face of plasticity in connected circuits, we therefore asked what role the homeostatic integrator could play in the ring attractor framework.

To address this question, we used the sleep homeostasis model proposed in [125] as a starting point. The connectome shows that this circuit is not isolated but interacts with the head direction system (Fig. 2.2A). When connectivity in this circuit is fixed, however, the increasing activity of R5 neurons (which encode sleep drive) decreases the amplitude of the bump of activity in the ring attractor (Fig. 2.2D). To overcome this problem of vanishing activity, we therefore propose a model with plasticity in R5 neurons (which is experimentally observed) and with hypothesized recurrent plasticity between wedge neurons. In this model (Fig. 2.2C), sleep drive balances plasticity in wedge neurons, which are now able to maintain a bump of activity that evolves towards a constant amplitude setpoint over long-timescales. The model also allows variability in the bump amplitude in short-timescales with external

(for example visual or self-motion related) input (Supplementary Fig. S2.3), consistent with experimentally observed behavior-related changes in bump amplitude[450].

However, prolonged activity during wakefulness ultimately leads to unstable behavior (oscillations in Figs 2.4C and 2.5A). Therefore, to restore the connectivity in the head direction system to baseline, we introduced a sleep phase, in agreement with models of sleep homeostasis [125], where the synaptic connections between wedge neurons are reset by LTD. While the time course and dynamics of this reset are not known, we here investigated two alternatives. In one case, while dFB neurons inhibit input, the ring attractor resets to its initial state while the bump stays in place (Supplementary Fig. S2.10). In the second case, an anti-Hebbian rule resets the ring attractor with autonomous dynamics. These dynamics are linked to the dynamics during wakefulness through their spatial (Fig. 2.6A and 2.6B) but not through their frequency distributions (Fig. 2.6A and 2.6C). The amplitude of the bump during autonomous dynamics is at setpoint level, that is, at the level of activity to which the amplitude settles in the absence of (visual or idiothetic) input.

In the proposed model, heterogeneities in recurrent connections of wedge neurons can also lead to drift during the wake phase with intermittent inputs (see Supplementary Fig. S2.8). While this is consistent with the heterogenities observed in the connectome (Supplementary Fig. S2.1B), we maintained a low drift by having plasticity rules with sufficiently slow dynamics and assuming homogeneous activation of wedge neurons over time (Supplementary Fig. S2.9). Other solutions to avoid drift in ring attractors have however been developed (for example [427, 428, 429]).

Many aspects of this model can also be captured by a simpler two-population model, which shows similar dynamics and related boundaries between the different dynamic regimes (Figs 2.3B and 2.4B).

The introduction of plasticity was motivated by the observation of structural, synaptic and functional changes in R5 neurons [123, 186, 207] as well as their interaction with the head direction system as suggested by the connectome [437, 443, 454]. The proposed combined sleep homeostasis and ring attractor model can capture this increase in activity in R5 neurons during wakefulness [123, 207] (Fig. 2.5A and Supplementary Fig. S2.7A, fourth row).

Additionally, in the proposed models, sleep deprivation leads to a qualitative change in the behavior of R5 neurons towards oscillatory dynamics which is reminiscent of the experimentally observed transition to bursting dynamics [123] or increase in oscillatory dynamics [186]. Whether sleep deprivation compromises the head direction system in behaving flies is currently not known, although navigation related memories are for example affected by sleep deprivation in bees [455, 456].

The proposed model relies on several hypotheses that could be tested experimentally, summarized in Table 2.1. First, we assume that the bump amplitude in wedge neurons evolves towards a setpoint in the absence of changing input (consistent with experiments

[313]). We further hypothesize LTP and LTD plasticity in the recurrent connections of wedge neurons during wakefulness and sleep respectively (which could also be achieved through an intermediate population [311] such as EL neurons, see Supplementary Fig. S2.1B). This plasticity in w_{EE} is assumed to be Hebbian plasticity, potentially produced by correlated activity between neighboring wedge neurons. The switch in the plasticity rule between wakefulness (LTP) and sleep (LTD) has been proposed in several models of sleep (for example [409]; see [395] for review). A potential mechanism could for example be neuromodulation of an STDP gate [457, 458], which has been observed in insects [459, 460] and could involve the strong innervation of the central complex by neuromodulatory neurons [461]. For example, ExR1 neurons described in [125] (modeled in Fig. 2.1A and B) could produce the switch in plasticity between sleep and wake phases, potentially through neuromodulation (similar to the related serotonergic ExR3 neurons [438, 443, 462]). Finally, we assume LTP in connections from wedge to ring neurons (w_{IE}) and slowly increasing firing rate in R5 neurons during wakefulness (consistent with experiments [123]). During sleep, we hypothesize that these connections are reset and R5 neurons slowly decrease their firing rate.

The model makes several predictions. First, the model predicts that prolonged wakefulness leads to oscillation in wedge and R5 neurons, due to LTP in the circuit. Second, as a result of this plasticity, the bump width changes with w_{EE}, decreasing over time spent awake due to LTP in wedge neurons and therefore increasing spatial resolution (and *vice versa* during sleep, Supplementary Fig. S2.5C). Generally, there is a range of bump widths that can be sustained by the ring attractor (Fig. 2.4). Third, extended wakefulness can disrupt the head direction system by producing oscillatory or bursting behavior and will lock the bump position in place (independent of external input, Fig. 2.5A, sleep deprivation). Additionally, sleep results in autonomous dynamics in the ring attractor model (Fig. 2.5), with the network transitioning towards faster dynamics towards the end of the sleep phase (Supplementary Fig. S2.9). Such autonomous dynamics are reminiscent of activity of the head direction system observed in mice during sleep [453].

The resulting weakening of synaptic strength during sleep underlies several hypotheses about sleep function [395, 411, 412, 435]. The approach implemented here is based on the idea of reverse learning [411, 412, 414]: during sleep, attractors within the ring attractor network generated during wake phase are removed and the corresponding increased weights are weakened. Autonomous dynamics during sleep could be functionally relevant for memory consolidation and organization [463]. For instance, flies could partially replay (in wedge neurons) trajectories during sleep that they performed during navigation in the wake phase (see Fig. 2.6A), which could be used by downstream circuits to consolidate navigation-related memories. Navigation memories are for example consolidated during sleep in bees [455], and replay of neural activity in the central complex during sleep has been suggested to consolidate courtship memory in flies [177].

While synaptic changes during sleep and wakefulness are observed across the fly brain

(for example [206]), one could hypothesize that such activity-related changes are stronger in areas where activity is persistent with a possible role in working memory, such as the head direction system [313, 332]. Therefore, inhibitory R5 neurons might increase their activity faster and require resetting through sleep sooner than other transiently active neurons, ultimately being responsible for signaling sleep drive. We additionally did not differentiate between different ring attractor inputs (for example visual or idiothetic) and such different signals could also be integrated in different ring neurons or homeostats [20] (taking for example into account that visual experience increases sleep need [464]).

The connectome shows that both the head direction as well as the sleep homeostasis circuits encompass a large number of connected cell types in the central complex [443, 465]. Nevertheless, strongly simplified models of ring attractor networks with only a limited subset of actually involved cell types have proven useful for the description of the head direction system. Similarly, for the sleep homeostasis circuit, many more connected cell types could be considered and we here only investigated a simplified network that nevertheless can capture several experimental observations.

Circadian input could be integrated in the proposed model to synchronize sleep and wake phases to day and night cycles. This input would need to interact with the sleep switch (dFB neurons), as experimentally observed [466]. For example, inhibitory circadian input to dFB neurons could delay the switch to sleep (similar to sleep deprivation), while excitatory circadian input to dFB neurons could promote early sleep.

Overall, the interaction of the homeostatic integrator and the head direction systems together with mounting evidence for a close structure-function relationship in these circuits, suggest that a relationship between the control and function of sleep could be established in this network using theoretical modeling and experiments.

2.5 Methods

2.5.1 Anatomy based on the fly connectome

The connectivity of the proposed model is based on the fly connectome [437] and incorporates the populations R5 (ER5), ExR1, EPG and EL, as described in the Neuprint database. Each population and its innervation in the ellipsoid body are shown in Supplementary Fig. S2.1A. EL and EPG neurons, respectively, have diagonal connectivity matrices within and across populations as shown in Supplementary Fig. S2.1B.

2.5.2 Numerical simulation of models

We numerically solved all models with forward Euler with a time step of $dt = 0.0001$ seconds. Our code is implemented in Python, and is available at https://gitlab.com/

anflorescaesar/integration_of_sleep_pressure_and_navigation_simulations

2.5.3 Sleep homeostasis circuit

In this and the following, we use rate-based models to simulate dynamics of entire neural populations and dynamics of single wedge neurons. The differential equations used to model the sleep homeostasis circuit are as follows:

$$\begin{cases} \tau_{R5}\dot{r_{R5}}(t) = -r_{R5}(t) + [r_{ExR1}(t)]_+ \\ \tau\dot{r}_{ExR1}(t) = -r_{ExR1}(t) + [1 - r_{dFB}(t)]_+ \\ \tau\dot{r}_{dFB}(t) = -r_{dFB}(t) + [G(r_I) - d(t)]_+. \end{cases} \tag{2.1}$$

The variables $r_I(t)$, $r_{ExR1}(t)$ and $r_{dFB}(t)$ are the population firing rates of R5 neurons, ExR1 neurons and dFB neurons, respectively. τ_I is the time constant of R5 neurons (on the order of hours) and τ is the effective population time constant (in the millisecond range). $[\cdot]_+$ is a threshold-linear function to ensure positive-valued firing rates. The variable $d(t)$, which can take values 0 or 1, represents an input to dFB neurons such as a wake-promoting dopaminergic signal [308]. The switch behavior of dFB neurons is modeled by simple hysteresis (Fig. 2.1C), according to the following equation:

$$G(r_{R5}) = \begin{cases} 0 & \text{if} \quad r_{R5}(t) < r_I^{(max)} \quad \text{and} \quad \dot{r_{R5}}(t) > 0 \\ 1 & \text{if} \quad r_{R5}(t) \geq r_I^{(max)} \quad \text{and} \quad \dot{r_{R5}}(t) > 0 \\ 1 & \text{if} \quad r_{R5}(t) > r_I^{(min)} \quad \text{and} \quad \dot{r_{R5}}(t) < 0 \\ 0 & \text{if} \quad r_{R5}(t) \leq r_I^{(min)} \quad \text{and} \quad \dot{r_{R5}}(t) < 0 \end{cases} \tag{2.2}$$

Such a switch behavior in dFB neurons could be implemented, for example, by adding an additional wake-promoting population, which together with dFB neurons, could mutually inhibit each other to create a flip-flop switch, similar to sleep models proposed in mammals [400, 401, 405, 467]. Candidates for the wake-promoting population in the fly are dopaminergic neurons in the PPM3 and PPL1 clusters [308]. Alternatively, this switch behavior could be generated by a single-cell mechanism in dFB neurons, which are known to increase excitability with extended wake time [308].

In this model, the wake and sleep time depend on the effective time constant τ_{R5} and the thresholds $r_I^{(min)}$ and $r_I^{(max)}$. The time spent in the sleep phase, t_S (sleep time) as a function of the time spent in the wake phase, t_W (wake time), can be computed by solving the differential equation for R5 neurons, r_{R5}, during the sleep phase and wake phase, respectively:

$$t_S(t_W) = \tau_{R5} log\Big(\frac{1 + (r_I^{(min)} - 1)e^{-t_W/\tau_{R5}}}{r_I^{(min)}}\Big) \tag{2.3}$$

Considering that t_W is small, we can expand this expression in a Taylor series, taking only first order terms:

$$t_S \approx \frac{1 - r_I^{(min)}}{r_I^{(min)}} t_W \tag{2.4}$$

For small waking time periods, the sleep time t_S increases linearly, resulting in sleep rebound as required for homeostasis (increased time spent awake leads to more sleep afterwards). However, for long wake times, the preceding sleep time saturates at a constant value $t_S^{(sat)}$, given by the following expression:

$$t_S^{(sat)} = \tau_{R5} log\Big(\frac{1}{r_I^{(min)}}\Big) \tag{2.5}$$

This saturation time prevents very large sleep times after large preceding wake times, and it is also a feature observed experimentally [267].

2.5.4 Sleep homeostasis and ring attractor with fixed connections

We asked how increasing activity in R5 neurons affects the head direction circuit in the absence of plasticity. Given the fact that R5 and wedge neurons are connected, we modeled a ring attractor network where wedge neurons encode head direction and R5 neurons provide increasing inhibitory input to wedge neurons. The model is shown schematically in Fig. 2.2A and described by the following system of equations:

$$\begin{cases} \tau \dot{r}_E^{(i)}(t) = -r_E^{(i)}(t) + \Big[\sum_j^N w_{EE}^{(ij)} r_E^{(j)}(t) - w_{ER5} r_{R5} + \theta + I^{(i)}(m,t)\Big]_+ & \text{for} \quad i = 1, ..., N \\ \tau_{R5} \dot{r}_{R5}(t) = -r_{R5}(t) + \Big[\sum_j^N w_{R5E}^{(j)} r_E^{(j)}(t) + r_{ExR1}(t)\Big]_+, \end{cases} \tag{2.6}$$

where $r_E(t)^{(i)}$ represents the activity of a wedge neuron i (in total, $N = 32$), $r_{R5}(t)$ is the population activity of R5 neurons and the time constants, τ_{R5} and τ, are the same as in the sleep homeostasis model. We only model the wake phase for simplicity, where dFB neurons are assumed to have zero activity and activity in ExR1 neurons is defined as $r_{ExR1}(t) = 1$, similar to the sleep homeostasis model. We neglect the connection from wedge to ExR1 neurons for simplicity, since we focus on the interaction between wedge and R5 neurons. The weights w_{AB} represent the connectivity from population B to population A. The recurrent connectivity $w_{EE}^{(ij)}$ is a matrix, in which for a given postsynaptic wedge neuron, i, the element (ij) is given by a gaussian function that depends on the distance to the presynaptic wedge neuron j along the ring, given by Eq (2.31) (see for example Fig. 2.4A). In this model, the synaptic weight w_{R5E} is tuned such that the activity of ring neurons increases, as in the sleep homeostasis model.

Fig. 2.2B shows a simulation of the model, where a rotating input $I(m,t)$ is provided to wedge neurons at 0.5 Hz (top row, blue). The activity of R5 neurons increases, as imposed by our parameter choice (third row, red). The wedge neurons, (second row, green) follow the rotating input while receiving this increasing inhibition, such that the bump amplitude decreases over time until inhibition gets strong enough so that the bump vanishes.

2.5.5 Two-population model with plasticity for R5 and wedge neurons

To simplify the analysis and build intuitions about the complete ring attractor model combined with the sleep homeostasis circuit, we first developed a simpler model. This model is a population model based on an excitatory-inhibitory network [448] (Fig. 2.3A) and describes the interaction between wedge and R5 neurons. The respective dynamics are described by the following system of differential equations:

$$\begin{cases} \tau \dot{r}_E(t) = -r_E(t) + \Big[w_{EE}(t) r_E(t) - w_{EI} r_I(t) + \theta \Big]_+ \\ \tau \dot{r}_I(t) = -r_I(t) + \Big[w_{IE}(t) r_E(t) \Big]_+, \end{cases} \tag{2.7}$$

where $r_E(t)$ and $r_I(t)$ are the firing rates at time t of wedge neurons and ring neurons, respectively, w_{AB} is the synaptic weight from population B to population A, θ is a constant background input onto wedge neurons, $[\cdot]_+$ is a threshold-linear function to ensure positive-valued firing rates, and τ is the effective population time constant. Note that now we model R5 neurons with a time constant τ on the millisecond range, in contrast with the previous models.

2.5.5.1 Plasticity rules

We introduce plasticity rules for the excitatory weights w_{EE} and w_{IE} during the wake phase:

$$\begin{cases} \tau_{EE} \dot{w}_{EE}(t) = c r_E(t) r_E(t) \\ \tau_{IE} \dot{w}_{IE}(t) = c r_I(t) r_E(t) \Big(r_E(t) - r_0 \Big), \end{cases} \tag{2.8}$$

During the sleep phase we change the plasticity rule in w_{EE} , while leaving unchanged the plasticity rule in w_{IE}:

$$\begin{cases} \tau_{EE} \dot{w}_{EE}(t) = -c r_E(t) r_E(t) \\ \tau_{IE} \dot{w}_{IE}(t) = c r_I(t) r_E(t) \Big(r_E(t) - r_0 \Big), \end{cases} \tag{2.9}$$

where τ_{EE} and τ_{IE} are time constants, r_0 is a positive presynaptic threshold, and c is a proportionality constant. While the first plasticity rule is a linear Hebbian rule, the second

is a triplet rule with presynaptic threshold. These plasticity rules can be extracted from a general form of Hebbian plasticity. A general Hebbian plasticity rule for a synaptic weight w_{ij} can be defined as follows:

$$\tau_{ij}\dot{w}_{ij} = F(w_{ij}, r_i, r_j), \tag{2.10}$$

where τ_{ij} is the time constant of the rule, and $F(\cdot)$ is a function that depends on the synaptic weight, w_{ij}, and on pre- and postsynaptic activities, r_j and r_i, respectively [449]. The function $F(\cdot)$ needs to fulfill Hebb's condition: to produce a change in the synaptic weight w_{ij}, the pre- and postsynaptic neurons must be active: $r_i > 0$, $r_j > 0$. In principle, this function is unknown, but we can expand it in a Taylor series [449] around $r_I = r_E = 0$:

$$\tau_{ij}\dot{w}_{ij} \approx c_{00} + c_{10}r_i + c_{11}r_j + c_{20}r_i^2 + c_{21}r_ir_j + c_{22}r_j^2 + c_{30}r_i^3 + c_{31}r_i^2r_j + c_{32}r_ir_j^2 + c_{33}r_j^3 + O(r^4), \tag{2.11}$$

where each coefficient depends on the connection strength $c_{mn} = c_{mn}(w_{ij})$. The values of these coefficients determine the plasticity rule. For instance, Hebbian plasticity rules that are linear in the neural activities can be obtained by setting second or higher order coefficients to zero[449]. Keeping higher order coefficients leads to rules with non-linearities.

We assume that the plasticity rule in $w_{EE}(t)$ during the wake phase is linear, obtained by setting $c_{21} = c$ and all other coefficients to zero, while the plasticity rule in w_{IE} is non linear on the presynaptic neural activity, obtained by setting $c_{21} = -cr_0$, $c_{32} = c$ and the other coefficients to zero (Eq (2.9)). To ensure that synapses remain excitatory or inhibitory throughout the system's dynamics at any time, the plasticity rules are threshold-rectified at zero if the synaptic weights are zero:

$$\begin{cases} \dot{w}_{EE}(t) = \left[\dot{w}_{EE}(t)\right]_+ & \text{if} \quad w_{EE}(t) = 0 \\ \dot{w}_{IE}(t) = \left[\dot{w}_{IE}(t)\right]_+ & \text{if} \quad w_{IE}(t) = 0. \end{cases} \tag{2.12}$$

Finally, we note that the dynamics of the plasticity rules are much slower than the dynamics of neural populations, so that $\tau_{EE}, \tau_{IE} >> \tau$. The parameters for the two-population model used for simulations are shown in Table S2.1, but the following stability analysis is performed without any assumption on the parameter values. Also note that the plasticity rules produce changes in the weights w_{EE} and w_{IE} that are proportional to neural activities, r_E and r_I. These changes are scaled by the constants τ_{EE} and τ_{IE}, which are constants with units in seconds, but do not define an exponential decay as for example the time constant τ. Therefore, the constant c is introduced and tuned experimentally such that the values of τ_{EE} and τ_{IE} define the timescale of the simulations.

2.5.5.2 Stability of the two-population model

2.5.5.2.1 Fast-timescale limit

In the fast-timescale limit, we can assume that $\tau_{EE}, \tau_{IE} \longrightarrow \infty$, meaning that synaptic plasticity is sufficiently slow compared to the dynamics of the neural populations so that it can be assumed to be constant. This allows us to study the dynamics of the model at the timescale of τ (milliseconds range). In that case, we can treat the synaptic weight w_{EE} as a free parameter with a fixed value, assuming that w_{IE} has already evolved through its plasticity rule to its equilibrium value, $r_E \longrightarrow r_0$. Therefore, for a given value of w_{EE}, we set the value of w_{EI} such that the fixed point for the wedge neurons is r_0. In this way, the value of w_{IE} is coupled to the value of w_{EE}. The stability of the 2-dimensional system given by equations in (2.7) is then analyzed with respect to the value of w_{EE}. Since the system is piecewise linear due to the threshold function $[\cdot]_+$, we perform a linear analysis assuming that the inputs to the neurons are positive. Under these conditions, the fixed point of the system, (r_E^*, r_I^*), is given by the following expressions:

$$\begin{cases} r_E^* = w_{EE} r_E^* - w_{EI} r_I^* + \theta = r_0 \\ r_I^* = w_{IE} r_0. \end{cases} \tag{2.13}$$

Since we force the fixed point of wedge neurons to be r_0, we can extract the equilibrium value of w_{IE} as a function of w_{EE}:

$$w_{IE} = \frac{\theta}{w_{EI} r_0} + \frac{w_{EE} - 1}{w_{EI}}. \tag{2.14}$$

The fixed point of the system can be described with respect to w_{EE} as:

$$\begin{cases} r_E^* = r_0 \\ r_I^* = \frac{\theta}{w_{EI}} + r_0 \frac{w_{EE}-1}{w_{EI}} \end{cases} \tag{2.15}$$

Both the fixed point of ring neuron activity, r_I^*, and the equilibrium value of the connectivity, w_{IE}, depend linearly on w_{EE}, implying that if w_{EE} increases, both w_{IE} and r_I^* increase as well as long as the fixed point is stable. We analyze the stability of the system by calculating the eigenvalues:

$$\lambda_\pm = \frac{1}{2\tau}\left((w_{EE} - 2) \pm \sqrt{(w_{EE} - 2)^2 - \frac{4\theta}{r_0}} \right). \tag{2.16}$$

Both eigenvalues are shown in Supplementary Fig. S2.2A with respect to different values

of w_{EE}. This leads to four different cases:

$$\begin{cases} (1) & w_{EE} \in \left[1, \quad 2 - 2\sqrt{\theta/r_0}\right] \\ (2) & w_{EE} \in \left(2 - 2\sqrt{\theta/r_0}, \quad 2\right] \\ (3) & w_{EE} \in \left(2, \quad 2 + 2\sqrt{\theta/r_0}\right] \\ (4) & w_{EE} > 2 + 2\sqrt{\theta/r_0} \end{cases} \tag{2.17}$$

In case (1), both eigenvalues are real and negative: the fixed point is stable (Eq (2.15)). In case (2), the real part of the eigenvalues is negative and the imaginary part is non-zero: the system evolves towards the fixed point with damped oscillations. In case (3), the real part of the eigenvalues is positive and the imaginary part is non-zero: the system diverges towards infinity, oscillating with amplitudes which increase exponentially. In case (4), the eigenvalues are real and positive: the fixed point is unstable. This analysis predicts a bifurcation in the stability of the fixed point when $w_{EE} = 2$. This behavior is shown in Fig. 2.3C.

The non-linearity of the linear threshold function changes the behavior of the model slightly. While the behavior stays the same for the cases (1), (2) and (4), because the model is mostly in the linear regime, case (3) differs and the non-linearity produces stable cycles around the fixed point. This behavior is found empirically from simulating the non-linear model, and is summarized in Fig. 2.3B.

2.5.5.2.2 Slow-timescale limit

In the slow-timescale limit, we consider the fact that the firing rates change sufficiently fast compared with the synaptic weights so that these changes can be considered instantaneous ($\tau \longrightarrow 0$). This allow us to study the dynamics of the model on the timescale of τ_{EE} and τ_{IE} (minutes to hours range). We therefore analyze the conditions under which the synaptic rules in Eqs (2.8) and (2.9) stabilize the model. We again first consider the linear range of the function $[\cdot]_+$ where the inputs to the neurons are positive. We approximate the instantaneous value of the firing rates in Eq (2.7) as follows:

$$\begin{cases} r_E = w_{EE}(t) r_E - w_{EI} r_I + \theta \\ r_I = w_{IE}(t) r_E \end{cases} \tag{2.18}$$

This linear system allows extracting the values of r_E and r_I in terms of the synaptic weights as:

$$\begin{cases} r_E = \frac{\theta}{1 - w_{EE} + w_{EI} w_{IE}} \\ r_I = \frac{w_{IE}\theta}{1 - w_{EE} + w_{EI} w_{IE}} \end{cases} \tag{2.19}$$

We can now compute the vector field for wedge and ring neuron activity as a consequence of the slow dynamics of synaptic plasticity:

$$\begin{cases} \dot{r_E} = \frac{\partial r_E}{\partial w_{EE}} \dot{w}_{EE} + \frac{\partial r_E}{\partial w_{IE}} \dot{w}_{IE} \\ \dot{r_I} = \frac{\partial r_I}{\partial w_{EE}} \dot{w}_{EE} + \frac{\partial r_I}{\partial w_{IE}} \dot{w}_{IE} \end{cases} \tag{2.20}$$

2.5.5.3 Two-population dynamics during wakefulness

Considering the plasticity rules during the wake phase (2.8), Eq (2.20) leads to the following system of differential equations:

$$\begin{cases} \dot{r_E} = \frac{c(w_{EI} r_I \tau_{EE} - \tau_{IE})}{\tau_{EE} \tau_{IE}} \frac{r_E^3}{\theta} \Big(- r_E + \Big(1 + \frac{\tau_{IE}}{w_{EI} r_I \tau_{EE} - \tau_{IE}} \Big) r_0 \Big) \\ \dot{r_I} = \frac{r_I^3 r_E}{\theta} \Big(\frac{c}{\tau_{EE}} + \frac{c(1 - w_{EE})}{\tau_{IE}} (r_E - r_0) \Big) \end{cases} \tag{2.21}$$

The second equation gives the dynamics of ring neurons, which increase activity with c/τ_{EE}. The first equation gives the dynamics of the population of wedge neurons approaching a setpoint only when the effective decay time constant (the first factor in the right hand side) is positive, otherwise the equation diverges to infinity and the system is unstable. This gives the following criterion for τ_{EE} and τ_{IE}:

$$\frac{\tau_{EE}}{\tau_{IE}} > \frac{1}{w_{EI} r_I} \tag{2.22}$$

This relationship supports the idea that plasticity in w_{IE} has to be fast enough with respect to the LTP in w_{EE}; otherwise, if w_{EE} increases faster than w_{IE}, the model diverges. Let us compute the upper limit of inequality (2.22), which corresponds to the minimum of r_I. For that, we approximate the firing rate of wedge neurons by $r_E = r_0$, and $r_I = w_{IE} r_0$. Then, we can write w_{IE} as a function of w_{EE} as in Eq (2.14). The upper limit of inequality (2.22) will therefore happen at the minimum of w_{EE}. As the minimum is $w_{EE} = 1$, the upper limit of the stability condition is:

$$\frac{\tau_{EE}}{\tau_{IE}} > \frac{1}{\theta}. \tag{2.23}$$

When this condition holds, the setpoint of wedge neurons in Eq (2.21), which is not r_0 as approximated previously, is given by

$$r_E^* = \Big(1 + \frac{1}{w_{EI} r_I \frac{\tau_{EE}}{\tau_{IE}} - 1} \Big) r_0, \tag{2.24}$$

which is generally different from r_0 due to the inertia of the dynamics of w_{EE}. In the limit $\tau_{EE} \longrightarrow \infty$ (no plasticity in w_{EE}), the fixed point is r_0, as expected from the fast-timescale analysis.

S2.2B shows the vector field for the system of Eqs (2.21). The green line shows the trajectory of the Supplementary Fig. setpoint in wedge neurons as the activity of ring neurons increase. As r_I increases due to increasing w_{EE}, the setpoint in r_E approaches r_0.

During wakefulness, the fixed point for wedge neurons r_E^* remains mostly constant, and the fixed point for ring neurons r_I^* changes with w_{EE} (Fig. 2.3B). If $w_{EE} \leq 2$ (light green region), the fixed point (r_E^*, r_I^*) is stable, and both neural populations evolve towards these values. With increasing w_{EE}, the fixed point of ring neurons r_I^* also increases while the fixed point of wedge neurons r_E^* remains constant. If w_{EE} increases further to $2 < w_{EE} \leq 2(1 + \sqrt{\theta/r_0})$, the model enters a regime of stable oscillations (light orange region of Fig. 2.3B). In this regime, both neural populations oscillate around the fixed point with a frequency that changes with w_{EE} (see Supplementary Fig. S2.2A), as explained in the fast-timescale limit. In addition, ring neurons increase their amplitude of oscillations as w_{EE} increases. Finally, when $w_{EE} \geq 2(1 + \sqrt{\theta/r_0})$ (light red region), the fixed point is unstable and the activity of both populations diverges.

Fig. 2.3C illustrates the dynamics of the full system, i.e. the activity of wedge and ring neurons, $r_E(t)$ and $r_I(t)$, as well as synaptic weights, $w_{EE}(t)$ and $w_{IE}(t)$. In the beginning (light green region), the fixed point of ring and wedge neurons is stable because $w_{EE} < 2$. When this boundary is crossed, the system enters the regime of stable oscillations (light orange region). Also, in the stable region of the simulation in Fig. 2.3C, w_{EE}, w_{IE} and ring neuron activity r_I increase, while the activity of wedge neurons r_E remains constant as imposed by conditions (i)-(iii). w_{EE}, w_{IE} and r_I constitute therefore a measure of how far the network has moved from its initial state.

2.5.5.4 Two-population model dynamics during sleep

In order to reset the system back to its stable state ($w_{EE} < 2$) after prolonged activity (wakefulness), we introduce a sleep phase with inverted plasticity [411, 412, 414]. For this, we assume that during sleep the recurrent connection between wedge neurons, w_{EE}, gets weaker through LTD [395, 414], while the plasticity rule for w_{IE} is the same as in the wake phase (Eq (2.9)).

We can perform the same analysis during sleep as in the wake phase by considering the plasticity rule in Eq (2.9) during sleep, so that the Eqs (2.20) lead to the following system of differential equations:

$$\begin{cases} \dot{r_E} = \frac{c(w_{EI} r_I \tau_{EE} + \tau_{IE})}{\tau_{EE}\tau_{IE}} \frac{r_E^3}{\theta} \Big(-r_E + \Big(1 - \frac{\tau_{IE}}{w_{EI} r_I \tau_{EE} + \tau_{IE}}\Big) r_0 \Big) \\ \dot{r_I} = \frac{r_I^3 r_E}{\theta} \Big(-\frac{c}{\tau_{EE}} + \frac{c(1 - w_{EE})}{\tau_{IE}} (r_E - r_0) \Big). \end{cases} \tag{2.25}$$

The second equation shows how ring neurons decrease their activity with c/τ_{EE}, at the same rate as in the wake phase. The first equation shows a fixed point for wedge neurons

that is lower than r_0, due to the inertia of a decreasing w_{EE} during sleep, given by:

$$r_E^* = \Big(1 - \frac{1}{w_{EI} r_I \frac{\tau_{EE}}{\tau_{IE}} + 1}\Big) r_0. \tag{2.26}$$

Supplementary Fig. S2.2C shows the vector field given by Eq (2.25) during the sleep phase, where the trajectory of the setpoint of wedge neurons (the green line) diverges from r_0 as the activity of ring neurons decreases.

The impact of LTD on the model during sleep can be understood by inspecting Fig. 2.3B: with decreasing value of w_{EE}, the fixed points become stable (light green) and the activity of ring neurons decreases (as shown in the fast-timescale limit). The switch between the wake and sleep phases is performed by dFB neurons that sense activity of R5 neurons [123]. Since R5 and dFB are not anatomically but functionally connected [123], we apply a low-pass filter to the activities of R5 neurons, which act as an input to dFB neurons and remove possible oscillations. We refer to this filtered activity as the switching signal, and it is modeled, together with dFB neurons as follows:

$$\begin{cases} \tau_f \dot{r}_I^{(f)}(t) = -r_I^{(f)}(t) + r_I(t) \\ \tau \dot{r_{dFB}}(t) = -r_{dFB}(t) + \Big[G(r_I^{(f)}(t)) - d(t)\Big]_+ \end{cases} \tag{2.27}$$

where τ_f is the time constant of the low-pass filter $r_I^{(f)}$ and $r_{dFB}(t)$ is the activity of dFB neurons with a switching behavior modeled by Eq (2.2). The variable $d(t)$ is a variable intended to produce sleep deprivation.

Fig. 2.3D shows a simulation of the model combining subsequent wake (white regions), where dFB neurons are inactive, and sleep phases (grey), where dFB are active. During wakefulness, w_{EE} and w_{IE} undergo LTP and the activity of R5 neurons increases (light red line in second row in Fig. 2.3D) and r_E is constant. When the switching signal (dark red line in second row) crosses an upper threshold, $r_I^{(max)}$, dFB neurons switch the model to sleep. During sleep, w_{EE} undergoes LTD due to the switch in plasticity, while the activity of R5 neurons decreases. w_{IE} also undergoes LTD (note that the plasticity rule does not change) since it follows the trend of w_{EE} to impose the set-point r_0 to the wedge neurons.

Therefore, sleep resets synaptic plasticity and activity of R5 neurons. Once the switching signal reaches a lower threshold, $r_I^{(min)}$, the model is switched back to the wake phase. In the third wake phase, we simulated sleep deprivation by setting $d(t) = 1$ (top orange region). Here, w_{EE} crosses the bifurcation boundary, $w_{EE} > 2$, and the model enters the domain of stable oscillations.

During the following sleep phase, the system needs more time to fully reset and reach the lower threshold. Such sleep rebound after sleep deprivation is an experimentally described feature of sleep homeostasis circuits [23, 125].

The time that the system spends in the sleep and wake phases is determined by the time constants of the plasticity rules, τ_{EE} and τ_{IE}, and the upper and lower thresholds of

the switching signal, $r_I^{(min)}$ and $r_I^{(max)}$. In our simulations, we set τ_{EE} and τ_{IE} to yield dynamics on the timescale of seconds (for ease of visualization), but larger values lead to similar behavior on longer timescales (minutes or hours, see Supplementary Fig. S2.8).

2.5.6 Ring attractor network with plasticity

We expand the two-population model to a ring attractor network. A total of $N = 32$ individual wedge neurons are modeled by $r_E^{(i)}(t)$. For simplicity, ring neurons are modeled as a population, $r_I(t)$. The model is schematically shown in Fig. 2.2D. The dynamics of the ring attractor network are given by the following equations:

$$\begin{cases} \tau \dot{r}_E^{(i)}(t) = -r_E^{(i)}(t) + \Big[\sum_j^N w_{EE}^{(ij)}(t) r_E^{(j)}(t) - w_{EI} r_I(t) + \theta + I^{(i)}(m) \Big]_+ & \text{for} \quad i = 1, ..., N \\ \tau \dot{r}_I(t) = -r_I(t) + \Big[\sum_j^N w_{IE}^{(j)}(t) r_E^{(j)}(t) \Big]_+. \end{cases} \tag{2.28}$$

The synaptic plasticity rules are also extended from the two-population model during the wake phase:

$$\begin{cases} \tau_{EE} \dot{w}_{EE}^{(ij)}(t) = c r_E^{(i)}(t) r_E^{(j)}(t) & \text{for} \quad i, j = 1, ..., N \\ \tau_{IE} \dot{w}_{IE}^{(i)}(t) = c r_I(t) r_E^{(i)}(t) \Big(r_E^{(i)}(t) - r_0 \Big) & \text{for} \quad i = 1, ..., N, \end{cases} \tag{2.29}$$

and during the sleep phase:

$$\begin{cases} \tau_{EE} \dot{w}_{EE}^{(ij)}(t) = -c r_E^{(i)}(t) r_E^{(j)}(t) & \text{for} \quad i, j = 1, ..., N \\ \tau_{IE} \dot{w}_{IE}^{(i)}(t) = c r_I(t) r_E^{(i)}(t) \Big(r_E^{(i)}(t) - r_0 \Big) & \text{for} \quad i = 1, ..., N. \end{cases} \tag{2.30}$$

We initialize the synaptic weights $w_{EE}^{(ij)}$ with a Gaussian function with amplitude $w_{EE}^{(max)}$ and standard deviation σ:

$$w_{EE}^{(ij)} = w_{EE}^{(max)} \exp\left(- \frac{\Big(\min\Big[|i-j|, \quad N - |i-j| \Big] \Big)^2}{2\sigma^2} \right). \tag{2.31}$$

Additionally we provide a Gaussian input to the ring attractor around a given wedge neuron m with amplitude I_{max} and standard deviation I_σ:

$$I^{(i)}(m,t) = I_{max} \left[\exp\left(- \frac{\Big(\min\Big[|i - m(t)|, \quad N - |i - m(t)| \Big] \Big)^2}{2 I_\sigma^2} \right) - r_{dFB}(t) \right]. \tag{2.32}$$

This input allows changing the position of the bump in the simulations, and can represent visual or idiothetic input to update the head direction of the animal.

We use the low-pass filtered activity of ring neurons to switch between sleep and wake phases, as in Eq (2.27). The values of the parameters in Table S2.2 are used in all simulations unless stated otherwise.

Synaptic plasticity in ring and wedge neurons has been discussed in several studies [123, 186, 207, 431, 432]. Note that we here focus on plasticity in the connections from wedge to ring neurons, while leaving the connectivity in the opposite direction constant. This is in contrast with [431, 432], where plasticity from ring to wedge neurons is assumed, while the other direction is left constant. This choice is motivated by the increasing activity in R5 neurons during the wake phase[123], which could be explained by the growth of dendritic synaptic sites (pre-synaptic plasticity), for instance from wedge to R5 neurons – consistent with the data and interpretation in [123] –, but not by the growth of axonal synaptic sites (post-synaptic plasticity).

2.5.7 Ring attractor network: bump stability analysis

To analyze to stability of the ring attractor model, we use an approach similar to the one in the fast-timescales analysis of the two-population model. First, we assume no plasticity in the recurrent connections $w_{EE}^{(ij)}$ but only in $w_{IE}^{(ij)}$,

$$\begin{cases} \tau_{EE}\dot{w}_{EE}^{(ij)}(t) = 0 \\ \tau_{IE}\dot{w}_{IE}^{(i)}(t) = cr_I(t)r_E^{(i)}(t)\Big(r_E^{(i)}(t) - r_0\Big) \qquad \text{for} \qquad i = 1, ..., N. \end{cases} \tag{2.33}$$

We analyze the stability and behavior of the network while gradually changing the values $w_{EE}^{(ij)}$. We initialize the ring attractor network with a bump profile, where neuron number 16 has maximum activity $r_E^{(16)} > r_E^{(j)}, \forall j \neq 16$. Given that only the connections $w_{IE}^{(i)}$ are plastic, the activity of ring neurons converges to a stable value given by

$$r_I \longrightarrow w_{IE}^{(16)} r_0. \tag{2.34}$$

This can be understood by looking at the plasticity rule for $w_{IE}^{(i)}$ (2.33). First, all the synaptic weights evolve so that wedge neuron 16 approaches the activity r_0. As all wedge neurons receive the same global inhibition, and wedge neuron 16 has maximum activity, the activity of the other wedge neurons is lower than r_0. At this point, the weights $w_{IE}^{(k)}$ for wedge neurons $k \neq 16$ with non-zero activity, decrease over time until reaching zero. On the other hand, if a wedge neuron $k \neq 16$ has zero activity, it does not provide any input to the ring neurons. As for wedge neuron 16, the synaptic plasticity rule changes the value of $w_{IE}^{(16)}$ such that its activity approaches r_0. An example of this behavior can be seen in Supplementary Fig. S2.4A, where we initialize the system with an input such that the peak of the bump is at wedge neuron 16. The synaptic weights $w_{IE}^{(k)}$ for wedge neurons $k \neq 16$ which have non-zero activity evolve towards zero.

The value of $w_{IE}^{(16)}$ is determined by the bump profile, because $r_E^{(16)}$ is receiving input from any wedge neuron with non-zero activity. Thus $w_{IE}^{(16)}$ has to balance the total excitation to set the activity of the wedge neuron 16 to r_0. Furthermore, the bump profile is determined by the parameters of the recurrent connectivity profile $w_{EE}^{(ij)}$, i.e. $w_{EE}^{(max)}$ and σ (Eq (2.31)). If we fix the amplitude $w_{EE}^{(max)}$ and increase the standard deviation σ, the width of the bump, that is the number of active wedge neurons, decreases. This is because more wedge neurons are providing input to wedge neuron 16 as σ increases, and the value of $w_{IE}^{(16)}$ increases to set $r_E^{(16)} = r_0$, which in turn provides more inhibition through ring neurons to all the wedge neurons and lowers their activities, reducing at the same time the bump width. This behavior is seen in Supplementary Figs. S2.4A and S2.4B.

The bump also shows oscillatory behavior (Supplementary Fig. S2.4C) depending on the value of σ. In general, the state of the ring attractor network and its stability can be described in terms of the recurrent connectivity distribution, $w_{EE}^{(ij)}$, consistent with the fast-timescale limit analysis in the two-population model.

To investigate how the behavior and stability of the ring attractor network depend on the recurrent connections $w_{EE}^{(ij)}$, we simulated the ring attractor model for a grid of values for the parameters $w_{EE}^{(max)}$ and σ:

$$\begin{cases} w_{EE}^{(max)} \in [0.1, 0.6) & \text{with step} \quad 0.005 \\ \sigma \in [1, 6) & \text{with step} \quad 0.05. \end{cases} \tag{2.35}$$

In total, we performed 10000 simulations where we initialize the bump peak in wedge neuron 16 with a predefined input of 0.5 seconds, and let the network evolve for 10 seconds. We then analyzed the stability and behavior of the system in the last second of each simulation, therefore assuming that the state of the network does not change. Supplementary Fig. S2.4 shows an example of 3 simulations with different σ values; the light orange band across all simulations highlights the region used for analysis.

In this region we computed for each simulation the following:

- **Oscillation frequency**: the frequency at which wedge neuron 16 oscillates. For this, we computed the Discrete Fourier Transform, and the resulting peak value corresponds to the oscillation frequency.

- **Mean bump FWHM**: the mean value over time of the full width at half maximum of the bump, a proxy for the width of the bump.

- **Maximum bump peak**: the maximum firing rate of wedge neuron 16 over time.

- **Mean bump peak**: the mean firing rate over time of wedge neuron 16. If the bump does not oscillate, this value is equivalent to the maximum bump peak value.

- **Mean ring neuron activity**: the mean of ring neuron activity over time.

These measures are displayed in Supplementary Fig. S2.5B-F, as a function of the recurrent connectivity parameters $w_{EE}^{(max)}$ and σ. Supplementary Fig. S2.5B shows how the network starts oscillating with increasing $w_{EE}^{(max)}$ and σ. On the other hand, the FWHM in Supplementary Fig.S2.5C shows how at low $w_{EE}^{(max)}$ and σ values, the bump disappears and all wedge neurons have constant activity at r_0. As the parameter values increase, a bump of activity appears and the FWHM decreases, as observed in Fig. 2.4C and Supplementary Figs. S2.4A and B. Finally, the activity of ring neurons increases as $w_{EE}^{(max)}$ and σ increase.

We further characterise the behavior and stability of the bump in the network with the total excitatory connectivity to the wedge neuron with maximal activity, i.e. wedge neuron 16, $w_{EE}^{(16,sum)}$:

$$w_{EE}^{(16,sum)} = \sum_{j}^{N} w_{EE}^{(16,j)}. \tag{2.36}$$

Supplementary Fig. S2.5A highlights the isolines where $w_{EE}^{(16,sum)}$ is constant for different values of $w_{EE}^{(max)}$ and σ. Note how the constant values of $w_{EE}^{(16,sum)} = 2$ and $w_{EE}^{(16,sum)} = 2(1 + \sqrt{\theta/r_0})$ coincide with the boundaries of the different dynamic regimes. Therefore, the quantity $w_{EE}^{(16,sum)}$ has in the ring attractor model a similar role as does the recurrent connection w_{EE} in the two-population model. For $w_{EE}^{(16,sum)} < 1$, the bump disappears, similar to the two-population network model when $w_{EE} < 1$. However, unlike in the two-population model, which is unstable for $w_{EE} > 2(1+\sqrt{\theta/r_0})$, in the ring attractor network, for $w_{EE}^{(16,sum)} > 2(1 + \sqrt{\theta/r_0})$ the wedge neurons are strongly inhibited by high activity in ring neurons.

From the above analysis, we extracted regions of stability that are shown in Fig. 2.4B. Constant lines of $w_{EE}^{(16,sum)}$ are computed as follows: in the continuous limit, i.e. $N \longrightarrow \infty$, the total excitatory connectivity is given by the following integral:

$$w_{EE}^{(16,sum)} = \int w_{EE}^{(max)} e^{\frac{x^2}{2\sigma^2}} dx = w_{EE}^{(max)} \sigma \sqrt{2\pi}. \tag{2.37}$$

Therefore, the isolines of constant $w_{EE}^{(16,sum)}$ are given by $w_{EE}^{(max)} = w_{EE}^{(16,sum)}/\sigma\sqrt{2\pi}$. For the discrete case, we empirically found $w_{EE}^{(16,sum)}$ to be well approximated by:

$$w_{EE}^{(max)} = \frac{w_{EE}^{(16,sum)}}{K\sigma}, \tag{2.38}$$

for any constant line $w_{EE}^{(16,sum)}$, where $K \approx 2.697$.

2.5.8 Ring attractor network: autonomous bump path analysis

To simulate how the bump in the ring attractor changes position to update the head direction during the wake phase, we use a simple clockwise or counter-clockwise rotating input with

frequency f defined by:

$$m(t) = \pm fNt. \tag{2.39}$$

$m(t)$ is the wedge neuron where the ring attractor receives the Gaussian input $I^{(i)}(m(t))$ (Eq (2.32)), and it is a cyclic variable, so that:

$$\begin{cases} \text{if} \quad m(t) = N+1 \quad \longrightarrow \quad m(t) = 1 \\ \text{if} \quad m(t) = 0 \quad \longrightarrow \quad m(t) = N. \end{cases} \tag{2.40}$$

During the sleep phase, the bump in the ring attractor shows autonomous dynamics (Fig. 2.5A). To investigate the relationship between the path of the bump during sleep and in the preceding wake phase, we use a sinusoidal input during the wake phase, defined by the amplitude A, frequency f, and the center C:

$$m(t) = C + Asin(2\pi ft). \tag{2.41}$$

An example of this input with different frequencies f and centers C is shown in Fig. 2.6A. We can obtain the position of the bump during wake and sleep phases as:

$$P_{bump}(t) = \text{argmax}_i \Big[r_E^{(i)}(t) \Big], \tag{2.42}$$

so that the position of the bump corresponds to the wedge neuron with maximum activity. We can now compute the distribution of times that the bump is localized around each wedge neuron i during sleep and wake phases, respectively, as:

$$\begin{cases} t_{wake}^{(i)} = \int_{wake} \delta\Big(P_{bump}(t) - i \Big) dt \\ t_{sleep}^{(i)} = \int_{sleep} \delta\Big(P_{bump}(t) - i \Big) dt, \end{cases} \tag{2.43}$$

where $\delta(\cdot)$ is the Dirac delta function and integrals extend over the wake and sleep phases. Fig. 2.6B shows these distributions normalized for the three wake phases in Fig. 2.6A and their following sleep phases. The distributions are very similar, meaning that during the sleep phase, the bump revisits the same wedge neurons that were active during the wake phase.

We further asked how the autonomous bump path changes during sleep with respect to the amplitude of the sine-shaped input, A, and frequency, f, during sleep. We first fixed the frequency of the input at $f = 1Hz$ and the center at $C = 16$ while varying the amplitude in the range of $[0, 15]$ with an increment of 1. This resulted in 15 simulations where we computed the standard deviation of the bump path during sleep and wake:

$$\begin{cases} \text{STD}_{wake} = \sqrt{\frac{1}{T_{wake}} \int_{wake} \Big(P_{bump}(t) - 16 \Big)^2 dt} \\ \text{STD}_{sleep} = \sqrt{\frac{1}{T_{sleep}} \int_{sleep} \Big(P_{bump}(t) - 16 \Big)^2 dt}, \end{cases} \tag{2.44}$$

where T_{wake} and T_{sleep} are the duration of wake and sleep phases, respectively. Fig. 2.6C shows the standard deviation in both phases with respect to the amplitude A. Note the similarity between both phases.

Secondly, we fixed the value of the amplitude at $A = 8$ and the center at $C = 16$ while varying the frequency, f, in the range $[0.1, 1.5]$ at increments of $0.1Hz$, resulting in 15 simulations. We quantify the number of cycles during both the sleep and wake phase. During the wake phase, the number of cycles is proportional to the input frequency f. During sleep, however, Fig. 2.6C, bottom, shows that the number of cycles of the autonomously rotating bump does not change as the input frequency increases. An example of this can be seen in Fig. 2.6A, where we increase the frequency in consecutive wake phases and the path of the bump during sleep does not increase its rotation frequency.

2.5.9 Ring attractor network: bump drift during wake phase

In the simulations and analyses above, we provided input during the wake phase and the ring attractor network closely followed the input with a bump of activity. However, a ring attractor network should be able to sustain the bump of activity in the absence of input. It is known that small changes in the synaptic connections of wedge neurons $w_{EE}^{(ij)}$ can cause drifts of the bump in the absence of input [427, 428, 429].

To test for drift during the wake phase, we used a flashing rotating input that turns on and off. The input around a wedge neuron m is on for 0.2 sec (Eq (2.32)), and then is turned off for 0.3 sec. Therefore, for N neurons, the rotating input frequency is $1/(0.5N)$. Supplementary Fig. S2.8A shows such a simulation with three wake and sleep phases and Supplementary Fig. S2.8B-D show blow-ups around different times. Note how the bump drifts from the provided visual input, due to the synaptic changes in $w_{EE}^{(ij)}$.

This drift depends on the plasticity time constants. For instance, Supplementary Fig. S2.9 shows a simulation with 100 times larger time constants, $\tau_{EE} = \tau_{IE} = 5000$ seconds. The duration of wake and sleep phases are now on the order of hours, compared to the simulation in Supplementary Fig. S2.9. Note in the blow-ups of Supplementary Fig. S2.9B-D that the bump of activity is sustained during the off time of the visual input without drifting. Since there are many more rotations during the wake phase and the synaptic changes in $w_{EE}^{(ij)}$ are very small in each rotation, the weights increase all together very homogeneously.

2.6 Supplementary information

τ	τ_f	c	τ_{EE}	τ_{IE}	w_{EI}	θ	r_0	$r_I^{(min)}$	$r_I^{(max)}$
0.01	2	0.005	50	50	0.5	10	10	20	35

Supplementary Table S2.1: Parameter values used in the two-population model. Time constants τ, τ_f, τ_{EE} and τ_{IE} are measured in seconds. We consider the rest dimensionless quantities.

τ	τ_f	c	τ_{EE}	τ_{IE}	w_{EI}	θ	r_0	$r_I^{(min)}$	$r_I^{(max)}$	$w_{EE}^{(max)}$	σ	I_{max}	I_σ
0.01	2	0.005	50	50	0.5	10	10	22	30	0.3	1.5	5	2

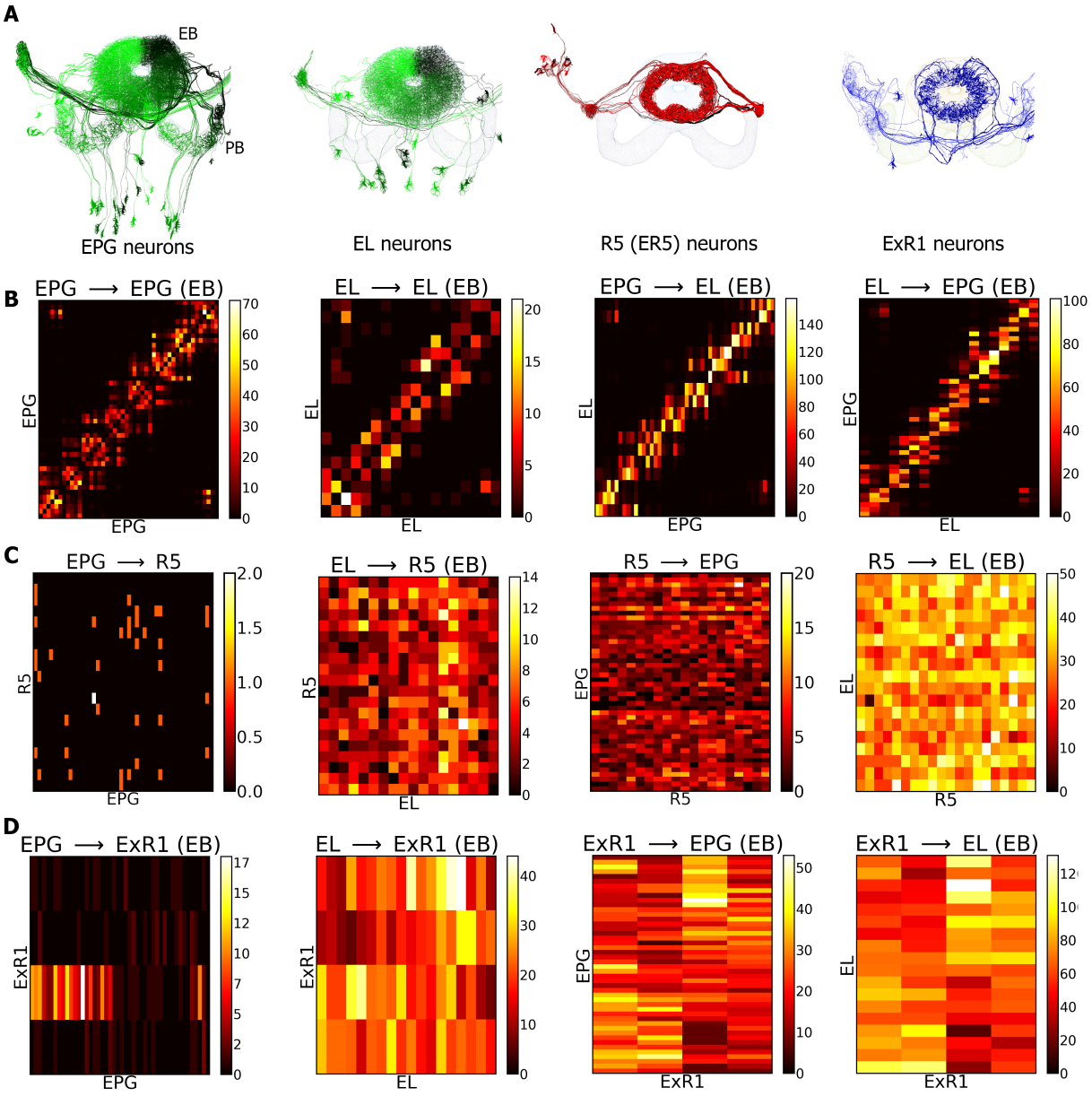
Supplementary Table S2.2: Parameter values used in the ring attractor network. As in the previous model, time constants τ, τ_f, τ_{EE} and τ_{IE} are measured in seconds. We consider the rest dimensionless quantities.

2.6.1 Ring attractor network: resetting the weights during sleep without autonomous activity

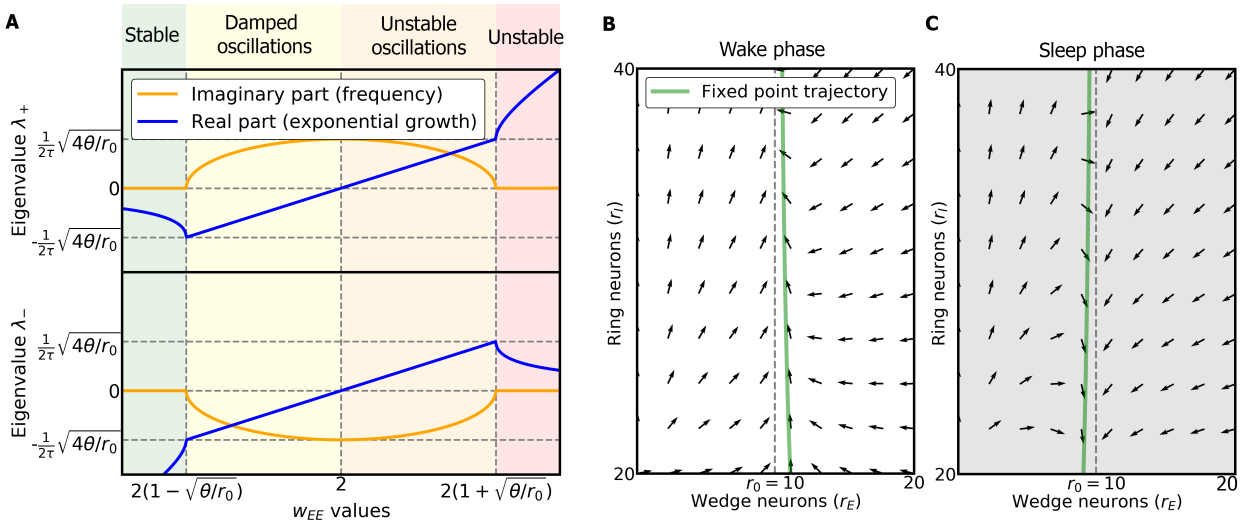
Assuming anti-Hebbian plasticity in the ring attractor network during sleep leads to autonomous dynamics (section 2.7). A different way to reset the network connectivity $w_{EE}^{(ij)}(t)$ is to relax it to its initial values over the sleep phase:

$$\tau_{EE} w_{EE}^{(ij)}(t) = -w_{EE}^{(ij)}(t) + w_{EE}^{(ij)}(0) \qquad \text{for} \qquad i,j = 1,...,N. \tag{2.45}$$

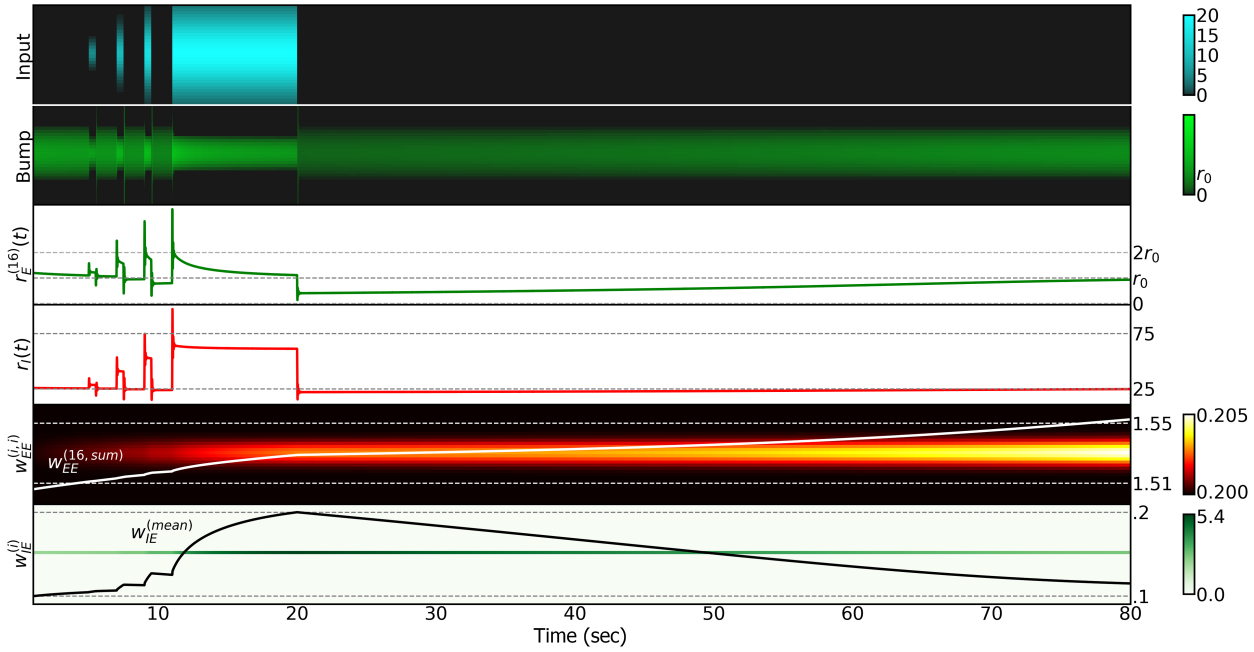
S10A Fig. shows a simulation of the ring attractor model using this type of plasticity during sleep. During the wake phase the dynamics of the model does not change (top, white regions). However, during sleep the plasticity rule keeps the bump in wedge neurons in place (top, grey regions), maintaining the last head direction of the fly before the sleep phase while the activity of R5 neurons slowly decreases. As with the two-population model (Methods 4.5), the timescale of sleep and wake phases depends on the time constants of the plasticity rules.



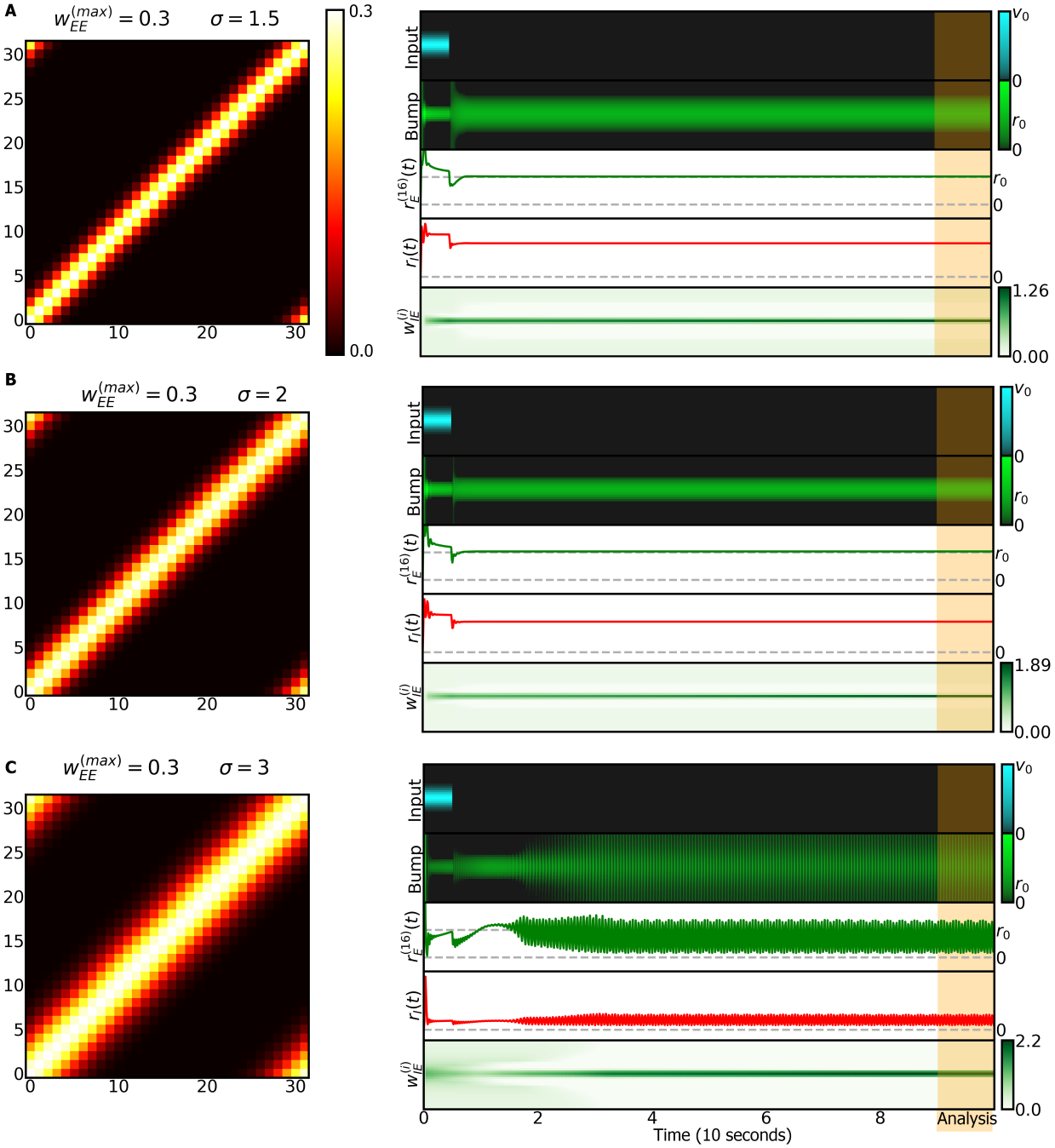
Supplementary Figure S2.1: Connectivity between the navigation-related populations (EPG and EL) and sleep-related populations (R5 and ExR1). A: On the left, neural projections of EPG and EL, referred as wedge neurons (green). On the right, neural projections of R5 (red) and ExR1 (blue). B: Recurrent connectivity between wedge neurons. The matrix in each figure represents the number of synaptic sites between presynaptic neurons (horizontal axis) and postsynaptic neurons (vertical axis)[437]. C: Connectivity between wedge neurons and R5 neurons in both directions. D: Connectivity between wedge neurons and ExR1 neurons in both directions. Data and neurons are reproduced from [437].



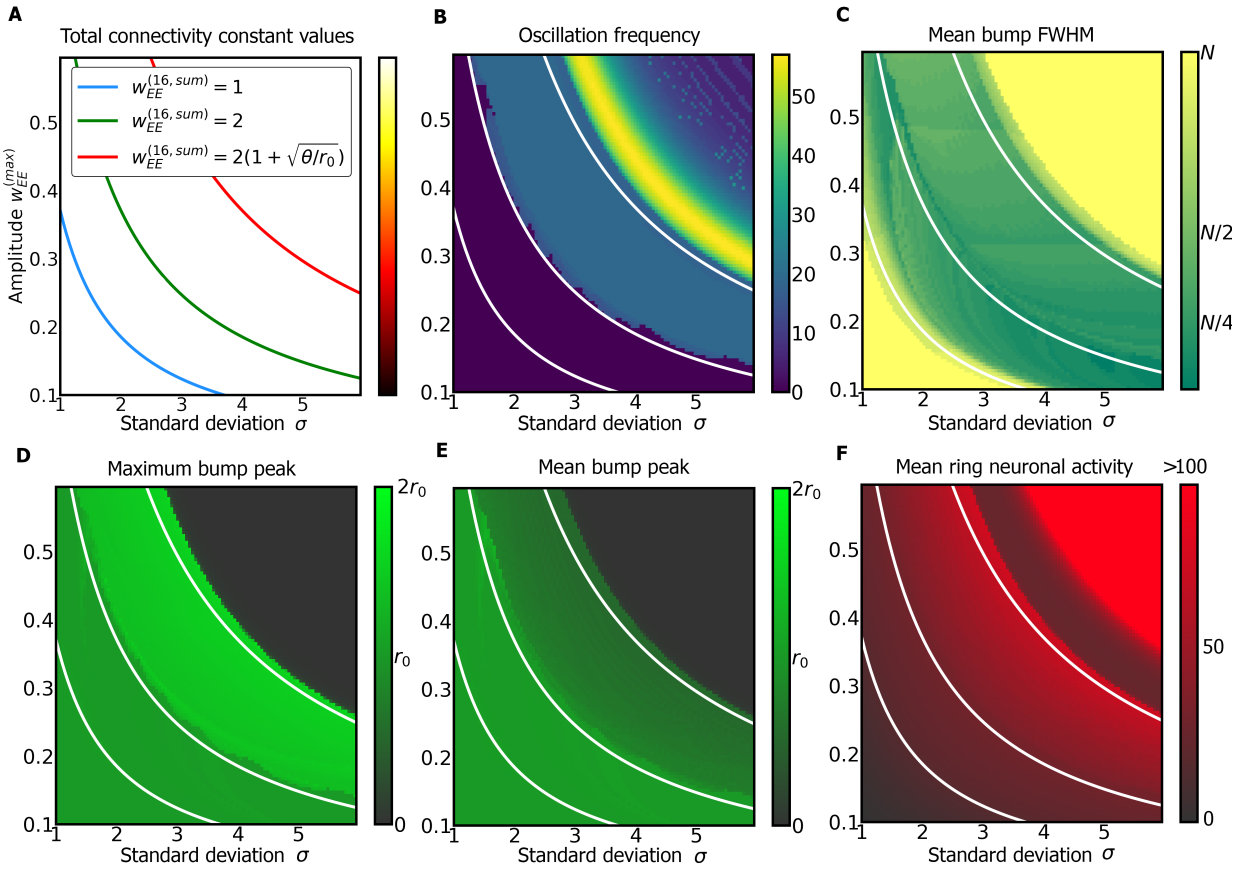
Supplementary Figure S2.2: Analysis of the two-population model in the fast and slow-timescale limits. A: Eigenvalues in the two-population model in the fast-timescales limit. The real (in blue) and imaginary (in orange) parts of the eigenvalues are plotted as a function of w_{EE}. B: Vector field of wedge and ring neurons dependent on synaptic plasticity during the wake phase in the slow-timescale limit. The green line represents the set point trajectory of wedge neurons. C: Vector field of wedge and ring neurons due to plasticity in the sleep phase in the slow-timescale limit. The green line is the trajectory of the set point in wedge neurons.



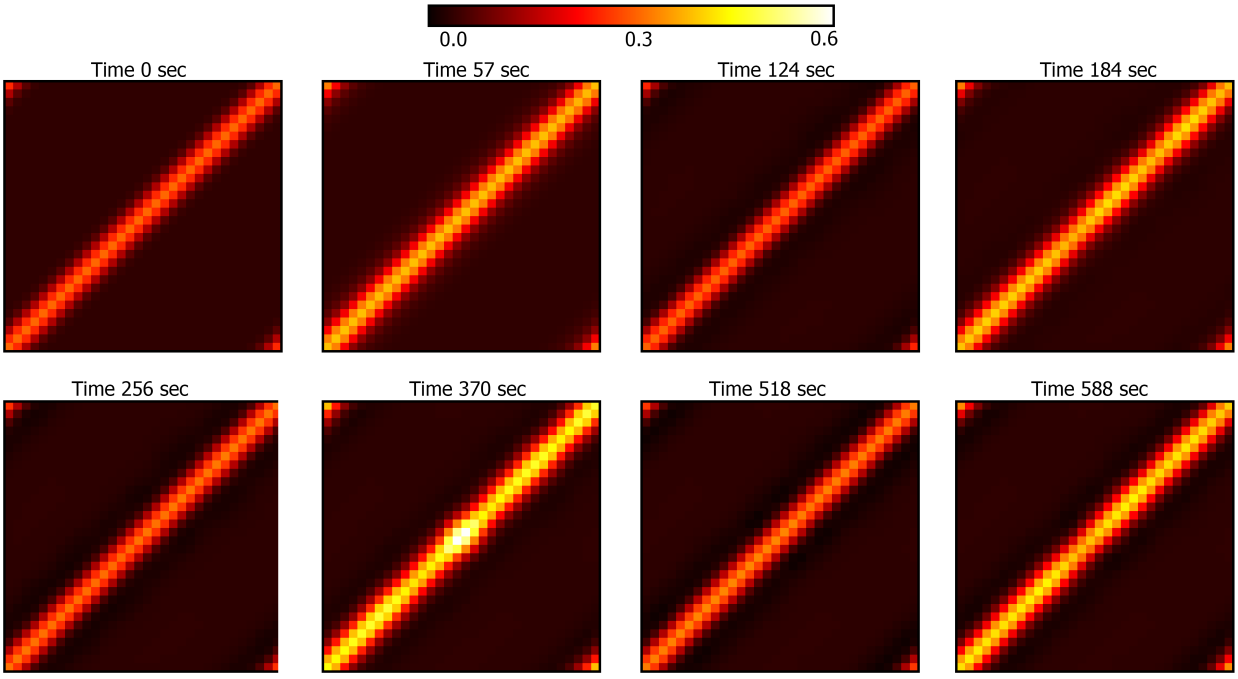
Supplementary Figure S2.3: Bump profile in the ring attractor network in response to inputs of different amplitudes I_{max} and standard deviations I_σ. When input (first row) is provided to the ring attractor the plasticity rule for $w_{IE}^{(i)}$ brings the activity of the wedge neuron $r_E^{(16)}$ (where the bump peak is located, second row) back to r_0 (third row). The bump is not constrained to have constant activity (third row), but always relaxes towards r_0 over time in the absence of changing input. For ease of visualization, we used a slower time constant for the plasticity of $w_{EE}^{(ij)}$ ($\tau_{EE} = 1000000$), thus avoiding oscillations in the bump throughout the simulation.



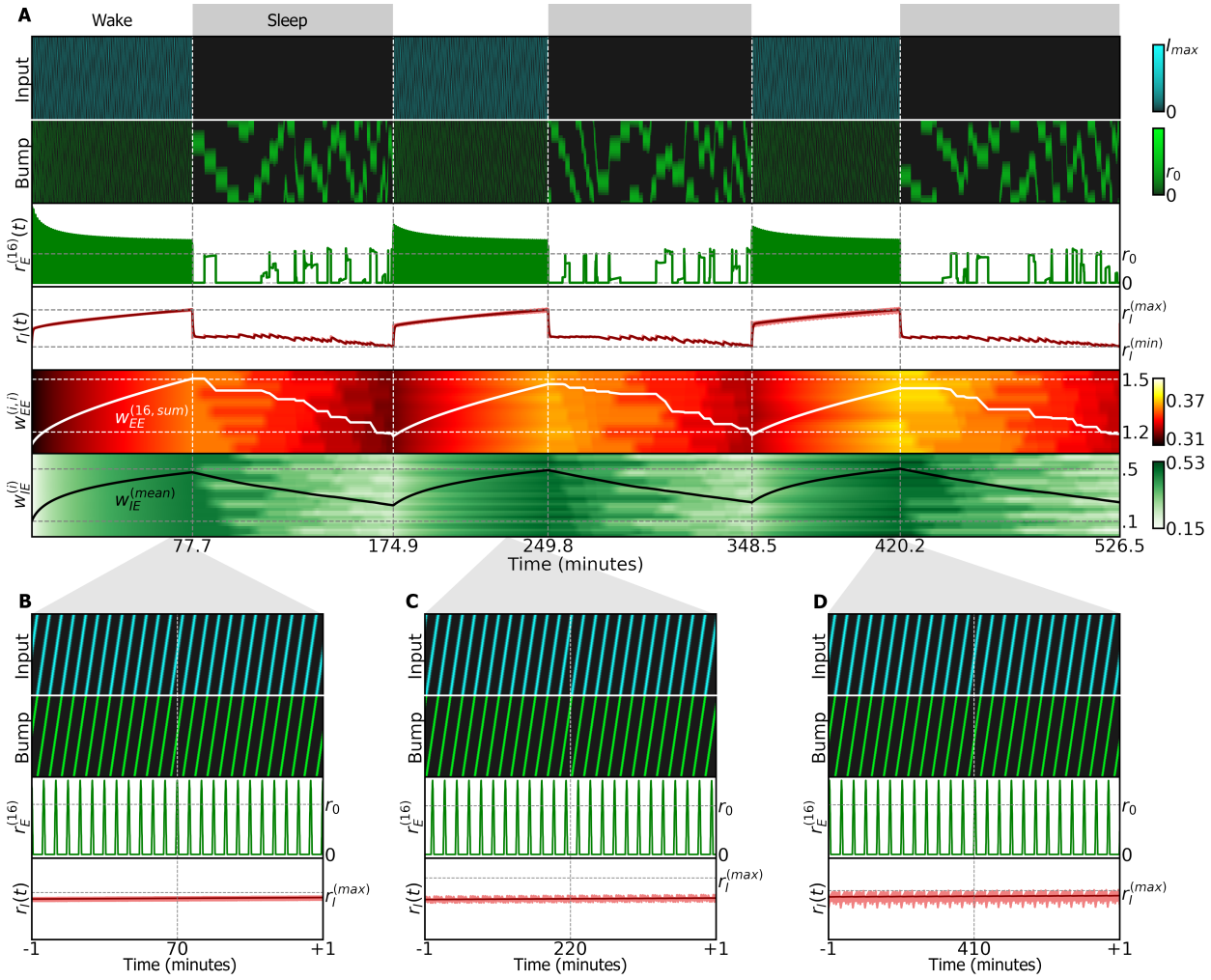
Supplementary Figure S2.4: Ring attractor network with no plasticity in $w_{EE}^{(ij)}$ and different initial distributions of weights. A: Left: initial $w_{EE}^{(ij)}$ values; right: 10 seconds of simulated dynamics. First row: input positioning the bump around wedge neuron 16. Second row: bump profile over time. Third row: activity of wedge neuron 16 evolving towards r_0 due to plasticity in $w_{IE}^{(i)}$. Fourth row: activity of ring neurons. Fifth row: the synaptic weights $w_{IE}^{(i)}$. The orange band at the end of the simulations represents the period in which the stability of the bump is analyzed. B: Same as A but with larger σ. C: Same as A, B but again increasing σ. In this simulation, the bump shows stable oscillations.



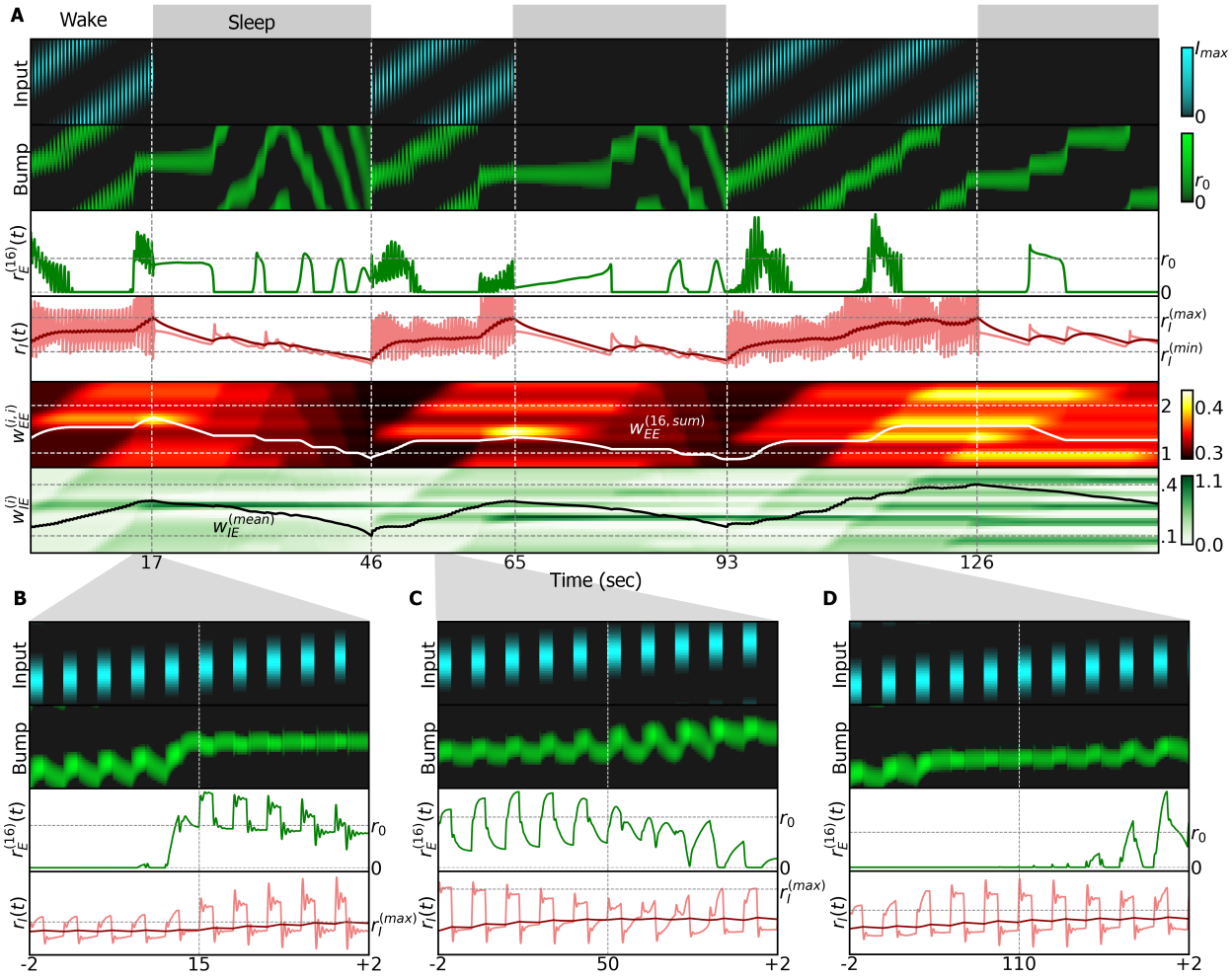
Supplementary Figure S2.5: Stability analysis of the bump in the ring attractor network. All subfigures are plots of different measures as a function of σ and $w_{EE}^{(max)}$, which parameterize the initial synaptic weights $w_{EE}^{(ij)}$ (Methods (2.5.7)). All variables in B, C, D, E, and F are calculated in a time window of 1 sec at the end of each simulation (orange area in Fig. 2.3). A: Isolines of $w_{EE}^{(16,sum)}$. These isolines are overlaid in white in the other subfigures and represent approximate boundaries of stability. B: Frequency of the oscillations in the bump across the analysis time window. Above the isoline $w_{EE}^{(16,sum)} = 2$, the bump oscillates. C: Mean FWHM over the analysis time window. Below the isoline $w_{EE}^{(16,sum)} = 1$ and above the isoline $w_{EE}^{(16,sum)} = 2(1+\sqrt{\theta/r_0})$, there is no bump because the FWHM is equal to the number of neurons, N. D: Maximum peak of the bump in the analysis time window (maximum activity of wedge neuron 16, $max(r_E^{(16)}(t))$). Below the isoline $w_{EE}^{(16,sum)} = 2$, the maximum is r_0 as forced by the plasticity rule in $w_{IE}^{(i)}$. Between the isolines $w_{EE}^{(16,sum)} = 2$ and $w_{EE}^{(16,sum)} = 2(1+\sqrt{\theta/r_0})$, the bump oscillates and the amplitude is given by the maximum, in this case $2r_0$. Above $w_{EE}^{(16,sum)} = 2(1+\sqrt{\theta/r_0})$, there is close-to-zero activity in wedge neurons, since the maximum is near zero. E: Mean of the bump peak over the analysis time window (mean activity of the wedge neuron 16, $< r_E^{(16)}(t) >$). In case of no oscillations, this value should be equivalent to the maximum bump peak in panel D. During oscillations, the value closely represents the center of oscillations. Note that between isolines $w_{EE}^{(16,sum)} = 2$ and $w_{EE}^{(16,sum)} = 2(1+\sqrt{\theta/r_0})$ this value is lower than r_0. F: Mean activity over the analysis time window of ring neurons, $< r_I(t) >$. Below the isoline $w_{EE}^{(16,sum)} = 2(1+\sqrt{\theta/r_0})$, the activity of ring neurons increases. Above the isoline, the activity of ring neurons first decreases and then rapidly increases. We clipped the values of the mean activity above 100 to facilitate visualization, but the increment of activity in this area reached values over 1000.



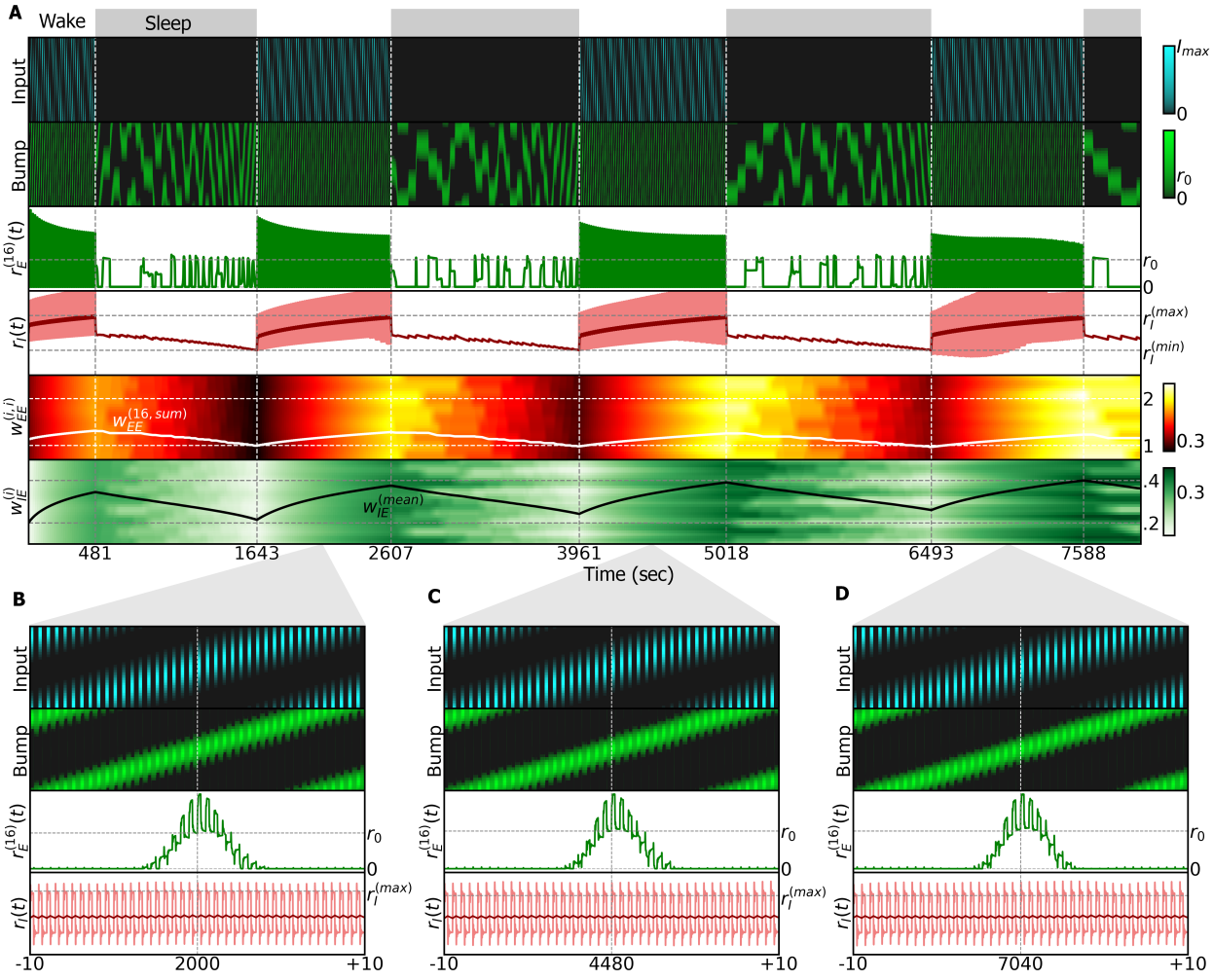
Supplementary Figure S2.6: Values of the synaptic weights $w_{EE}^{(ij)}$ in the simulation of Fig. 2.4. From left to right and from top to bottom: each plot shows the values each time there is a switch between wake and sleep phase and *vice versa*. Top, left: initial values of the weights set by the initial values of $w_{EE}^{(max)}$ and σ in Table B in 2.6. Top, center left: weights at the end of the first wake phase. Top, center right: after the subsequent sleep phase. Top, right: after the second wake phase. Bottom, left: weights after the second sleep phase. Bottom, center left: after sleep deprivation. Bottom, center right: after sleep rebound. Bottom, right: weights after the third wake phase. Note how the weights after each wake phase are increased (specially after sleep deprivation in the sixth plot) and how the sleep phase resets the weights to close to the initial conditions.



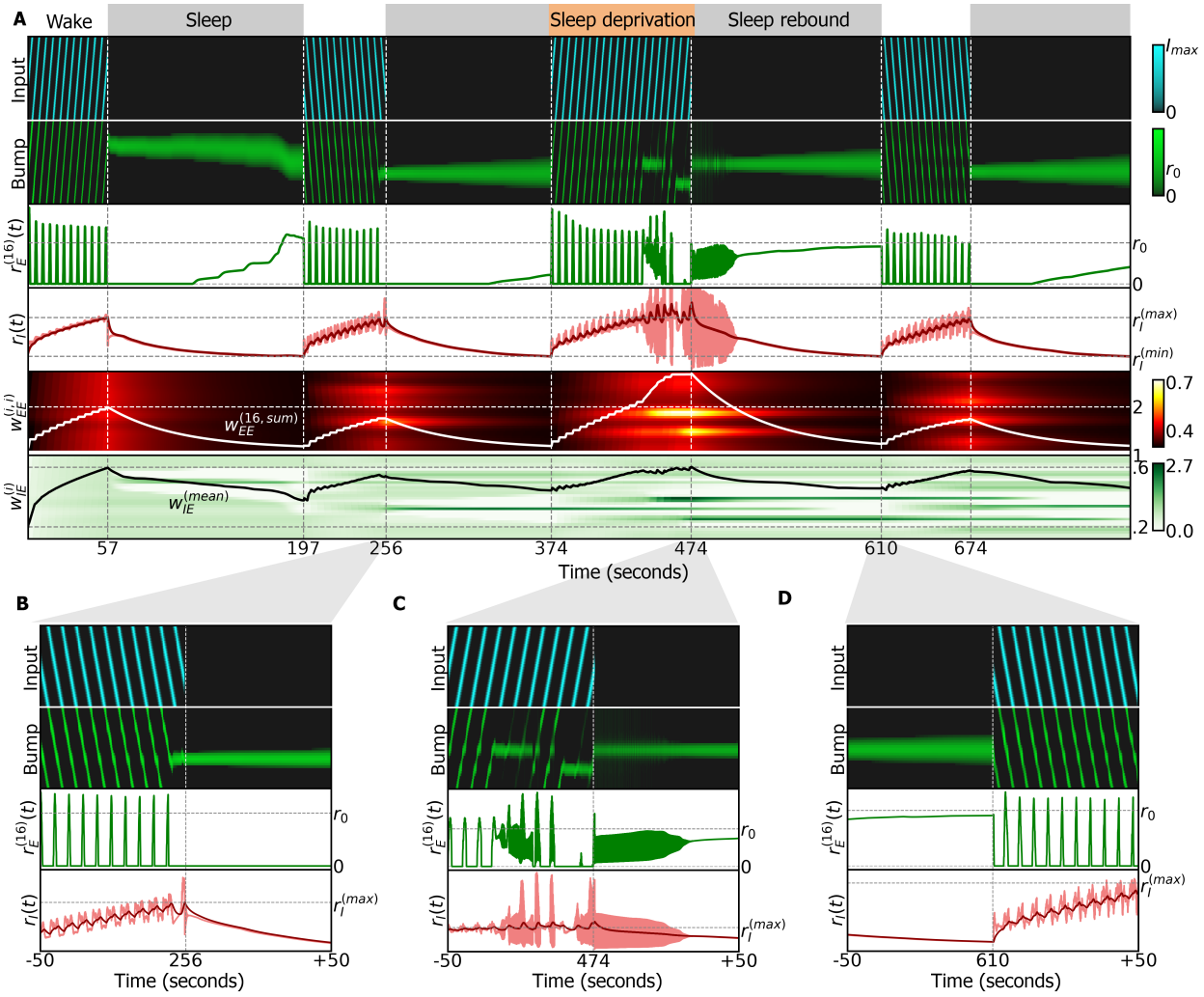
Supplementary Figure S2.7: Simulation of the ring attractor network with flashing input during the wake phase with slow plasticity time constants (details in Methods(2.5.9)). The time constants τ_{EE} and τ_{IE} in this simulation are 210 times larger than in Table B in 2.6. We decreased the time resolution of the simulation (time step is 0.001 seconds) and decreased the value $r_I^{(max)}$ to 30. A: Full simulation with three wake phases and three sleep phases. We used the same input rotation as in Fig. 2.5 (rotating input at $0.5Hz$). B: Blow-up around 70 minutes in the first wake phase of the simulation. C: Blow-up around 220 seconds in the second wake phase. D: Blow-up around 410 seconds in the third wake phase. Note that the duration of sleep and wake phases are now on the order of hours due to the increased time constants in the plasticity rules.



Supplementary Figure S2.8: Simulation of the ring attractor network with flashing input during the wake phase (details in Methods(2.5.9)). A: Simulation with three wake phases and three sleep phases. A flashing input that turns on and off is provided during the wake phase. During the off period, the ring attractor sustains a bump of activity that drifts due to changes in the synaptic weights $w_{EE}^{(ij)}$. B: Blow-up around 15 seconds in the first wake phase of the simulation. C: Blow-up around 50 seconds in the second wake phase. D: Blow-up around 110 seconds in the third wake phase.



Supplementary Figure S2.9: Simulation of the ring attractor network with flashing input during the wake phase with slow plasticity time constants (details in Methods(2.5.9)). The time constants in this simulation are 100 times larger than in the previous ring attractor simulations. A: Full simulation with three wake phases and three sleep phases. We used the same input rotation frequency as in Supplementary Fig. S2.6. As in Supplementary Fig. S2.6, we provide a flashing input that turns on and off during the wake phase. B: Blow-up around 2000 seconds in the first wake phase of the simulation. C: Blow-up around 4480 seconds in the second wake phase. D: Blow-up around 7040 seconds in the third wake phase. Note how the duration of sleep and wake phases are now on the order of hours due to the increased time constants in the plasticity rules. Note also how the bump of activity is sustained in place without drifting after the input switches off.



Supplementary Figure S2.10: Simulation of ring attractor combined with sleep homeostasis model, using an exponentially decaying plasticity rule during sleep (see 2.6). A: Entire simulation over a period of 800 seconds. White and grey regions indicate the sleep and wake phases, and correspond to dFB neurons switching off and on, respectively. Top row: input (inhibited during the sleep phase), alternating between clockwise and counter-clockwise rotations at $0.5Hz$. Second row: ring attractor bump activity. Third row: activity of wedge neuron 16. Fourth row, light red: activity of R5 neurons. Dark red: filtered activity. Switching between sleep and wake is carried out by dFB neurons that switch on and off depending on filtered activity crossing thresholds $r_I^{(min)}$ and $r_I^{(max)}$. In the third wake epoch, sleep deprivation is produced by extending the inhibition of dFB neurons ($d(t) = 1$ during the orange top layout). Fifth row: diagonal elements of the connectivity matrix $w_{EE}^{(ij)}$. The white line is the sum of all excitatory connections to wedge neuron 16. It passes threshold 2 at around 240 seconds leading to oscillations. The full connectivity matrix $w_{EE}^{(ij)}$ at the switch times is shown in Supplementary Fig. S2.6. Sixth row: connectivity $w_{IE}^{(i)}$; black line is the mean value. B: Blow-up around 256 seconds: switch from wake to sleep phase. C: Blow-up around 474 seconds: extended wake phase leads to oscillatory behavior. Circuit switches to sleep. **C** Blow-up around 610 seconds: switch from sleep to wake phase.

Chapter 3

Automated long-term two-photon imaging in head-fixed walking *Drosophila*

Preparations for imaging in behaving flies allow recordings of only a few hours (see sections 1.7.3.1 and 1.7.3.4). Recordings over long timescales were implemented either in constrained, non-behaving flies [294, 390], which makes it difficult to assess the state of the animal and preparation, or using intermittent imaging, where the animal is reintroduced into the microscope every day for a few minutes [363]. Therefore, recordings over multiple days have not been achieved (see section 1.7.3.4).

Testing the predictions and hypothesis developed in Chapter 2 requires monitoring neural activity across multiple timescales in behaving flies during wakefulness and during sleep. Recordings at fast timescales are thus needed to capture the dynamics of neural populations, such as compass neurons encoding heading direction [313]. Long timescales are also necessary for monitoring slow transients of neural activity during the day, such as the ones that were proposed to occur for R5 neurons, which have however only been investigated in brain explants and not in behaving animals [123, 186].

This chapter describes a set of technical improvements and innovations for both the dissection of flies as well as for imaging in behaving flies that allow recordings across multiple timescales, in walking and sleeping flies, as well as during feeding with an automated feeder. As a proof-of-principle experiment, long-term imaging is validated by monitoring the dynamics of the well-characterized compass neurons for up to 7 days. The resulting automated long-term imaging technique, where flies are automatically fed at preset time intervals, now routinely allows imaging of flies behaving in virtual reality over multiple days.

This chapter contains the following peer-reviewed publication:

[28] **Flores-Valle, A., Honnef, R. and Seelig, J.D.**
Automated long-term two-photon imaging in head-fixed walking Drosophila.
Journal of Neuroscience Methods 368 (2022): 109432.

Author	**Contribution in [28]**
Flores-Valle, A.	- Conceptualization - Setup design - Setup building - Experiments - Analysis - Visualization - Writing
Honnef, R.	- Setup design - Setup building
Seelig, J.D.	- Conceptualization - Setup design - Setup building - Supervision - Writing

3.1 abstract

The brain of *Drosophila* shows dynamics at multiple timescales, from the millisecond range of fast voltage or calcium transients to functional and structural changes occurring over multiple days. To relate such dynamics to behavior requires monitoring neural circuits across these multiple timescales in behaving animals.

Here, we develop a technique for automated long-term two-photon imaging in fruit flies, during wakefulness and extended bouts of immobility, as typically observed during sleep, navigating in virtual reality over up to seven days. The method is enabled by laser surgery, a microrobotic arm for controlling forceps for dissection assistance, an automated feeding robot, as well as volumetric, simultaneous multiplane imaging.

The approach is validated in the fly's head direction system and walking behavior as well a neural activity are recorded. The head direction system tracks the fly's walking direction over multiple days.

In comparison with previous head-fixed preparations, the time span over which tethered behavior and neural activity can be recorded at the same time is extended from hours to days. Additionally, the reproducibility and ease of dissections are improved compared with manual approaches. Different from previous laser surgery approaches, only continuous wave lasers are required. Lastly, an automated feeding system allows continuously maintaining the fly for several days in the virtual reality setup without user intervention.

Imaging in behaving flies over multiple timescales will be useful for understanding circadian activity, learning and long-term memory, or sleep.

3.2 Introduction

The brain of *Drosophila* shows dynamics at multiple timescales, from single action potentials to functional and structural changes across multiple days. Such slow changes occur for example due to sleep [20], circadian rhythms [294, 390], or memory consolidation [177, 468]. To relate fast and slow activity changes across these conditions therefore requires monitoring neural circuits over multiple timescales in behaving animals [469].

While head-fixed walking preparations allow imaging of neural activity during behavior [331], experiments typically last on the order of an hour, and two-photon imaging [355] over multiple timescales, including naturally occurring extended epochs of immobility, a prerequisite for sleep, has so far not been achieved. A preparation for widefield bioluminescence imaging for over up to 12 hours through a resealed opening in the fly's head was developed in [470]. Repeated imaging over up to 50 days was achieved with the help of a transparent window in [363] and allowed functional imaging in an epifluorescence widefield microscope after anesthetizing and reintroducing the fly into the setup for each experiment. Three-photon imaging of neural activity in intact walking flies over 12 hours was performed for

bright and large neurons close to the surface of the brain [471].

Here, we describe a method for multi-day two-photon calcium imaging in behaving fruit flies over up to seven days. Continuous monitoring of behavior, which included sleep and circadian modulation, in a virtual reality setup was combined with intermittent, fast volumetric imaging of calcium activity during between 8 to 16 percent of the time (imaging every 5 minutes in trials of either 30 or 60 seconds throughout the duration of the experiments).

For this, a transparent window was inserted into the fly's head [363], using a cost effective laser surgery approach combined with a microrobotic arm for operating forceps under a dissection microscope. The imaging and behavior experiments did not require supervision, with an automated feeding system maintaining the fly over the course of the experiment. Simultaneous two-plane imaging [369] allowed volumetric recording of neural activity at high frame rates. We validated the method in wedge neurons, also known as EPG neurons, in the head direction system of the fly [306, 313].

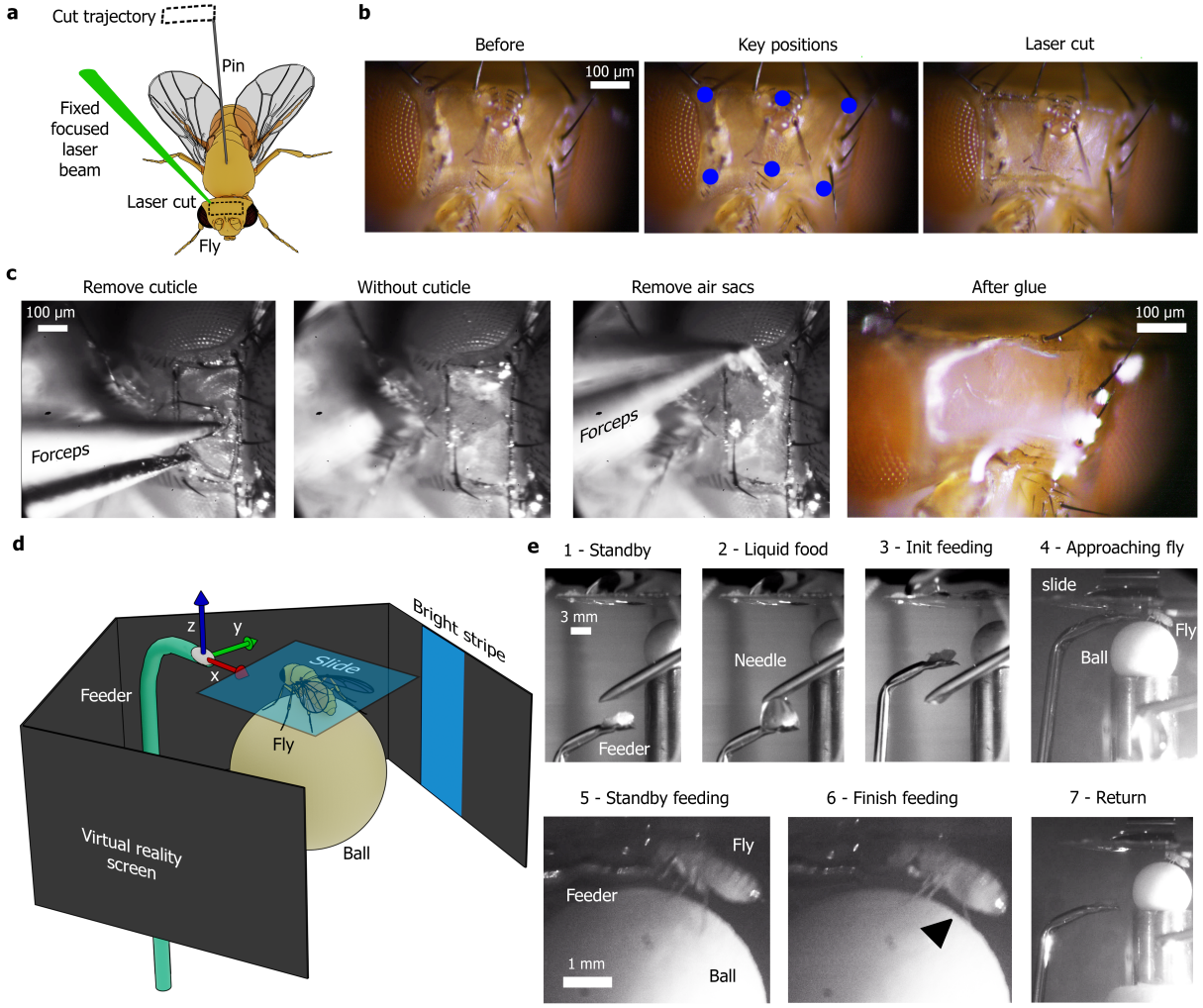


Figure 3.1: Long-term imaging preparation. **a** Schematic of laser cutting. The fly attached to a pin is moved while a laser beam cuts the cuticle. **b** Head of the fly (top view) before laser cutting, with key positions of trajectory, and after cutting. **c** Top view of head with motorized forceps removing cuticle and air sacs. The window is sealed using transparent glue[363]. **d** Schematic of VR and feeding setup: the fly is glued to a slide and placed on a ball under the microscope (not shown) surrounded by a screen for virtual reality projection and an automated feeding system. **e** 1 - Side view of fly and feeder in standby position (4 hours). 2 - Refilling of feeder every 2 minutes. 3, 4 - Feeder approaches fly. 5 - Feeding the fly. 6 - Increased abdomen volume from the ingested food indicated with arrowhead. 7 - Feeder returns to home position. In all experiments, flies were fed for 2 minutes every 4 hours.

3.3 Results

3.3.1 Laser surgery

A window for imaging through the cuticle was cut using a laser [363] (Fig. 3.1a and b, and Methods). Different from previous approaches [363, 472], which used an expanded pulsed UV excimer laser at 193 nm, we here used a focused visible continuous wave laser (Lassos Lasertechnik, YLK Series, 561 nm) with comparatively low power (30 mW was required for cutting) and cost. The fly (glued to a pin with its head fixed with respect to the thorax, see Methods) was moved against the stationary laser focus using a cost-effective, three-axis motorized micromanipulator (see Methods 3.5.1). A path for the laser was defined in three dimensions on the fly's head, allowing arbitrary geometries for the resulting opening in the cuticle (Fig. 3.1b). A single pass through the laser focus was sufficient to cut the cuticle.

3.3.2 Microrobotic arm for surgery assistance

After laser surgery, the fly on the pin was transferred to a dissection microscope. The pin was attached to a micromanipulator and was positioned on a cold plate at 4 degrees Celsius to anesthetize the fly. To assist with dissections, a microrobotic arm for controlling forceps was used to lift off the cut cuticle as well as to remove the underlying air sacs (see Methods 3.5.3, Fig. 3.1c). The position, orientation, and grip of the pair of forceps were controlled with a joystick.

The forceps were positioned at an angle of 45 degrees with respect the table and the fly was positioned on a cold plate angled downwards at approximately 20 degrees with respect to the table to easily access the brain. The tip of the forceps (see Fig. 3.2 and Methods 3.5.3 for details) was inserted into the cut to grab and slowly retract the cuticle. After cleaning the tip of the forceps, it was repositioned and the air sacs were similarly removed. er the cuticle, closing the forceps to grab the cuticle, and retracting the forceps to detach the cuticle from the brain.

The opening in the fly's head was sealed by manually applying UV glue [363] with a pin, here we used UV highgloss finish (DETAX, Freeform, 02204), and cured for twice 15 seconds with UV light. The fly was then glued to a microscope cover slide for imaging, either after first leaving the fly to recover overnight in a vial with food [363] (fly 3, Supplementary Fig. S3.6 and S3.7, and fly 4, Supplementary Fig. S3.8) or directly after surgery (fly 1, Fig. 3.4, and fly 2, Supplementary Fig. S3.5). The fly glued to the microscope slide was finally positioned on an air supported ball in a VR system (Fig. 3.1d) under a two-photon microscope [157, 331].

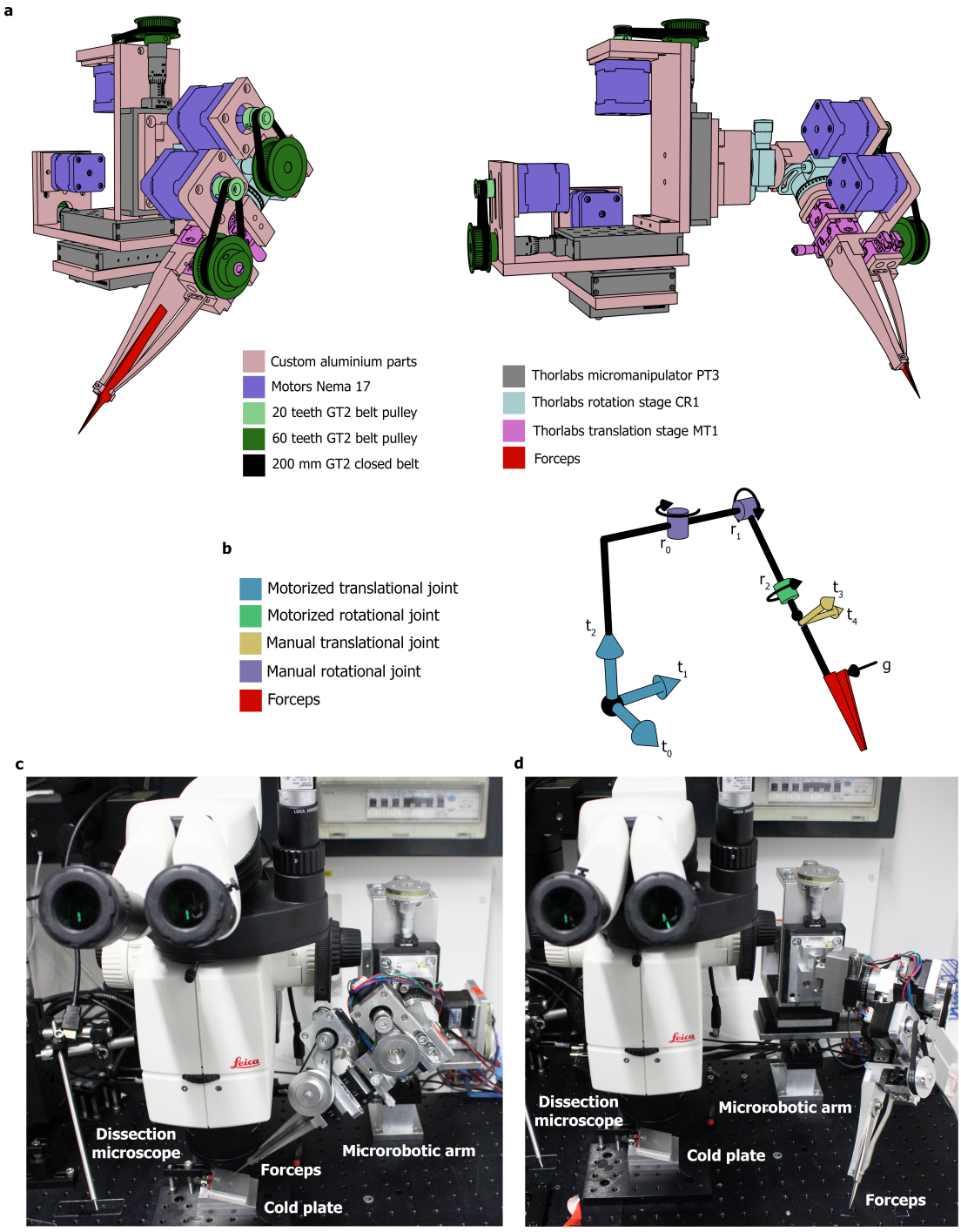


Figure 3.2: Microrobotic arm for dissection assistance. **a** Two different views of 3D model of microrobotic arm with forceps. **b** Scheme of dynamics with different joints and forceps. **c** Setup with microrobotic arm with forceps under the dissection microscope. **d** View of setup with retracted forceps (using joint r_0), for example for cleaning the tip of the forceps during dissections.

3.3.3 Volumetric two-photon imaging

For two-photon imaging of calcium activity we implemented a fast volumetric approach with two axially extended Gaussian beams. The focal planes of the two beams were axially offset and recorded simultaneously using temporal multiplexing [29, 369, 473] (Fig. 3.3b) which allowed covering the entire structure of interest in a single scan at 60 Hz. The extended imaging volume also minimized artefacts resulting from axial brain motion and corresponding changes in fluorescence intensity.

The laser power at the sample was 6 mW for each beam. The microscope optics and electronics were similar to the one described in [29] with temporal mutliplexing implemented in the Scanimage photon counting mode [29, 474]. The two beams had a path length difference of approximately 2 m, corresponding to a time delay of about 6 ns, and were linearly and orthogonally polarized (Fig. 3.3b). Beam diameter and collimation were adjusted with two lenses (Thorlabs achromatic doublets). The microscope objective (16X Nikon CFI LWD Plan Fluorite Objective, 0.80 NA, 3.0 mm WD) was underfilled, resulting in elongated beam profiles with an axial standard deviation of 4μm and 7μm, respectively, and the beam maxima were offset by 7μm (Fig. 3.3c).

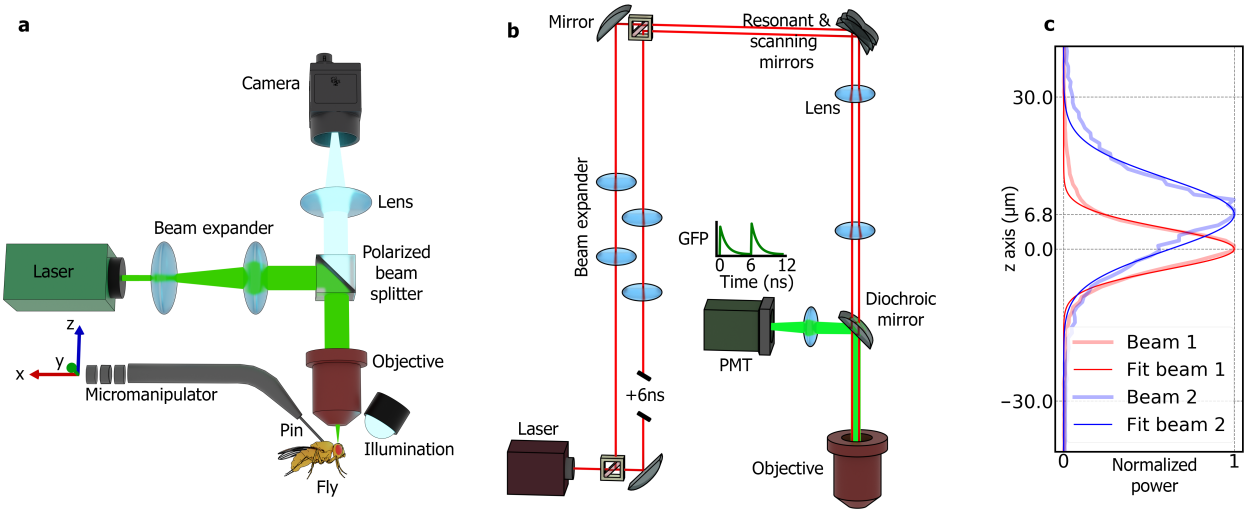


Figure 3.3: Optical setups. **a** Schematics of setup for laser cutting. The laser beam is fixed and the fly is moved along three axes (x, y and z) with a custom motorized micromanipulator. A camera and custom microscope are used to set the key points on the fly's head that define the cutting trajectory. **b** Two-photon microscope with two Gaussian beams that are temporally offset by 6 ns for simultaneous imaging in two different focal planes using temporal multiplexing [369]. **c** Normalized axial (z axis) profiles of the two beams fitted with a Gaussian function.

For long-term imaging experiments, data was recorded in continuous trials of 30 (flies 3 and 4) or 60 seconds (flies 1 and 2), with a break of 5 minutes between trials. Recordings were stopped for 2 minutes per day for refilling the liquid food deposit. The number of trials,

the time of each trial, the total time during which calcium activity was recorded, as well as the total time and temperature of the experiment are shown for each fly in Supplementary Table S3.1.

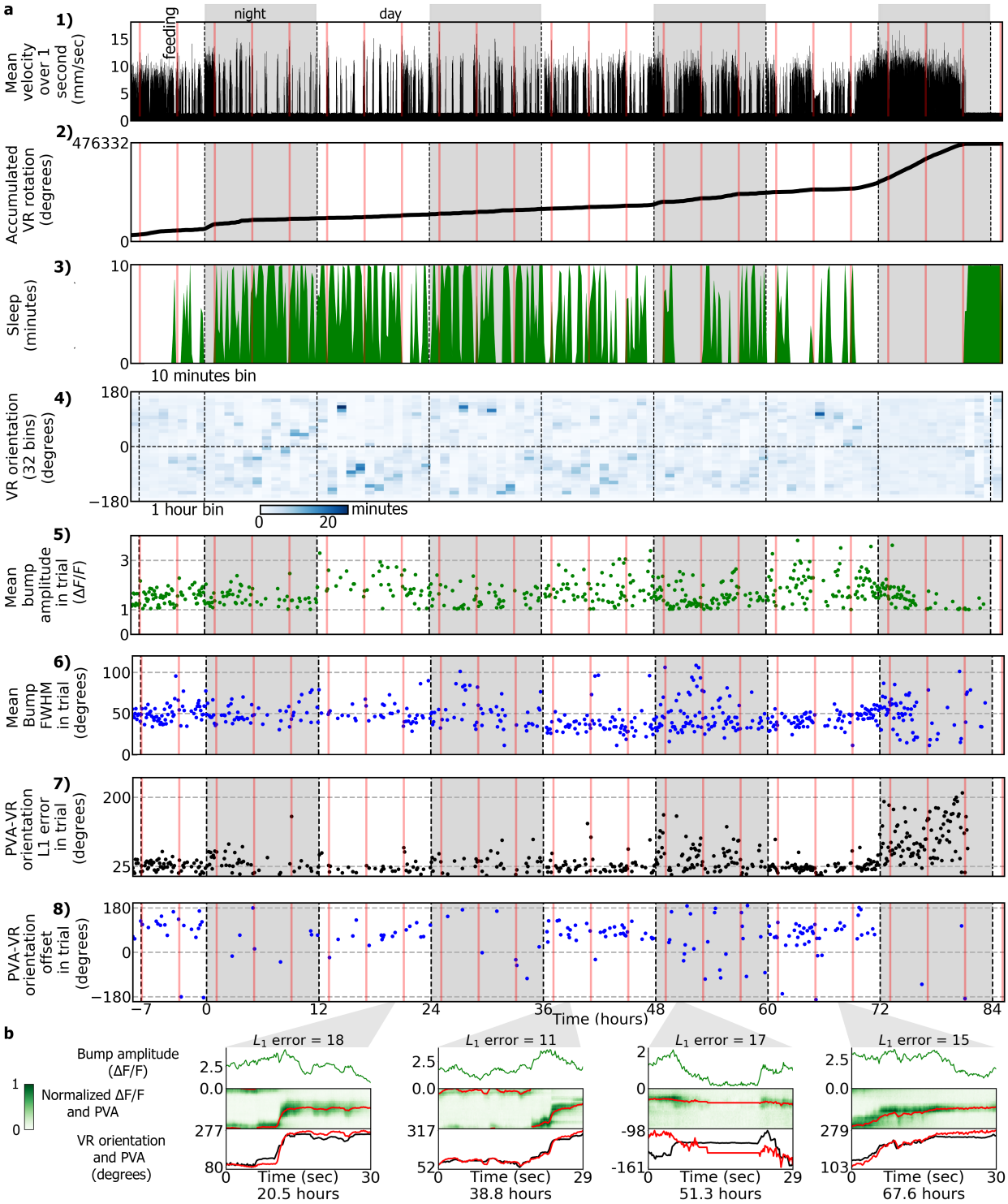
3.3.4 Feeding robot

To maintain the fly over multiple days in the VR setup, a robot was developed for automated feeding of the fly on the ball (Fig. 3.1d and e). A feeder tube can be used for imaging the midgut over up to 16 hours [475]. Installing such a tube during the entire duration of the experiment was however not compatible with virtual reality, where it blocks the fly's view. Therefore a motorized micromanipulator (see Methods 3.5.1) was used to automatically introduce and remove a feeder at preset intervals during the experiment. The feeder consisted of an appropriately shaped needle (Fig. 3.1e and Supplementary Fig. S3.2b) with a piece of cotton inserted into the tip [475]. This needle was parked in a standby position outside the fly's field of view and only approached the fly for feeding (Fig. 3.1d, e, Supplementary Fig. S3.2b).At the beginning of a multiday experiment, the feeding position of the needle was defined such that the fly could extend its proboscis into the food (as monitored with two cameras (Basler acA640-750um) from different angles, Fig. 3.1 d). Further, a trajectory for approaching the needle to the fly's proboscis and then retracting it to a standby position outside the fly's field of view was defined (Fig. S3.2 b).A second needle continually refilled the feeding needle in the standby position with liquid food to keep the cotton moist. This refilling needle was connected through tubes to an elevated liquid food container with an electromagnetic valve (electric solenoid valve working at 24V) for timing the refilling process (see Figure S3.2b). The valve was controlled by an Arduino Uno connected to a host computer that opened the valve every 2 minutes for 0.5 seconds.

The feeder was programmed to feed the fly for 2 minutes every 4 hours. The intervals and duration for feeding were chosen such as to maintain the fly over multiple days but also to ensure sufficient walking activity (which typically decreased after feeding) for monitoring activity in the head direction system of the walking fly.

3.3.5 Calcium imaging over multiple days

For validation of the long-term imaging approach, we monitored calcium activity in wedge neurons in the head direction system of flies walking with a single bright stripe in a VR setup [313] during the day (12 hours) and in darkness during the night (12 hours). The temperature of the preparation was controlled with a perfusion system circulating water under the objective (see Methods 3.5.5 and Supplementary Fig. S3.2c). Locally controlling the temperature under the objective was able to compensate for changes in setup temperature or room temperature in an efficient way. Calcium activity was recorded in trials of 60 (fly



2) or 30 seconds (flies 1, 3 and 4) every five minutes over a total duration of up to seven days, while behavior was monitored continuously.

Wedge neurons encode the head direction of the fly, for example with respect to a bright stripe, in a bump of activity that moves along the ellipsoid body (EB) [313]. To show

Figure 3.4: Imaging and behavior experiment for fly 1. **a**: row **1):** velocity of the fly averaged in bins of 10 minutes. Vertical red lines indicate feeding, while white and grey regions indicate day and night. Row **2)**: accumulated rotation of the fly in the VR. Row **3)**: sleep time in bins of 10 minutes. Row **4)**: time distribution of the VR orientation. The VR orientation is divided into 32 angular bins and 1 hour temporal bins. Row **5)**: mean bump amplitude of wedge neurons in each trial. Row **6)**: mean bump FWHM of wedge neurons in each trial. Row **7)**: L_1 error between the PVA and the VR orientation in each trial. Row **8)**: offset between the PVA and VR orientation in each trial. **b** Example trajectories of activity in wedge neurons in different trials at different times in the experiment. For each of the four trials, top row: amplitude of the bump. Second row: change in fluorescence of wedge neurons (green image) together with the calculated PVA (red line). Bottom row: unwrapped trajectory of the VR orientation (black line) together with the PVA (red line) with PVA-VR orientation offset removed. L_1 error is indicated at the top for each trial.

that neural activity could be recorded reliably in walking animals over multiple days, we therefore verified that the bright stripe in the VR was accurately tracked by the bump in the EB. Bump position (measured with the population vector average (PVA) over 32 regions of interest tiling the EB, Supplementary Fig. S3.4b) tracked the bright bar during the day (as measured with L_1 error between the population vector average of bump activity and the stripe position (equation 3.8)) and with an error during the night, as previously described [313] (Figures 3.4 and 3.5, and Supplementary Figures S3.5, S3.6, S3.7, S3.8). This, together with the animal's walking activity, indicated that neural activity and behavior could be recorded reliably.

Wedge neuron activity was typically higher during the day with visual stimulation than during the night (Fig. 3.5ii). Feeding did not impact wedge neuron activity, but did change walking activity during the night in flies 1, 2 and 4 (Fig. 3.5i). As observed in freely moving flies, walking activity was interrupted by bouts of immobility, both, during the day and night (Figures 3.4 and Supplementary Figures S3.5, S3.6, S3.7, and S3.8) and (in fly 3) showed circadian modulation (Supplementary Figures S3.6 and S3.7). Bouts of immobility or walking activity were also not affected by the onset of the imaging trial and the switching on of the laser.

For fly 2, which was used for imaging immediately after surgery, the L_1 error was large during the first hours of the experiment, even though a bump was visible, and this data was not included in the average statistics (Fig. 3.5). Changes in the dynamics over long timescales were also observed in fly 3 after 5 days. The L_1 error increased while the correlations stayed high (Supplementary Fig. S3.9a), corresponding to a change in the gain of the head direction system with respect to ball rotation. Under these conditions, we observed (after the 5th day) autonomous activity of the bump while the fly was standing still on the ball during the night (Supplementary Fig. S3.9b). This likely indicates a

deterioration of the head direction system, potentially due to phototoxicity, since overall walking behavior was not visibly affected.

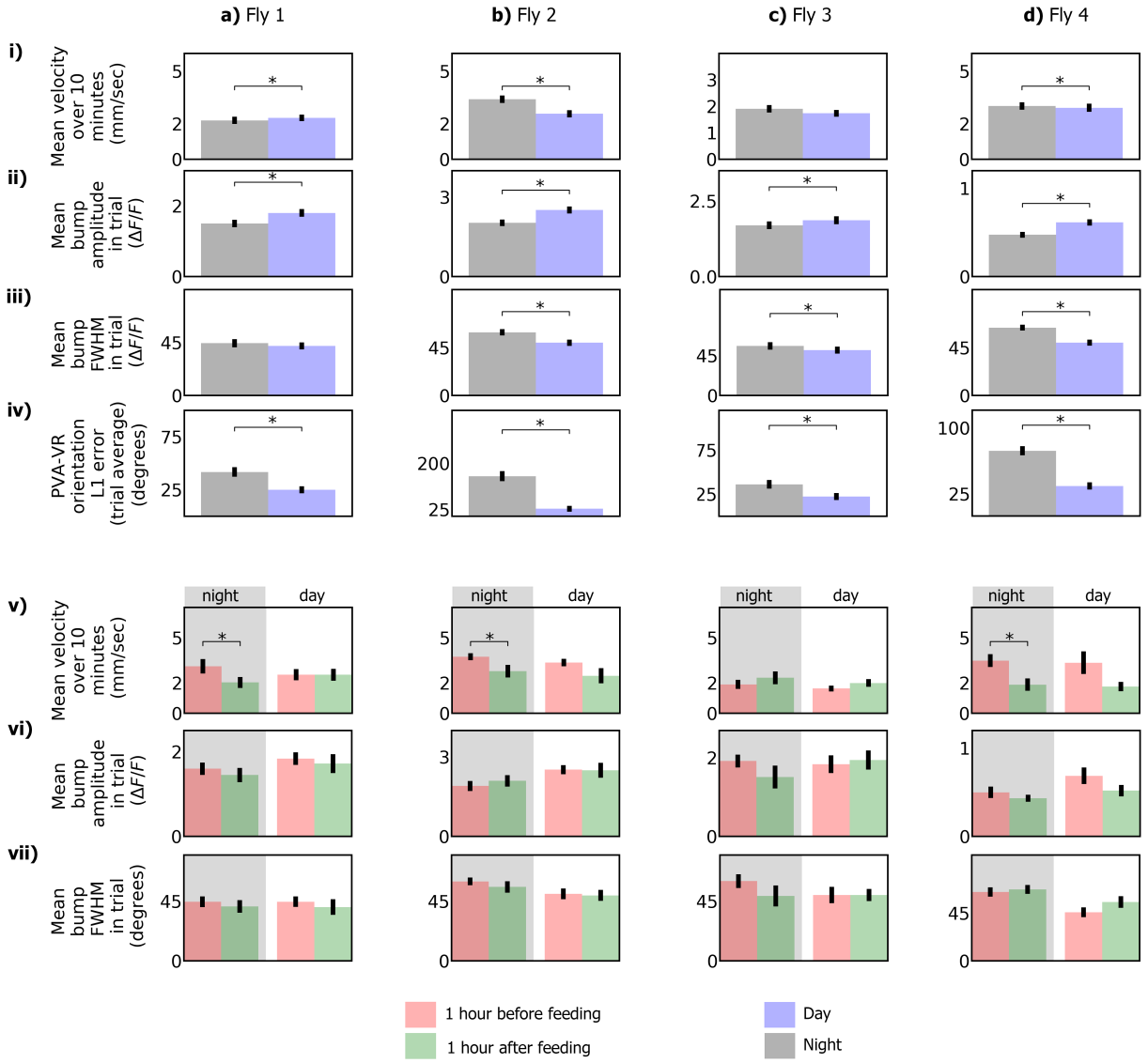


Figure 3.5: Statistical analysis of experiments. Top, row **i)**: mean velocity over 10 minutes during day and night for fly 1 (**a**), fly 2 (**b**), fly 3 (**c**), and fly 4 (**d**). Row **ii)**: mean bump amplitude in trial, row **iii)**: mean bump FWHM in trial, and row **iv)** L_1 error between bump position (PVA) and visual stimulus orientation (VR). Bottom, row **v)**: mean velocity during 1 hour before feeding and 1 hour after feeding for fly 1 (**a**), fly 2 (**b**), fly 3 (**c**), and fly 4 (**d**). Row **vi)**: mean bump amplitude. Row **vii)**: mean bump FWHM. Kolmogorow-Smirnow tests were performed for data in **i)**, **ii)**, **iii)** and **iv)**, while two t-tests were performed for data in **v)**, **vi)** and **vii)**. The p-values were corrected using a multi-test correction (FDR) across flies. A total of 4 FDR tests were performed for each quantity and asterisks indicate statistical significance (corrected p ¡ 0.05, see Methods 3.5.11 for details). The sample size used for the statistical analysis of each quantity is shown in Table S3.3.

3.4 Discussion

We developed a preparation for intermittent functional calcium imaging over up to 7 days during continuous navigation in virtual reality. The behavior and imaging experiments, using volumetric, simultaneous two-plane two-photon imaging, were fully automated and didn't require intervention while the fly was maintained in the VR with an automated feeding system. The preparation opens up the opportunity to investigate neural circuits underlying behavior across multiple timescales, from fast calcium dynamics to changes that occur over multiple days. Monitoring behavior continuously, also between the intermittent imaging sessions as was done here, will be useful for relating behavior to neural activity changes in the context of circadian activity, learning and long-term memory, or sleep.

Functional imaging during sleep has so far only been performed in flies that were placed on the ball for short periods of time [476]. Similarly, circadian activity has so far only been investigated in immobilized animals [294, 390]. The long duration of our experiments resulted in the observation of multiple epochs of extended naturally occurring immobility. Sleep behavior is commonly assessed by immobility of flies for more than 5 minutes, and we used this definition for characterizing the behavior on the ball. Whether the observed state of immobility in this tethered preparation also fulfills other criteria of sleep, such as an increased arousal threshold, will need to be investigated in future experiments.

Fly walking activity depended on temperature, and feeding (decreasing after feeding during the night, Fig. 3.5), which could be adjusted to increase or decrease the amount of sleep or walking activity. The automated feeding setup will also be useful for studying feeding behavior or drug application in behaving animals during functional imaging.

The reproducibility and ease of dissections was improved compared to manual approaches[331], only requiring minimal manual manipulations under the dissection microscope for applying glue. This, together with the extended lifetime and improved health of the fly, even without feeding, makes this approach also attractive for imaging experiments over short timescales (after leaving the flies to recover for several hours [363]). Compared to previous laser surgery approaches [363], a comparatively low cost continuous wave laser was used for surgery in a scanning configuration. This approach allows greater flexibility in terms of head orientation and the geometry of the cut, which is defined in all three spatial dimensions and therefore is not limited to a single focal plane.

Compared to three-photon experiments in intact animals, which still need to be tested for calcium imaging in deeper structures, the approach used here has the advantage that it is compatible with more widely available one- or two-photon imaging approaches [363]. While previous approaches used widefield imaging for monitoring calcium dynamics[363, 470], increased fluorescence background makes this less suitable for imaging in deeper structures and visible excitation light interferes with behavior. We here therefore used two-photon imaging with an axially extended focal volume based on two simultaneously recorded focal

planes using temporal multiplexing. These experiment could also be performed without multiplexing by averaging the signal of the two beams in a single detection channel.

The elongated focal volume resulting from the two extended, axially overlapping Gaussian beams reduced sensitivity to axial brain motion and therefore only lateral motion correction was sufficient for reliably extracting changes in calcium signals. Recording the two beams independently using temporal multiplexing additionally allows axial motion correction [477] which will further improve the accuracy of imaging experiments. Fluorescence was recorded intermittently to minimize photobleaching and phototoxicitiy. Longer continuous recording times could potentially be achieved with methods that can reduce the required fluorescence intensity for extracting calcium signals, for example using deep learning [478].

Overall, long-term imaging in fruit flies walking in VR is expected to contribute to an understanding of the dynamics of neural circuits in a variety of behaviors that bridge multiple timescales, for example circadian rhythms, learning and long-term memory, or potentially sleep.

3.5 Methods

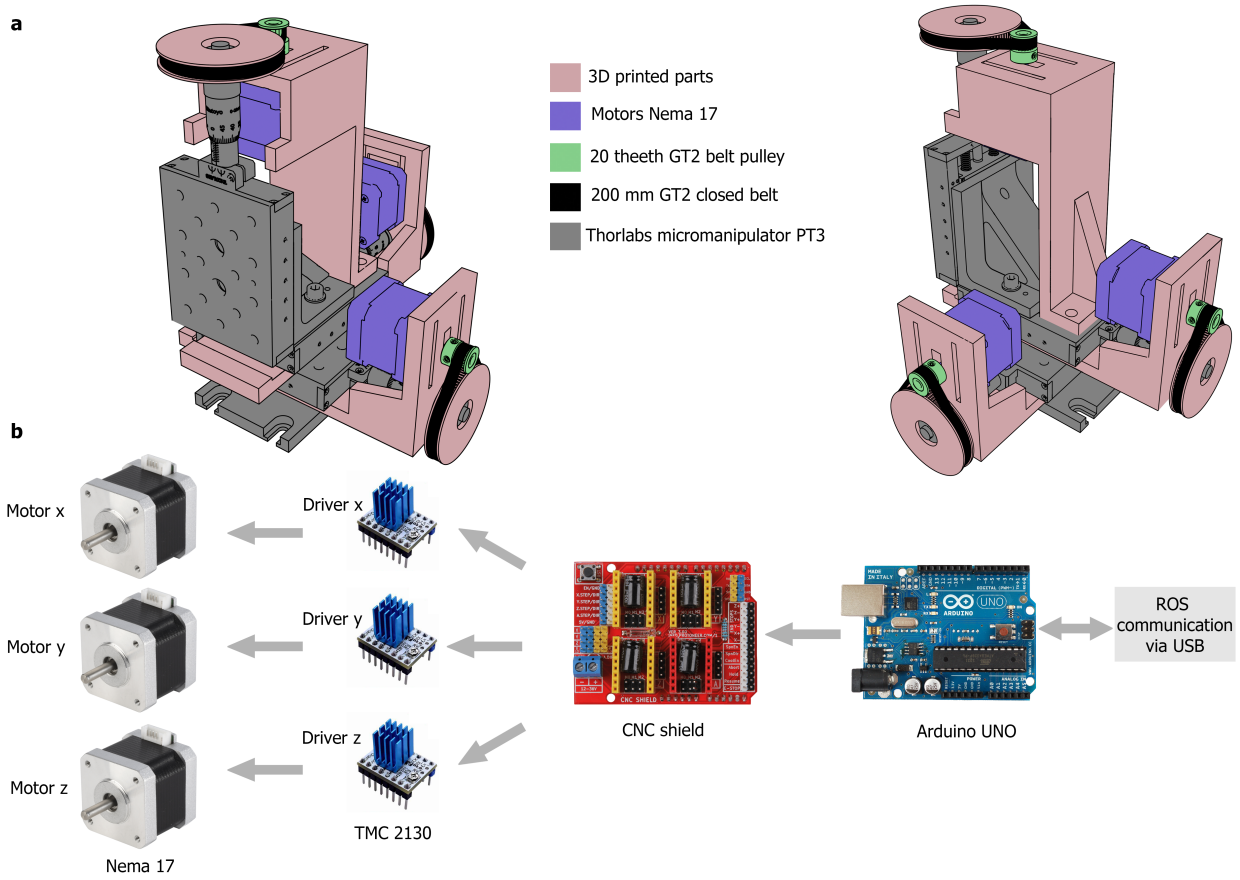
3.5.1 Motorized micromanipulators for fly feeding and laser surgery

For both, feeding the fly on the ball as well as for moving the fly across the laser beam for surgery, we motorized a three-axis micromanipulator (Thorlabs, PT3 with 25 mm travel). Fig. S3.1a shows the mechanical assembly and the control configuration. Each axis was controlled with a stepper motor (Nema 17). Motor torque was transmitted to the micromanipulator actuator through a closed loop toothed belt (GT2 with 6mm width and 200mm length, black parts in Fig. S3.1a), that connected a metal gear attached to the motor axis (20 teeth GT2 belt pulley with 5mm bore, green parts in Fig. S3.1a) and a custom 3D printed gear with 92 teeth attached to the micromanipulator axis. The three motors were supported by 3D printed parts, shown in red in Fig. S3.1a. All 3D printed parts were printed using a Prusa, i3 MK3S printer. Using micro-stepping of the stepper motors (3200 steps per revolution) and gear reduction, the micromanipulator produced a translational resolution of 0.06μm per motor step in each axis.

The stepper motors were controlled through Arduino Uno using a CNC shield with TMC2130 motor drivers powered with 12V. Arduino Uno was connected through USB to a host computer running ROS (Robot Operating System) under Linux. The connection diagram is shown in Fig. S3.1b. Custom control software implemented in Python sent motor commands through serial communication at 30 Hz, while Arduino Uno returns the absolute angular position of each motor at 10 Hz. Multiple micromanipulators could be connected to a single computer through USB ports.

Each micromanipulator was controlled in open loop through either velocity or absolute

position commands from the host computer. A custom command line interface was developed in Python to control each micromanipulator with three control modes: (1) 'stop', where the micromanipulator is standing still. (2) 'manual', where the user can move the micromanipulator using a joystick (Logitech Extreme 3D pro joystick); velocity commands are sent to the motors proportional to the displacements of the joystick axes (absolute maximum velocity can also be adjusted from one of the joystick's axes). (3) 'auto' mode, in which the user can program instructions, via the command line interface, that the micromanipulator repeats sequentially in a loop. Additional instructions can be defined, such as a wait instruction, where the manipulator waits for a defined amount of seconds before moving to the next instruction. This is used in the feeding robot during the standby and feeding states (Fig. 3.1e, panels 1 and 5).



Supplementary Figure S3.1: Motorization of micromanipulator. **a** Two views of 3D model with different parts labeled in different colors. **b** Electronics for controlling Nema 17 motors. Motors are controlled by TMC 2130 drivers attached to CNC shield connected to Arduino UNO. Arduino UNO is connected to a host computer that interacts within the ROS framework by receiving motor commands and sending motor absolute positions.

3.5.2 Laser surgery setup

The laser was expanded and collimated with two lenses to fill the back aperture of the microscope objective (Olympus Plan N 10x/0.25 air objective) over a dichroic mirror (Semrock). A white light LED was used to illuminate the fly and to image its head through the same objective with an additional lens (Thorlabs AC254-250-A) onto a color camera (Basler acA1920-155uc). Laser power was adjusted to 32 mW at the focal plane. The laser beam was additionally pulsed with a mechanical shutter (Thorlabs SH05/M, opened for 15 milliseconds every 45 milliseconds), resulting in an average power of 8 mW at the focus.

The fly, tethered to a pin, was attached to a motorized micromanipulator. This custom-motorized micromanipulator, based on a manual translation stage (Thorlabs, PT1), had a 'manual' control mode, where the position of the fly was controlled by the experimenter using a joystick, and an 'auto' control mode, where the fly was moved along a trajectory through previously defined key positions (see section 3.5.1 for details). First, the head of the fly was positioned (in 'manual' mode) in the field of view of the microscope with the help of three cameras. Two cameras (Basler acA640-750um) had a large field of view for easily positioning the fly in the center of the microscope, and one camera provided the view through the microscope.

After moving the fly's head into focus, 'manual' mode was again used to move the fly's head to 6 key positions (each with three spatial coordinates), defining the trajectory for laser cutting (see Fig. 3.1b, center). After defining the key positions, another motorized micromanipulator in 'manual' mode was used to move a metal shim with a v-shaped incision over the fly's head to protect the eyes from laser light. The motorized micromanipulator with the fly attached was then set to 'auto' mode, so that the fly's head was automatically moved across a trajectory through the previously defined key positions. Finally, the laser shutter was manually opened to cut the cuticle in one pass over the defined key positions.

3.5.3 Microrobotic arm

A 3D model of the microrobotic arm is shown in Fig. 3.2a. Fig. 3.2c shows the setup with the microrobotic arm with forceps and the dissection microscope. Forceps were from Dumont, #5SF. The microrobotic arm was built using translation and rotation stages from Thorlabs that were motorized with stepper motors (Nema 17) (see Fig. 3.2a), similar to the motorized micromanipulator described in section 3.5.1. The microrobotic arm had the following joints: three motorized translational joints (Thorlabs PT3), t_0, t_1, and t_2, three rotational joints r_0, r_1 and r_2, and opening and closing of the forceps (Thorlabs MT1), g, by actuating one of the forceps arms, as shown Fig. 3.2b. The rotational joint r_0 was a swivel mount that was used to easily remove the forceps from under the dissection microscope for cleaning the tip of the forceps with a paper tissue during dissections (see Fig. 3.2d). On the

other hand, r_1 and r_2 used a rotational stage (Thorlabs CR1), and only r_2 was motorized with an attached motor. Micro-stepping of the stepper motors (3200 steps per revolution) together with gear reduction, provided a resolution of 0.10μm per step in translational joints, including the joint closing and opening the forceps, g, and 0.002 degrees per step in the rotational joint r_2. Two additional one-axis translation stages (Thorlabs MT1) were used without motors to correct the offset between the tip of the forceps and the center of rotation of the r_2 joint to ensure that the rotation occurs around the tip of the forceps. To control the five stepper motors, similar electronics were used to the one in the motorized micromanipulators. TMC2130 drivers were used to move the stepper motors, which were plugged into two CNC shields and these connected to a Teensy board 4.0 (which allows faster communication with the computer and therefore leads to smoother control), which was connected to a host computer through a USB port and received velocity commands for each motor. All the joints of the microrobotic arm were controlled with a single joystick (Logitech Extreme 3D pro joystick) through custom software in Python (host computer) and c++ (on the Teensy board). Velocity sensitivity could be adjusted on the joystick for faster or finer movements in each joint.

3.5.4 Fly stocks and preparation

We used 8-10 days old female flies expressing GCaMP7f (flies 1, 2 and 3) or GCaMP8f (fly 4) in wedge neurons (UASGCaMP7f;R60D05-GAL4 and UASGCaMP8f;R60D05-GAL4[313]). Flies were reared at 25 degrees with a 12 hour day-night cycle. During long-term imaging, the same time schedule was followed for switching the VR stimulus on and off.

Flies were haphazardly picked from a vial, briefly anesthetized on ice and attached to a pin mounted on a three-axis micromanipulator with UV glue after immobilizing them in an elongated opening in an aluminum wedge on a cold plate a 4 degrees Celsius [154, 331]. The head of the fly was immobilized by additionally adding two drops of glue with a pin between the thorax and the head close to the eye or occasionally covering the top part of the eye. The pin with the fly was then transferred to the laser cutting setup and an opening was cut into the cuticle as described below (section 3.3.1). The cut cuticle and underlying air sacs were removed with a microrobotic arm with forceps as described below (section 3.3.2). A drop of a glue (DETAX, Freeform, 02204) was placed in the opening and distributed over the edges of the cuticle around the opening with a pin, and then cured with UV light (UV gun as in [331]) for twice 15 seconds from each side of the fly's head. Flies were then detached from the pin by gently pushing against the thorax close to the attached pin with forceps.

For each experiment we prepared up to six flies. Each surgery took about 20 minutes. After surgery, flies were glued to a microscope cover slide (22 mm $\times$ 22 mm, thickness No. 1, Cat. No. 631-0124) while cold anesthetized, either after being transferred to a vial (flies

3 and 4) and left to recover over night, or directly after surgery and left to recover for about 30 minutes (flies 1 and 2).

To attach flies to the cover slide, UV glue (Norland Optical Adhesive 68[363]) was distributed at the center of a cover slide, in a thin layer to minimize optical aberrations. The fly was positioned upside down with its head and part of the thorax on top of the glue layer under a dissection microscope (Leica M205 C, Planapo 10x objective) with forceps, gently pushed against the surface and the glue was cured with UV light for twice 15 seconds from different angles. Additionally, in flies 3 and 4 the antennae were covered with UV glue, to exclude that potential activity in the EB during immobility could be due to movement of the antennae.

For imaging, the microscope slide was fixed to a custom-designed aluminium holder in the microscope using two screws (Fig. S3.2a). The holder was further attached to a micromanipulator using a magnetic mount (Thorlabs KB25) and the fly was centered on the ball [331]. We then monitored neural activity of the fly with the microscope and its walking behavior on the ball for about 5 minutes and either started the long-term experiment or tested a different fly if imaging quality or behavior weren't satisfactory. A total of 8 flies were selected for long-term imaging after surgery, 4 of them (all glued to the glass immediately after surgery) died after at least 12 hours of recordings, the other flies lasted between 2 and 7 days (flies 1,2,3 and 4).

Liquid fly food was prepared at the beginning of the experiment and stored at 4 degrees Celsius. 0.5 L of distilled water, 50 g extracted yeast, and 25 g sucrose was heated to 60 degrees for 10 minutes. After cooling down to room temperature, 0.75 g methyl 4-hydroxibenzoate, 1.25 mL Ethanol and 1 mL Propionic acid were added. The food was stored at 4 degrees. The experiment's liquid food deposit was refilled once a day with a mixture of 200 mL liquid food and 200 mL of distilled water.

Beam profiles were measured with z-stacks recorded with 1μm diameter fluorescent beads (average of 10 stacks). Fig. 3.3c (semitransparent red and blue lines) shows measured normalized beam profiles fitted with the following Gaussian function:

$$G(z) = exp\Big(- \frac{(z - \mu_z)^2}{2\sigma_z^2}\Big), \tag{3.1}$$

with maximum μ_z and standard deviation σ_z^2 (Fig. 3.3C, solid red and blue lines).

3.5.5 Temperature control

We used a perfusion system (Multichannel Systems, PPS2 Peristaltic Perfusion System) to control the temperature during imaging. This perfusion system continuously circulated water between the objective and the cover slide in a closed loop at a desired temperature. Water was first heated to 40 degrees in a beaker and then cooled down to 10 degrees inside

	Number of trials	Trial time (seconds)	Total time of calcium imaging (hours)	Total time of the experiment (hours)	Temperature (degrees)
Fly 1	1019	30	8.5	94.0	20
Fly 2	486	60	8.0	49.2	22
Fly 3	1798	30	15.0	166.6	20
Fly 4	544	30	4.5	42.0	22

Supplementary Table S3.1: Trials, timings and temperatures of the long-term imaging experiments for each recorded fly.

the tube leading to the objective before reaching the final temperature in a temperature controlled needle dispensing it onto the microscope slide (Mutlichannel Systems, PH01 Perfusion Canula, only heating). Water was removed through a second needle, as shown in Fig. S3.2c. Preheating of water to 40 degrees before cooling was necessary to avoid the formation of bubbles under the objective. The temperature at the objective was set to 22 degrees for flies 1 and 2, and to 20 degrees for flies 3 and 4.

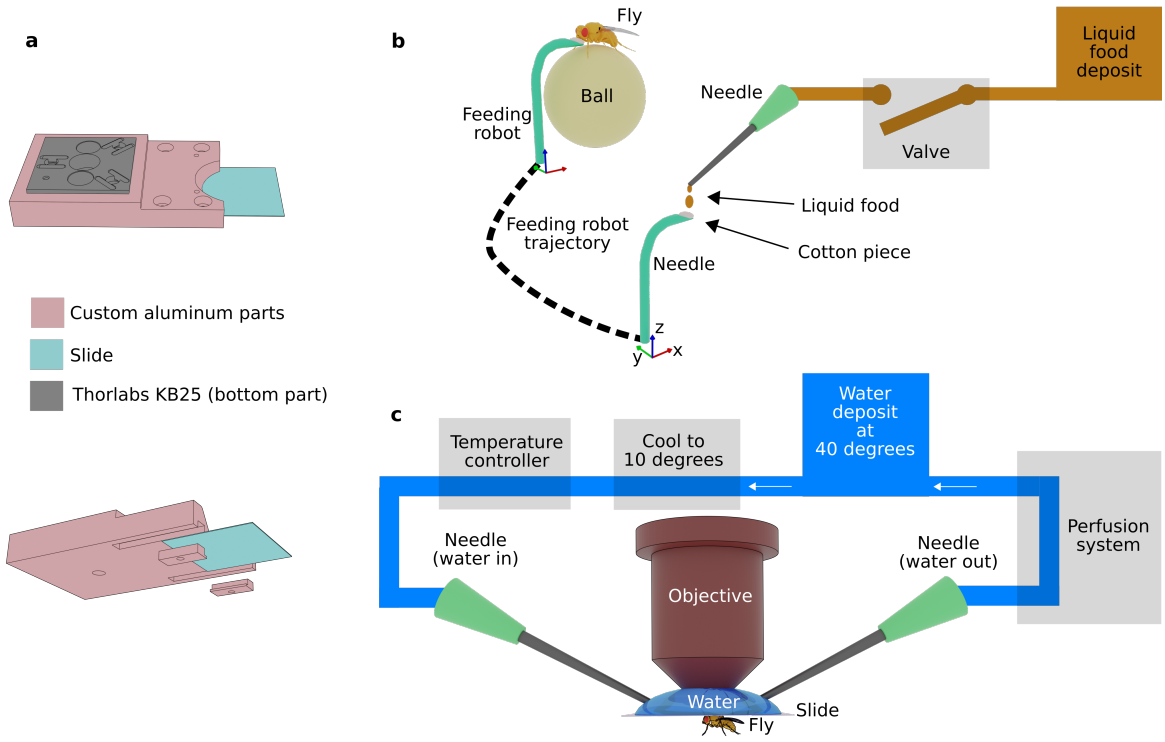
3.5.6 Virtual Reality setup

Ball motion was tracked with a single camera (Basler acA640-750um) and a single bright stripe was projected onto a five-sided screen using a virtual reality (VR) system based on two DMDs updated at 120 Hz[157]. Ball motion was tracked using optical flow [157] at 300 Hz. Compared with [157] ball tracking frame rate was decreased to increase the camera exposure time and reduce the required IR light intensity. The screen was made of semi-transparent paper (Hobbycut Mylarfolie Schablonen-Material) that was attached to a pentagonal frame printed with a 3D printer (Prusa, i3 MK3S) out of transparent PLA filament. The screen was mounted in parallel to the microscope platform. The vertical stripe used for behavior experiments was oriented orthogonally with respect to the platform. A total of four cameras were monitoring the behavior of the fly and the feeder through the semi-transparent screen. The screen had a radius of 30 mm and a height of 70 mm. The fly was at the center of the pentagonal screen, at a height of 20 mm from the top.

A laser (Toptica, ibeam Smart, 488 nm) was used as a light source and was modulated to only switch on during the turnaround of the resonant mirror where imaging data is not recorded [479, 480]. Additionally laser line and complementary emission filters were used to reduce the light on the PMT.

3.5.7 Hardware and software synchronization

Three computers were connected in a local network. The flow of information between the three computers and experiment hardware is shown in Fig. S3.3. One computer (Windows



Supplementary Figure S3.2: **a** Different views of holder for microscope cover slide with glued fly. **b** Components of feeding system. A needle with a piece of cotton inserted at the tip, is parked in standby under another refilling needle. Refilling is controlled by a valve that opens and closes every 2 minutes, connected to a liquid food deposit. After 4 hours of standby, the feeding needle moves along a trajectory to feed the fly on the ball. **c** Temperature control of the water between the objective and microscope cover slide. Water in a container is heated to 40 degrees and a perfusion system circulates the water to a cooling chamber where it is cooled down to 10 degrees. From there, water is heated again to the desired temperature by a temperature controller and finally circulated under the objective, as commonly done to prevent formation of bubbles under the objective.

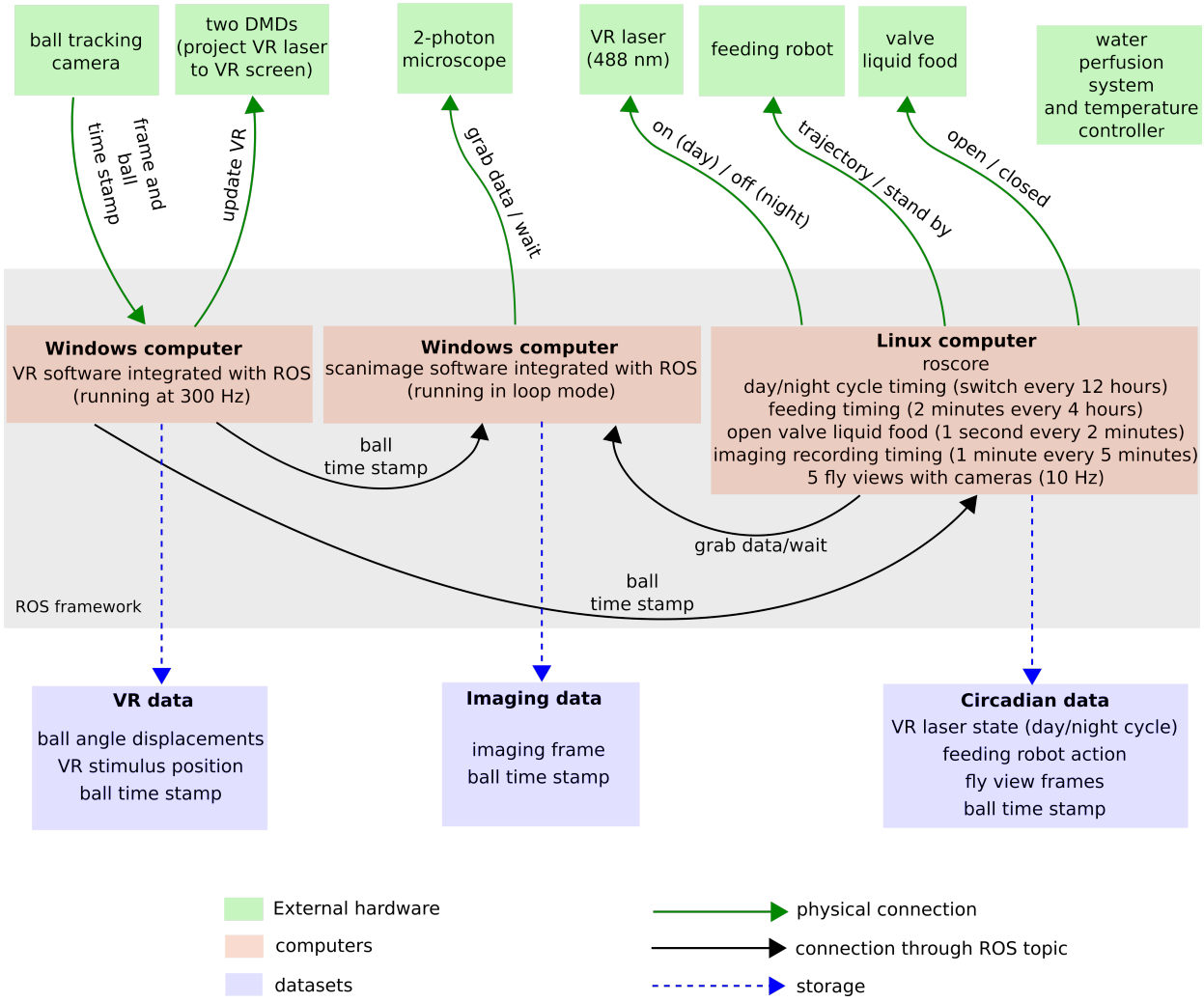
10) ran the VR software which was integrated with ROS (Robot Operating System) for Windows, and published through the network in a ROS topic at 300 Hz. The time stamp of each frame collected by the camera which tracked the movements of the ball (ball time stamp). This ball time stamp was used as the common time for all events throughout the

entire experiment. A second computer (Windows 10) running Scanimage [474] integrated with ROS (ROS toolbox in Matlab R2016b), was subscribed to the ball time stamp ROS topic. This modified Scanimage version additionally saved a file containing the ball time stamp corresponding to each Scanimage imaging frame. Scanimage ran continuously in its loop mode while being subscribed to a ROS topic to receive grab and stop commands which were sent from a third computer to control the timing of imaging recordings. This third computer (Ubuntu 18.04 LTS and ROS melodic) ran Roscore and other ROS nodes that were also subscribed to the ball time stamp ROS topic. The ROS nodes in this computer were custom-developed in Python and included: a node that controlled the day and night cycle by modulating the power (on and off) of the VR laser beam, and stored the state of the laser with the corresponding ball time stamp; a node to control the robotic feeder, which stored the actions of the robot in the 'auto' mode with the corresponding ball time stamp; software controlling the timing for opening the liquid food valve; a node showing all frames at 10 Hz, combining different views of the fly (front, zoomed in front, left, zoomed in left, and left top) from five different cameras (Basler Basler acA640-750um), and stored each camera frame (fly view frame) with its corresponding ball time stamp; and software that published in a ROS topic grab and stop commands that were received by Scanimage to record imaging data.

3.5.8 Data storage and preprocessing

Each computer stored a dataset, resulting in three datasets per experiment that included VR data, imaging data and circadian data, as shown in Supplementary Fig. S3.3. The three datasets were joined together and kept in a external storage unit for data analysis. The amount of data for single flies ranged from 0.5 Tb up to to 1.5 Tb. Scanimage time stamps were synchronized with ball time stamps with a conversion factor measured form simultaneously recorded data, and either time stamps were used.

For data analysis, we described the data of a single fly in DataFrames using the library Pandas, which contained, for example, the link to the file directory of each single imaging frame, together with its corresponding ball time stamp, the corresponding interpolated VR (ball displacements and VR stimulus position), circadian data (light state and feeding robot actions), and the corresponding fly view frame closest to that particular time stamp. This way of organizing the data allowed access to all data without having to load them into memory. We divided the data into continuous recordings of imaging data (trials) lasting for 60 seconds in experiment 1 and 2 and 30 seconds for experiments 3 and 4.



Supplementary Figure S3.3: Schematic of setup control. Three different computers communicate trough the ROS framework synchronized to the ball tracking time. The first computer runs the VR software that obtains the ball tracking data and projects the bright stripe onto the VR screen using two DMDs, similar to [157]. The second computer controls the 2-photon microscope and receives commands for recording imaging data. The third computer controls the day and night cycle, the feeding robot, and obtains views of the fly from different cameras. Each computer stores a dataset for analysis.

3.5.9 Imaging data analysis from EPG neurons

The first step for data analysis of each trial was to correct the lateral motion between two-photon images (referred as xy motion). First, for a trial a template was constructed by averaging over the first 20 frames. The xy offset for the remaining frames in the trial with

	Averaged imaging frames for lateral motion correction	Averaged imaging frames in template	Amplitude threshold A_{th} ($\Delta F/F$)	Fluorescence threshold F_{th} ($\Delta F/F$)	Linear velocity threshold v_{th} (mm/sec)	L_1 error threshold (degrees)	Time range for statistical analysis (hours)
Fly 1	10	3600	1	0.6	0.1	50	[-7, 68]
Fly 2	20	7200	1	0.6	0.1	50	[0, 39]
Fly 3	10	3600	1	0.6	0.1	25	[-10, 84]
Fly 4	10	3600	0.3	0.35	0.1	25	[-5, 30]

Supplementary Table S3.2: Parameter values used in each experiment for data analysis.

respect to the template was computed using a phase correlation algorithm implemented in the Skimage library [481]. Using the xy offset, all frames in the trial were aligned, which included 3600 (for flies 1, 3 and 4) or 7200 frames (for fly 2), and the average of these frames was used as a common template for all the remaining trials (see Fig. S3.4a). The offset of every frame in all trials was computed with respect to the common template using the same algorithm. To improve the xy motion correction, we averaged up to 20 frames and used either a Gaussian or a median filter to smooth frames, as shown in Fig. S3.4a. These setting were selected once for each fly and maintained over all trials.

After correcting lateral motion, a total of 32 wedge-shaped regions of interest (ROIs) were defined and the sum of intensity in each ROI was computed for each frame.

For each trial, two intensity matrices, I_1 and I_2, corresponding to the two simultaneously recorded imaging planes were obtained. Each intensity matrix included the intensity in each ROI computed from 10 averaged frames, providing a time resolution of 0.17 seconds. Both matrices had a size of $32 \times T/m$, where T is the number of frames in a trial per simultaneous plane, and $m = 10$ is the number of averaged frames (Fig. S3.4b). We then computed the change in fluorescence for each recorded plane, $(\Delta F/F)_1$, and $(\Delta F/F)_2$, as

$$\begin{cases} (\Delta F/F)_1(i,t) = \frac{I_1(i,t) - I_1^0(i)}{I_1^0(i)} & \text{for each ROI} \quad i = 0, ..., 31 \quad t = 0, ..., T/m \\ (\Delta F/F)_2(i,t) = \frac{I_2(i,t) - I_2^0(i)}{I_2^0(i)} & \text{for each ROI} \quad i = 0, ..., 31 \quad t = 0, ..., T/m, \end{cases} \tag{3.2}$$

where $I_1^0(i)$ and $I_2^0(i)$ are the baseline activity of each ROI i for each plane defined as the mean of 10% of imaging frames with lowest activity in ROI i. We finally combined the change in fluorescence in each plane to obtain the fluorescence matrix:

$$\Delta F/F = \frac{(\Delta F/F)_1 + (\Delta F/F)_2}{2}. \tag{3.3}$$

With this fluorescence matrix, we computed the amplitude of the bump of activity in wedge neurons, $A(t)$, as the maximum value in $\Delta F/F$ at a given time t:

$$A(t) = max_i(\Delta F/F(i,t)), \tag{3.4}$$

and the full width at half maximum, FWHM(t).

To observe how the bump amplitude and bump width changed over time, we computed the mean bump amplitude in the trial, $< A >$, and the mean bump full width at half maximum in each trial, $<$ FWHM $>$,

$$\begin{cases} < A >= \frac{1}{T'} \sum_{t \text{ where } A(t) > A_{th}} A(t) \\ < FWHM >= \frac{1}{T'} \sum_{t \text{ where } A(t) > A_{th}} FWHM(t) \end{cases} \quad \text{where} \quad T' = \sum_{t \text{ where } A(t) > A_{th}} 1 \tag{3.5}$$

filtering out times where the bump amplitude, $A(t)$, was lower than a threshold, $A_{th} = 1$. This avoided averaging over times where a bump was not visible when the fly was not moving. Figures 3.4, S3.5, S3.6, S3.7 and S3.8 show the mean bump amplitude in each trial, $< A >$ (row 4)). The row 5) shows $< FWHM >$.

We then computed the bump position in wedge neurons in each trial using algorithm 1. For this, first the time t where the change in fluorescence is largest per trial, t_{max}, was determined. Then the population vector average (PVA) at time t_{max} was calculated as $PVA(t_{max}) = pva(t_{max})$, with the function $pva(t)$ for time t defined as:

$$pva(t) = \frac{32}{2\pi} arctan2\left(\frac{1}{32} \sum_{i=0}^{32} \Delta F/F(i,t) \sin\left(\frac{2\pi i}{32}\right), \frac{1}{32} \sum_{i=0}^{32} \Delta F/F(i,t) \cos\left(\frac{2\pi i}{32}\right) \right) \tag{3.6}$$

Finally, the PVA was computed backwards and forwards in time from t_{max}. If the maximum change in fluorescence at time t was larger than the threshold F_{th}, the PVA was computed as $PVA(t) = pva(t)$. Otherwise it was assigned the next or previous value, $PVA(t+1)$ or $PVA(t-1)$, depending on the direction of time:

The PVA in the range of $[0, 32]$ was scaled to $[-180, 180]$, corresponding to the VR orientation, $R(t)$. The PVA and VR orientation were both unwrapped to compute the PVA-VR orientation offset, PVA_0, for each trial. The PVA-VR orientation offset was computed as the mean of the offset between the two variables at times when the bump amplitude, $A(t)$, was larger than the threshold A_{th}:

$$PVA_0 = \frac{1}{T'} \sum_{t \text{ where } A(T) > A_{th}} \Big(R(t) - PVA(t)) \Big) \quad \text{where} \quad T' = \sum_{t \text{ where } A(T) > A_{th}} 1 \tag{3.7}$$

Then, the L_1 error between the PVA, with offset PVA_0 subtracted, and the VR orientation was found as:

$$L_1 = \frac{1}{T} \sum_{t=0}^{T} \Big| (PVA(t) - PVA_0) - R(t) \Big| \tag{3.8}$$

This error indicated how well the PVA encoded the VR orientation. In trials where the fly was not moving, this error was close to zero. Values of L_1 error in trials where the mean velocity during the trial v^{trial} was lower than a threshold $v^{trial} < v_{th} = 0.1mm$ could therefore be removed. The values for the L_1 error are shown in the row 7) of Fig. 3.4, and Supplementary Figures S3.5, S3.6, S3.7 and S3.8.

Algorithm 1 Calculation of PVA for each trial

$t_{max} = argmax_t\Big(\Delta F/F(i,t)\Big)$
$PVA(t_{max}) \longleftarrow pva(t_{max})$
$t \longleftarrow t_{max} - 1$
for $t \geq T/m$ **do** ▷ Backwards in time
  if $max\Big(\Delta F/F(t,i)\Big) < F_{th}$ **then**
    $PVA(t) \longleftarrow PVA(t+1)$
  else
    $PVA(t) \longleftarrow pva(t)$
  end if
  $t \longleftarrow t - 1$
end for
$t \longleftarrow t_{max} + 1$
for $t \leq T/m$ **do** ▷ Forward in time
  if $max\Big(\Delta F/F(t,i)\Big) < F_{th}$ **then**
    $PVA(t) \longleftarrow PVA(t-1)$
  else
    $PVA(t) \longleftarrow pva(t)$
  end if
  $t \longleftarrow t - 1$
end for

In addition, to analyze changes in PVA-VR orientation offset, PVA_0, over the course of the experiment, we selected the offset in trials where both the mean velocity in the trial was higher than the threshold v_{th}, and where the L_1 error was lower than a second threshold, L_1^{th}. This threshold was selected at $L_1^{th} = 25$ degrees for flies 3 and 4, and $L_1^{th} = 50$ degrees for flies 1 and 2, since the trial duration for the latter was twice as long and therefore larger errors accumulated. PVA-VR orientation offsets with high L_1 error were removed since in this case the PVA_0 offset was not reliable. Cases where the L_1 error was large included trials during the night (See Fig. 3.5). Another source of large L_1 error were fast rotations of the fly that resulted in very fast bump movement with low fluorescence intensity that was therefore not recognized by the algorithm 1. All parameter values for analysis of each fly are shown in Supplementary Table S3.2.

3.5.10 Behavioral data analysis for each fly

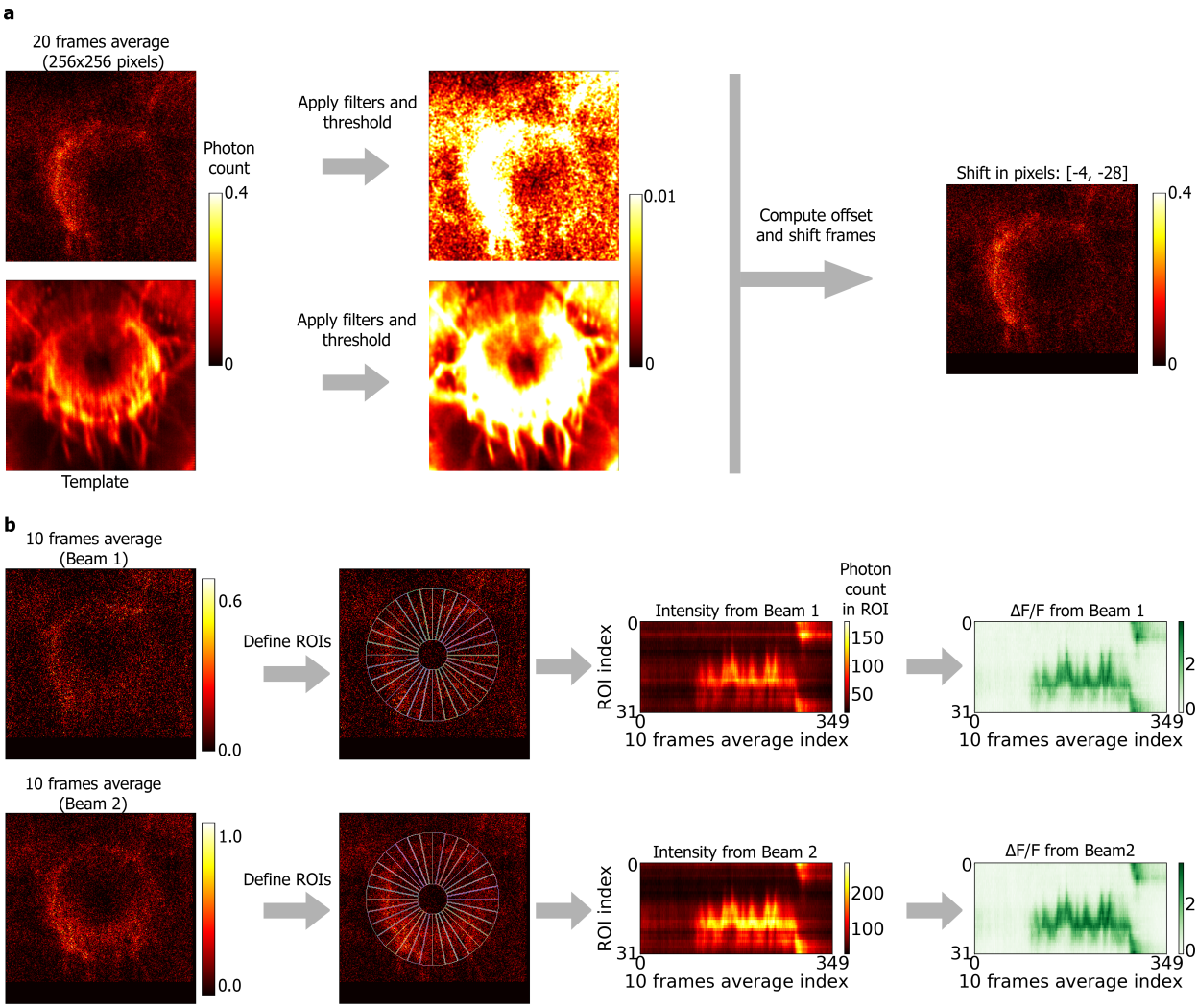
Fly behavior was extracted from ball movements recorded over the entire experiment, also in between imaging trials. Ball tracking [157] provided the angular displacement of the ball along the three axes of rotation, ($b_x(k)$, $b_y(k)$, $b_z(k)$), at a rate of 300 Hz for time stamp k. We first computed the linear velocity of the fly in mm/sec as:

$$v(k) = R_b \frac{\sqrt{b_x(k)^2 + b_y(k)^2 + b_z(k)^2}}{\Delta t} \tag{3.9}$$

where $R_b = 3$ mm is the radius of the ball and $\Delta t = 1/300$ sec is the time between consecutive frames. We then computed the mean velocity of the fly over 10 minutes by averaging v(k) over 10 minute bins (Fig. 3.4 and Supplementary Figures S3.5, S3.6, S3.7 and S3.8, row 1)).

Since the ball tracking algorithm shows slow drift due to imaging noise, we defined a velocity threshold, $v_{th} = 0.1$ mm that was used to detect sleep events. Sleep was defined as the velocity being below v_{th} for at least 5 minutes [20]. To display sleep events, we finally computed the amount of sleeping time in bins of 10 minutes (Fig. 3.4 and Supplementary Figures S3.5, S3.6, S3.7 and S3.8, row 3)). That the fly was not moving during these times could additionally be verified by simultaneously recorded videos of the fly on the ball.

Walking direction of the fly was computed from the accumulated VR rotation (Fig. 3.4 and Supplementary Figures S3.5, S3.6, S3.7 and S3.8, row 2)). The distribution of VR orientation over time in a histogram with a bin width of VR angular range [-180, 180] divided by 32 (wedges) over 1 hour is shown in Fig. 3.4 and Supplementary Figures S3.5, S3.6, S3.7 and S3.8, row 4).



Supplementary Figure S3.4: Analysis of imaging data. **a** In each trial, lateral motion is corrected using a template. Left side: 20 frames are averaged and Gaussian and threshold filters are applied to both the template and the 20 averaged frames (center). A phase correlation algorithm is used to compute the offset from the template and the 20 averaged frames are shifted to match the template (right). **b** 10 frames were averaged in the planes recorded from each beam (left) and 32 ROIs (center left) were defined to calculate the intensity over time within each ROI (center right). The change in fluorescence $\Delta F/F$ was calculated for each beam (right) and the final change in fluorescence was the average of the two.

3.5.11 Statistical analysis of behavior and imaging data

For each fly we compared the following quantities across trials between day and night: (i) walking velocity, (ii) mean bump amplitude per trial, (iii) mean bump FWMH per trial, and (iv) L_1 error. Walking (or ball) velocity was averaged over 10 minutes, as described in section 3.5.10, while the other quantities were obtained for each trial, as explained in

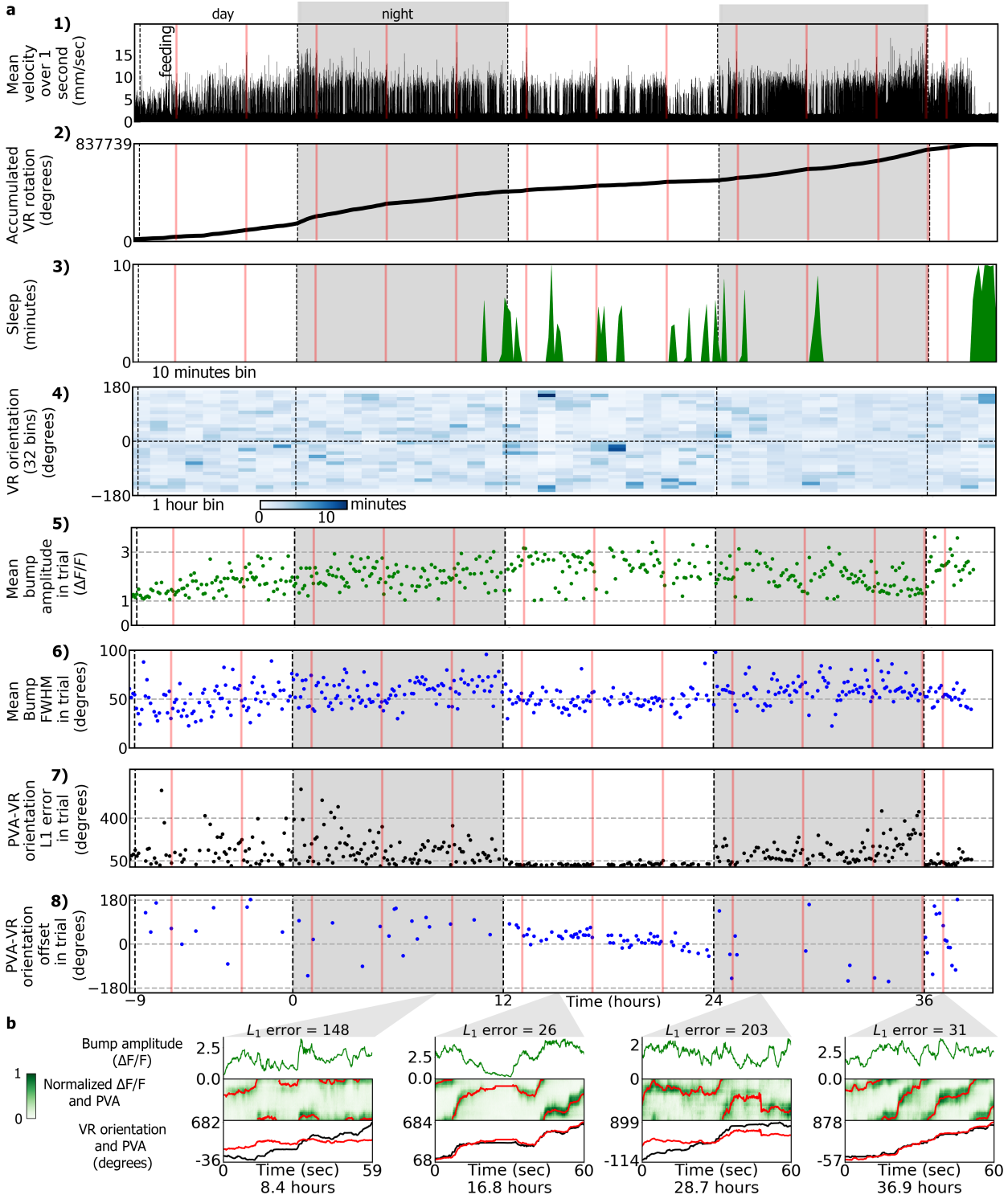
section 3.5.9. For (ii), (iii) and (iv) only trials where the fly was moving were included (only trials with a mean velocity larger than a threshold velocity v_{th}). Statistical significance was assessed with Kolmogorow-Smirnow (KS) test (in Scipy [482]). The obtained p-values from all the KS tests were corrected across flies using the Benjamini-Hochberg[483] or false discovery rate (FDR) (in Statmodels[484]). A total of 4 FDR tests were performed for each quantity. The FDR correction reduced false positive results, providing a set of corrected p-values. Additionally, only time intervals where wedge neurons tracked the bright stripe in the VR well were included (see Table S3.2, last column). The compared quantities were considered true positives (that is, significant) when the corrected p-values were lower than 0.05, and were indicated by an asterisk in Fig. 3.5 i), ii), iii) and iv).

In addition, the effect of feeding on (v) the velocity of flies, (vi) the mean bump amplitude per trial and (vii) the bump FWHM per trial was analyzed. For comparison, 1 hour before feeding and 1 hour after feeding, both during the day and during the night, and within the same time interval, as in the previous analysis (see Table S3.2), were considered. For these data we performed two t-tests, one with values during the day and the other with values during the night. We again used the FDR correction across flies to obtain corrected p-values for all compared quantities, and significance (corrected p ¡ 0.05) was indicated with an asterisk in Fig. 3.5 v), vi), and vii).

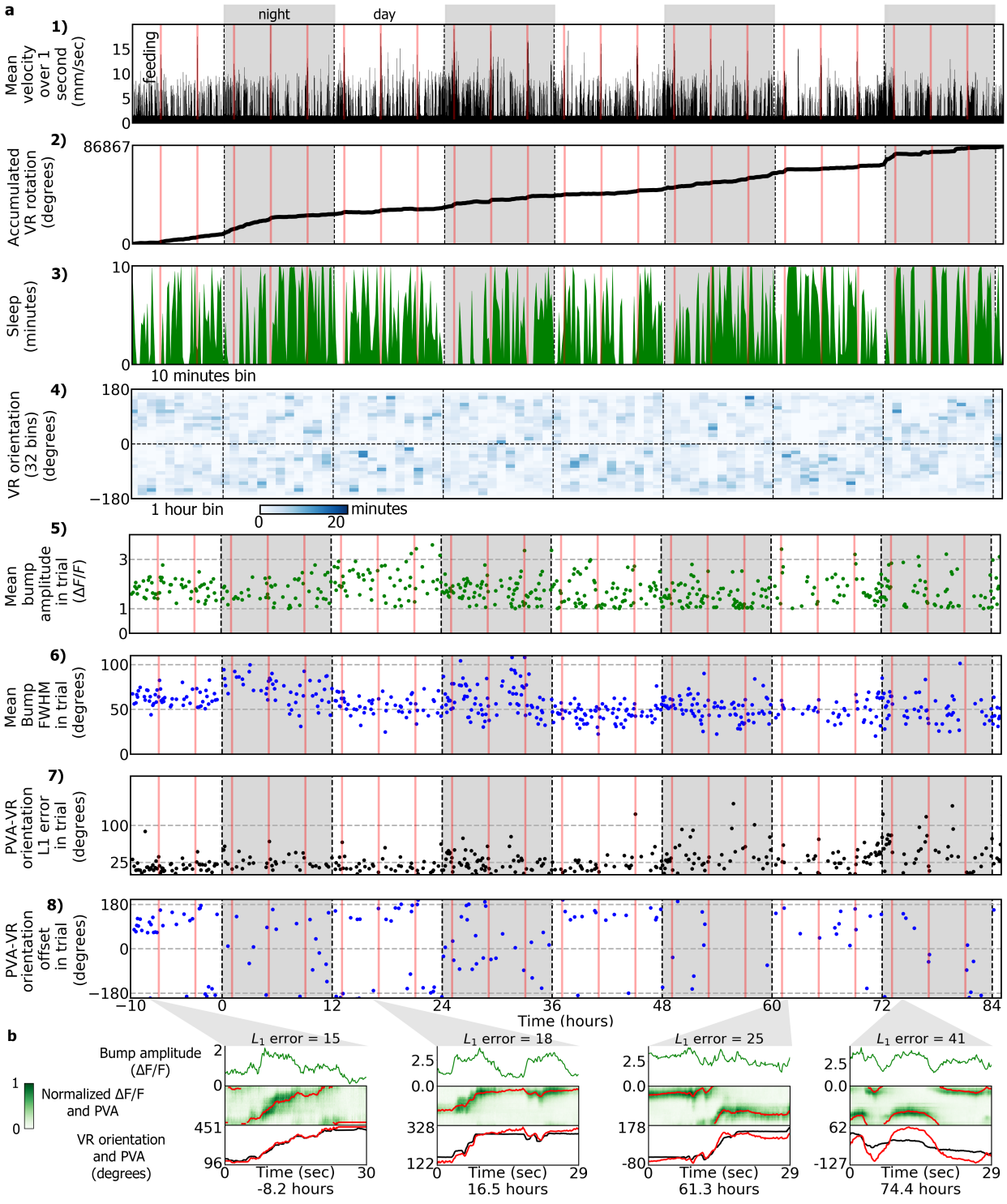
Statistical significance in velocity was found for 3 out of 4 flies during the night (Fig. 3.5 v)). The sample size used in each test for each quantity is shown in Table S3.3.

	Fly 1		**Fly 2**		**Fly 3**		**Fly 4**	
	Day	**Night**	**Day**	**Night**	**Day**	**Night**	**Day**	**Night**
i) Mean velocity over 10 minutes	214	234	90	140	275	278	100	107
ii) Mean bump amplitude in trial	215	160	95	196	180	187	184	195
iii) Mean bump FWHM in trial	215	160	95	196	180	187	184	195
iv) PVA-VR orientation L1 error (trial average)	215	160	95	196	180	187	184	195
v) Mean velocity over 10 minutes before and after feeding	10	9	7	4	11	12	4	5
vi) Mean bump amplitude in trial before and after feeding	10	9	7	4	11	12	4	5
vii) Mean bump FWHM in trial before and after feeding	10	9	7	4	11	12	4	5

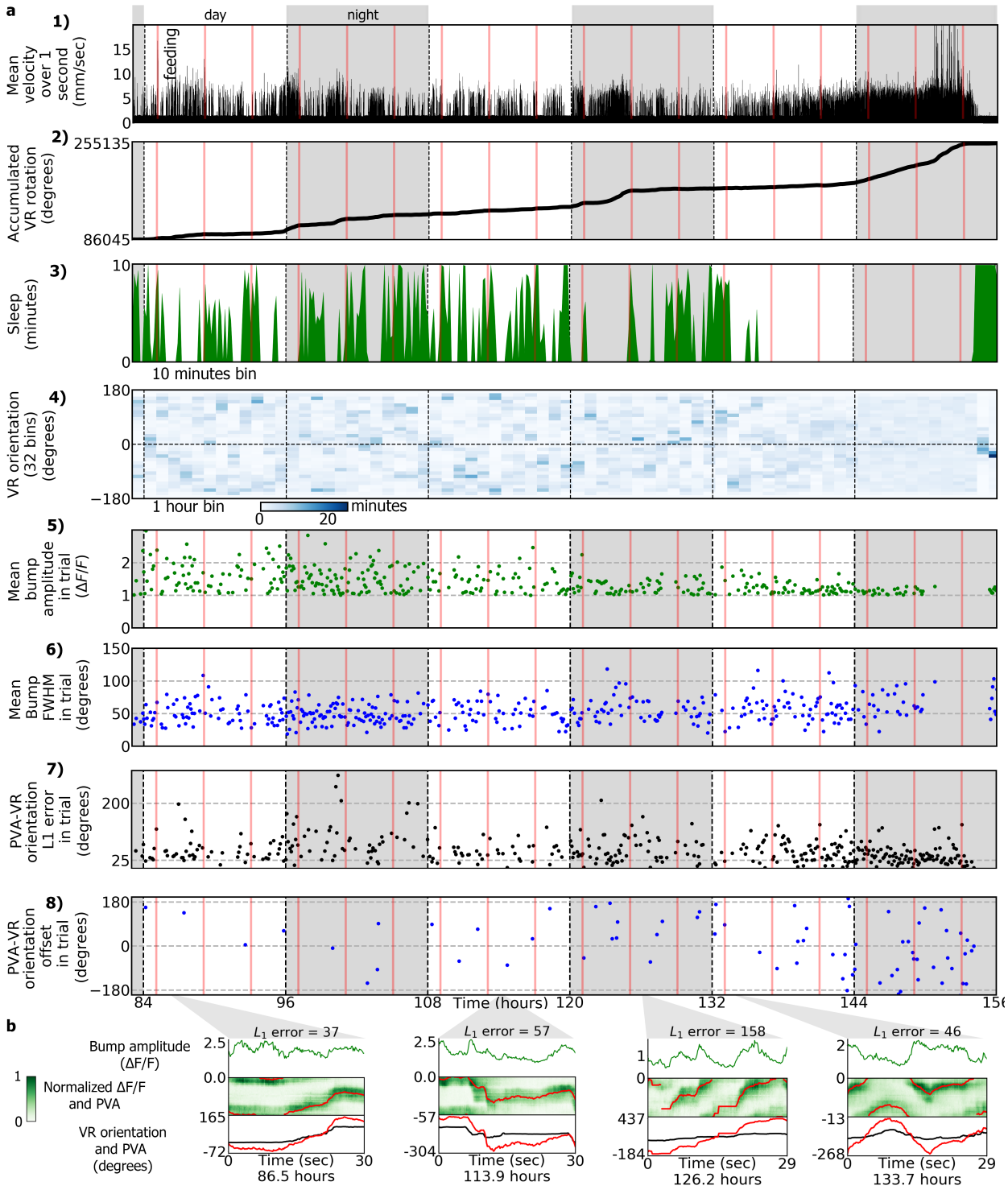
Supplementary Table S3.3: Sample size used for the statistical analysis shown in Fig. 3.5. For quantities v), vi) and vii), the number of samples before and after feeding is the same, shown here both during the day and during the night.



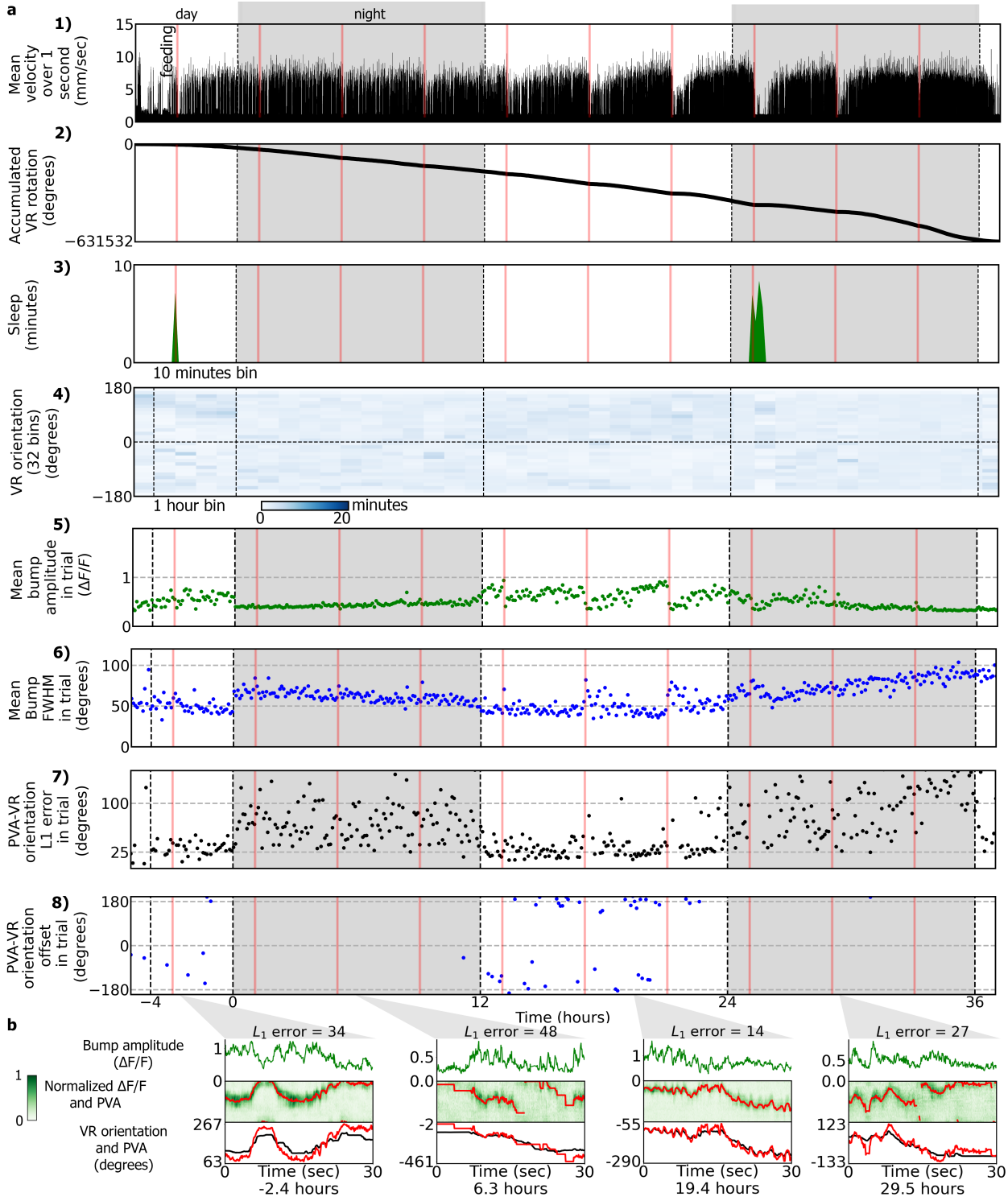
Supplementary Figure S3.5: Imaging and behavior experiment for fly 2. See figure legend of Fig. 3.4 for details.



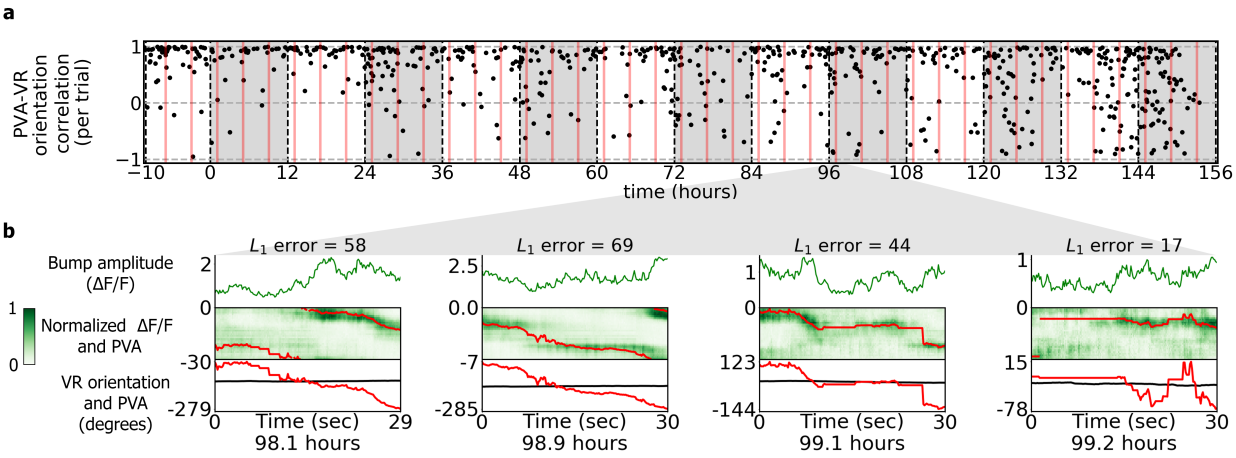
Supplementary Figure S3.6: Imaging and behavior experiment for fly 3, first part. See figure legend of Fig. 3.4 for details.



Supplementary Figure S3.7: Imaging and behavior experiment for fly 3, second part. See figure legend of Fig. 3.4 for details.



Supplementary Figure S3.8: Imaging and behavior experiment for fly 4. See figure legend of Fig. 3.4 for details.



Supplementary Figure S3.9: PVA-VR correlation and bump drift in fly 3. **a** Pearson correlation between the PVA and VR orientation in each trial remains high for all trials, whereas the L_1 error increases after the 5th day (Fig. S3.7, row 7)). **b** Examples of trials during the night where the bump drifts while the fly is standing still on the ball. The antennae of the fly were glued. Such strong autonomous dynamics was only observed after the L_1 error increased during the day, potentially due to phototoxicity.

Chapter 4

Techniques for improving imaging using temporal multiplexing

Recording calcium activity from neurons distributed in three dimensions requires monitoring sample volumes at high temporal resolution. Additionally, imaging in behaving animals is often limited by brain motion, and three-dimensional motion correction can also benefit from volumetric recordings at high temporal resolution (as reviewed in section 4.2). For example, the method described in Chapter 3 for long-term imaging in behaving *Drosophila* does not fix the proboscis or remove muscles in the fly head, as previous methods do [330, 331], resulting in comparatively larger brain motion.

In scanning microscopy, the most common implementation of volumetric imaging relies on scanning multiple focal planes at different axial positions in order to record different slices of the sample (as described in 1.7.3.2), resulting in comparatively low volume rates.

This chapter introduces two novel methods that use temporal multiplexing (described in Fig. 1.11) first for increasing temporal resolution in volume imaging and second for correcting brain motion.

The first method consists of a tomography approach where four projections of the sample at different angles are recorded in the duration that it would typically take to obtain just one frame. Off-line tomography reconstruction combined with deep learning then yields the 3D structure of the sample based on these four projections.

The second method records two different focal planes of a 3D sample simultaneously, and an off-line algorithm estimates and corrects motion perpendicular to the focal plane based on the recorded data.

These methods improve the volume imaging rate compared to traditional methods. In addition, the second technique allows imaging in behaving flies, including during feeding, and was used to correct brain motion in all the imaging experiments reported in Chapter 5.

This chapter contains the following peer-reviewed publications:

[29] **Flores-Valle, A. and Seelig, J.D.**
Two-photon Bessel beam tomography for fast volume imaging.
Optics express 27.9 (2019): 12147-12162.
(section 4.1)

[30] **Flores-Valle, A. and Seelig, J.D.**
Axial motion estimation and correction
for simultaneous multi-plane two-photon calcium imaging.
Biomedical Optics Express 13.4 (2022): 2035.
(section 4.2)

Author	**Contribution in [29] (section 4.1)**	**Contribution in [30] (section 4.2)**
Flores-Valle, A.	- Conceptualization - Investivation - Methodology - Analysis - Visualization - Writing	- Conceptualization - Investivation - Methodology - Experiments - Analysis - Visualization - Writing
Seelig, J.D.	- Conceptualization - Setup design - Setup building - Experiments - Supervision - Writing	- Conceptualization - Setup design - Setup building - Supervision - Writing

4.1 Two-photon Bessel beam tomography for fast volume imaging

4.1.1 abstract

Light microscopy on dynamic samples, for example neural activity in the brain, often requires imaging volumes that extend over several 100 μm in axial direction at a rate of at least several tens of Hertz. Here, we develop a tomography approach for scanning fluorescence microscopy which allows recording a volume image in a single frame scan. Volumes are imaged by simultaneously recording four independent projections at different angles using temporally multiplexed, tilted Bessel beams. From the resulting projections, three-dimensional images are reconstructed using inverse Radon transforms combined with convolutional neural networks (U-net).

4.1.2 Introduction

In many fluorescence microscopy experiments samples show dynamics which evolves not in a single focal plane but in a volume. For example, imaging neural activity in the brain requires monitoring multiple cells that are distributed in three dimensions [485, 486]. In this situation, the temporal resolution of the microscope needs to match the time scale of the sample dynamics, which for neural activity monitored with calcium indicators, lies in the range of several tens of Hertz [366, 485, 487].

While such imaging rates are standard for scanning a single plane, they are more difficult to reach for volumes. The scan rate is ultimately limited by the requirement of integrating a sufficient number of photons per scanned pixel. To overcome this limit, solutions for volume imaging have been developed that scan multiple pixels in parallel [366, 487]. Multifocal microscopy, for example, images several spots at the same time, but requires detectors with multiple pixels making this approach susceptible to scattering (for example when imaging in tissue) [366, 488]. Multiple focal spots can also be imaged in parallel with single pixel detectors: by introducing temporal offsets between different (typically pulsed) beams, fluorescence emission can be sorted into different temporal channels [369, 370].

To speed up volume imaging rates, extended volumes - instead of multiple focal spots - can be excited at the same time, for example using Bessel beams, Airy beams, line foci or light sheets [487, 489, 490]. Combined with camera detectors at an angle to the axis of excitation, as for example in Bessel beam light sheet microscopy [489], these approaches work best for weakly scattering samples [366, 487], but Bessel beams or line foci [488] can also be used for imaging with non-descanned PMT detection. This is more suitable for imaging in scattering tissue and results in a projection of the entire imaging volume along the beam axis [373, 374, 377, 378, 379]. While for Bessel beams this approach offers the

advantage of recording from an entire volume in a single frame scan, it comes at the cost of losing all axial resolution.

Axial resolution was restored in experiments that used two Bessel beams which imaged the sample at different angles [377, 378, 379] for generating two different projections. These projections were either recorded sequentially [377, 378] or simultaneously (as required for moving samples such as brain tissue *in vivo*) in a single channel by averaging over two different projections [379]. From these projections axial information was recovered based on the distance between prominent, sparse features such as fluorescent beads or cell bodies [378, 379].

Recording multiple projections at different viewing angles generally forms the basis for reconstructing volumes in tomographic imaging [491]. While such tomographic approaches have been implemented for fluorescence microscopy by rotating the samples with respect to the illumination direction [492, 493], this is not compatible with most *in vivo* imaging preparations. A tomography approach compatible with fluorescence microscopy for *in vivo* imaging has recently been developed with Gaussian line foci generating projections in the focal plane and was combined with scanning the objective along the axial direction to record volumes [488].

We here develop a tomography method based on Bessel beams. Volume information is obtained from four independent projections recorded at the same time, in a single frame, from four different angles by scanning temporally multiplexed, tilted Bessel beams. For volume reconstruction we combine inverse Radon transforms adapted for Bessel beam scanning with machine learning [491, 494, 495, 496, 497, 498]. Machine learning has been shown for example in optical phase imaging to allow high resolution reconstruction from sparse projections at shallow angles similar to the ones used here [496]. We show that three-dimensional convolutional neural networks (U-net) trained on suitable datasets similarly improve reconstructions in Bessel beam tomography. This scanning microscopy method allows volumetric imaging with non-descanned detection in a single frame scan.

4.1.3 Results

4.1.3.1 Setup

The setup is based on a custom built two-photon scanning microscope controlled by Scanimage (Vidrio) in a resonant scanning configuration with photon counting. The microscope optics was adapted to scan four tilted Bessel beams across the sample as described in the following. Four different projections were generated by using four different Bessel beams tilted with a mean angle of 13.25 (standard deviation 2.75) degrees with respect to the optical axis and an azimuth separation of approximately 90 degrees between neighboring beams (see Table S4.1.1 and Supplementary Fig. S4.1.1 for more details and for quantification).

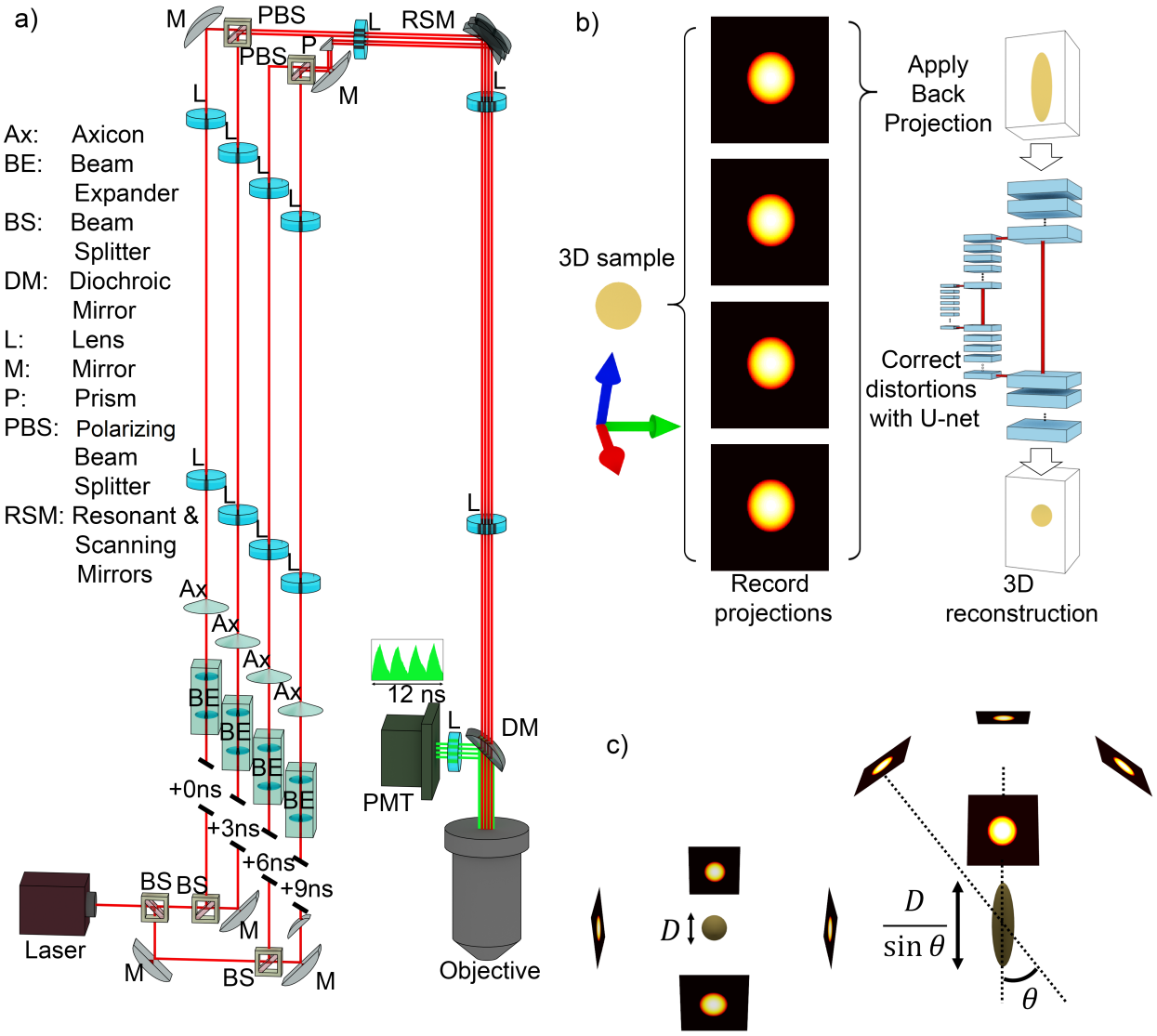


Figure 4.1: (a) Schematic of the experimental setup. A laser beam is split into four temporally offset beams using beam splitters (BS). Each beam is converted into a Bessel beam with independently adjusted beam parameters. The Bessel beams excite the volume from four different sides. Inset: Fluorescence emission is detected in four temporally separated channels. (b) Workflow for volumetric reconstruction: four projections are recorded from a three dimensional (3D) sample and back projection is applied to obtain its 3D tomographic reconstruction. Then, a U-net is applied to correct distortions in the reconstructed sample. (c) Illustration of 3D tomography with different viewing angles. Left side: projections parallel to the xy plane allow a perfect reconstruction of a sphere of diameter D. Right side: projections at an oblique angle θ produce a reconstructed sphere elongated in the z axis by a factor of $1/\sin(\theta)$. This is corrected for by using convolutional networks. Projection images are obtained by bidirectional raster scanning of tilted Bessel beams across the sample (see Methods for details).

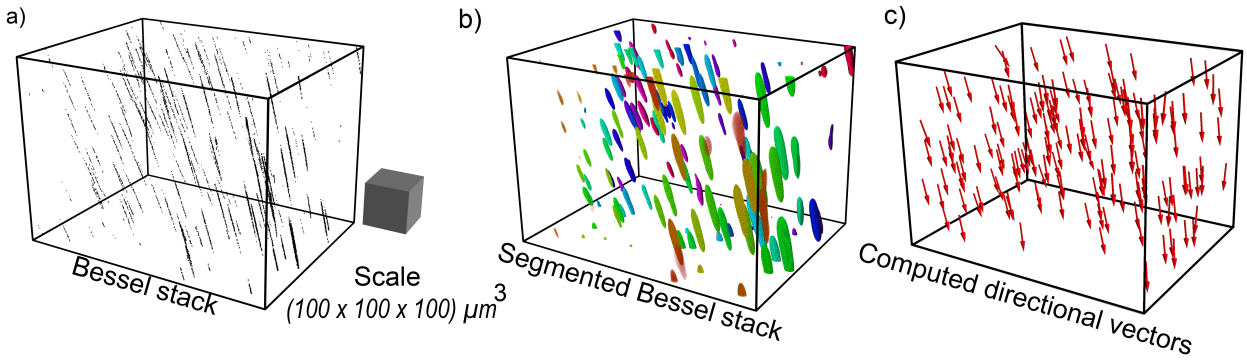


Figure 4.2: Calibration procedure for a single Bessel beam. (a) A volumetric sample of 1μm diameter beads in Agarose recorded with a Bessel beam with 1μm step size in the axial direction (z-axis), resulting in a Bessel beam z-stack. (b) For segmenting different beams, we applied a Gaussian filter with standard deviation of 5 pixels ,thresholded the image with its mean value and binarized it. Segmented beams are colored randomly for visualization. (c) Using Principal Component Analysis (PCA) we computed the center of each beam and the directional vector at its center. These vectors are used in linear regression to compute the directional vector field for each the Bessel beam z-stack. Viewing angles were selected for best visibility of the vector fields.

The setup is shown in Fig. 4.1(a) and pictures of the setup are shown in Supplementary Fig. S4.1.2(a) and (b). A laser beam (Coherent Discovery, 120 fs pulse width) is split into four beams with non-polarizing plate beam splitters and the (nevertheless polarization dependent) splitting ratio is additionally balanced using a half-wave plate for each beam (not shown). The beams are separated with a delay of 3 ns (corresponding to a 1 m additional path length per beam) [369, 370] which allows distinguishing the different projections with a single detector using photon counting at a time resolution faster than the pulse repetition rate, provided that the fluorescence lifetime is shorter than the pulse separation [369]. The beam width and collimation is adjusted for each beam with a telescope (two achromatic lenses, one mounted on a translation stage).

Each beam is sent through an axicon (AX252-B, all optical components were from Thorlabs unless otherwise noted) for generating a Bessel beam. The beam is collimated after the axicon with an achromatic lens (AC254-100-B) and the resulting ring is imaged onto the back focal plane of the microscope objective. For this, the ring is first demagnified and imaged onto the scan mirrors using a telescope (AC254-200-B and AC254-100-B), with the latter lens common to all four beam paths. The scan mirror is imaged onto the back focal plane of the objective using a scan lens (AC300-050-B) and tube lens (AC508-300-B).

To achieve tilted illumination from four opposing azimuth angles (see Fig. 4.3), the last lens in each beam path (before the beams are recombined) is displaced laterally and/or vertically for each beam, resulting in an off-center Bessel ring in each quadrant of the back focal plane of the objective. The displacement was in the range of 1-2 mm in the respective

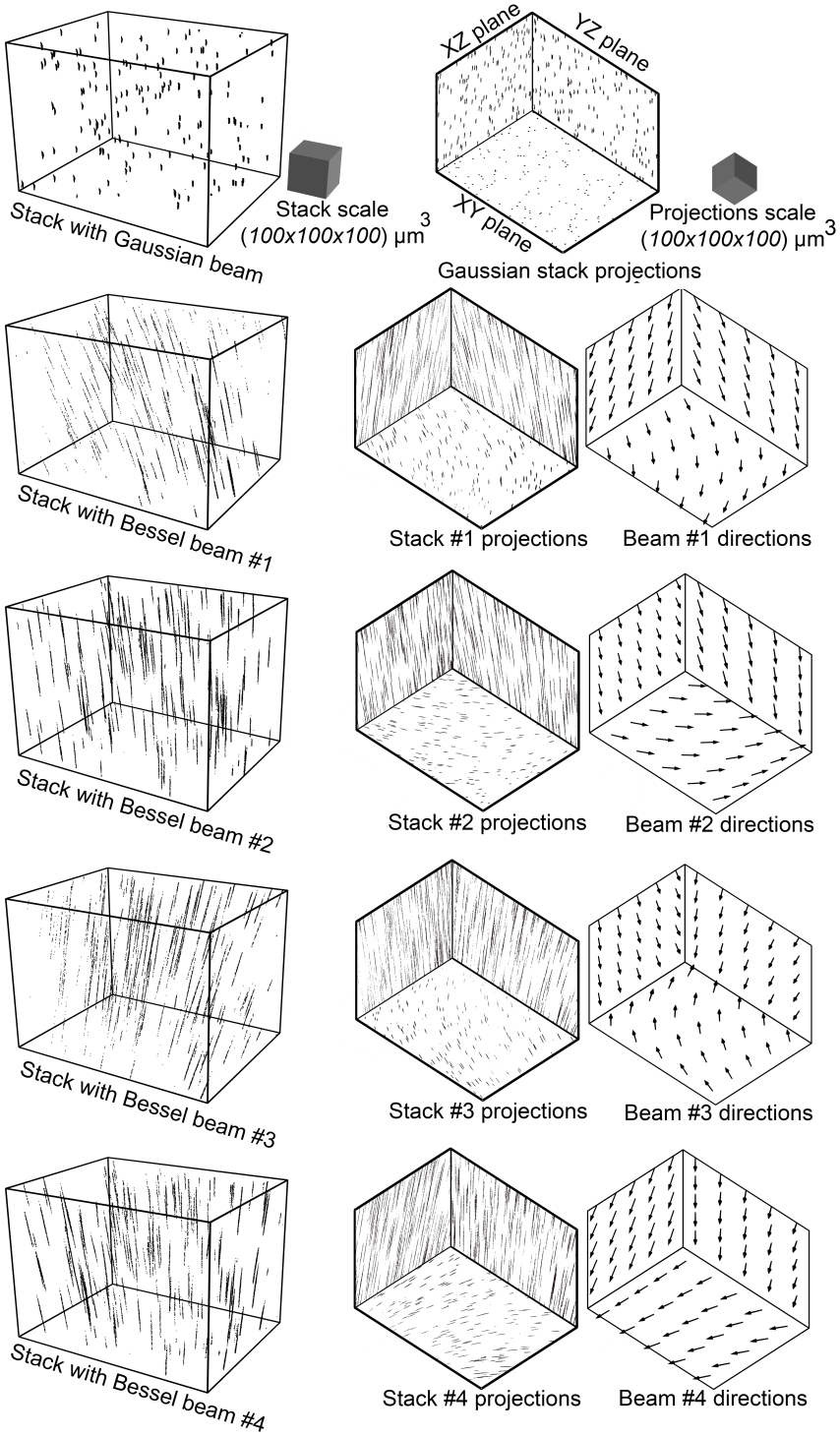


Figure 4.3

direction and was adjusted while observing the projection of the Bessel ring at the back aperture of the objective. The Bessel ring diameters at the back aperture of the objective were slightly below half the objective aperture diameter and allowed laterally displacing the

Figure 4.3: Directional vector fields of each Bessel beam measured and computed from a volumetric sample of $1\mu m$ diameter beads. Top row: sample recorded with a Gaussian beam (left side) and projections of the volume in the xy, xz and yz planes, respectively (right side). Second row to bottom row: volumetric samples recorded by the four Bessel beams (left side) and plane projections (center). The extrapolated vector field for each beam (right side) is shown in plane projections. The elevation angle is centered around 166.75 ± 2.75 degrees, see Table S4.1.1 and Supplementary Fig. S4.1.1 for more details and quantification of vector fields. Viewing angles were selected for best visibility of the vector fields and projections, respectively.

beam without clipping. The four rings projected onto the back aperture of the objective are shown in Supplementary Fig. S4.1.2(c).

Depending on the parameters and methods used to generate Bessel beams, different profiles in terms of width, length and axial intensity distribution result [375]. The axial intensity profile additionally depends on the placement of the collimating lenses [375, 379]. Here, we aimed for a beam length of about 80 μm as a compromise between recording a sufficiently large volume while limiting the power required for two-photon excitation in each beam. The maximum power per beam used in the experiments was 90 mW measured at the entrance aperture of the resonant scanner. In each beam path the collimating lens was placed 11.5 cm behind the axicon, the first lens of the telescope was placed 30 cm behind the collimating lens which was separated by 28 cm from the lens common to all beam paths. The focal length of each beam was iteratively adjusted based on the two-photon point spread function by changing the beam collimation using the translation stage in the beam expander [379].

The four beams are recombined by first combining pairs of beams - after adjusting their polarizations othogonally with a half-wave plate (not shown) - with a polarizing beam splitter cube. All four beams are then combined with a right angle reflecting prism positioned just before the common telescope lens (that forms the demagnified image of the Bessel ring on the scan mirror). The reflecting prism is positioned laterally into the beam path using a translation stage, reflecting two beams at 90 degrees while allowing the other two beams to pass near the edge of the prism. This is possible without clipping any of the beams by laterally displacing the two passing beams into the appropriate neighboring quadrants in the objective back focal plane (as required for tilting of the Bessel beams).

An additional Gaussian beam path (not shown) was used for recording reference image z-stacks. A flip mirror was used to direct the beam through a telescope towards a polarizing beam splitter cube mounted on a magnetic mount that was manually inserted before the resonant scanner.

All experiments were performed with a custom-built two-photon microscope controlled with Scanimage (Vidrio) [474] with a resonant scanner (resonant scan box, Sutter Instru-

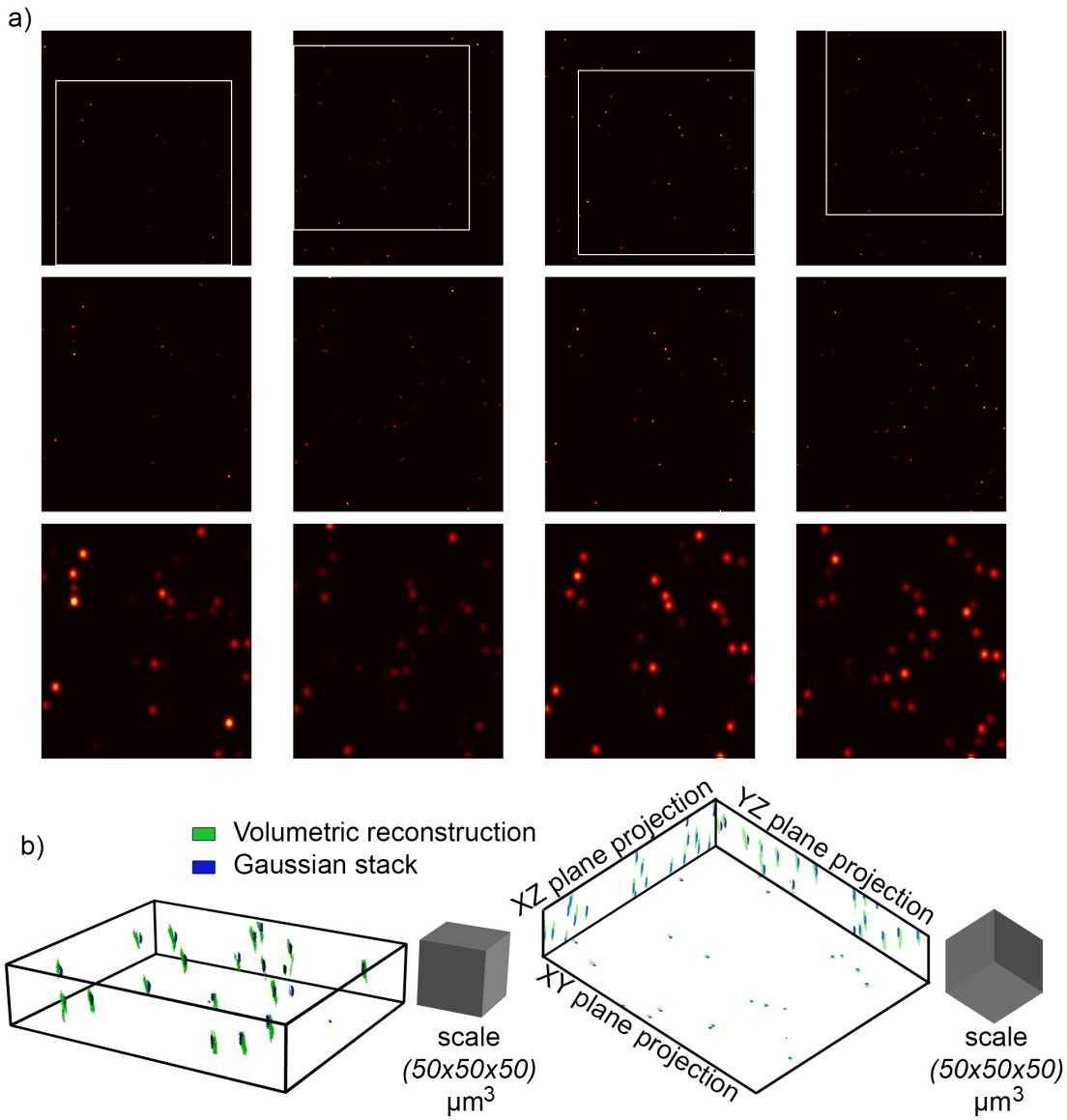


Figure 4.4: Tomographic reconstruction of $1\mu m$ diameter beads. (a) Top row: projections for each Bessel beam of a volumetric sample. The white frames indicate the overlap between the four Bessel beam projections and any bead within this area is visible in all projections. Center row: cropped projections corresponding to the overlapping area (white frames). Bottom row: cropped projections after applying a Gaussian filter with standard deviation of 5 pixels to improve bead visibility. (b) Reconstruction of the beads (using only back projection, no convolutional networks) in green, compared to the volume recorded with the Gaussian beam (ground truth). A single frame required for reconstruction was recorded at the same time in each channel with 512×512 pixels at 30 Hz. As described in the results section, the tomographic reconstruction only shows regions in which all four beams intersect. Due to the offsets between the different projections, some of the beads near the borders of the reference volume are therefore not reconstructed.

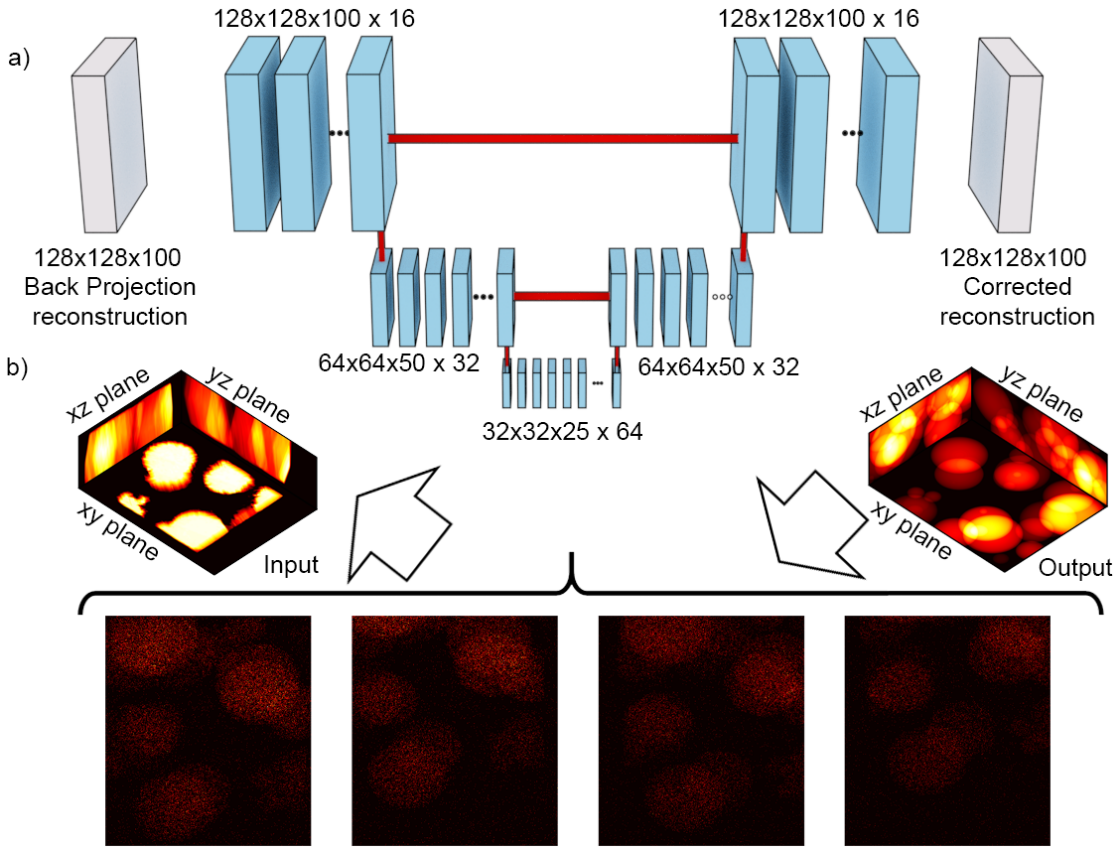


Figure 4.5: U-net architecture and simulated data. (a) U-net: each step in the network is composed of 3D convolution, batch normalization and max pooling in 3D in the encoding part while the decoding part is composed of 3D convolution, batch normalization and up sampling in 3D. (b) Simulated data used for training the network. The simulated 3D samples consist of ellipsoids of different sizes and serve as the output of the network. Four projections are generated from each simulated sample volume with addition of shot noise (bottom part). These four projections are produced using the calibration vector fields obtained experimentally. Applying back projection to these four projections yields a volume image. The black region in the reconstructed volume results from the cropping of the projections due to the offset between the different Bessel beam projections. This reconstructed volume serves as the input of the network, while the original volumes serves as the output.

ments) and components similar to the ones described in [331]. Scanimage allows FPGA-based (National Instruments, PXIe-7975R) photon counting, in our setup at a time resolution of 1.28 GHz (16 time bins between laser pulses at 80 MHz repetition rate). The resonance frequency of the resonant scan mirror was 8 kHz and images were acquired using bidirectional scanning (images are acquired during both movement directions across the sample). Overlaying the four beams resulted in a combined pulse repetition rate of 320 MHz and therefore four time bins per beam. To suppress cross talk between the fluorescence de-

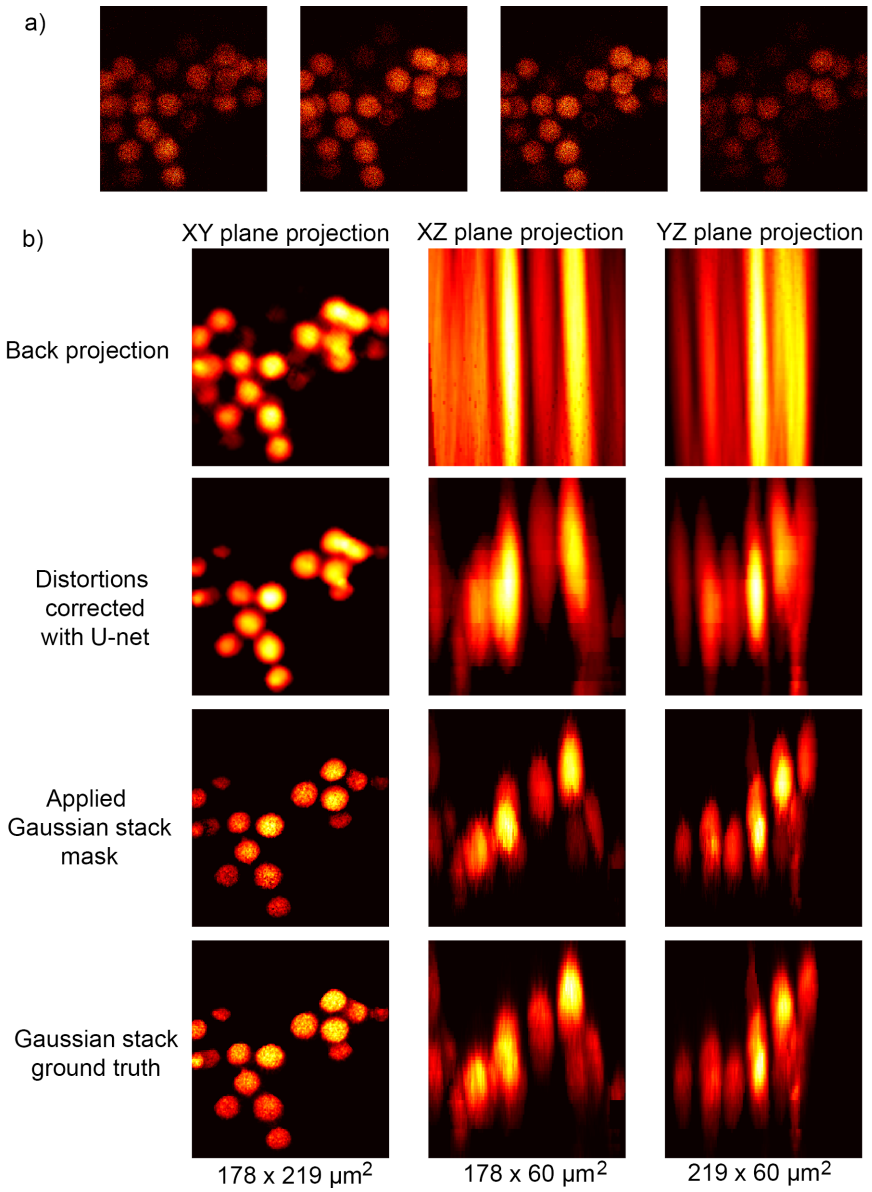


Figure 4.6: Tomography on pollen grain sample. (a) Four projections recorded from a 3D sample of pollen grains. (b) Plane projections of the volumetric reconstructions. Top row: back projection shows poor resolution in the z axis since the object approaches the beam length. The second row shows the reconstruction after applying the U-net. The third row additionally applies a mask recorded with the Gaussian beam (see text for details). The bottom row shows the reference Gaussian stack. The dimensions of the images are indicated for each image in the bottom row. A single frame required for reconstruction was recorded at the same time in each channel with 512×512 pixels at 30 Hz.

cays excited by the different beams, only three time bins were used for each beam and the intensity in these three bins was averaged into one channel (or image) using the scanning control software. The four different channels were selected with the help of the fluorescence

decay time histogram displayed in the scanning control software.

4.1.3.2 Tomographic volume reconstruction

A typical 3D tomography approach, for example in medical imaging, acquires 2D projections of a sample by varying the azimuth angle at a fixed elevation of 90 degrees, as illustrated on the left side of Fig. 4.1(c). Changing the elevation to an oblique angle as shown on the right side of Fig. 4.1(c) distorts the reconstruction by a factor of $1/\sin(\theta)$. Using tilted Bessel beams to record projections results in a distortion along the z axis and this was (partially) corrected for using machine learning. The workflow of our tomography approach is shown in Fig. 4.1(b): first, four projections are recorded from a 3D sample by scanning the four different Bessel beams accross the sample, second, back projection is applied resulting in a distorted 3D reconstruction and, and third, a convolutional neural network (3D U-net [499, 500, 501]) is used to recover the 3D object. These steps are described in more detail below.

4.1.3.2.1 Radon transform for Bessel beam scanning

For volume reconstruction we developed a 2D Radon transform based approach for Bessel beam scanning with tilted beams. In this approach, the amount of light emitted following excitation at a given point $\mathbf{x} \in \mathbb{R}^3$ in a volumetric sample is described with a function $f : \mathbb{R}^3 \to \mathbb{R}$. The Bessel beam is approximated as a line segment of length ℓ with constant intensity centered at a point $\mathbf{x}_c \in \mathbb{R}^3$ and a direction given by the normalized vector $\hat{\mathbf{s}} \in \mathbb{R}^3$ with a parameter t. The total amount of light emitted by the sample due to excitation by the beam is then described in terms of the Radon transform along the segment:

$$[\Re f](\mathbf{x_c}, \hat{\mathbf{s}}, \ell) = \int_{-\ell/2}^{\ell/2} f(\mathbf{x_c} + t \cdot \hat{\mathbf{s}}) dt. \tag{4.1}$$

We define an image of size $(2N+1) \times (2N+1)$ as a function $I : \{\mathbb{Z} \cap [-N, N]\} \times \{\mathbb{Z} \cap [-N, N]\} \to \mathbb{R}$ representing the intensity of a pixel at a position with integer indices (ν, μ). To create an image, the Bessel beam is scanned with the two scanning mirrors across the field of view and for each pixel the resulting intensity is recorded. When scanning the tilted Bessel beams we observed small changes of both the vector $\mathbf{x_c}$ and the direction vector $\hat{\mathbf{s}}$ across large fields of view compared to a Gaussian reference z-stack, see Fig. 4.3 and Table 1 for quantification. Both vectors are therefore described as vector fields depending on the pixel coordinates (ν, μ): the offset vector field, $\mathbf{x_c} = \mathbf{x_c}(\nu, \mu, z)$, and the the direction vector field, $\hat{\mathbf{s}} = \hat{\mathbf{s}}(\nu, \mu, z)$ and axial position z. A general expression for the intensity in each pixel is then given by:

$$I(\nu,\mu) = [\Re f](\nu,\mu) = \int_{-\ell/2}^{\ell/2} f\Big(\mathbf{x_c}(\nu,\mu) + t\cdot\hat{\mathbf{s}}(\nu,\mu)\Big)dt. \tag{4.2}$$

4.1.3.2.2 Calibration of Bessel beam projections

The vector fields $\mathbf{x_c^{(i)}}$ and $\hat{\mathbf{s}}^{(\mathbf{i})}$ are required for reconstructing the volumetric sample $f(\mathbf{x})$ from its projections $I^{(i)}(\nu,\mu;z)$ and are measured experimentally for each projection $I^{(i)}$ with a volumetric sample of 1 μm diameter fluorescent beads (Fluoresbrite, Cat. No. 17154-10, Polysciences) suspended in 2% Agarose (Agarose LE, M 3044, Glenaxxon) (see Fig. 4.2(a) and Fig. 4.3). For this, a z-stack was recorded while scanning the four Bessel beams resulting in volumes of 2D projections, $V^{(i)}(\nu,\mu,z) \equiv \{I^{(i)}(\nu,\mu;z)/z \in [z_{min}, z_{max}]\}$. As quantified in Table 1, variations of the vector field in z-direction were small and are ignored in the following.

The recorded volumes were segmented using the mean value after Gaussian filtering with standard deviation of 5 pixels for noise reduction (manually tuned for optimizing segmentation) as threshold, see Fig. 4.2(a) and (b). The center position of each segmented bead b, $(\nu_c^{(i,b)}, \mu_c^{(i,b)}, z_c^{(i,b)})$, was identified using the *skimage* function *regionprops* and Principal Component Analysis (PCA) was applied to obtain the axis with the highest eigenvalue as the direction vector $\hat{\mathbf{s}}^{(i,b)}$ at the center point $(\nu_c^{(i,b)}, \mu_c^{(i,b)}, z_c^{(i,b)})$ as well as the length of the beam $\ell^{(i,b)}$, see Fig. 4.2(c) and Fig. 4.3.

Making use of all beads measured in each z-stack i and the corresponding directional vectors,

$$S^{(i)} \equiv \{\hat{\mathbf{s}}^{(i,b)}(\nu_c^{(i,b)}, \mu_c^{(i,b)}, z_c^{(i,b)})/b = 0, 1, ..., (N_b^{(i)} - 1)\}, \tag{4.3}$$

we used linear regression to obtain the directional vector field across the entire field of view (ν,μ,z),

$$\hat{\mathbf{s}}^{(\mathbf{i})}(\nu,\mu,z) \approx A_s^{(i)}\cdot(\nu,\mu,z)^T + \mathbf{B_s^{(i)}}, \tag{4.4}$$

where A_s is a 3×3 matrix while $\mathbf{B_s}$ is a bias vector, which are both parameters fit to the data $S^{(i)}$.

The length of the beam in each z-stack i is considered constant, and it is computed as the average value of the lengths obtained for all beams:

$$\ell^{(i)} = \frac{1}{N_b^{(i)}}\sum_{b}^{N_b^{(i)}} \ell^{(i,b)}. \tag{4.5}$$

Due to the selected beam length and collimation of the tilted Bessel beams, the different beams do not meet at the center of the field of view (similar to [379]). This offset leads to cropping of the projections, see Fig. 4.4(a) top row for full frames and Fig. 4.4(a) center row for cropped frames (as indicated by the white frames). (An additional cropping is introduced

by the offset between reference z-stack recorded with a Gaussian beam used for calibration and the z-stack recorded with the Bessel beam (referred to as a Bessel beam z-stack below).) For tomographic reconstructions, this offset was corrected for by computing an offset vector field. For this, one Bessel beam z-stack was used as a reference. For each centroid of each bead in the segmented Bessel beam z-stack the offset vector to the same bead imaged in the three other segmented Bessel beam z-stacks was computed. Interpolating the offset vectors using linear regression for all three z-stacks results in the offset vector field:

$$\mathbf{x_c^{(i)}}(\nu,\mu,z) \approx A_c^{(i)} \cdot (\nu,\mu,z)^T + \mathbf{B_c^{(i)}}. \tag{4.6}$$

4.1.3.2.3 Back projection

Using the calibrated vector fields $\mathbf{x_c}^{(i)}$, $\hat{\mathbf{s}}^{(i)}$, and length $\ell^{(i)}$ for each projection i, the inverse Radon transform, $\Re^{(-1)}I^{(i)}$, can be applied to any projection $I^{(i)}(\nu,\mu)$, where the pixels of $I^{(i)}$ are projected along the corresponding direction vector $\hat{\mathbf{s}}^{\mathbf{(i)}}$ and translated with its corresponding offset vector $\mathbf{x_c^{(i)}}$. This results in a 3D image:

$$\left[\Re^{(-1)}I^{(i)}\right](\nu,\mu,t) = \begin{cases} I^{(i)}(\nu,\mu) - \mathbf{x_c^{(i)}}(\nu,\mu,c_z) - t\cdot\hat{\mathbf{s}}^{\mathbf{(i)}}(\nu,\mu,c_z) & \text{if} \quad t \in \left[-\frac{\ell^{(i)}}{2},\frac{\ell^{(i)}}{2}\right] \\ 0 \quad \text{otherwise} \end{cases} \tag{4.7}$$

The parameter t needs to be discretized: $t = t_{min}, (t_{min}+z_{res}), ..., (t_{max}-z_{res}), t_{max}$, where z_{res} gives the z resolution. We obtain an approximated reconstruction of the volume as the sum of the the inverse Radon transforms (back projection):

$$R(\nu,\mu,t) = \sum_i \left[\Re^{(-1)}I^{(i)}\right](\nu,\mu,t). \tag{4.8}$$

For small objects, such as the fluorescent beads in Fig. 4.4), the back projections were additionally filtered by setting the 3D image to zero if not all four inverse Radon transforms overlapped in a given position (ν, μ, t). For this filtering, a binary image was computed from each inverse Radon transform (obtained from equation (7)) by applying a Gaussian filter with 1 pixel standard deviation and thresholding to the mean value of the inverse Radon transform. This was done for each projection, and the binary inverse Radon transforms were then summed to form a thresholded back projection. The maximum value of the thresholded back projection is 4 (only 4 projections). This image was binarized, setting values below 4 to zero, creating a back projection mask with a value of 1 where the four beams intersect. The actual back projection obtained from equation (8) was finally multiplied element-wise with the back projection mask so that the density of the resulting image was non-zero only where the 4 beams intersected. The recorded projections are shown in Fig. 4.4(a) and the

resulting reconstructed volume with only intersecting regions of the four beams as well as a comparison with the Gaussian reference z-stack is shown in Fig. 4.4(b) (no convolutional networks were applied for this reconstruction).

4.1.3.2.4 Neural networks for distortion correction

For objects that are of similar size to the Bessel beam focal length, the back projected volume will extend over the entire axial range of the sampled volume due to the shallow projection angles. Neural networks were used to correct for distortions and to recover axial resolution in this situation, (see Fig. 4.1(b) and (c)).

A three dimensional U-net (Fig. 4.5(a)) was trained using simulated 3D samples consisting of ellipsoids of different sizes with homogeneous constant density (ranging from $1\mu m$ to 40 μm) (Fig. 4.5(b)). Using the Radon transform approach, four projections were generated from each simulated 3D sample using the vector fields measured during calibration and shot noise was added to simulate detection noise (Fig. 4.5(b), bottom row). From these four projections a (distorted) 3D volume was reconstructed using back projection and a back projection mask (as described above) to obtain reconstructions based on all four beams (Fig. 4.5(b), left side). This reconstructed volume served as input to a 3D U-net (dimension $128x128x100$ pixels) and the original simulated 3D sample (same dimension of $128x128x100$) served as the output. The number of data samples generated was 1000.

Networks were built and trained using Python and $keras$ with $tensorflow$ as the backend [502]. The 3D U-net had 804809 parameters and was composed of blocks formed in the first part by 3D convolutional layers, batch normalization and 3D max pooling. After the bottleneck we used a combination of 3D convolutional layers, batch normalization and 3D upsampling layers to deconvolve the 3D image and recover the corrected reconstruction (Fig. 4.5).

The model was trained on a desktop computer running Ubuntu with an Intel Xeon (R) CPU E5-1650 v4 @ 3.60GHz x 12 processor and a TITAN XP graphics card, that allowed to train the network for 100 epochs with batches of 5 samples in about 5 hours. The loss function was the mean squared error between the original simulated image and the network output and we used Adam optimizer to train the neural network. Results of applying this network on a pollen grain volume sample (Mixed Pollen Grains, part number 304264, Carolina) are shown in Fig. 4.6, where Fig. 4.6(a) shows the four recorded projections and Fig. 4.6(b), top row, shows the reconstruction using back projection. The back projection of the pollen grains was again filtered by a back projection mask to base the reconstruction on all four projections. The Gaussian filter of the back projected mask had again 1 pixel standard deviation and the threshold was the mean of the inverse Radon transform of each projection. Due to the (compared with the beam length) large size of the pollen grains, almost no axial resolution is recovered using back projection (Fig. 4.6(b), top row).

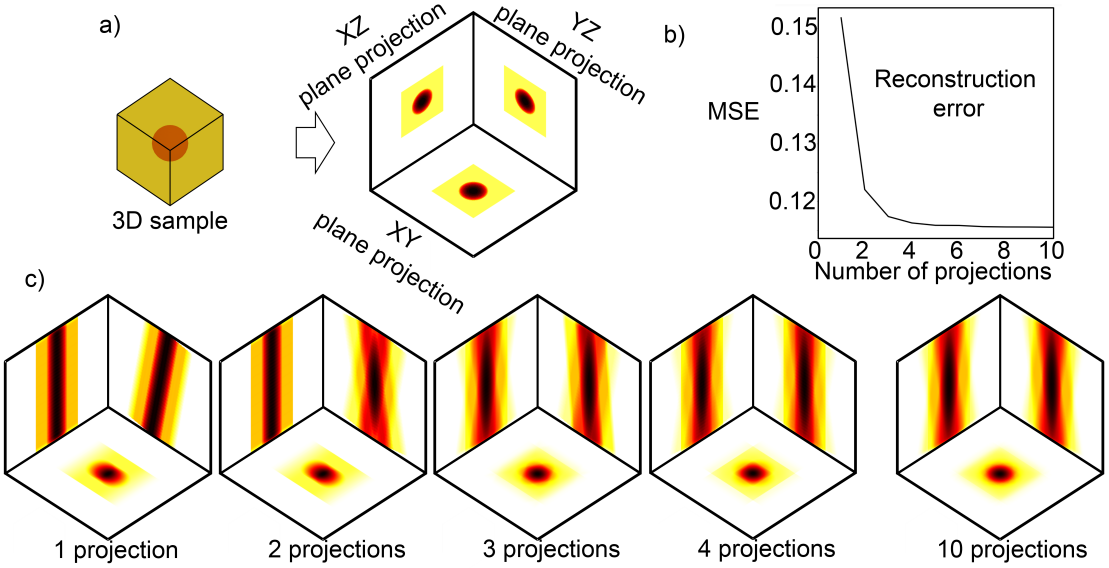


Figure 4.7: Simulated reconstruction error of 3D tomography depends on number of projections for the given isolated sample. (a) A homogeneous cube that contains a homogeneous sphere with higher density and its projection in the xy, xz and yz planes (for visualization). (b) Mean Square Error (MSE) between the simulated 3D sample and the reconstructed sample using back projection as a function of the number of recorded projections using a constant elevation angle of 170 degrees. (c) Projections of the reconstructed sample considering $1, 2, 3, 4$, and 10 projections, respectively.

However, axial information can be partially recovered with the U-net (Fig. 4.6(b), second row, compare to Fig. 4.6(b), last row for ground truth).

For samples which do not change their structure during the observation time but only their intensity a Gaussian reference z-stack could first be recorded for obtaining structural information and Bessel beam tomography for subsequently monitoring activity at high temporal resolution [375]. We tested this approach by generating a structure-mask from the Gaussian z-stack by filtering it in the xy-plane with a Gaussian filter with 1 pixel standard deviation, thresholding it at the mean value, binarizing and downsampling it to 128 pixel resolution by averaging over four pixels. The resulting mask was multiplied with the volume reconstructed using combined back projection and U-net filtering (Fig. 4.6(b), second row) and resulted in the reconstruction shown in Fig. 4.6(b), third row. The accuracy of the reconstructed intensities in this case still depends on the quality of the tomographic reconstruction.

4.1.4 Discussion

We introduced a tomography method for scanning fluorescence microscopy: volumes were imaged in a single frame scan using temporally multiplexed and tilted Bessel beams for

recording independent projections at four different viewing angles with a single objective. A tomographic reconstruction approach suitable for scanning with tilted Bessel beams was developed combining Radon transforms with three dimensional convolutional networks (3D U-net). We recovered volume information using fluorescent beads (Fig. 4.4) and pollen grain samples (Fig. 4.6). The frame rate depended on the resolution of the image and was 30 Hz for images with 512×512 pixel resolution (and increases with fewer pixels, for example 90 Hz for 128 pixel resolution) and the largest reconstructed volumes was $179\mu m \times 219\mu m \times 60\mu m$ (Fig. 6).

Imaging using extended beams, lines or light sheets offers a promising approach for increasing the imaging rate beyond point scanning methods [366, 485, 486, 487]. Different from approaches that detect fluorescence using a camera, Bessel beam tomography uses non-descanned PMT detection. This is an advantage for imaging in tissue, since, although scattering affects the infrared excitation light, it does not lead to cross talk of the more strongly scattering visible emission between different detection channels or pixels [366, 490].

The depth of the field of view depends on the length of the Bessel beam and can be adjusted. For for *in vivo* two-photon imaging the power that can be sent into the sample is a limiting factor. Here we used a maximum of 90 mW per beam at a combined pulse rate of 360 MHz. Fluorescence excitation could likely be optimized by using lasers with higher energy per pulse and lower repetition rate without exceeding the damage threshold [487]. Lower repetition rates would also reduce crosstalk between channels and would allow imaging with fluorophores with longer lifetimes, such as typical genetically encoded calcium indicators. Additionally, using higher numerical aperture objectives (we here used 0.8) or using a larger fraction of the available N.A. at the cost of smaller tilt angles could further improve the lateral beam resolution and two-photon excitation efficiency. Bessel beam tomography could also be performed using single photon excitation, where laser power would not be a problem, or using three-photon excitation.

Different from previous approaches with tilted Bessel beams [377, 378, 379] we simultaneously recorded independent projections using temporal multiplexing. The advantage of simultaneous instead of sequential recordings [377, 378] lies in the increased frame rate and makes the measurement less sensitive to motion artefacts (which would interfere with the tomographic reconstruction) as typically observed in *in vivo* imaging. Increasing the number of projections to four is advantageous for volume reconstruction at shallow angles as illustrated in Fig. 4.7 and adding more projections is expected to only add a limited benefit for an isolated object. Different from another recent tomography approach [488], projections here were recorded along the optical axis instead of across the focal plane. While the axial projections at shallow angles come at the cost of lower resolution it is compatible with a standard 2D scanning configuration and doesn't require axial scanning.

For volume reconstruction we used Radon inverse transforms combined with machine learning and adapted it for the presented Bessel beam scanning configuration. We modeled

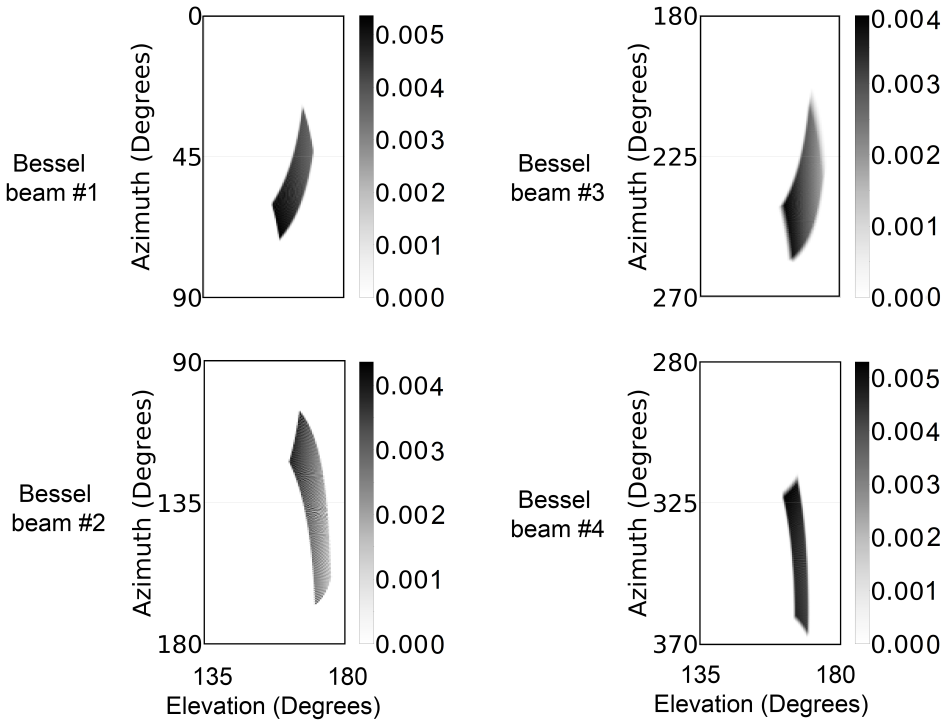
the Bessel beam as a constant line segment for computational simplicity, but models of the actual point spread function could be used for computing the inverse Radon transform.

Approaches combining imaging physics and machine learning have been successfully applied in other tomography techniques for improving the reconstruction from sparse, shallow angle projections [491, 494, 495, 496, 497, 498]. Overall, the quality of the reconstruction depends on the neural network model and training data. Our networks were limited by GPU memory and therefore only low resolution images (128 pixel resolution instead of 512) were used. Training the network models on higher resolution images will likely improve the reconstruction. Additionally, we used a limited training data set based on simulated, randomly distributed homogeneous spheres to approximate the pollen grain sample. Training a network on this data set was sufficient for partially reconstructing axial information, but as expected didn't recover higher resolution features of the sample, such as small spikes on the pollen grains. The quality of the reconstruction is expected to improve if the training data is more similar to the sample. Therefore, increasing the training data set to include large numbers of more realistic samples and, if necessary, increasing the model complexity will allow to further improve the reconstruction. It will be interesting to explore in how far denser and less regular samples can be reconstructed with Bessel beam tomography and suitable training data sets. While for an isolated object four projections suffice for reconstruction (see Fig. 7), for denser samples, the reconstruction would be expected to improve with the number of projections.

Overall, Bessel beam tomography is suitable for fast imaging of sparse volumetric samples that can be accessed only with a single objective, a situation that is commonly encountered when imaging neural activity from cell bodies in the brain.

4.1.5 Supplementary information

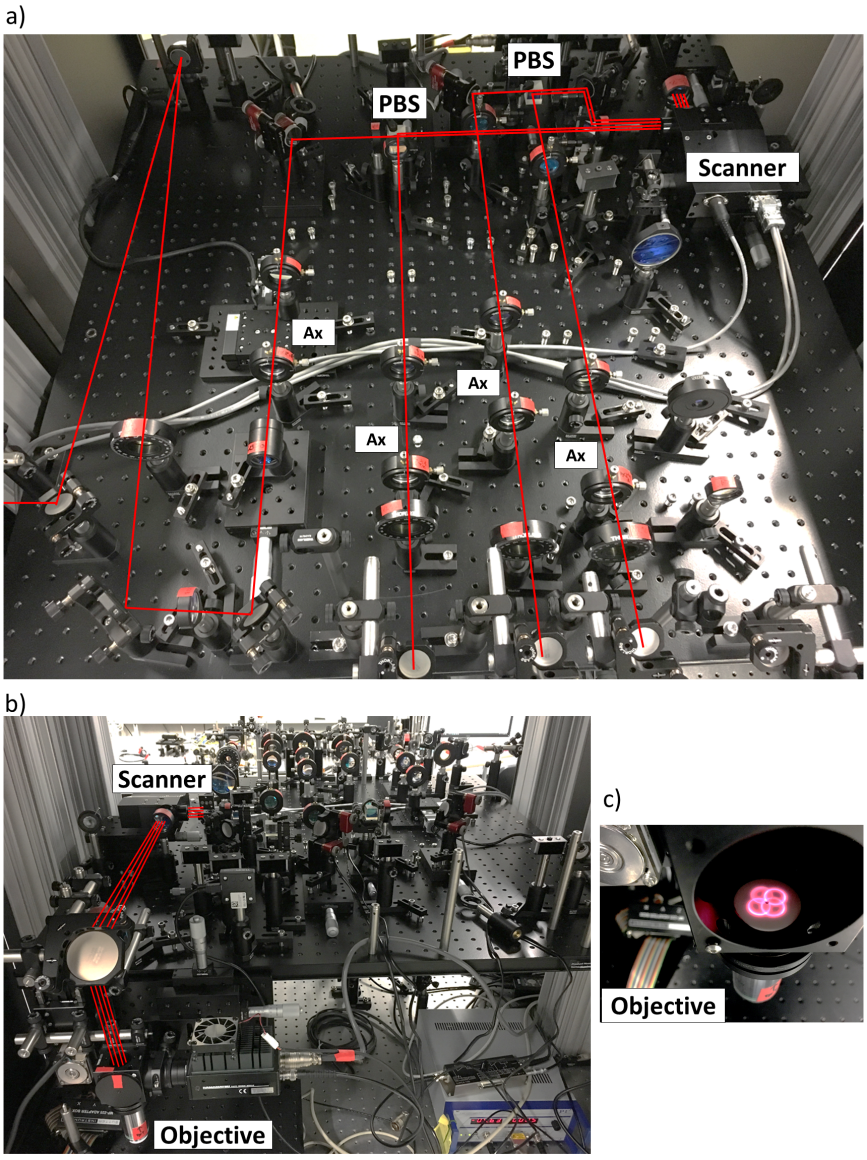
Table 1 shows the variation of the elevation and azimuth angles for each Bessel beam across an entire z-stack. For each beam, a total of 10^6 vectors were generated from the linear interpolation equation (4) after calibration, and the mean and standard deviation (std) of the beam angle with respect to the x-axis (azimuth) and z-axis (elevation) were computed for each of these vector fields. In the third column the change of direction of each Bessel beam with respect to the z axis (over a larger volume than used in experiments) is shown. Generating 10^4 vectors in the top layer ($z = 200\mu m$) and 10^4 vectors in the bottom layer $z = 0\mu m$ from equation (4), the angle between each pair of vectors corresponding to the same pixel locations as well as the mean and standard deviation for all vectors were computed. The mean difference for each beam was close to zero and therefore any z-dependence of the vector fields could be ignored in the reconstruction.



Supplementary Figure S4.1.1: 2D normalized distribution of the elevation (horizontal axis) and azimuth (vertical axis) angles for each Bessel beam. The distribution is computed from the interpolation equation (4), using a total of $N = 10^6$ vectors. See Table S4.1.1 for mean values of the distributions.

Supplementary Table S4.1.1: Variation of elevation and azimuth angle of Bessel beam vector fields

	Elevation mean ± std (degrees) $N = 10^6$	Azimuth mean ± std (degrees) $N = 10^6$	Top-bottom angle difference mean ± std (degrees) $N = 10^4$
Bessel beam #1	164 ± 3	53 ± 10	$0,54 \pm 0.01$
Bessel beam #2	169 ± 3	133 ± 15	$0,11 \pm 0,01$
Bessel beam #3	168 ± 3	237 ± 12	$1,71 \pm 0.11$
Bessel beam #4	166 ± 2	310 ± 21	$0,75 \pm 0.04$



Supplementary Figure S4.1.2: Pictures of the setup. (a) Top view of beam path before entering the resonant scanner and after the delay lines. Four independent Bessel beams are generated with four axicons and combined with polarizing beams splitters (PBS) and a reflecting prism (to combine all four beams) as shown schematically in Figure 1. Delay lines are not shown. Red lines schematically illustrate the beam paths and the number of parallel lines illustrate the number of combined beams. Rotation mounts contain half-wave plates and are not shown in the schematic in Fig. 1. (b) View of microscope with beam path illustrated between the scanner and the microscope objective, passing through scan lens and tube lens and reflected with a mirror into the objective. (c) Picture of the four Bessel beams at the back aperture of the objective with the laser tuned to 680 nm. A 1 inch diameter alignment disk was placed in the back aperture for taking the picture. The diameter of the back aperture is 20 mm. The back focal plane of the objective (Nikon MRP07220 - CFI-75 LWD 16x/ 0.80/ 3,00 water dipping) is at 42.6mm from the specimen surface. The collimation of each beam was iteratively adjusted to obtain four beams with similar focal length. This results in the four rings having different diameters, which is due to the different initial collimations of the beams resulting from the 1 m additional path lengths of each beam.

4.2 Axial motion estimation and correction for simultaneous multi-plane two-photon calcium imaging

4.2.1 abstract

Two-photon imaging in behaving animals is typically accompanied by brain motion. For functional imaging experiments, for example with genetically encoded calcium indicators, such brain motion induces changes in fluorescence intensity. These motion related intensity changes or motion artifacts can typically not be separated from neural activity induced signals. While lateral motion, within the focal plane, can be corrected by computationally aligning images, axial motion, out of the focal plane, cannot easily be corrected.

Here, we developed an algorithm for axial motion correction for non-ratiometric calcium indicators taking advantage of simultaneous multi-plane imaging. Using temporally multiplexed beams, recording simultaneously from at least two focal planes at different z positions, and recording a z-stack for each beam as a calibration step, the algorithm separates motion related and neural activity induced changes in fluorescence intensity. The algorithm is based on a maximum likelihood optimisation approach; it assumes (as a first order approximation) that no distortions of the sample occurs during axial motion and that neural activity increases uniformly along the optical axis in each region of interest.

The developed motion correction approach allows axial motion estimation and correction at high frame rates for isolated structures in the imaging volume *in vivo*, such as sparse expression patterns in the fruit fly brain.

4.2.2 Introduction

Using optical microscopy for investigating neural circuits *in vivo*, and particularly in behaving animals, is complicated by movement of the brain with respect to the focal plane [329, 381, 383, 384, 385]. In many preparations, such as mice or fruit flies, movement is reduced by mechanically stabilizing the brain, which however often still leaves residual motion [329] and additionally can be invasive [331, 342].

In *in vivo* preparations, the brain moves in all three spatial dimensions, laterally, within the focal plane, as well as axially, out of the focal plane. Since the lateral resolution of the microscope is higher than the axial resolution, lateral motion is easier to detect [384]. Lateral motion can be corrected by post processing with a range of different methods, resulting in sequences of images aligned to a common field of view [329, 380, 381, 382, 383, 384].

Motion in axial direction, however, can usually not be corrected using post-processing. Axial motion leads to variations in the recorded fluorescence intensity due to changes in

sample excitation. Generally, such changes cannot be disentangled from intensity fluctuations of the indicator resulting from neural activity [385]. Additionally, sample movement, which for example in mice lies in the range of a few micrometers [329, 385], can exceed the focal range of the two-photon microscope [355] and therefore lead to loss of information [503].

Algorithms similar to those used for lateral motion correction have also been applied for time series of volume images (z-stacks). For small axial displacements, two-color labeling can be used for motion correction (see [389] for a recent example of this approach). Recording time series of z-stacks with sufficient axial resolution however limits the frame rate in each focal plane [474, 504]. Faster axial correction speeds can be achieved by actively tracking moving brain samples. Taking advantage of a reference signal, for example a reflected beam [386], behavioral parameters [387], or fluorescent fiducials such as cell bodies [385, 388] or fluorescent beads [385], the focal plane or additionally the region of interest (ROI) can be updated in a closed-loop configuration. Repositioning of the ROI at high frame rates and in fast control cycles however requires specialized hardware allowing random access scanning [385]. Additionally, introducing fiducials, typically fluorescent beads, is often impractical and invasive, for example when imaging in the brain of *Drosophila*. Similarly, naturally occurring fiducials such as cell bodies are often not present in the imaging volume. Further, often only a single fluorescent dye, for instance a non-ratiometric calcium indicator, is used.

Alternatively to recording volume images in z-stacks, simultaneous multi-plane imaging allows recording a limited number of focal planes at the same time [29, 369, 370, 371, 505, 506, 507]. Similar to imaging in a single focal plane, multi-plane recordings are still subject to axial motion artifacts. However, the correlated intensity changes across simultaneously recorded focal planes that result from sample motion, allow inferring motion information. This has been used for tracking fluorescent beads using temporally multiplexed and axially offset beams [508, 509, 510].

Here, we develop an approach for axial motion estimation and correction in the brain for two-photon functional imaging with non-ratiometric calcium indicators. The approach does not require fiducials and can be applied for isolated neural structures inside the imaging volume. The technique relies on an optimization algorithm that estimates axial brain motion as well as disentangles motion and neural activity related fluorescence changes based on simultaneous imaging in at least two focal planes. The algorithm is demonstrated using simulations with two and four simultaneously recorded focal planes, as well as validated using *in vivo* imaging in behaving fruit flies.

4.2.3 Results

4.2.3.1 Outline of motion correction approach

In simultaneous multi-plane imaging, motion along the axial direction displaces the sample at the same time in all focal planes. This correspondingly leads to related intensity changes in the different planes. For functional imaging with calcium indicators, changes in intensity due to sample motion are additionally confounded with neural activity related intensity changes. For disentangling these two contributions we developed an optimization based correction approach.

The experimental setup is shown in Fig. 4.2.1B and was previously described [507]. Simultaneous two-plane imaging was implemented with two temporally offset beams (by 6 ns) recorded independently using temporal multiplexing [369]. The axial profiles of the two beams are shown in Fig. 4.2.1C.

The different steps of the correction approach are outlined in Fig. 4.2.1A. First, a calibration stack of the sample is recorded with the two temporally multiplexed beams (Fig. 4.2.1A,1)). This stack is averaged over 10 recordings (see Methods for details) so that intensity variations due to motion are averaged out. For subsequent combined functional imaging and motion estimation, the sample is then approximately centered between the two beams such that it is always visible in both focal planes (Fig. 4.2.1A, 2)). After recording a time series (Fig. 4.2.1A, 3)) and computationally removing lateral motion, the correction algorithm extracts axial sample motion. Using the estimated axial motion and the z-stacks, the intensity recorded by each beam at each focal plane is finally corrected for motion (Fig. 4.2.1A, 5)).

The algorithm does not require a second activity-independent label for motion estimation, such as a fluorescent bead of a different color. It however relies on the assumption that neural activity induced fluorescence changes occur with a constant gain factor from baseline in axial direction (see Supplementary Fig. S4.2.1 for an illustrative example). Additionally, the method requires that the structure of interest is always visible in both focal planes and isolated, meaning that no other structures move in and out of the imaging volume. Depending on the sample and its typical motion, the separation between focal planes as well as the axial width of the beams therefore needs to be adjusted.

The algorithm finds and corrects axial motion by optimizing a cost function. The cost function is derived and explained in detail in Methods in several steps. First an analytical approximation for a one dimensional sample is developed to illustrate the workings of the algorithm before introducing the general case with multiple ROIs. Both, the one dimensional as well as the full algorithm are demonstrated in simulations. We then test the algorithm experimentally. First, we estimate controlled focal plane motion in a sample labeled with green fluorescent protein. Then, in addition to motion, we also estimate controlled variations in fluorescence intensity. Next, we correct neural activity recorded with

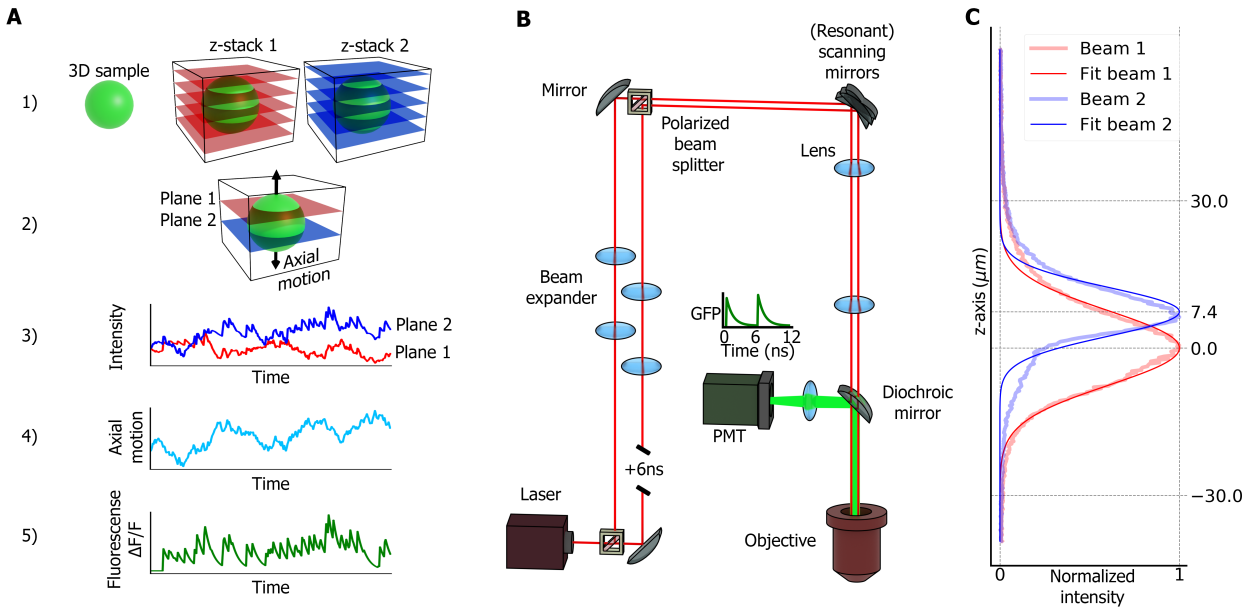


Figure 4.2.1: Approach and setup for motion estimation and correction. **A** Outline of method: 1) Calibration step: two stacks of the sample are recorded simultaneously in two different, axially offset focal planes. 2) Fluorescence intensity of the sample is recorded simultaneously in two planes and the sample moves in axial direction (z-axis). 3) Changes in intensities over time in each plane have two contributions: axial motion as well as neural activity. 4) The algorithm uses the recorded stacks to estimate axial motion of the sample from intensities recorded in the two planes. 5) Changes in fluorescence, $\Delta F/F$, are corrected to remove the contribution of axial motion, yielding motion corrected, neural activity related fluorescence changes. **B** Optical setup: two Gaussian beams are temporally offset by 6 ns, allowing simultaneous imaging in two different planes using temporal multiplexing. **C** Normalized profiles of the two beams along the z-axis fitted with Gaussian functions.

a genetically expressed calcium indicator for controlled motion. Finally, the algorithm is applied for measuring and correcting actual brain motion.

4.2.3.2 Motion estimation and correction algorithm

The motion estimation and correction algorithm is shown schematically in Fig. 4.2.1A and proceeded along the following steps:

- **1)** First, we recorded a total of 10 z-stacks of the sample with each beam, using the Fast z mode in Scanimage with a piezoelectric objective actuator. The fast-z mode in scanimage enables recording of z-stacks by continuously recording frames while moving the objective with a piezoelectric actuator linearly along the z-axis. The z-stacks were obtained over 100μm along the z-axis in steps of 0.25μm, at a resolution of 256 x 256

pixels at $60Hz$ frame rate. Stacks were recorded simultaneously with the two beams. The time to record the 10 stacks was approximately 67 seconds.

- **2)** We recorded time series of the sample simultaneously in two focal planes at $60Hz$, with the same resolution and zoom as the stacks, providing a total of T frames for each beam. Lateral motion correction (i.e., along the x and y-axis) was performed using the phase correlation algorithm from Skimage [481] in Python. The phase correction algorithm computes the relative lateral offset between two images by obtaining the phase shift between the Fourier transforms of both images [511]. We defined a template as the average of the first 10 frames of the two-plane time series recordings and computed the offset of each subsequent frame in the time series with respect to this template [382, 507]. Additionally, all frames in the stacks recorded in step 1 were similarly aligned with respect to their respective templates and the aligned 10 stacks for each beam were finally averaged.

- **3)** We defined $N = 32$ regions of interest (ROIs) corresponding to the structural arrangement of wedge neurons [507]. The intensity of each ROI i was computed for each beam, $I_{1,i}(t)$ and $I_{2,i}(t)$, at every recorded frame, $t = 1, ..., T$, by summing over all pixels within the ROI. We also computed the intensity of each ROI i in each averaged z-stack in step 2, producing a total of 400 slices of each ROI i profile recorded by each beam along the z-axis, $I_{1,i}^{(stack)}(z)$ and $I_{2,i}^{(stack)}(z)$.

- **4)** For each frame t, we estimated axial motion of the sample. First, we computed the log-likelihood of the sample at any z-position in the stacks, described by Eq. (4.9) and derived from Eq. (35). Then we filtered the log-likelihood over time with a Gaussian kernel $f(t, \sigma)$ (Eq. (20)), and estimated the axial motion of the sample, $\hat{z}(t)$, by obtaining the z position that maximized Eq. (4.10). An estimation error, $E(t)$ was additionally computed using Eq. (4.11).

$$L(z,t) = \\ -\frac{N}{2}\log(2\pi) - \frac{1}{2}\sum_{i=1}^{N}\log\left(2\frac{(I_{1,i}^{(stack)}(z))^2}{(I_{2,i}^{(stack)}(z))^3}\right) - \sum_{i=1}^{N}\frac{(I_{2,i}^{(stack)}(z))^3}{(I_{1,i}^{(stack)}(z))^2}\left(\frac{I_{1,i}(t)}{I_{2,i}(t)} - \frac{I_{1,i}^{(stack)}(z)}{I_{2,i}^{(stack)}(z)}\right)^2. \tag{4.9}$$

$$L_f(z,t) = \sum_{t'=0}^{T} f(t'-t, \sigma_t)L(z,t'), \tag{4.10}$$

$$E(t) = \frac{1}{N}\sum_{i=0}^{N}\Big(\frac{I_{1,i}(t)}{I_{2,i}(t)} - \frac{I_{1,i}^{(stack)}(\hat{z}(t))}{I_{2,i}^{(stack)}(\hat{z}(t))}\Big)^2. \tag{4.11}$$

- **5)** The motion estimation is used to remove axial motion-related changes in the measured intensities $I_{1,i}(t)$ and $I_{2,i}(t)$, using Eq. (4.12). Finally, the corrected change in fluorescence in each ROI i, $\Delta F/F_i$, is computed according to Eq. (4.13).

$$\begin{cases} I_{1,i}^{cor}(t) = \frac{I_{1,i}(t)}{I_{1,i}^{stack}(\hat{z}(t))} \\ \\ I_{2,i}^{cor}(t) = \frac{I_{2,i}(t)}{I_{2,i}^{stack}(\hat{z}(t))}. \end{cases} \tag{4.12}$$

$$\text{corrected} \quad \Delta F/F_i(t) = \frac{1}{2}\Big(\frac{I_{1,i}^{cor}(t) - F_{1,i}^0}{F_{1,i}^0} + \frac{I_{2,i}^{cor}(t) - F_{2,i}^0}{F_{2,i}^0}\Big) \quad \text{for } i = 1, ..., N, \tag{4.13}$$

The previous steps are also summarized in Algorithm 2.

4.2.3.3 Motion correction in simulated data for a single voxel

The motion correction algorithm was first verified using simulated data (Fig. 4.2.2). For this purpose, we defined an arbitrary one dimensional sample extended along the optical axis (z-axis, Fig. 4.2.2A, top). We additionally defined two Gaussian beams with different beam profiles and intensities, similar to the ones used in the experiment (Fig. 4.2.2A, top). The profiles of the beams along the z-axis must cover the axial range of sample motion, keeping the sample always visible with both beams. Note that the use of different beam profiles is not a requirement for the motion correction algorithm, both profiles can be similar as long as they are offset along the z-axis.

At the beginning of the simulated experiment, a z-stack is computed for each beam (Fig. 4.2.2A, bottom, see Methods for details). The sample is assumed to move along the z-axis as well as change its intensity due to neural activity (Fig. 4.2.2B). We assume that activity changes occur homogeneously along the optical axis, that is, with a multiplicative factor with respect to the fluorescence baseline (see Supplementary Fig. S4.2.1).

A simulated time series of sinusoidal axial sample motion combined with stochastic changes in neural activity is shown in Fig. 4.2.2C, top row. The resulting intensity time series, recorded simultaneously in two focal planes, are shown in Fig. 4.2.2C, second row.

Algorithm 2 Motion estimation and correction algorithm

record_stacks() ▷ 1)
record_sample_activity() ▷ 2)
correct_lateral_motion()
define_ROIs(N) ▷ 3)
for $t = 1, ..., T$ **do** ▷ Loop for time steps
  for $i = 1, ..., N$ **do** ▷ Loop for ROIs
    $I_{1,i}(t), \quad I_{2,i}(t) \leftarrow$ compute_intensity_in_ROI(i)
    $I_{1,i}^{(stack)}(z), \quad I_{2,i}^{(stack)}(z) \leftarrow$ compute_stack_intensity_in_ROI(i)
  end for
  $\hat{z}(t) \leftarrow \text{argmax}_z \Big[L_f(z,t) \Big]$ ▷ 4) Eq. (4.10)
  $E(t) \leftarrow$ estimate_error(t) ▷ Eq. (4.11)
  for $i = 1, ..., N$ **do** ▷ Loop for ROIs
    $I_{1,i}^{(cor)}(t) \leftarrow$ correct_intensity$\Big(I_{1,i}(t), \quad I_{1,i}^{(stack)}(\hat{z}(t)) \Big)$ ▷ 5) Eq. (4.12)
    $I_{2,i}^{(cor)}(t) \leftarrow$ correct_intensity$\Big(I_{2,i}(t), \quad I_{2,i}^{(stack)}(\hat{z}(t)) \Big)$
    $\Delta F/F_i \leftarrow$ compute_fluorescence_change$\Big(I_{1,i}^{(cor)}(t), \quad I_{1,2}^{(cor)}(t) \Big)$ ▷ Eq. (4.13)
  end for
end for

Based on the recorded intensity time series, the optimization algorithm accurately estimates both, sample motion as well as motion-corrected, activity related changes in fluorescence intensity (Fig. 4.2.2C, third and bottom rows).

4.2.3.4 Motion correction in simulated data for multiple voxels

The algorithm was further validated with simulated data with multiple one dimensional voxels, representing regions of interests (ROIs) defined on a three dimensional sample (see next section and Methods for details). For this, neural activity in a ring attractor was simulated, similar to experimentally observed data [313, 507]. A random distribution of the axial position of the different ROIs was assumed, reflecting structural variability (Fig. 4.2.3A, top row). Neural activity in this kind of network is centered in a bump and we here assumed that the bump of activity moves at constant velocity around the ring attractor. To simulate brain motion, the sample was oscillated with respect to the two focal planes along the axial direction (Fig. 4.2.3A, bottom). As for the case of a single voxel, a z-stack is computed using both beams. Intensity measurements from both beams are subjected to noise, similar to experimental recordings (see Methods for details). The algorithm assumes that all ROIs undergo the same axial motion. Therefore, all ROIs contribute to estimating motion (Fig. 4.2.3C, first row).

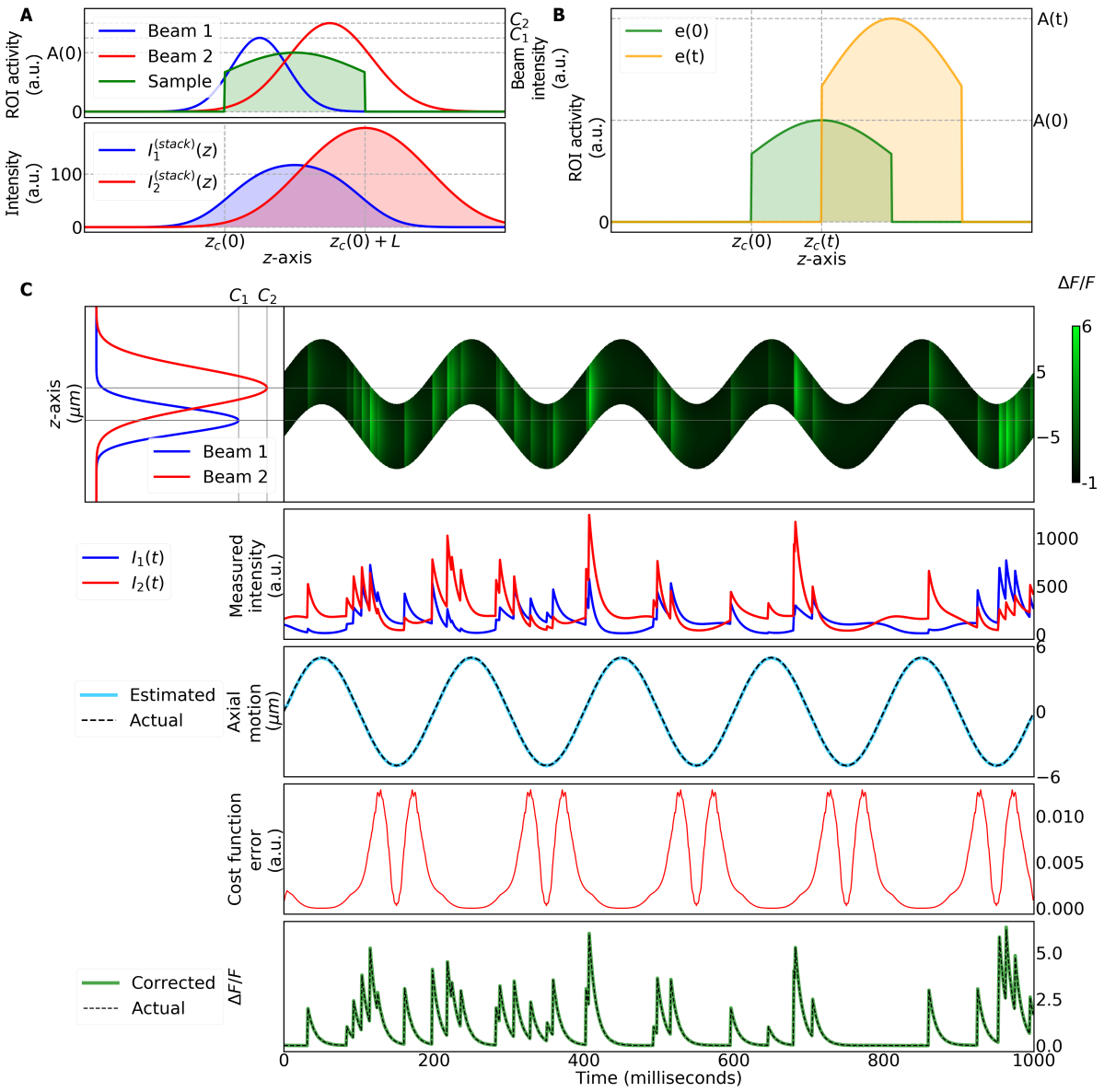


Figure 4.2.2: Motion correction in a simulated single ROI. **A** Top: axial intensity profiles of the two simulated beams and the simulated sample (ROI) at time $t = 0$. Bottom: two stacks recorded from the sample at time $t = 0$ with the two beams. **B** Example of axial motion and activity of the ROI. Sample profile along the z-axis at time $t = 0$ is shown in green. At time $t > 0$, the offset of the ROI along the z-axis changes while its activity increases. **C** Simulation of ROI activity and motion along the z-axis over time. Top row, left side: beam profiles. Right side: sample moves along z-axis over time. Color indicates sample neural activity. Second row: resulting intensities measured by each beam have two different contributions, motion and activity. Third row: comparison of actual and estimated axial motion. Fourth row: cost function error of the motion estimation algorithm (see Methods for details). Bottom row: actual and estimated, corrected changes in neural activity induced $\Delta F/F$.

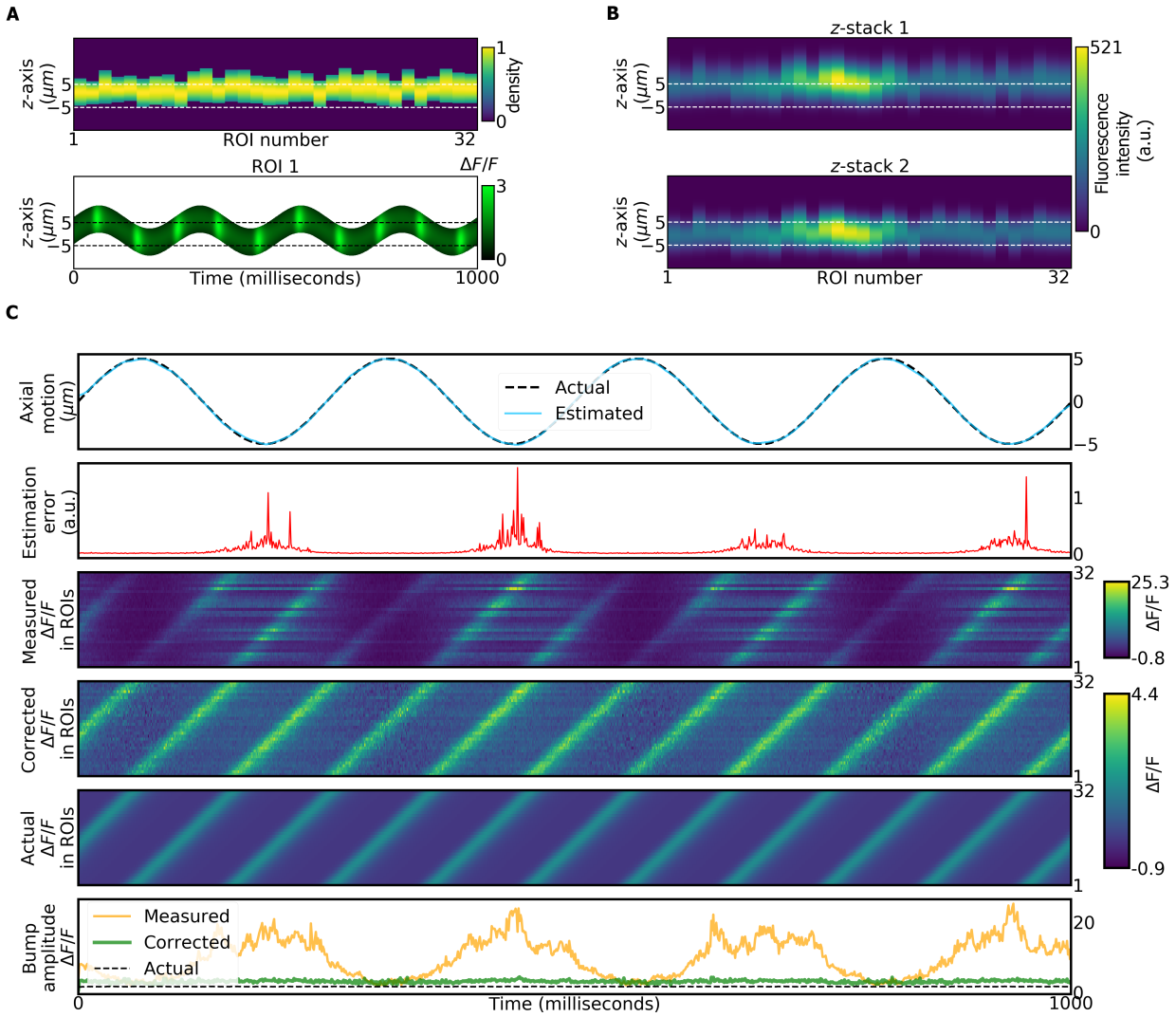


Figure 4.2.3: Motion correction in a simulated ring attractor with 32 ROIs. **A** Top: normalized intensity profiles of the ROIs, which are simulated with varying lengths and offsets along the z-axis. **B** Bottom: ROI 1 moves along the z-axis over time while its activity ($\Delta F/F$) changes (see C for all ROIs). **B** Top: stacks of the ROIs obtained with first beam. Bottom: same for second beam. **C** Simulation of ROIs with axial motion and activity changes over time. All ROIs move together, while activity changes independently in each ROI. First row: comparison of actual and estimated axial motion of ROIs. Second row: cost function error of the motion estimation algorithm. Third row: measured changes in fluorescence with combined activity changes and axial motion. Fourth row: changes in fluorescence after motion correction. Fifth row: actual changes in fluorescence due to activity. Bottom row: comparison of the averaged measured, corrected and actual bump amplitudes in the ROIs (see Methods for details on all steps).

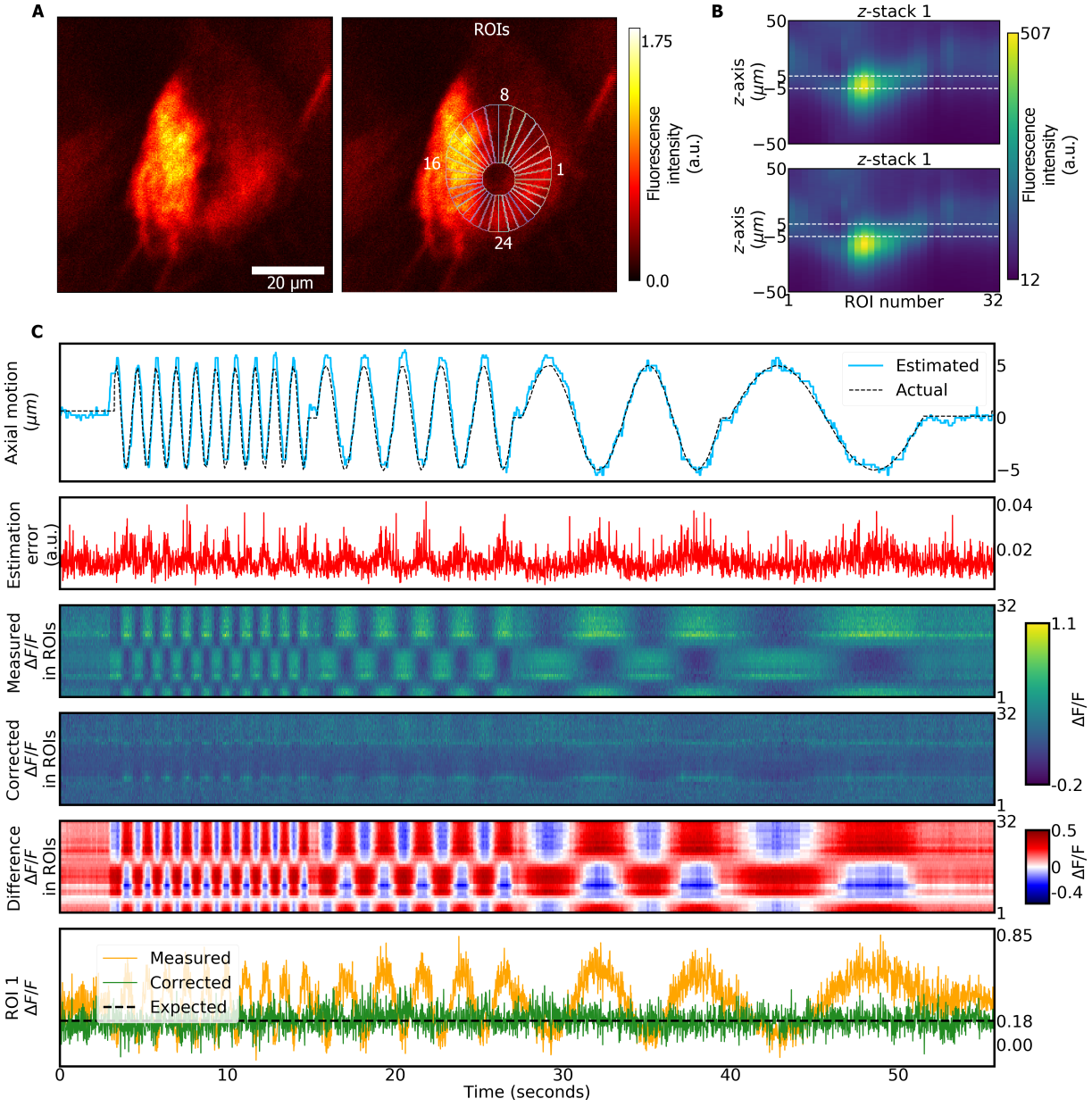


Figure 4.2.4: Axial motion estimation and correction in GFP labeled neurons. **A** Left side: average over all frames of the experiment. Right side: 32 ROIs are defined. **B** Stacks recorded from each ROI with first (top) and second (bottom) beam, respectively. **C** Top row: actual and estimated axial motion. Second row: cost function error of motion estimation (see Methods for details). Third row: measured fluorescence changes in each ROI. Fourth row: corrected fluorescence changes in each ROI. Fifth row: difference between corrected and measured fluorescence changes for each ROI. Bottom row: measured, corrected, and expected changes in fluorescence for ROI 1 (representative for all ROIs).

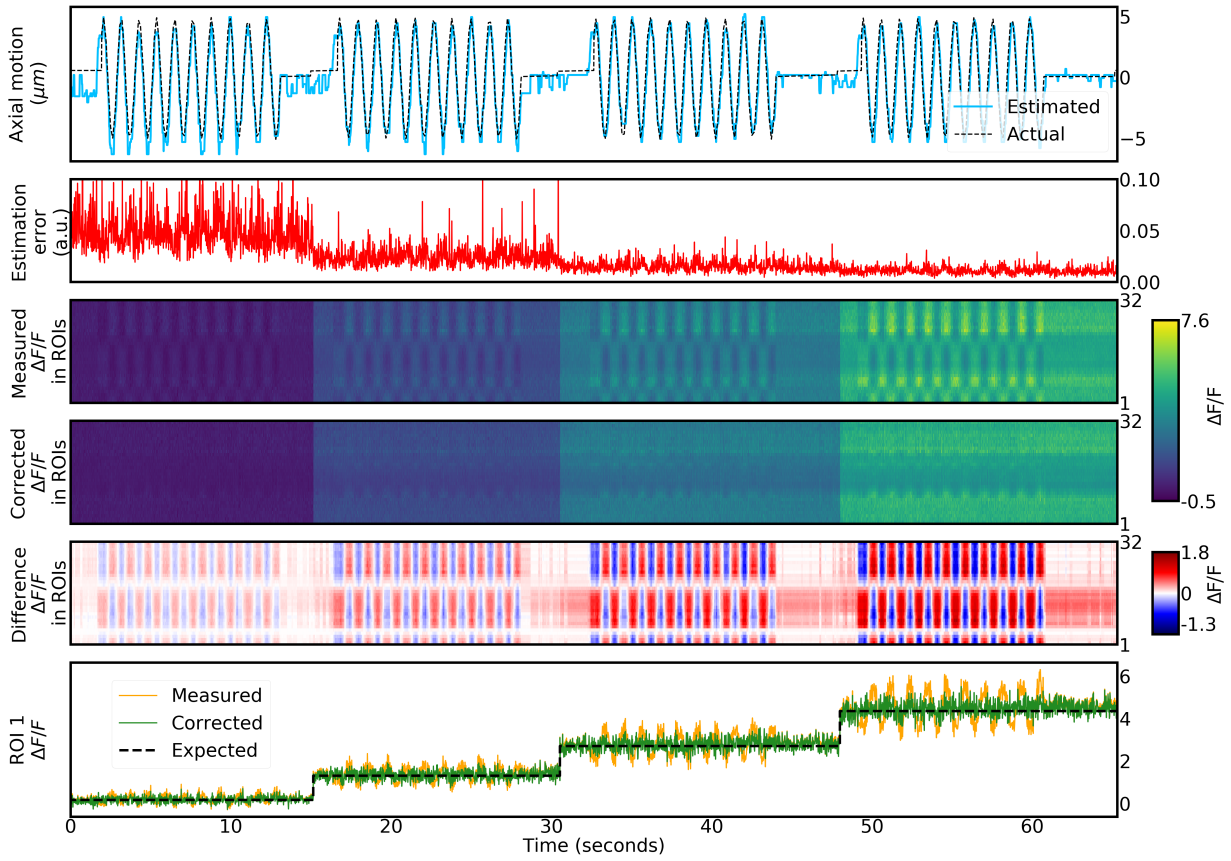


Figure 4.2.5: Axial motion estimation and correction in GFP labeled neurons at different laser powers, simulating changes in neural activity. The definition of ROIs and the recorded stacks are the same as in Fig. 4.2.4A and B, respectively. Top row: comparison between actual and estimated axial motion. Second row: cost function error of motion correction algorithm. Third row: measured changes in fluorescence in each ROI. Fourth row: corrected changes in fluorescence in each ROI. Fifth row: difference between corrected and measured changes in fluorescence for each ROI. Bottom row: comparison between measured, corrected and expected changes in fluorescence for ROI 1 (see Methods for details).

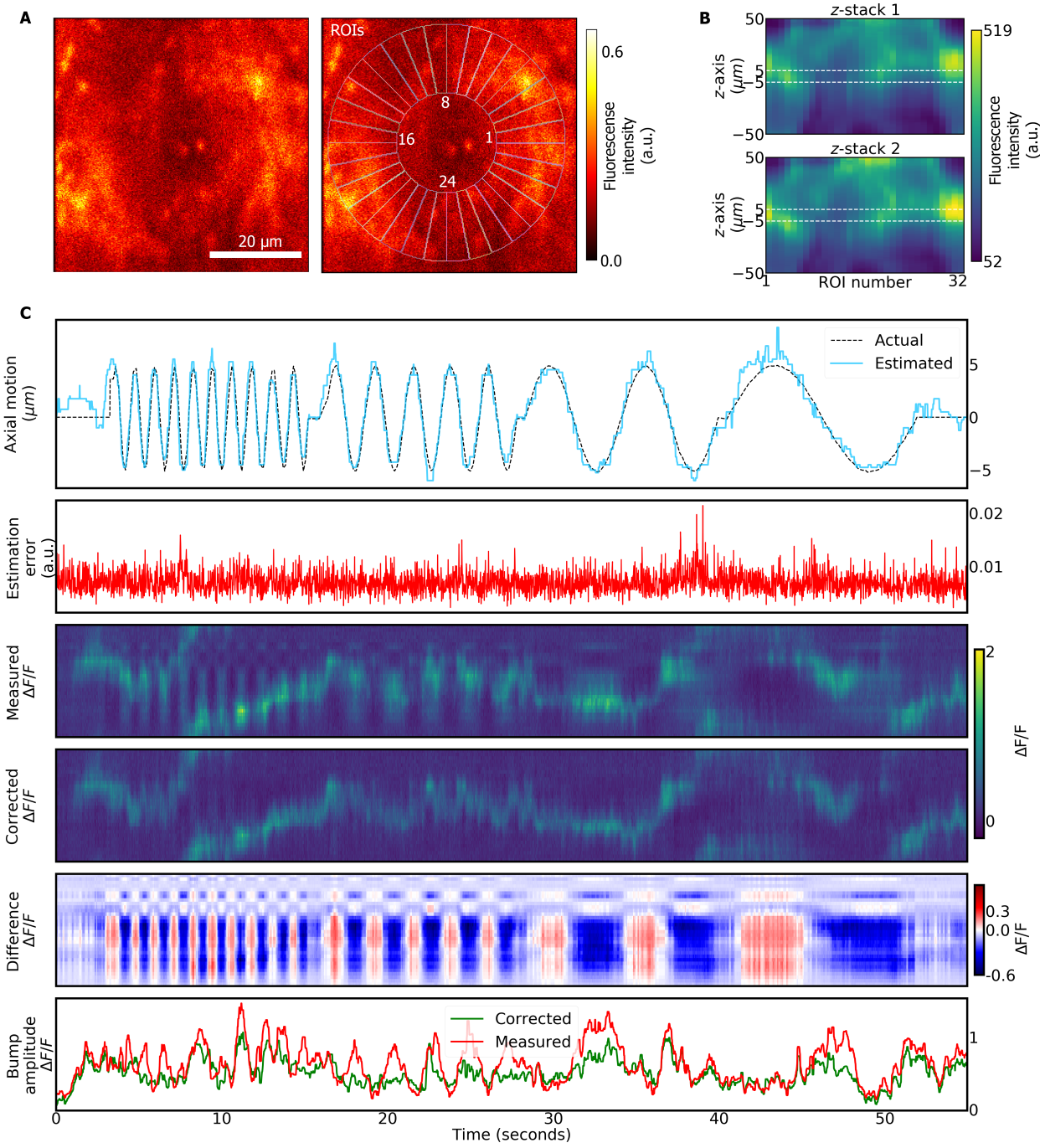


Figure 4.2.6: Motion estimation and correction in wedge neurons labeled with jGCaMP8f during controlled axial motion. **A** Left side: average over all frames. Right side: definition of 32 ROIs. **B** Z-stacks recorded by the first beam (top) and second beam (bottom). **C** First to fifth row: same as Fig. 4.2.4C. Bottom row: measured and corrected fluorescence signals (bump amplitude, see Methods for details).

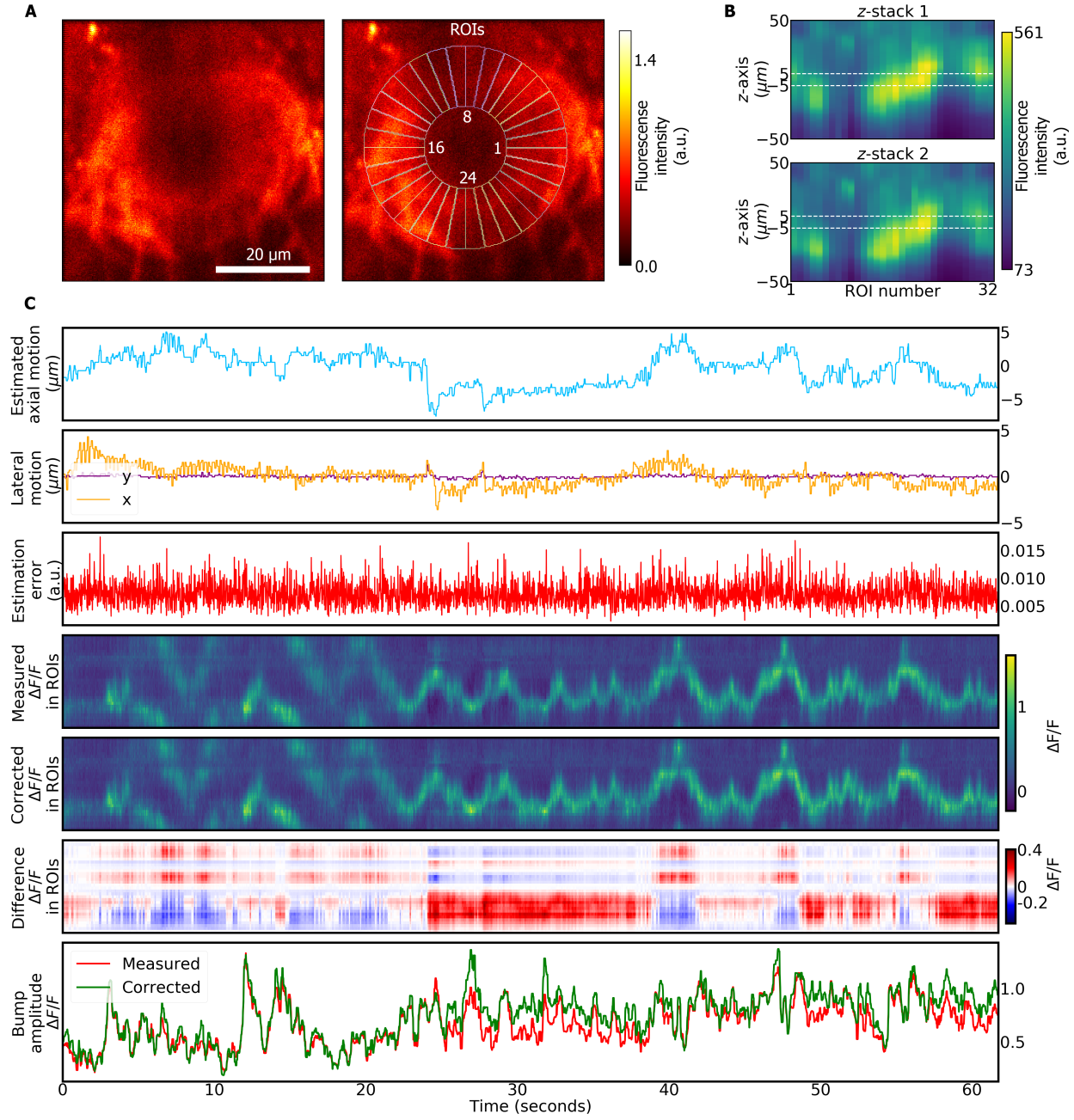


Figure 4.2.7: Motion estimation and correction in wedge neurons labeled with jGCaMP8f. **A** Left side: average over all frames. Right side: definition of 32 ROIs. **B** Stacks recorded by the first beam (top) and second beam (bottom). **C** First to sixth row: same as Fig. 4.2.4C, additionally including lateral motion estimated from computationally aligning frames (second row). Bottom row: measured and corrected fluorescence signals (bump amplitude, see Methods for details).

The bump of activity traveling with continuous velocity across the different ROIs is shown before correction in Fig. 4.2.3C, third row, as well as after correction in Fig. 4.2.3C, fourth row, and compared with the actual bump activity in Fig. 4.2.3C, fifth row. As also seen in the average over all ROIs (Fig. 4.2.3C, bottom row), the algorithm accurately corrects motion artifacts in the estimation of fluorescence changes.

4.2.3.5 Estimation and correction of controlled sample motion *in vivo*

The motion correction algorithm was experimentally tested by controlled variation of the focal plane in neurons labeled with green fluorescent protein (GFP, Figs. 4.2.4 and 4.2.5). For this, GFP was expressed in wedge neurons of the head direction system of the fruit fly [313] (R60D05-GAL4, Fig. 4.2.4A, left side). The fly's proboscis was fixed with wax to prevent brain motion [331]. To simulate sample motion, the axial position of the microscope objective was modulated sinusoidially at a range of frequencies using a piezoelectric objective actuator (P-725.4CD, Physik Instrumente) by up to $10\mu m$ at different frequencies ($1Hz$, 0.5 Hz, $0.2Hz$, $0.1Hz$, see Methods for details).

The motion correction algorithm was applied for estimating axial motion from data simultaneously recorded in two focal planes as follows. At the beginning of the experiment a total of 10 z-stacks were recorded with both beams. Each z-stack contained a total of 400 slices covering $100\mu m$ along the z-axis in steps of $0.25\mu m$. The resolution of each slice was 256×256 pixels and images were recorded at $60Hz$. Even though there was no lateral brain motion during these experiments, the piezoelectric objective actuator produced lateral displacements at different z-positions. Therefore, we defined a template, consisting of the 10 first images acquired during the experiment, and all images, including those of the z-stacks, were aligned with respect to this template using a phase correlation algorithm (as implemented in Skimage [481], see Methods). After alignment, the 10 z-stacks were averaged and a total of $N = 32$ ROIs were defined along the dendritic toroidal structure as described previously [507] (Fig. 4.2.4A, right side). The intensities recorded in the z-stacks were further filtered using a median filter with a window size of 20 slices to remove noise. The filtered intensities for all ROIs are shown in Fig. 4.2.4B for both beams.

Axial motion in the time series data was estimated by computing the value of the log-likelihood function (Eq. (4.10)) in all 400 slices of the z-stacks with a time window of size $\sigma_f = 3$. Then, the slice $\hat{z}(t)$ that maximized the log-likelihood function was determined. The axial motion estimation was obtained in steps of $0.25\mu m$, which is the step size of the recorded stacks. The resulting resolution of axial motion estimation however depends on the profile of the z-stack, which in turn depends on the ROI densities and beam profiles. For example, Supplementary Fig. S4.2.3 shows a simulation for a single voxel defined with a very wide rectangular ROI density along the z-axis, producing z-stacks without axial structure (Supplementary Fig. S4.2.3A). In this case, the motion correction algorithm cannot estimate

the precise axial position of the sample around the center of the ROI (see Supplementary Fig. S4.2.3B, third row), because the ratio between the stacks, $I_1^{(stack)}(z)/I_2^{(stack)}(z)$, is constant. There are however no changes in fluorescence intensity between the two recorded intensities, and therefore the activity correction of the sample (Supplementary Fig. S4.2.3B, fourth row) is not affected by the inaccuracy of the estimated axial motion.

As seen in Fig. 4.2.4C, top row, the algorithm accurately estimates motion. The cost function error (Fig. 4.2.4C, second row, calculated using Eq. (4.11)) indicates that the accuracy of the estimate is similar across all positions.

The fluorescence intensities were corrected using Eq. (23), and the corrected $\Delta F/F$ was computed using Eq. (4.13) (Fig. 4.2.4C, fourth row). This was compared to the measured $\Delta F/F$, obtained from Eq. (47) (Fig. 4.2.4C, third row). The strong changes in measured fluorescence intensity, or motion artifacts, across ROIs in Fig. 4.2.4C, third row, are removed after correction and all ROIs show constant fluorescence profiles, as expected for GFP labeled neurons (Fig. 4.2.4C, fourth row). This is also seen in the average intensities for a representative ROI (Fig. 4.2.4C, bottom row). The offset (from 0) in the corrected $\Delta F/F$ value is due to an arbitrary definition of the baseline as the fraction of 10 percent lowest intensities (see Supplementary Fig. S4.2.2 for details).

4.2.3.6 Estimation and correction of controlled sample motion and intensity variations

To estimate at the same time motion related as well as activity induced intensity changes, we varied the focal plane (as described above) together with the laser power, resulting in different levels of fluorescence intensity in a GFP labeled sample (Fig. 4.2.5). Four epochs of sinusoidal focal plane modulations at a frequency of $1Hz$ were combined with increasing the laser power in steps, simulating different neural activity levels. Recordings of time series and z-stacks, image preprocessing as well as motion estimation and correction were performed as described above.

Motion was again estimated accurately (Fig. 4.2.5, top row). Additionally the algorithm correctly estimated the different motion corrected intensity levels (Fig. 4.2.5, third to fifth row). This is also seen in the average changes across all regions of interest (Fig. 4.2.5, bottom row). As expected, the cost function error (Fig. 4.2.5, second row) decreased with increased signal-to-noise ratio resulting from the increased fluorescence signal. Motion estimation always occurs on a single frame basis (smoothed with a Gaussian kernel with a standard deviation of 3 frames, see Methods), so that faster variations in intensity would result in similar estimates.

4.2.3.7 Estimation and correction of controlled motion for *in vivo* two-photon calcium imaging

We next corrected controlled motion of the focal plane in a sample expressing the calcium indicator jGCaMP8f [344] in the head direction system of the fly [313]. The fly walked in a virtual reality setup on an air supported ball [507] and the proboscis of the fly was fixed to prevent uncontrolled sample motion. Controlled focal plane motion was again generated by actuating the objective by up to $10\mu m$ at different frequencies ($1Hz$, $0.5Hz$, $0.2Hz$, $0.1Hz$). Images (z-stack and time series) were recorded, corrected for lateral motion, and filtered as described above and motion correction proceeded along the same steps (Eqs. (4.10), (23), (4.13), and (47)).

Again, $N = 32$ ROIs were defined (Fig. 4.2.6A, right side) and Fig. 4.2.6B shows the intensity profiles of all ROIs for both beams.

The estimated axial motion is compared with the actual motion of the piezoelectric objective actuator in Fig. 4.2.6C, first row. The measured $\Delta F/F$ as well as the corrected $\Delta F/F$ values are shown in Fig. 4.2.6C, third and fourth rows. The difference between the corrected and measured $\Delta F/F$ is shown in Fig. 4.2.6C, fifth row. The estimation error (Eq. (4.11)) indicates that motion was tracked with similar quality across all axial positions. The last row in Figs. 4.2.6C compares corrected and measured bump amplitudes (see Methods), which was smoothed using a Gaussian filter with a standard deviation in the kernel of 5 frames. Motion correction was able to remove motion artifacts, resulting in a smooth movement of the bump across the ellipsoid body as expected [313].

4.2.3.8 Estimation and correction of brain motion for *in vivo* two-photon calcium imaging in behaving animals

Finally, motion was corrected in a naturally moving brain during *in vivo* calcium imaging in a fly walking in a virtual reality setup [331, 507], without fixing the fly's proboscis or removing muscles in the head. Motion estimation and correction proceeded as described in the previous section.

We measured brain motion of up to $10\mu m$ (Fig. 4.2.7C, top row) and corrections induced changes in the values of $\Delta F/F$ of up to 40%, as seen in the difference (Fig. 4.2.7C, sixth row) between uncorrected and corrected $\Delta F/F$ (4.2.7C, fourth and fifth row, respectively). The bump amplitudes of the corrected and measured $\Delta F/F$ are shown in Fig. 4.2.7, bottom row, and were computed using Eq. (7) and smoothed using a Gaussian filter with standard deviation of 5 frames.

4.2.3.9 Algorithm for imaging with four simultaneously recorded focal planes

The developed technique can be extended to more than two focal planes (for example four beams as in [370]). Supplementary Fig. S4.2.4 shows a simulation with four axially separated beams. A single ROI was simulated for simplicity (Supplementary Fig. S4.2.4A, top) and the resulting z-stacks for all four beams are shown in Supplementary Fig. S4.2.4A, bottom. Using more than two beams allows for example increasing the axial resolution or axial range.

The code of the axial motion correction algorithm, together with the simulations, can be found in the following git repository: https://gitlab.com/anflores/axial_motion_correction

4.2.4 Discussion

We developed a method for correcting motion artifacts for two-photon calcium imaging that result from axial sample movement. The method relies on simultaneous multi-plane imaging with at least two axially offset focal planes [369]. As verified with simulations (Figs. 4.2.2 and 4.2.3 and Supplementary Fig. S4.2.4), by controlled motion of the focal plane (Fig. 4.2.4, 4.2.5, 4.2.6), as well as by controlled changes in fluorescence intensity (Fig. 4.2.5), the developed optimization algorithm can estimate as well as correct motion with non-ratiometric indicators in isolated structures in the imaging volume.

The method was applied for correcting motion artifacts that are observed when imaging *in vivo* in the brain of fruit flies. Since motion can be corrected without additional mechanical stabilization (Fig. 4.2.7), such as removing muscles or immobilizing the proboscis [331], the approach simplifies imaging in flies and improves the viability of the preparation. Since brain motion in the fly as observed here (about $10\mu m$, see Fig. 4.2.7) lies in a similar range as observed in other species [385], the technique could also similarly be applied in other animals.

Compared with motion correction that relies on recording time series of z-stacks [474, 504], the approach developed here benefits from high frame rates (for example 60 Hz at 256×256 pixels in each plane). Compared with closed-loop correction [385, 386, 387, 388], the microscope does not require custom modifications and is compatible with multi-beam scanning as implemented in commercially available scanning software (Scanimage [474]). Further, the developed method does not use an independent tracking fiducial, such as a fluorescent bead or cell body.

That motion is estimated directly from the sample labeled with calcium indicator, leads however to the following two conditions: First, changes in fluorescence due to calcium activity need to occur with a constant gain factor axially along the entire ROI (see Supplementary Fig. S4.2.1 for illustration). Given that controlled motion is accurately corrected in a sample expressing jGCaMP8f (Fig. 4.2.6), this is a valid approximation for the sample used here. Second, the structure of interest needs to be isolated in the imaging volume at all times.

This means that no (partial) structures can move in and out of the imaging volume. Since the algorithm relies on measuring intensity changes along the optical axis, such appearing or disappearing features would lead to erroneous corrections.

Further, the algorithm requires that each ROI must be visible at all times in both focal planes. This condition can be satisfied by adjusting the separation and axial extension of the beams such that the moving object is always within their axial range. Here, beam conditions were optimized for imaging with commonly used GAL4 fly lines labeling subsets of neurons in the central brain. We used two axially extended beams, since we imaged from a relatively large structure. However, the technique could equally be applied for smaller structure with diffraction limited beams. Beam separation and parameters could additionally be adjusted on a sample by sample basis using for example electrically tunable lenses or spatial light modulators. The method can also be similarly extended to more simultaneously recorded focal planes (see [367] for an overview of different multiplane imaging approaches) as shown in simulations (Supplementary Fig. S4.2.4) which could be used to extend the axial range or resolution. Instead of using simultaneously recorded planes the method could be applied with sequentially recorded planes [512, 513], as long as the sample moves slowly compared with the time it take to switch between focal planes. Additionally, the algorithm requires that lateral motion is corrected first using standard motion correction algorithms and for reliable image alignment therefore sufficient intensity is needed in each channel. Similarly, the ROIs must be defined over a sufficient number of pixels so that the intensity distribution in each ROI is approximately normal.

Overall, the developed method allows correction of lateral and axial brain motion in two-photon calcium imaging experiments from isolated structures in the imaging volume, such as sparse expression patterns in the brain of *Drosophila*, with non-ratiometric indicators.

4.2.5 Supplementary information: Methods

4.2.5.1 Microscope setup

The setup was described in [507]. Briefly, two axially offset Gaussian beams were used to record in two different focal planes using temporal multiplexing [369]. Temporal multiplexing was performed using Scanimage in photon counting mode [474]. The diameter and collimation of each beam was adjusted with two lenses (Thorlabs achromatic doublets), while the two beams were linearly and orthogonality polarized and delayed by $2m$, as shown in Fig. 4.2.1B. The beams were focused at the samples with a power of $6mW$ for each beam by underfilling the objective of the microscope (16X Nikon CFI LWD Plan Fluorite Objective, 0.80 NA, 3.0 mm WD). This created elongated beam profiles along the axial direction (Fig. 4.2.1). The full width at half maximum was adjusted to $9\mu m$ and $16\mu m$ (computed from the standard deviations: FWHM = 2.4σ), respectively, and the peaks of

the two beams were separated by $7\mu m$.

4.2.5.2 *Drosophila* preparation

Imaging in behaving flies we performed as described in [507]. Briefly, We used 7-10 days old female flies, either expressing GFP or GCaMP8f in wedge neurons (R60D05-GAL4). We performed laser surgery to remove the cuticle over the brain. The cuticle and underlying tissue were then removed either with a microrobotic arm or manually under a dissection scope [507]. Finally, a drop of glue was placed on the opening (DETAX, Freeform, 02204). The flies expressing GCaMP8f were left to recover over night [507], while flies expressing GFP were imaged directly after surgery.

For the fly expressing GFP, as well as for the fly in Fig. 4.2.6 the proboscis was fixed with wax to prevent brain motion [331]. For imaging, flies were glued to a cover slide ((22 mm × 22 mm, thickness No. 1, Cat. No. 631-0124, see [507] for details of the preparation).

4.2.5.3 Extracting head direction from calcium signals

We computed the trajectory of the bump of activity along the ROIs, $b(t)$, based on the ROI position with maximum fluorescence value of the corrected $\Delta F/F$:

$$b(t) = argmax_i \Big[\quad \text{corrected} \quad \Delta F/F_i(t) \quad \Big] \tag{4.14}$$

We then used this trajectory to compute the bump amplitude in both, measured and corrected $\Delta F/F$, in the ROIs along the bump trajectory:

$$\begin{cases} \text{corrected bump amplitude}(t) = \text{corrected} \quad \Delta F/F_{b(t)}(t) \\ \text{measured bump amplitude}(t) = \text{measured} \quad \Delta F/F_{b(t)}(t) \end{cases} \tag{4.15}$$

4.2.5.4 Analytical approximation of motion correction algorithm for a single ROI

While motion correction was performed numerically as described in Algorithm 2, we here first explain the operation of the algorithm using an analytical approximation, assuming continuous time and z-axis, first for a single ROI defined on a 3D sample in the absence of noise.

A single ROI is a voxel extended along the z-axis, which is described as a function $e(A, z)$ representing the number of fluorescent proteins, for example GFP or GCaMP, inside the ROI at a given z position. The function $e(A, z)$ changes over time depending on a variable A, $A = A(t)$, representing neural activity in each ROI. Generally, the ROI function, $e(A, z)$, could have any form. As an example, Fig. S4.2.1A shows a ROI function defined by the

following Eq.:

$$e(A,t) = A\exp\left[\frac{(z+p_1)^2}{2\sigma^2}\right] + A^2\exp\left[\frac{(z+p_2)^2}{2\sigma^2}\right], \tag{4.16}$$

where $p_1 = -5\mu m$ and $p_2 = 5\mu m$ represent the center of two Gaussians with standard deviation $\sigma = 2.5\mu m$. In this case the activity A changes the Gaussian peaks by different amplitudes (Fig. S4.2.1A), meaning that fluorescence changes heterogeneously at different z positions. This could for example be the case if two different dendrites of a neuron receive inputs with different strengths.

To simplify the problem of motion estimation and correction, we can approximate the ROI function to first order with a Taylor series around $A = 0$:

$$e(A,z) \approx e(0,z) + \frac{\partial e(A,z)}{\partial A}\Big|_{A=0} A. \tag{4.17}$$

The derivative of $e(A,z)$ with respect to A and evaluated at $A = 0$ is a function that only depends on z, which we call $\rho(z)$. On the other hand, $e(0,z)$ is the baseline fluorescence indicator distribution along the z-axis which is not modulated by the activity A of the ROI. We assume for simplicity that $e(0,z)$ is negligible, assuming that there is an activity baseline, A^0, much larger than $e(0,z)$:

$$A^0\rho(z) \quad >> \quad e(0,z) \tag{4.18}$$

With this approximation, we can write the ROI function as:

$$e(A,z) = A\rho(z) \tag{4.19}$$

The function $\rho(z)$ describes a density of fluorescence proteins along the z-axis, while A increases activity inside the ROI homogeneously. In the following we refer to $\rho(z)$ as the ROI density while A is called the ROI activity. An example of Eq. (4.19) is given in Fig. S4.2.1B, where $\rho(z)$ is defined by the following expression:

$$\rho(z) = \exp\left[\frac{(z+p_1)^2}{2\sigma^2}\right] + \exp\left[\frac{(z+p_2)^2}{2\sigma^2}\right] \tag{4.20}$$

In addition, we assume that the ROI undergoes axial (along the z-axis) motion, described with a time-dependent variable, $\Delta z(t)$, which changes the offset of the ROI density along the z-axis. Assuming no distortion in the sample during axial motion, the ROI density remains constant but moves along the z-axis. Therefore, the ROI function is finally approximated as:

$$e(t,z) = A(t)\rho(z - \Delta z(t)) \tag{4.21}$$

Eq. (4.21) allows us to separate the ROI function, $e(t,z)$, into two parts, one which depends on the activity of the ROI, $A(t)$, which is independent of the z-axis, and another one that depends on the motion of the sample, $\rho(z - \Delta z(t))$.

This first order approximation, which was valid in the biological samples used for the experiments, allows us to develop an algorithm to estimate and correct the axial motion of the sample. The goal of the algorithm is to estimate axial motion, $\Delta z(t)$, as well as to extract the activity, $A(t)$.

The ROI activity is measured using two beams described by two functions, $g_1(z)$ and $g_2(z)$, which represent the shape of the beams along the z-axis. For the algorithm to work, these two beams must have different profiles along the z-axis (to provide unique information about the sample) and must be integrable, meaning that their integral must be finite. In practice, we assume that these are Gaussian beams centered at different positions along the z-axis, while their width along the z-axis and power can be different. At each time, t, both beams excite the sample with a time delay (on the order of the fluorescence lifetime), and produce two independently measured fluorescence signals.

The intensity of each fluorescence signal associated with each beam, $I_1(t)$ and $I_2(t)$, is the integral of the excitation of each beam within the ROI along the z-axis:

$$\begin{cases} I_1(t) = \int_{-\infty}^{\infty} e(t,z) g_1(z) dz \\ \\ I_2(t) = \int_{-\infty}^{\infty} e(t,z) g_2(z) dz. \end{cases} \tag{4.22}$$

Since the ROI activity, $A(t)$, is independent of z (Eq. (4.21)), we can write the measured intensities as:

$$\begin{cases} I_1(t) = A(t) G_1(\Delta z(t)) \\ I_2(t) = A(t) G_2(\Delta z(t)), \end{cases} \tag{4.23}$$

where G_1 and G_2 are two functions defined by the integral over the excitation of each beam at the ROI density, $\rho(z - \Delta z(t))$, and only depend on the axial motion of the sample, $\Delta z(t)$. Eq. (4.23) describes how changes in the measured intensities, $I_1(t)$ and $I_2(t)$, can have two different contributions: the activity of the ROI and the axial motion of the sample.

For estimating axial motion of the sample, $\Delta z(t)$, a calibration step is first performed. At the beginning of the experiment ($t = 0$), a z-stack is recorded with each beam by moving the two beams simultaneously and continuously along the z-axis. We assume that the ROI activity and axial motion of the sample, $A(0)$ and $\Delta z(0)$, do not change when recroding the stack. Moreover, and without loss of generality, we define the origin of the axial motion while recording the stacks so that $\Delta z(0) = 0$. In practice, the assumption that $A(0)$ and $\Delta z(0)$ do not change is achieved by averaging over several stacks (see Results with biological samples expressing GFP or GCaAMP8f). The algorithm however works with arbitrary activity $A(0)$ during z-stack acquisition. Since moving the beams is equivalent to moving the sample in

the opposite direction while leaving the beams fixed, the stacks are defined as follows:

$$\begin{cases} I_1^{(stack)}(z) = A(0)\int_{-\infty}^{\infty}\rho(z'-z)g_1(z')dz' \\ \\ I_2^{(stack)}(z) = A(0)\int_{-\infty}^{\infty}\rho(z'-z)g_2(z')dz' \end{cases} \tag{4.24}$$

This equation can be expressed as

$$\begin{cases} I_1^{(stack)}(z) = A(0)G_1(z) \\ I_2^{(stack)}(z) = A(0)G_2(z) \end{cases} \tag{4.25}$$

The ratios $I_1(t)/I_2(t)$ and $I_1^{stack}(z)/I_2^{stack}(z)$ do not depend on the activity and we use this to define the following cost function,

$$J_{L_2}(z,t) = \left(\frac{I_1(t)}{I_2(t)} - \frac{I_1^{stack}(z)}{I_2^{stack}(z)}\right)^2 = \left(\frac{G_1(\Delta z(t))}{G_2(\Delta z(t))} - \frac{G_1(z)}{G_2(z))}\right)^2 \tag{4.26}$$

The cost function $J_{L_2}(z)$ is minimized at time t when $z = \Delta z(t)$. This optimization is used to find the axial motion of the sample, $\Delta z(t)$, using the stacks. We will show in the following sections (Eq. (4.9)) that the shape of this cost function arises from a expectation–maximization approach. To take into account that the axial motion of the sample is correlated in time, we modified Eq. (4.26), with a Gaussian filter over time:

$$J_{L_2}(z,t) = \int_{-\infty}^{\infty} f(t'-t,\sigma_t)\left(\frac{I_1(t)}{I_2(t)} - \frac{I_1^{stack}(z)}{I_2^{stack}(z)}\right)^2 dt' \tag{4.27}$$

where $f(t-t',\sigma)$ is a Gaussian kernel centered at time t with standard deviation σ_t, defined as:

$$f(t'-t,\sigma) = \exp\Big[-\frac{(t'-t)^2}{2\sigma_t^2}\Big] \tag{4.28}$$

Eq. (4.27) provides a filtered estimate of the axial motion of the sample by weighting contributions from several intensity measurements. This cost function assumes that changes in axial motion within the Gaussian kernel are small. The standard deviation, σ_t, is a manually-set parameter that provides the size of the time window considered for the axial motion estimation.

To find the axial motion of the sample at any time t, we find the z-position in the stack, $\hat{z}(t)$, that minimizes the cost function.

$$\hat{z}(t) = \text{argmin}_z\Big[\quad J(z,t)\quad\Big] \tag{4.29}$$

The value of the cost function evaluated at the estimated displacement, $\hat{z}(t)$, provides a measure for the quality of the optimisation result at time t.

$$\text{cost function error}(t) = J(\hat{z}(t), t) \tag{4.30}$$

Once the the motion of the sample is estimated, we correct the measured intensities by dividing the intensity recorded by each beam by its corresponding stack, evaluated at the estimated slice $\hat{z}(t)$ at any time t:

$$\begin{cases} I_1^{cor}(t) = \frac{I_1(t)}{I_1^{stack}(\hat{z}(t))} = \frac{A(t)}{A(0)} \frac{G_1(\Delta z(t))}{G_1(\hat{z}(t))} \\ \\ I_2^{cor}(t) = \frac{I_2(t)}{I_2^{stack}(\hat{z}(t))} = \frac{A(t)}{A(0)} \frac{G_2(\Delta z(t))}{G_2(\hat{z}(t))} \end{cases} \tag{4.31}$$

This correction eliminates the contribution of the axial motion of the sample from the measured intensities if the axial motion estimation is correct, i.e. $\hat{z}(t) = \Delta z$, leaving only the contributions made by changes in the activity $A(t)$. Finally we can compute the relative change in fluorescence, $\Delta F/F$, using the corrected intensities:

$$\Delta F/F(t) = \frac{1}{2}\Big(\frac{I_1^{cor}(t) - F_1^0}{F_1^0} + \frac{I_2^{cor}(t) - F_2^0}{F_2^0}\Big) = \frac{A(t) - A^0}{A^0} \tag{4.32}$$

where F_1^0 and F_2^0 are the baselines of the intensities $I_1^{cor}(t)$ and $I_2^{cor}(t)$ respectively, corresponding to the ROI activity baseline, A^0. The baselines F_1^0 and F_2^0 are obtained by computing the mean value of the lowest 10% values of the corrected intensities, I_1^{cor} and I_2^{cor}, respectively.

4.2.5.5 Simulation of a moving single ROI

To demonstrate how this algorithm works for a single ROI, we simulated a single ROI along the z-axis described by Eq. (4.19) with an activity density defined as

$$\rho(z) = \begin{cases} \frac{2}{3} + \frac{1}{3}\sin\Big[(z - z_0)\frac{\pi}{L}\Big] & \text{if} \quad z_0 > z > z_0 + L \\ 0 & \text{otherwise,} \end{cases} \tag{4.33}$$

where $z_0 = -5\mu m$ and $L = 10\mu m$. The ROI undergoes axial motion over time, as defined by Eq. (4.21) and shown in Fig. 4.2.2B, described by the following Eq.:

$$\Delta z(t) = z_{amp} \sin(2\pi f_z t) \tag{4.34}$$

where $z_{amp} = 5\mu m$ and $f_z = 5Hz$ are the amplitude and frequency of a simulated sinusoidal axial motion. The activity of the sample, $A(t)$, is modeled by a differential Eq.:

$$\tau_A \dot{A}(t) = -A(t) + 1 + \epsilon_A, \tag{4.35}$$

where $\tau_A = 10ms$ is a time constant, and ϵ_e is a stochastic input to the sample that produces spikes along the simulation with 0.5% probability and positive amplitude.

To record the activity of the sample, we defined two beams with Gaussians axial profiles, according to the following equation:

$$g_i(z) = C_i e^{-(z-d_i)^2/(2\sigma_i^2)} \qquad \text{for } i = 1, 2, \tag{4.36}$$

where $C_1 = 1.25a.u.$ and $C_2 = 1.5a.u.$ define the maximum beam power and $\sigma_1 = 2\mu m$ and $\sigma_2 = 3\mu m$ are the widths (standard deviations) along the z-axis. The two beams are offset in axial direction, $d_1 = -2.5\mu m$ and $d_2 = 2.5\mu m$. The shape of the beams is shown at the top of Fig. 4.2.2A, together with the ROI function at time $t = 0$, $e(0, z)$.

A z-stack of the sample at time $t = 0$ is defined in the absence of axial motion, $\Delta z(0) = 0$, and activity is defined as $A(0) = 1$. The stack is simulated by recording the activity of the sample while moving the beams along the the z-axis from $-25\mu m$ to $25\mu m$ in steps of $0.05\mu m$, resulting in a convolution between the beams and the sample according to Eq. (4.24) (Fig. 4.2.2A). Only a single stack without averaging is used for simulations.

Next, combined sample motion and activity are simulated for 1000 milliseconds. The equation for the activity, $A(t)$, is solved using forward Euler with a time step of $dt = 0.001$ milliseconds. The intensity of each beam is given by Eq. (4.22). The result of the simulation is shown in Fig. 4.2.2C, where the first row shows the moving sample and its activity, and the second row shows the intensities recorded in each beam.

To estimate sample motion, $\hat{z}(t)$, at each instant t, we computed the value of the cost function (Eq. (4.27)) at all z positions of the stacks (from $-25\mu m$ to $25\mu m$ in steps of $0.05\mu m$). Finally, motion at time t, $\Delta z(t)$, is estimated according to Eq. (4.29), by finding the position $\hat{z}$ that minimizes the cost function across all z values. The third row in Fig. 4.2.2B shows the real versus the estimated motion of the sample. The error of the optimisation process is calculated using Eq. (4.30) and shown in the fourth row of Fig. 4.2.2.

Finally, the recorded intensities are corrected using the estimated axial motion and Eq. (4.31), and changes in fluorescence intensity, $\Delta F/F$, are computed from the corrected intensities, according to Eq. (4.32). The last row in Fig. 4.2.2 shows the actual and the corrected changes in fluorescence, respectively. The actual $\Delta F/F$ is calculated according to the following Eq.:

$$\text{actual} \quad \Delta F/F = \frac{A(t) - A^0}{A^0} \tag{4.37}$$

where A^0 is an activity baseline calculated as the average of the lowest 10% values of $A(t)$.

4.2.5.6 Algorithm for motion estimation and correction for several ROIs with noise

We now extend the approach developed above to a sample with multiple ROIs. In addition we now consider that the measurements are noisy. We assume rigid three-dimensional sample motion, with negligible elastic deformations or changes in orientation.

We record a total of T pair of images, $M_1(t)$ and $M_2(t)$, one for each beam, for $t = 1, ..., T$ and assume that all images are aligned, that is, corrected for lateral motion. We define N ROIs on the images and each ROI i describes an area on the images containing n_i pixels. The sum of the values of all the pixels of each image inside this area, $M_1^{(w,h)}(t)$ and $M_1^{(w,h)}(t)$, where $(w, h) \in$ ROI i, provides a pair of intensity measurements of the ROI i in each pair of images at time t:

$$\begin{cases} I_{1,i}(t) = \sum_{(w,h)\in ROI_i} M_1^{(w,h)}(t) \\ I_{2,i}(t) = \sum_{(w,h)\in ROI_i} M_2^{(w,h)}(t). \end{cases} \tag{4.38}$$

The fluorescence signals detected by the PMT are subjected to shot noise and the intensities in each pixel follow independent Poisson distributions. If the number n_i of pixels in each ROI i is large, each pair of intensity measurements approaches the following normal distributions:

$$\begin{cases} I_{1,i}(t) \sim \mathcal{N}\Big(\mu_{1,i}(t), \mu_{1,i}^2(t)\Big) \\ I_{2,i}(t) \sim \mathcal{N}\Big(\mu_{2,i}(t), \mu_{2,i}^2(t)\Big) \end{cases} \tag{4.39}$$

where $\mu_{1,i}$ and $\mu_{2,i}$ are the means of the normal distribution for each beam, respectively.

Using the first-order Taylor expansion (Eq. (4.17)), we can approximate each ROI function i by the following expression:

$$e_i(t, z) = A_i(t)\rho_i(z - \Delta z(t)) \quad \text{for } i = 1, ..., N \tag{4.40}$$

where $A_i(t)$ and $\rho_i(z - \Delta z(t))$ are the activity and density of each ROI i, respectively, during the acquisition t. We again assume that the ROI moves in the axial direction, given by $\Delta z(t)$. Then, we can approximate the means of the intensity distributions, $\mu_{1,i}(t)$ and $\mu_{2,i}(t)$, as

$$\begin{cases} \mu_{1,i}(t) = A_i(t)G_{1,i}(\Delta z(t)) \\ \mu_{2,i}(t) = A_i(t)G_{2,i}(\Delta z(t)) \end{cases} \quad \text{for } i = 1, ..., N \quad , \tag{4.41}$$

where $G_{1,i}(\Delta z(t))$ and $G_{2,i}(\Delta z(t))$ are functions defined by the integral of the excitation of each beam at each ROI density, $\rho_i(z)_i$.

We now take the ratio of the intensities for each ROI i at each acquisition t, $I_{1,i}(t)/I_{2,i}(t)$, since the ratio of the mean values $\mu_{1,i}(t)/\mu_{2,i}(t)$ does not depend on the ROI acivity, $A_i(t)$. The ratio of these two normal variables is well approximated by a normal distribution

around the mean of the ratio, $\mu_{1,i}(t)/\mu_{2,i}(t)$, if the means are positive and the coefficients of variation, $\delta_{1,i}(t) = \sqrt{\mu_{1,i}(t)}/\mu_{1,i}(t)$ and $\delta_{2,i}(t) = \sqrt{\mu_{2,i}(t)}/\mu_{2,i}(t)$ are smaller than 0.1 [514].

$$\frac{I_{1,i}(t)}{I_{2,i}(t)} \sim \mathcal{N}\left(\frac{\mu_{1,i}(t)}{\mu_{2,i}(t)}, \quad 2\delta_{2,i}^2(t)\left(\frac{\mu_{1,i}(t)}{\mu_{2,i}(t)}\right)^2\right) \tag{4.42}$$

Assuming that all ROIs undergo the same axial motion, Δz, we can compute the log-likelihood for the ROIs with respect to their axial position, Δz, at acquisition t:

$$L\left(\Delta z \quad | \quad \frac{I_{1,1}(t)}{I_{2,1}(t)}, \ldots \frac{I_{1,N}(t)}{I_{2,N}(t)}\right) =$$
$$-\frac{N}{2}\log(2\pi) - \frac{1}{2}\sum_{i=1}^{N}\log\left(2\delta_{2,i}^2(t)\left(\frac{\mu_{1,i}(t)}{\mu_{2,i}(t)}\right)^2\right) - \sum_{i=1}^{N}\frac{1}{\delta_{2,i}^2(t)}\left(\frac{\mu_{2,i}(t)}{\mu_{1,i}(t)}\right)^2\left(\frac{I_{1,i}(t)}{I_{2,i}(t)} - \frac{\mu_{1,i}(t)}{\mu_{2,i}(t)}\right)^2, \tag{4.43}$$

where the mean of the ratio distributions depends only on the axial motion $\Delta z(t)$, and not on the activity of the ROIs:

$$\frac{\mu_{1,i}(t)}{\mu_{2,i}(t)} = \frac{G_{1,i}(\Delta z(t))}{G_{2,i}(\Delta z(t))} \tag{4.44}$$

To compute the ratio of the means for each ROI i, we used z-stacks recorded at the beginning of the experiment, $t = 0$. Each slice in each stack is aligned to remove lateral motion using phase correction[481], and the intensity for each ROI i in each z-slice is computed, $I_{1,i}^{(stack)}(z)$ and $I_{2,i}^{(stack)}(z)$. During the acquisition of the stack, both axial motion and activity of each ROI are considered constant, while the noise in the intensities of the slices in the stacks are assumed zero. Therefore, the intensity of each ROI in each slice of the stacks is given by the following equation:

$$\begin{cases} I_{1,i}^{(stack)}(z) = A_i(0)G_{1,i}(z) \\ I_{2,i}^{(stack)}(z) = A_i(0)G_{2,i}(z) \end{cases} \tag{4.45}$$

In practice, the previous assumptions are achieved by averaging several stacks and applying a median filter (see Results). We can now approximate the mean of the ratio distribution by the ratio of the intensities in the stacks at the slice Δz:

$$\frac{\mu_{1,i}(t)}{\mu_{2,i}(t)} = \frac{I_{1,i}^{(stack)}(\Delta z(t)))}{I_{2,i}^{(stack)}(\Delta z(t))}. \tag{4.46}$$

Finally, we can write the log-likelihood (Eq. 4.43) using the stacks as a function of z at each acquisition, t:

Note that $L(z,t)$ has a quadratic difference between the ratio of the stacks and the ratio of intensities (right side of Eq. (4.9)), similar to the cost function defined for a single ROI

(Eq. (4.26)), which was minimized due to the change in sign. The log-likelihood function, however, weights (left factor on the third term in Eq. (4.9)) and offsets (second term in Eq. (4.9)) this quadratic difference, taking into account more strongly ROIs that are less noisy to estimate the axial motion, i.e., the intensity of those ROIs with lower values (and therefore lower standard deviation in their distributions).

Since axial motion is correlated in time, we use a Gaussian filter similar to Eq. (4.27)) in the log-likelihood: where the kernel $f(t'-t,\sigma_t)$ is defined in Eq. 4.28. Again, the variable σ_t is manually set, and defines the size of the time window considered for the sum of log-likelihoods.

Since the z-stacks have a finite number of slices, we can compute the value of $L_f(z,t)$ numerically for each slice z and then estimate the axial motion of the sample, $\hat{z}(t)$, at each time t, from the slice z that maximizes the log-likelihood function, $L_f(z,t)$:

$$\hat{z}(t) = \text{argmax}_z\Big[L_f(z,t)\Big]. \tag{4.47}$$

We provide an estimation error, $E(t)$, by computing the standard deviation of the difference between the ratio of recorded intensities and the ratio of the means:

$$E(t) = \frac{1}{N}\sum_{i=0}^{N}\Big(\frac{I_{1,i}(t)}{I_{2,i}(t)} - \frac{\mu_{1,i}(t)}{\mu_{2,i}(t)}\Big)^2 \tag{4.48}$$

and using Eq. (4.46), this error can be expressed as:

Next, we correct the measured intensities from each beam using the estimated axial motion and extending Eq. (4.31) to N ROIs:

This correction eliminates the axial motion contribution from the intensity measurements. However, note that this correction inherits the noise from the measured intensities $I_{1,i}(t)$ and $I_{2,i}(t)$. According to Eq. (4.39), both intensity corrections are obtained according to the following normal distribution:

$$\begin{cases} \hat{I}^{cor}_{1,i}(t) \sim \mathcal{N}\Big(1,1\Big) \\ \hat{I}^{cor}_{2,i}(t) \sim \mathcal{N}\Big(1,1\Big) \end{cases} \tag{4.49}$$

Finally, we compute the change in fluorescence for each ROI i as follows:

where $F^0_{1,i}$ and $F^0_{2,i}$ are the baselines of the intensities, $I^{cor}_{1,i}$ and $I^{cor}_{2,i}$ that correspond to the activity baseline of each ROI, A^0_i. As for the case of a single ROI, we compute the baselines $F^0_{1,i}$ and $F^0_{2,i}$ from the average of the 10% lowest values of $I^{cor}_{1,i}(t)$ and $I^{cor}_{2,i}(t)$ respectively, for each ROI i.

4.2.5.7 Simulation of several moving ROIs

We demonstrate how the algorithm works for a simulation of $N = 32$ moving ROIs with noise. In this simulation it is assumed that lateral motion of a 3D sample is already corrected

and the ROIs are defined. The density of each ROI is defined along the z-axis according to the following equation:

$$\rho_i(z) = \begin{cases} \frac{1}{C_i}\left(a_i^0 + a_i^1 sin\left[(z - z_{0,i})\frac{\pi}{L_i}\right]\right) & \text{if} \quad z_{0,i} > z > z_{0,i} + L_i \\ 0 & \text{otherwise,} \end{cases} \tag{4.50}$$

where a_i^0 and a_i^1 are random coefficients for each ROI obtained from an uniform distribution in the range $[1, 2]$ and $z_{0,i}$ and L_i are a random origin and random length for each ROI, sampled from a uniform distribution in the range of $[-2, -5]$ and $[10, 15]$, respectively. The constant C_i normalizes the density of each ROI so that $\rho_i(z)$ is in the range of $[0, 1]$. Fig. 4.2.3A, top, shows the density of each ROI used in the simulation.

The motion of all ROIs is modeled as in the simulation in section 4.2.5.5 using Eq. (4.34) with a frequency of $f_z = 8Hz$. The activity of each sample is modeled as:

$$\tau_A \dot{A}_i(t) = -A_i(t) + 1 + U(t, i), \tag{4.51}$$

where $\tau_A = 10ms$ is the time constant and $U(t, i)$ is an input defined as a rotating Gaussian along the ROIs:

$$U(t, i) = U_{max} \exp\left[- \frac{min\Big[\quad |i - v(t)|, \quad N - |i - v(t)|\Big]^2}{2\sigma^2} \quad \right] \tag{4.52}$$

where $U_{max} = 2$ is the amplitude, $\sigma = 2$ is the width of the Gaussian and $v(t)$ rotates the input with respect to the ROIs at a frequency of $f_u = 10Hz$, according to

$$v(t) = \quad \text{mod } (f_u N t, N), \tag{4.53}$$

where mod $(\cdot, \cdot)$ indicates the modulo operation. The activity of the ROIs is again solved using forward Euler with a time step of $dt = 0.001$ millisecond. An example of ROI 1 undergoing axial motion while receiving the rotating input is shown in Fig. 4.2.3A, bottom, while the rotating input in all the ROIs during the simulation is shown in Fig. 4.2.3C, fourth row.

Two beams, defined again by Eq. (4.36), were used to record the fluorescence change in all ROIs. At time $t = 0$ we recorded a z-stack using 1000 slices (from $-25\mu m$ to 25μ in steps of $0.05\mu m$), assuming no axial motion of the sample, $\Delta z(0) = 0$. The recorded z-stacks are shown in Fig. 4.2.3B. Note that the activity during the z-stack acquisition is higher around the ROI 16. The algorithm can estimate and correct the axial motion with arbitrary activity $A_i(0)$ in the z-stack.

After defining the stacks, the intensities at time t in two simultaneous planes for each ROI i are simulated, $I_{1,i}(t)$ and $I_{1,i}(t)$, with changing axial position and ROI activity. The

intensities in each plane are sampled from a Gaussian distribution, given by Eq. (4.39), where the mean values $\mu_{1,i}(t)$ and $\mu_{2,i}(t)$ are computed using Eq. (4.41).

To estimate axial motion of the sample, $\Delta z(t)$, we computed the value of the log-likelihood function in Eq. (4.10) at all 1000 z positions of the stacks, at any time t, using a time window of size $\sigma_t = 3$. The estimated axial motion is then obtained by the slice in the $z-$stacks, $\hat{z}(t)$, that maximizes the log-likelihood function. The first row of Fig. 4.2.3C shows the estimated compared to the actual axial motion during the simulation, while the estimation error, computed by Eq. (4.11), is shown in the second row of Fig. 4.2.3C.

Next we corrected the measured intensities from each beam and each ROI using the estimated axial motion and Eq. (4.12). The change in fluorescence of the corrected intensities, corrected $\Delta F/F_i(t)$, is computed using Eq. (4.13) and shown in Fig. 4.2.3C, fourth row. This is compared with the actual $\Delta F/F_i(t)$ (Fig. 4.2.3C, fifth row), which is computed as:

$$\text{actual} \quad \Delta F/F_i(t) = \frac{A_i(t) - A_i^0}{A_i^0}, \tag{4.54}$$

where A_i^0 is the baseline activity of each ROI i, obtained from the average of the 10% lowest values of $A(t)$. Fig. 4.2.3C, third row, shows the change in fluorescence measured without motion correction. This measured $\Delta F/F_i(t)$ is obtained by the following Eq.:

$$\text{measured} \quad \Delta F/F_i(t) = \frac{1}{2}\Big(\frac{I_{1,i}(t) - I_{1,i}^0}{I_{1,i}^0} + \frac{I_{2,i}(t) - I_{2,i}^0}{I_{2,i}^0}\Big), \tag{4.55}$$

where $I_{1,i}^0$ and $I_{2,i}^0$ are the baseline measured intensities for each beam, obtained by the mean value of the 10% lowest values of $I_{1,i}(t)$ and $I_{2,i}(t)$, respectively. These baseline values are affected by axial motion and therefore changes in fluorescence appear much larger (Fig. 4.2.3C, third row) when the sample is out of focus due to the resulting low intensities. Further, the corrected $\Delta F/F$ is larger than the actual $\Delta F/F$ (Fig. 4.2.3, fourth and fifth row). This is due to noise in the measurements, which produces lower baselines values, $F_{1,i}^0$ and $F_{2,i}^0$. These lower values follow from averaging over the lowest 10% values of the corrected intensities (see for example Fig. S4.2.2B) instead of taking the mean value of the distribution.

4.2.5.8 Simulation for motion estimation and correction with four simultaneously recorded focal planes

Here, we extend the motion correction algorithm to four beams using simulations. For simplicity we consider only a single ROI. The ROI density is defined again by Eq. (4.33). Four different Gaussian beams are defined, according to the following equation:

$$g_j(z) = C_j e^{-(z-d_j)^2/(2\sigma_j^2)} \qquad \text{for } j = 1, 2, 3, 4, \tag{4.56}$$

where $C_1 = 1, C_2 = 1.5, C_3 = 2$ and $C_4 = 0.5$ are the maximum beam powers, and $\sigma_1 = 3$, $\sigma_2 = 3$, $\sigma_3 = 2$ and $\sigma_4 = 3$ are the beam widths (standard deviations) along the z-axis. Each beam is offset from the previous one by $3.33\mu m$ ($d_1 = -5$, $d_2 = -1.67$, $d_3 = 1.67$ and $d_4 = 5$). The beam profiles, as well as the ROI densities, are shown in Fig. S4.2.4A, first row.

First, a stack is recorded by continuously moving each beam long the z axis, from $-25\mu m$ to 25μ in steps of 0.05μ. The stack obtained for each beam is shown in the second row of S4.2.4A. We assume that the ROI undergoes axial motion over time, defined by Eq. (4.34), while its activity changes according to (4.35). We ran the simulation for a total of 1000 milliseconds using forward Euler with a time step of $dt = 0.001$. Both activity and axial motion of the ROI are shown in the first row of Fig. S4.2.4B. At each time step t each beam recorded intensity from the sample according to the following equation:

$$I_j(t) = A(t)G_j(\Delta z(t)) \qquad \text{for } j = 1, 2, 3, 4 \tag{4.57}$$

where the functions $G_j(\Delta z(t))$ represent the integration of the excitation of each beam j at the ROI density. The intensities recorded by each beam are shown in the second row of Fig. S4.2.4.

To estimate the axial motion of the ROI, we extended the cost function for two beams (Eq. 4.27) and defined the following cost function for four beams:

$$J^{(4)}_{L_2}(z,t) =$$
$$\int_{-\infty}^{\infty} f(t'-t,\sigma_t)\left[\alpha_{12}\left(\frac{I_1(t)}{I_2(t)} - \frac{I_1^{stack}(z)}{I_2^{stack}(z)}\right)^2 + \alpha_{23}\left(\frac{I_2(t)}{I_3(t)} - \frac{I_2^{stack}(z)}{I_3^{stack}(z)}\right)^2 + \alpha_{34}\left(\frac{I_3(t)}{I_4(t)} - \frac{I_3^{stack}(z)}{I_4^{stack}(z)}\right)^2\right]dt', \tag{4.58}$$

where $f(t'-t,\sigma_t)$ is the Gaussian kernel defined by Eq. (4.28), and the parameters α_{12}, α_{23} and α_{34} are computed at each time step t defined as:

$$\alpha_{jk} = \begin{cases} 1 & \text{if} \quad I_j(t), I_k(t) > I_{th} \\ 0 & \text{otherwise,} \end{cases} \tag{4.59}$$

where $I_{th} = 0.1$ is a minimum intensity threshold. The parameters α_{jk} are used to only take into account measured intensities at t if the ROI is within the field of view of beams j and k. When the intensity recorded by one of the beams is lower than I_{th}, the ROI is considered outside of the z-field of view of the beam and therefore its contribution to the cost function of Eq. (4.58) is discarded by the α_{jk} parameters.

We estimated the axial motion of the single ROI by finding the slice in the stacks, $\Delta z(t)$, at any time step t, that minimized the cost function (4.58). Both the estimated and actual axial motion are shown in Fig. S4.2.4B, third row. The cost function error, shown Fig.

S4.2.4B, fourth row, is given by the value of the cost function evaluated at the estimated axial motion, $J_{L_2}^{(4)}(\Delta z(t), t)$.

Finally, the intensity of each beam is corrected using the following expression:

$$I_j^{cor}(t) = \frac{I_j(t)}{I_j^{stack}(\hat{z}(t))} \qquad \text{for } j = 1, 2, 3, 4 \tag{4.60}$$

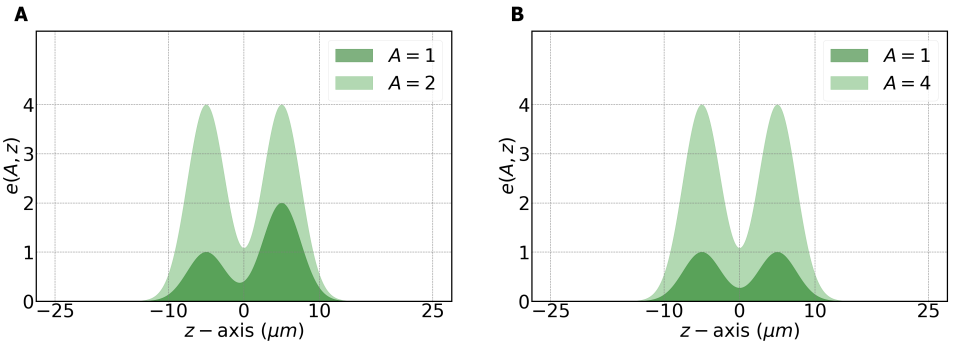
and the corrected fluorescence change, $\Delta F/F$ is computed from the corrected intensities:

$$\Delta F/F(t) = \frac{1}{4}\sum_{j=1}^{4}\left(\frac{I_j^{cor}(t) - F_j^0}{F_j^0}\right) \qquad \text{for } j = 1, 2, 3, 4, \tag{4.61}$$

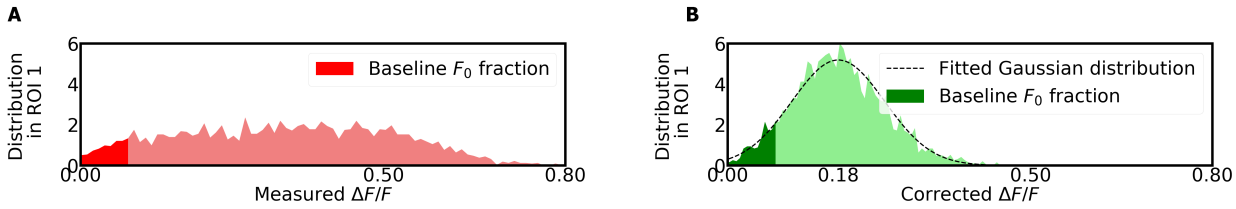
where F_j^0 is the baselines of the intensity I_j^{cor}, computed from the average of the 10% lowest values of $I_j^{cor}(t)$ for beam $j = 1, ..., 4$. The last row of Fig. S4.2.4B shows the corrected, actual, and measured $\Delta F/F$. The actual $\Delta F/F$ is computed according to Eq. 4.37. The measured $\Delta F/F$ is the fluorescence change that would be measured assuming no motion correction, given by:

$$\text{measured} \quad \Delta F/F = \frac{1}{4}\sum_{j=1}^{4}\frac{I_j(t) - I_j^0}{I_j^0}, \tag{4.62}$$

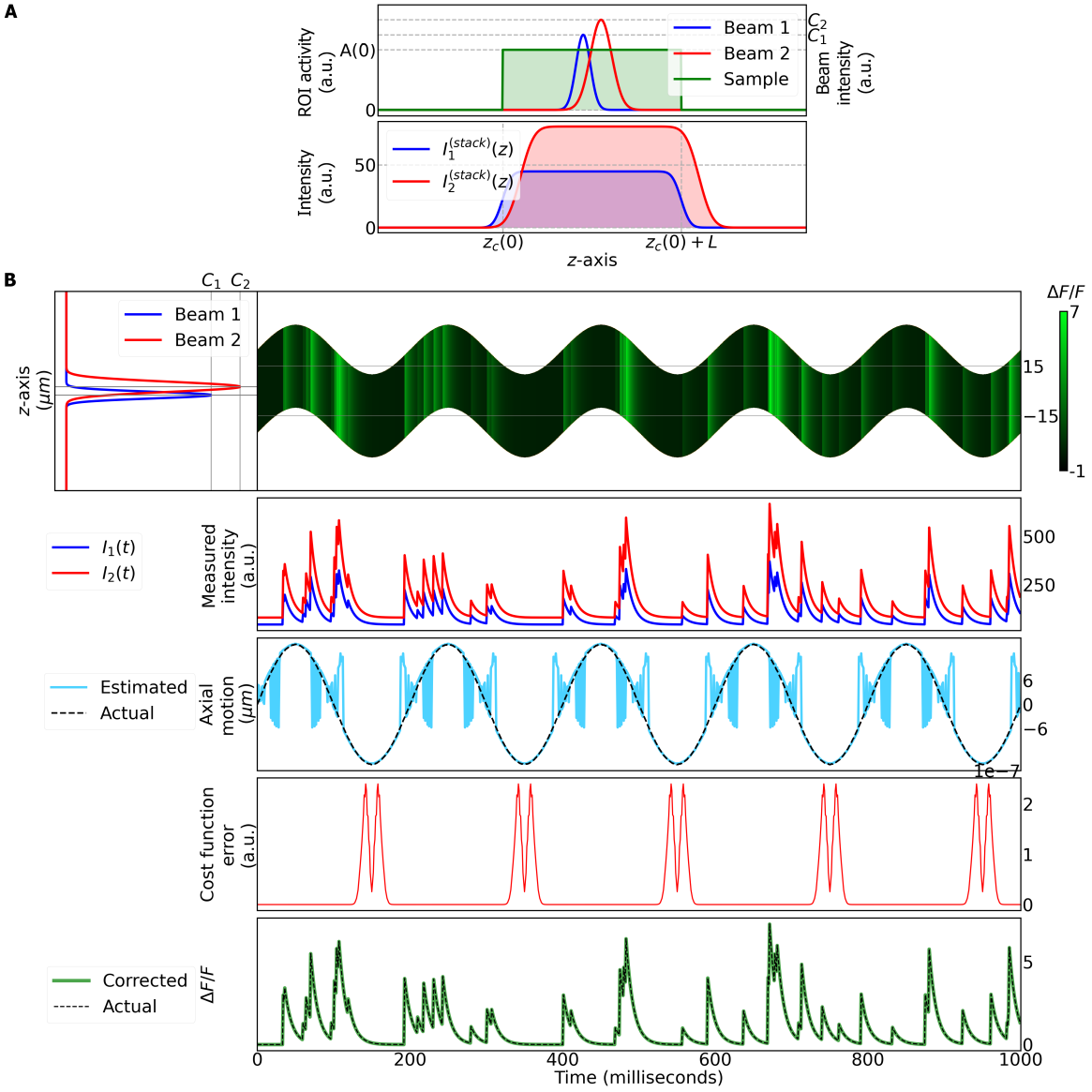
where I_j^0 is the baseline measured intensity, obtained by the mean value of the 10% lowest values of $I_j(t)$ for each beam $j = 1, ..., 4$.



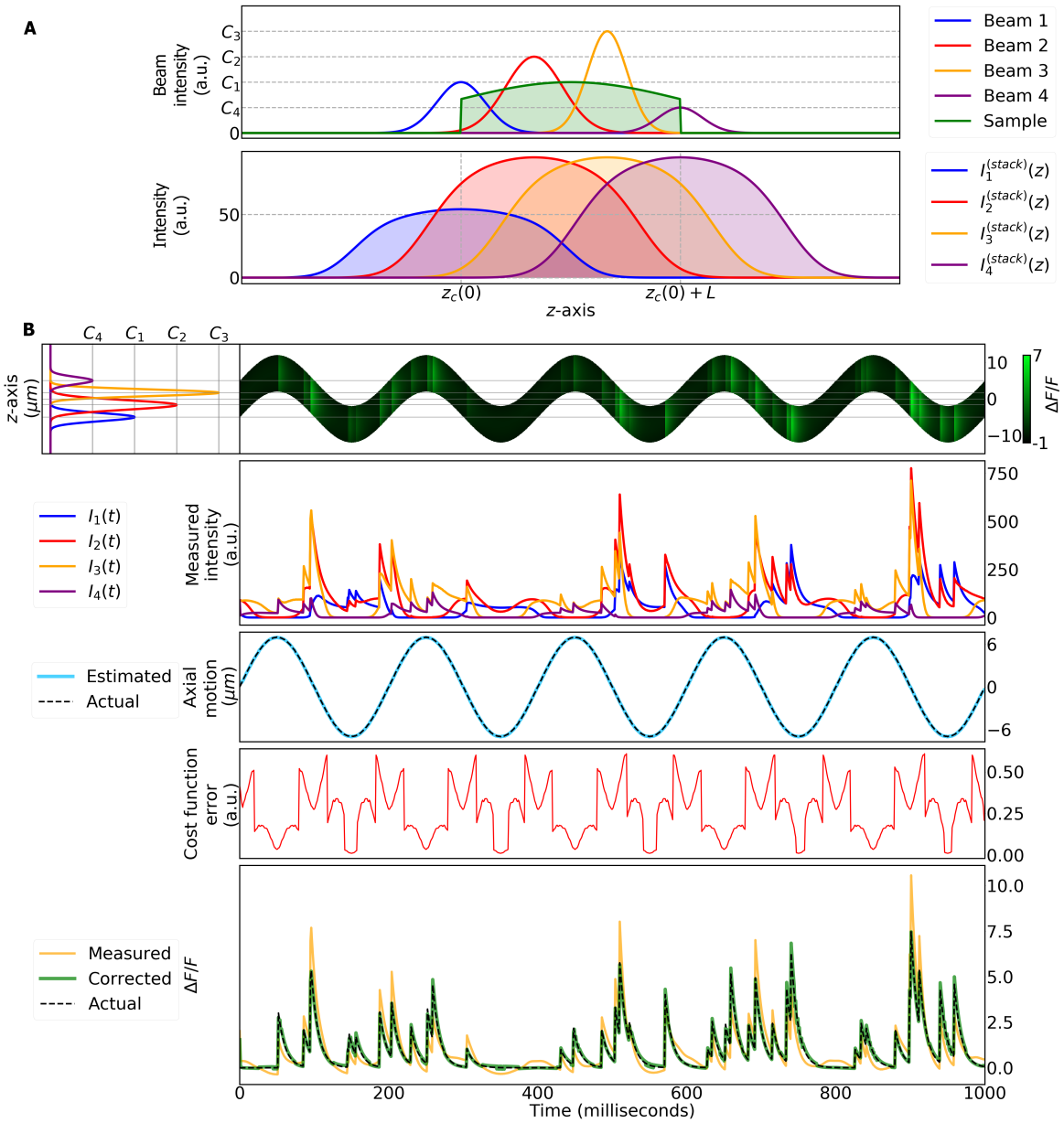
Supplementary Figure S4.2.1: Example of two different ROI functions. A ROI function defined by Eq. 4.16, where the activity A modulates heterogeneously the function along the z-axis. Such modulation can not be corrected with the developed algorithm. **B** ROI function defined by Eq. 4.20, where the activity A homogeneously modifies the ROI function along the z-axis. An underlying assumption of the algorithm is that activity is modulated in such a homogeneous fashion from baseline.



Supplementary Figure S4.2.2: Distributions of fluorescence changes for ROI 1 in the experiment shown in Fig. 4.2.4. **A** Distribution of the measured $\Delta F/F$ for ROI 1. This distribution is affected by axial motion. The distribution of the measured $\Delta F/F$ for ROI 1 is not Gaussian due to the axial motion **B** Gaussian distribution of the corrected $\Delta F/F$ for ROI 1. Since the fluorescence baseline is calculated from the average of 10% lowest values, the mean of the distribution of corrected $\Delta F/F$ is not centered around 0, as one would expect for GFP (no fluorescence changes).



Supplementary Figure S4.2.3: Simulation of a single moving voxel stacks which have a flat axial profile. **A** Top row, defined flat and elongated ROI densities at time $t = 0$ as well as the profiles of the beams along the z-axis. Bottom row, stack of the sample at time $t = 0$ obtained for each beam. **B** First row, left side: profile of the two beams along the z-axis. Right side: activity and axial motion of the ROI over time. Second row: intensity measured with each beam over time. Third row: estimated and actual axial motion of the ROI over time. Fourth row: cost function error evaluated at the estimated axial position. Bottom row: measured, corrected and actual activity of the ROI over time.



Supplementary Figure S4.2.4: Simulation of a single moving voxel for a configuration with four temporally mulitplexed beams. **A** Top row, ROI density at time $t = 0$ as well as the profiles of the four beams along the z-axis. Bottom row, stack of the sample at time $t = 0$ obtained for each beam. **B** First row, left side: profile of the four beams along the z-axis. Right side: activity and axial motion of the ROI over time. Second row: intensity measured with each beam over time. Third row: estimated and actual axial motion of the ROI over time. Fourth row: cost function error evaluated at the estimated axial position. Bottom row: measured, corrected and actual activity of the ROI over time.

Chapter 5

Calcium dynamics of sleep homeostasis in *Drosophila* during walking and feeding behavior

Different populations of neurons and glia are important for sleep in *Drosophila*. Due to the technical challenges with recording the brain during sleep in behaving flies, these cells were typically not monitored during behavior. However, in particular for sleep homeostasis, it is important to record neural dynamics during behavior since most of the naturally occurring sleep bouts in flies have a duration of tens of minutes. Changes at the timescale of minutes are difficult to describe with methods that separate behavior and recordings in the brain. In such experiments, flies are sleep deprived for several hours after which flies need to be prepared for experiments before recordings can start.

In the central complex, a circuit that regulates sleep homeostasis has been reported, reviewed in section 1.6.1, shown in Fig. 1.10D, and modeled in Chapter 2. The dynamics of these neurons have however been inferred from *ex vivo* physiology experiments and electrophysiology over short timescales [123, 125, 186].

Using the developed methods for long-term imaging and brain motion correction (Chapter 3 and section 4.2, respectively), this chapter investigates the calcium dynamics of multiple cellular populations involved in sleep. By probing the arousal threshold of flies in the imaging setup, which increases as flies spend more time immobile, we confirm that sleep can be observed during imaging. The developed approach is therefore suitable for investigating the dynamics of sleep circuits. Monitoring calcium activity from ensheathing glia (Fig. 1.8C) in the central complex reveals the dynamics of a sleep homeostat, with calcium increasing during wakefulness, saturating during sleep deprivation, and decreasing during sleep, as expected based on conceptual models such as the two-process model (see section 1.5).

The observed ensheathing glia dynamics are however not a simple reflection of the ac-

tivity of sleep-related central complex neurons in the same brain compartments. On the contrary, dFB and R5 neurons (see section 1.6.1) do not show a simple correlation with sleep or wakefulness, as would have been predicted based on previous work [123, 125, 186]. Interestingly, the dynamics of dFB neurons are in particular modulated by feeding and walking activity.

This chapter thus reveals a new component of sleep regulation in *Drosophila*. The dynamics of a sleep homeostat that integrates time spent awake and resets during sleep is characterized for the first in behaving animals. Interestingly, sleep homeostasis is distributed over multiple different neuropils or brain compartments, thus offering an architecture for how sleep need could be integrated across different brain areas.

This chapter contains preliminary experiments and results.
It is additionally based on the following bioRxiv publication:

[31] **Flores-Valle, A. and Seelig, J.D.**
Dynamics of a sleep homeostat observed in glia during behavior.
bioRxiv (2022): 2022-07.

Author	**Contribution in [31]**	**Contribution in this chapter**
Flores-Valle, A.	- Conceptualization - Methodology - Experiments - Analysis - Visualization - Writing	- Conceptualization - Methodology - Experiments - Analysis - Visualization - Writing
Seelig, J.D.	- Conceptualization - Methodology - Experiments - Supervision - Writing	- Conceptualization - Methodology - Experiments - Supervision - Writing

5.1 abstract

An animal's need to sleep grows with time spent awake and decays again during sleep. In the brain, a homeostatic process or signal has been proposed to represent sleep need, steadily increasing during wakefulness and gradually decreasing during sleep [267, 269]. However, such dynamics of a sleep homeostat, capturing the changing need to sleep in real time depending on behavior, has so far not been observed in identified cells [277, 515, 516, 517].

Here, using a system that we developed for monitoring calcium activity over multiple days in head-fixed, walking fruit flies [28, 30], we find that a class of glia in the fly brain, called ensheathing glia [224, 226, 237], shows dynamics expected of a sleep homeostat for the short sleep bouts observed in the fly. Calcium levels in these cells – monitored in a central brain area important for memory, navigation and sleep – integrate different kinds of behavioral effort during wakefulness, reset during rest and sleep, and saturate under sleep deprivation. We further show that ensheathing glia dynamics are not a simple reflection of other sleep-related populations of neurons in the central complex, which do not track sleep-wake behavior in a similarly reliable way. Instead, we find that activity in such neurons depends on the feeding state of the fly.

The dynamics of the sleep homeostat, observed in glia of different brain compartments agree with conceptual model expectations [267, 269, 406, 518]. Ensheathing glia therefore act as a system for tracking sleep need distributed across brain areas.

5.2 Introduction

Sleep is important for a number of processes in the brain, many of which are related to plastic changes, such as learning and memory or clearing of waste products [7, 20, 277, 519]. *Vice versa*, the experience during wakefulness, in particular the duration of time spent awake, but also for example learning or injury, impact subsequent sleep across species [7, 277].

How neural circuits in the brain integrate the time spent awake as well as specific behaviors for homeostatic sleep regulation is however little understood [277, 515, 516, 517]. Recent experiments in mice that take advantage of calcium imaging during behavior point to the importance of glia for sleep homeostasis [229, 235, 236, 520, 521, 522, 523].

In *Drosophila*, a circuit for sleep regulation has been investigated in the ellipsoid body (EB) and fan-shaped body (FB) of the central complex [20, 21, 27, 123, 125, 186], an area in the center of the fly brain important for memory and navigation [306]. Sleep depriving flies for several hours led to an increase of activity in calcium or electrophysiology recordings in neurons and astroglia recorded in brain explants [123, 129, 186].

While glia constitute about 10 percent of the cells in the fly brain and they are important for sleep regulation [22, 261], little is known about their dynamics. About a third of the glia in the fly brain are ensheathing glia [224]. Removal of the excitatory amino acid transporter 2 (Eaat2) from ensheathing glia increases sleep [226, 252], thus indicating a role of these cells in sleep regulation.

In flies, sleep processes occur at the timescale of minutes [190, 194] and many short bouts of sleep are distributed throughout the day and night with a mean duration of around 20 minutes [105, 106, 195]. A frequently used definition of sleep assumes at least 5 minutes of immobility [19, 119], and already shorter periods of rest lead to reduced responsiveness to sensori stimulation [190, 195]. Whether the sleep homeostatic signal that are measured after many hours of sleep deprivation [123, 186] allow keeping track of such much shorter intervals critical for wake and sleep [105, 106, 195] is not known.

This motivates experiments in behaving animals where neural activity and behavior are recorded at the same time and which therefore do not have to rely on extended periods of sleep deprivation. For this purpose, we developed methods for two-photon [355] calcium imaging in head-fixed walking flies [28], including an approach for correction of axial brain motion during volumetric multiplane imaging [30], that allow combined neural and behavior recordings over multiple days while the fly is maintained in a virtual reality setup.

Here, using the developed methods we monitor the activity of a subset of neurons and glia that are important for sleep over several days. We find that ensheathing glia activity can be well described with exponential dynamics, consistent with a sleep homeostat as proposed in conceptual models [269]. In particular, we show that ensheathing glia monitor sleep and wakefulness more reliably than sleep related neurons in the central complex. We additionally find that activity of sleep-related neurons in the fan-shaped body can be explained by taking

into account feeding behavior, emphasizing the importance of monitoring neural circuits in central brain areas in behaving flies [306].

5.3 Results

5.3.1 Expected time constants of sleep homeostasis

A sleep homeostat needs to keep track of time spent awake and sleeping, which can be achieved by continuously integrating time [267, 406, 518]. The time constants of such a homeostat are therefore expected to lie in the range of the naturally occurring sleep bouts.

Walking flies show a distribution of bouts of rest or sleep of different lengths during the day and night [18, 19, 105, 106]. The resulting sleep bout duration depends on the sensitivity of movement detection, but lies around 20 minutes [105, 106]. To confirm that the sleep bout duration is robust against the sensitivity with which shorter bouts of movement are detected, we quantified the distribution of sleep in flies walking in a rectangular chamber by tracking their position and velocity with a camera (Fig. 5.1a and b, Supplementary Fig. S5.1a and b, see Methods). We removed short periods of movement between consecutive bouts of immobility (Fig. 5.1c) and computed the distribution of sleep bouts for all flies. Even when filtering out movement periods of 2 minutes, 90% of sleep bouts were shorter than 50 minutes during the day and night (Fig. 5.1 d), with even shorter sleep bouts in constant darkness (Supplementary Fig. S5.1c), setting a range for the expected dynamics of a sleep homeostat in the tens of minutes.

5.3.2 Glia activity varies across the day

To monitor the dynamics of ensheathing glia during sleep and wakefulness, we expressed the calcium indicator jGCaMP8m [344] using the GAL4 line R56F03 [16, 224] and imaged in the EB and FB (Fig. 5.1e and f) as well as the lateral accessory lobe (LAL, Supplementary Fig. S5.5a), a neuropil associated with the central complex. In these experiments, flies walked on an air supported ball in a virtual reality setup in closed-loop with a single dark stripe on a bright background during the day, and in darkness during the night (12 hours light/dark cycle, Fig. 5.1g) [28].

Freely walking flies approached the food at different intervals and for different durations (Fig. 5.1h, see Methods). To replicate similar conditions for tethered walking flies, we fed the fly every 26 minutes for 2 minutes. Feeding during long-term imaging was performed without interrupting the experiments using an automated feeder (Fig. 5.1g) [28]. In these imaging experiments we observed slow transients of calcium that varied across multiple days in both the EB and FB (Fig. 5.1i and Supplementary Fig. S5.2). Approaching the feeder to the fly led to spikes of activity (Fig. 5.1i) in calcium and walking traces, but on

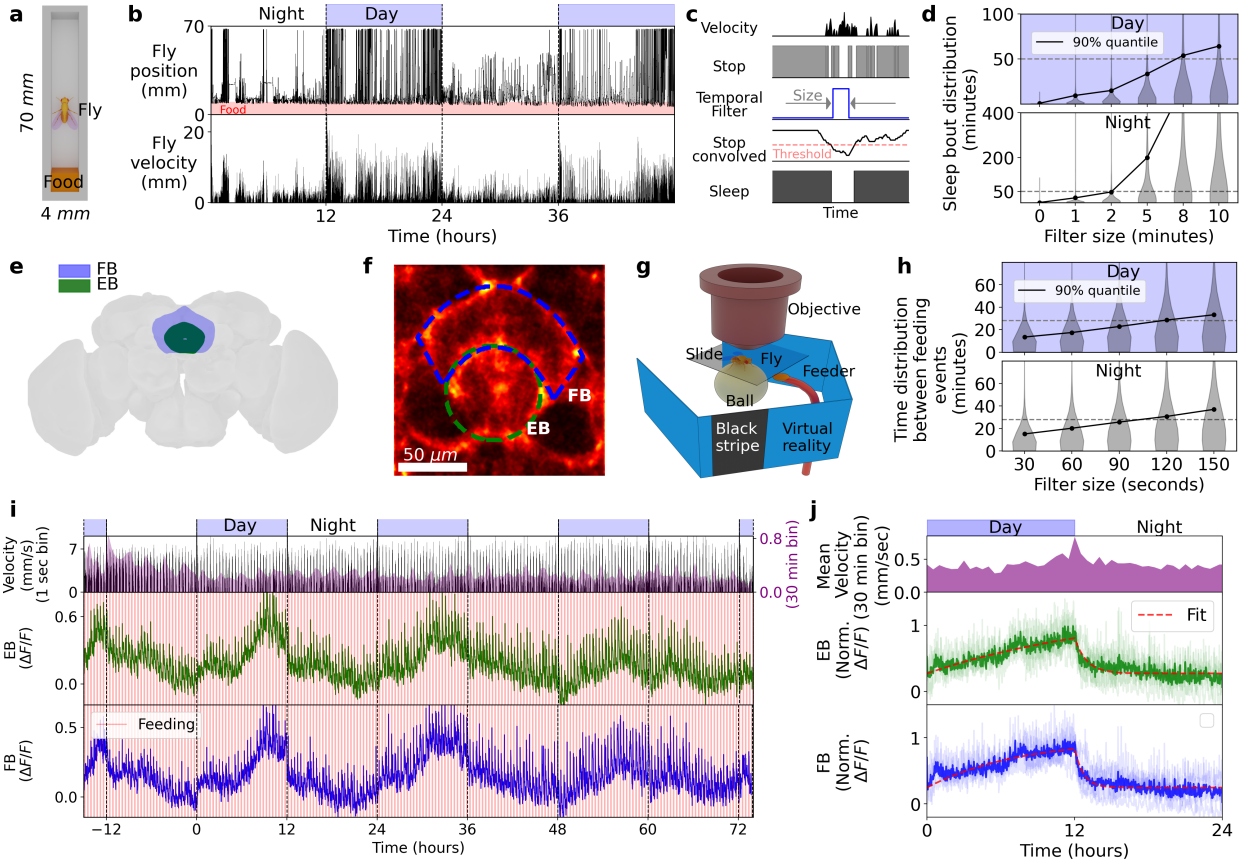


Figure 5.1: Sleep and feeding behavior in freely moving flies and long-term calcium imaging in ensheathing glia. **a** The position of flies walking in a rectangular chamber with food is tracked from the top with a camera. **b** Position along the rectangular chamber and velocity over two days for a single fly. **c** Velocity (first row) is thresholded to find bouts of immobility ('stop', second row). A temporal filter (third row) is convolved with the stop state of the fly (fourth row) and a threshold is used to characterize sleep (fifth row). **d** Distribution of sleep bouts for a total of 15 flies during the day and night as a function of filter size. **e** EB and FB in the *Drosophila* brain. **f** Ensheathing glia express jGCaMP8m and regions of interest (ROIs) for analyzing fluorescence in EB (green) and FB (blue). **g** Setup for long-term imaging: a fly is glued to a cover slide and navigates on an air supported ball in VR under the microscope objective. **h** Distribution of time between feeding events in freely moving flies as a function of filter size (see Methods). **i** Long-term calcium imaging in a fly walking in VR over 89 hours. Top row: day and night cycle in VR. Second row from top: absolute ball velocity in 1 second bins. Third and fourth rows: calcium activity (100 hours high-pass-filtered, see Methods) in EB and FB. Red lines indicate time of feeding (every 26 minutes). **j** Average of 5 flies over 24 hours (see Methods). Top row shows day and night cycle. Mean velocity binned over 30 minutes is shown in the second row. The third and fourth rows show average calcium activity in the EB and FB.

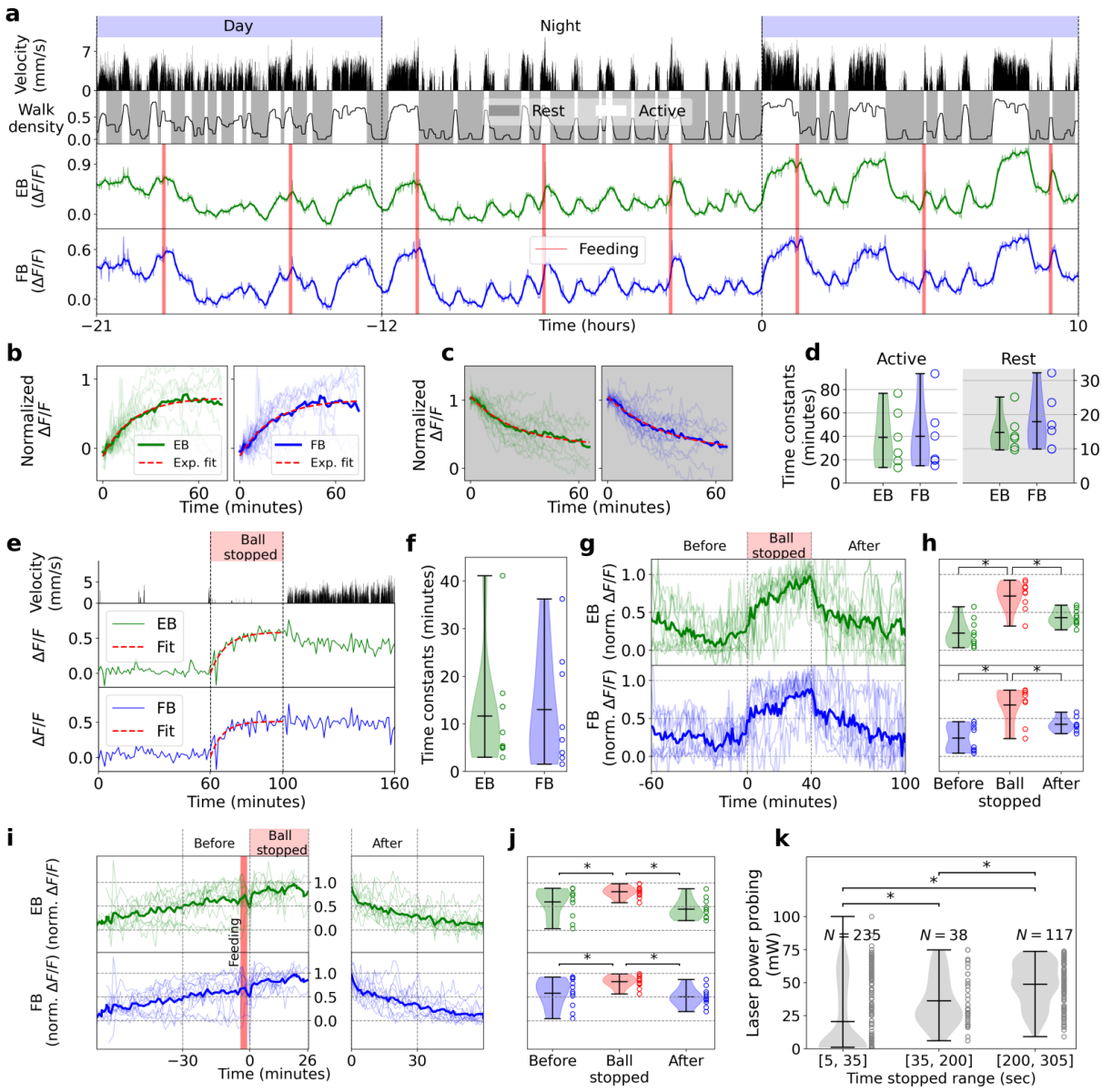


Figure 5.2

average, calcium activity slowly increased across the day, and reset during the first part of the night (Fig. 5.1j). We also observed similar dynamics when flies were fed every 16 minutes (Supplementary Fig. S5.3). These calcium oscillations could result from slow accumulation of calcium due to the fly being more active during the day than during the night, consistent with homeostatic activity. Alternatively, such calcium oscillations could also be due to circadian modulation independent of behavior [22].

Figure 5.2: Calcium dynamics in ensheathing glia increases due to effortful behavior and decreases during rest. **a** Long-term recording of a single fly over 31 hours. Top row: day and night cycle in VR. Second row from top: absolute ball velocity. Third row: walk density obtained by low-pass filtering (cut-off period of 6 minutes) of 'walk' (walk: 1 if the fly has non-zero velocity in 1 second bins, 0 otherwise). Active and rest states were defined when the walk density was above or below a threshold (see Methods). Fourth and fifth row: calcium activity (24 hours high-pass-filtered, see Methods) in EB and FB ensheathing glia over time, respectively. Red lines indicate time of feeding. **b** Single traces of increasing normalized calcium activity (see Methods) during active states (thin lines), average (thick line), and exponential fit (red) for EB and FB. **c** Same as b but during rest state, fitted with exponentials (red). **d** Time constants for exponential fitting during active (white region) and rest states (grey region) for EB and FB. Violin plots represent distribution of time constants for 6 flies (circles), short horizontal black lines show maximum, mean, and minimum values in descending order. Time constants were not significantly different between EB and FB using t-test ($p > 0.05$). **e** Calcium activity during effort with blocked treadmill ball. Second row: velocity of fly over time (zero while stopping the ball). Third and fourth row: ensheathing glia activity and exponential fit (red) in EB and FB, respectively. **f** Time constants of exponential fits while ball was stopped for $N = 10$ trials in 5 flies. **g** Normalized fluorescence traces of activity in EB and FB before, during, and after ball was stopped (top row). Second and third row: single trials (thin lines) and average (thick lines) in EB and FB, respectively. **h** Normalized fluorescence levels (y-axis shared with panel g) before, during, and after ball stopping (60, 40, and 60 minutes average), respectively. Statistical significance was assessed using t-test. **i** Calcium activity during effortful behavior after feeding. Normalized fluorescence traces of glia activity in EB and FB before feeding, after feeding while the ball was stopped, and after releasing the ball (for $N = 11$ trials in 5 flies). Normalized fluorescence levels (y-axis shared with panel j) before feeding, after feeding while stopping the ball, and after releasing the ball (30, 26, and 30 minutes average); asterisks represent statistical significance for p-values less than 0.05 using t-test. **k** Laser power required to wake up the fly based on the previous durations of immobility. Durations of immobility are arranged in three different time ranges; the number of probing trials is indicated at the top (for a total of 6 flies). Statistical significance was assessed with Kolmogorov–Smirnov test. Asterisks in all the panels indicate p-values less than 0.05.

5.3.3 Glia activity monitors active and rest states

To distinguish these two possibilities, a second feeding protocol where the fly was fed only every four hours was used, which often led to epochs of continuous walking activity (often before feeding) or rest (often after feeding). Under these conditions, ensheathing glia in EB, FB, and LAL showed pronounced calcium fluctuations (Fig. 5.2a, Supplementary Figs. S5.4a-e and S5.5b). To determine whether the overall trend of these fluctuations was consistent with the dynamics of a sleep homeostat, we subdivided the fly's behavior coarsely into active and rest epochs (a higher-resolution analysis is performed in the next sections). We first distinguished only two behavioral states based on the fly's walking activity: 'walk' (fly is walking) and 'stop' (fly is standing still as assessed based on ball velocity, second row in Fig. 5.2a and Methods). We then selected epochs of at least 10 minutes during which the fly was walking most of the time (active, third row in Fig. 5.2a) or immobile most of the time (rest, third row in Fig. 5.2a) by thresholding the 'walk density', obtained by low-pass filtering of 'walk' (see Methods).

Fluorescence traces were averaged over the selected active and rest epochs (Figs. 5.2b and c, and Supplementary Fig. S5.6). The averaged fluorescence could be well fitted with exponentials (see Methods), a common model for homeostatic activity [273, 524] (red line in Figs. 5.2b and c, and Supplementary Fig. S5.6). The resulting rise and decay rates of the exponentials, defined by their time constants, are shown in Fig. 5.2d for 6 flies for EB and FB, respectively. Thus, consistent with the behavior of a sleep homeostat, activity levels changed exponentially on the minutes timescale during epochs where the animals were predominantly active or resting, respectively. Dynamics in the LAL were similar to those observed in EB and FB (Supplementary Fig. S5.5b).

5.3.4 Glia monitor behavioral effort

Sleep behavior was often correlated with feeding (red lines in Fig. 5.2a and Supplementary Fig. S5.4a-e), with flies increasingly walking more with time elapsed since feeding and sleeping more after feeding (as observed in freely walking flies [21, 94]). We therefore first asked, whether the increase in fluorescence levels in ensheathing glia was specifically due to walking, or whether other effortful behaviors could also cause similar activity changes. To address this question, we immobilized the ball for epochs of 40 minutes while the fly was in the VR setup, and recorded behavior and glia activity in the EB and FB (Fig. 5.2e and Supplementary Fig. S5.7). Movement of the ball was blocked by pushing it against the ball holder with the tip of a brush, positioned close to the fly with a motorized remote controlled micromanipulator. This induced the fly to continually push or pull the ball; if the fly stopped moving, the brush was slightly repositioned and due to the induced perturbation the fly resumed active behavior.

As seen in the resulting fluorescence traces and averages in Fig. 5.2g, this led to a steady increase in or saturation of calcium levels similar to the dynamics observed due to walking activity (Fig. 5.2b) with slightly faster time constants (Figs. 5.2f). This shows that glia calcium activity increases (Fig. 5.2h) not only due to coordinated walking but also due to other effortful behaviors.

We next asked, whether feeding was responsible for the decay of calcium activity, or whether this was due to the fly often resting after feeding. We sleep deprived the fly immediately after feeding by stopping the ball as above (Fig. 5.2i and Supplementary Fig. S5.8). This not only suppressed resetting, but slightly increased calcium signals after feeding (5.2j). This indicates that immobility and resting, and not feeding, was responsible for the decay of calcium levels.

5.3.5 Flies sleep during imaging

To determine whether epochs of immobility on the ball correspond to sleep, we tested whether the arousal threshold, the required stimulus strength to induce a behavioral response in the resting fly, increased with the duration of immobility, as expected for sleep [190]. We tested the arousal threshold during long-term imaging with an infrared laser beam pointed at the fly's abdomen. At the start of each trial for probing the threshold, we ensured that the fly was first awake by closing and opening the air stream to the air supported ball every second for 3 seconds (see Methods), which stimulated the fly to walk. Then, using an automated control loop for monitoring ball velocity, we detected bouts of immobility. After either 30 seconds or 5 minutes of immobility, the power of the heating laser was gradually ramped up until the fly started walking (see Methods). To ensure that flies were completely still during the detected epochs of immobility, we classified behavior recorded with a camera using deep learning in post-processing (see Methods and Supplementary Fig. S5.20). Removing those sections where the fly was grooming resulted in the final bouts of immobility between 5 seconds and 5 minutes. A single trial of arousal threshold probing is shown in Supplementary Fig. S5.9a. Fig. 5.2k shows that longer periods of immobility required higher laser powers for a behaivoral response, therefore indicating that the arousal threshold increases over the duration of immobility consistent with sleep observed in freely moving flies [18, 19, 190] (see Supplementary Fig. S5.9b-g for individual flies).

5.3.6 Sleep deprivation saturates glia activity

A signature of a sleep homeostat is that it saturates and plateaus under sleep deprivation [267, 269]. Sleep deprivation for extended periods of time leads to rebound sleep in flies [18, 19, 21]. The amount of rebound sleep however depends on the method of sleep deprivation. Sleep deprivation which avoided strong mechanical perturbation, resulted in less than one

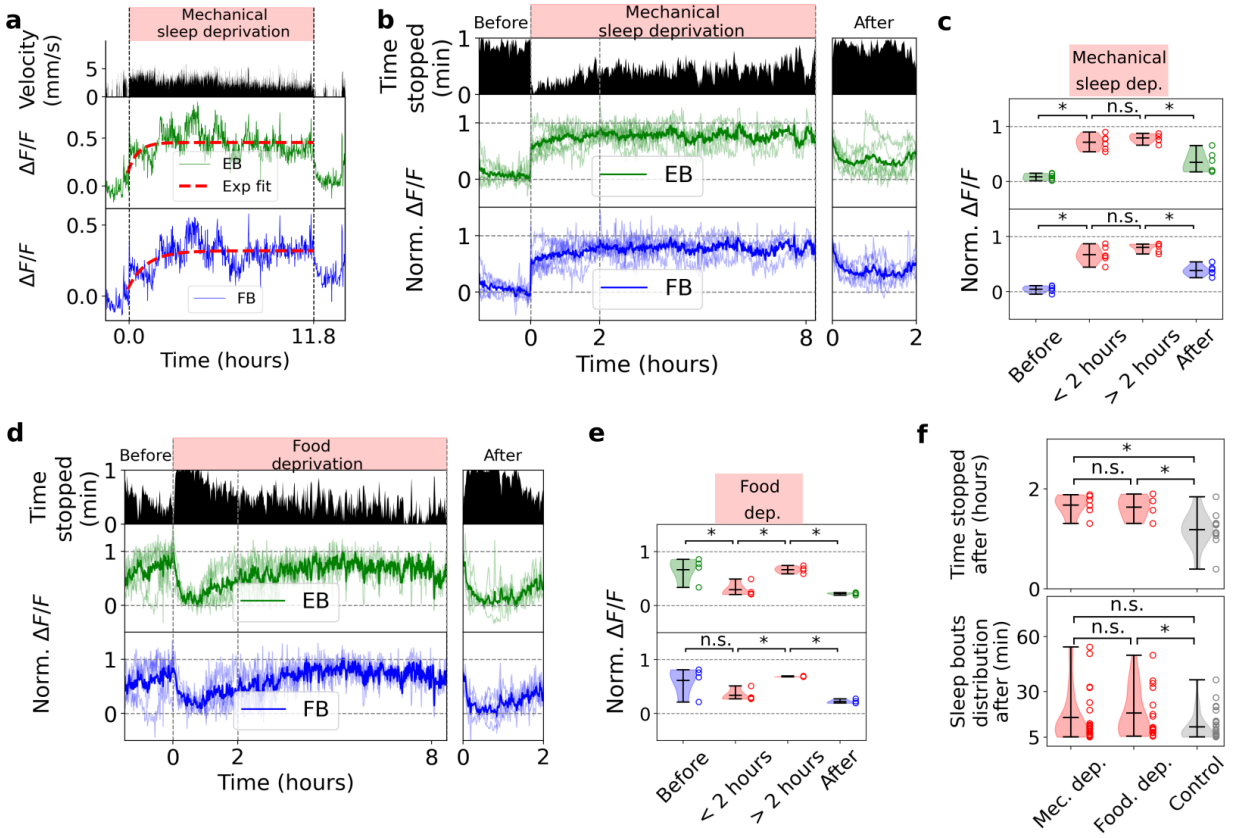


Figure 5.3

hour of mean rebound sleep after 12 hours of sleep deprivation [134].

To sleep deprive flies during long-term imaging, we periodically opened and closed the air stream supporting the ball with a valve at 1 second intervals for 6 seconds every 20 seconds, similar to sleep deprivation in freely walking flies [123, 134, 186], which induced short bouts of fast walking when the ball was free to rotate. Calcium activity saturated and plateaued in EB, FB (Fig. 5.3a and b, and Supplementary Fig. S5.10a) and LAL (Supplementary Fig. S5.5c). Calcium activity saturated before 2 hours and remained high (Fig. 5.3c), with occasional fluctuations around the saturation level (indicated by an exponential fit, red line in Fig. 5.3a).

For comparison, we also used food deprivation to sleep deprive flies. Absence of food and starvation induce hyperactivity or foraging behavior and prevent sleep [21, 525, 526, 527] and in some flies resulted in long epochs of continued fast walking. Single trials and average activity of 4 flies that were continuously walking for at least 3 hours following food deprivation with fluorescence traces normalized for comparison, are shown in Fig. 5.3d (see Supplementary Fig. S5.10b for individual trials). Starvation-induced walking produced a slow increase of glia calcium activity (Fig. 5.3d), and, similar to mechanical sleep deprivation, calcium activity saturated after 2 hours (Fig. 5.3e).

Figure 5.3: Glia activity due to sleep deprivation. **a** Behavior and calcium activity in EB and FB ensheathing glia under mechanically induced sleep deprivation. Top row: time interval where sleep deprivation was applied. Second row: fly velocity. Third and fourth row: activity of glia with exponential fit for visualization of plateau level (red) during mechanical sleep deprivation for EB and FB, respectively. **b** Mechanical sleep deprivation for $N = 6$ trials in 5 flies (including fly in a). Top row as in a. Second row: average time stopped over time, calculated in bins of 1 minute. Third and fourth row: normalized fluorescence traces of ensheathing glia activity in each fly (thin lines) and average (thick line, at least 2 flies) in EB (green) and FB (blue), respectively, shown during up to 8 hours of mechanical sleep deprivation. Times of mechanical sleep deprivation varied between flies (see Supplementary Fig. S5.10a. **c** Average fluorescence distributions before (over 1.5 hours), during the first 2 hours of sleep deprivation, between 2 and 8 hours of sleep deprivation, and after (2 hours). **d** Same as b but during food deprivation for $N = 4$ trials in different flies. Top row shows the time interval (in red) between two consecutive feeding events. Times of food deprivation varied between flies (see Supplementary Fig. S5.10b). **e** Same as c but for food deprivation. **f** Top row: time being stopped over 2 hours for each trial after mechanical sleep deprivation, food deprivation, and for control trials ($N = 10$ in 6 flies). Bottom row: distribution of sleep bouts (longer than 5 minutes) over the 2 hours after mechanical sleep deprivation, starvation induced sleep deprivation, and in control flies. Asterisks in all panels indicate statistical significance (p ¡ 0.05) using t-test (panels c,e and the top row of f) and Kolmogorov–Smirnov test in the bottom row of f.

After the offset of mechanically or food induced sleep deprivation, flies became less active (right side of Fig. 5.3b and d), and glia activity returned to lower levels. Flies displayed rebound sleep and showed an average of 1.68 and 1.64 hours of immobility in the two hours after the offset of mechanical and starvation induced sleep deprivation, respectively, compared to 1.19 hours in control flies (top row in Fig. 5.3f, see Methods). The difference between sleep-deprived and control flies (around 30 minutes more in sleep-deprived flies on average) is consistent with the time that it takes to reset glia activity to baseline levels (Fig. 5.2d). Additionally, for mechanical sleep deprivation more sleep bouts with duration over 5 minutes were observed (5.3f).

5.3.7 Glutamate changes faster than calcium

Ensheathing glia are important for glutamatergic signaling [226] and glutamatergic neurons show activity correlated with walking [528]. We therefore tested whether the slow calcium dynamics observed in glia corresponded to the accumulation of extracellular glutamate. The glutamate sensor iGluSnFR was expressed in ensheathing glia and we performed long-term imaging experiments as before [529, 530].

Glutamate activity was correlated with walking (Fig. 5.4a and Supplementary Fig.

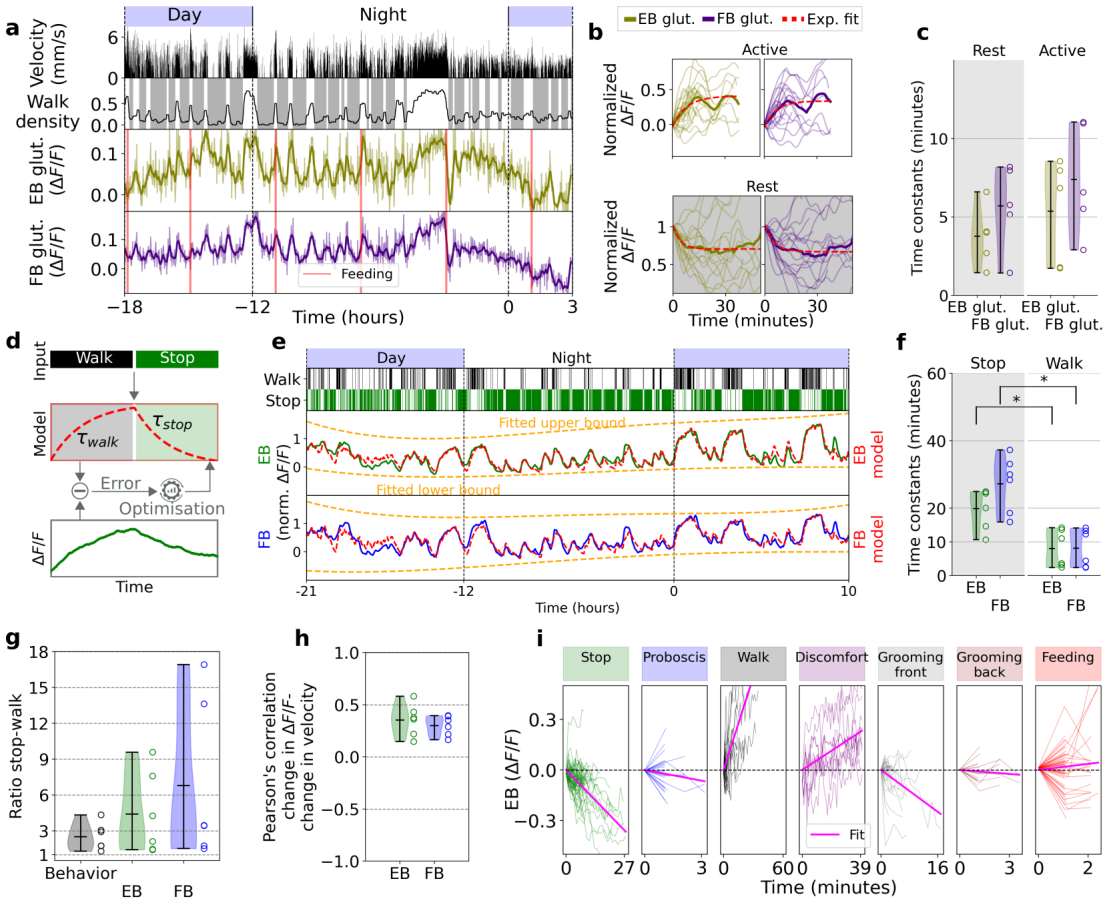


Figure 5.4

S5.11). We again defined active and rest epochs based on the velocity of the fly and fitted exponential curves for EB and FB fluorescence traces (Fig. 5.4b and Supplementary Fig. S5.12). Extracellular glutamate increased during active epochs and decreased during rest (Fig. 5.4b). However, time constants were faster than those obtained for calcium (compare Fig. 5.4c and Fig. 5.2d), indicating that calcium does not simply reflect extracellular glutamate concentration.

5.3.8 Homeostat model describes glia activity

Homeostatic activity can be modeled as exponentially decaying during sleep and exponentially approaching a saturation level during wake [267, 273, 524]. We therefore quantified whether calcium from ensheathing glia integrates behavioral history, that is, wake and sleep, according to such homeostatic dynamics across timescales. For this purpose, we fitted a differential equation with two time constants for charging and resetting of the homeostat, respectively, to ensheathing glia calcium activity dependent on behavioral state (see Methods). As illustrated in Fig. 5.4d, the behavioral states, here 'walk' and 'stop', are passed to

Figure 5.4: Glia glutamate dynamics and two-state model for calcium dynamics. **a** Glutamate long-term imaging in EB and FB. Similar to 5.2a for glutamate. Top row: day and night cycle in VR. Second row: fly velocity. Third row: walk density with rest (grey region) and active (white region). Fourth and fifth row: extracellular glutamate activity in EB and FB, respectively. Thick lines indicate band-pass filtered signal (0.1 hours). **b** Single traces of increasing normalized glutamate activity (see Methods) during active state (thin lines), with average (thick line) and exponential fit (red) for EB and FB. **c** Time constants for exponential fit during active (white region) and rest (grey region) for extracellular glutamate in EB and FB in $N = 5$ flies. **d** Schematic of model fitting approach for calcium imaging: behavior (walk, stop) is integrated as model input with corresponding time constants and fitted to glia calcium activity using optimization. **e** Band-pass filtered (0.5 to 12 hours) calcium activity in EB and FB over time. Top row: 'walk' state (velocity larger than zero in 1 second bins). Second and third row: activity in EB and FB. Red line: fitted homeostat model (two-state model); orange lines: fitted corrections for fluorescence levels (see Methods). **f** Distributions of time constants for 'stop' and 'walk' states from model fitting for $N = 6$ flies in EB (green) and FB (blue). Asterisks represent statistical significance with p-values lower than 0.05 using t-test. **g** Ratios of time in 'stop' and 'walk' states (black) and ratio of time constants between 'stop' and 'walk' state in EB (green) and FB (blue) for each fly ($N = 6$). Ratios were not significantly different, p-values were above 0.05 using t-test. **h** Correlation coefficients as in e for $N = 6$ flies. All flies had p-values lower than 0.05 (see Supplementary Fig. S5.19 and Table S5.5). **i** Fluorescence traces from EB and linear fit (pink line) over time intervals of seven behaviors which were classified using deep learning (see Supplementary Fig. S5.20 and Methods).

the model which represents homeostat activity and differentially increases or decreases with time constants characterizing the exponential dynamics. The time constants of the model are fitted to ensheathing glia activity using an optimization approach (see Methods). After fitting, the homeostat model [406, 518] describes ensheathing glia activity over the time course of the experiments based on behavior (31 hours in Fig. 5.4e, see also Supplementary Fig. S5.13).

The resulting rise and decay time constants for 6 flies in EB and FB, respectively, are shown in Fig. 5.4f (see also Supplementary Fig. S5.13). Time constants in Fig.5.2d were more similar between rise and decay than those obtained by model fitting (Fig. 5.4f). This is due to the fact that active and rest states in Fig.5.2b and c were determined using low-pass filtering of the animal's walking activity (Fig.5.2a), thus resulting in rest states that still contained a fraction of walking activity, and *vice versa* for active states.

Models with two different rest states, distinguishing between epochs with less and more than 5 minutes of immobility (defining sleep [119]), were implemented as well, but the time constants for resetting the homeostat between these two rest states were not significantly different, even when defining a sleep state as starting only 5 minutes after the onset of immobility (see Supplementary Figs. S5.15, S5.16, and Methods). This shows that the homeostat resets similarly in short and long bouts of immobility, consistent with the observation that already short bouts of immobility show features of sleep [190, 195].

Ensheathing glia integrate activity over long timescales (tens of minutes) as indicated by the time constants resulting from model fitting (Fig. 5.2f). Modulations of fluorescence signals were however already observed at the timescale of 1 minute when comparing changes in walking velocity with changes in high-pass filtered calcium signals ($\Delta F/F$, Fig. 5.4h, Supplementary Fig. S5.19, and Methods). Thus, the accumulation of such faster fluctuations could lead to the integrated activity observed over longer timescales.

5.3.9 Homeostat integrates multiple behaviors

Different behaviors contribute differently to sleep need and are therefore expected to charge the sleep homeostat with different time constants [20, 21, 277]. We therefore tested whether a more detailed analysis, distinguishing multiple behaviors, could improve model fitting. Behavior on the ball, which was monitored with a camera throughout the experiments, was classified into the following 7 categories using deep learning with 1 second resolution (similar to [531], Supplementary Fig. S5.20): immobility (stop), proboscis extension, walking, discomfort (where the fly was pushing or pulling the ball), grooming of the front, grooming of the back, and feeding (see Methods).

We used the intervals where flies performed one of the defined behaviors continuously over consecutive imaging epochs to assess whether they contributed to an increase or decrease of calcium activity. As expected, glia activity decreased when flies were stopped, but also

during proboscis extension and grooming. Glia activity increased with walking, feeding (during which flies were often walking), and discomfort (Fig. 5.4i and Supplementary Fig. S5.17a).

We next fitted a model to obtain the time constants for each of the seven behaviors (Supplementary Fig. S5.17b). This model predicts that resetting of the homeostat occurs faster during proboscis extension and back-grooming than during immobility, and also resets during front-grooming, although more slowly than during immobility. Proboscis extension and back-grooming was only observed in short bouts, and rarely over more than two consecutive imaging epochs (Supplementary Fig. S5.18a). Consistent with this observation, proboscis extension has been described to occur during a deep sleep state, and other brief movements have also been observed during sleep [18, 105, 195].

5.3.10 Glia and neuron dynamics

A homeostatic circuit that acts after sleep deprivation for several hours has been described in the central complex [27, 123, 125, 186]. We therefore asked whether these sleep-related neurons in EB and FB would also show homeostatic activity for naturally occurring sleep bouts, that is on shorter timescales and without sleep deprivation.

Ring neurons (R5) have been proposed to encode sleep pressure by increasing calcium activity [123, 186]. We recorded calcium activity of R5 neurons in the EB with two different Gal4 lines, R58H05 and R88F06 (Supplementary Fig. S5.21a and b), different calcium indicators (GCaMP7f, GCaMP8f, and GCaMP8m), as well as different imaging protocols (Fig. 5.5a and Supplementary Figs. S5.22, S5.25, and S5.29, see Methods).

We monitored a second component of the sleep control circuit in the central complex, the dFB neurons labeled by R23E10 (Supplementary Fig. S5.21c), a 'sleep switch' that is frequently used to induce sleep [122, 176, 177]. We used again different calcium indicators (GCaMPf and GCaMP8m), as well as different imaging protocol (Fig. 5.5b and Supplementary Figs. S5.30 and S5.31, see Methods).

To determine whether these neurons could encode sleep homeostasis similar to ensheathing glia, we first again determined active and rest epochs based on behavior (Fig. 5.5c,d and Supplementary Figs. S5.23, S5.27, and S5.32). We then computed the correlation between active (Fig. 5.5e) or rest epochs (Fig. 5.5f) and the normalized calcium activity of neurons and glia (to avoid saturation we limited this analysis to traces of 30 minutes, Fig. 5.5e). For a sleep homeostat, the correlation should be positive during active epochs (increasing activity over time) and negative during resting epochs (decreasing activity over time). This was on average the case for both neurons and glia, with however considerably higher correlation for glia than for R5 neurons (Fig. 5.5e and f, left side). dFB neurons displayed high correlations during active epochs, while the slope of decreasing activity in dFB neurons was close to zero during rest epochs (Supplementary Fig. S5.40, see Methods).

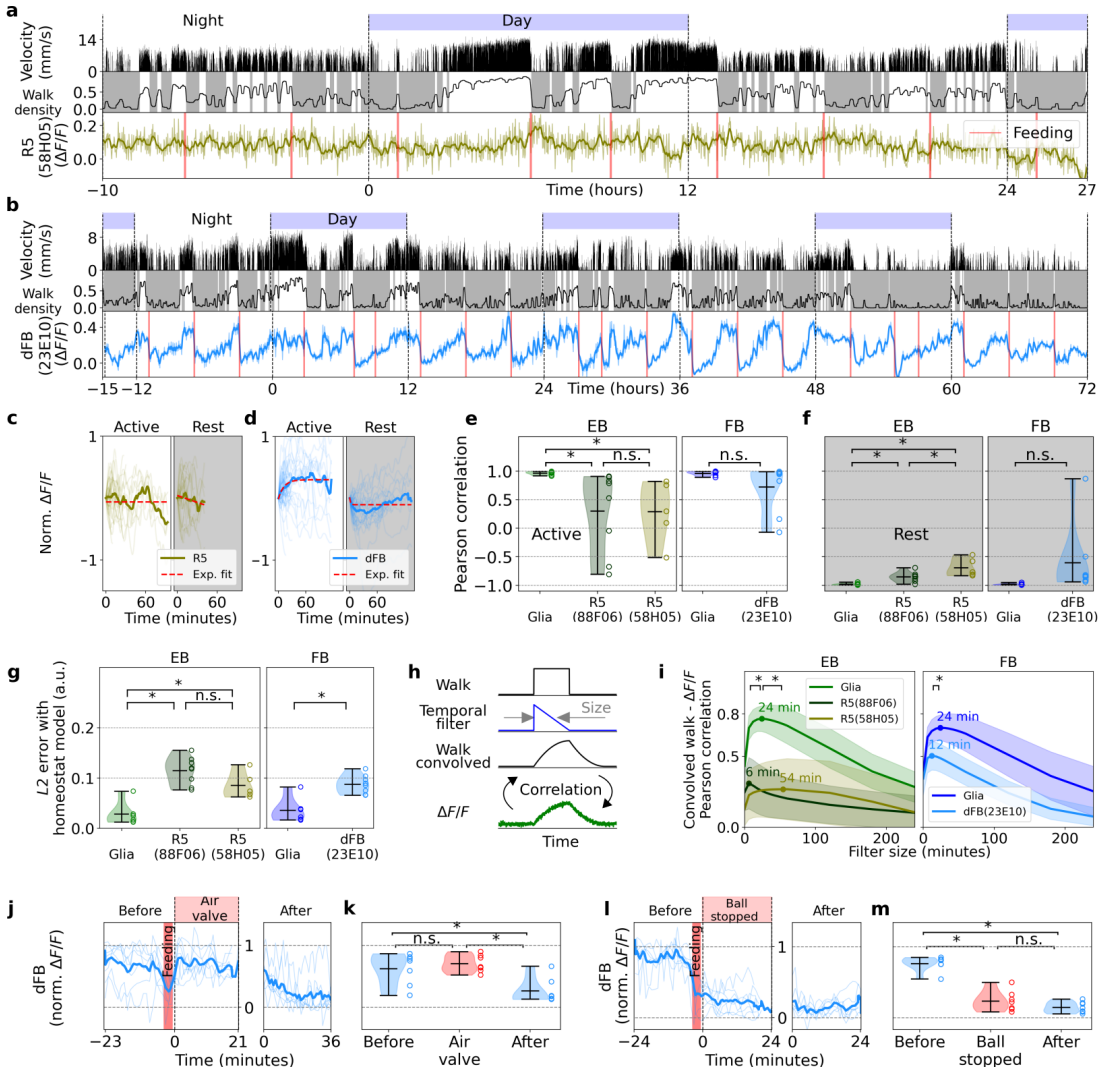


Figure 5.5

We further tested whether the homeostat model which describes calcium activity in glia could fit activity of R5 and dFB neurons (Supplementary Figs. S5.24, S5.28, S5.29, S5.36, and S5.37 and Methods). However, Fig. 5.5g shows that the L2 error between the fitted model and normalized activity was larger for both neural populations than for glia.

Finally, we computed the convolution between walking activity with a triangular-shaped temporal filter, which produces an exponential increase during 'walk' bouts and an exponential decrease during 'stop' bouts at a rate defined by the filter size (Fig. 5.5h, see Methods). We computed the correlation between activity in neurons and glia with the corresponding signal resulting from the convolution of different temporal filter sizes with 'walk' (Fig. 5.5i). Although this method makes the convolved walk signal increase and decrease with the same time constant (defined by the filter size), the correlation with glia activity was nevertheless high and peaked at a filter size of 24 minutes, similar to the dynamics obtained with previ-

Figure 5.5: Calcium dynamics in sleep-related neurons and comparison with ensheathing glia **a** Long-term imaging in R5 neurons (labeled by R58H05). Top row: day and night cycle in the VR. Second row: fly velocity. Third row: 'walk' density, rest (grey region), and active epochs (white region). Fourth row: calcium activity in R5 neurons. Thick line is low-pass filtered (0.1 hours cut off period). **b** Same as a, but imaging in dFB neurons (labeled by R23E10). **c** Normalized individual (thin lines) and average (thick lines) fluorescence traces, as well as exponential fits (red lines, see Methods), during active and rest epochs for R5 neurons shown in a. **d** Same as c, but for dFB neurons shown in b. **e** Left side: Pearson correlation between the time flies are active and the average fluorescence traces for glia (in the EB, $N = 6$), as well as R5 neurons labeled by R88F06 ($N = 8$) and R58H05 ($N = 5$)). Right side: same as left side, but for glia (in the FB, $N = 6$) and dFB neurons ($N = 8$). **f** Pearson correlation between time resting and average fluorescence traces from glia and neurons, as in e. **g** $L2$ error between fitted homeostat model and calcium activity from glia and neurons in EB (left) and FB (right). **h** Approach followed to compute correlation between calcium activity and convolved 'walk'. First, walk is obtained from the behavior of the fly (first row). Then, 'walk' is convolved with a triangular temporal filter with a defined size (second row) to obtain 'convolved walk'. Finally, the correlation between calcium activity and 'convolved walk' is obtained. Pearson correlation between 'convolved walk' and calcium activity for different filter sizes (x-axis) for glia and neurons in EB (left) and FB (right). **j** Calcium activity in dFB neurons during sleep deprivation by perturbing the ball-supporting air stream after feeding. Normalized fluorescence traces of dFB activity (thin lines) and average (thick lines) before feeding, after feeding while the air valve was perturbing the ball, and after offset of the perturbation. **k** Normalized fluorescence levels (y-axis shared with panel j) before feeding, after feeding during sleep deprivation, and after offset of sleep deprivation. Sleep deprivation was performed by periodically interrupting air stream to ball. **l**, **m** Same as j and k, respectively, but with sleep deprivation by blocking the ball to induce effortful behaviors. Asterisks in all panels indicate statistical significance using t-test ($p < 0.05$).

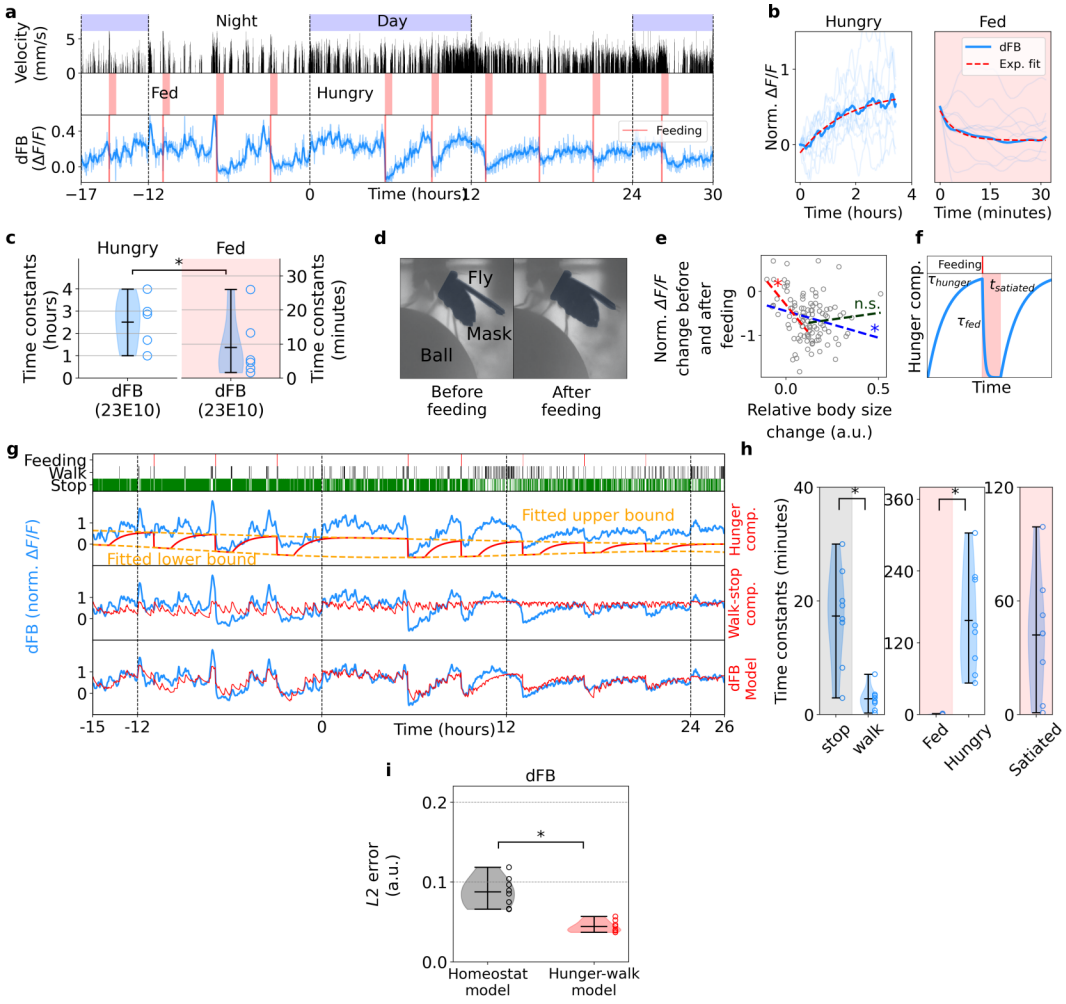


Figure 5.6

ous methods (Figs. 5.2d and 5.4f). The correlation for R5 and dFB neurons was positive but lower compared to glia activity (Fig. 5.5i, see Methods).

Taken together, activity observed in ensheathing glia is not a simple reflection of activity in homeostatic circuits of the central complex. Additionally, as the above analysis shows, ensheathing glia are a better predictor of sleep and wake behavior and sleep homeostasis in the fly than either R5 or dFB neurons.

5.3.11 Hunger state encoded in dFB neurons

While activity in dFB neurons was often correlated with walking activity and rapidly reset during feeding, resetting additionally depended on the behavioral state. If the fly was sleep deprived immediately after feeding by opening and closing the valve that controlled the air stream to the ball (mostly inducing quick bouts of fast walking), fluorescence activity increased again (Fig. 5.5j, k and Supplementary Fig. S5.35). If the fly was sleep deprived

Figure 5.6: Feeding-related modulation in dFB neurons. **a** Long-term imaging in dFB neurons. Top row: day and night cycle in VR. Second row: fly velocity. Third row: 'hungry' epochs before feeding (white region) and 'fed' epochs after feeding (red region). Fourth row: calcium activity in dFB neurons. Thick line indicates low-pass filtering (with 0.1 hours cut-off period). **b** Normalized individual (thin lines) and average (thick lines) fluorescence traces and exponential fits (red lines, see Methods) during hungry and fed epochs from the recording in dFB neurons shown in a. **c** Time constants of fitted exponentials during hungry and fed epochs ($N = 8$ flies). Asterisk indicates statistical significance using t-test (p ¡ 0.05). **d** Side view of a fly during a long-term imaging recording before feeding (hungry, left side) and after feeding (fed, right side). Mask of abdomen (highlighted in dark color) for computing change in size. **e** Normalized fluorescence change against relative change in body size (see Methods) between 10 minutes before and 10 minutes after feeding. The blue line represents a linear fit over all points, while the red and green lines represent a linear fit over the first half and second half of relative body size change, respectively. Asterisks indicate the statistical significance of each fit using Pearson correlation (p ¡ 0.05). **f** Parametrization (three parameters, τ_{hunger}, τ_{fed} and $t_{satiated}$) of the hunger component of the 'hunger-walk' model. Before a feeding event (top row in red) the hunger component increases with the time constant τ_{hunger} and resets after feeding with the time constant τ_{fed} for a given time $t_{satiated}$. **g** Fitting of the hunger-walk model to activity of dFB neurons. Top row: events of feeding as well as walking and stopping bouts of the fly. Second, third and fourth row: normalized fluorescence (blue) and the fitted hunger component, 'walk-stop' component, and the 'hunger-walk' model (obtained from the two previous combined components), respectively (red). **h** Time constants ($N = 8$ flies) of stop and walk (left, from the stop-walk component), and time constants of 'fed', 'hungry', and 'satiated' (center and right, from the hunger component). Asterisks indicate statistical significance using t-test (p ¡ 0.05). $L2$ error between the fitted homeostat and 'hunger-walk' models and the normalized activity of dFB neurons. Asterisk indicates statistical significance using paired t-test.

by blocking the ball (which resulted in the fly pushing and pulling on the ball but not coordinated walking), fluorescence reset (Fig. 5.5l, m, and Supplementary Fig. S5.34) indicating that dFB neurons monitor feeding as well as walking state.

Further, activity of dFB neurons often increased with time since the last feeding, with no strong correlation with walking activity (see for example Fig. 5.5b), suggesting that these neurons could encode a homeostatic drive to eat or hunger. We therefore first analyzed the dynamics of dFB activity with respect to feeding by fitting exponentials (see below for a more detailed model). The average fluorescence traces were divided into two epochs, one where the fly was hungry (defined as 3.5 hours before feeding) and one where the fly was fed (defined as 30 minutes after feeding, see Fig. 5.6a and b, Supplementary Fig. S5.33, and Methods). The time constants during epochs where the fly was hungry were in the order of hours (Fig. 5.6c). The time constants for resetting after feeding were in the range of minutes, but they might not reflect the actual dynamics of dFB neurons after feeding, since resetting depended also on the fly behavioral state (Fig. 5.5j-m).

To describe the dynamics of dFB neurons we thus used a model with a hunger component, which increases and decreases with respect to feeding events (Fig. 5.6f) and a 'walk' component, reflecting walking activity as in the homeostat model (Fig. 5.4d, see Methods). The two components were combined and fitted together to the normalized fluorescence of dFB neurons ('hunger-walk' model, Fig. 5.6g and Supplementary Figs. S5.38 and S5.39). Fig. 5.6h shows the fitted time constants, showing slow calcium dynamics similar to glia activity during the stop state (in the order of minutes), while the fed time constant is close to zero indicating that dFB activity resets immediately at feeding. Flies stayed satiated (where the hunger component did not increase) on average for around 40 minutes, although this varied between flies (Fig. 5.6h). The fitted 'hunger-walk' model (Fig. 5.6g and Supplementary Figs. S5.38 and S5.39) produced a lower error with dFB activity (Fig. 5.6i) and statistically significant better fits (see Table S5.4 and Methods) than the homeostat model (Supplementary Figs. S5.36 and S5.37).

Flies were not ingesting the same amount of food from the feeder during all feeding events, and often ate less at the beginning of the experiment. To address whether the reset of dFB neurons after feeding depended on the amount of food ingested, we computed the relative change in size of the abdomen between 10 minutes before and 10 minutes after feeding (Fig. 5.6d, see Methods). Change in fluorescence of dFB neurons was correlated with change in abodmen size, with larger decays in fluorescence when flies ate more (Fig. 5.6e). This correlation was stronger for small changes in body size, indicating that the reset of dFB neurons saturates after a certain increase in the volume of the abdomen (see Methods).

5.4 Discussion

Ensheathing glia show the characteristics expected of a sleep homeostat [267, 269]: calcium levels increase with behavioral activity or effort during wakefulness, decay when the fly is sleeping, resting, extending its porboscis, or grooming (Fig. 5.2a-d, and Supplementary Figs. S5.4, S5.6, and S5.13), and saturate during sleep deprivation (Fig. 5.3), all with an exponential time course. For example resetting of the homeostat to below 2% from baseline occurs over about 4 time constants or 60 to 120 minutes, a time span that covers a large fraction of the sleep bouts observed in freely walking flies [18, 105, 106] (Figs. 5.1d, 5.2d and 5.4f).

The homeostat resets similarly during short and longer epochs of immobility, as shown when comparing sleep bouts of less and more than five minutes duration (see the three-state homeostat model in Methods (Supplementary Figs. S5.15 and S5.16). The arousal threshold increased with time spent resting (Fig. 5.2k and Supplementary Fig. S5.9b-g), as previously observed during extracellular recordings in tethered walking flies [193], thus indicating that flies indeed sleep in these experiments. The time constants of were faster for charging than for resetting of the homeostat (Fig. 5.4f and Supplementary Fig. S5.18a), consistent with the observation that flies sleep more than they are awake over a 24 hour period [105, 106]. A model differentiating between 7 different behavioral states (seven-state homeostat model) improved fitting accuracy and indicated that variability in charging and resetting dynamics depended on behavior (Supplementary Figs. S5.17 and S5.18). Reaching the upper or lower thresholds of the sleep homeostat did not automatically trigger awakening or sleep; long bouts of activity with a saturated homeostat were however only observed under sleep deprivation (Fig. 5.3b and d).

Glia activity does not simply reflect neural activity of sleep related neurons in the enclosed central complex compartments and additionally predicts wake and sleep bouts more reliably than neurons (Fig. 5.5e-i). Ring neurons that increase activity after extended sleep deprivation [123, 186] were not well described with a homeostatic model, yielded weaker predictions for distinguishing wake and sleep states, and had faster time constants than ensheathing glia. Activity of dFB neurons, which are frequently used as a 'sleep-switch' to induce sleep [176], could be well described by taking into account walking activity and hunger, but not with a sleep homeostat model (Fig. 5.6g-i and Supplementary Figs. S5.36, S5.37, S5.38, and S5.39). The rapid reset of activity after feeding in dFB neurons depended on the behavioral state of the fly, which was not the case for ensheathing glia. Glia activity remained high during sleep deprivation after feeding, whereas in dFB neurons only walking activity, and not other effortful behaviors, could suppress resetting (Fig. 5.2i and j). The magnitude of the fluorescence decay after feeding in dFB neurons additionally depended on the amount of food ingested by the fly (Fig. 5.6d and e).

Feeding related signals in the fan-shaped body and modulatory activity in dFB neurons

in immobilized preparations were described in [532, 533, 534]. Since the central complex is at the center of sensorimotor integration [306], hunger and sleep related signal thus could modulate behavioral decisions in this network [535].

Sleep is linked to feeding and more broadly to energy homeostasis across species [261, 536, 537]. Fly glia are important for supplying energy to neurons, and ensheathing glia could contribute to this for example by sensing glutamate [261]. Consistent with this idea, we observed an increase or respectively a decrease of extracellular glutamate at ensheathing glia during active and inactive, or wake and sleep states.

Ensheathing glia form a barrier around brain compartments [224, 225] and could therefore integrate activity of the underlying circuits, for example by sensing glutamate. A potentially similar integration of local neural activity was performed computationally by integrating electrical cortical activity recorded in mice, and approach that resulted in a sleep homeostat [185].

If ensheathing glia integrate activity of the underlying brain regions, glia around different brain compartments could show different calcium dynamics, for example due to locally different activity and resulting sleep needs [59, 185, 538]. *Vive versa*, the similarities in the navigation related neural activity between brain compartments in the central complex [306, 313, 539] could lead to the similarities in calcium glia dynamics observed in EB and FB. Additionally, calcium dynamics in glia in the LAL (Supplementary Fig. S5.5), a brain area which has not been associated with sleep circuits, were similarly to those in EB and FB.

Calcium levels in glia have been suggested as a mechanism for integrating neural activity and providing feedback to underlying neural circuits by modulating their environment [58, 540]. Modulation of sleep circuits by glia has for example been described in C. elegans [541, 542]. The action of ensheathing glia could include the regulation of glutamate in the enclosed circuits [226, 247]. In mice, microglia generate inhibitory feedback and suppress activity of glutamatergic neurons [543], a mechanism which could also play a role in sleep regulation in an adenosine-dependent manner [544]. Recent evidence suggests that ensheathing glia could also release adenosine with increasing calcium levels [545]. Adenosine seems however not to be important for sleep control in the fly [99]. An alternative gliotransmitter could be taurine which promotes sleep in flies and is also regulated by ensheathing glia [252].

Overall, ensheathing glia offer a sleep homeostat distributed across different brain areas. Combining imaging in behaving flies over long timescales with a range of behavior paradigms, including learning, as well as the genetic tools available in the fly will enable the brain-wide investigation of the interplay between behavior, sleep homeostasis and sleep function.

5.5 Methods

5.5.1 *Drosophila* preparation

All flies were reared in an incubator at 25 degrees with a 12 hour light/dark cycle. For freely moving experiments we used 7 days old female flies expressing jGCaMP8m in ensheathing glia (UAS-jGCaMP8m;56F03-GAL4). Flies were first anesthetized using ice and placed individually in rectangular chambers with food (Fig. 5.1a).

For imaging experiments, the same 12 hour light/dark cycle from the incubator was used in the VR during imaging experiments. All the experiments for imaging were performed on female flies between 3 and 8 days old. To record calcium activity from ensheathing glia, we expressed jGCaMP8m using the Gal4 line 56F03 (UAS-jGCaMP8m;56F03-GAL4). Experiments for monitoring extracellular glutamate were performed by labeling the glutamate sensor iGluSnFR in ensheathing glia (UAS-iGluSnFR;56F03-GAL4). To monitor activity from R5 ring neurons we used two different Gal4 lines: 58H05-GAL4, for which we expressed jGCaMP8m (UAS-jGCaMP8m;58H05-GAL4), and 88F06-GAL4 for which we expressed jGCaMP8m, 8f or 7f (UAS-jGCaMP8m;88F06-GAL4, UAS-jGCaMP8f;88F06-GAL4 and UAS-jGCaMP7f;88F06-GAL4, respectively). Activity from dFB neurons was monitored by expressing jGCaMP8m or jGCaMP8f in 23E10-GAL4 (UAS-jGCaMP8m;23E10-GAL4, UAS-jGCaMP8f;23E10-GAL4).

Before imaging experiments, flies were dissected using laser surgery as described in described[28] to insert a transparent window into the cuticle [363]. The cut cuticle and air sacks were removed under a dissection microscope using forceps, either manually or with a microrobotic arm [28]. The opening was sealed with a drop of transparent UV glue (Freeform, UV fixgel composite). Between 2 and 5 flies were dissected at a time and were left to recover in vials with food for 1 to 3 days before imaging. Flies were then glued to a glass slide using UV glue and transferred to the long-term imaging setup. Flies were selected for imaging based on the optical access to the structures of interest which varied dependent on dissections. Only data recorded at least 48 hours after surgery was included in the analysis.

5.5.2 Setup for experiments with freely walking flies

Flies were placed in transparent chambers of 70×4 mm (Fig. 5.1a) and activity was recorded in 15 chambers using a camera from above with a resolution of 1920×1080 pixels running at 30 Hz. A rectangular grid of IR LEDs illuminated the chambers from below through a diffuser. A high-pass filter (Thorlabs FGL780S) in front of the camera rejected white light from LEDs, which recreated the same 12 hour light /dark cycle from the incubator where flies were reared. Since flies needed to adapt to the new environment, the first day of the

experiment was discarded, and we only considered the subsequent two days for the following analysis.

Tracking of the fly positions was done offline, using color segmentation in OpenCV and Python, by extracting the dark color of the flies from the bright background. The position and velocity of each fly in its chamber were further smoothed using a Kalman filter. Fig. 5.1b shows examples of the position along the chamber and the velocity of one fly. Supplementary Fig. S5.1a and b shows the mean velocity of 15 flies with a light/dark cycle and in darkness conditions over 48 hours, respectively. In both conditions, flies displayed circadian activity.

To find epochs of immobility, we set the velocity of each fly to zero if a fly did not move at least 0.25 body lengths in a second (a body length is defined as 2.5 mm) (Fig. 5.1c, first row). We then computed each fly's "stop" binary profile over time from the velocity (Fig. 5.1c, second row). To compute sleep bouts, we used different temporal filters with a size of 1,2,5,8 and 10 minutes (Fig. 5.1c, third row) to convolve stop bouts (Fig. 5.1c, third row). This temporal filter allows removing small bouts of movement of the fly (depending on the filter size) between stop epochs. Sleep was then obtained by thresholding the convolved walk at the value of 0.5 (Fig. 5.1c, fourth row). The distribution of continuous sleep bouts was computed for each filter size during the day and night (Fig. 5.1d), and during darkness (Supplementary Fig. S5.1c), where the 90% quantile of the distribution is highlighted. A filter size of 2 minutes, which already removes up to 1 minute of walking in between stop epochs, produces a distribution where 90% of sleep bouts are below 50 minutes (Fig. 5.1d). Sleep bouts were even shorter in dark conditions, where even using a filter size of 10 minutes, which removes 5 minutes of walking in between stop bouts, led to a distribution where 90% of sleep bouts were below 40 minutes (Supplementary Fig. S5.1c).

To compute how frequently flies eat in the freely moving experiments, we thresholded the position of the fly when it was close to the food (at around 7 mm in the chamber, see Fig. 5.1b). As before, we used a temporal filter with different sizes (30, 60, 90, 120, and 150 seconds) to filter out small movements of the fly entering and leaving the food and defining feeding events. We then obtained the distribution of time duration between consecutive feeding events during the day and night for different filter sizes (Fig. 5.1h). Using a filter size of 120 seconds, 90 % of the times between consecutive feeding events were around 26 minutes during both the day and night. This result was therefore used for some of the long-term imaging experiments in ensheathing glia, where the flies were fed every 26 minutes (Fig. 5.1i and j, and Supplementary Fig. S5.2) or every 16 minutes (Supplementary Fig. S5.3).

5.5.3 Imaging setup

The setup for long-term imaging was as described in [28]. For recording volumetric calcium activity and to reduce brain motion artifacts, two axially offset focal planes were recorded

at the same time with beams with an extended focal length, with temporally multiplexed acquisition [28]. This setup allowed motion correction at high time resolution in all three dimensions as described in [30]. Fly behavior and virtual reality projection was implemented as previously described [28, 157].

5.5.4 Data acquisition

At the start of each long-term imaging experiment, a z-stack of 100 μm depth with an axial resolution of 0.25 μm was recorded, which was used for z-motion correction in post-processing [30] (see next section). Additionally, an automated robotic feeder was configured at the beginning of the experiment, which fed flies every 4 hours for 2 minutes [28]. Imaging data was recorded at a resolution of 256 $\times$ 256 pixels at 60Hz. In most of the experiments, we recorded for 1 second with a wait time of 60 seconds between consecutive recordings, resulting in a total imaging time of 1.6% of the duration of the experiment, which helped to reduce photobleaching and phototoxicity. However, we additionally used a different protocol in four other flies, where we recorded for trials of 30 seconds with a wait time of 5 minutes between trials, which resulted in a total imaging time of 11% of the duration of the experiment (Supplementary Figs. S5.31g and S5.26f-h). A side view of the fly was recorded with a camera at 10 Hz with a resolution of 640 $\times$ 480 during the whole experiment, which was used later for behavior classification. The VR, implemented as described [27, 157] displayed a dark stripe on a bright background using a blue laser (488 nm), which was switched off during the night for 12 hours. The VR night and day cycle was synchronized to the day and night cycle used in the fly incubator before the experiment. Ball movement was tracked at 200 Hz and a calibration factor for the frame rate and lighting conditions was determined for calculating ball velocities. The water temperature at the objective was 22 degrees [28].

Flies were left to recover for at least 2 days before imaging started. In some of the flies, imaging started after only 1 day of recovery, but the first day was excluded from data analysis. Food deprivation was performed in some of the flies in the middle of the experiment. Recordings of calcium activity in ensheathing glia are shown in Figs. 5.1i, 5.2a and e, and Supplementary Figs. S5.2, S5.3, S5.4, S5.7, S5.8 and S5.5. Recordings of glutamate activity in ensheathing glia are shown in Fig. 5.4a and Supplementary Fig. S5.11. Recordings of calcium activity in R5 neurons using 58H05-GAL4 are shown in Fig. 5.5a and Supplementary Fig. S5.22, and recordings using 88F06-GAL4 are shown in Supplementary Figs. S5.25 and S5.26. Finally, recordings of calcium activity in dFB neurons are shown in Fig. 5.5b and Supplementary Figs. S5.30, S5.30, S5.35 and S5.34.

5.5.5 Data post-processing

Imaging data was corrected for lateral motion by alignment with respect to a template (average of the first 60 frames) using cross-correlation (Fig. 5.2f). The z-stack was also aligned with respect to this template. Then, 24 regions of interests (ROIs) were defined for EB, 24 for FB (Fig. 5.2f shows the combined ROIs in the EB and FB, also for the case of R5 and dFB neurons), and 24 for LAL (in the two flies in Supplementary Fig. S5.5). The intensity of each ROI was computed by summing all pixel values within each ROI per frame as well as in each frame in the z-stack. The intensity of the ROIs was then used to estimate the z-motion of the sample for each imaging frame as described in [30]. The resulting z-motion over the time of the experiment was filtered using a median filter with 1000 points to discard high-frequency motion, and found maximum displacements of around $10um$ along the z-axis. The filtered z-motion was used to estimate the fluorescence of each ROI corrected from z-motion[30]. Differences between corrected and uncorrected fluorescence was generally low, with maximum differences of 0.1 $\Delta F/F$ due to the extended focal volume used for imaging [30].

The 200Hz used to track ball motion underestimated ball displacements in the 3 axes by a factor of 0.50 compared to using 500 Hz tracking as in [157]. This factor was experimentally measured by rotating manually the ball 3600 degrees, which resulted in approximately 1809 degrees tracked displacements. Therefore ball displacements during long-term imaging were corrected in the post-processing and used to compute the absolute velocity of the fly in bins of 1 second using the ball radius ($3mm$).

To fit exponentials and all the models implemented to fluorescence traces (see sections below), we first smoothed the fluorescence signal from any of the experiments using a low-pass filter with a cut-off period of 15 minutes (thick lines Figs. 5.2a, 5.4a, 5.5a,b and Supplementary Figs. S5.4, S5.11, S5.22, S5.25, S5.26, S5.30, and S5.31). Then we normalized the filtered fluorescence, $F(t)$, by remapping the 10% and 90% quantiles of $F(t)$ ($Q_{10\%}$ and $Q_{90\%}$, respectively) to the values 0 and 1, respectively, following this equation:

$$\text{Normalized } F(t) = \frac{F(t) - Q_{10\%}}{Q_{90\%} - Q_{10\%}} \tag{5.1}$$

This processing was performed to reliably compare glia and neurons in Fig. 5.5e-i, since different recordings have different fluorescence dynamic ranges and different noise levels. By smoothing and normalizing fluorescence traces from all experiments, we ensured that correlations (Fig. 5.5e, f and i) and errors from model fittings (Fig. 5.5g and Fig. 5.6i) were correctly compared across recordings.

5.5.6 Behavior classification

Fly behavior was monitored during the entire experiment using a camera (Supplementary Fig. S5.20A) under IR illumination at 10 frames per second (fps) [28]. Based on blocks of 10 consecutive frames (1 second time resolution), we classified the following 7 behaviors (rows in Supplementary Fig. S5.20A): Stop: the fly does not move. Proboscis: the fly does not move but extends and retracts the proboscis. Walk: the fly walks on the ball. Discomfort: the fly pushes or pulls the ball. Grooming front: grooming of head and proboscis with front legs. Grooming back: grooming of the abdomen and wings with hind legs. Feeding: fly is fed with the feeding robot.

We used a 3D convolutional neural network (3D CNN) to classify the behavior based on 10 frames. The field of view of the camera (with resolution 640×480 pixels) was cropped around the fly and was resized to a resolution of $256x256$ pixels. The architecture of the 3D CNN is shown in Supplementary Fig. S5.20B, where each convolutional block consisted of a 3D convolutional layer with a $3x3x3$ kernel size and rectified linear unit activation function (ReLU), a dropout layer with a rate of 0.2 to prevent overfitting, and 3D max pooling with size $2x2x1$. The filters of the convolutional layer increased by a factor of 2 in each consecutive convolutional block. Finally, a dense layer with a softmax activation function assigned a value to each class. The 3D CNN had a total of around 6.5M trainable parameters.

A total of 45610 manually labeled frames from 10 different flies were used for training. The dataset was normalized to train the network with the same number of samples for each class. We further increased this dataset with data augmentation that randomly transformed the input frames by changing illumination, translation, rotation and/or scale during training. To train the network we used TensorFlow with a binary cross-entropy loss function and Adam as optimizer. After 150 epochs with a batch size of 50 samples, the loss function reached a minimum saturation value in about 2 hours, using 4 QUADRO GPUs.

To test the performance of the network, we used 2410 labeled frames, which were augmented to a total of 20000 with the previously described augmentation transformations. The accuracy of the network to predict the right class of behavior was 98.6%, and the normalized confusion matrix for each class is shown in Supplementary Fig. S5.20C. An example of behavior classification is shown in Supplementary Fig. S5.17b.

5.5.7 Probing of arousal threshold

For probing the arousal threshold of the fly during long-term imaging, we used a total of 6 flies where we recorded calcium activity (data not included) from ensheathing glia using the same protocol as before. We recorded multiple trials of probing the arousal threshold in each fly. Trials were initiated automatically using custom software (see N for each fly

in Supplementary Fig. S5.9b-g). At the beginning of each trial, the amount of expected sleep time for probing the arousal threshold was selected, randomly setting it to 30 seconds or 5 minutes. Then the fly was stimulated to walk by closing and opening the air stream of the ball repeatedly 3 times during 6 seconds (1 second closed and 1 second open). This ensured that the fly was awake at the beginning of each trial. After this, velocity of the fly on the ball (thresholded to remove tracking noise) was monitored in real-time to detect epochs of walking or immobility. A timer was used to measure the time the fly was stopped since since the end of the last walking bout (non-zero velocity). If this time reached the previously selected duration (30 seconds or 5 minutes), the probing of the arousal threshold started. Probing the arousal threshold was performed through an IR laser (Toptica, ibeam-smart-785-S-HP with pulse option, 785 nm), by ramping the power from 0 to $100mW$ in steps $1mW$ every second. When the fly started to walk, due to the heating effect of the IR laser, the trial finished and the IR laser was turned off. During probing with the IR laser, the shutter of the two-photon laser was closed and imaging data was not recorded, since the combined power the of two-photon and heating lasers would distort the detection of the threshold. After one trial was finished, the next trial started after 10 minutes of waiting. Experiments for each fly were performed for at least 1 day, resulting in several hundreds of trials in each fly.

During these experiments, we recorded the ball velocity and fly behavior with a camera as usual, as well as the IR laser power. We then used the 3D CNN to classify the behavior in post-processing. For each trial, we compute the actual elapsed time that fly was immobile (either in the 'stop' state or 'proboscis' state) prior to the arousal threshold probing, in order to filter grooming events. Only trials with prior times of immobility larger than 5 seconds were considered, therefore the times of immobility ranged from 5 seconds to 5 minutes. During the probing period in each trial, we obtained the required laser power to awake the fly. The fly was considered awake when it showed walking, discomfort, or grooming behaviors (obtained from the 3D CNN classification). An example of a trial for arousal threshold probing is shown in Supplementary Fig. S5.9a.

We computed the distribution of IR laser power required to awake the fly prior to three different immobility time intervals: [5, 35], [35, 200], and [200, 305] seconds. These distributions are shown in Supplementary Fig. S5.9b-g for individual flies, and in Fig. 5.2k for all flies. Asterisks indicate statistical significance using t-test (p-value ¡ 0.05). As shown for individual flies as well as for all flies (Fig. 5.2k and Supplementary Fig. S5.9b-g), longer prior time of immobility required higher IR laser powers to awake the flies, confirming that the arousal threshold increases with time of immobility during our long-term recordings.

5.5.8 Fitting of fluorescence traces during 'active' and 'rest' states

Sleep is commonly identified in flies as bouts of quiescence that last at least 5 minutes [19, 119], a threshold that has also been used for assessing sleep in tethered walking flies [192, 546]. However, shorter bouts of quiescence already show many of the characteristics of sleep [194]. The distribution of bouts of times that the flies did not walk for our experiments is shown in Supplementary Fig. S5.14 for the recordings in ensheathing glia. We compare the amount of sleep according to a 5 minutes threshold, according to only distinguishing between walking and stopping, and according to the 'rest' and 'active' states (used in Fig. 5.2a) in Table S5.1.

To find epochs of at least 10 minutes during which the fly was walking most of the time (active) or sleeping most of the time (rest), we proceeded as follows: Walking velocity on the ball (with a diameter of 3 mm) was averaged over one second. Velocities below a threshold of 0.25 body lengths per second (body length defined again as 2.5 mm) were set to zero to remove tracking noise, and we defined a binary walk state of the fly, $w(t)$, when the thresholded velocity was non-zero ($w(t) = 1$). We defined active and rest states where the fly was walking or standing still most of the time. To calculate these states, we used a walk density, which was defined as alow-pass filter of the walk state with a period of 0.1 hours (6 minutes). Active and rest states were defined based on the walk density being above or below a threshold of 0.5, respectively (Fig. 5.2a and Supplementary Figs. S5.4, S5.11, S5.22, S5.25, S5.26, S5.30, and S5.31). We cut the normalized fluorescence from each recording (equation (5.1)) into N_a traces of at least 10 minutes of continuous active epochs, $F^i_{active}(t)$ for $i = 1, ...N_a$ and at least 4 trace trances were used from each fly to obtain the normalized averaged fluorescence over active epochs, which was fitted with a rising exponential (Figs. 5.2b, 5.4b, and 5.5c, and left side in Supplementary Figs. S5.6a-e, S5.12a-d, S5.23a-d, S5.27a-h, and S5.32a-g). The exponential was defined by the following equation:

$$\hat{F}_{active}(t) = A_{active}(1 - e^{-t/\tau_{active}}) + C_{active}. \tag{5.2}$$

Here, A_{active} is the saturation level of the exponential, C_{active} is an offset and τ_{active} is the time constant.

Fluorescence traces for the rest state were similarly selected as epochs of at least 10 minutes. At least 4 normalized fluorescence tracnes were used to obtain the normalized average fluorescence over rest epochs, which was fitted with a resetting exponential (Figs. 5.2c, 5.4b, and 5.5d, and right side in Supplementary Figs. S5.6a-e, S5.12a-d, S5.23a-d, S5.27a-h, and S5.32a-g). The resetting exponential was defined by the following equation:

$$\hat{F}_{rest}(t) = A_{rest}e^{-t/\tau_{rest}} + C_{rest}. \tag{5.3}$$

Here, A_{rest} is the amplitude, C_{rest} is an offset and τ_{rest} is the time constant of the decay.

Fly	Sleep using ball velocity (stop) (% per hour)	Sleep using walk density (rest) (% per hour)	Sleep with 5 minutes threshold (% per hour)
1	50.0	49.1	18.7
2	56.8	51.5	28.8
3	68.1	61.0	33.6
4	70.8	51.6	30.4
5	57.6	46.0	19.1
6	76.4	61.2	31.0

Supplementary Table S5.1: Percentage of time sleeping per hour for each fly according to the different definitions used in the paper.

The time constants during active and rest states from activity in glia and in extracellular glutamate are shown in Figs. 5.2d and 5.4c.

5.5.9 Sleep deprivation

Sleep deprivation was performed for recordings in ensheathing glia. Mechanical sleep deprivation was performed in a total of 5 flies over 3.6 and 8.2 hours, by opening and closing the air stream of the ball repeatedly 3 times for 6 seconds (alternating betwen 1 second closed and 1 second open) every 20 seconds. This stimulated flies to walk and prevented sleep. Food deprivation was performed for a total of 4 flies between 4 and 16 hours. Individual recordings for both conditions are shown in Supplementary Fig. S5.10a and b, respectively, where exponentials were fitted for visualization (equation (5.2)).

For each fly, we computed the 'stop' state of the fly (zero velocity) in 1 second bins. We then averaged the 'stop' time for all flies over 1.5 hours before sleep deprivation and over 8 hours of sleep deprivation (left side, first row in Fig. 5.3b and d). We computed the average of the fluorescence in the EB and FB, which were first normalized through equation (5.1) (left side, second and third row in Fig. 5.3b and d, respectively). At least two flies were considered for the average over the sleep deprivation period. The average 'stop' time and fluorescence were also computed over 2 hours after sleep deprivation (right side in Fig. 5.3b and d). We then computed the distribution of the mean values of the normalized fluorescence in each fly over 1.5 hours before sleep deprivation, over the first 2 hours of sleep deprivation, after the first 2 hours of sleep deprivation, and over 2 hours after sleep deprivation (Fig. 5.3c and e). Statistical significance between these distributions was assessed using t-test (p-value ¡ 0.05).

We also calculated the distribution of 'stop' time after 2 hours of sleep deprivation from the 'stop' state in each fly, as well as the duration of immobility bouts that were larger than 5 minutes (Fig. 5.3f). For control flies, we used the recordings from Supplementary Fig. S5.4, which had identical conditions as sleep-deprived flies except for sleep deprivation. We

then computed the distribution of 'stop' time over 2 hours at the time of the day when sleep deprivation finished for the sleep-deprived flies, as well as the distribution of sleep bout duration for all flies (Fig. 5.3f). Statistical difference between distributions was assessed again using t-test (p-value ¡ 0.05).

5.5.10 Homeostat model

The homeostat model was fitted to activity of glia, R5 neurons, and dFB neurons. For model fitting, fluorescence was filtered and normalized as described before (equation (5.1)). In the homeostat model we did not distinguish between immobility and sleep, but distinguished two behavioral states based on the fly's walking activity for charging and resetting of the homeostat, respectively: 'walk' and 'stop'. The homeostat model was fitted over the time range of each experiment, defined by $[T_{min}, T_{max}]$ for 'stop' and 'walk' periods of the fly. The 'stop' behavior of the fly, $s(t)$, was set to 1 when the velocity of the fly was below a threshold of (0.25 body lengths per second, to remove tracking noise level) and a value of 0 otherwise. Conversely, the 'walk' state of the fly, $w(t)$, was assigned a value of 1 for velocities higher than the threshold and 0 otherwise (top rows in Fig. 5.4e, and Supplementary Figs. S5.13, S5.24, S5.25, S5.26, S5.36, and S5.37). The time resolution for distinguishing between 'stop' and 'walk' was 1 second. The following model was used for fitting:

$$\dot{h}_v(t) = s(t)\frac{1}{\tau_s}\Big(- h_v(t) + L(t)\Big) + w(t)\frac{1}{\tau_w}\Big(- h_v(t) + U(t)\Big). \tag{5.4}$$

Here, $h_v(t)$ describes the fluorescence signal ($\Delta F/F$) or homeostat, while $s(t)$ and $w(t)$ act as binary weights for each behavior. Therefore only one behavioral state contributes to the homeostat at any given time. τ_s and τ_w are the time constants for the stop and walk states, and $L(t)$ and $U(t)$ are functions that describe the lower and upper bounds of the homeostat, respectively (yellow lines in Fig. 5.4e, and Supplementary Figs. S5.13, S5.24, S5.25, S5.26, S5.36, and S5.37). These bounds were allowed to vary with time to take into account slow modulations in fluorescence that are unavoidable during long-term imaging recordings, such as photobleaching, circadian modulation, or slow changes in calcium levels potentially due to phototoxicity. These changes affect both baseline levels as well as the dynamic range of fluorescence signals over time. Therefore these upper and lower bounds allowed to correct for dynamic range and baseline changes, and were defined as Bezier curves:

$$\begin{cases} U(t) = \sum_k^K C_k u_k \\ L(t) = \sum_k^K C_k l_k, \end{cases} \quad \text{where} \quad C_k = \binom{K}{k} \Big(\frac{T_{max} - t}{T_{max} - T_{min}}\Big)^{K-k} \Big(\frac{t - T_{min}}{T_{max} - T_{min}}\Big)^{k} \tag{5.5}$$

These curves were fitted at the same time as the parameters of the model. The Bezier curves were parameterized by points separated by at least 6 hours, which defined the number of

parameters K for each experiment as

$$K = \lfloor \frac{T_{max} - T_{min}}{6 \text{ hours}} \rfloor, \tag{5.6}$$

where $\lfloor \cdot \rfloor$ indicates the floor division operation. For each experiment we fitted the 2 time constants τ_s and τ_w, and the K upper and lower bound parameters, u_k and l_k:

$$\{\tau_s, \tau_w, u_1, ..., u_K, l_1, ..., l_k\}. \tag{5.7}$$

The fitting procedure is described in the next section. The fitted homeostat model for glia activity is shown in Fig. 5.4e and Supplementary Fig. S5.13; for R5 neurons in Supplementary Figs. S5.24, S5.25, and S5.26; and for dFB neurons in Supplementary Figs. S5.36 and S5.37. All the fitted time constants for stop and walk and their estimated errors are shown on the left side of all the previous s., and the combined time constants for glia are shown in Fig. 5.4f, where asterisks show statistical significance (p-values lower than 0.05) between the walk and stop states in the EB (green) and FB (blue) using t-test.

5.5.11 Three-state homeostat model

This model was only fitted for glia activity, where fluorescence was filtered and normalized as described before (equation (5.1)). In this model, we distinguished two states for resetting the homeostat: a 'stop' state where the fly was at rest (as assessed by ball velocity) for less than 5 minutes, and a sleep state, where the fly was at rest for epochs lasting more than 5 minutes.

$$f(t) = \{\text{Stop}(t),\ \text{Sleep}(t),\ \text{Walk}(t)\} \tag{5.8}$$

The following model was used for fitting:

$$\dot{h_s}(t) = \sum_{i}^{N_s} f_i(t) \frac{1}{\tau_i} \Big(- h_s(t) + F(w_i, t) \Big). \tag{5.9}$$

Here, $h_s(t)$ describes the fluorescence signal ($\Delta F/F$) or homeostat, and $f_i(t)$ acts as a mask for each state, and therefore only the assigned behavior contributes to the homeostat at any given time (similar to the 2-state model). τ_i is a time constant for each behavior i, and w_i is the weight with which each behavior contributes to the homeostat, -1 for 'stop' and 'sleep' states and +1 for 'wake'. F is a function that describes the upper and lower bounds of the homeostat,

$$F[w_i, t] = \begin{cases} U(t) & \text{if } w_i = 1 \\ L(t) & \text{if } w_i = -1, \end{cases} \tag{5.10}$$

where functions $U(t)$ and $L(t)$ are the upper and lower bounds defined in equation (5.5), similarly to the previous homeostat model.

For each model we fitted the N_s time constants τ_i and the K upper and lower bound parameters, u_k and l_k:

$$\{\tau_1, ..., \tau_{N_s}, u_1, ..., u_K, l_1, ..., l_k\} \tag{5.11}$$

An example of the model fitting for glia activity in the EB and FB is shown in Supplementary Fig. S5.15a. The fitted time constants for each of the states, as well as their estimated errors in EB and FB, are shown in Supplementary Fig. S5.15b. The distribution of time constants for each state in the EB and FB is shown in Supplementary Fig. S5.15c. Only time constants with an estimated error lower than 0.2 times its fitted value were included to discard estimated time constants with high error. Asterisks in Supplementary Fig. S5.15c indicate statistical significance (p-values lower than 0.05) between different behaviors in EB (green) and FB (blue) using t-test.

We also asked if the homeostat would reset differently after 5 minutes of immobility. For this purpose, we defined a sleep state only after the fly was stopped for 5 minutes and fitted again equation 5.9. Supplementary Fig. S5.16a shows an example for glia activity in the EB and FB, together with the fitted time constants in Supplementary Fig. S5.16b. The distribution for time constants with an estimated error lower than 0.2 times its value are shown in Supplementary Fig. S5.16c for EB and FB. We did not find statistical significance between the time constants of the 'sleep' and 'stop' states using t-test.

5.5.12 Seven-state homeostat model

Only activity of glia, which was filtered and normalized as described before (equation (5.1)), was fitted to a homeostat model using the classified behaviors (an example is shown in the top row of Supplementary Fig. S5.17b. We fitted the dynamics of the homeostat with a model taking into account the $N_b = 7$ classified behaviors from the 3D CNN:

$$b(t) = \{\text{Stop}(t), \text{Proboscis}(t), \text{Walk}(t), \text{Discomfort}(t), \text{Grooming front}(t), \text{Grooming back}(t), \text{Feeding}(t) \tag{5.12}$$

Each behavior, $b_i(t)$, was assigned a binary value, $b_i(t) \in \{0, 1\}$, and only one behavior had value 1 at any given time, corresponding to the maximum class value predicted by the 3D CNN. The time resolution for the classification of behavior was 1 second.

We used the following model to fit the data:

$$\dot{h_b}(t) = \sum_{i}^{N_b} b_i(t) \frac{1}{\tau_i} \Big(- h_b(t) + F(w_i, t) \Big). \tag{5.13}$$

Here, $h_b(t)$ describes the fluorescence signal ($\Delta F/F$) or homeostat, and $b_i(t)$ acts as a mask for each behavior, and therefore only the assigned behavior contributes to the homeostat at any given time (similar to the 2-state model). τ_i is a time constant for each behavior i, and w_i is the weight with which each behavior contributes to the homeostat, which can take

only two values: $w_i \in \{-1, 1\}$. When a weight is $w_i = -1$, the homeostat decreases while the fly performs the behavior, while with $w_i = 1$, the homeostat increases.

F is a function that describes the upper and lower bounds of the homeostat, given by equation (5.10), similarly to the previous 2- and 3-states model.

Fitting this differential equation requires determining for each behavior whether it charges or resets the homeostat, that is, contributes with a negative or positive weight to the model. To determine the weight of each behavior in the model, we used fluorescence traces from flies that performed one of the 7 behaviors for at least two consecutive imaging epochs (120 seconds). For 'discomfort' we used fluorescence traces recorded when the ball was stopped (Fig. 5.2e and Supplementary Fig. S5.7), since this behavior was not observed continuously for 120 seconds when the ball was free to rotate. For the rest of the behaviors, we used fluorescence traces from the recordings of ensheathing glia in 6 flies. For each behavior, all traces were aligned at the origin ((thin lines in Fig. 5.4i for the EB and Supplementary Fig. S5.17a for the FB)) and linear regression was used to determine the slope. If the slope was positive for a behavior, the weight was set to 1 and otherwise to -1 (negative slope, magenta lines in Fig. 5.4i). We repeated the same procedure for FB and found the same weights as in EB (Supplementary Fig. S5.17a). For each model we fitted the N_b time constants τ_i and the K upper and lower bound parameters, u_k and l_k:

$$\{\tau_1, ..., \tau_{N_b}, u_1, ..., u_K, l_1, ..., l_k\}. \tag{5.14}$$

Models were fitted independently to EB and FB data.

The fitting procedure is explained in the next section. Since some behaviors were very rare in some of flies, the estimation error for model fitting was large for some of the time constants. Therefore only time constants with an estimated error lower than 0.2 times its fitted value were included in the distribution of the time constants for each behavior in Supplementary Fig. S5.18a. Asterisks in Supplementary Fig. S5.18a indicate statistical significance (p-values lower than 0.05) for behaviors in the EB (green) and FB (blue) using t-test.

5.5.13 Hunger-walk model

Only dFB neurons were fitted to the hunger-walk model, where fluorescence was filtered and normalized as described before (equation (5.1)). This model contained two different components that contributed differently: a hunger component, and a walk-stop component. The hunger component was fitted from the feeding events of the fly. We defined a "hungry" variable, hungry(t), defined as 0 between a feeding event and a time after feeding, called satiated time $t_{satiated}$, and as 1 after the satiated time and the next feeding event. Another variable, fed(t), was defined as 1 after feeding and before the satiated time, and as 0 otherwise. Therefore fed(t) = 1 − hungry(t). The satiated time, $t_{satiated}$, interpreted as the

time during which the hunger component resets and stays low, was fitted as a model parameter. The hunger component, h_{hunger}, was therefore fitted using the following differential equation:

$$\dot{h_{hunger}}(t) = \text{hunger}(t)\frac{1}{\tau_{hunger}}\Big(-h_{hunger}(t)+U(t)\Big)+\text{fed}(t)\frac{1}{\tau_{fed}}\Big(-h_{hunger}(t)+L(t)\Big). \quad (5.15)$$

Here, hungry(t) and fed(t) act as a mask and therefore only the assigned variable contributes to the hunger component at any given time (similar to the 2-state model). τ_{hungry} and τ_{fed} are the time constants that describe the increase and decrease of the hunger component, respectively. The hunger component and its parameters are shown in Fig. 5.6f. $U(t)$ and $L(t)$ represent the upper and lower bounds, defined in equation (5.5), which were fitted together with the parameters.

The walk-stop component, $h_v(t)$, was defined as in the homeostat model (equation (5.4), but the upper and lower bouts were set constant, $U(t) = 1$ and $L(t) = 0$.

Finally, the hunger-walk model was defined as the weighted sum of the hunger and walk-stop components as follows:

$$h_{hunger-stop} = h_{hunger} + w_v h_v(t) \quad (5.16)$$

where w_v was a weight that indicated the contribution of the walk-stop component, which was also fitted. In summary, for this model we fitted the following 6 parameters,

$$\{\tau_{hungry}, \tau_{fed}, t_{satiated}, \tau_w, \tau_s, w_v\}, \quad (5.17)$$

as well as the parameters that defined the upper and lower bounds of the hunger component, u_k and l_k from equation (5.5). The fitting procedure is explained in the next section, and the fitted models are shown in Fig. 5.6g and Supplementary Figs. S5.38 and S5.39. The fitted time constants of all flies are shown in Fig. 5.6h, where only parameters with an estimated error lower than 0.2 times their fitted value were included. Asterisks in . 5.6h indicate statistical significance (p-values lower than 0.05) for behaviors in the EB (green) and FB (blue) using t-test.

5.5.14 Model fitting

Fitting of models was performed using the function *curve fit* in Scipy [547] in Python. Given a set of initial values of the parameters, we integrated each model with the corresponding equation, for example using equation 5.4 for the 2-state model, equation 5.9 for the 3-state model and equation 5.13 for the 7-state model, from their corresponding states over time, using Euler integration (with 1 second steps). Since the fluorescence data was not recorded continuously, we then interpolated the values of the model in agreement with the times of the

recordings. Finally, we obtained an $L2$-error function between the interpolated model values and fluorescence data. The parameter values were updated iteratively from the Jacobian of the error function, and the minimum was found using the trust region reflective algorithm as optimization method.

To prevent parameters from taking forbidden values during optimization, we used parameter bounds. For the homeostat model, as well as the 3-state and 7-state homeostat models, time constants the allowed range was $[0, 2]$ hours. For the hunger-walk model, time constants were allowed in the range of $[0, 2]$ hours except for the time constant for "hungry", $_tau_{hungry}$, where the allowed range was [0, 6] hours. The allowed range for the weight w_v in the hunger model was [0,1], and the allowed range for the upper and lower bound parameters, u_k and l_k, were $[-1, 0]$ and $[0, 2]\Delta F/F$, respectively.

We computed the error or variance of each parameter from the covariance matrix between all parameters, which was returned by the function *curve fit*. This error indicated one standard deviation error of the parameter, obtained as the square root of the corresponding diagonal element in the covariance matrix. In all models, parameters with errors lower than 0.2 times the magnitude of the fitted parameter were considered for distribution analysis (Fig. 5.4f, 5.1h and Supplementary Figs. S5.15, S5.16, and S5.18a).

5.5.15 Comparison between models

We asked whether the 7-state homeostat model fitted the glia activity better than the homeostat model. In this case, the homeostat model is a nested model, the 7-state homeostat model, which means that the homeostat model and its parameters are included in the 7-state homeostat model and parameters. We therefore asked if a null hypothesis holds, which establishes that the more complex (7-state homeostat) model does not fit fluorescence data significantly better than the simpler model (homeostat model). For this purpose we used a F-test [548].. Since the more complex model has different numbers of parameters than the simpler model, we can compute the F-statistic of the F-test, as:

$$\text{F-statistic} = \frac{(R_{simple} - R_{complex})/(N_{complex} - N_{simple})}{R_{complex}/(N_F - (N_{compex})}, \tag{5.18}$$

where R_{simple} and $R_{complex}$ are the residual sum of squares for the simpler and the more complex model, respectively (same as $L2$-error), N_{simple} and $N_{complex}$ are the number of parameters for the simpler and more complex model, respectively (in this case $N_{complex} - N_{homeostat} = 5$) and N_F is the number of fluorescence points that was used for fitting both models. The F-statistic value can then be used to generate a p-value, rejecting the null hypothesis stated above if it is lower than 0.05. If the null hypothesis is rejected, we can conclude that the more complex model fits the data significantly better than the simpler model.

Fly	L2 error in 2-state model (EB)	L2 error in 7-state model (EB)	F-statistic (EB)	p-value (EB)
1	3.479988	3.478012	0.32	0.9
2	3.063297	2.696925	70.74	1.1e-16
3	4.955734	4.186857	56.23	1.1e-16
4	4.281183	4.167001	13.01	1.6e-12
5	1.520076	1.658245	-40.54	1.0
6	11.306768	10.176129	61.61	1.1e-16

Supplementary Table S5.2: Comparison between 2-state and 7-state models in the EB

Fly	L2 error in 2-state model (FB)	L2 error in 7-state model (FB)	F-statistic (FB)	p-value (FB)
1	3.588580	3.246188	59.59	1.1e-16
2	0.784993	0.733569	36.50	1.1e-16
3	3.402890	2.818227	63.52	1.1e-16
4	1.604965	1.512774	28.95	1.1e-16
5	2.616210	2.554074	11.84	2.4e-11
6	5.747171	5.153419	63.90	1.1e-16

Supplementary Table S5.3: Comparison between the 2-state and 7-state models in the FB

The L2-errors between each pair of models for each fly in EB and FB are shown in Supplementary Fig. S5.18b, while the L2-errors, F-statistic values, and p-values comparing each pair of models in EB and FB are shown in Tables S5.2, S5.3. This analysis concludes that the 7-state homeostat model provides a better fit for the glia data than the homeostat model.

We performed a similar analysis to compare the homeostat model with the hunger-walk model fitted to dFB neurons. As before, the homeostat model was a nested model of the hunger-walk model. We computed the F-statistic between the two models (being the homeostat model the simpler model, while the hunger-walk model is the more complex model) from equation 5.18 and obtained the corresponding p-values. The L2-errors between each pair of models fitted for each fly in shown in Fig. 5.6i, while the L2-errors, F-statistic values, and p-values are shown in Table S5.4. Since all the p-values were lower than 0.05, we conclude that the hunger-walk model fits the activity of dFB neurons better than the homeostat model.

5.5.16 Velocity modulation of glia activity

To assess the influence of fly velocity at short timescales in calcium activity from glia, we computed the mean velocity of the fly during each 1 second imaging epoch, and used a high-pass filter to calculate fluorescence oscillations below periods of 0.5 hours. Supplementary Fig. S5.19a shows the mean velocity of fly 1 in each trial (black) as well as the high-pass filtered fluorescence in EB (green) and FB (blue). Each data point in Supplementary Fig.

Fly	L2 error in homeostat model	L2 error in hunger-walk model	F-statistic	p-value
1	0.093624	0.041422	1395.11	1.110223e-16
2	0.131172	0.055818	790.07	1.110223e-16
3	0.084375	0.057946	233.75	1.110223e-16
4	0.075678	0.058143	90.18	1.110223e-16
5	0.101618	0.045378	635.48	1.110223e-16
6	0.065754	0.039686	84.41	1.110223e-16
7	0.066197	0.037298	498.03	1.110223e-16
8	0.101609	0.043907	1574.07	1.110223e-16

Supplementary Table S5.4: Comparison between the homeostat model and hunger-walk model for dFB neurons

Fly	Number of points	Pearson's correlation (EB)	Pearson's correlation (FB)	p-value (EB)	p-value (FB)
1	1664	0.46	0.37	5.3e-86	3.8e-56
2	1543	0.31	0.25	1.7e-35	4.5e-23
3	680	0.12	0.16	1.2e-03	3.8e-04
4	1065	0.61	0.44	2.1e-108	3.6e-51
5	1283	0.37	0.25	2.3e-43	1.0e-19
6	904	0.28	0.28	1.2e-17	2.9e-18

Supplementary Table S5.5: Pearson's correlation between the changes in high frequency fluorescence fluctuations (change in $\Delta F/F$) and changes in velocity.

S5.19a was separated by the time difference between consecutive imaging recordings of 60 seconds. We computed the change in mean velocity and the change of $\Delta F/F$ in EB and FB between consecutive epochs, Supplementary Fig. S5.19b-g. We fitted a linear regression (red line in Supplementary Fig. S5.19b-g) and computed the Pearson's correlation between the change in velocity and change in $\Delta F/F$ for the EB and FB, finding a positive correlation for each fly with p-values lower than 0.05 (see Fig. 5.4h and Table S5.5).

5.5.17 Comparison between activity of ensheathing glia and neurons

The dynamics of activity in ensheathing glia, R5, and dFB neurons were compared with respect to how well they described a sleep homeostat. For this, we used three different methods. In a first approach, we reasoned that a homeostatic signal should increase over active epochs, producing a positive correlation with the time during which the fly was active, and decrease over epochs or rest or sleep, thus producing a negative correlation the time spent resting or sleeping. We therefore computed the Pearson correlation between the averaged normalized traces over 30 minutes of active and rest epochs (Figs. 5.2b,c and 5.5c,d and Supplementary Figs. S5.6, S5.23, S5.27, and S5.32). We distinguished between the EB

and FB neuropils and compared the distributions of correlation values in the EB between glia and R5 neurons and the distribution of correlation values in the FB between glia and dFB neurons (Fig. 5.5e and f). To assess whether the distributions of correlation values were statistically different we used t-test. Asterisks in Fig. 5.5e and f represent p-values lower than 0.05.

Alternatively, we compared the normalized average traces to a linear fit (Figs. 5.2b,c and 5.5c,d and Supplementary Figs. S5.6, S5.23, S5.27, and S5.32) during the first 30 minutes of rest and activity. The slope of this fit for each fly, shown in Supplementary Fig. S5.40, represents how fast activity increases towards a maximum value during active epochs (Supplementary Fig. S5.40, left side), and how fast activity decreases during epochs of rest to baseline (Supplementary Fig. S5.40, right side). Statistical differences of the slope distributions were again assessed using t-test and are represented by asterisks (p-value ¡ 0.05) in Supplementary Fig. S5.40. The slope for a homeostatic signal that increases and decreases linearly over 30 minutes of activity or rest should be 1 and -1, respectively. Glia activity was very close to these values (Supplementary Fig. S5.40), while the slope for dFB neurons during rest is close to zero.

As a second approach, we calculated the $L2$-error of the homeostat model fitted for glia and R5 neurons. We again distinguished between neuropils and compared the $L2$-error of glia in the EB and of R5 neurons, as well as glia in the FB and dFB neurons (Fig. 5.5g). Statistical significance was assessed using t-test, where asterisks indicate that p-values were lower than 0.05.

As a third approach, we computed the convolution of the binary 'walk' state of the fly, $w(t)$ (assigned with a value of 1 for velocities higher than the threshold and 0 otherwise, as in the homeostat model, first row in Fig. 5.5h), with a temporal filter, $T_f(t)$. The temporal filter had a triangular shape (second row in Fig. 5.5h) defined by a filter size, s_f, as:

$$T_f(t) = \left[1 - \frac{1}{s_f}t\right]_+ \tag{5.19}$$

where $[\cdot]_+$ represents a threshold-linear function to ensure only positive values. The convolution between the 'walk' state and the triangular filter produced the 'convolved walk' (third row in Fig. 5.5h), which exponentially increased when the 'walk' state was 1 and exponentially decreased otherwise. The increase and decrease was the same, defined by the filter size s_f. The 'convolved walk' can therefore be used to compute the Pearson correlation with the normalized fluorescence (as previously described, see equation (5.1)) for different filter sizes s_f. We used a total of 34 temporal filters, ranging from 0 to 60 minutes in steps of 6 minutes, and from 1 hour to 25 hours in steps of 1 hour. The average correlation for glia in the EB and R5 neurons, and for glia in the FB and dFB neurons, is shown with colored lines in Fig. 5.5i, while the standard deviation of the correlation from each group is represented by semi-transparent colored regions around the average in Fig. 5.5i. Only filter sizes lower

than 240 minutes were considered, as larger filter sizes produced close to zero correlation. We obtained the maximum value of the averaged correlation and its corresponding filter size (colored numbers in Fig. 5.5i) and assessed the statistical difference between these maxima using t-test. Statistical significance was indicated by asterisks in Fig. 5.5i (p-values ¡ 0.05)

5.5.18 Fitting of fluorescence traces during 'hungry' and 'fed' states

This analysis was only performed for dFB neurons and was similar to the analysis using active and rest epochs. We defined 'hunger' and 'fed' epochs to characterize the trend of activity of dFB neurons. Fed epochs were defined over the first 30 minutes after a feeding event, while hungry epochs were defined as starting 30 minutes after a feeding event and lasting until the next feeding. At least 4 normalized fluorescence traces were used to obtain the normalized average fluorescence over hungry or fed states, which was fitted with a rising exponential (equation (5.2)) or a resetting exponential (equation (5.3)), respectively (Fig. 5.6b and Supplementary Fig. S5.33). The time constants of the fitted exponentials are shown in Fig. 5.6c, where the asterisk indicates statistical significance (p-value ¡ 0.05) using t-test.

5.5.19 Change in body size before and after feeding

This analysis was only performed for dFB neurons. We asked whether the reset of activity of dFB neurons was linked with how much food flies were ingesting at each feeding event. We therefore used the side view of the fly in the video recorded during the experiment 10 minutes before feeding and 10 minutes after feeding. Using color segmentation in OpenCV, we obtained a mask of the fly that only included the abdomen and the wings (Fig. 5.6d). We did not include the legs or the head in this mask, as flies could for example move the legs or extend the proboscis, producing an enlarged body size. We computed the area of the mask before and after feeding, A_{before} and A_{after}, respectively, and calculated the relative body size change between feeding events, ΔA_r as follows:

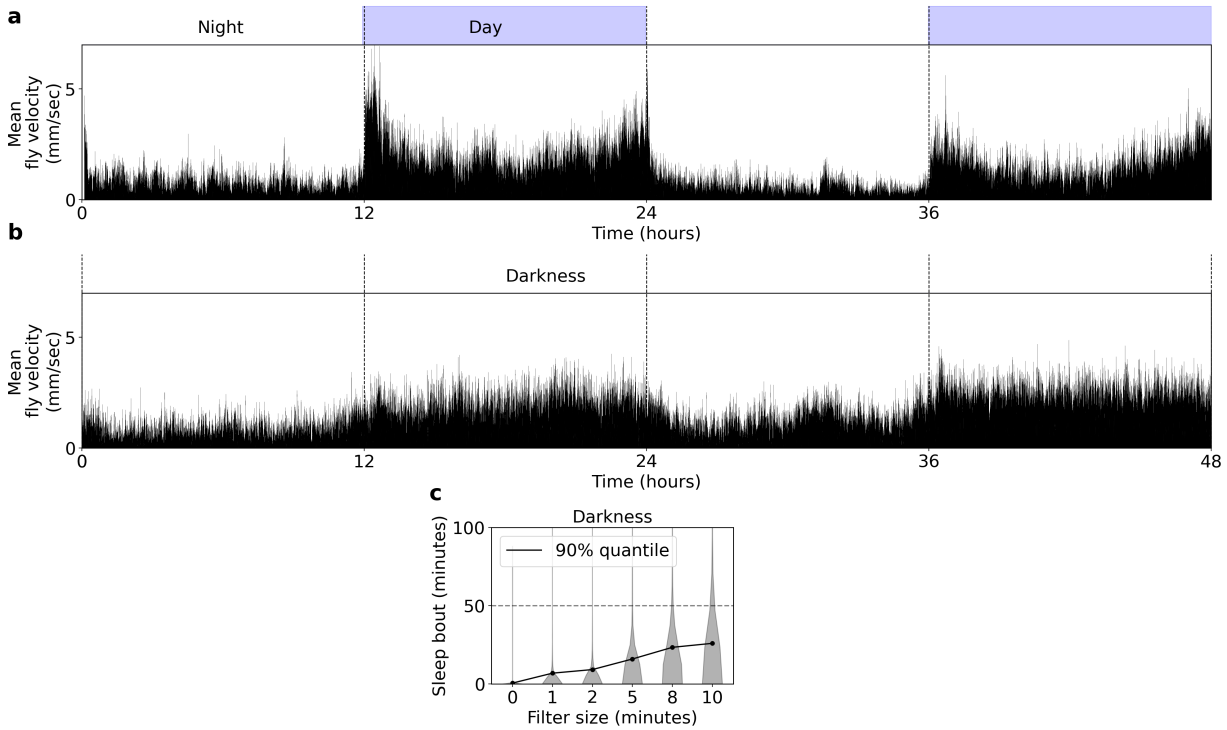
$$\Delta A_r = \frac{A_{after} - A_{before}}{A_{before}} \tag{5.20}$$

The relative body size changes between feeding events were then compared to the corresponding difference in activity of dFB neurons before and after feeding. For this, we averaged the activity of dFB neurons over the last 10 minutes before a feeding event, $< F >_{before}$, and over the next 10 minutes after feeding, $< F >_{after}$, and obtained the difference, $< \Delta F >=< F >_{before} - < F >_{after}$. We obtained a total of 107 pairs of relative body size change and fluorescence change from 8 flies, shown in Fig. 5.6e. We computed

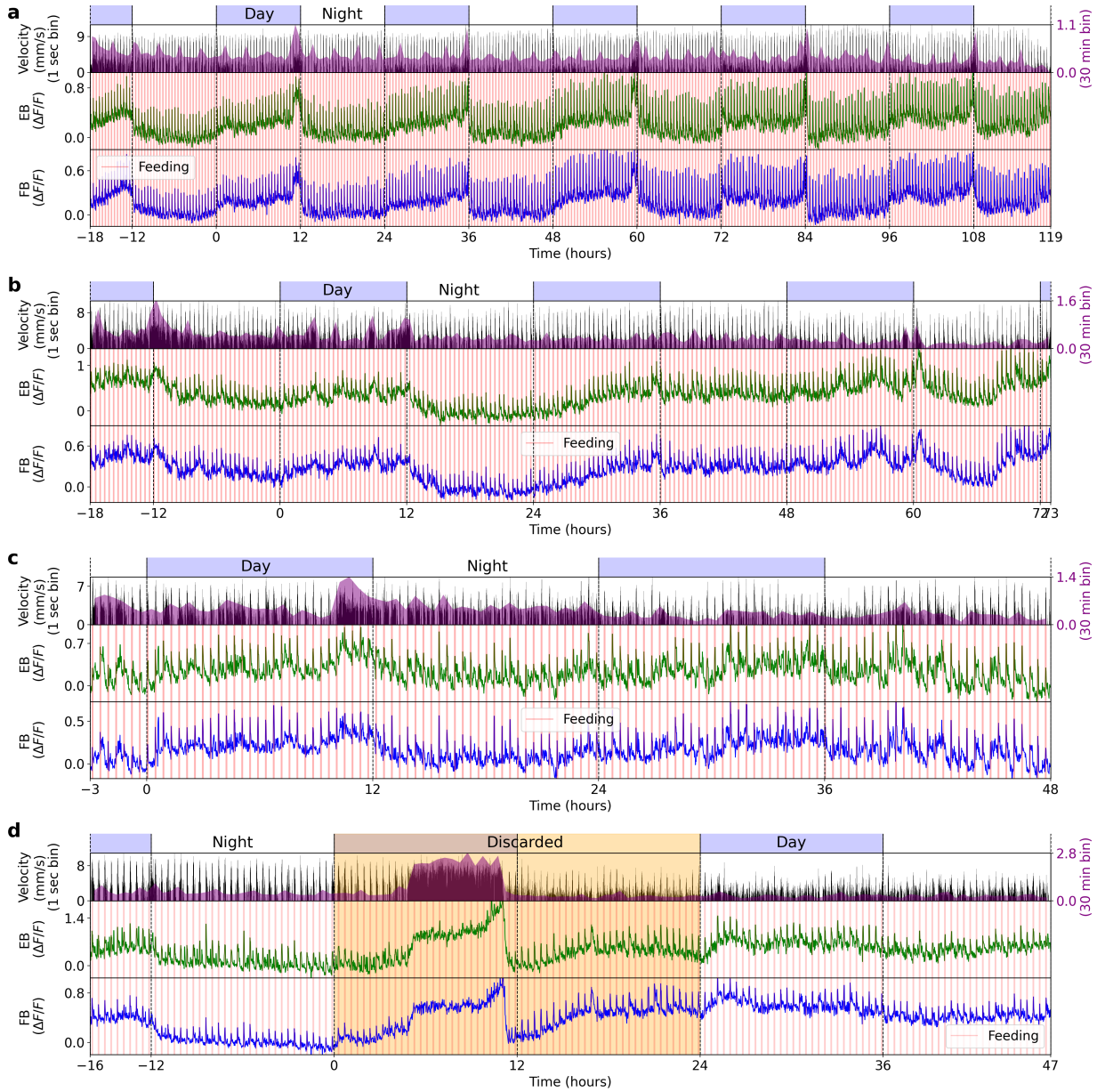
	Correlation coefficient	**p-value**
All pair of points	-0.25	0.011
0% to 50% quantile in relative body size change	-0.56	1.57e-5
50% to 100% quantile in relative body size change	0.09	0.501

Supplementary Table S5.6: Pearson correlation and p-values for the relative body size changes and changes in activity of dFB neurons before and after feeding events.

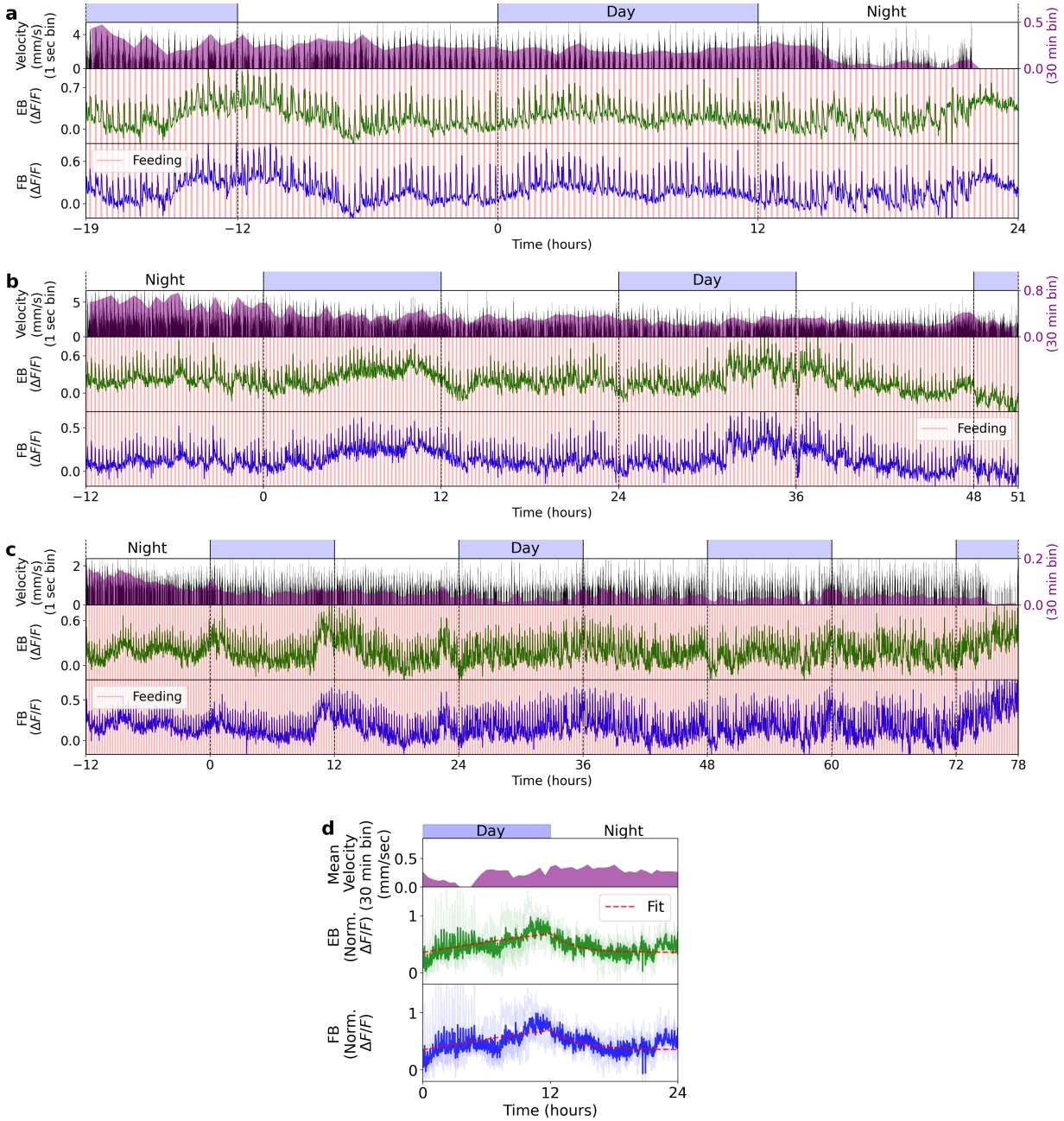
the Pearson correlation between all pairs of points, as well as during the first half of the lowest relative body size change values (50% quantile) and the second half, shown in Table S5.6. While the correlation was positive and statistically significant (p-value ¡ 0.05), this correlation was stronger for lower relative body size change values (Table S5.6).



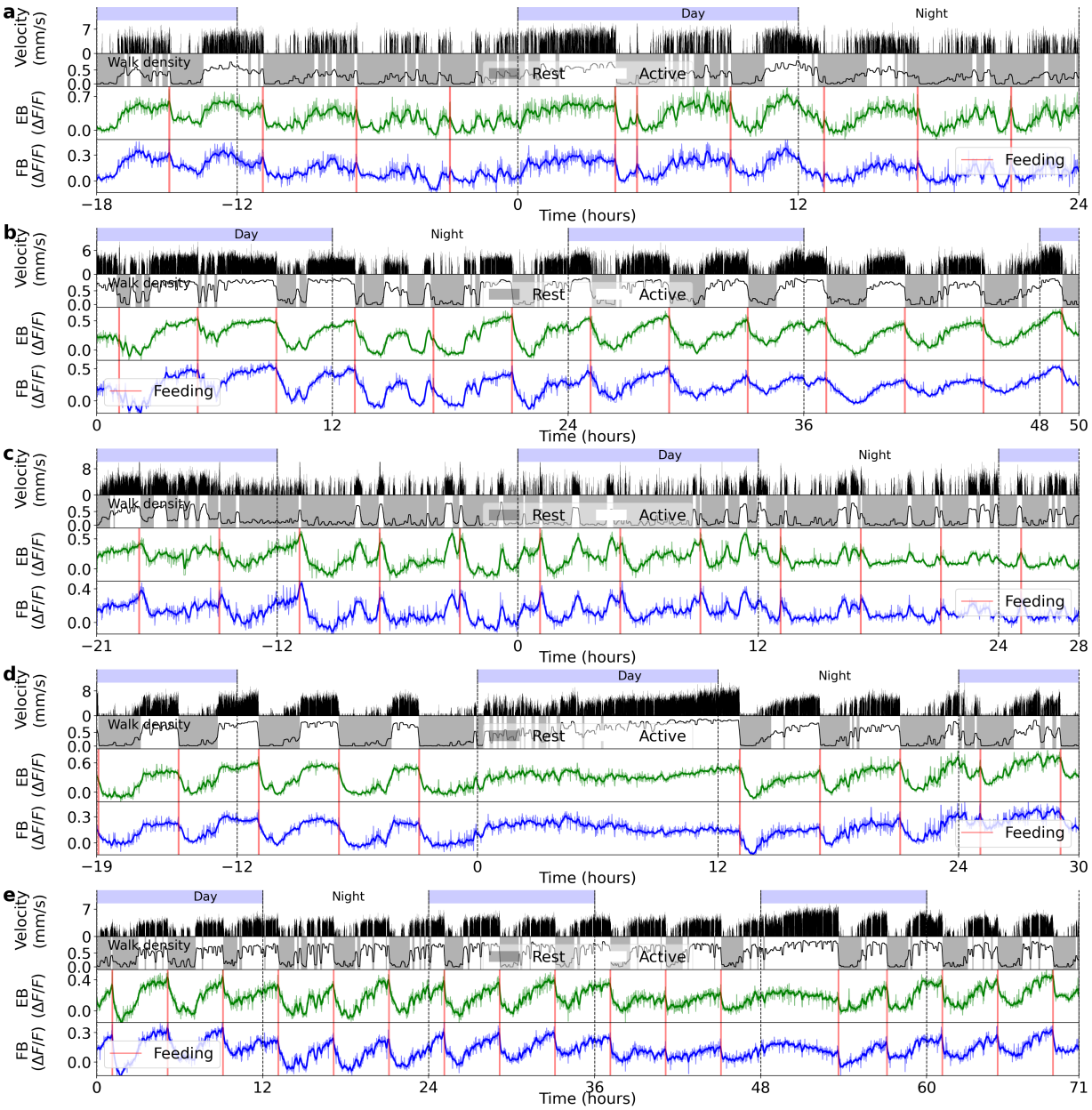
Supplementary Figure S5.1: Behavioral activity of freely moving flies. **a** Mean fly velocity in 1 second bins over 48 hours with 12 hours of light (day) and 12 hours of darkness (night). **b** Same as in a, but in constant darkness. **c d** Distribution of sleep bouts for a total of 15 flies in complete darkness (from b) as function of filter size.



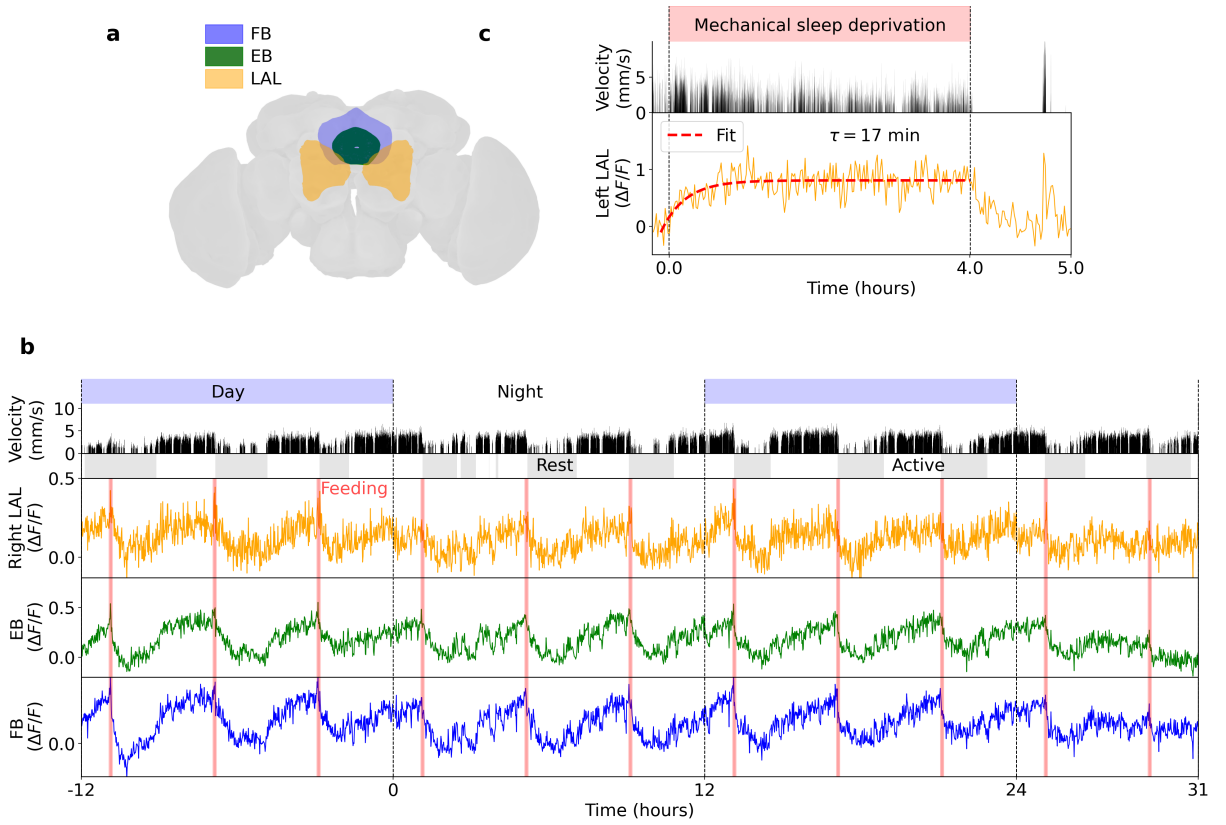
Supplementary Figure S5.2: Four different recordings in ensheathing glia where flies are fed every 26 minutes. **a** Top row: day and night cycle in VR. Second row: in black, velocity of the fly in 1 second bins. Purple: velocity of the fly in 30 minutes bins. Third and fourth row: Calcium activity from ensheathing glia in the EB (green) and FB (blue). Vertical red lines indicate feeding events. **b-d** Same as a. Each panel shows different flies. In panel d, the orange area was discarded from the average in Fig. 5.6j, since there was an epoch of increased walking and calcium activity between hours 5 and 11. The reason for this increase during the recording is unknown, but probably an unexpected event during the recording such as a sudden increase in two-photon laser power or temperature produced it, which made the fly very active. We therefore excluded also the subsequent 12 hours of the experiment where the fly was recovering.



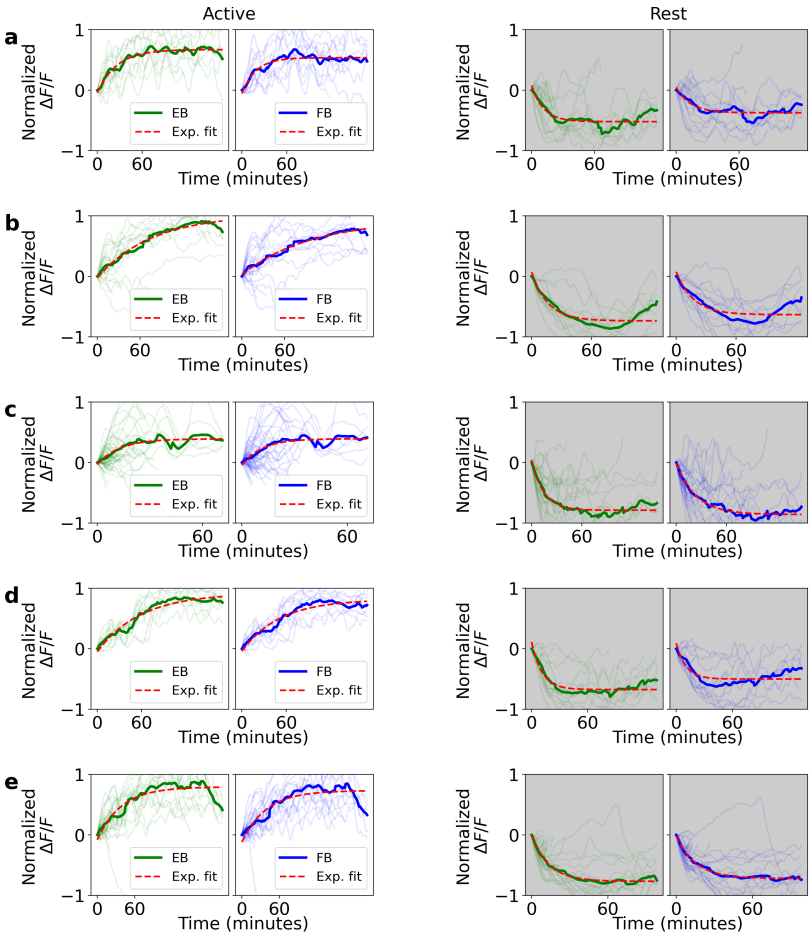
Supplementary Figure S5.3: Three different long-term imaging recordings in ensheathing glia where flies are fed every 16 minutes. **a** Top row: day and night cycle in VR. Second row: in black, velocity of the fly in 1 second bins. Purple: velocity of the fly in 30 minutes bins. Third and fourth row: Calcium activity of ensheathing glia in the EB (green) and FB (blue), respectively. Vertical red lines indicate feeding events. **b, c** Same as a, but for different flies. **d** Average of previous recordings (in a, b and c) over 24 hours. Top row: day and night cycle. Second row: Mean velocity of all flies over 30 minutes bins. Third and fourth row: average glia activity in the EB (green) and FB (blue). Red lines indicate exponential fits during the day and night (see Methods).



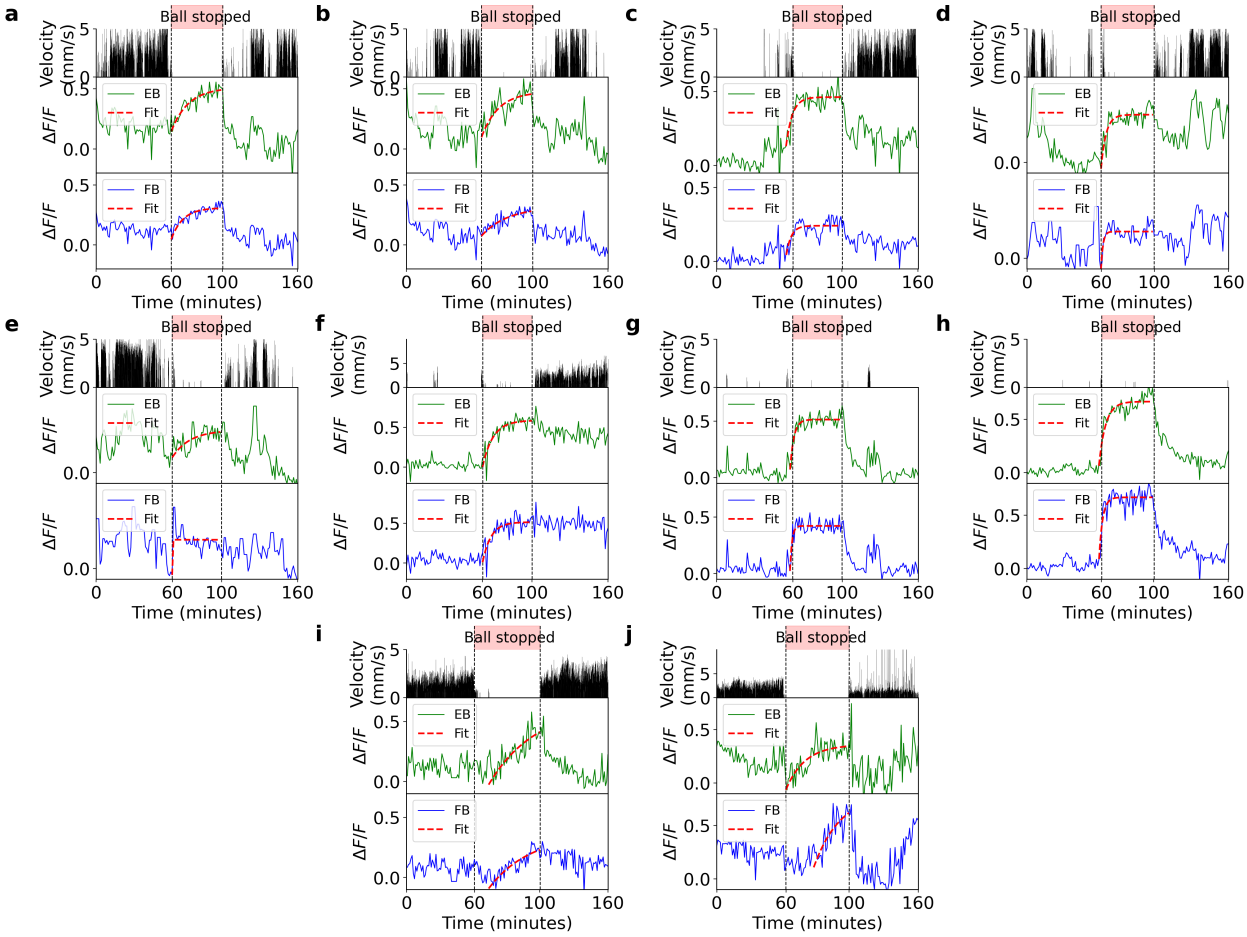
Supplementary Figure S5.4: Five different recordings in ensheathing glia where flies are fed every 4 hours. **a** Top row: day and night cycle in VR. Second row: velocity of the fly in 1 second bins. Third row: walk density (see Methods) and rest (grey region) and active (white region) epochs. Fourth and fifth row: Calcium activity of ensheathing glia in the EB (green) and FB (blue), respectively. Thick lines indicate low-pass filter with a 0.1 hours cut-off period, while vertical red lines represent feeding events. **b-e** Same as a. Each panel shows different flies.



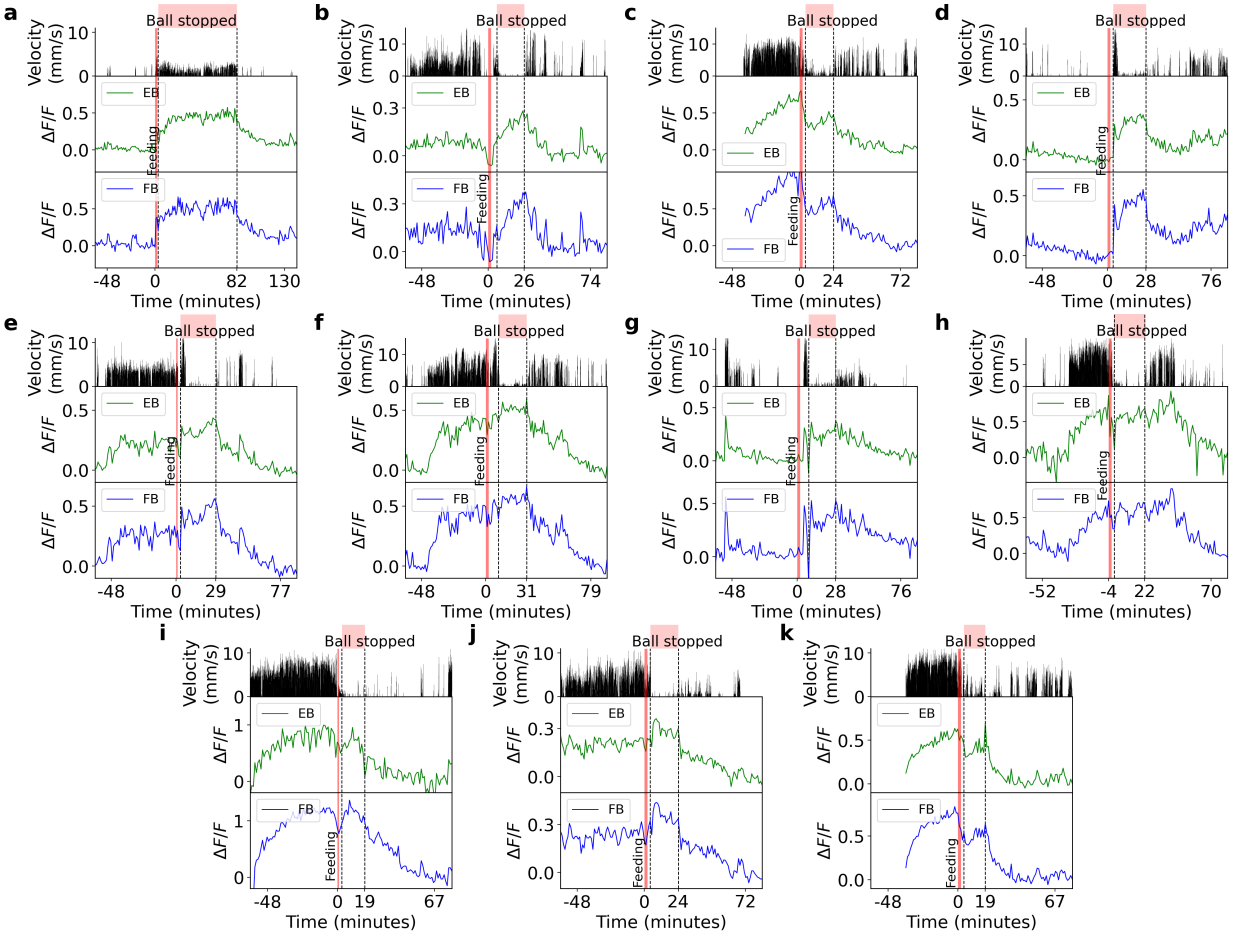
Supplementary Figure S5.5: **a** Schematic of EB, FB and left and right LAL in the fly brain. **b** Activity of LAL, EB and FB over time (fly 5). First row shows day and night cycle in VR, second row shows fly velocity, third row shows rest (grey areas) and active (white areas) behavioral states. The bottom 3 rows show activity in the right LAL and activity in the EB and FB for comparison, respectively. **c** Mechanical sleep deprivation of fly (top row) walking in VR with velocity shown in the second row and the recorded activity in the left LAL (third row). Sleep deprivation was achieved by periodically touching the fly, which was walking in VR, with the tip of a brush on a automated micromanipulator.



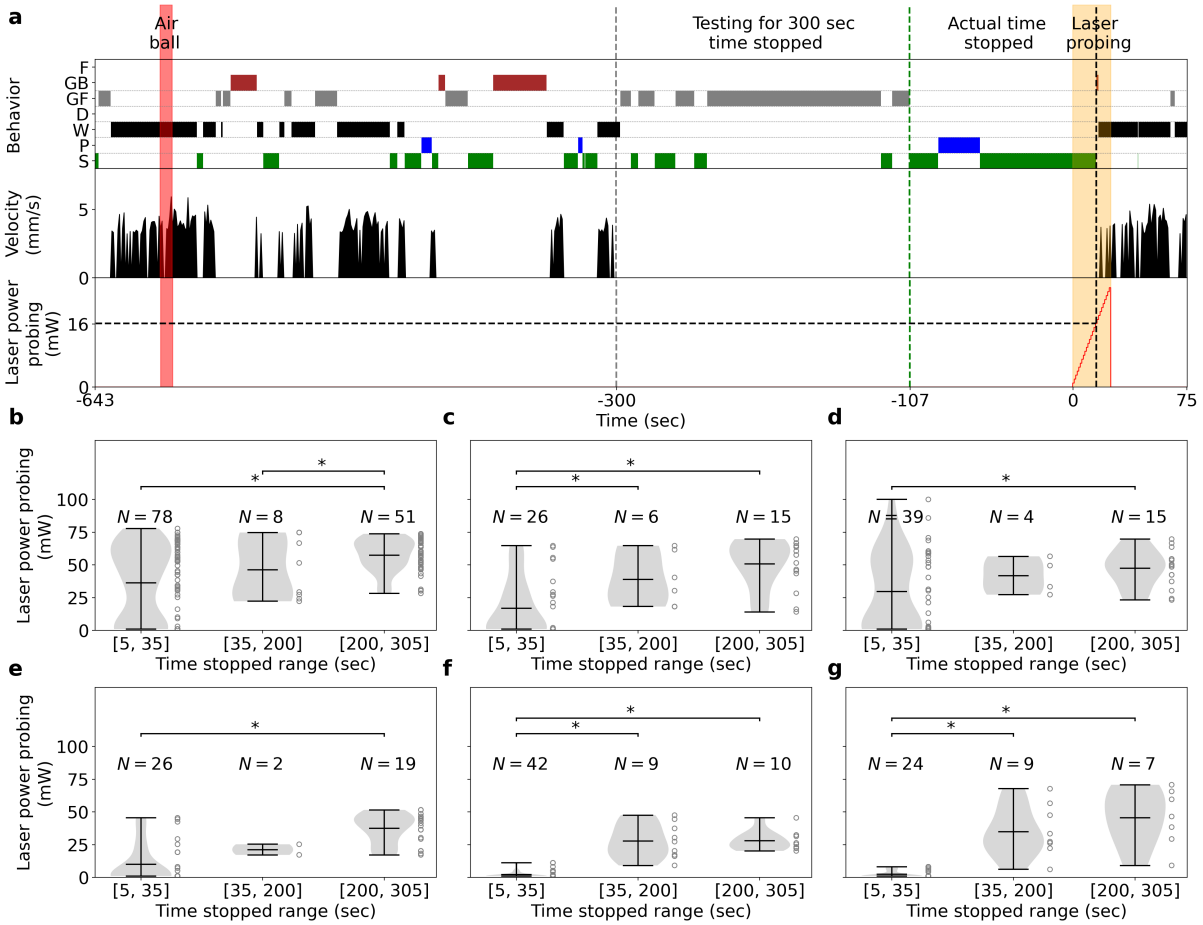
Supplementary Figure S5.6: Normalized fluorescence traces during active and rest epochs for 5 flies. **a** Left side: single (thin lines) and average (thick lines) normalized fluorescence traces in the EB (green) and FB (blue) during active epochs. Red lines indicate exponential fit. Right side: same as left side, but during rest epochs. **b-e** Same as a. Each panel is obtained from different flies.



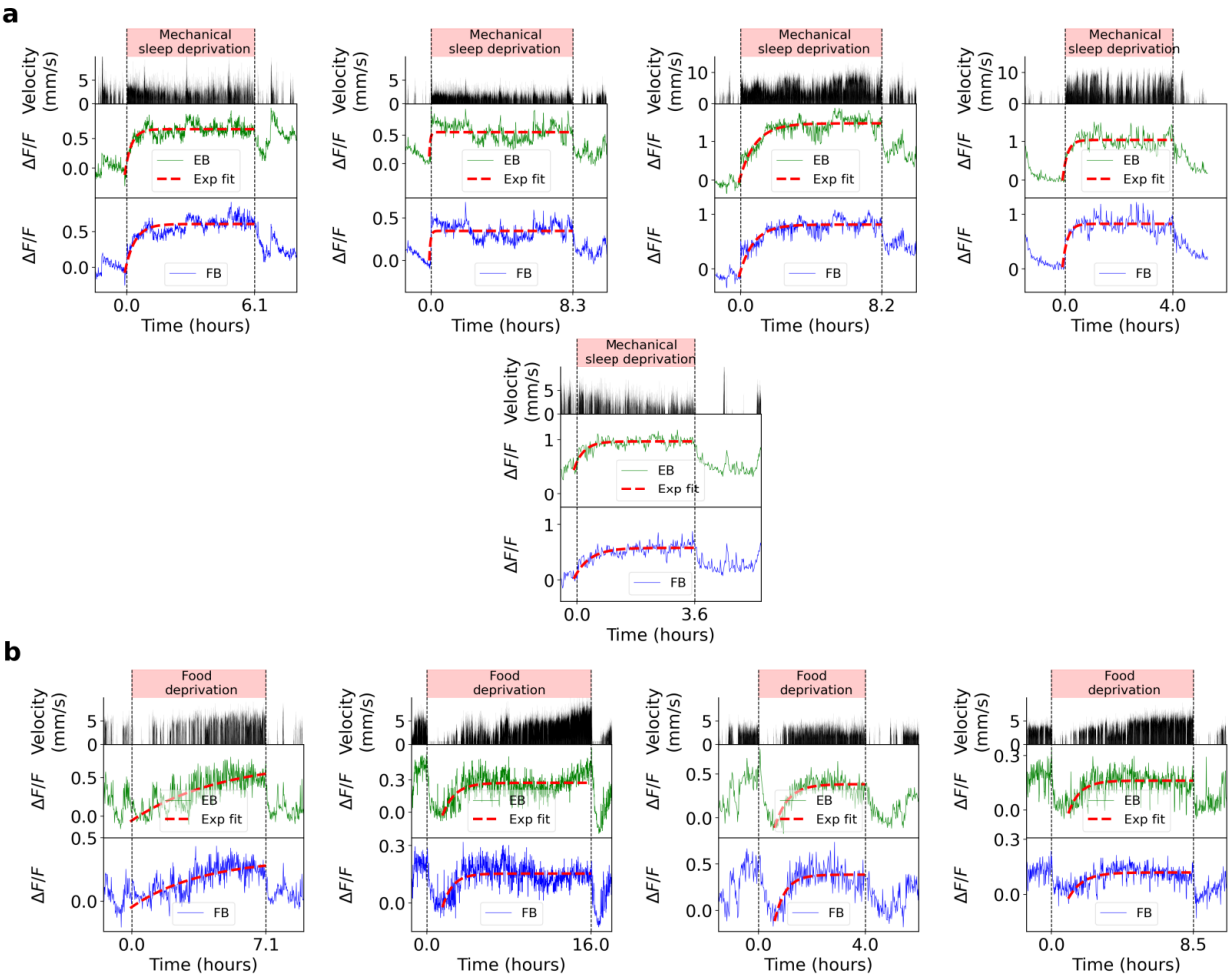
Supplementary Figure S5.7: Trials where the ball was blocked during recordings in glia. **a** First row: time where the ball was stopped (red region). Second row: velocity of fly. Third and fourth row: Calcium activity of ensheathing glia in the EB (green) and FB (blue), respectively. Red lines are exponential fits. **b-j** Same as a. Each panel represents a different trial.



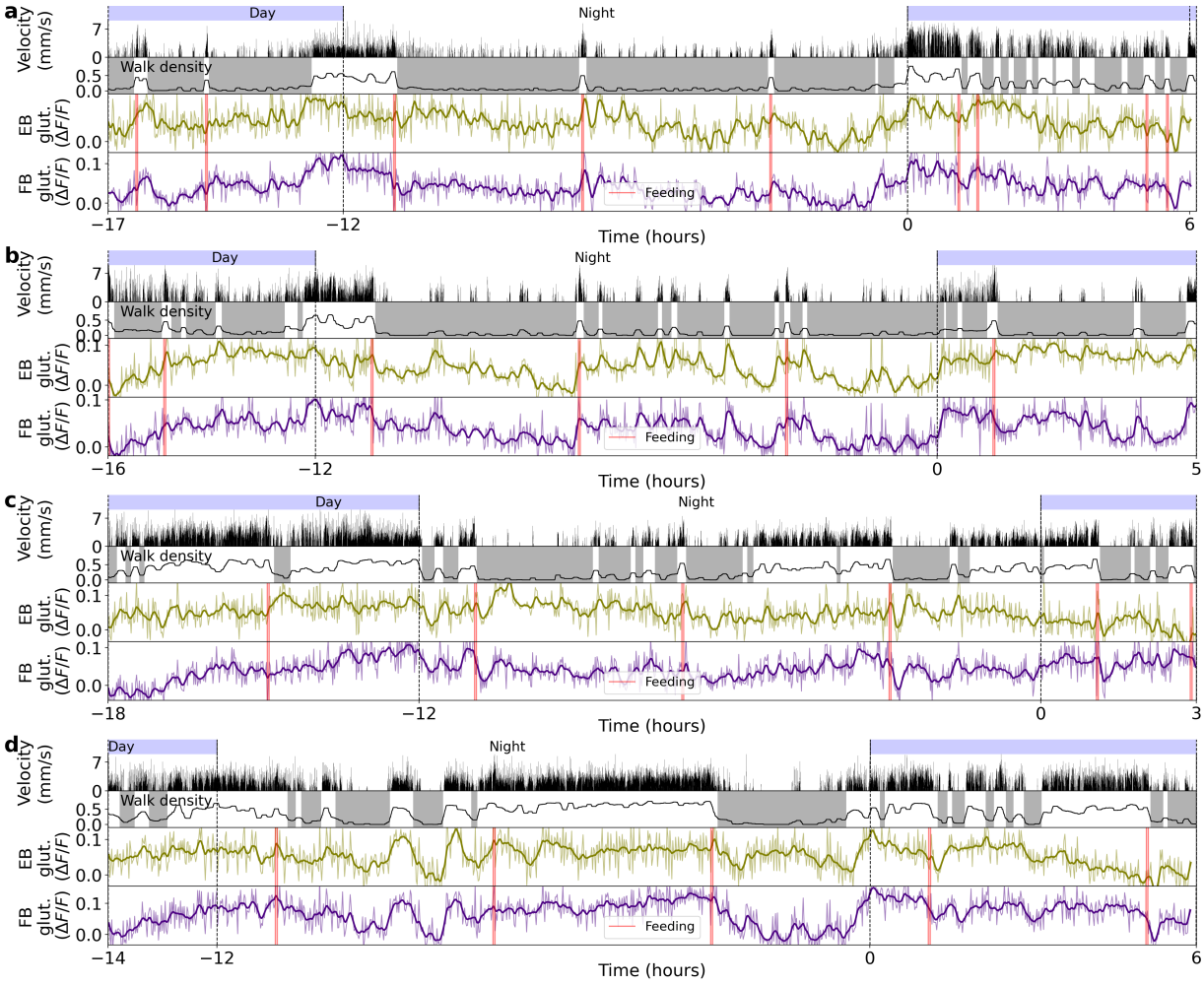
Supplementary Figure S5.8: Trials where the ball was blocked after feeding while activity in glia was recorded. **a** First row: time where the ball was stopped (red region). Second row: velocity of the fly. Third and fourth row: Calcium activity from ensheathing glia in the EB (green) and FB (blue). Vertical red line indicates feeding before blocking the ball. **b-k** Same as a. Each panel represents a different trial.



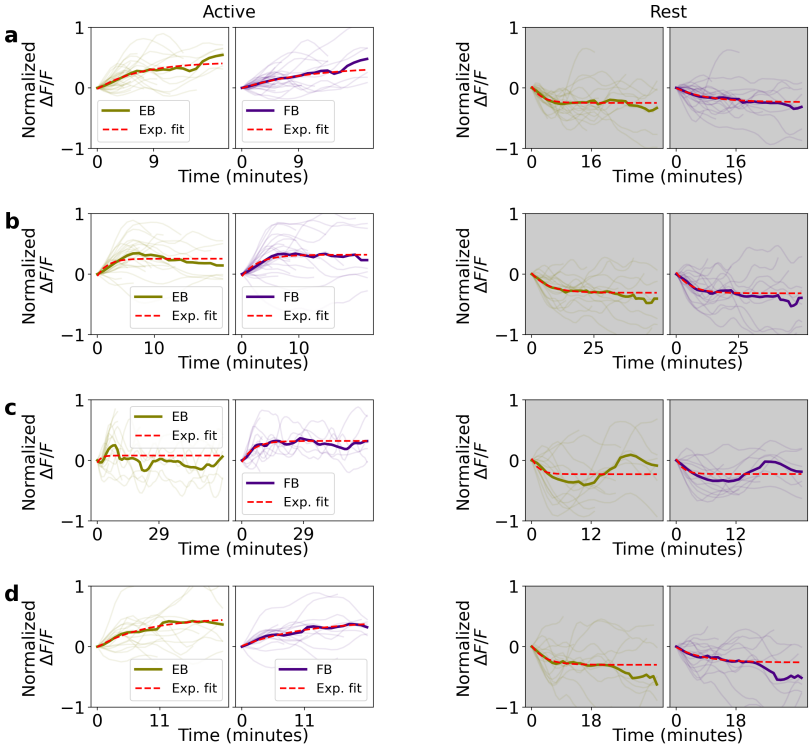
Supplementary Figure S5.9: **a** Example of trial protocol for testing arousal threshold after 300 seconds of immobility of a fly on the ball. First, the air ball is switched on and off (red area) to ensure the fly is awake. Fly stops walking for 300 seconds (fly velocity is zero in second row) and laser (third row) starts probing the arousal threshold of the fly by increasing its power every 0.5 seconds (orange area). Laser is switched off when the fly starts walking again (velocity higher than 0). Post processing: behavior classification (first row) is used to compute the actual time fly was immobile, without grooming (107 seconds in this trial), as well as the actual laser power the fly reacts to by grooming, discomfort, or walking during laser probing (16 mW in this trial). **b,c,d,e,f,g** Distribution of laser powers at which fly wakes up for all trials at different for different durations of immobility for 6 different flies. Asterisks indicate statistical significance using t-test (p-value lower than 0.05).



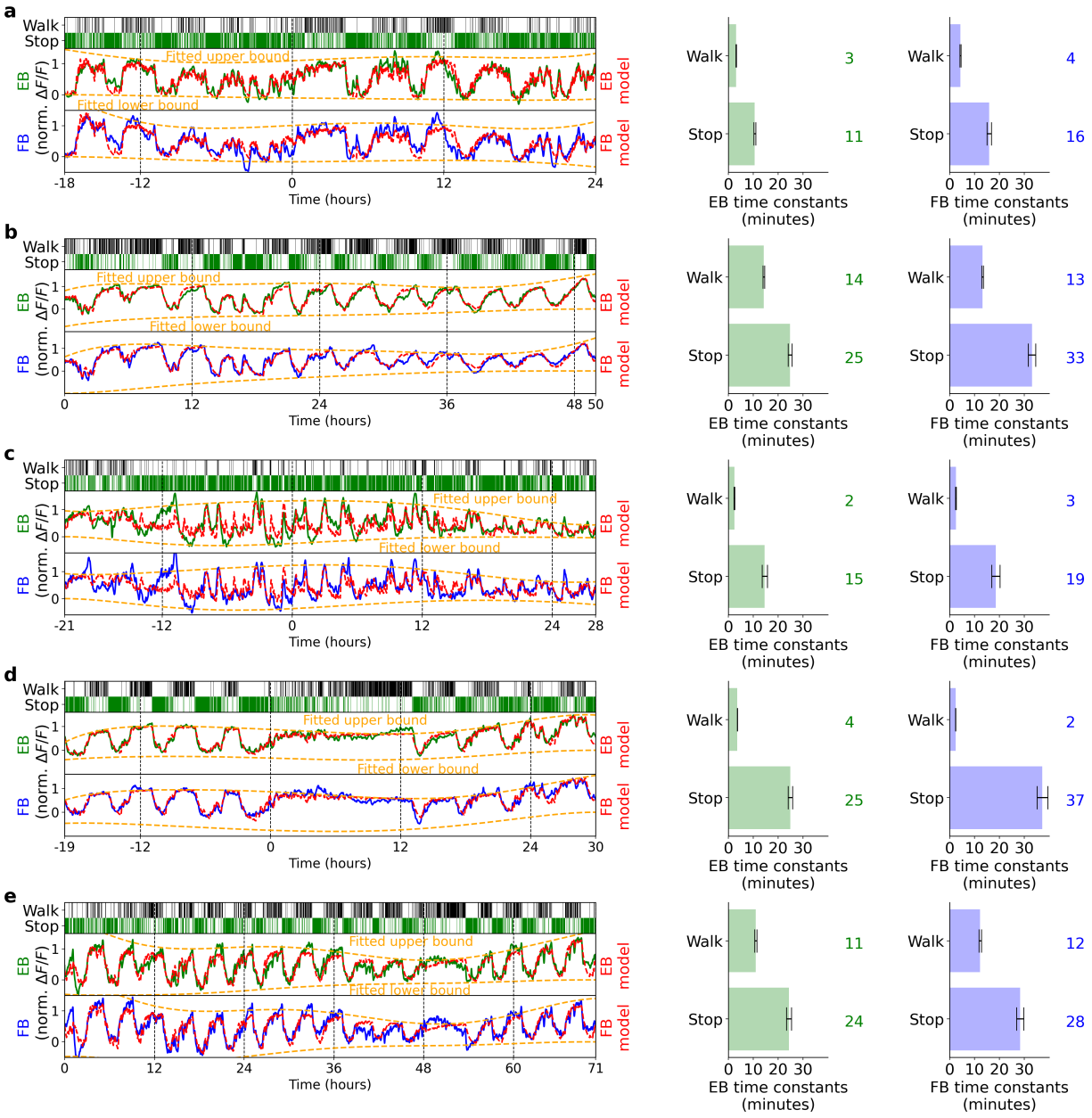
Supplementary Figure S5.10: Glia activity during mechanical sleep deprivation (a) and food deprivation (b) in each trial. Each panel shows the velocity over time (second row), and glia activity in EB (third row) and FB (fourth row) during either mechanical sleep deprivation or food deprivation (first row) for 6 and 4 trials, respectively. Exponential fits are shown for visualization of saturation levels.



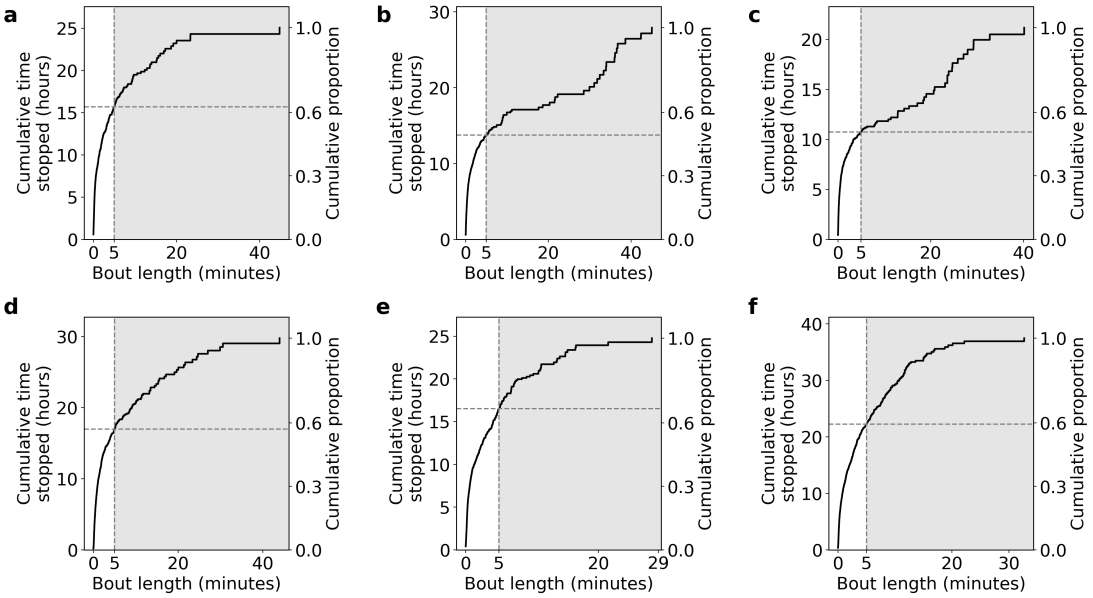
Supplementary Figure S5.11: Four different recordings using glutamate sensor expressed in ensheathing glia. **a** Top row: day and night cycle in VR. Second row: velocity of the fly in 1 second bins. Third row: walk density (see Methods) and rest (grey region) and active (white region) epochs. Fourth and fifth row: Calcium activity from ensheathing glia in EB (green) and FB (blue). Thick lines indicate low-pass filter with a 0.1 hours cut-off period. Vertical red lines represent feeding events. **b-d** Same as a. Each panel shows different flies.



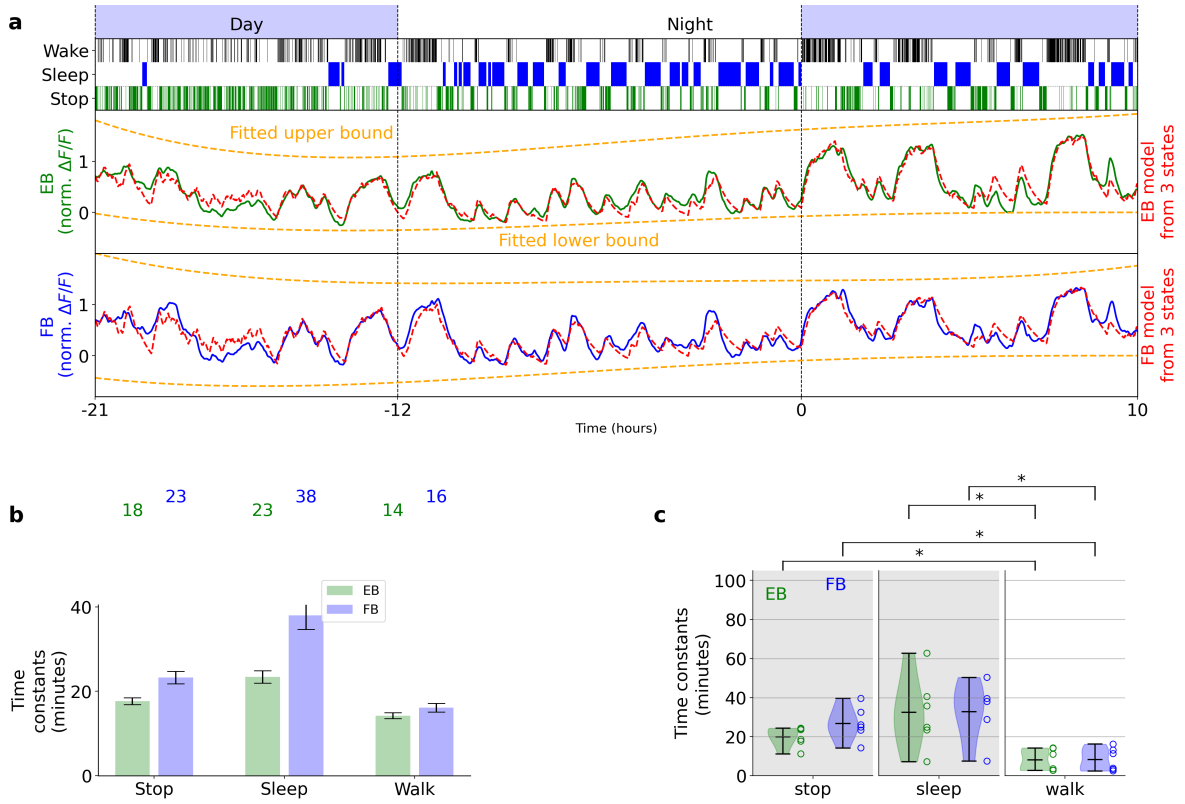
Supplementary Figure S5.12: Normalized fluorescence traces recorded with glutamate sensor during active and rest epochs for 4 flies. **a** Left side: single (thin lines) and average (thick lines) normalized fluorescence traces in EB (olive) and FB (indigo) during active epochs. Red lines indicate exponential fit. Right side: same as left side, but during rest epochs. **b-d** Same as a. Each panel is obtained from different flies.



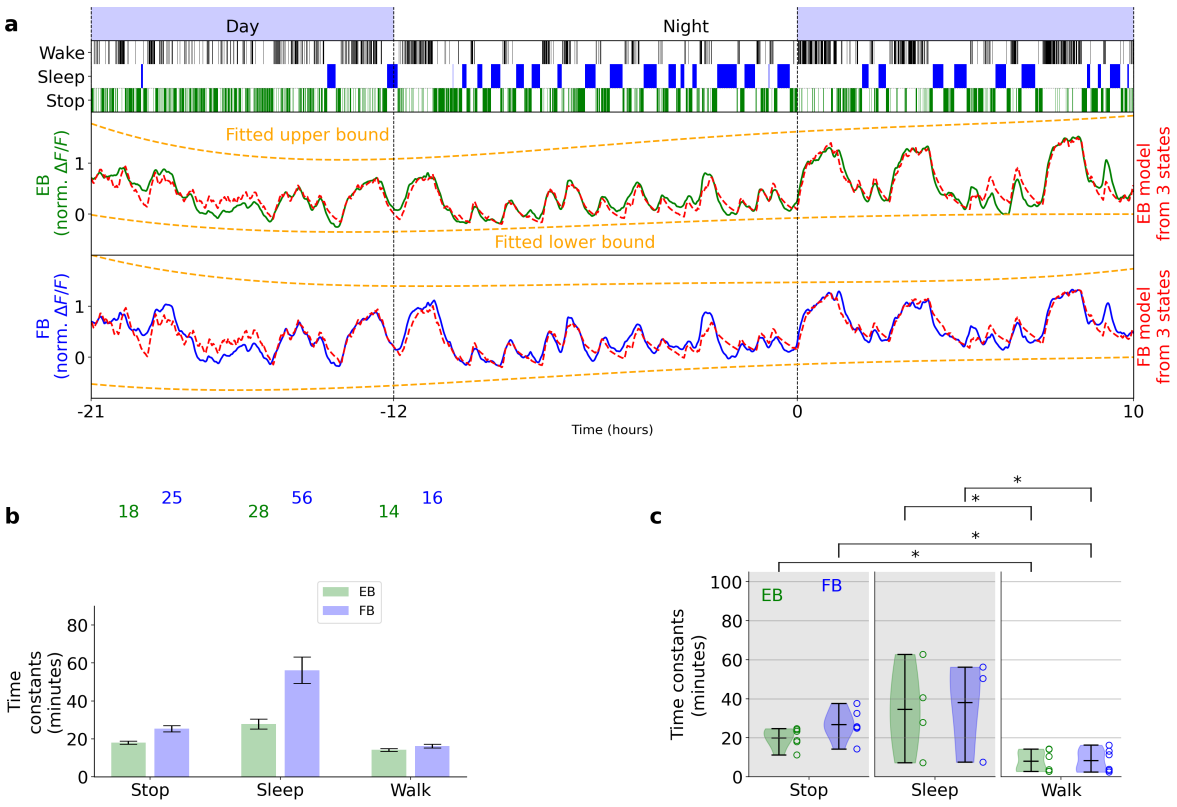
Supplementary Figure S5.13: Fitting glia activity with homeostat 2-state model. **a** Left side: top row shows walking and stopping bouts of a fly. Second and third row: Normalized fluorescence in the EB (green) and FB (blue). Red lines show fitted model, while orange lines represent fitted upper and lower bounds of the model. Right side: fitted time constants from EB (green) and FB activity (blue). Grey lines indicate error bars of estimated time constants (see Methods). Green and blue numbers show approximated value of the fitted time constants. **b-e** Same as a. Each panel represents a fitted model for each fly.



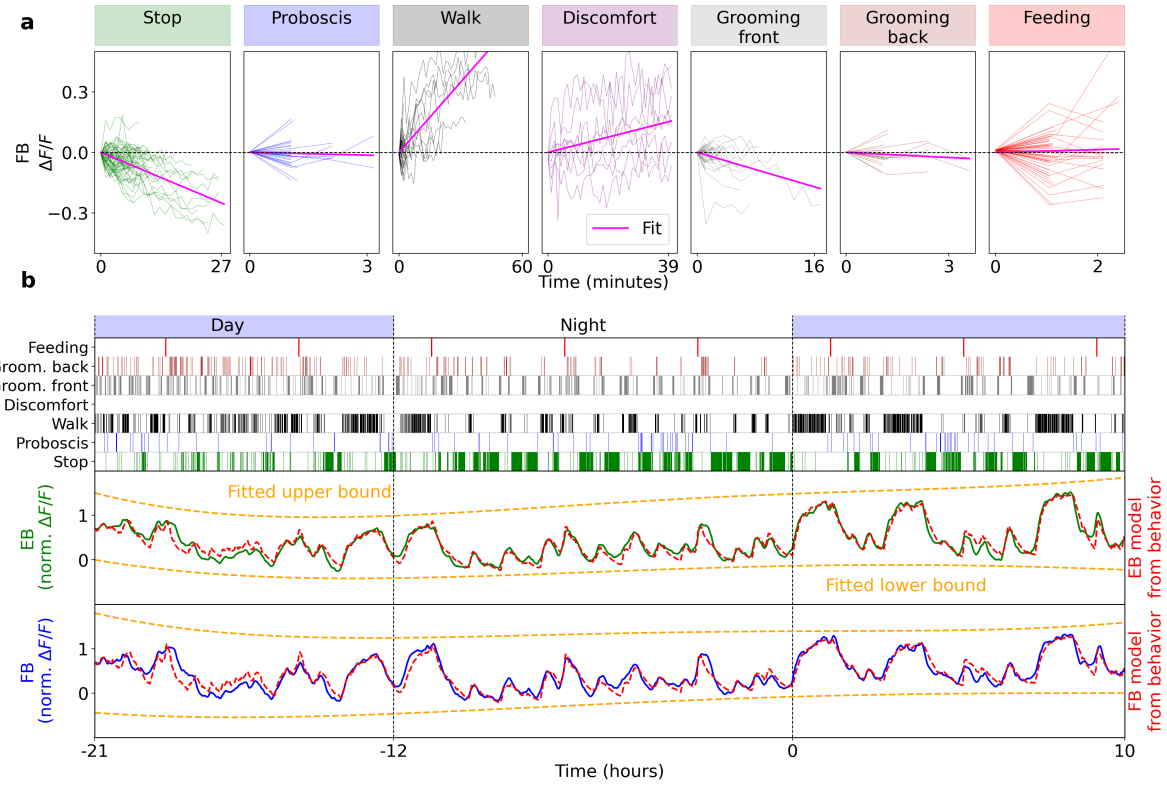
Supplementary Figure S5.14: Cumulative time that each fly stops (left y-axis) and corresponding proportion over the total stop time (right y-axis) as a function of the stop duration (**a-f** correspond to flies 1-6). Bouts where the fly stops for less than 5 minutes (white background) correspond to around 0.6 of the total stop time across flies.



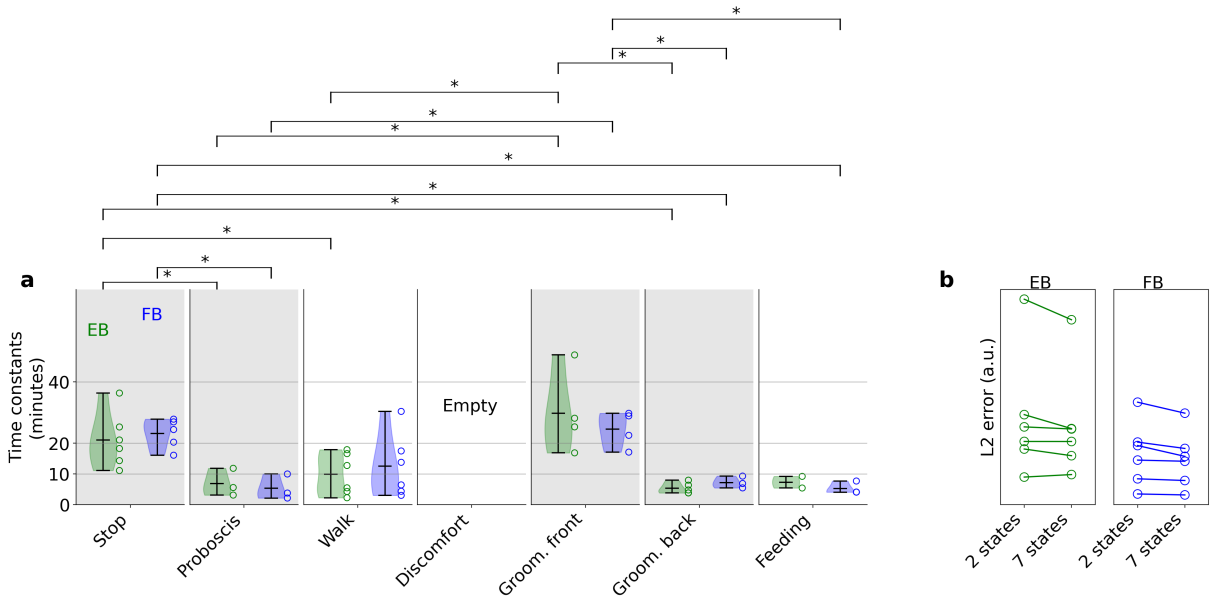
Supplementary Figure S5.15: Fitting glia activity with 3-state homeostat model defining a 'sleep' state as epochs where the fly was stopped for more than 5 minutes. **a** First row shows day and night cycle in VR, second row shows behavior of fly 1 extracted from ball velocity. Sleep is defined as epochs where the fly stops walking for at least 5 minutes. The third and fourth rows show fitting of the 3-state model (red line) and corresponding bounds (orange lines) in EB and FB, respectively. **b** Time constants of 3 states resulting from fitting in a for EB (green) and FB (blue). **c** Distribution of time constants for the 3 states for $N = 6$ flies. Asterisks represent statistical significance between states, with p values lower than 0.05 using t-test.



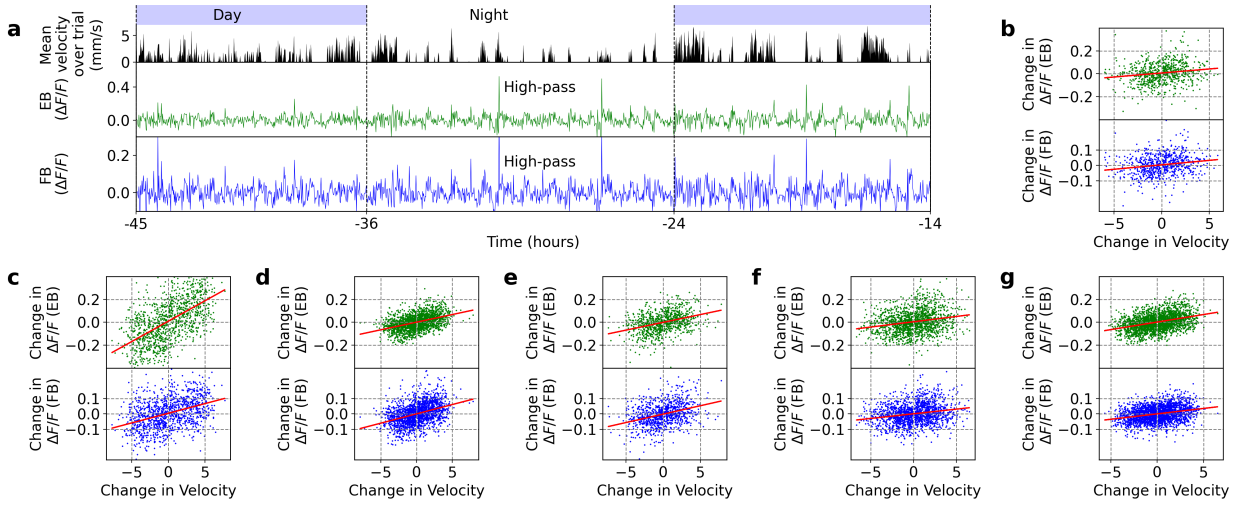
Supplementary Figure S5.16: Fitting glia activity with the 3-state homeostat model with a 'sleep' state define as only after 5 minutes of immobility. Same as Supplementary Fig. S5.15.



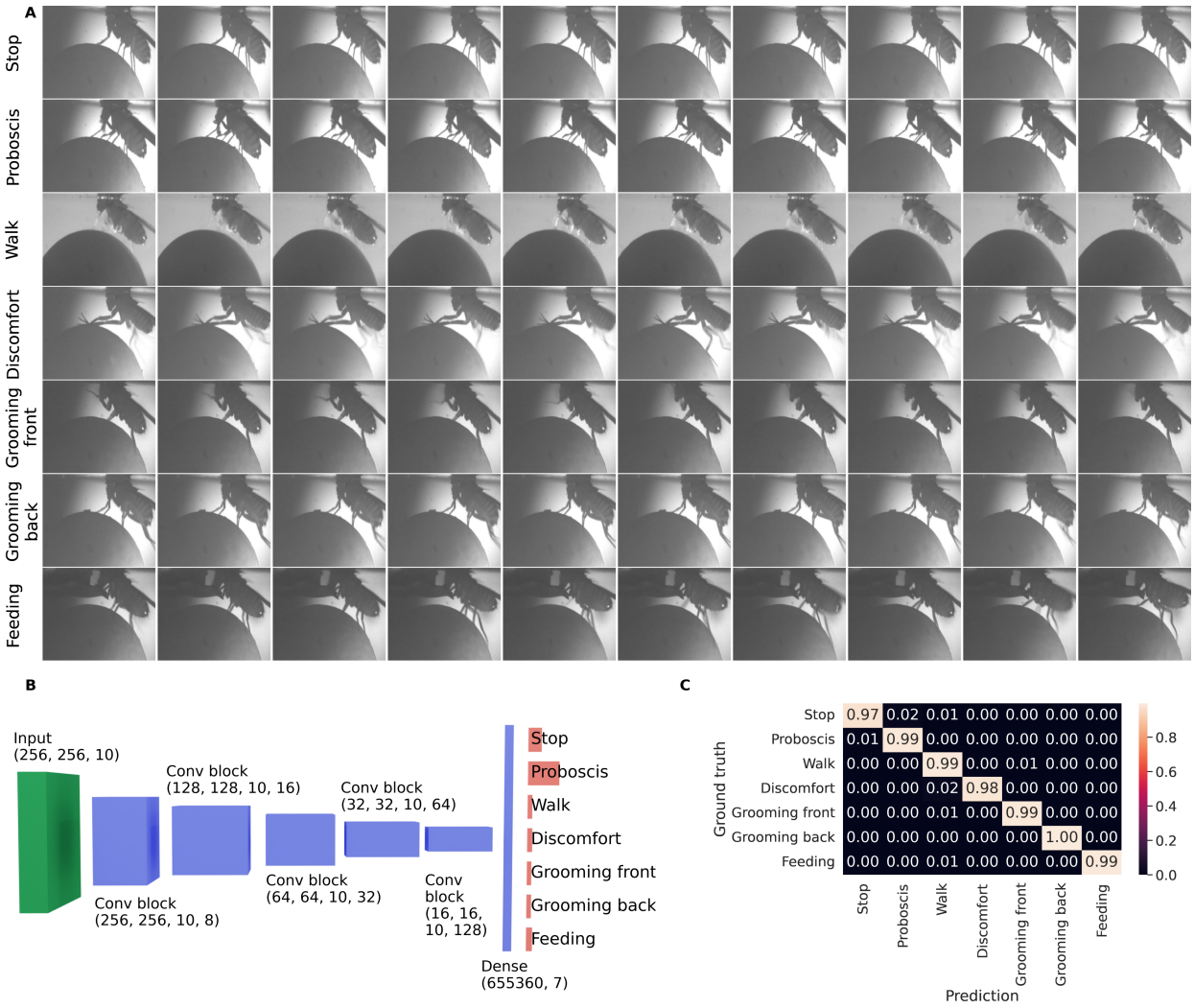
Supplementary Figure S5.17: Fitting calcium activity with 7 behavioral states (seven-state homeostat model). **a** Determination of sign of weights of each behavior for model fitting. Fluorescence FB traces while fly is performing the respective behavior for at least to consecutive fluorescence recordings (2 minutes, combined across flies, see Methods). Purple shows linear fit, negative slope results in negative weight, and *vice versa*. Flies were often walking fast during feeding, likely resulting in increasing fluorescence. Note that scale on y-axes differs between plots. **b** Model fitting with 7 states. Top: day-night cycle. Second row: classified fly behavior over time. Third row: band-pass filtered activity of glia in the EB (green line); red line shows model fit, orange lines show fitted correction of fluorescence levels. Fourth row: same as third row for FB.



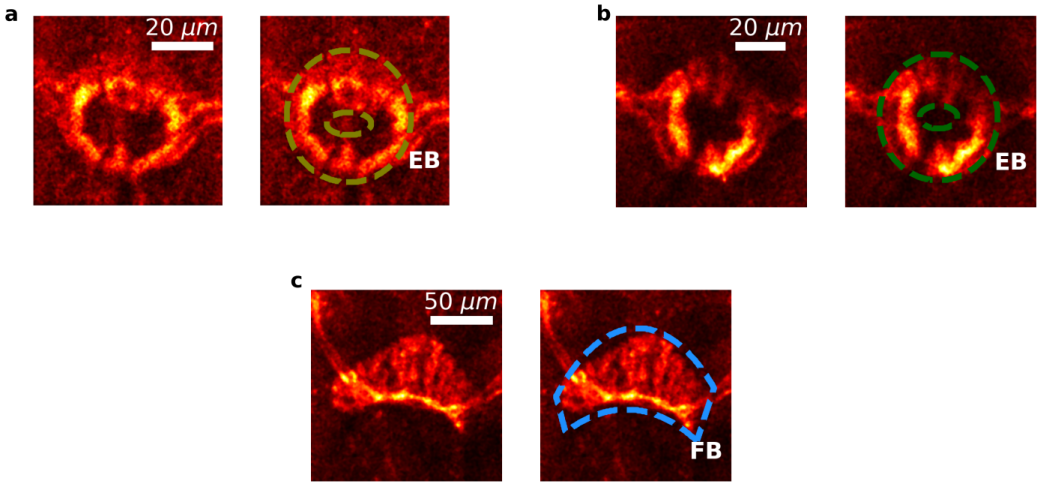
Supplementary Figure S5.18: Significance levels for behaviors in 7-state homeostat model. Time constants of the 7 classified behaviors fitted in 7-state model for the EB (green) and FB (blue, Supplementary Fig. S5.17a). Only time constants with an error of less than 20% were included in the histograms (see Methods). Asterisks include statistical significance between all possible pairs of fitted time constants, based on p-values lower than 0.05 using t-test. **b** Comparison between the 2-state and 7-state models in the EB (left) and FB (right). L2-error between fit and data for $N = 6$ flies.



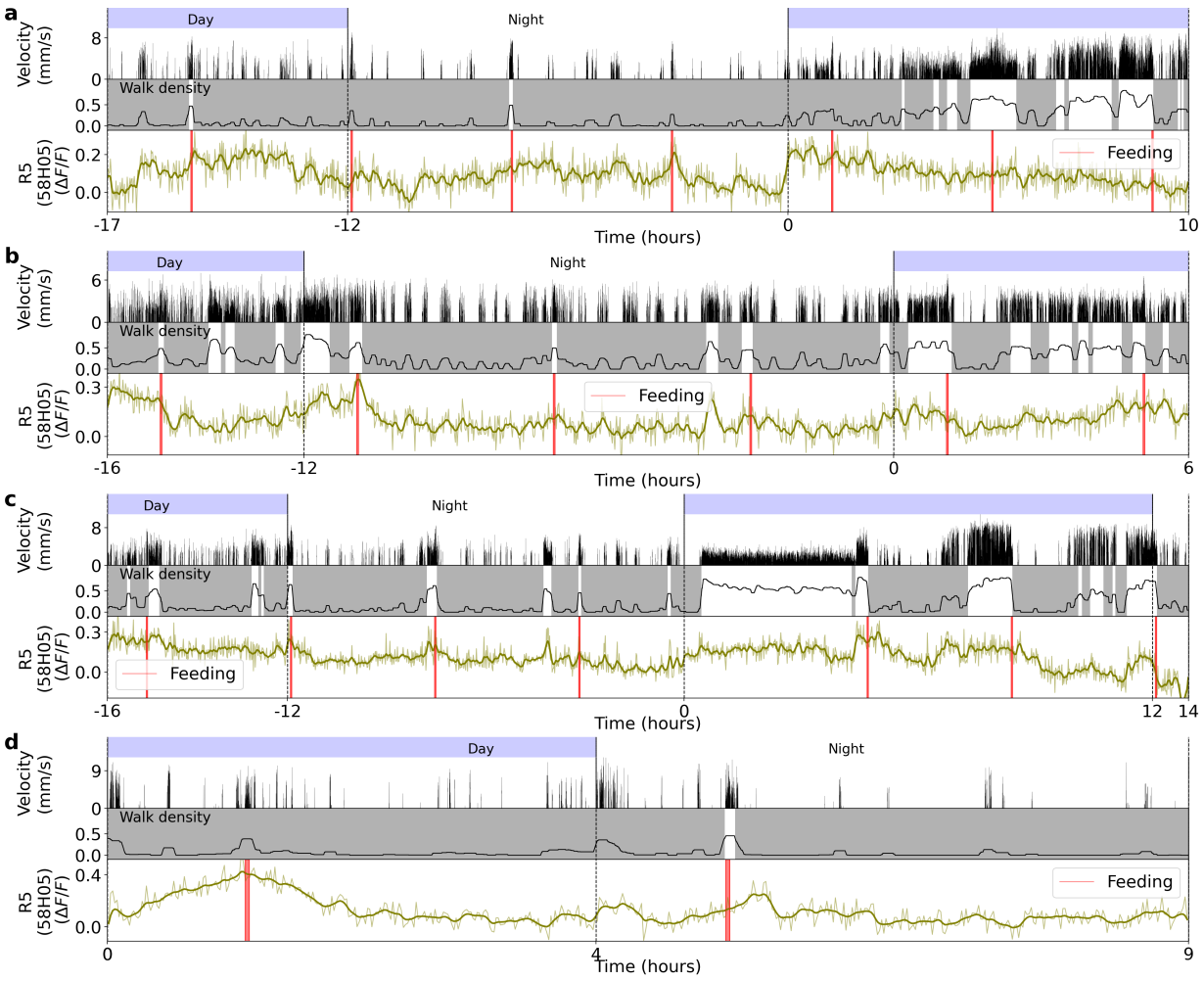
Supplementary Figure S5.19: **a** Top row shows day and night cycle in VR over time and second row shows mean velocity during recording epoch (1 second). Second and third row show fluorescence signals in the EB and FB, respectively. Fluorescence was filtered with a high-pass filter for periods higher than 0.5 hours. **b** Correlation between mean velocity over trial and high-pass filtered fluorescence. **c-g** Same as b but for 5 different flies.



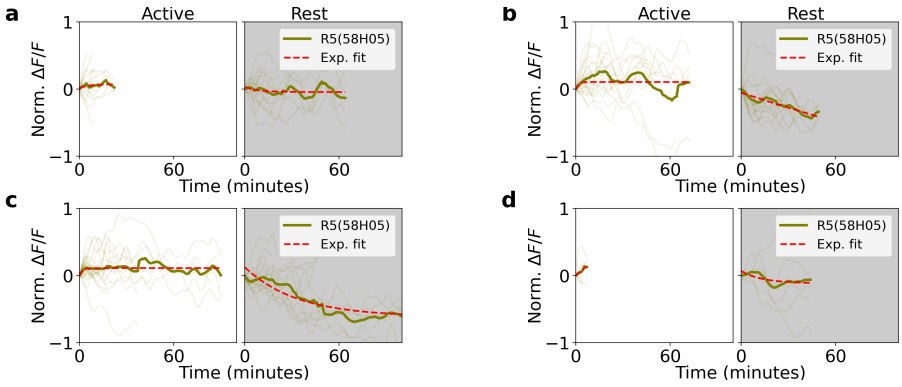
Supplementary Figure S5.20: Classification of the behavior of the fly on the ball during long-term imaging. **a** A 3D CNN with 10 consecutive frames of images with a side view of the fly on the ball is used to classify 7 different behaviors (y-axis). Each row in the plot corresponds to 10 consecutive frames where the fly performs the labeled behavior. **b** Architecture of the 3D CNN. **c** Confusion matrix for each behavior for prediction of the 3D CNN (x-axis) on a test dataset that was manually labeled (ground truth along y-axis).



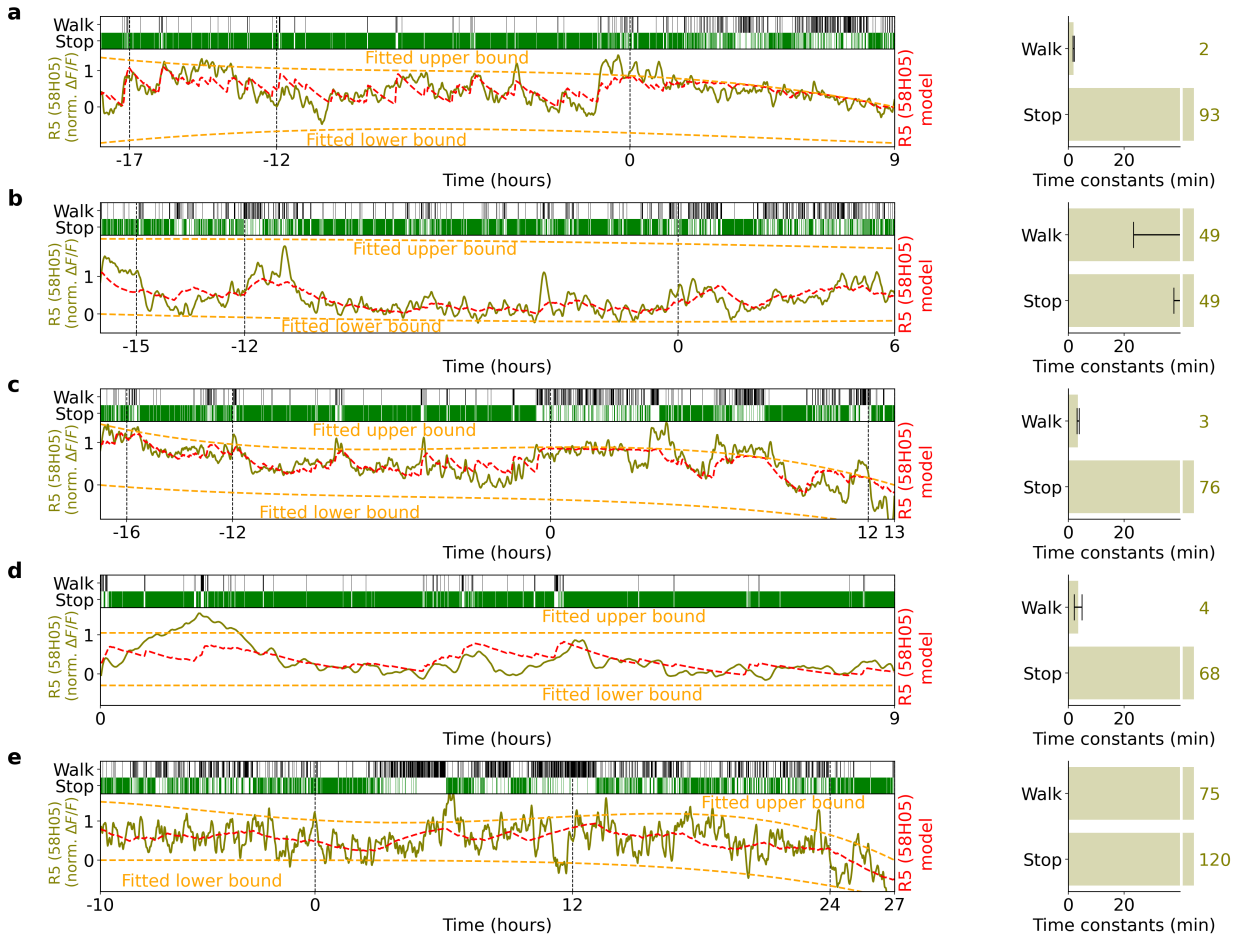
Supplementary Figure S5.21: Regions of interests (ROIs) for recordings of R5 and dFB neurons. **a** On the left, R5 neurons labeled by 58H05-GAL4. On the right, ROI along the ring-shaped projections of R5 neurons for calculating fluorescence changes. **b** Same as in a, but for R5 neurons labeled by 88F06-GAL4. **c** Same as a and b, but for dFB neurons labeled by 23E10-GAL4.



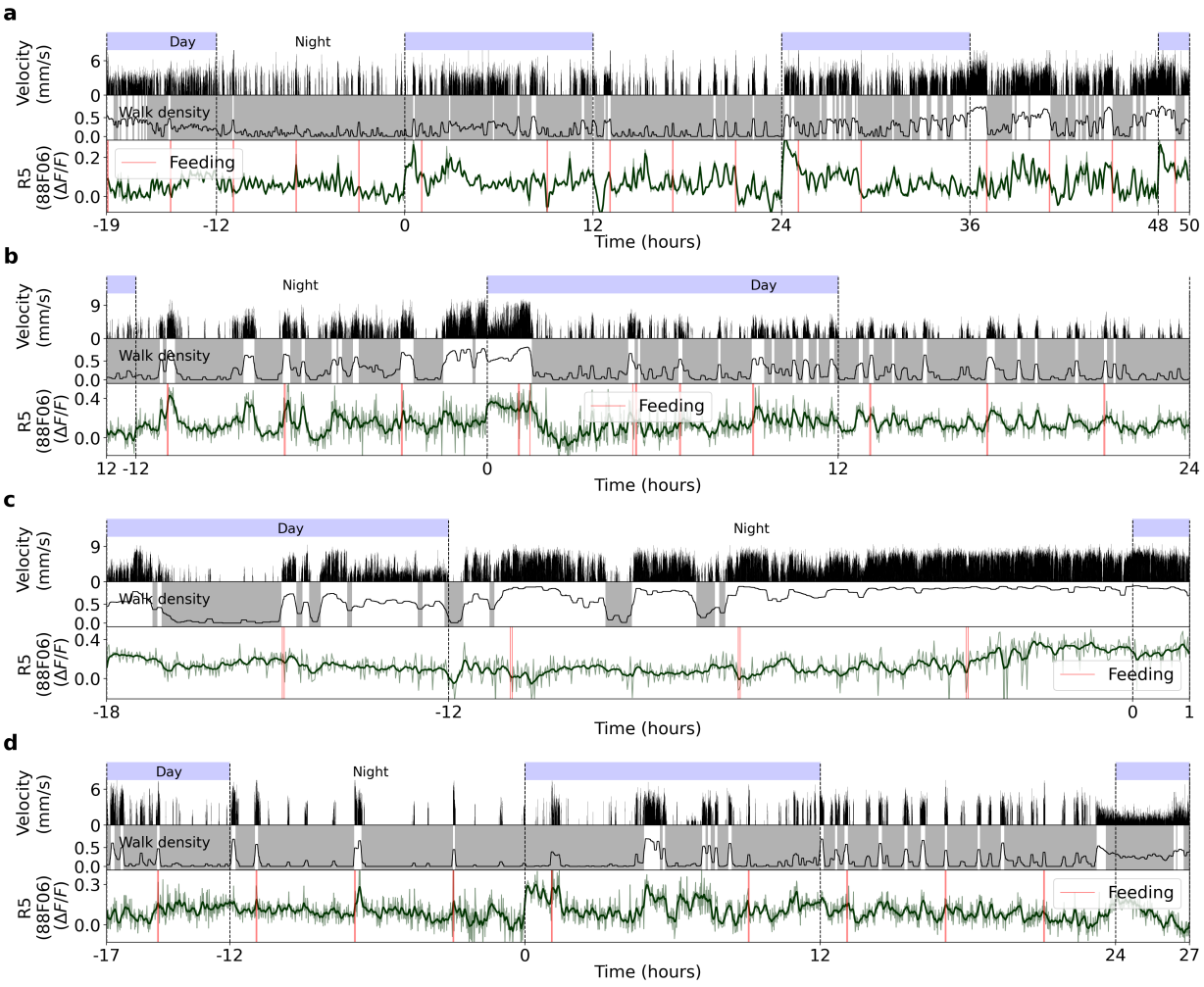
Supplementary Figure S5.22: Four different long-term imaging recordings of calcium activity in R5 neurons labeled by 58H05-GAL4. **a** Top row: day and night cycle from the VR. Second row: velocity of the fly in 1 second bins. Third row: walk density (see Methods) and rest (grey region) and active (white region) epochs. Fourth row: Calcium activity from R5 neurons. The thick line indicates a low-pass filter with a 0.1 hours cut-off period. Vertical red lines represent feeding events. **b-d** Same as a. Each panel shows different flies.



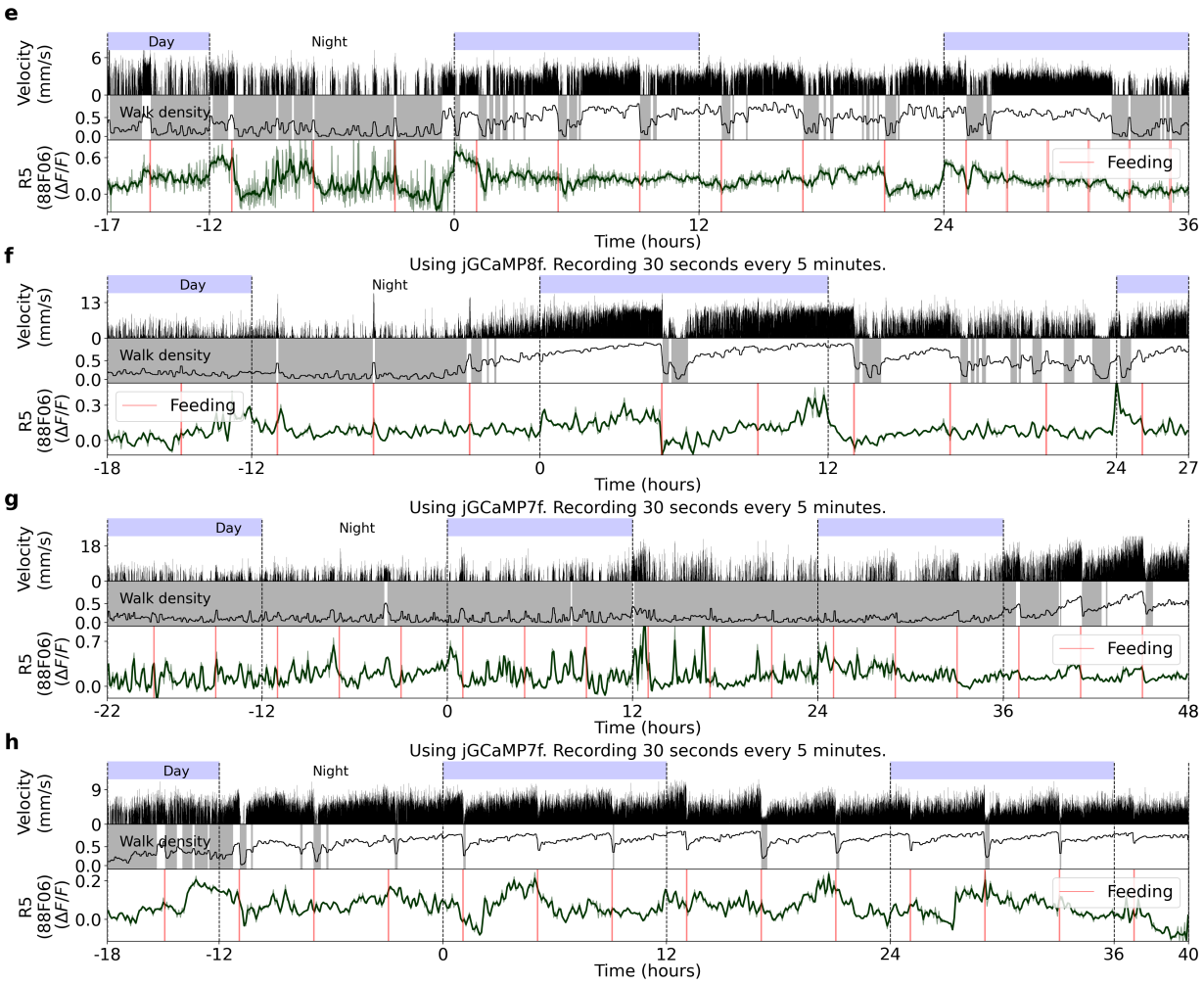
Supplementary Figure S5.23: Normalized fluorescence traces during active and rest epochs for four flies in R5 neurons (labeled by 58H05-GAL4). **a** Left side: single (thin lines) and average (thick lines) normalized fluorescence traces from activity in R5 neurons during active epochs. Red lines indicate exponential fit. Right side: the same as the left side, but during rest epochs. **b-d** Same as a. Each panel is obtained from different flies.



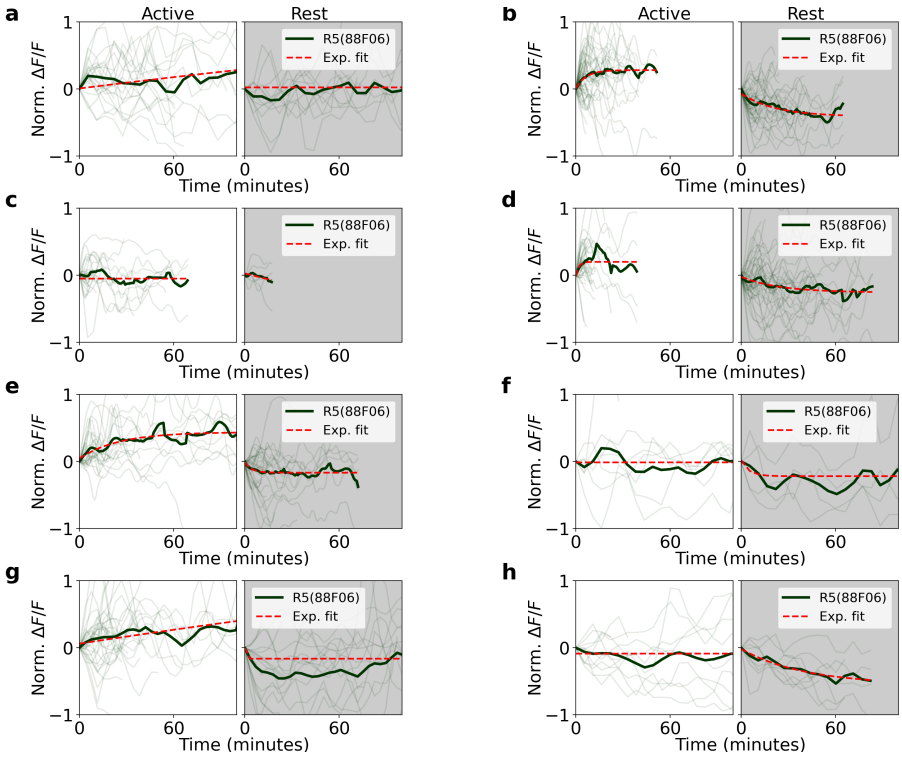
Supplementary Figure S5.24: Fitting calcium activity from R5 neurons (labeled by 58H05-GAL4) with the 2-state homeostat model. **a** Left side: the top row shows walking and stopping bouts of a fly. Second row: Normalized fluorescence from R5 neurons. Red lines show the fitted model, while orange lines represent the fitted upper and lower bounds of the model. Right side: fitted time constants from the model. Grey lines indicate error bars of the estimated time constants (see Methods), while colored numbers show the approximated value of the fitted time constants. **b-d** Same as a. Each panel represents a fitted model for each fly.



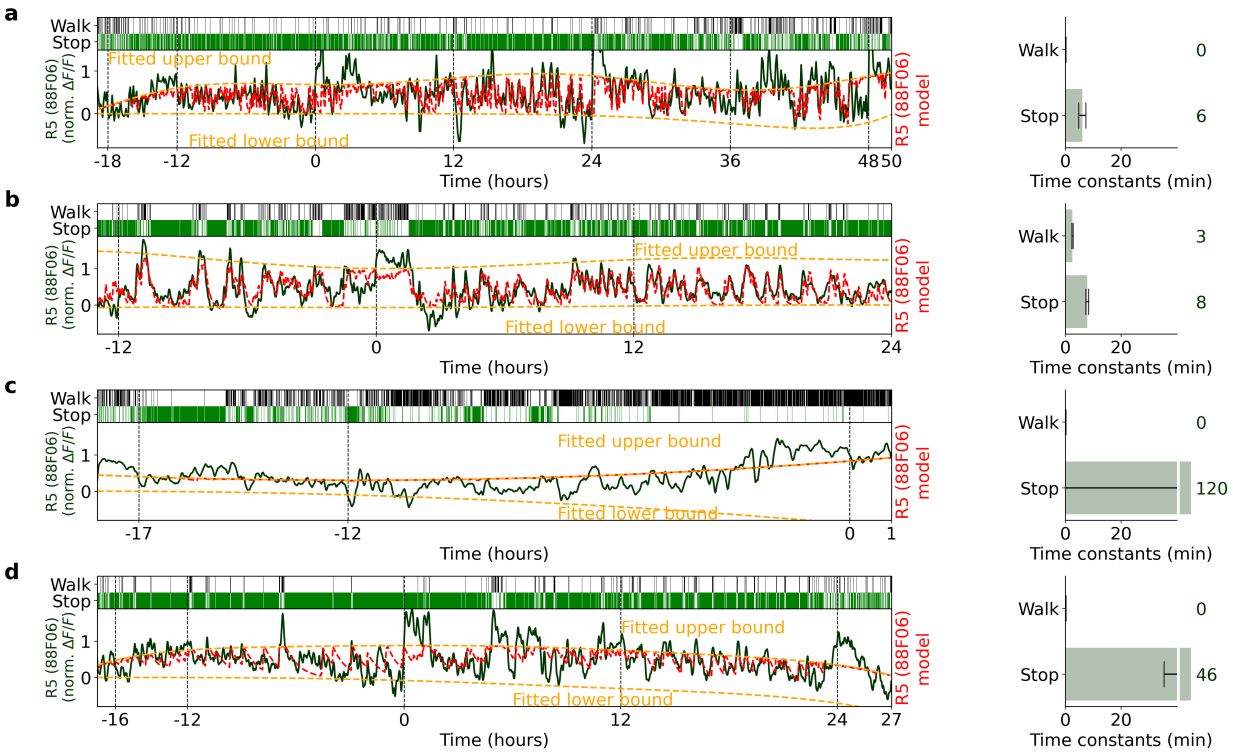
Supplementary Figure S5.25: Four different recordings of calcium activity in R5 neurons labeled by 88F06-GAL4. **a** Top row: day and night cycle in VR. Second row: velocity of fly in 1 second bins. Third row: walk density (see Methods), rest (grey region) and active (white region) epochs. Fourth row: Calcium activity of R5 neurons. Thick line indicates low-pass filtering with a 0.1 hours cut-off period. Vertical red lines represent feeding events. **b-d** Same as a. Each panel shows different flies.



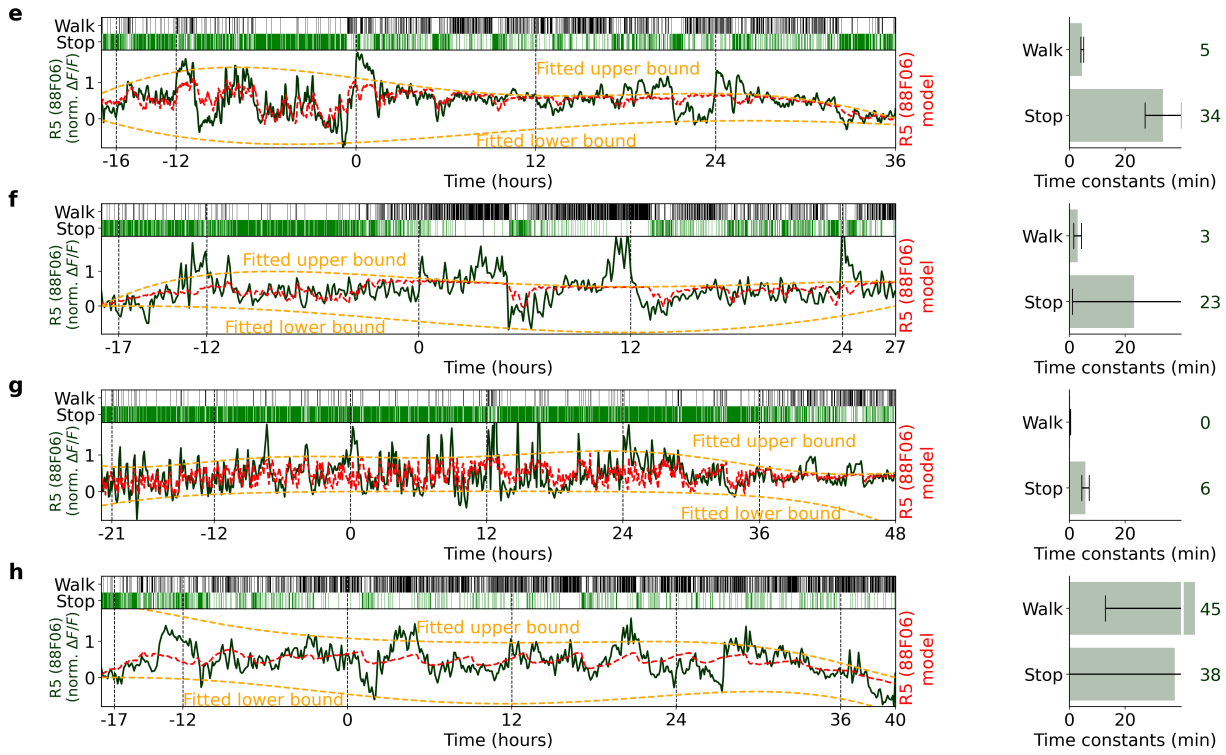
Supplementary Figure S5.26: Four more recordings of calcium activity in R5 neurons labeled by 88F06-GAL4. Same as Supplementary Fig. S5.25



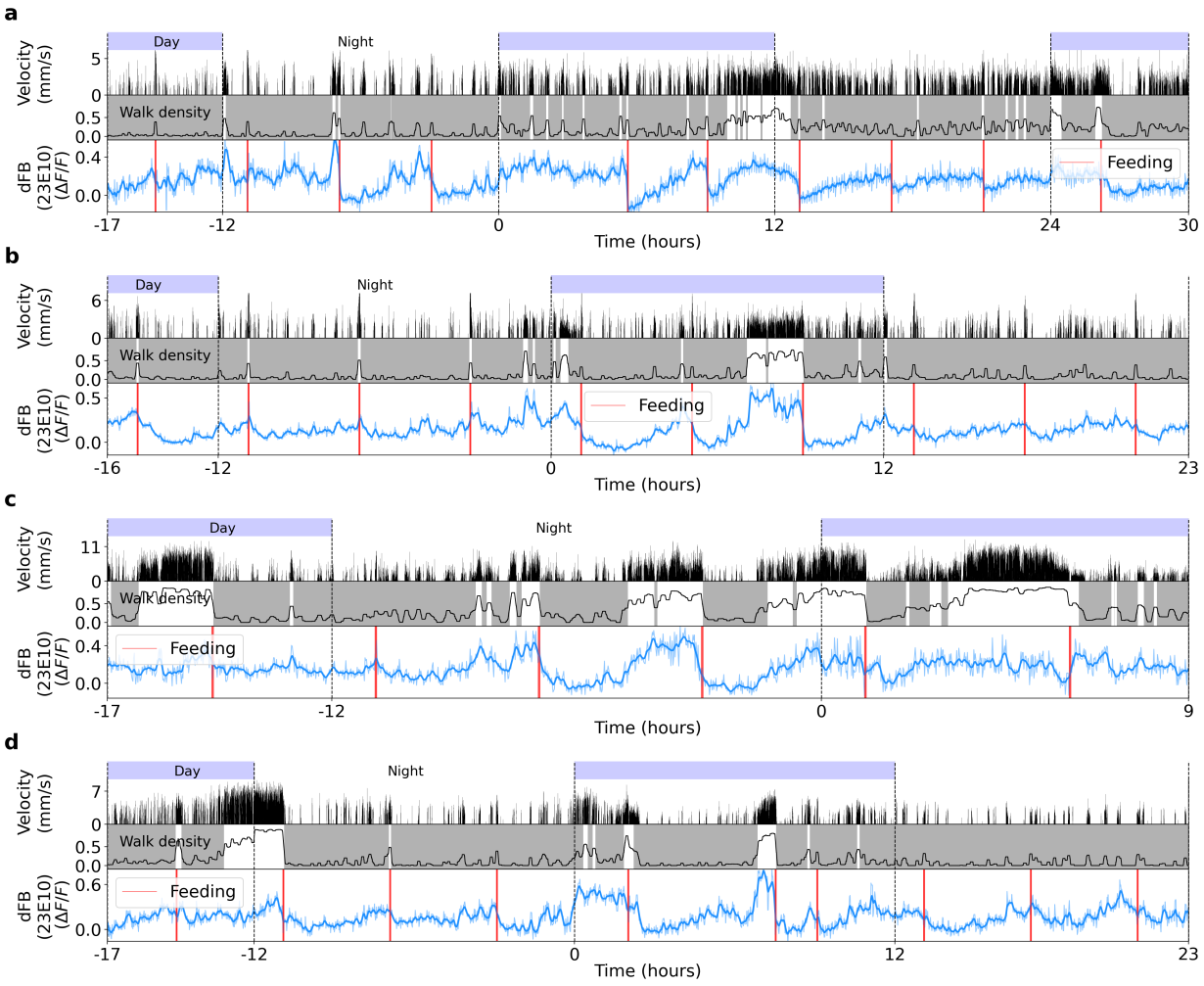
Supplementary Figure S5.27: Normalized fluorescence traces during active and rest epochs for eight flies in R5 neurons (labeled by 88F06-GAL4). **a** Left side: single (thin lines) and average (thick lines) normalized fluorescence traces of activity in R5 neurons during active epochs. Red lines indicate exponential fit. Right side: the same as left side, but during rest epochs. **b-d** Same as a. Each panel is obtained from different flies.



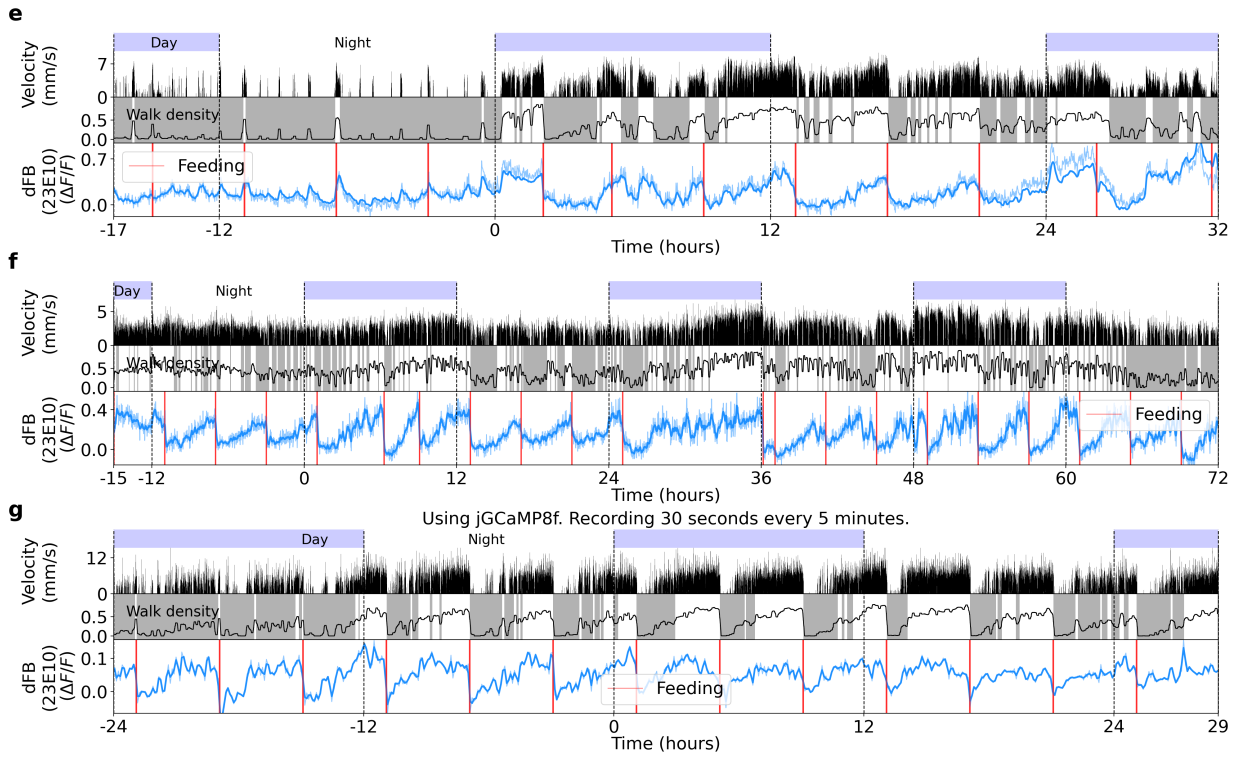
Supplementary Figure S5.28: Fitting calcium activity of R5 neurons (labeled by 88F06-GAL4) with 2-state homeostat model. **a** Left side: stop row shows walking and stopping bouts of a fly. Second row: Normalized fluorescence of R5 neurons. Red lines show the fitted model, while orange lines represent fitted upper and lower bounds of model. Right side: time constants obtained from model fitting. Grey lines indicate error bars of estimated time constants (see Methods), while colored numbers show approximated values of fitted time constants. **b-d** Same as a. Each panel represents a fitted model for each fly.



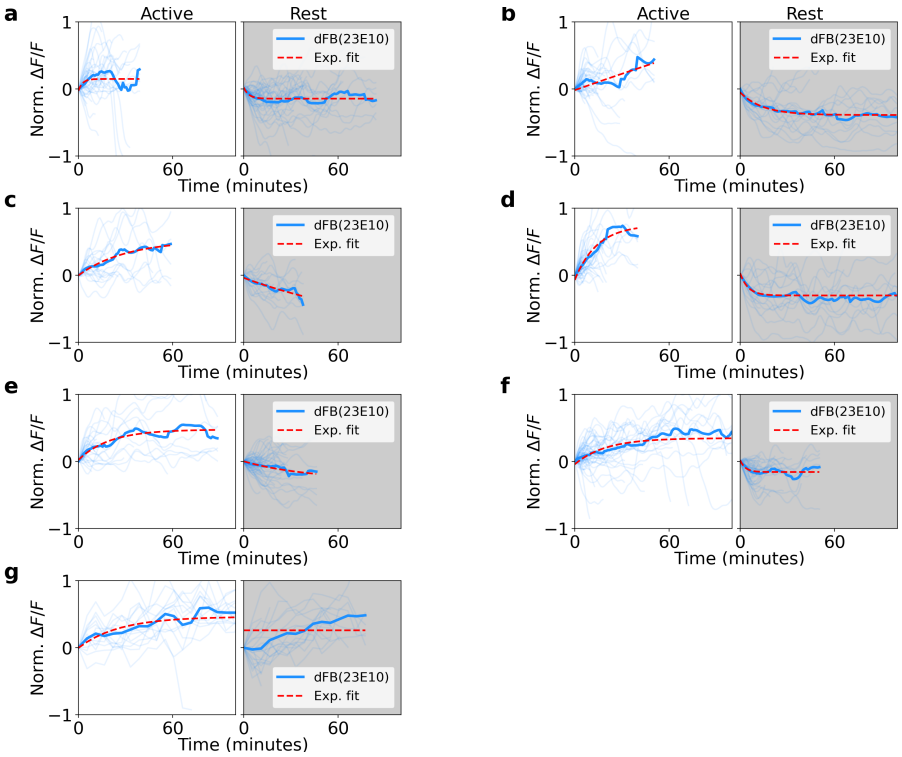
Supplementary Figure S5.29: Four more recordings and fits of 2-state homeostat model with calcium activity of R5 neurons (labeled by 88F06-GAL4). Same as Supplementary Fig. S5.28.



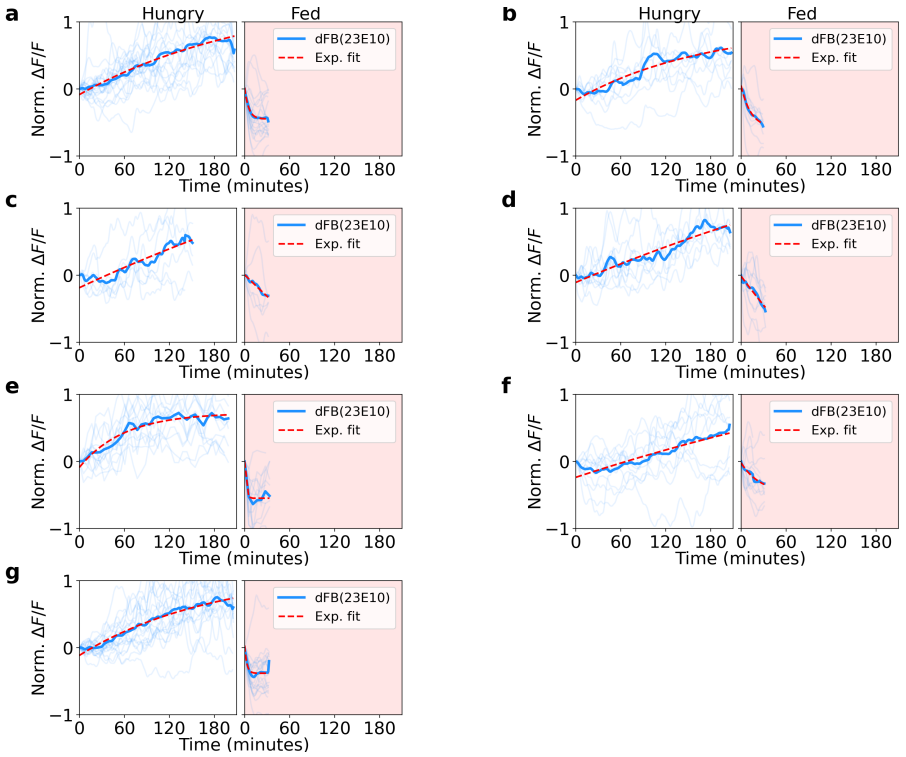
Supplementary Figure S5.30: Four different recordings of calcium activity in dFB neurons labeled by 23E10-GAL4. **a** Top row: day and night cycle in VR. Second row: velocity of fly in 1 second bins. Third row: walk density (see Methods), rest (grey region) and active (white region) epochs. Fourth row: Calcium activity of dFB neurons. The thick line indicates low-pass filter with a 0.1 hours cut-off period. Vertical red lines represent feeding events. **b-d** Same as a. Each panel shows different flies.



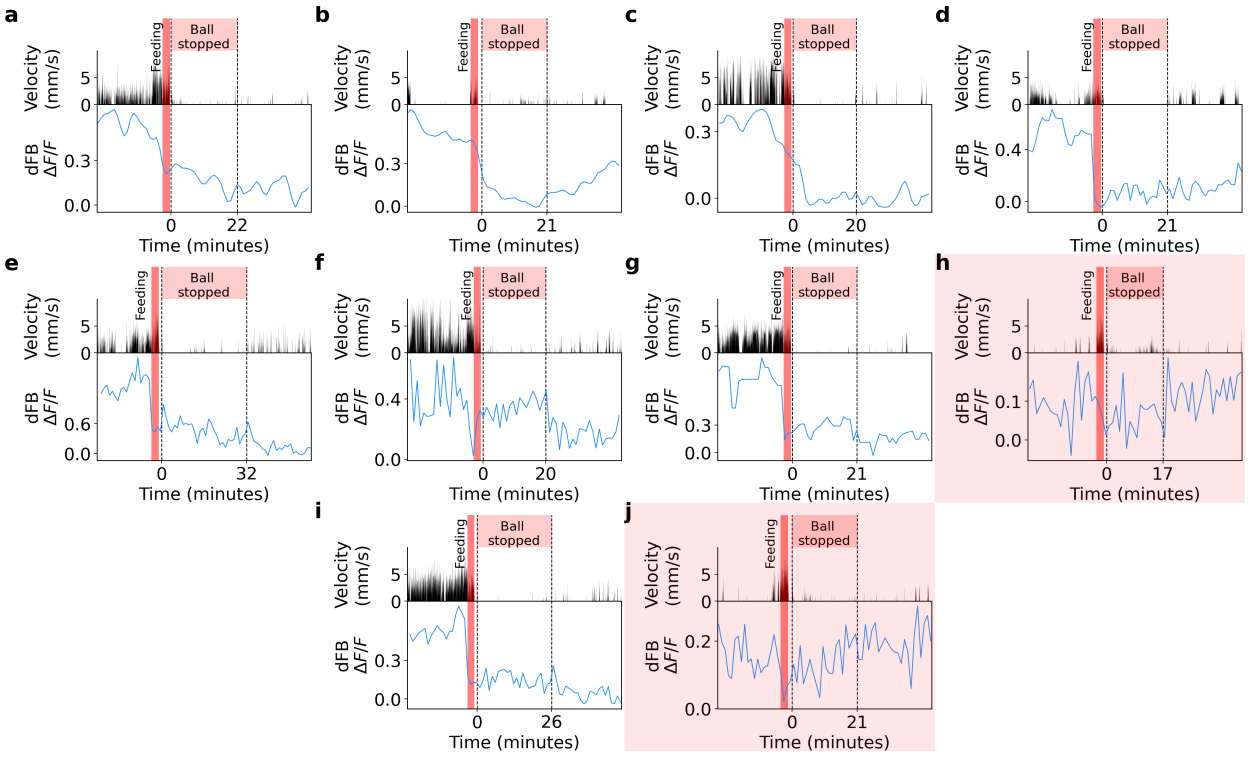
Supplementary Figure S5.31: Three recordings of calcium activity in R5 neurons labeled by 23E10-GAL4. Same as Supplementary Fig. S5.30



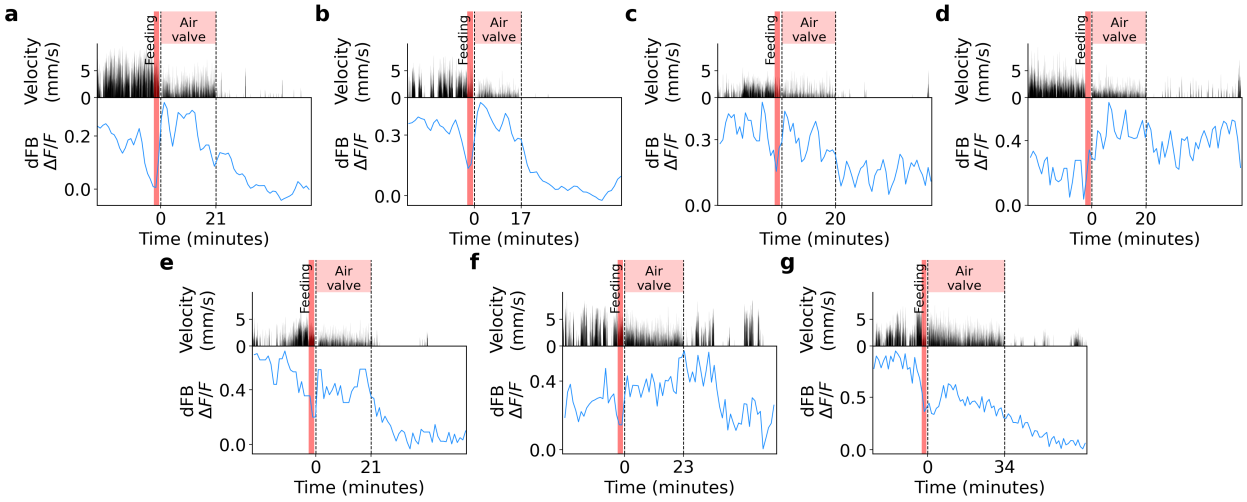
Supplementary Figure S5.32: Normalized fluorescence traces during active and rest epochs for seven flies in dFB neurons (labeled by 23E10-GAL4). **a** Left side: single (thin lines) and average (thick lines) normalized fluorescence traces of activity in dFB neurons during active epochs. Red lines indicate exponential fit. Right side: same as the left side, but during rest epochs. **b-d** Same as a. Each panel is obtained from different flies.



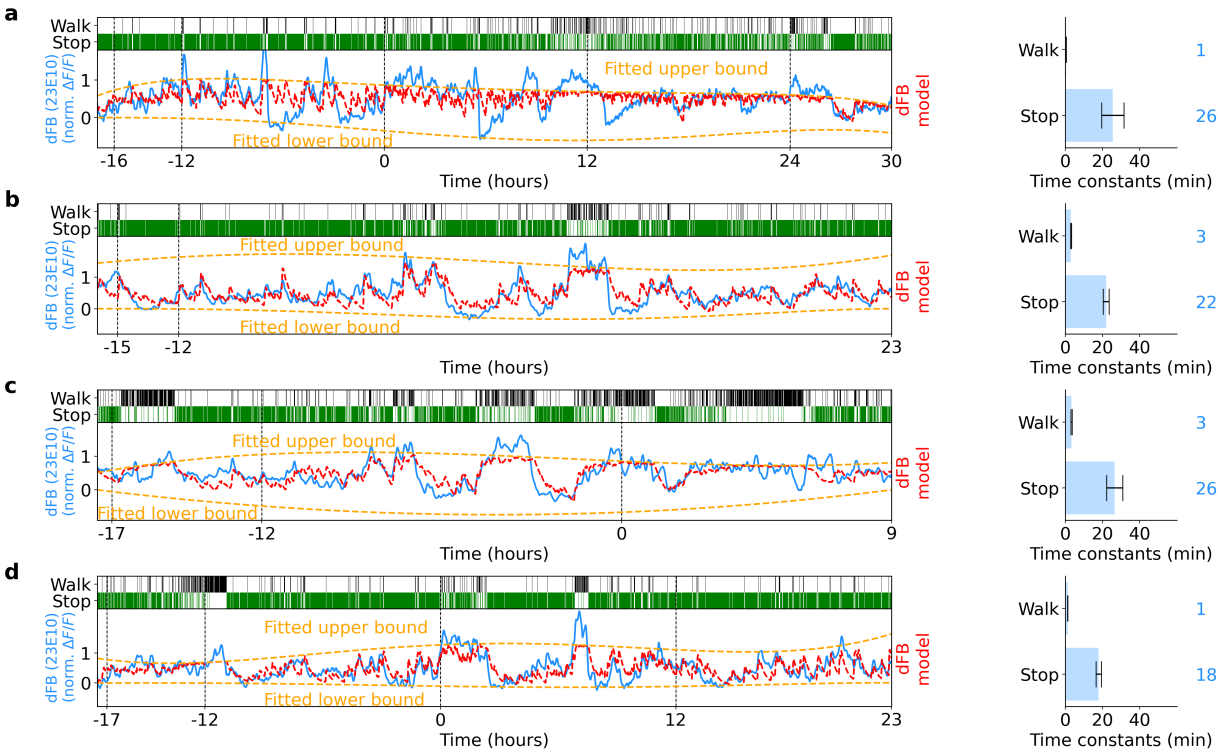
Supplementary Figure S5.33: Normalized fluorescence traces during hungry and fed epochs for seven flies in dFB neurons (labeled by 23E10-GAL4). **a** Left side: single (thin lines) and average (thick lines) normalized fluorescence traces of activity in dFB neurons during hungry epochs. Red lines indicate exponential fit. Right side: same as the left side, but during fed epochs. **b-d** Same as a. Each panel is obtained from different flies.



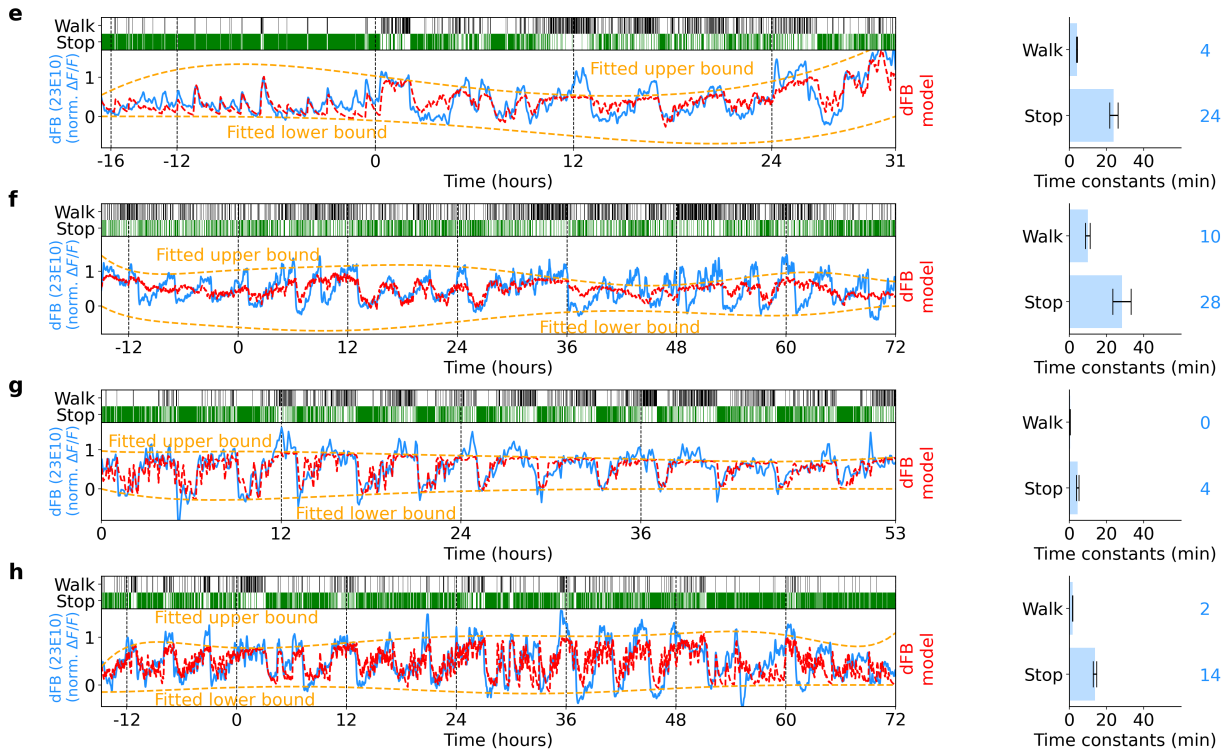
Supplementary Figure S5.34: Trials where the ball was blocked after feeding while activity in dFB neurons was recorded. **a** First row: time where the ball was stopped (red region). Second row: velocity of the fly. Third row: Calcium activity dFB neurons. The vertical red line indicates the feeding event before blocking the ball. **b-j** Same as a. Each panel represents a different trial. Trials h and j were not considered for the analysis (highlighted in red) because dFB neurons had low activity levels before feeding.



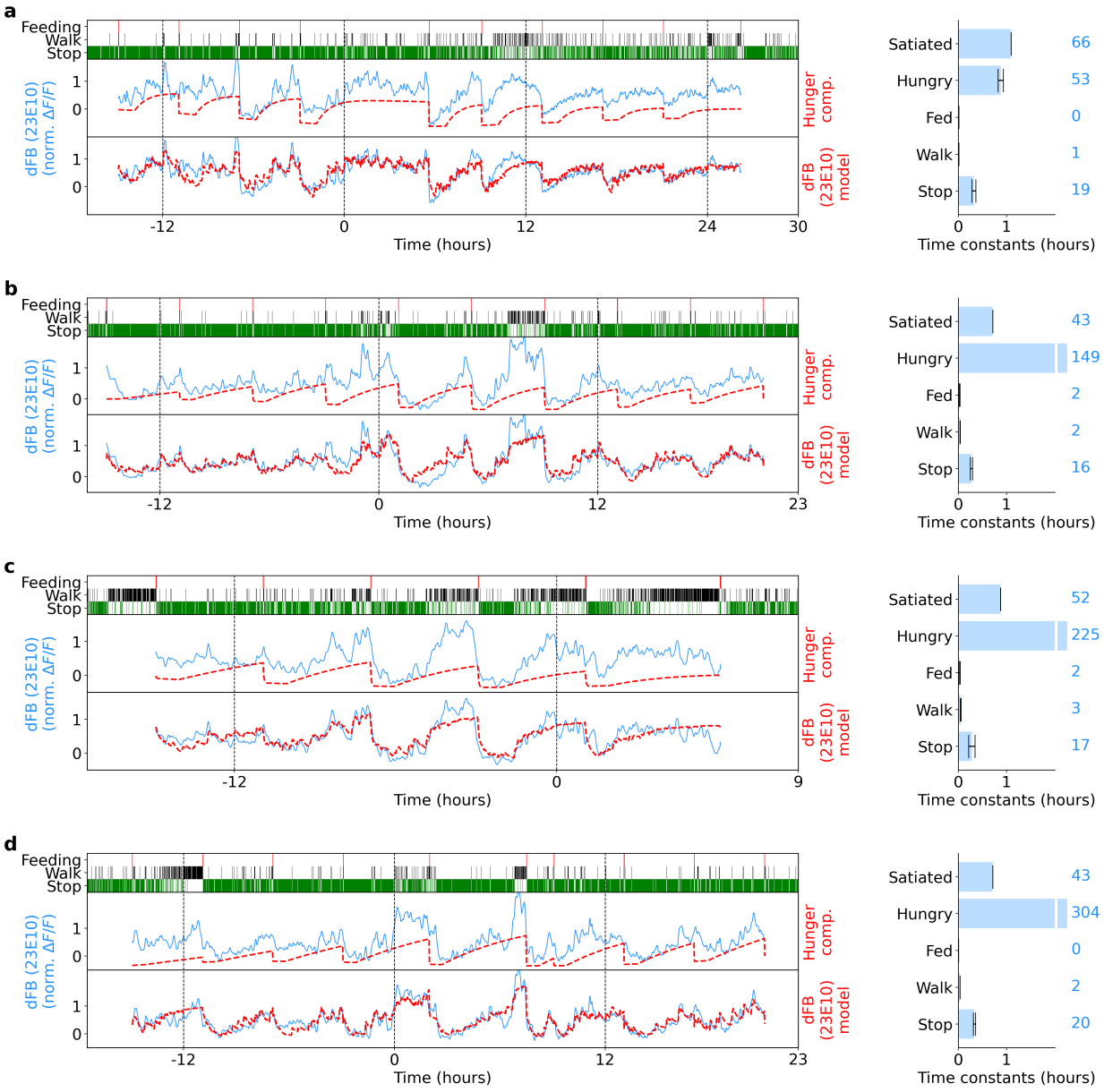
Supplementary Figure S5.35: Trials where air supply of the ball was intermittently interrupted to promote walking after feeding, while activity in dFB neurons was recorded. **a** First row: times where the ball was perturbed by the air valve (red region). Second row: velocity of the fly. Third row: Calcium activity in dFB neurons. The vertical red line indicates feeding event before perturbing the ball. **b-g** Same as a. Each panel represents a different trial.



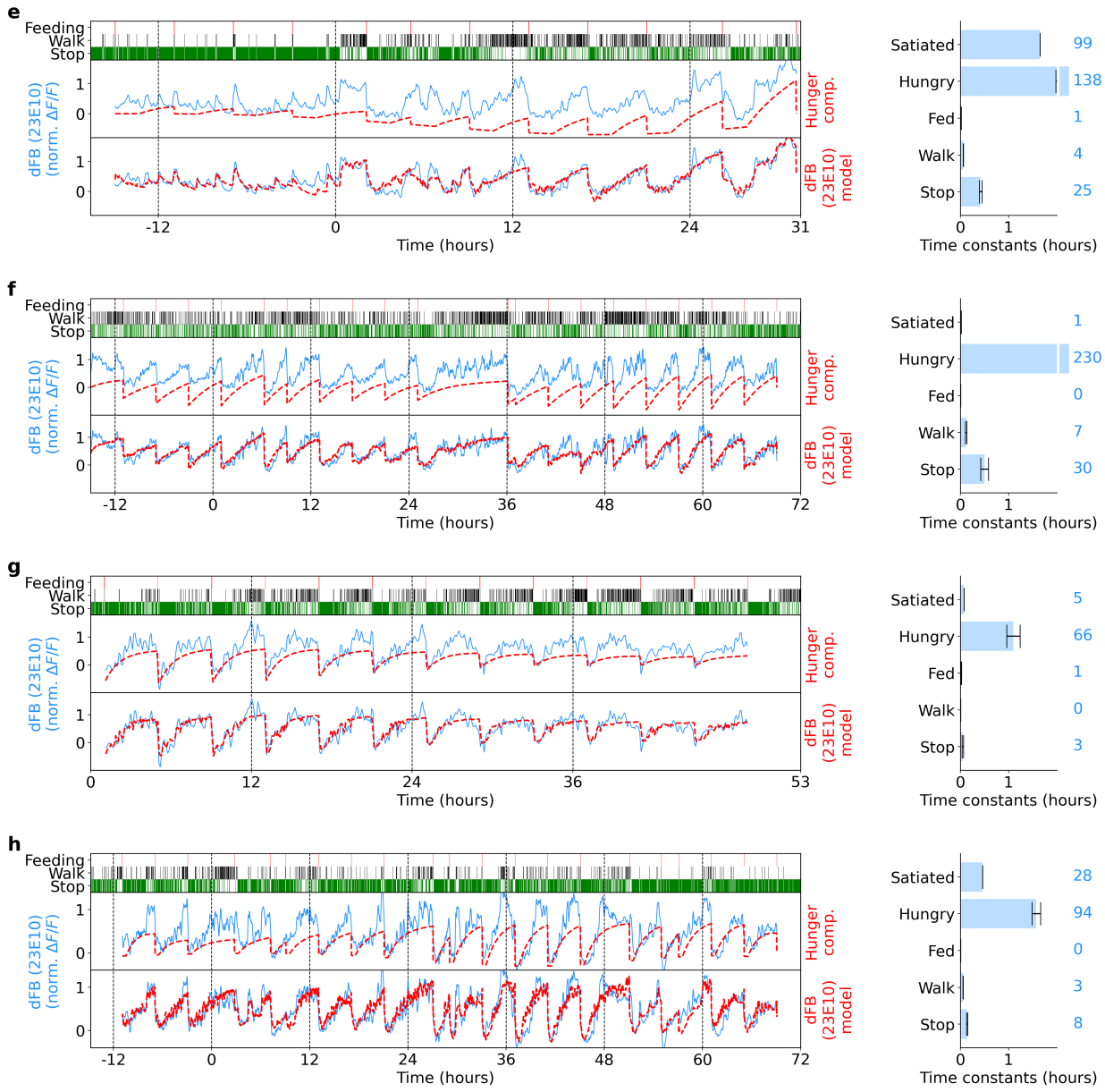
Supplementary Figure S5.36: Fitting calcium activity of dFB neurons (labeled by 23E10-GAL4) with 2-state homeostat model. **a** Left side: top row shows walk and stop bouts of a fly. Second row: Normalized fluorescence of dFB neurons. Red lines show fitted model, orange lines represent fitted upper and lower bounds of the model. Right side: fitted model time constants. Grey lines indicate error bars of estimated time constants (see Methods), while colored numbers show the rounded value of the fitted time constants. **b-d** Same as a. Each panel represents a fitted model for each fly.



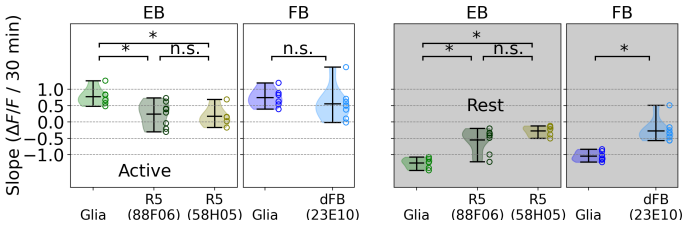
Supplementary Figure S5.37: Four more experiments and fits of the 2-state homeostat model with calcium activity of dFB neurons (labeled by 23E10-GAL4). Same as Supplementary Fig. S5.36.



Supplementary Figure S5.38: Fitting calcium activity of dFB neurons (labeled by 23E10-GAL4) with hunger-walk model. **a** Left side: top row shows feeding events as well as walk and stop bouts of a fly. Second row: normalized fluorescence of dFB neurons in blue. Red line shows hunger component fitted by the model. Third row: normalized fluorescence of dFB neurons in blue and fitted hunger-walk model in red. Right side: fitted time constants from the model. Grey lines indicate error bars of estimated time constants (see Methods), while colored numbers show their approximated fitted value. **b-d** Same as a. Each panel represents a fitted model for a different fly.



Supplementary Figure S5.39: Another four experiments with dFB neurons and fits of hunger-walk model to calcium activity (labeled by 23E10-GAL4). Same as Supplementary Fig. S5.38.



Supplementary Figure S5.40: Left side: slope of a linear fit between time that flies spent in active epochs and average fluorescence traces from glia and neurons in EB and FB. Right side: same as left side but during resting epochs.

Chapter 6

Autonomous activity in the head direction system of *Drosophila* during learning

In the mammalian brain, sleep is a dynamic state where spatio-temporal activity patterns in single neurons and neural populations are observed. These dynamic patterns are also investigated in the context of learning and memory, for example in experiments that investigate neural activity reactivation or replay (see 1.3.1). Less is known about the neural dynamics in circuits of the fly brain during sleep, and how these dynamics are linked to learning and memory. Several neural populations in the central complex, such as those innervating different layers of the fan-shaped body (FB) or ring neurons of the ellipsoid body (EB), are important for spatial and visual learning (see section 1.2.4). However, investigating neural dynamics underlying spatial learning requires assays that replicate similar behavior in head-fixed behaving animals.

Section 6.1 describes an assay and a novel virtual reality setup for studying spatial and visual learning in *Drosophila*, based on the visual place learning assay for freely moving flies [146, 164] described in section 1.7.4 and Fig. 1.12. Using this setup, a spatial learning behavior similar to place learning in freely walking flies is replicated in tethered flies and during calcium imaging (section 6.2).

Section 6.2 further describes autonomous or drift neural dynamics when the fly is standing still and during sleep in a set of neurons of the central complex: the PFR neurons in the FB. PFR neurons are part of the head direction system and represent the traveling direction of the fly in a world coordinate frame of reference [305, 323].

PFR neurons are monitored during learning in the developed assay. They are also monitored during subsequent sleep to investigate the potential role of autonomous activity during resting periods with respect to learning. Although these are still ongoing experiments, autonomous activity from PFR neurons during rest and sleep is characterized, showing

similar activity patterns as during navigation but faster temporal dynamics.

One of the predictions of the model developed in Chapter 2 is the autonomous activity in the head direction system of the fly. Additionally, autonomous dynamics from PFR neurons are reminiscent of activity reported in the mammalian head direction system during sleep (see section 1.3.1).

This chapter contains the following peer-reviewed publication in section 6.1:

[32] **Flores-Valle, A. and Seelig, J.D.**
A place learning assay for tethered walking Drosophila.
Journal of Neuroscience Methods 378 (2022): 109657.

This chapter additionally contains preliminary experiments and results in section 6.2

Author	**Contribution in [32] (section 6.1)**	**Contibution in section 6.2**
Flores-Valle, A.	- Conceptualization - Setup design - Setup building - Methodology - Experiments - Analysis - Visualization - Writing	- Conceptualization - Setup design - Setup building - Methodology - Experiments - Analysis - Visualization - Writing
Honnef, R.	- Setup building	- Setup design - Setup building
Seelig, J.D.	- Conceptualization - Setup design - Setup building - Supervision - Writing	- Conceptualization - Setup design - Setup building - Supervision - Writing

6.1 A place learning assay for tethered walking *Drosophila*

6.1.1 abstract

Drosophila shows a range of visually guided memory and learning behaviors, including place learning. Investigating the dynamics of neural circuits underlying such behaviors requires learning assays in tethered animals, compatible with *in vivo* imaging experiments. Here, we introduce an assay for place learning for tethered walking flies. A cylindrical arena is rotated and translated in real time around the fly in concert with the rotational and translational walking activity measured with an air supported ball, resulting in a mechanical virtual reality (VR). Navigation together with heat-based operant conditioning allows flies to learn the location of a cool spot with respect to a visual landmark. Flies optimize the time and distance required to find the cool spot over a similar number of trials as observed in assays with freely moving flies. Additionally, a fraction of flies remembers the location of the cool spot also after the conditioning heat is removed. Learning tasks have been implemented in tethered flying as well as walking flies. Mechanically translating and rotating an arena in concert with the fly's walking activity enables navigation in a three dimensional environment. In the developed mechanical VR flies can learn to remember the location of a cool place within an otherwise hot environment with respect to a visual landmark. Implementing place learning in a tethered walking configuration is a precondition for investigating the underlying circuit dynamics using functional imaging.

6.1.2 Introduction

Navigation related circuits in mammals are important for the encoding of memories [549, 550, 551]. Basic elements of circuits for spatial navigation as well as spatial and visual memories have also been described in *Drosophila* (see for example [144, 146, 306, 313, 332]). *Drosophila* also increasingly offers the tools to describe learning and memory at the level of reconstructed neural circuits as well as with molecular specificity [552]. How memories are encoded in the fly brain at the level of the dynamics of neural circuits is however little understood. Investigating such dynamics requires behavioral assays that can be combined with functional imaging [331].

Drosophila shows a range of spatial as well as visually guided learning behaviors, often relying on heat for conditioning [136]. In the heat-box assay, a fly learns to remember the cooler side of a chamber after the offset of the conditioning heat [163, 553, 554, 555, 556]. In the place learning assay, flies navigate in a circular arena with visual cues on its walls, similar to the Morris water maze [557]. In this assay, flies learn the place of a cool spot on an otherwise aversively hot platform with respect to visual landmarks [146, 164, 558].

Several assays have also been developed for visual learning in tethered flies, both, for flying [144, 145, 559, 560, 561, 562] as well as walking flies [160]. In tethered flying flies, the animals can for example be trained to associate a safe, unheated flight direction with a visual pattern [144, 559, 560, 561]. Tethered walking flies were trained to turn in a preferred direction using heat or optogenetically induced rewarding stimuli (without a visual VR) [563]. In a tethered walking assay [160] based on a VR projection system and optogenetically induced sugar or heat sensation for conditioning, flies learned to distinguish between different shapes displayed in a three dimensional virtual space.

Projector-based virtual reality approaches allow flexibly generating visual stimuli [154, 160]. However, in how far virtual reality can accurately reproduce the visual stimuli seen in a three-dimensional environment is more difficult to asses. Parameters such as brightness and contrast, surface texture of objects, or lighting and shadows, need to be chosen out of a wide parameter space that is additionally constrained by the characteristics of the projection system, including the light source, frame rate, or projection screen.

While not offering the flexibility of LED displays or projectors, rotating cylinders have been traditionally used for virtual reality experiments in flies [149, 564] (see also [154] for discussion), in particular also for learning experiments in tethered flying flies [144, 559, 560, 561]. Using such cylinders for implementing a virtual reality in a configuration that not only takes into account rotation but also translation, requires however that the axis of rotation of the arena is laterally displaced in concert with the animals translational walking activity.

Here, we describe a mechanical VR based on a cylindrical arena that rotates as well as translates around the fly in concert with its walking activity in real time. For this purpose, a rotating cylindrical arena [144, 149, 559, 560, 561, 564] is additionally physically translated depending on the walking trajectory recorded on an air supported ball.

We use this setup to implement a place learning assay in tethered walking flies. Similar to the place learning assay in freely walking flies [146, 164, 558], the animals learn to remember the location of a cool or safe spot with respect to a visual landmark. We observe similar learning dynamics as described in freely moving (individual) flies. Additionally, in a small fraction of flies, we find that a memory of the cool spot is retained also after the offset of the heating stimulus. Overall, the developed mechanical VR for tethered walking flies captures essential elements of place learning observed in freely walking animals in a configuration that is compatible with functional imaging experiments.

6.1.3 Materials and Methods

6.1.3.1 Mechanical VR

The mechanical VR has 3 degrees of freedom (DOF): one rotational DOF, θ, which allows the fly to rotate around its own axis and therefore to assume different orientations with

respect to the arena (as in traditional one DOF cylindrical arenas), and two translational DOF, x and y, which allow the fly to change position in the arena. For this purpose, a translation stage with two DOF is mounted on top of a rotation stage (one DOF). The assembly of the mechanical VR, with the different components in different colors, is shown in Fig. 6.1A and B. Each degree of freedom is controlled with an independent motor. To prevent vibrations generated by the motors or by movement of the arena from affecting fly behavior, all moving parts were mechanically isolated from the stationary parts (the fly and fly mount, ball and ball holder, cameras, laser and corresponding optical elements). All stationary parts were mounted on a vibration isolating optical table and the moving parts were attached to a scaffold standing on the floor and providing a slightly elevated platform above the optical table (see Supplementary Fig. S6.1.1).

6.1.3.1.1 Rotation

Rotation of the mechanical VR was implemented using a slip ring. The slip ring (Senring, part H90185-0310-09S) has a central opening with a diameter of $90mm$ and has an outer diameter of $185mm$. An air supported ball as well as a camera for tracking the ball are mounted inside this opening (Fig. 6.3A, see section 6.1.3.2). This opening allowed mechanically isolating the ball holder and camera from vibrations generated by movement of the arena by placing them on the optical table. All moving components of the mechanical VR were mounted on platform positioned with a scaffold above the optical table (see Supplementary Fig. S6.1.1). The fly, standing on top of the ball, is always at the center of the slip ring. Apart form providing mechanical support for rotating the translation stage mounted on top (see next section), the slip ring allows passing electric signals across the rotational joint without twisting any cables or wires. Seven electrical contacts are provided at the stationary part of the slip ring and are transferred to the rotating end, as shown in Fig. 6.2B. Of the 7 transferred contacts, 6 are used for controlling the translational motors (see next section), x and y, and 1 contact is used to power the LED strip that illuminates the pattern on the walls of the mechanical VR (in this case a single blue stripe).

The parts for implementing rotation of the mechanical VR are shown in Fig. 6.1C. A brushless motor drives a 30 teeth belt pulley attached to its axis (Maedler, 17223000). The motor is connected through a closed belt (100mm length, 9mm width, Maedler, 17312600) to the slip ring through a custom-made metal belt pulley with 112 teeth. The belt pulley is mounted around the rotating part of the slip ring. This configuration results in a ratio of 3.73 between motor and slip ring rotations.

The brushless motor (Odrive, D5065 270KV) has an encoder attached (Odrive, CUI AMT102-V) through a 3D printed enclosure, as shown in Fig. 6.2A. The encoder reads the absolute position of the motor, which is controlled in closed-loop with an Odrive board (Odrive 3.6, version 56 V, powered at 24 V, Fig. 6.2A). Since the encoder registers 8192

counts per revolution, together with the reduction ratio of the belt pulleys, the rotational DOF in the mechanical VR has a resolution of $0,012$ degrees.

6.1.3.1.2 Translation

The stage for translating the mechanical VR with two DOF (x and y) is shown in Fig. 6.1D. This stage was mounted on top of the slip ring such that the entire translation stage rotates around the fly on the ball. Translational motion was achieved with closed loop stepper motors (MKS SERVO42, shown in purple in Fig. 6.1D) with belt pulleys attached to the motor axis (GT2 Belt pulleys, shown in green in Fig. 6.1D). These motors moved a toothed belt (GT2 belt, 6mm width) attached to a custom aluminium mount connected to a carriage block (MGN12H slide block). The carriage block slid smoothly on a rail guide (MGN12 linear rail, shown in yellow in Fig. 6.1D).

The stepper motors were controlled with an Arduino DUE, which received commands from a computer connected via USB. The Arduino DUE sends 4 signals through the slip ring (Fig. 6.2B), including the direction of movement (dir) and the number of steps (step) to control each motor. After passing through the slip ring, these signals connect to a CNC shield, which acted as a control interface and was connected to the x- and y-motors. The CNC shield was mounted on the translation stage and rotated together with the x- and y-motors around the central axis of the slip ring. We used microstepping (16 microsteps) to control each stepper motor, which resulted in a displacement resolution of 80 steps per mm in each axis.

6.1.3.2 Ball tracking

All three DOF of ball motion are tracked at 300 Hz using a camera and an optic flow based algorithm [157] which provides three orthogonal angular velocity components (Fig. 6.3A). The rotational and translational DOF of the arena are updated accordingly (in closed loop) by projecting the ball movement into a plane (see Section 6.1.3.6). The parts of the setup used for tracking ball movement are shown in Fig. 6.1.3.2B. A custom-made ball with a radius of 3 mm freely rotates in a holder on air [331]. A right angle prism mirror (Thorlabs, MRA05-P01) mounted at the same height as the ball in the back of the fly (with respect to the walking direction on the ball) reflected light at 90 degrees into a camera mounted below the ball holder. The ball was illuminated with two IR LEDs (Thorlabs, LED851L, only one shown in Fig. 6.3B for simplicity). All these components were installed in the center opening of the slip ring.

6.1.3.3 Cylindrical arena and visual stimuli

A cylindrical arena with a diameter of $200mm$ and a height of $85mm$ was printed out of black plastic (PLA, Fig. 6.3C). This cylinder had a rectangular opening with width of $25mm$ and height of $67mm$, which defined the shape of a single vertical stripe. Behind this opening a green or blue transparent paper (Conrad, green/blue foil sheet) and a white LED strip (see Figure 6.3C) were attached. An Arduino UNO was used for switching the LED strip on and off. The fly was positioned at $1cm$ above the bottom of the cylindrical arena such that the bright stripe was just above the fly.

6.1.3.4 Aversive heat stimulus

We used an infrared laser (Toptica, ibeam-smart-785-S-HP with pulse option, 785 nm) to generate and aversive heat stimulus for operant conditioning [144, 145, 559, 560, 561, 562, 563]. The setup is shown in Fig. 6.3B: the laser was focused with a lens (Thorlabs, AC254-300-B) and had a power of 7 mW after the shutter. We used a mirror mounted in a kinematic mirror mount just after the focusing lens to direct the laser beam towards the thorax of the fly from the top. The position of the beam was adjusted with an IR sensitive camera after mounting the fly on the ball with the help of the kinematic mirror mount. During the place learning experiment, the laser was pulsed using an Arduino UNO at 1KHz with a 50% duty cycle, using a PWM signal, resulting in a power of 3.5mW at the laser output. The power of the laser was adjusted such that flies responded to laser illumination with increased walking activity. The same power was fused for all flies.

6.1.3.5 Hardware and software control

A computer running Ubuntu 18.04LTS was used for the high level control of the mechanical VR. We used the framework ROS (Robot Operating System), which allows integration and communication of different algorithms written in different programming languages (C++ and Python) within the same computer. The software and hardware used to control the mechanical VR are schematically shown in Fig. 6.4.

Four different algorithms, or ROS nodes (light red boxes in Fig. 6.4), were running at the same time, and communicated with each other through ROS topics (buses to exchange unidirectional messages, black arrows in Fig. 6.4). The first node contained the ball tracking algorithm [157], written in C++, which was fed by frames from a camera (Basler acA640-750um) and detected ball motion (see Section 6.1.3.2). The ball tracking node then continuously sent the integrated position and orientation of the ball movement (see Section 6.1.3.6) through a ROS topic to the mechanical VR driver node, written in Python. This node computed the fly position and orientation in the arena from the kinematics and collisions (see Section 6.1.3.6) and continuously sent commands via USB to the

Odrive board and Arduino DUE to control the motors. The node was also responsible for storing data, which included the ROS time stamp (a time stamp shared across all ROS nodes), as well as position, orientation, and velocity of the fly. Finally, the mechanical VR driver node continuously sent the fly position and orientation through a ROS topic to the place learning node, which controlled the light for the visual stimuli (which was switched off for resetting the arena), and triggered the laser for the aversive heat stimulus using an Arduino UNO connected via USB (see Section 6.1.3.4). This node also sent the control mode of the mechanical VR (explained below) through a ROS topic. Finally, the fly view node was fed by frames from a camera (Basler acA640-750um) to store videos of the fly during the experiments with the respective ROS time stamp for each frame.

The mechanical VR had two different control modes: 'open-loop' and 'closed-loop'. The open-loop mode was used to move the arena to a specific position and orientation without taking into account movements of the ball, and was used to reset the position and orientation of the mechanical VR to the starting position and orientation during place learning experiments (see Section 6.1.4.2). The 'closed-loop' mode was used to move the mechanical VR according to the movements of the ball and allowed the fly to navigate.

6.1.3.6 Kinematics and collision avoidance

The ball tracking algorithm[157] outputs the angular velocity vector at any time t, $\psi(t) = (\psi_x(t), \psi_y(t), \psi_z(t))^T$. This angular velocity is transformed to linear velocity (in mm/s) projected onto the plane given by its components $v_x(t)$ and $v_y(t)$, and angular velocity around an axis normal to the plane, $v_\theta(t)$ as follows:

$$\begin{pmatrix} v_x(t) \\ v_y(t) \\ v_\theta(t) \end{pmatrix} = \begin{pmatrix} 0 & 0 & r^{ball} \\ r^{ball} & 0 & 0 \\ 0 & 1 & 0 \end{pmatrix} \begin{pmatrix} \psi_x(t) \\ \psi_y(t) \\ \psi_z(t) \end{pmatrix}, \tag{6.1}$$

where $r^{ball} = 3mm$ is the radius of the ball. The velocity components $v_x(t)$ and $v_y(t)$ were defined in the fly reference system, shown in Fig. 6.3E and were then integrated at 300Hz to compute ball position and orientation, $(x^{ball}(t), y^{ball}(t), \theta^{ball}(t))^T$, which was finally sent to the mechanical VR driver node with a ROS topic.

The mechanical VR driver was running at 50 Hz, and generated motor commands from the ball readout. The θ motor operated in position-control mode using the Odrive board (Fig. 6.2A), which took as a continuous input the absolute orientation measured in turns per second. The command to control this motor, θ^{cmd}, was computed as:

$$\theta^{cmd}(t) = G_r\Big(\theta^{ball}(t) - \theta_0\Big)\frac{R}{2\pi}, \tag{6.2}$$

where G_r is the rotational gain, which is set to 1 unless specified otherwise, θ_0 is a fixed offset from the ball orientation, and $R = 3.73$ is the rotation ratio of the pulley system.

The actual orientation of the fly in the arena at any time, $\theta^f(t)$, was obtained by measuring the absolute orientation of the encoder that was attached to the θ motor, which was sent by the Odrive board to the computer and scaled taking into account the rotation ratio, R.

The x and y motors were controlled in velocity-control mode using an Arduino DUE with custom software written in C++. The Arduino DUE took as a continuous input the velocity of each motor. Therefore, the mechanical VR driver node first computed the fly velocity in the stationary arena frame of reference (see Fig. 6.3E), (v_x^f, v_y^f), from the current and previous ball positions, which were defined in the fly reference system, rotated by the current orientation of the fly, θ^f:

$$\begin{pmatrix} v_x^f(t) \\ v_y^f(t) \end{pmatrix} = \begin{pmatrix} sin\theta^f(t) & -cos\theta^f(t) \\ -cos\theta^f(t) & -sin\theta^f(t) \end{pmatrix} \frac{G_t}{\Delta t} \left[\begin{pmatrix} x^{ball}(t) \\ y^{ball}(t) \end{pmatrix} - \begin{pmatrix} x^{ball}(t-\Delta t) \\ y^{ball}(t-\Delta t) \end{pmatrix} \right]. \tag{6.3}$$

Here, G_t was the translation gain, which unless otherwise specified was set to 1, and $\Delta t \approx 1/50$ seconds. This velocity was further transformed to obtain the motor commands, $(v_x^{cmd}, v_y^{cmd}) = K(v_x^f, v_y^f)$, where $K = 80$ steps per mm. The actual position and orientation of the fly in the cylindrical arena, (x^f, y^f), was obtained by measuring the absolute positions of the encoders attached to the x and y motors, (e_x, e_y), which were sent from the Arduino DUE to the computer, and then transformed to mm as:

$$\begin{pmatrix} x^f \\ y^f \end{pmatrix} = \frac{1}{K} \begin{pmatrix} e_x \\ e_y \end{pmatrix} - \begin{pmatrix} x_0 \\ y_0 \end{pmatrix}, \tag{6.4}$$

where $(x_0, y_0)^T$ are fixed offsets that set the origin at the center of the cylindrical arena.

To ensure that the fly did not collide with the walls of the cylindrical arena with radius $100mm$, we limited walking activity to a circle of radius $R_{max} = 64mm$ (the circular 'walking limit' of the fly, see Fig. 6.6A). If the fly reached this limit or walked beyond it, only the velocity component tangential to the circular walking limit was updated and the forward velocity (in radial direction) was set to zero. For this, the fly position from the center of the arena was computed as:

$$\phi = arctan2(y^f(t), x^f(t)). \tag{6.5}$$

The tangent vector, $\hat{\mathbf{t}}$, and normal vector, $\hat{\mathbf{n}}$, for the fly position and orientation with respect to the circular walking limit were computed as:

$$\begin{cases} \hat{\mathbf{t}} = (sin\phi, -cos\phi)^T \\ \hat{\mathbf{n}} = (cos\phi, -sin\phi)^T. \end{cases} \tag{6.6}$$

If the velocity of the fly, $\mathbf{v^f} = (v_x^f, v_y^f)^T$, was in the direction outward from the circular walking limit, as determined using the sign of the dot product between the fly velocity and

the normal vector to the walking limit,

$$\mathbf{v^f} \cdot \hat{\mathbf{n}}, \tag{6.7}$$

the fly velocity was set to its projection along the tangent direction of the circular walking limit:

$$\mathbf{v^f} \quad \longleftarrow (\mathbf{v^f} \cdot \hat{\mathbf{t}})\hat{\mathbf{t}}. \tag{6.8}$$

This projection allowed the fly to move sideways along the circular walking limit, but prevented it from approaching the arena walls closer than the limit.

The delay between ball rotation and the induced rotation of the mechanical VR was around $298ms$, while the delay between forward movement of the ball and translation of the mechanical VR was around 75 ms. These values were obtained experimentally by using a camera to capture motion of the ball and mechanical VR at the same time at a rate of 1000 frames per second. Optical flow was used to estimate both, ball and mechanical VR motion, and the delay was found using the peak of the cross-correlation function between the two motion signals.

The rotational delay was affected by the PID controller of the brushless motor. Since the mechanical VR arena has a large inertia along the rotational axis, the PID values were tuned manually so that mechanical VR rotation was a low-pass filtered version of ball rotation. This prevented sudden changes of direction and accelerations while rotating the mechanical VR, which would require high peak currents that could break the motor and its driver board.

6.1.3.7 *Drosophila* preparation

We used wild type female flies from Michael Dickinson's lab (a gift from Bettina Schnell) that were 3 to 5 days old . The flies were kept in an incubator at 25 degrees on a 12 hour light/dark cycle and were reared on Wuerzburg food [565]. The experiments were performed at room temperature (23 degrees) and towards the evening of the flies' day, between hours 8-12, where hour 0 is defined at the transition from dark to light. Several flies were tethered at the same time on a cold plate using UV glue [154] and tethered to a pin. The experiment started with an accomodation period of 5 minutes during which the fly was freely navigating in the arena.

6.1.4 Results

6.1.4.1 Setup

The mechanical VR setup is shown in Fig. 6.1. A cylindrical arena rotates as well as translates with respect to the fly walking on an air supported ball [331, 566]. The azimuthal orientation and the position of the axis of rotation of the cylinder are updated in real time

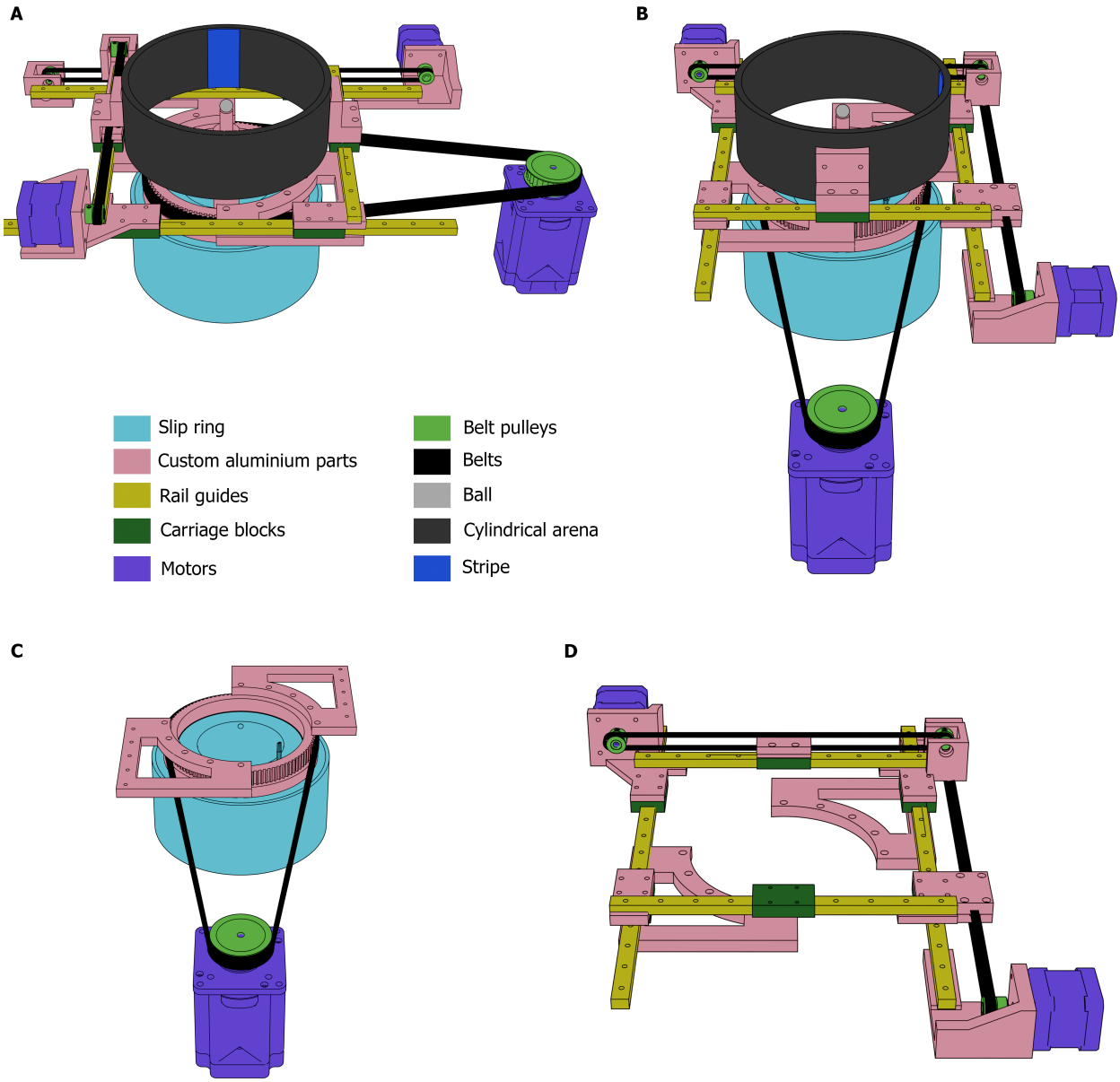


Figure 6.1: Mechanical VR. **A** Mechanical VR setup with rotation and translation mechanisms that move the cylindrical arena around the air supported ball on which the tethered fly walks. The different components of the setup are labeled with different colors (see legend in figure). **B** Same as A shown from a different perspective. **C** The components of the setup that enable the rotation of the cylindrical arena. **D** The components of the setup that enable the translation of the arena along two orthogonal axes.

depending on the fly's walking activity. The cylindrical arena can rotate without limits in either direction, while the translation of the arena is limited by its diameter.

Ball movement is tracked using optic flow [157] and the fly's trajectory is projected into

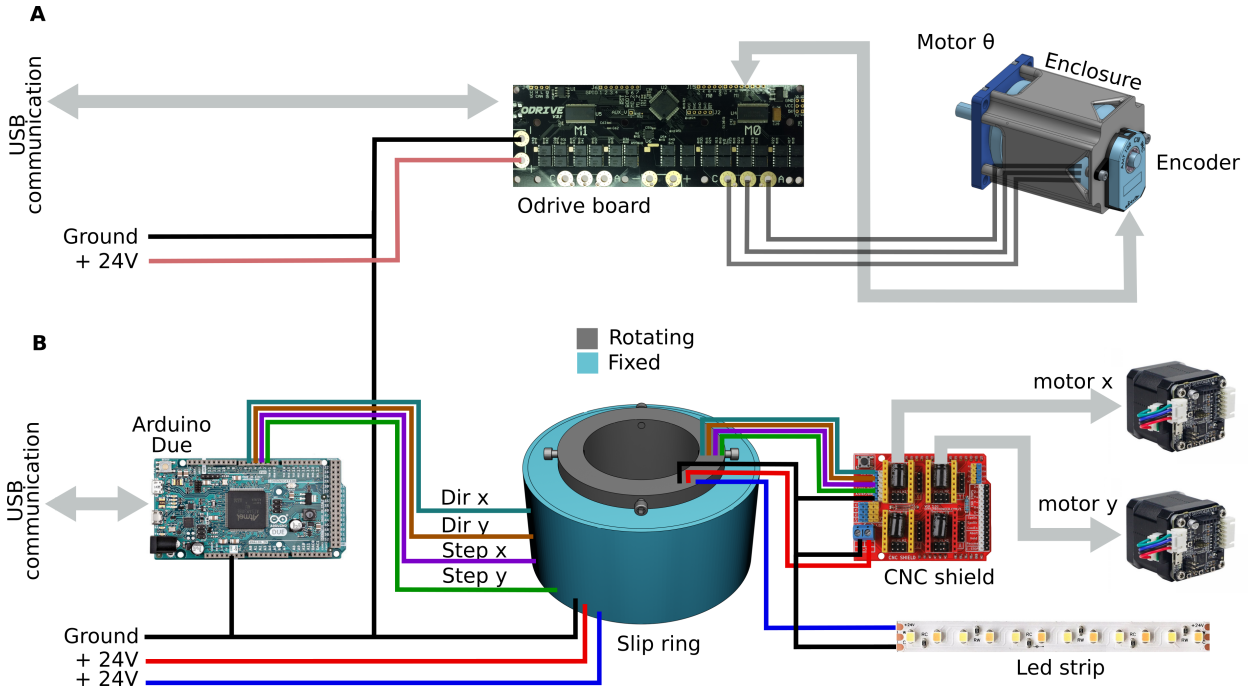


Figure 6.2: Control of the mechanical VR **A** Components for controlling the rotation include an Odrive board and a brushless motor with an attached encoder. **B** Components for controlling translation, including an Arduino DUE that sends motor commands through a slip ring to a CNC shield, which is connected to stepper motors with attached encoders. An LED strip, powered by wires passing through the slip ring, provides the illumination for the bright stripe in the cylindrical arena.

a two-dimensional plane. Rotation of the arena is achieved with a custom-motorized slip ring. The slip ring allows transferring electrical contacts across the rotational joint, from the stationary part that is mounted on the table, to the rotating part, which rotates around the fly positioned in the center of the ring. On top of the rotating part of the slip ring, a two-dimensional custom-motorized translation stage moves a cylindrical arena along two perpendicular axes. All motors used silent drivers, which made the noise produced by the mechanical VR lower than the background noise of the lab. For the experiments described here, an arena with a single bright stripe of either blue or green color was used (see Fig. 6.3C). Control software and electronics were integrated using ROS. An infrared laser was switched on an off depending on the fly's location in the arena.

6.1.4.2 Place learning with respect to a visual landmark

We first tested whether flies showed an intrinsic orientation preference when walking in an arena with a single bright green stripe on an otherwise black background. Using a single color stripe was motivated by combining the mechanical VR setup with calcium imaging,

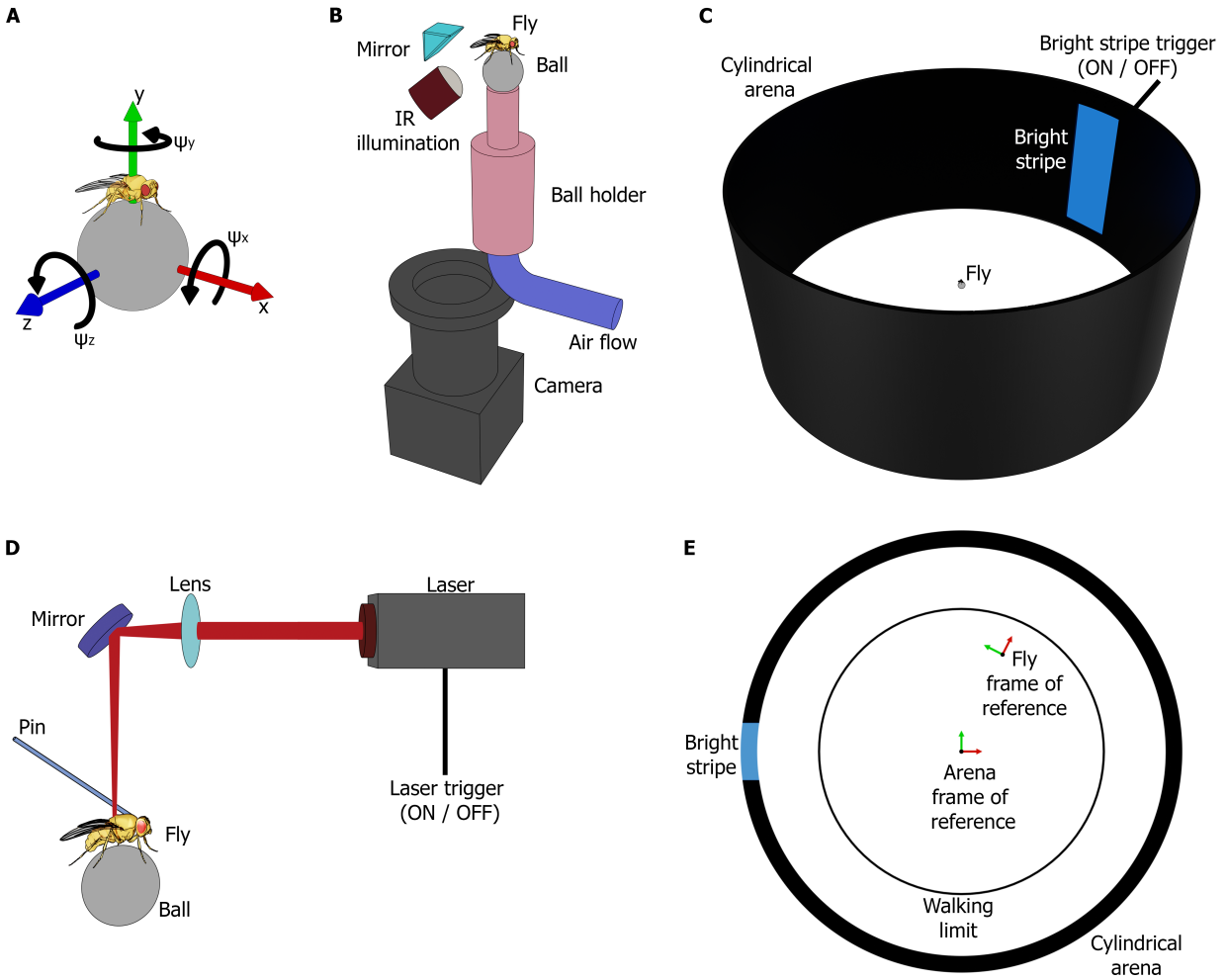


Figure 6.3: Ball tracking, conditioning IR laser, and arena. **A** Angular velocity of the ball decomposed in its three orthogonal axes detected by the ball tracking algorithm[157]. **B** The fly is positioned on an air supported ball mounted on a ball holder [331]. An infrared (IR) LED illuminates the ball and a camera records ball motion using a correlation based algorithm [157] with a reflecting prism mirror mounted at the same level as the ball behind the fly and reflecting the light by 90 degrees into a camera mounted vertically below the mirror. Mounting the camera vertically minimizes the footprint of the tracking setup and allows the mechanical VR to closely approach the ball. **C** Cylindrical arena that is rotated and translated around the fly with the bright stripe, which can be switched on and off with a trigger signal. **D** An IR laser is used as an aversive stimulus for heating the fly. The beam is focused onto the fly through a lens reflected off a mirror mounted above the fly, and directed to the thorax of the fly using an adjustable mirror mount. **E** Top view of the cylindrical arena, with the circular walking limit and the two frames of reference.

where light from a visual stimulus below or above the spectral emission peak of the calcium indicator can be filtered out. We tested the orientation preference when flies could only

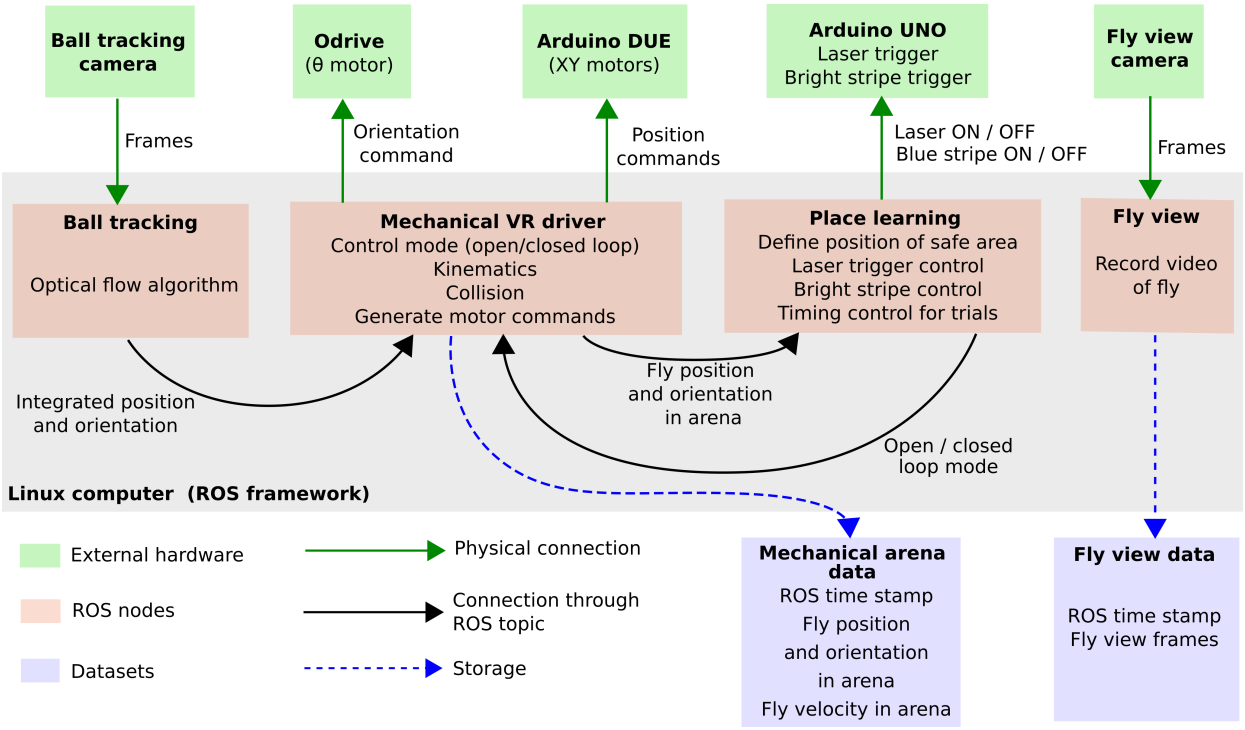


Figure 6.4: Overview of hardware and software components of the mechanical VR. Hardware components (in green, top) connect to a single computer running ROS with four different ROS nodes that communicate with each other and log the data during the experiment.

control rotation (R, no translation). Additionally, we tested the orientation preference when the (same) flies were in control of both, translation as well as rotation (R+T, after having first performed the rotation only experiment). The mechanical VR with both rotation and translation (R + T) is shown in Supplementary Video 1 during a closed loop navigation experiment.

We tested 9 flies, each walking for 15 minutes under both conditions, while an infrared laser was focused on their thorax from above which induced walking. Flies showed a different orientation preference between the R and R+T conditions (Fig. 6.5A), avoiding the green stripe during rotation only (R) and walking towards the striped when in control of both, rotation and translation (R + T, Fig. 6.5D). Flies also showed different directional rotation and forward velocity distributions under the two conditions (6.5B and C, respectively), displaying more rotation and forward walking around the green stripe during R+T (Fig. 6.5E and F, respectively). Statistical significance was assessed using the t-test with p-values lower than 0.05 (indicated by asterisks in Fig. 6.5D-F).

Since green visual stimuli can compromise compatibility of the mechanical VR setup with fluorescence imaging under a microscope, we next investigated the behavior of flies with a blue stripe. While flies in control of rotation and translation (R+T) with a green stripe did not show a preference for any of the four quadrants of the arena for 5 minutes

(green bars in Supplementary Fig. S6.1.2B), flies with a blue stripe avoided approaching the stripe and significantly preferred the opposite quadrant (blue bars in Supplementary Fig. S6.1.2B where statistical significance is indicated by asterisks using a t-test). While Fig. 6.5 shows a preference for the green stripe for an experiment lasting 15 minutes, the analysis for the quadrant preference in Supplementary Fig. S6.1.2B was performed for the first 5 minutes in the experiment with the green stripe. Note that the stripe preference shown in Fig. 6.5 does not imply that all flies where looking at the stripe from quadrant Q1, but also from other quadrants in the arena.

We next asked whether flies could learn to recognize a cool spot with respect to a visual landmark using operant conditioning with an aversive heat stimulus, similar to the place learning assay in freely walking flies [146, 164]. For this purpose, flies first explored the mechanical VR with the blue stripe for 5 minutes, without heating ('exploration phase'). After this, flies navigated with an infrared laser pointed at their thorax from above during 10 trials ('training phase', see Fig. 6.6A). A safe, cool spot (no laser illumination) was defined in front of the landmark in an otherwise aversively hot arena (green spot in Fig. 6.6B). Each trial started with the same initial position and orientation (Fig. 6.6B) of the fly (30 mm to the right of the center of the arena), with the cool spot located to the left of the fly at the opposite end of the arena. Whenever the fly entered the cool spot the laser was switched off. If the fly stayed in the cool spot for 30 seconds continuously without leaving, the bright stripe was switched off and the arena was reset to the starting position and orientation. If the fly did not find the cool spot after 5 minutes, the mechanical VR was reset and the next trial started. Each trial was initiated immediately after resetting the position and orientation of the mechanical VR, which took around 5 seconds. The laser as well as the light were switched back on at the start of the next trial. After 10 trials, the fly position and orientation were reset, and the fly was left to explore the arena again for 5 minutes without heating ('testing phase', see Fig. 6.6A).

An example of a learning experiment are shown in Fig. 6.6C and Supplementary Video 2 (corresponding to fly 5). The fly's walking trajectory in each trial is plotted in the arena frame of reference. Color indicates the time during the trial. The time it takes for the fly to reach the cool spot is indicated at the top; it includes the 30 seconds that the fly has to stay in the cool spot before resetting of the arena for the next trial. We performed this experiment with a total of 18 flies. Two flies were discarded for not being able to find the cool spot in any of the trials. Single trial trajectories for all remaining 16 flies are shown in Supplementary Video 3 and Supplementary Figs. S6.1.4 and S6.1.5, while the superimposed trajectories for all flies in each trial are shown (in different colors for each fly) in Fig. 6.6C. We computed the time it took to reach the cool spot, the total distance to the spot, and the mean velocity (calculated over the entire trial) in each trial for each of the 16 flies (Supplementary Fig. S6.1.6) The average improvement of the training time and distance as well as the mean velocity for all flies is shown in Fig. 6.7A, B and C, respectively. Flies

show improvement after trial 3 (statistically different from trial 1), while no difference in the mean velocity was observed across trials.

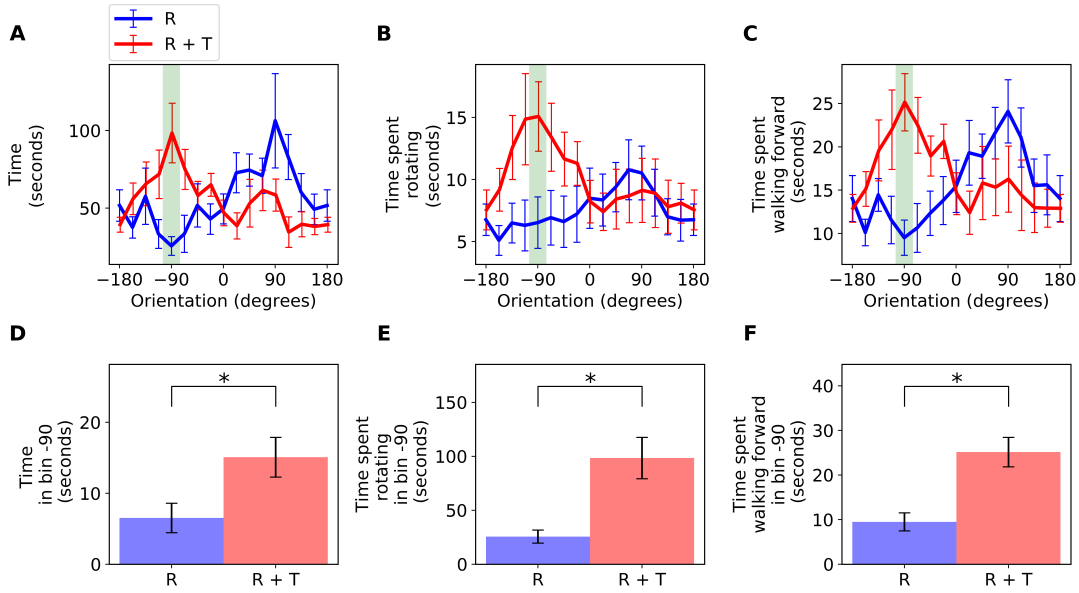


Figure 6.5: Difference in walking direction for 9 flies that can control either only rotation (R) (while positioned at the center of the cylindrical arena), or rotation together with translation (R + T) for 15 minutes in the mechanical VR. Flies were illuminated with the IR laser to encourage walking. **A** Mean time distribution of the orientation, divided in 16 bins of 22.5 degrees. The green bar indicates the position of the green stripe at -90 degrees, and error bars indicate the standard error of the mean (SEM). **B** Time that flies spent rotating with a rotational velocity higher than 22.5 degrees per second, as a function of the orientation. **C** Time that flies spent walking forward with a velocity higher than 0.5 mm per second, as a function of orientation. **D** Time distribution around the green stripe (bin -90 degrees). **E** Time spent rotating around the green stripe. **F** Time spent walking forward towards the stripe. The asterisks indicate statistical significance using a t-test, with $p = 0.034$, $p = 0.004$ and $p = 0.002$ for subfigures D, E and F respectively.

6.1.4.3 Place memory is preserved also after learning in a fraction of flies

We next tested whether flies retained their place preference after offset of the aversive conditioning stimulus. Monitoring flies for 5 minutes after the end of the last training session (testing phase), we found that 3 out of 16 flies returned to the cool spot in the absence of the conditioning stimulus with higher probability than observed in any of the flies before learning. Fig. 6.8A shows the trajectories of all flies during the exploration phase (5 minutes of closed loop walking without heat) before training starts (right side) as well as the time spent in the area that defined the cool spot during the subsequent learning

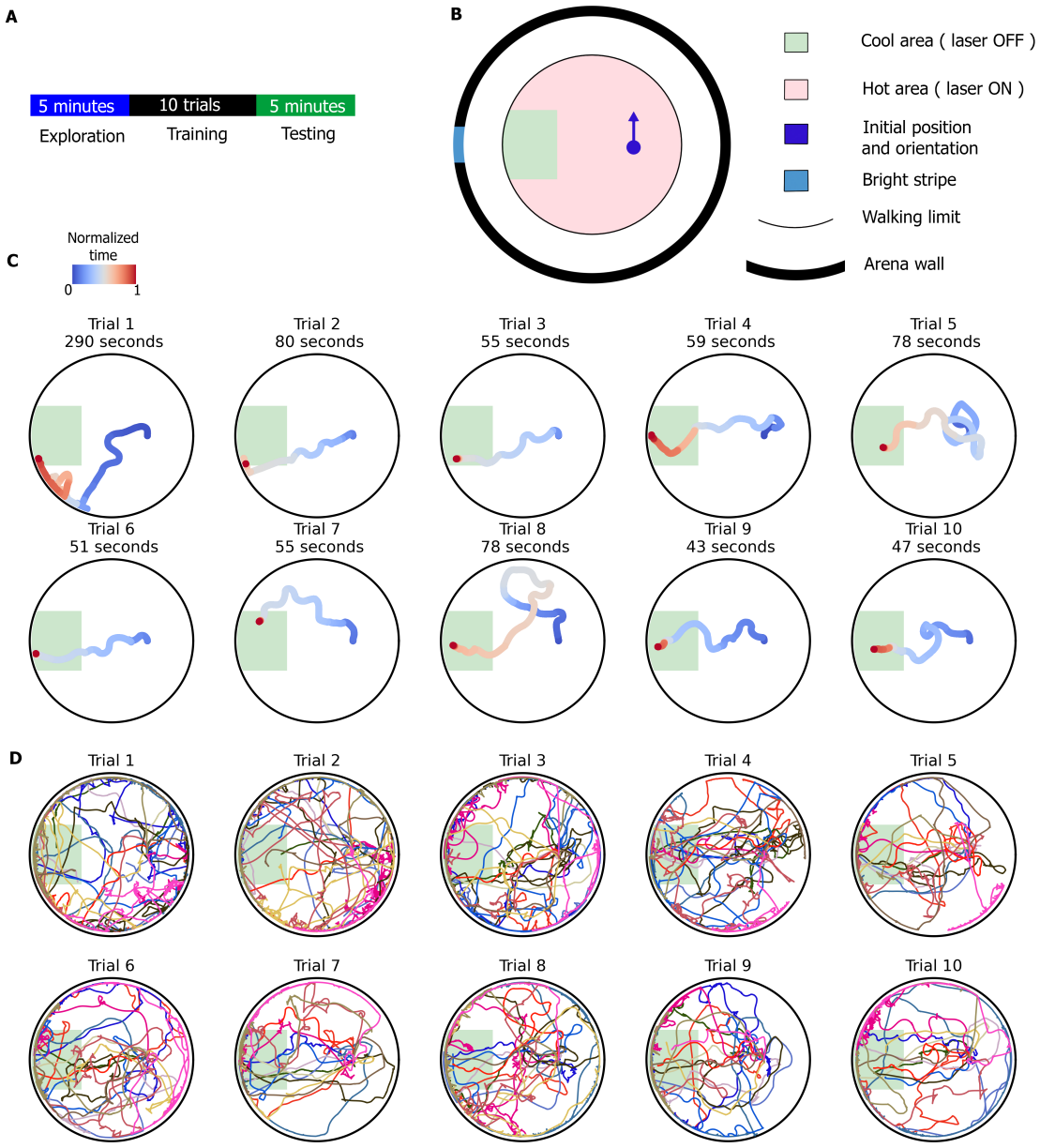


Figure 6.6: Place learning experiment with a single bright stripe. **A** Timeline of the experiment. First, flies freely explore the arena during 5 minutes. Then, they learn to find the cool spot during 10 trials using the heating laser, and finally freely explore the arena again during 5 minutes (testing). **B** Top view of the arena. The cool spot, where the laser was switched off, was defined as a square with sides of $50mm$ and its center located $50mm$ to the left of the center of the arena. The initial position of the fly was defined at $30mm$ to the right of the center of the arena. The bright stripe was placed right in front of the cool spot. **C** Trajectory of fly 11 for each trial. The color in the trajectory indicates the normalized time, the total time for reaching the cool spot is indicated at the top. **D** Trajectories of all 16 flies across all trials.

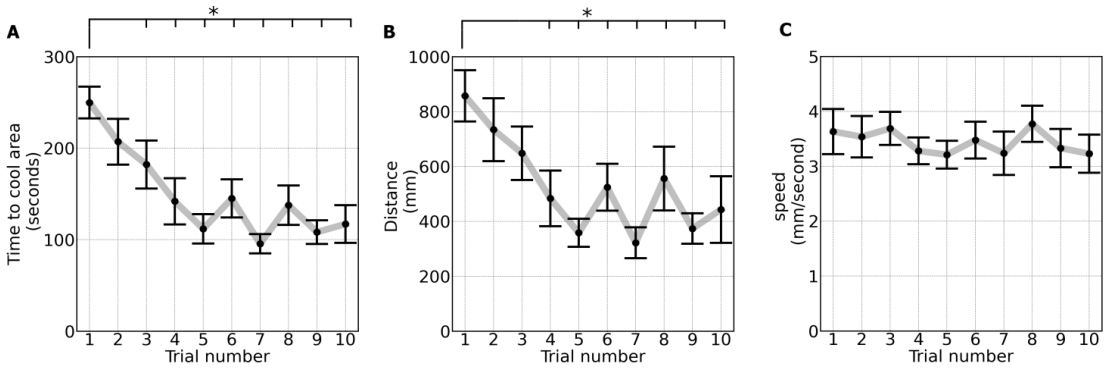


Figure 6.7: Training performance. **A** Average time across all 16 flies for reaching the cool spot (including the 30 seconds that flies had to spend in the cool spot before resetting). **B** Average distance that flies walked in each trial. **C** Average speed of the flies across each trial. Error bars represent the standard error of the mean (SEM). Asterisks indicate statistical significance between trial 1 and the rest of the trials, using a t-test with p-values below 0.05. For example in panel A, trial 1 is statistically different from the rest of the trials, except for trial 2.

experiment. Fig. 6.8B, left side, shows the trajectories of the 16 flies during the 5 minutes after the offset of the last learning trial (again without heat). The three flies shown in 6.8C showed an increased preference for the cool spot after training.

We also asked if the orientation preference of flies changed between the exploration phase and after training. Although the orientation distribution of flies did not change (Supplementary Fig. S6.1.3A), flies displayed more rotation and forward walking around the blue stripe than in other directions after training (S6.1.3B and C, respectively).

6.1.5 Discussion

We developed an assay for visually guided place learning in tethered walking *Drosophila*. The assay is based on a mechanical VR: using a two-dimensional translation stage on top of a rotation stage (slip ring), a cylindrical arena is rotated and translated around a stationary, tethered walking fly. The components used for the rotation stage included a brushless motor with a dedicated driver board to deal with the large rotational inertia of the mechanical VR and for allowing rapid changes in direction, while inexpensive stepper motors and components commonly found in 3D printers were used for the translation stage. The tethered fly can navigate inside the arena in real time on an air supported ball. The resulting mechanical VR ensures that the visual stimulus that the fly sees from any location along its virtual walking trajectory is similar to what it would perceive when navigating freely in the arena. Comparing navigation behavior of flies using only rotational control with combined rotational and translational control, we found that the orientation preference changed between the two conditions for a single green vertical stripe (Fig. 6.5).

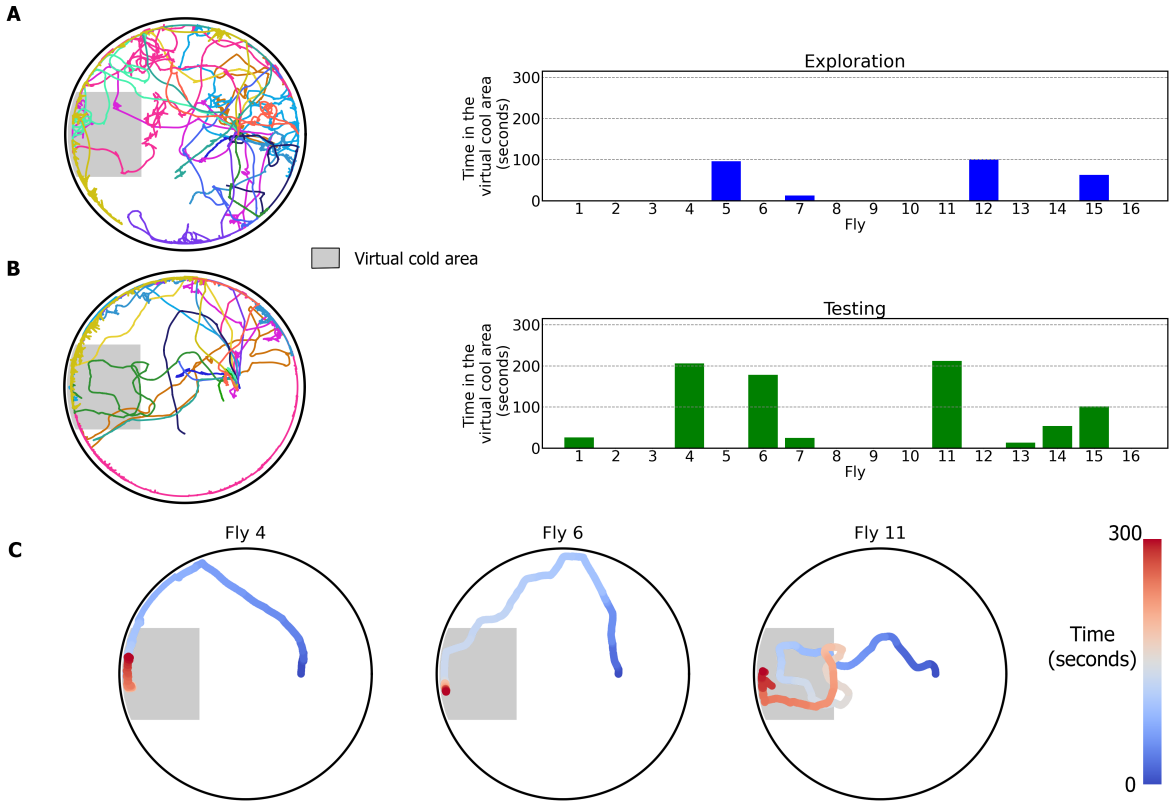


Figure 6.8: Fly behavior during the exploring phase and during the testing phase. **A**, left: trajectories of the 16 flies during the exploration phase, when the laser was switched off. Right: The time each fly spent in the virtual cool spot over 300 seconds. **B**, left: trajectories of the 16 flies in the testing phase during 300 seconds; the laser was again swiched off. Right: time that each fly spent in the virtual cool spot after training. **C** Examples of the trajectories of three flies (4, 6 and 11) during the testing phase that spent most of the time in the virtual cool spot after training.

In this setup, flies can learn to find the location of a cool spot with respect to a visual landmark under heat-based operant conditioning. The cool spot was located in front of a blue vertical stripe which did not elicit a strong orientation preference. The assay can replicate several of the characteristics of place learning observed in freely walking flies [146, 164, 558]. Similar to freely walking flies, the time and distance required for reaching the target is optimized over several trials. The time and distance optimization plateaus between 5 to 7 trials, similar to freely walking assays with individual flies [146, 164, 558]. Additionally, small oscillations in the performance after learning are observed in tethered as well as in freely walking flies after the opimization plateau is reached. Further, in a small fraction of flies, a memory of the cool spot is retained also after the conditioning heat stimulus is switched off (Fig. 6.8B). Flies also changed their rotation and walking velocity distributions before and after training (Supplementary Fig. S6.1.3B and C)

Tethered flying flies can learn to distinguish different visual patterns and such memories

are likely important for freely navigating flies [567]. These tethered flying assays however do not have a translational component which is required for gaining a more complete understanding of navigation circuits [567]. The combination of such translational and memory components has been investigated in experiments with flies walking in virtual reality landscape generated with projectors and operant conditioning using optogentically delivered rewarding and punishing stimuli [160].

The mechanical VR developed here ensures that flies see an actual three-dimensional environment from every point along their virtual trajectory. We used an IR laser as an aversive conditioning stimulus, similar to previous experiments [144, 559, 560, 561]. Flies did not show any visible decrease in performance over the run of the experiment due to heating (as for example indicated by the mean walking velocity across trials) and IR based conditioning avoids having to genetically label different classes of neurons.

The mechanical VR approach has some notable differences to projector base methods (for example [157, 160]). Projector based approaches rely on high frame rates. Achieving a large field of view that surrounds the entire animal with sufficient brightness and contrast is however not easily achieved. The mechanical VR solves problems of stimulus geometry, contrast and brightness in a simple way. Additionally, the continuous motion of the arena is not subject to potential flickering that could be perceived by the animal at low frame rates. A major difference to projector based setups is the comparatively long lag between ball motion and arena motion (around $298ms$ for rotation and 75 for translation, respectively). Interestingly, flies can nevertheless navigate in two dimensions under these conditions and show an intrinsic orientation preference for green stripes, as similarly observed with dark stripes [568, 569]. A tolerance for delays of up to 2 seconds for flies walking freely in a virtual reality environment has previously been described [568].

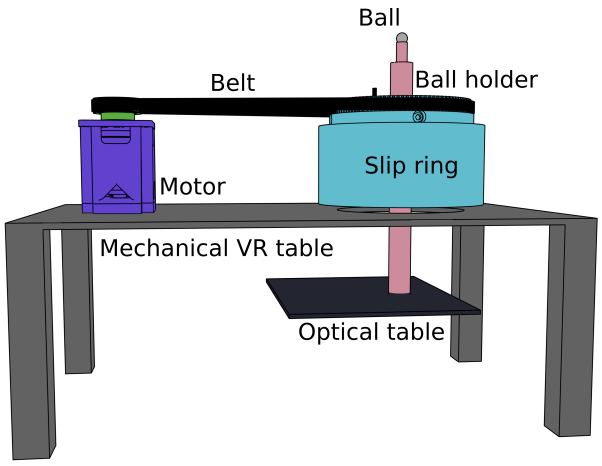
We used an arena with a single landmark (bright stripe) which induced only a weak place and orientation preference before training (see blue bars in Supplementary Fig. S6.1.2B and blue line in Supplementary S6.1.3A) with blue light. We observed reliable learning performance for the safe spot in front of the visual landmark. Potentially different visual stimuli could be used, for example more complicated visual patterns, although, as observed in freely moving flies[146, 164], the flexibility of place learning with respect to the choice of pattern is likely limited.

In addition to different patterns, also different arena sizes or arena shapes could be used, including structures inside the arena, such as mazes, which could potentially provide suitable cues for training. Using different arena shapes only requires that the geometry is integrated with the control software to configure the interaction of the fly with the physical arena boundaries. The mechanical VR will also allow to enrich the fly's experience with additional physical interactions, for example with food [507], wind [570] or touch.

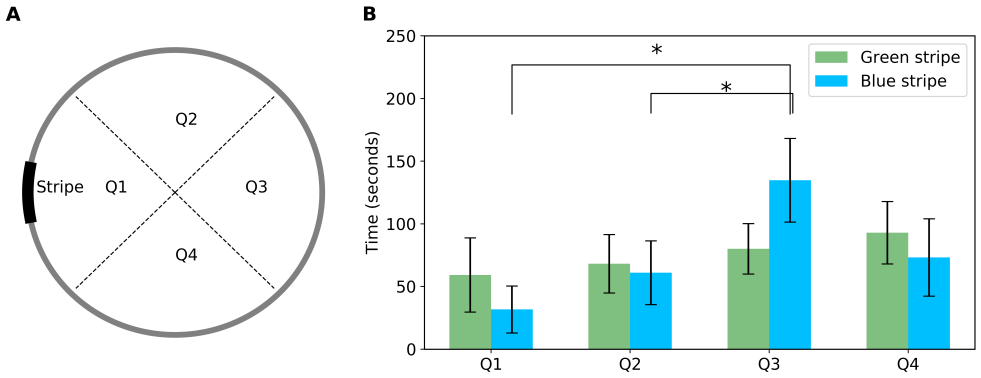
Likely, flies use a combination of idiothetic as well as visual cues for navigation [162, 553, 571, 572] and both components are integrated in the head direction circuits [306, 313].

The use of such idiothetic information has also been observed in tethered walking flies [572]. Idiothetic information could therefore also contribute to the place learning described here, which could be investigated in the future by comparing navigation after training with visual cues to navigation in darkness. In this situation, the control that tethered place learning offers in term of the starting position and orientation of the fly in the arena might prove advantageous.

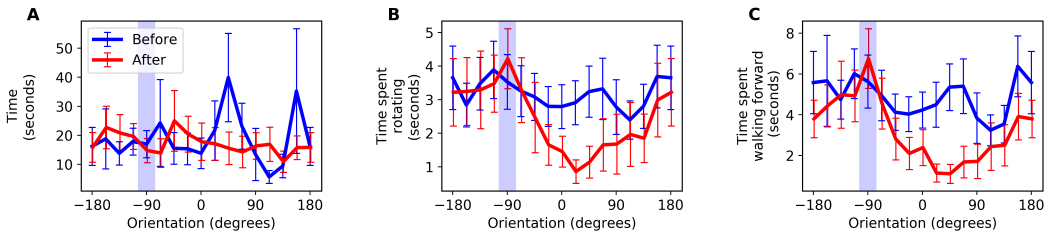
In walking flies, imaging can be performed over long periods of time, including multiple bouts of sleep and wakefulness [507]. Sleep is likely important for memory consolidation also in place learning in flies [130, 178] and imaging over long timescales [507] could be combined with place learning for investigating the impact of sleep or sleep deprivation on memory. More broadly, how such navigation memories could be encoded in the fly brain has been investigated using computational modeling (see for example [441, 573, 574]) and functional imaging in behaving and learning flies could be used to further constrain such models. Overall, combining the preparation developed here with two-photon imaging [331, 507] is expected to contribute to an understanding of neural circuits underlying place learning and memory.



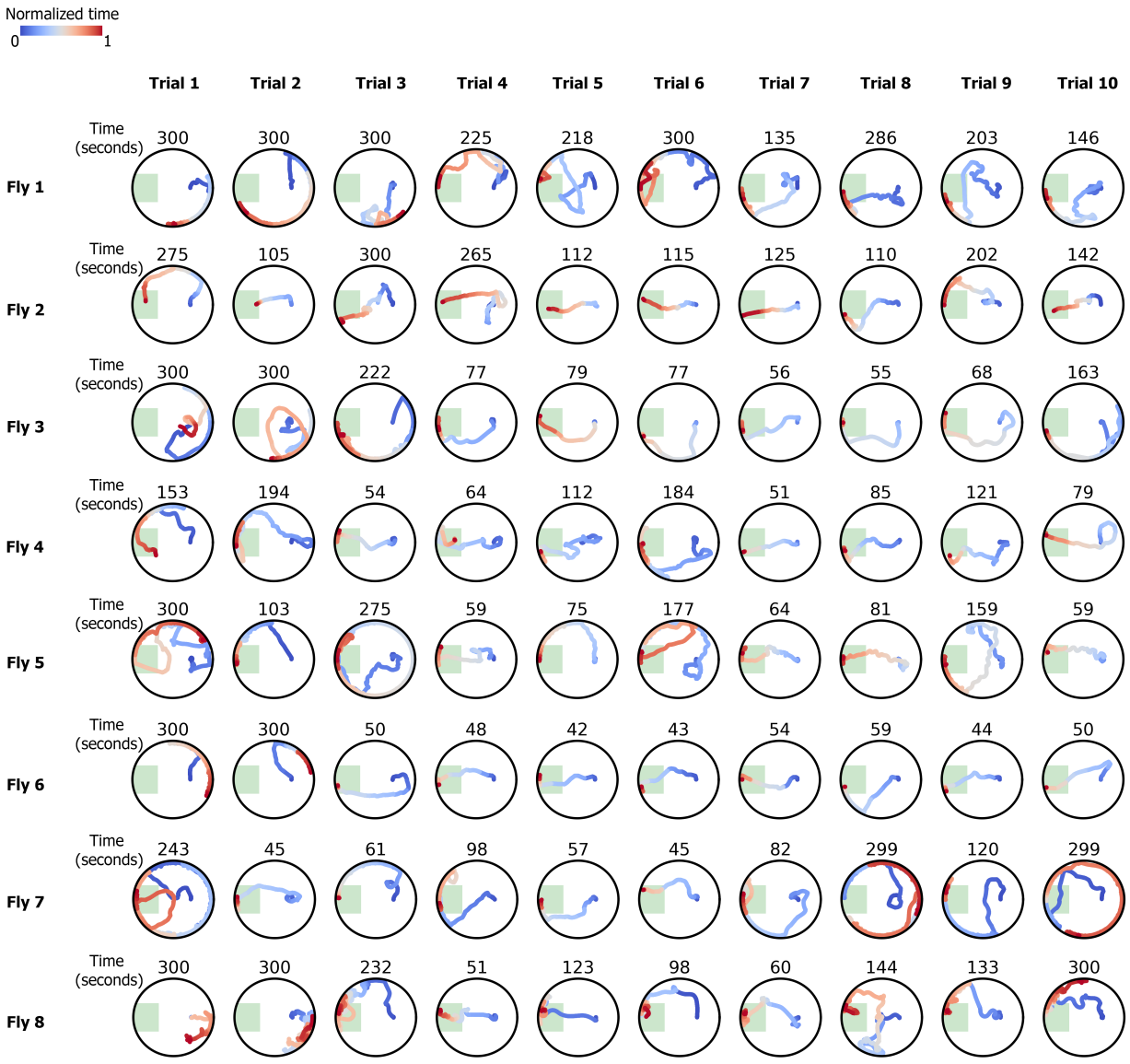
Supplementary Figure S6.1.1: Isolation of the mechanical VR with respect to the optical table (not drawn to scale, the optical table and scaffold (mechanical VR table) were of similar size). The fly and fly mount, laser and corresponding optical components, as well as the ball and cameras are placed on the optical table, whereas all moving parts are mounted on the mechanically isolated platform on a scaffold that is standing on the floor.



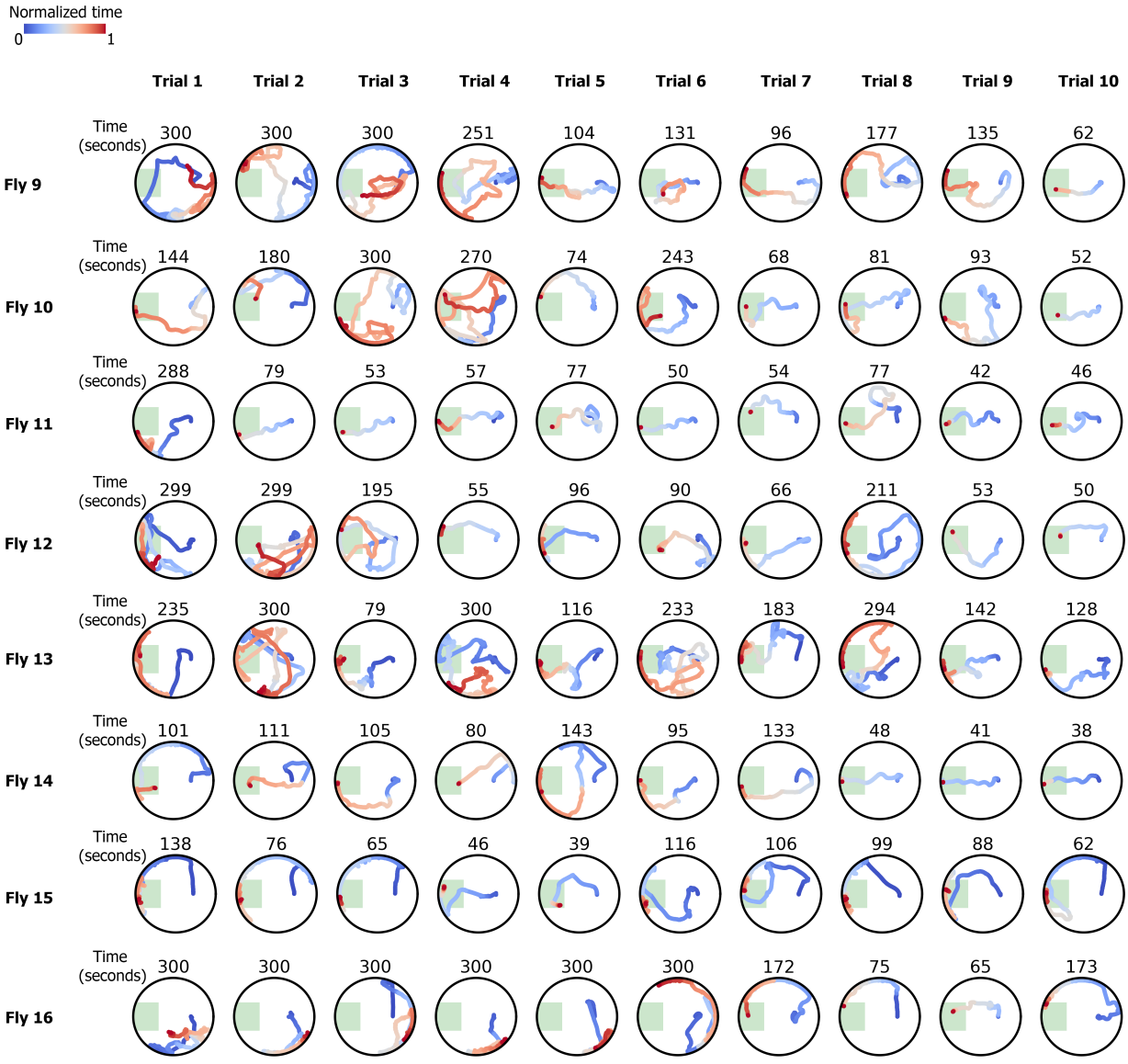
Supplementary Figure S6.1.2: Comparison between green and blue stripes during rotation and translation control for 5 minutes of walking. Flies walking with the green stripe were additionally illuminated with the IR laser to encourage walking. The 16 flies walking with the blue stripe were used for place learning. The data shown here was recorded during the 'exploration phase' at the beginning of the experiment (no laser heating). **A** The arena is divided into four quadrants, Q1, Q2, Q3 and Q4, where Q1 is the quadrant where the stripe is located (indicated by bold black line). **B** Time flies spent in each quadrant. Green and blue bars represent the average time of 9 and 16 flies with a green and a blue stripe in the arena, respectively. Error bars indicate the standard error of the mean (SEM). The asterisks indicate statistical significance between blue bars, using a t-test, with $p = 0.002$ between Q1 and Q3, and $p = 0.030$ between Q2 and Q3.



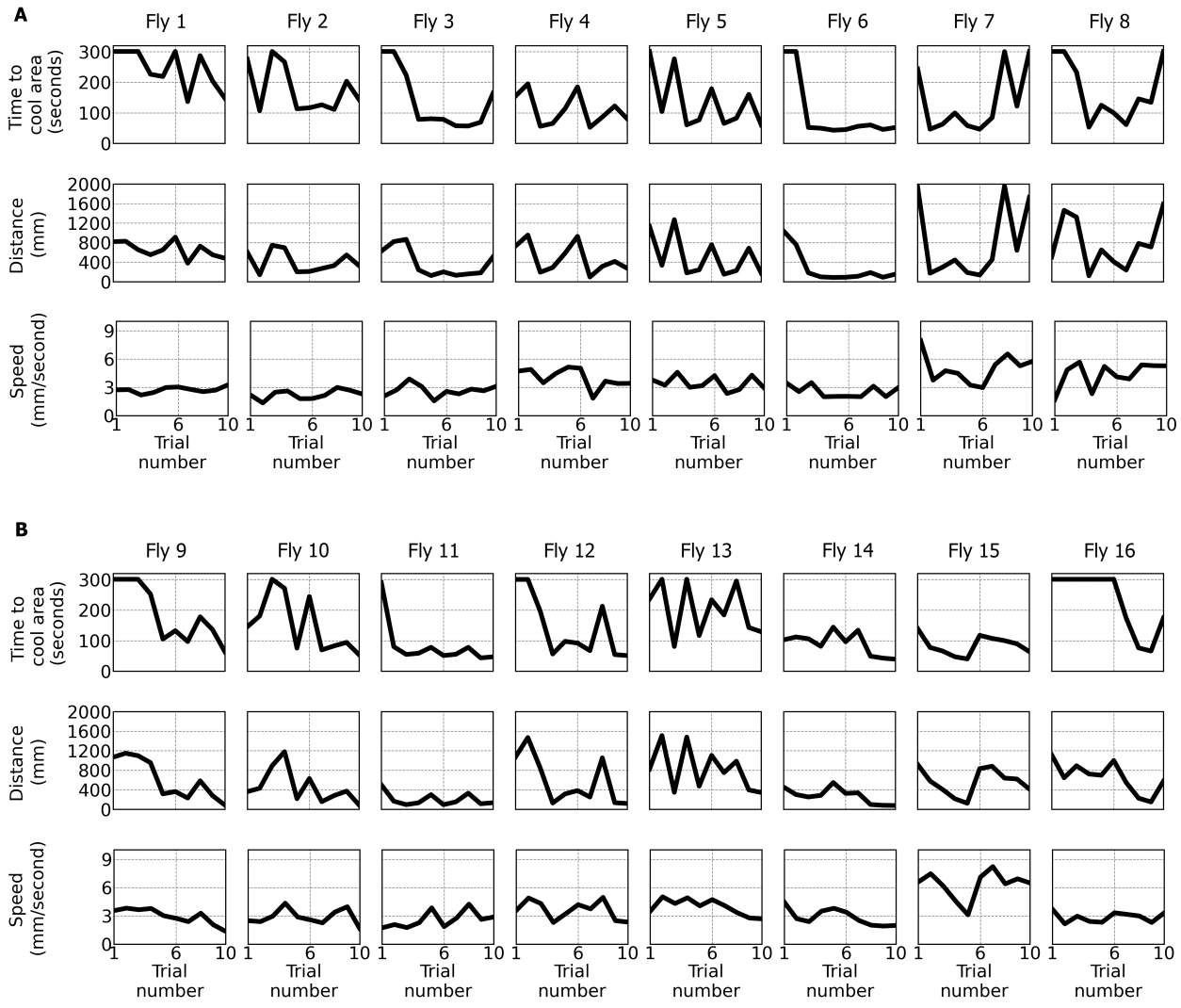
Supplementary Figure S6.1.3: Difference in walking direction for 16 flies that can control rotation and translation (R+T), before and after learning, for 5 minutes in the mechanical VR. **A** Mean time distribution of the orientation, divided in 16 bins of 22.5 degrees. The blue bar indicates the position of the blue stripe at -90 degrees, and error bars indicate the standard error of the mean (SEM). **B** Time that flies spent rotating with a rotational velocity higher than 22.5 degrees per second, as a function of the orientation. **C** Time that flies spent walking forward with a velocity higher than 0.5 mm per second, as a function of orientation.



Supplementary Figure S6.1.4: Trajectories of flies 1 to 8 across all trials during learning.



Supplementary Figure S6.1.5: Trajectories of flies 9 to 16 across all trials during learning.



Supplementary Figure S6.1.6: Performance of each fly during the training phase. **A** Time to reach the cool spot, total distance walked and mean speed across trials for flies 1-8. **B** The same for flies 9-16.

6.2 Autonomous activity in PFR neurons during place learning

6.2.1 abstract

Neural populations for navigation in mammals, such as place or head direction cells, show autonomous activity during rest and sleep which is important for planning, decision making, and learning. Whether such activity or drift also plays a functional role in the head direction system of the fruit fly is not known.

Here, we characterize autonomous activity in a population of neurons in the central complex, called PFR neurons, which are part of the head direction system of *Drosophila*. These neurons track head direction in flying and walking flies with a bump of activity. Different from other neurons in the head direction system of the fly, we find that PFR neurons show activity with a bump profile that drifts over time when the fly is standing still or sleeping with similar statistics as during navigation. Drift persists independently of the duration of immobility, measured for up to 500 seconds.

We ask whether drift dynamics during immobility is related to activity during behavior, as observed in place or head direction cells in mammals. To address this question, we develop an assay for spatial learning in tethered walking *Drosophila*, combined with two-photon calcium imaging. We find that drift shows similar spatial but faster temporal statistics during during rest than during walking.

These experiments show that drift is, as in mammals, an intrinsic feature of the *Drosophila* head direction system. Further, the developed setup will allow the characterization of neural dynamics during behavior and sleep.

6.2.2 Introduction

Spontaneous activity during rest or sleep is observed in mammals in different brain areas, such as in visual cortex [575, 576, 577] or in brain areas important for spatial navigation [578]. In spatial navigation tasks place cells show activity during rest or sleep that resembles activity observed during navigation across different timescales [199, 201, 577, 578, 579, 580, 581, 582, 583, 584, 585, 586]. This kind of activity has also been interpreted as intrinsic neural dynamics that is already present before learning [577, 583]. Spontaneous activity also occurs in head direction cells in mammals, which show activity similar to that observed during navigation during sleep or rest [453, 587]. Additionally, drift in the mammalian head direction system can be induced using visual stimulation [588].

In *Drosophila*, neural circuits important for navigation and memory have been located in the central complex, a brain area in the center of the fly brain [25, 306]. Memories for visual patterns have been associated with substructures of the central complex using behavioral

genetics [144, 145, 146, 565]. For example ring neurons of the ellipsoid body (EB), a neuropil in the central complex, are required for visual place learning [146]. Other ring neurons that discriminate visual features [155] as well as dopaminergic neurons are important for visual memory as shown using calcium imaging in flies performing pattern discrimination [159].

Multiple classes of columnar neurons that innervate different neuropils of the central complex, including the EB and the fan-shaped body (FB), encode head direction and keep track of the fly's orientation with respect to visual cues as well as in darkness [25, 306]. These columnar neurons encode head direction through a bump of activity that moves across different columns, and most of these neurons do not show activity drift during periods of rest [25, 28, 306, 313, 314, 316]. Instead, the bump positions was found to be stable during periods of rest over a few tens of seconds [313], or also during extended periods of immobility in recordings that lasted multiple days, both during the day (navigating in virtual reality) and during the night (navigating in darkness) [28].

Complementary to such a body centered representation of head direction [313, 314, 316, 443], other neurons encode the heading direction of the fly in a world centered coordinate system [323, 539]. Such representations have been associated with two populations of neurons in the FB, known as hΔB and PFR [323, 465, 539]. PFR neurons encode traveling direction independently of whether the fly is walking forward, backward, or sideways towards a goal with a bump of activity that can be described with a sinusoid [323, 539]. A single example of drift in PFR neurons when the fly was standing was shown in [539]. However, how such activity is related to activity observed during behavior, and what functional role such drift could have for navigation, is not known.

Spontaneous activity has also been described in other *Drosophila* neurons. For example, LFP recordings were used to measure oscillatory dynamics during sleep [193] and reactivation of neurons after learning occurred at the same timescale as enhanced sleep in freely walking flies [177]. Further, the slow decay of activity in ensheathing glia over tens of minutes additionally indicates that sleep is a dynamic state in the fly brain [31]. Modeling of sleep homeostasis in the head direction system proposed spontaneous activity as a mechanism to clear attractor states that form due to neural plasticity [27].

Here, we developed a setup for combined spatial learning and two-photon calcium imaging using a mechanically actuated virtual reality setup [28, 32]. We use this setup to characterize spontaneous activity in PFR neurons while the fly is walking, resting, or potentially sleeping. We find that PFR neurons show activity during rest which is similar to that observed during navigation: PFR activity during rest shows a single bump of activity which however moves faster during rest than during navigation. We further show that flies can learn a navigation task during two-photon imaging.

6.2.3 Results

6.2.3.1 PFR neurons

PFR neurons are columnar neurons that innervate the PB, FB, and ROB (round body), as shown in Fig. 6.2.1A. According to the connectome, there are two types of PFR neurons: PFRa and PFRb [443]. Both PFRa and PFRb neurons receive strong inputs from the hΔB neurons and transform the body-centric heading direction of the fly in the EB into world-centric coordinates in the FB [323, 539]. While the PFRa neurons stay in the same columns across PB and FB, the PFRb neurons make a one-column shift between PB and FB (Fig. 6.2.1B), suggesting that these neurons might move the bump around the FB, similar to PEN neurons for angular velocity integration in the EB [314, 316].

We used the Gal4 line R27G06 expressing GCaMP8m, shown in Fig. 6.2.1C, to study the dynamics of PFR neurons during learning, rest, and sleep. This GAL4 line labels PFR neurons as well as a set of columnar neurons in the EB, possibly EL or EPG neurons. This line has been previously used to describe how PFR neurons encode the head direction of the fly [465], and has also been identified as sleep-promoting [123].

6.2.3.2 Imaging in mechanical virtual reality setup

To study the dynamics of PFR neurons during learning and sleep we combined our previously developed paradigm for spatial learning in tethered walking flies [32] with simultaneous two-photon calcium imaging. First, flies were dissected to create a transparent window over the brain using UV glue, as previously described [28], and were left to recover for at least 2 days. Then flies were glued to a cover slide and placed under a two-photon microscope and on an air-suspended ball (Fig. 6.2.1E).

We used a mechanical virtual reality (VR) where a cylindrical arena rotates and translates around the fly in closed loop depending on ball motion tracked with a camera (Fig. 6.2.1D), allowing flies to navigate in 2 dimensions. The mechanical arena was larger than the one developed in [32], with a diameter of 500 mm and a height of 250 mm (see Fig. 6.2.1D, and 6.2.2A). The fly was at a height of 150 mm from the bottom of the arena. To avoid collisions with the microscope objective, the translation of the cylindrical arena was limited to a circle with a diameter of 270 mm; thus, the minimum distance between the fly and the arena wall was 165 mm. The mechanical VR contained two vertical stripes as visual cues (Figs. 6.2.1D and 6.2.2A), which were illuminated from the back with LEDs and covered with colored glass filters to spectrally separate the arena illumination from the detected fluorescence (see Methods). The glass filters were additionally covered with a white diffuser to avoid light reflections and the rest of the arena was covered with black paper. Only one stripe was self-illuminated with LEDs during the behavioral assay. This resulted in one bright stripe and one darker stripe that was not self-illuminated, but was visible due

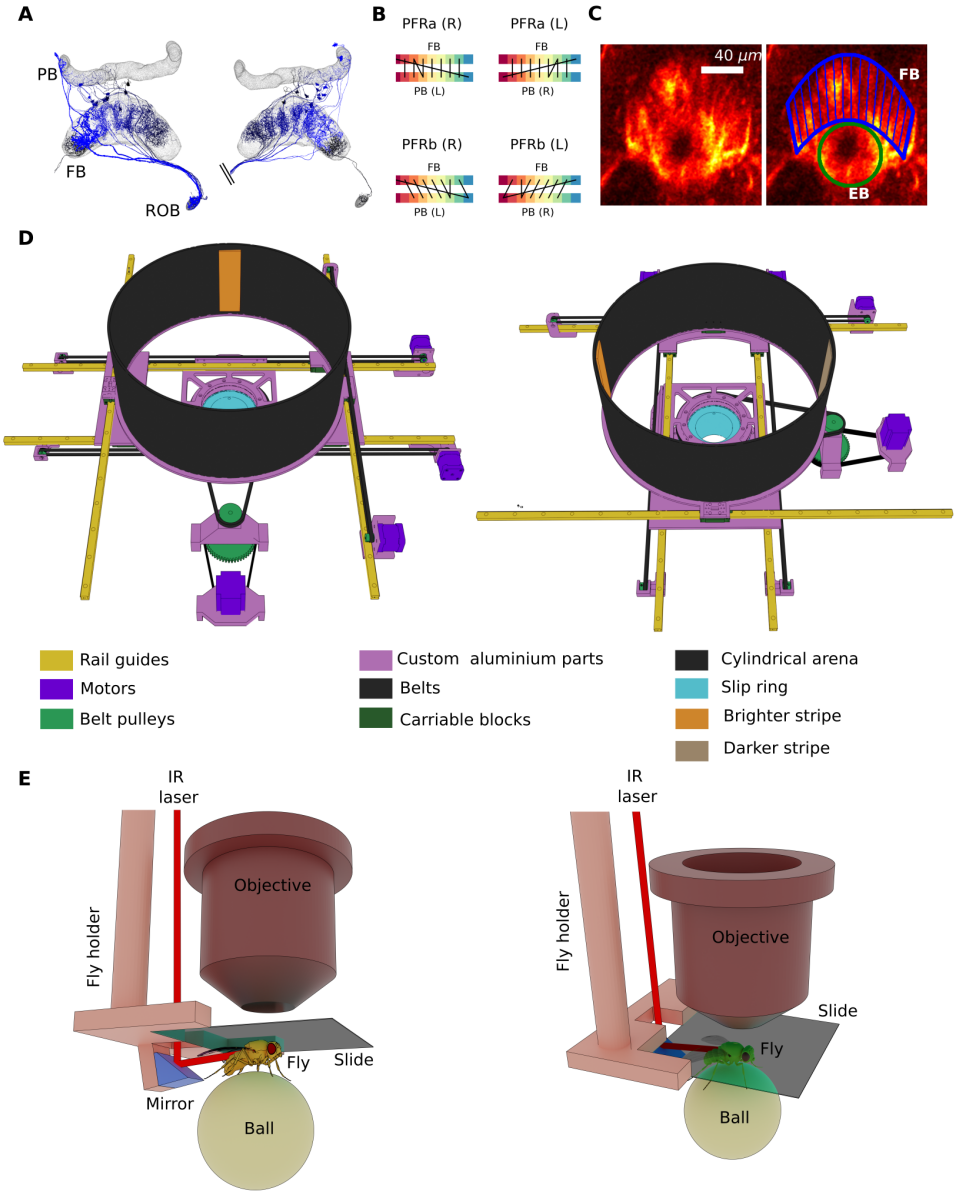


Figure 6.2.1

to the light reflected from the brighter stripe (see Fig. 6.2.2A).

6.2.3.3 Learning behavior

We implemented a spatial learning assay similar to [32] where flies had to find a cool area in the mechanical VR, which was simulated by switching off the IR laser that was pointed at the fly's abdomen (see Fig. 6.2.1E). The cool area was located in front of the brighter stripe, as shown in Fig. 6.2.2B.

Experiments ran for a total of 10 trials. In the first trial, the mechanical VR was set

Figure 6.2.1: PFR neurons and experimental setup. **A** PFRa neurons in the right and left hemisphere, respectively. This panel is obtained from the fly connectome[443] **B** Connectivity between the different columns on the right and left side of the PB (right and left, respectively) and FB for PFRa neurons (top) and PFRb neurons (bottom). **C** PFR neurons labeled by 27G06-GAL4 on the left. On the right, 16 different regions of interest (ROIs) are defined to compute the activity of PFR neurons across the different columns in the FB. **D** Mechanical virtual reality setup from two different views, colors are for visualization. The setup is described in detail in [32]. **E** A fly glued to a cover slide is attached to the fly holder and placed between the air-supported ball and the objective. The IR laser used as an aversive stimulus is focused on the back of the fly through an opening in the fly holder (visible on the left side) and with the help of a small mirror.

to its initial position (see Fig. 6.2.2B, left) and the fly started to navigate in closed loop while we recorded calcium activity in PFR neurons. The IR laser provided an aversive "hot" stimulus in pulses of 0.1 seconds at all positions of the arena except for the location of the cool area. To prevent flies from resting or grooming, the air supply for the ball was turned off for 0.1 seconds with an automated valve if the flies were not walking for more than 10 seconds, which stimulated flies to resume walking. The air valve was triggered by tracking of the velocity of the ball in real time [157].

Once the flies found the cool area and stayed inside for 10 seconds, a new trial started and the self-illuminated stripe switched to the diametrically opposite side of the arena (see Fig. 6.2.2B). The cool area was also switched to the side of the bright stripe. This had the effect of an instantaneous 180 degrees rotation of the arena from the perspective of the fly, similar to the place learning assay in freely moving flies [146].

If a fly did not find the cool spot within 15 minutes, a new trial started and both the cool area and the bright stripe were switched to the opposite side. Occasionally, flies were in the area to which the cool spot switched after 15 minutes, which made flies accidentally find the cool area immediately in the next trial (see for example trial 2 in Supplementary Fig. S6.2.3). This could have assisted some of the flies to navigate again to the bright stripe in subsequent trials.

We trained a total of 9 flies for 10 trials while continuously monitoring activity from PFR neurons as well as in the EB. Activity from PFR neurons was measured using regions of interest (ROIs) distributed across the FB, according to the columnar architecture and morphology of these neurons (Fig. 6.2.1C, right).

Fig. 6.2.2C shows the combined trajectories from all flies in every trial, while the top row of Supplementary Figs. S6.2.1-S6.2.9 show all the single trajectories as well as the recorded activity in the FB and EB for each trial in every fly. Flies displayed learning behavior by optimizing the time to reach the cool area over the 10 trials (first row in Fig. 6.2.2F on the left), similar to the learning behavior in tethered flies [32] and freely moving flies [146].

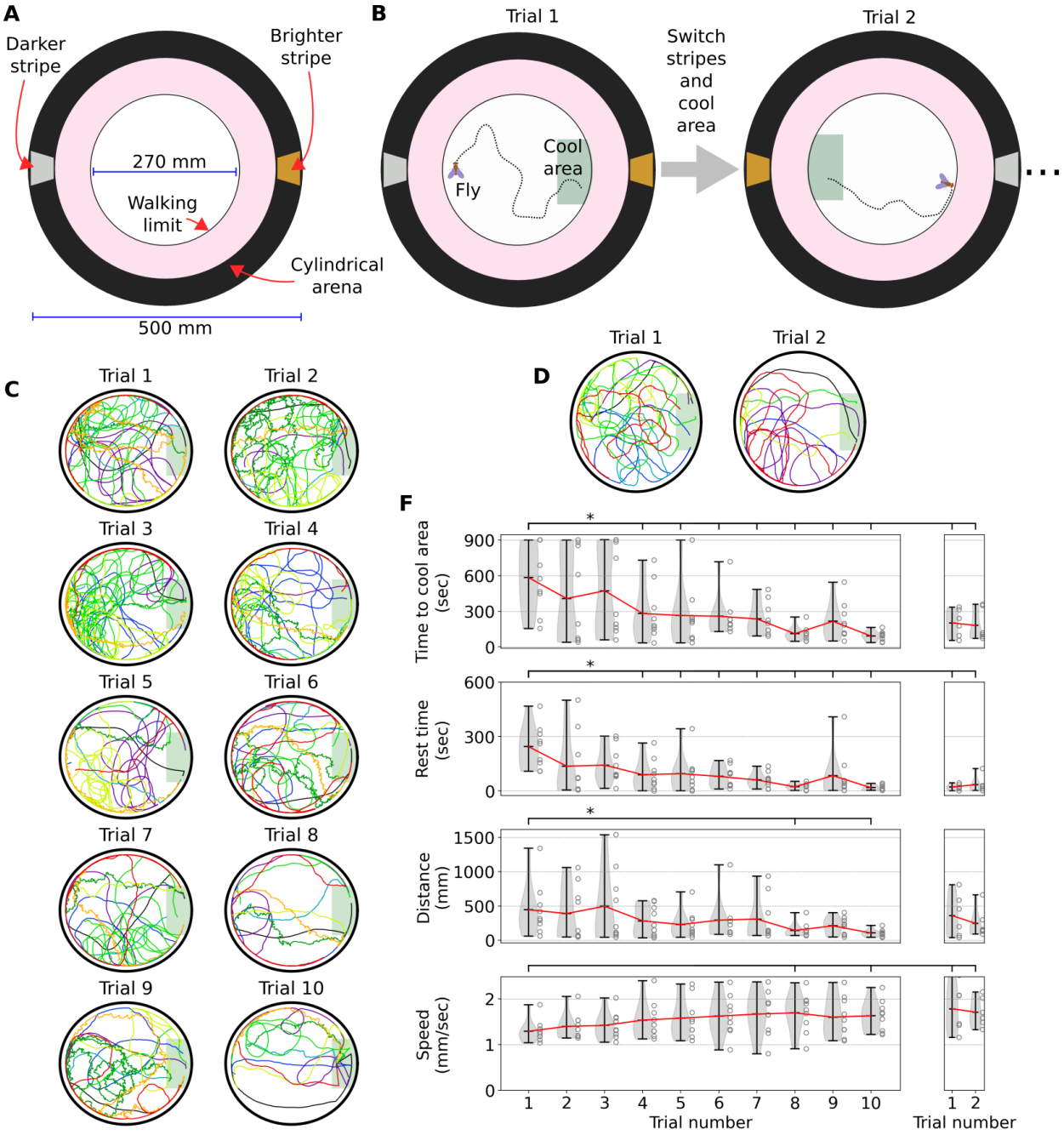


Figure 6.2.2

Flies additionally displayed a decrease in resting time and walking distance before reaching the cool area across the trials (second and third row in Fig. 6.2.2F on the left, respectively), as well as a slight increase in velocity in the final trials (last row in Fig. 6.2.2F on the left).

After 10 trials, the flies were left to navigate in the mechanical virtual reality for 20 minutes without any aversive stimulus (IR laser turned off), while keeping the same illumi-

Figure 6.2.2: Learning assay and performance of flies during learning. **A** Top view of VR cylindrical arena. Two stripes (one darker, one bright) at opposite sides of the arena serve as visual cues. A walking limit is defined to avoid collisions between the microscope objective and the arena walls. **B** Learning assay: First trial, left: the fly starts at a fixed position and orientation. After finding the cool area and staying inside for 10 seconds, both the cool area and stripes switch to the opposite side, and a new trial begins (right). **C** Trajectories of all flies ($N = 9$) across 10 trials in the mechanical VR (each color represents one fly). **D** Trajectories of flies over 2 trials after a break of 20 minutes ($N = 8$ and $N = 7$ for the first and second trials, respectively). **F** Learning performance of the flies for 10 trials (left) and for 2 trials after a break of 20 minutes (right). First row: the amount of time that flies took to find the cool area. Single grey points represent individual flies, violin plots represent the distributions at each trial, red line shows mean value. Second row: amount of time that flies were resting (i.e., not walking) over trials. Third row: the distance that flies walked over trials. Fourth row: Mean speed over trials. Asterisks represent statistical significance using t-test (p-values < 0.05) between the distributions in the first trial and the rest of the trials.

nation as during training (one of the stripes was switched on). During this period, flies often displayed epochs of immobility, some of which lasted for more than 5 minutes, a common threshold time used to define sleep in flies [18, 19]. After a break of 20 minutes, the same learning assay started again for 2 trials to assess if flies still remembered the location of the cool area. In the first and second trials after the break, one and two flies, respectively, were discarded after dying in the middle of the trial. All the trajectories for trials after the break are shown in Fig. 6.2.2D and in the second row of Supplementary Figs S6.2.1-S6.2.9 together with the recorded activity from PFR neurons and in the EB. After the 20 minutes break, flies still displayed a decreased time to reach the cool area, decreased resting time, and increased speed compared to the very first trial before the 20 minutes break (Fig. 6.2.2F, right), suggesting that flies still remembered the location of the cool area.

6.2.3.4 Drift activity while the fly is standing still

PFR neurons encode the heading direction of the fly [323, 465, 539] (Fig. 6.2.3A). We observed, as previously noted [539], that, when flies were standing still or grooming, PFR neurons showed activity that moved autonomously across the FB columns (Fig. 6.2.3B).

To quantify this autonomous activity we first tested whether PFR neurons produced a bump of activity when the fly was resting or whether any other activity profiles might occur. To assess this, we applied Principal Component Analysis (PCA) to the normalized fluorescence activity (Fig. 6.2.3C, fourth row, see Methods) to reduce the 16-dimensional fluorescence activity (defined by the 16 ROIs) to 2 dimensions. Fig. 6.2.4A shows the projection of the fluorescence at any time along the first two principal components (see

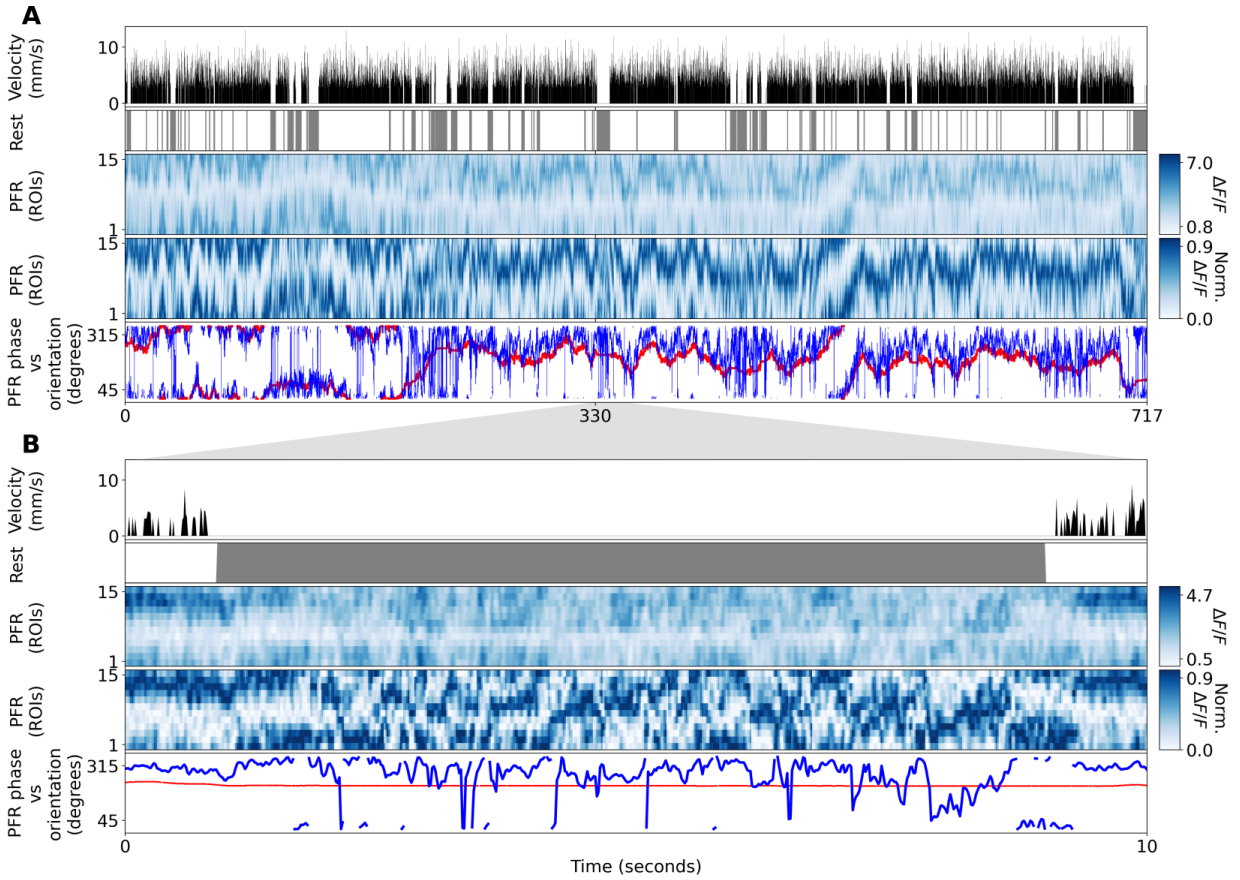


Figure 6.2.3: Activity of PFR neurons. **A** Example of activity of PFR neurons over one trial in one fly during the learning experiment. Top row: velocity of the fly in bins of 1 second. Second row: rest bouts of the fly defined by zero velocity. Third row: fluorescence of PFR neurons over 717 seconds. Fourth row: normalized fluorescence of PFR neurons (see methods). Fifth row: phase of PFR neurons (blue) and orientation of the fly on mechanical VR (red). **B** Same as A, but this panel shows zoom-in of a rest bout in the middle of the trial with a duration of 8 seconds.

Methods). During walking (velocity larger than zero), the embedded fluorescence organizes along a ring, and the phase at any time, defined as the angle of a point from the origin with respect to the x-axis, encodes the orientation of the fly in the arena (Fig. 6.2.4A and B, and Supplementary Figs. S6.2.10 and S6.2.11). However, during rest (zero velocity) the embedded fluorescence organizes in a disc with no clear correlation with the orientation of the fly (Fig. 6.2.4A and B, and Supplementary Figs. S6.2.10 and S6.2.11).

To illustrate why activity during rest organizes more broadly than during walking, we discuss what the distance from the origin encodes in the embedded manifold. For this purpose, we selected points of embedded fluorescence frames during rest at a constant distance from the origin at different radii (Fig. 6.2.4D, first row). Then we transformed these points back into their corresponding normalized fluorescence measured in each ROI (Fig.

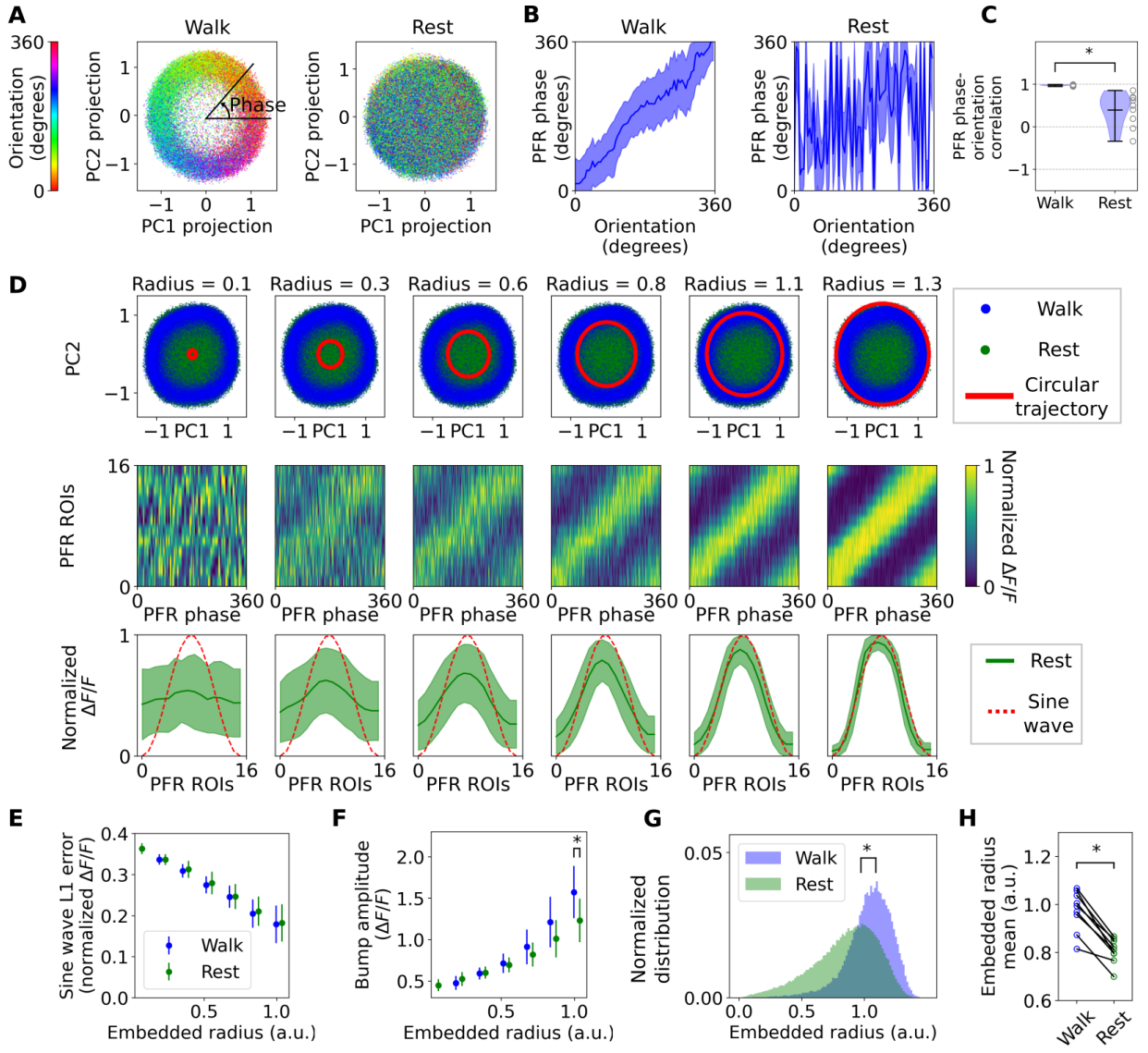


Figure 6.2.4

6.2.4D, second row). We then aligned the normalized fluorescence across the PFR phase to find the mean activity across the ROIs for a given radius in the embedded manifold (Fig. 6.2.4D, last row). Since the mean activity across the ROIs resembled a bump of activity, and has been previously proposed to have a sine wave shape [539], we computed the $L1$ error between a sine wave and the mean activity for each radius (last row in Fig. 6.2.4D, and 6.2.4E). This showed that the $L1$ error decreases as the radius increases, which was not statistically different between rest and walking bouts. We also computed the amplitude of the bump-like activity profile at different radii based on the recorded fluorescence, which increased with increasing embedded radius, and was higher during walking than during rest (Fig. 6.2.4F).

Figure 6.2.4: Dimensionality reduction for analysis of PFR neuron activity. **A** Normalized fluorescence of one fly projected along the first two principal components (PC1 and PC2) during walking (left) and during rest (right). Each point thus represents the embedded fluorescence at each time, and is colored according to the orientation of the fly at that time. The phase of PFR neurons at any time is defined as the angle between of a line from that point to the origin and the x-axis (left side). **B** PFR phase obtained from the embedded normalized fluorescence in panel A against the orientation of the fly for all times, during walking (left) and rest (right). Blue lines represent mean value, while the blue region represents the standard deviation. **C** Distribution of Pearson's correlation coefficients for $N = 9$ flies between the PFR phase and fly orientation during walking and rest. Asterisk indicates statistical significance using t-test (p-value < 0.05). **D** Characterization of PFR activity during rest from the embedded manifold. In the first row and for each column, blue and green points represent the projected fluorescence along the two principal components from panel A during walking and rest, respectively. Embedded fluorescence points with a constant distance from the origin (red circle) are obtained for different radii in each of the columns. These embedded fluorescence frames are transformed back to the original dimension in the second row, which shows the normalized fluorescence from PFR neurons over the PFR phase for different radii in the embedded manifold. The activity of PFR neurons is then aligned according to the phase (see Methods), resulting in an averaged bump-like (green lines) activity profile for different radii in the third row. Green regions indicate the standard deviation across the PFR phase, and red lines show a sine wave. **E** $L1$ error between a sine wave and aligned PFR activity against different radii from the embedded manifold, during rest and walking (green and blue, respectively), and for all flies ($N = 9$). Points indicate mean values, while error bars indicate standard deviation. **F** Amplitude of the bump-like profile against different radii from the embedded manifold for all flies. **G** Distribution of the radius in the embedded manifold during walking and rest from panel A (blue and green, respectively). Asterisk indicates statistical significance using Kolmogorow-Smirnow test (p-value < 0.05) **H** Mean of the embedded radius distribution during rest and walking for $N = 9$ flies. Asterisk indicates statistical significance using paired t-test (p-value < 0.05).

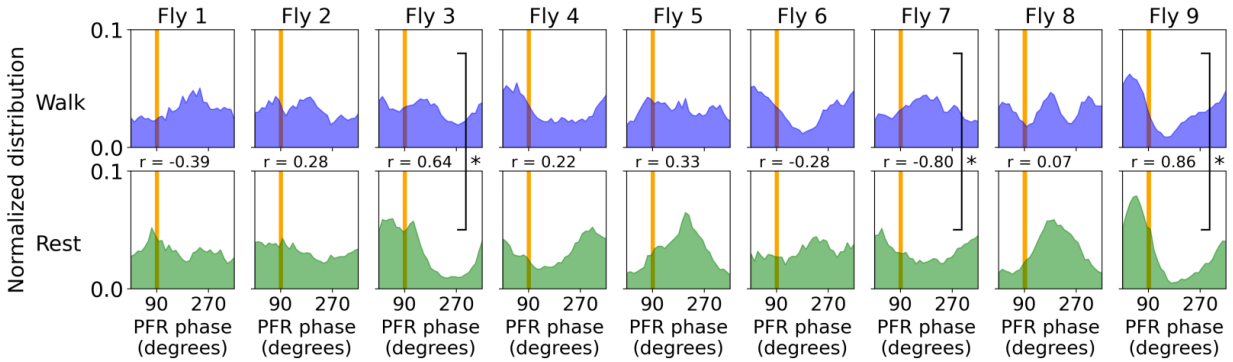


Figure 6.2.5: Normalized distributions of the PFR phase during walk (blue, top row) and rest (green, bottom row) for each fly over the whole learning experiment. The orange vertical line represents the orientation of the bright stripe. Comparison between walking and rest distributions in each fly was assessed using Pearson correlation, where the correlation value, r, is shown, and its significance is indicated through a vertical black line and asterisk between the two distributions.

Taken together, this analysis shows that PFR neurons display a bump-like activity profile during rest similar to the one during walking. However, the distribution of the embedded fluorescence is broader during rest (Fig. 6.2.4G and H), indicating that the amplitude during rest was on average smaller and that the fit to a sine wave was worse than during walking.

PCA provides a reliable way to obtain bump trajectories from the PFR phase. The embedded radius additionally provides information about how well activity from PFR neurons approximates a sine wave (Fig. 6.2.6A and B). We therefore ignored the PFR phase if the embedded radius was lower than 0.3 (Fig. 6.2.4D, second column), and assumed that the PFR phase in those instances stayed constant.

The distribution of the PFR phase during walking and rest epochs is shown in Fig. 6.2.5 for each fly over the course of the learning experiment. We used Pearson correlation between the rest and walking distributions to assess whether these distributions were similar in shape or not, which for example could be the case if the PFR phase during rest was revisiting the same angles as during walking. Although in some of the flies the PFR phase distribution during rest was correlated to the one during walking (fly 9, Fig. 6.2.5), other flies showed a negative correlations (fly 7, Fig. 6.2.5) or no clear correlations.

We then filtered the PFR phase using a median filter (see Methods) and computed the PFR phase velocity distribution during walking and rest. Both distributions followed a Gaussian-like distribution centered at zero (see Fig. 6.2.6C), but the standard deviations during rest were on average twice as large as during walking (Fig. 6.2.6D). This indicates that the PFR phase moves faster during a larger fraction of time during rest compared to walking.

We binned the velocity of the PFR phase over continuous rest and walking intervals and

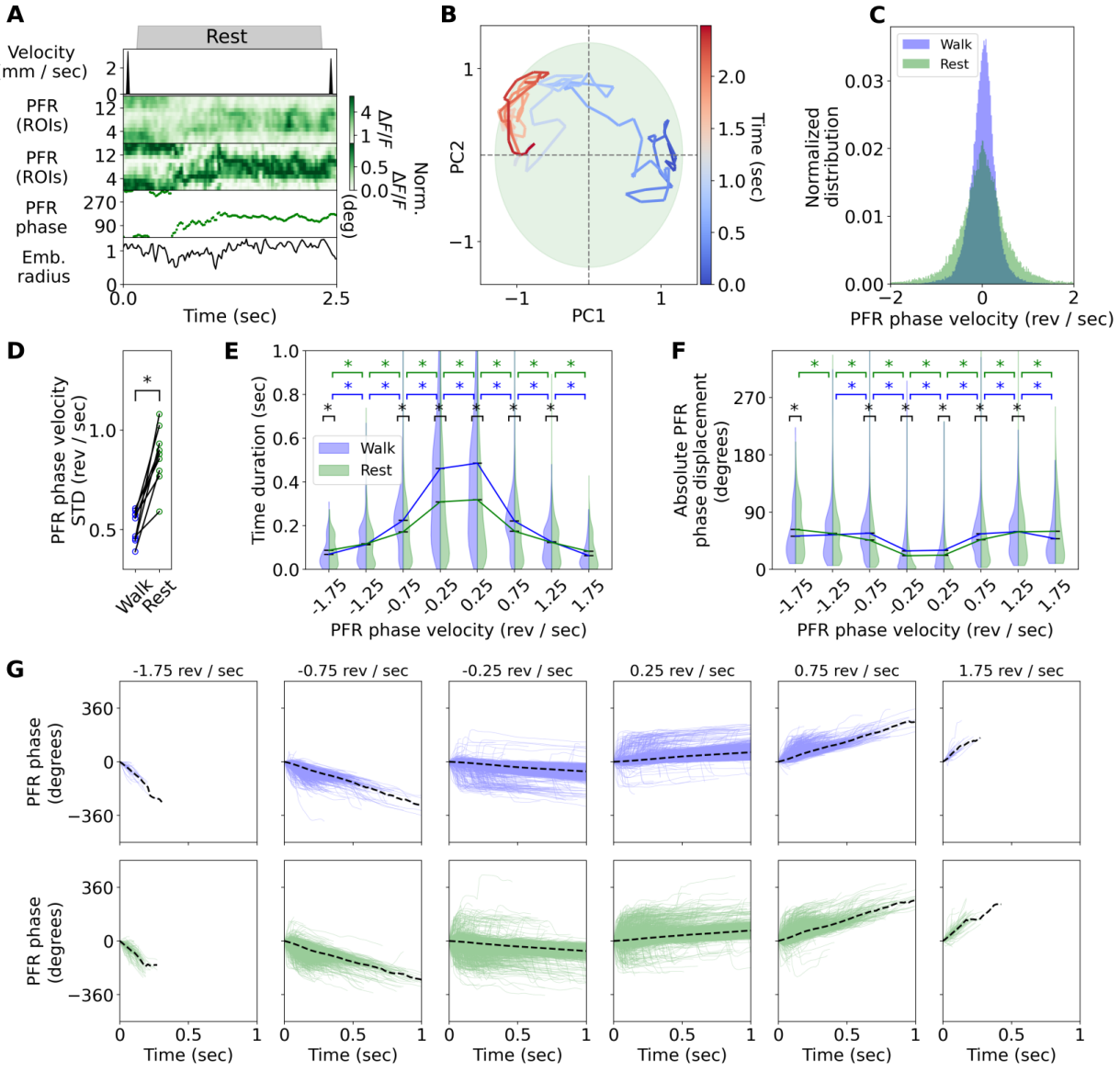


Figure 6.2.6

computed the distribution of times during which PFR phase was moving at a given binned velocity (Fig. 6.2.6E). Additionally, we computed the distribution of absolute PFR angle displacement at each binned velocity (Fig. 6.2.6F). Fig. 6.2.6G shows all the intervals of the PFR phase moving at nearly constant velocities.

In general, the PFR phase moved faster over a short amount of time and produced larger displacements. However, the PFR phase during walking stayed at a lower velocity for a longer time compared to resting (Fig. 6.2.6E). This suggests that the PFR phase moved fast in bursts of small time intervals below 0.5 seconds.

We additionally quantified the cumulative absolute drift of the PFR phase for all walking and rest bouts over the learning experiment (Fig. 6.2.7A, see Methods). We computed the

Figure 6.2.6: Velocity analysis for the phase of PFR neurons. **A** Example of a rest bout in a fly while recording PFR neurons. Top row: linear velocity of the fly. Second and third rows: fluorescence and normalized fluorescence of from PFR neurons, respectively. Fourth and fifth rows: PFR phase and embedded radius of PFR neurons over time obtained by dimensionality reduction. **B** Trajectory of the PFR phase from panel A across the embedded manifold. The green area represents the extent of the embedded manifold for visualization. **C** Normalized velocity distribution of the PFR phase during walking (blue) and rest (green) for a single fly over a whole recording. **D** Standard deviation of the PFR velocity distributions during walking and rest for $N = 9$ flies. Asterisk indicates statistical significance using a paired t-test (p-value < 0.05). **E** Distributions of the time duration that the PFR is moving at a given binned velocity for all flies ($N = 9$) during walking (blue) and rest (green). **F** Absolute displacement of the PFR phase moving at a given binned velocity for all flies during walking (blue) and rest (green). Asterisks in panels E and F indicate statistical significance (p-values < 0.05) between different binned velocities over walking (blue), over (green), and between the same binned velocity over walking and rest (black). **G** Example of intervals in time where the PFR phase is moving at a given binned velocity during walking (top row) and rest (bottom row). The black lines indicate the mean PFR phase over all intervals.

slope of the cumulative drift in each fly and for all walking and rest bouts, interpreted as the absolute PFR phase displacement per second (Fig. 6.2.7B), which shows that the PFR phase was drifting two times faster during rest than during walking.

6.2.3.5 Drift during sleep

After the first 10 trials, flies had a 20 minutes break where they displayed longer epochs of immobility over 5 minutes while activity from PFR neurons was being monitored. Fig. 6.2.7D shows an example of a rest bout with a duration of over 8 minutes. We asked whether the drift dynamics from PFR neurons changed with the time during which the fly was immobile. We therefore computed the absolute cumulative drift of the PFR phase over continuous rest bouts (Fig. 6.2.7C) and obtained the slope of the cumulative drift over time for different intervals of immobility (Fig. 6.2.7E). Interestingly, the drift in the PFR phase was slower in the first 5 seconds of immobility, and did not change nor disappear after longer times of immobility (Fig. 6.2.7E), suggesting that these neurons show autonomous activity potentially also during sleep.

6.2.4 Discussion

We developed a setup for two-photon imaging during spatial learning in walking flies. We used this setup to characterize spontaneous activity in PFR neurons. While this experiment and the analysis are still ongoing we here draw some first conclusions about drift activity

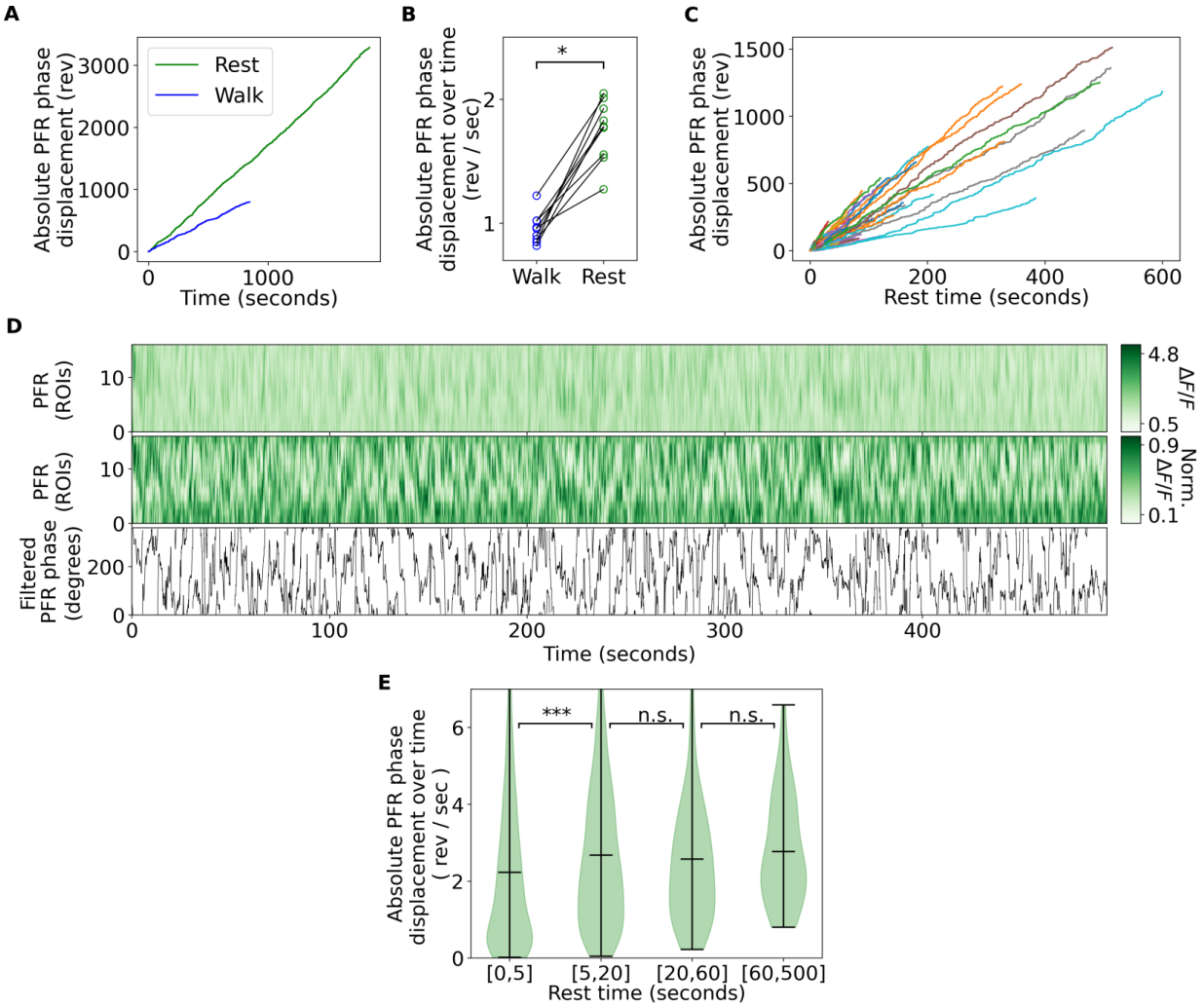


Figure 6.2.7: PFR displacement during rest and walking, and during sleep. **a** Absolute PFR phase displacements during discontinuous bouts of walking and rest for a single fly over the whole experiment. **b** Fitted slope of the absolute PFR phase displacement over time during walking and rest for all flies. The asterisk indicates statistical significance using a paired t-test (p-value < 0.05). **c** Absolute PFR phase displacement during continuous rest bouts over time. Each line represents a single rest bout longer than 0.5 seconds ($N = 3342$ from 6 flies). **d** Example of the drifting PFR activity over a rest bout that lasts more than 500 seconds. First row: fluorescence from PFR neurons in each ROI over time. Second row: normalized fluorescence from PFR neurons over time (see Methods). Third row: Filtered PFR phase over time, using a mean filter with a filter size of 0.5 seconds (see Methods). **f** Distributions of the absolute PFR phase displacement over time for different ranges of rest time. The three asterisks indicate statistical significance evaluated using Kolmogorow-Smirnow test (p-value < 0.0005).

in PFR neurons and briefly discuss potential reasons for drift that could be tested in future experiments.

First, PFR neurons show similar activity during navigation and during rest, with similar activity profiles. During rest, however, the autonomous dynamics in PFR neurons moved about two times faster than during navigation (Fig. 6.2.7A and B). This spontaneous activity was similar between short and long bouts of rest or sleep, although it was slower in the first 5 seconds of immobility (Fig. 6.2.7C and E).

Compared to learning experiments in flying flies [159], performing learning experiments in walking flies is in particular advantageous for investigating autonomous activity during rest and sleep, which occur naturally during walking while flight behavior needs to be interrupted. For example, behavior experiments for place learning have shown that performance deteriorates after sleep deprivation [166], an experiment that could be similarly implemented with the developed setup.

Autonomous activity at different timescales has been observed in the mammalian head direction system during sleep or rest [453, 587] as well as drifting activity after visual stimulation in darkness [588]. Spontaneous activity showed different statistics between wake and sleep in [587], while we here observed similar statistics during walking and rest. While replay of activity has also been observed using calcium imaging in mammals[589], a limitation of experiments in the fly using calcium indicators is the limited temporal resolution which would not allow detecting much faster dynamics during sleep [453, 587].

On a mechanistic level, the question of how drift occurs in head direction systems has been discussed computationally. To prevent drift in basic head direction models, the connectivity between neurons needs to be precisely tuned and symmetric, which seems implausible biologically. Therefore, multiple compensatory mechanisms have been suggested [419, 427, 428, 429, 590].

Several hypotheses for the function of spontaneous activity in mammals have been developed in the literature, some of which are briefly mentioned in the following. In the context of attractor networks, in particular two hypotheses have been discussed [201]. One assumes that drifts serves to reset unwanted attractor states [411], while the other assumes that autonomous activity in the form of replay supports learning and memory consolidation [591, 592]. The idea of unlearning attractors in the *Drosophila* head direction system was computationally explored in [27].

In place cells, the idea that autonomous sequences of activity are important for planning and learning has been investigated. For example, changes in spontaneous activity at behavioral decision points over learning have been observed [593, 594]. More broadly, related to the idea that autonomous activity could contribute to learning, much theoretical work has linked such activity to reinforcement learning [582, 595, 596, 597, 598, 599]. Autonomous activity could also represent internal models [575, 582] or generative models, generating activity patterns similar to those observed during behavior [201, 577]. Further, autonomous activity could play a role in memory consolidation or transfer [188].

Future analysis of the experiments presented here will focus on the autonomous dynamics

during learning, assessing whether these dynamics change with learning performance. The autonomous dynamics observed in the head direction system of the fly, which is also observed in the head direction system of mice during sleep [453], suggests further similarities between head direction dynamics across species.

6.2.5 Methods

6.2.5.1 Drosophila preparation

All flies used for experiments were reared in an incubator at a temperature of 23 degrees Celsius and subjected to a 12-hour light/dark cycle. Flies between 5 and 8 of age expressing jGCaMP8m in PFR neurons (UAS-jGCaMP8m;27G06-GAL4) were used for imaging. The dissection of the flies for inserting a transparent window into the cuticle was performed as described in [28]. First, the perimeter of the window was cut in the head using laser surgery. Then the cuticle and air sacks were removed under a dissection microscope using a microrobotic arm [28]. The opening was then sealed with a drop of transparent UV glue (Freeform, UV fixgel composite). Usually, between 3 and 5 flies were dissected in one day. Flies were allowed to recover after the dissection in isolation, in vials with food for 2 to 3 days before imaging. The flies were then glued to a glass slide with UV glue and transferred to the mechanical VR setup and under the two-photon microscope [355]. Flies that did not show the desired imaging quality (as assessed by the visibility of FB and EB) were discarded at this step. From the selected flies that started the experiment, a total of 10 flies were additionally excluded for reasons such as abnormal walking patterns, failure to reach the cool area after 5 trials, or death during the experiment.

6.2.5.2 Setup

6.2.5.2.1 Mechanical virtual reality

We combined a mechanical virtual reality (VR) setup similar to the one described in [32] with a custom two-photon microscope to allow for neural activity recordings during learning.

The mechanical VR allows flies to navigate in a cylindrical arena that translates and rotates around the fly. It has two main components: a rotational stage with a slip ring that allows continuous rotations, and a translation stage to offset the cylindrical arena from the center along two dimensions. We used a cylindrical arena with twice the size used in [32], with a diameter of 500 mm and a height of 250 mm, as shown in Fig. 6.2.2A. We used the same motors as in [32], since however the cylindrical arena was larger, the motor rotating the arena used a higher reduction ratio of 1:11, implemented with a pulley system, to transmit the rotation to the slip ring. This was necessary to address the increased inertia due to the larger size. Additionally, the translational stage was extended along the two dimensions to

allow for the required larger translations on the larger arena. The setup is shown in Fig. 6.2.1D.

To prevent vibrations from the motors to interfere with the fly and the two-photon microscope, the mechanical VR was mechanically isolated using a different mounted table, as described in [32].

The cylindrical arena contained two vertical stripes of 40 mm wide and 180 degrees apart (see Figs. 6.2.1D and 6.2.2A,B), which was illuminated from the back of the cylinder wall using white LEDs. The light from the LEDs was diffused using white paper and filtered using colored long-pass filters (Thorlabs, FGL550S), which prevented interference with the photomultiplier tube (PMT) for detecting fluorescence light. The LEDs in each stripe were independently controlled using an Arduino.

During imaging experiments, flies were positioned on an air-suspended ball at a height of 150 mm from the bottom of the cylinder. The motion of the ball when the fly was walking was measured using an optic flow-based algorithm [157] through a small mirror from the back and a camera from below, as described in [32]. To avoid collisions between the objective and the walls of the cylinder, we defined a walking limit in the mechanical VR with a diameter of 270 mm, as shown in Fig. 6.2.2A and as described in [32].

6.2.5.2.2 Aversive stimulus

An infrared laser (Toptica, ibeam-smart-785-S-HP with pulse option, 785 nm) was used to generate an aversive heat stimulus, similarity as in [32]. The IR laser was focused onto the thorax of the fly using a lens with help of a small mirror (Thorlabs, MRA05-P01) placed at the back of the fly holder (see Fig. 6.2.1E). Since each fly was glued slightly differently to the transparent slide, a camera was used at the beginning of the experiment to fine-tune the position of the IR beam after the fly had been placed on the ball with the aid of the kinematic mirror mount. During the learning experiment the IR laser power was set to 30 mW, while an arduino UNO was used to pulse the laser at a frequency of 0.2 Hz.

6.2.5.2.3 Two-photon microscope

We used a custom two-photon microscope setup similar to the one described in [28, 30]. This setup contains two axially offset beams with independently controlled focal planes that were offset in time by 6 ns to additionally detect them independently using temporal multiplexing. This setup configuration allows estimating and correcting axial motion by recording two different planes, one for each beam, using temporal multiplexing [30]. However, we instead combined these two beams to obtain only one plane with an effective extended focal length, allowing us to record volumetric calcium activity while decreasing the amount of two-photon laser power for imaging. Axial motion estimation and correction were therefore

not considered here, as axial motion during imaging produced little fluorescence changes in these neurons.

6.2.5.3 Experimental design

Flies were first allowed to explore the mechanical VR in closed loop for 10 to 30 minutes without imaging or without the IR laser. During closed loop, the mechanical arena ran with a translational gain of 1 and a rotational gain of 0.25, meaning that flies needed to rotate four revolutions on the ball to rotate the mechanical VR one revolution. After the exploration period, the learning experiment started for a total of 10 trials where both IR laser and two-photon laser were turned on.

Only for the first trial, the mechanical VR was autonomously reset to an initial position defined at $(-100, 0)$ mm from the center of the area and orientation of 0 degrees, as shown in the left of Fig. 6.2.2B. The cool area was defined as a square with origin $(150, 0)$ mm and length 60 mm. If a fly entered the cool area and stayed for 10 seconds, a new trial started where both the bright stripe and cool area were switched to the opposite side, which from the fly perspective supposed an instantaneous 180 degrees rotation of the cylindrical arena (see Fig. 6.2.2B, right). If a fly did not find the cool area in 15 minutes, a new trial started and the cool area and stripe were switched as usual. Sometimes flies were in the opposite side of the cool area when after 15 minutes the stripe and cool spot switched. This effect produced flies to accidentally find the cool area in the next trial (see for example trial 2 in Supplementary Fig. S6.2.3), which assisted some of the flies that were initially unattractive to the bright stripe.

To prevent flies from spending too much time grooming due to the IR laser, the air supply for the ball was turned off for 0.1 seconds if the flies were not walking for more than 10 seconds and then turn it back on again. This produced stimulated flies to start walking. Real-time tracking of the ball's motion was used to monitor the walking activity of the flies, triggering the air supply to turn off if the ball velocity was below a pre-defined threshold for 10 seconds. The air valve controlling the ball's air supply was controlled using an Arduino UNO.

After 10 trials, the mechanical VR was again reset to the initial position (-100, 0) mm and flies were let to walk around the mechanical VR without any IR laser (and therefore no cool area) for 20 minutes while recording calcium activity. In general, most of the flies become less active and even showed bouts of inactivity for more than 5 minutes, a threshold that is commonly used to define sleep.

After 20 minutes, the learning experiment was repeated for another 2 trials. One fly was discarded in the first trial, and another on in the second trial since they died between the trials.

6.2.5.4 Data acquisition

Behavioral data from the mechanical VR was obtained at 100 Hz, providing the time stamps of the experiment, the ball tracking data, and the position and orientation of the mechanical arena. The time stamps were sent through ROS 1 (Robot Operating System version 1) and through the local network to the computer running Scanimage that controlled the two-photon microscope. These time stamps were stored together with each recorded frame from the microscope and were later used to synchronize the behavior and imaging data.

The imaging data were obtained at a resolution of 256×256 pixels at approximately 60 Hz continuously during the whole experiment. Each experiment lasted between 1 and 2 hours in total, depending on the performance of the fly during learning.

6.2.5.5 Behavior data analysis

The linear velocity of the fly was first computed from the recorded ball velocity. We then thresholded the linear velocity to define bouts of resting (with zero linear velocity) or walking for each fly. This threshold was 0.125 mm/sec, which was adjusted to be right above the linear velocity noise level.

For each trial during learning, we computed the time that each fly took to find the cool area, the total time it was resting, as well as the distance each fly walked. The mean velocity was also computed for each fly and each trial when flies were not resting. All these quantities are shown in Fig. 6.2.2. We also computed the trajectory of each individual fly, and rotated them by 180 degrees in those trials where the stripe and cool area were on the left side. All the trajectories are shown in Fig. 6.2.2C and D, while single trajectories are shown in the top row of Supplementary Figs. S6.2.1-S6.2.9.

6.2.5.6 Imaging data analysis

For each fly, all recorded imaging frames were aligned to a common template to correct for lateral motion using cross-correlation. Once every frame was aligned, we defined a total of 16 regions of interest (ROIs) along the expression pattern in the FB, as well as in the EB, and computed the total intensity $I_i(t)$ within each ROI i and for each frame, associated with a time stamp t. Then, the fluorescence over the frames for each ROI was computed as

$$\Delta F/F_i(t) = \frac{I_i(t) - I_i^0}{I_i^0}, \tag{6.9}$$

where I_i^0 is the 0.1 quantile of the intensity $I_i(t)$. The activity of FB and EB over the trials for each fly is shown in Supplementary Figs. S6.2.1-S6.2.9. PFR neurons represent the orientation of the fly while walking straight with respect to the mechanical VR in a bump of activity that moves across the ROIs [323, 465, 539]. The offset between the bump of activity

and the orientation of the arena is different across flies [313]. To compute this offset, we first obtained the fluorescence of the ROIs only when the fly was walking, $\Delta F/F_i(t_{walk})$, and determined the center of the bump of activity, $C_i(t_{walk})$ at each time as the ROI with maximum fluorescence:

$$C_i(t_{walk}) = argmax_i\Big[F/F_i(t_{walk})\Big]. \tag{6.10}$$

We then transformed $C_i(t_{walk})$ into degrees and computed the offset with respect to the mechanical VR orientation as the mean angle difference. Although the activity of PFR neurons also shifts depending on the walking direction of the fly [539], on average this shift was canceled out over the whole experiment, allowing us to compute the offset reliably. Using this offset we aligned the ROIs with the arena angle. In this situation, the bump at position 0 encodes the orientation at 0 degrees, while the bump at position 16 encodes the orientation at 360 degrees.

6.2.5.6.1 Dimensionality reduction

The minimum and maximum fluorescence across the ROIs for each time was first calculated as

$$\begin{cases} \Delta F/F_{min}(t) = min_i(\Delta F/F_i(t)), \\ \Delta F/F_{max}(t) = max_i(\Delta F/F_i(t)). \end{cases} \tag{6.11}$$

Then we normalized the fluorescence at each time t in the range $[0, 1]$:

$$\text{Normalized } \Delta F/F_i(t) = \frac{\Delta F/F_i(t) - \Delta F/F_{min}(t)}{\Delta F/F_{max}(t) - \Delta F/F_{min}(t).} \tag{6.12}$$

We performed Principal Component Analysis (PCA) on the normalized fluorescence to reduce the 16 dimensions from the defined ROIs into two dimensions. The normalized fluorescence was therefore projected along the two first principal components at each time, $PC1(t)$ and $PC2(t)$. Fig. 6.2.4A and Supplementary Figs. S6.2.10 and S6.2.11 show the fluorescence along the two principal components for every fly during walking and during rest, $(PC1(t_{walk}), PC2(t_{walk}))$ and $(PC1(t_{rest}), PC2(t_{rest}))$. In these plots, each point therefore represents a snapshot in time of the projected fluorescence from the 16 ROIs, while the color represents the orientation of the fly at that particular time. The phase of PFR neurons, $\Phi(t)$, was then computed as the angle between each point and the origin,

$$\Phi(t) = arctan2\Big(PC2(t), PC1(t)\Big), \tag{6.13}$$

as shown in Fig. 6.2.4A. The PFR phase, $\Phi(t)$, provides a better description of the bump position than the previously used method in equation (6.10), which is more prone to noise in the fluorescence. The dimensionality reduction also allowed us to assess the neural activity profile during rest.

To compute the correlation between the PFR phase and the orientation of the fly, we used bins of 1 degree and computed the Pearson correlation between the orientation of the fly and the PFR phase during walking and rest, $\Phi(t_{walk})$ and $\Phi(t_{rest})$, respectively. Fig. 6.2.4B and Supplementary Figs. S6.2.10 and S6.2.11 show the binned orientation against the PFR phase for every fly, while Fig. 6.2.4C shows the Pearson correlation for all flies during rest and walking, which was statistically different using a t-test ($p < 0.05$).

We defined the embedded radius of each point in time as the distance from the origin. In the top row of Fig. 6.2.4D, different circular trajectories with 1 degree of resolution are shown for different radii. For each radius, we obtained the closest embedded fluorescence point and plot the corresponding normalized fluorescence of the 16 ROIs in the second row of Fig. 6.2.4D. We further aligned the normalized fluorescence and computed the mean, $\hat{B}(i)$, and standard deviation of the bump profile across the ROIs for each embedded radius, shown in the last row of Fig. 6.2.4D (green line and light green area, respectively). The L1 error between a sine wave (red line in the last row of 6.2.4D), defined as

$$S(i) = \frac{1}{2}\Big[sin\Big(\frac{2\pi i}{16}\Big) + 1\Big], \tag{6.14}$$

and the average bump profile $B(i)$ for each radius r was then computed as

$$L1 = \frac{1}{16}\sum_{i}^{16} |\hat{B}(i) - S(i)| \tag{6.15}$$

The $L1$ error was computed for all flies during walking and rest at 7 different radii equally spaced in the range of $[0.05, 1]$. Fig. 6.2.4E shows a tendency of decreasing $L1$ error as the embedded radius increases. Error bars represent the standard deviation for the 9 flies. Statistical difference between walking and rest L1 errors was assessed using t-test, however no significance ($p < 0.05$) was found.

We also computed the bump amplitude from the aligned fluorescence at each radius, again for all flies. Fig. 6.2.4F shows the bump amplitude against each radius, where the error bars represent the standard deviation for the 9 flies, and again the statistical difference between walking and rest was determined using t-test.

Fig. 6.2.4G shows the distribution of the embedded radius during walking and rest in a single fly, where the statistical difference between the two distributions was assessed with a Kolmogorov–Smirnov test. Fig. 6.2.4H shows the mean of the embedded radius distribution during walking and rest for all flies, where a t-test was used to measure the statistical difference.

We then computed the distribution of the PFR phase during rest and walking for each of the flies, shown in Fig. 6.2.5. We compared these distributions using Pearson correlation (shown between the first and second row in Fig. 6.2.5), and statistical significance was considered for p-values lower than 0.05 (indicated by asterisks in Fig. 6.2.5).

6.2.5.6.2 Analysis of PFR phase velocity

To analyze the velocity of the PFR phase during walking and rest, we first filtered the PFR phase using a median filter with a filter size of 31, which resulted in a filter size of approximately 0.53 seconds (since the time between consecutive PFR phase points is approximately 17 milliseconds). Fig. 6.2.6C shows the distribution of the PFR velocity during walking and rest for a single fly. Fig. 6.2.6D shows the standard deviation of the PFR velocity during walking adn rest for all flies, where a t-test was used to assess the statistical difference.

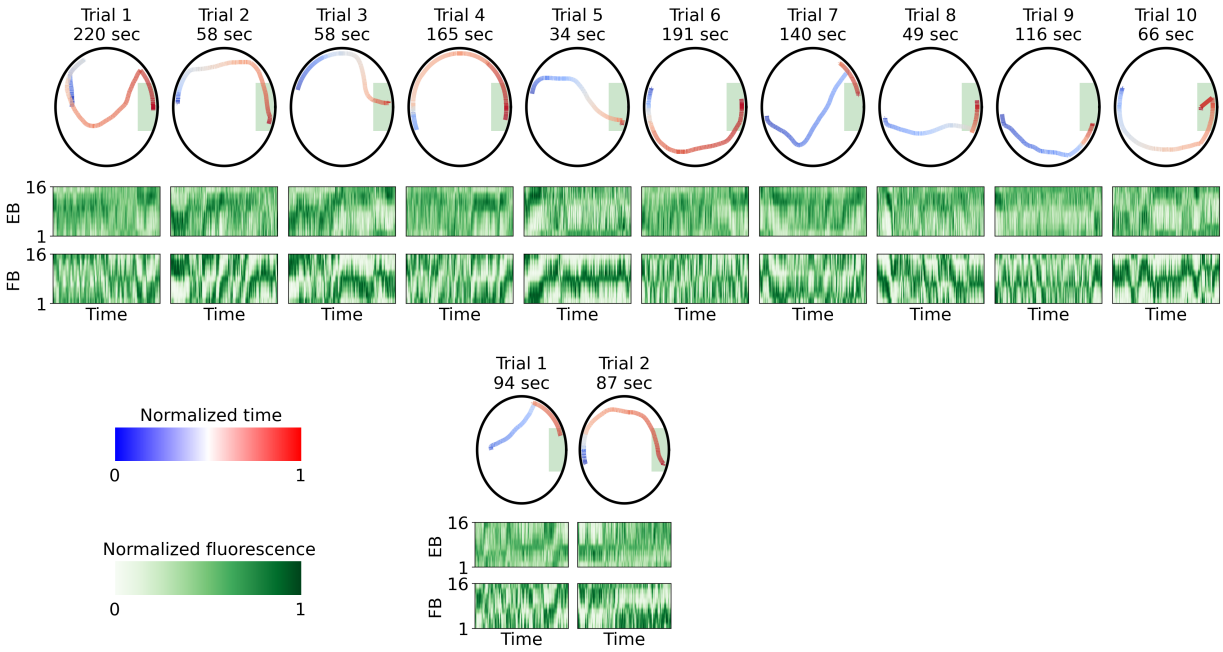
For all flies, we also computed the amount of time and the angular displacement that the PFR phase moved at the different speeds. For this, we obtained time intervals where a fly was resting during the experiment with a minimum duration of 0.5 seconds. Then we computed the velocity of the phase in these time intervals and binned the velocity between -720 and 720 degrees per second (or -2 and 2 revolutions per second) in steps of 180 degrees (or 0.5 revolutions per second). We then obtained all the time intervals where the PFR phase was moving at each binned velocity, shown in Fig. 6.2.6G, where the dashed black line represents the mean. Finally, for each phase interval moving at every binned velocity, we calculated the amount of time and the absolute PFR phase displacement, and the distributions are shown for all flies across the entire experiments in Fig. 6.2.6E and F, respectively.

We then computed the cumulative absolute displacement of the PFR phase during rest and walking, shown in Fig. 6.2.7A for one fly. For this, we joined walking and rest bouts, respectively, computed the displacement of the PFR phase between consecutive frames, and finally summed the displacements over time. The same analysis was performed for the rest of the flies (data not shown). Finally, we fitted a line to the absolute cumulative displacement during rest and walk, respectively, and obtained the slopes from each fit. The different slopes for each fly during rest and walk are shown in Fig. 6.2.7B, and statistical significance was assessed using a paired t-test (p-value < 0.05).

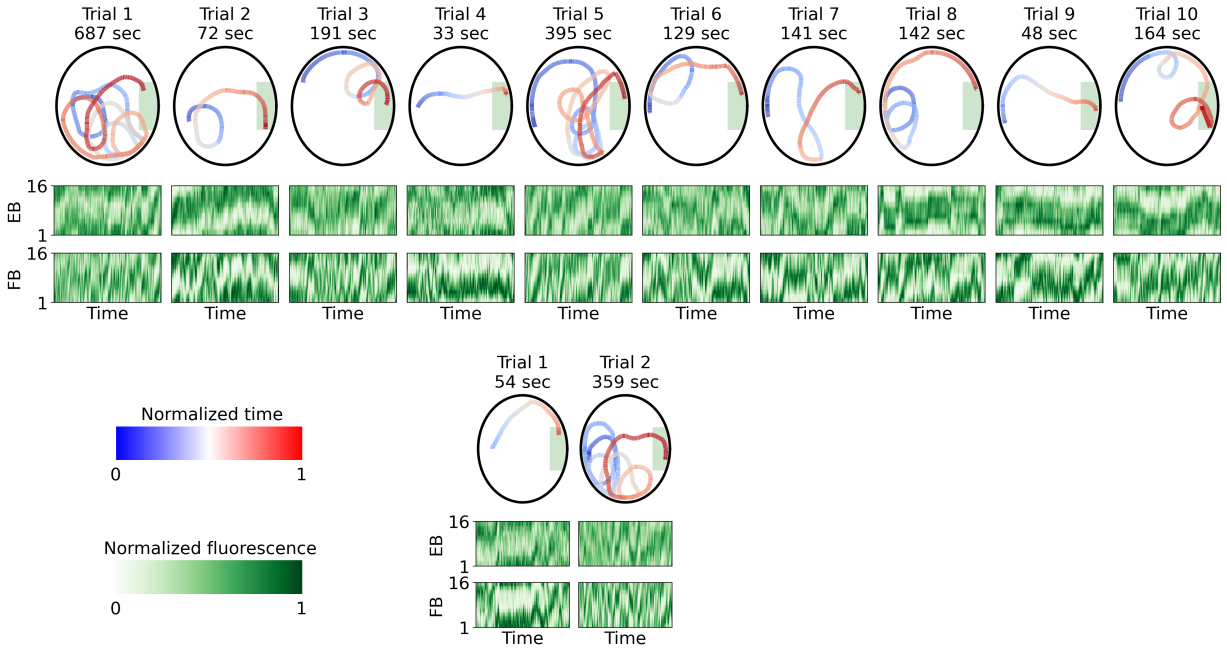
6.2.5.6.3 Analysis of the PFR phase during sleep

Longer resting bouts were observed in flies during the 20 minutes break after the first 10 trials. During these 20 minutes, we obtained continuous rest bouts by thresholding the ball velocity as previously described. Then we computed the absolute cumulative displacement of the PFR phase, similarly to the previous analysis, but now only during continuous rest bouts. The drift of all these epochs for $N = 9$ flies is shown in Fig. 6.2.7C. A long rest bout of more than 8 minutes, corresponding to one of the lines in Fig. 6.2.7C, is shown in Fig. 6.2.7D. Finally, we used all the rest bouts with different durations and fitted a line to the absolute cumulative drift for different time intervals of immobility, ranging between $[0, 5], [5, 20], [20, 60]$, and $[60, 500]$ seconds. The distributions of these fitted slopes for each

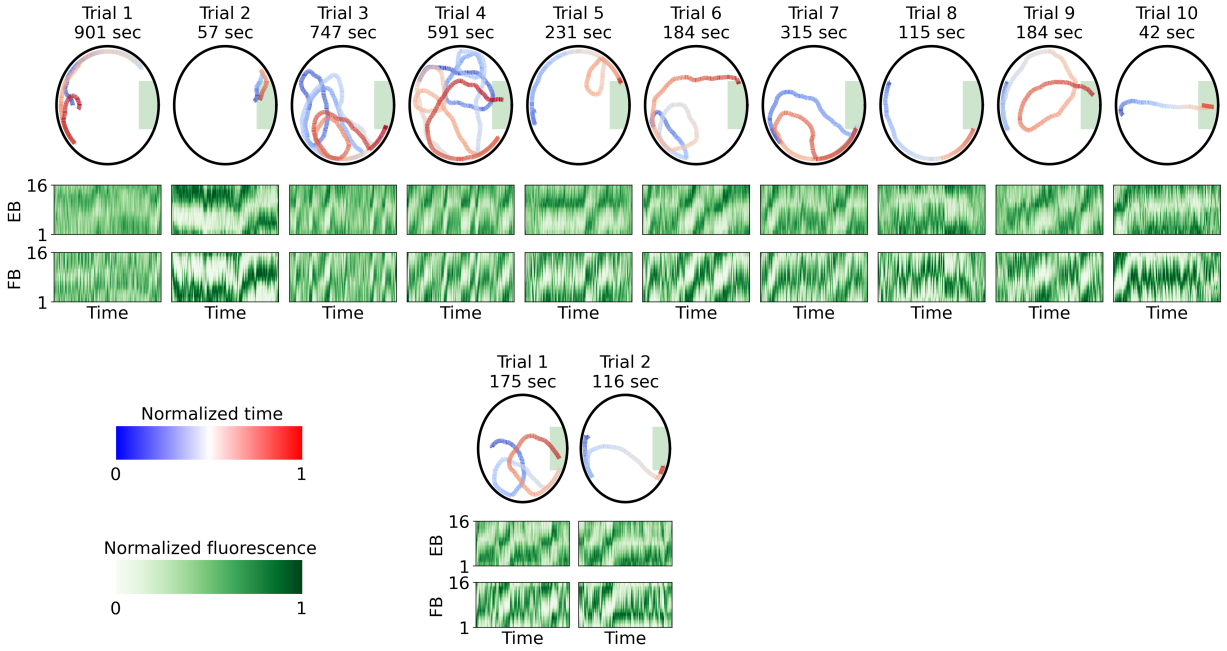
immobility time are shown in Fig. 6.2.7E, where statistical significance was assessed using Kolmogorow-Smirnow test. The three asterisks represent a p-value below 0.0005.



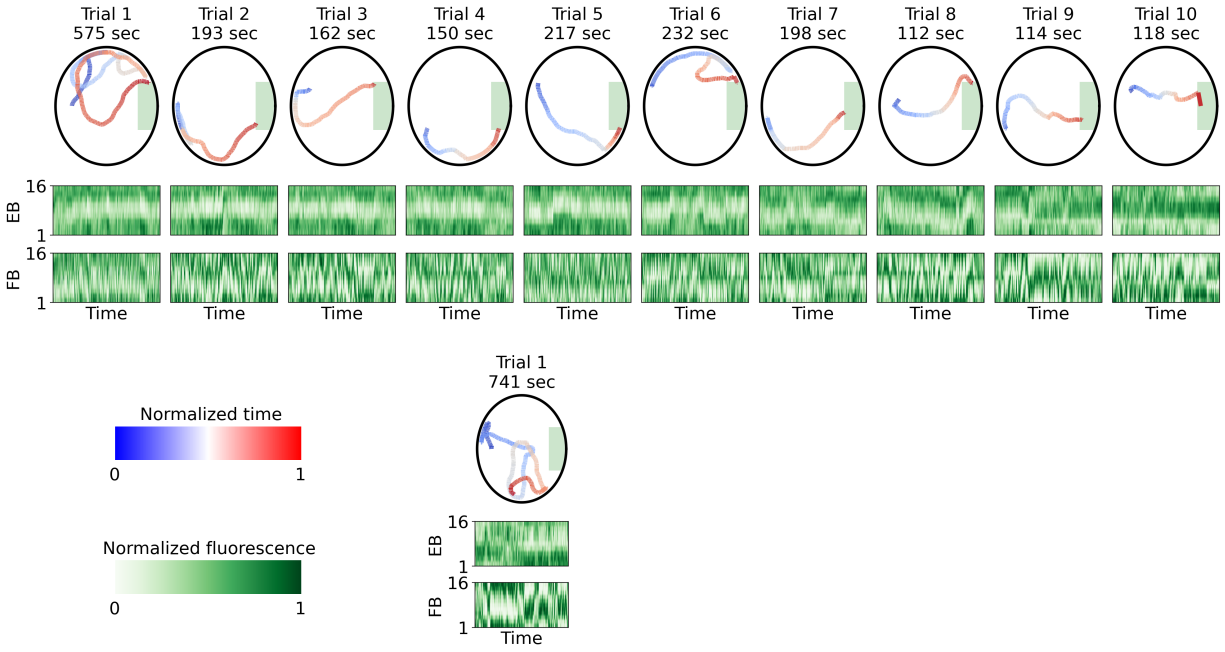
Supplementary Figure S6.2.1: Learning during imaging for fly 1. Upper half, top row: trajectory of the fly in the mechanical VR for 10 trials. Color of the trajectory represents normalized time. The time that the fly took to find the cool area for each trial is displayed at the top. Second row: normalized fluorescence recorded from the EB using 16 ROIs across different wedges, possibly from EL neurons, although crosstalk in ROIs between EB and FB could not be excluded. Third row: normalized fluorescence recorded from PFR neurons in the FB. Lower half: same as upper half, but for the 2 trials after the 20 minutes break.



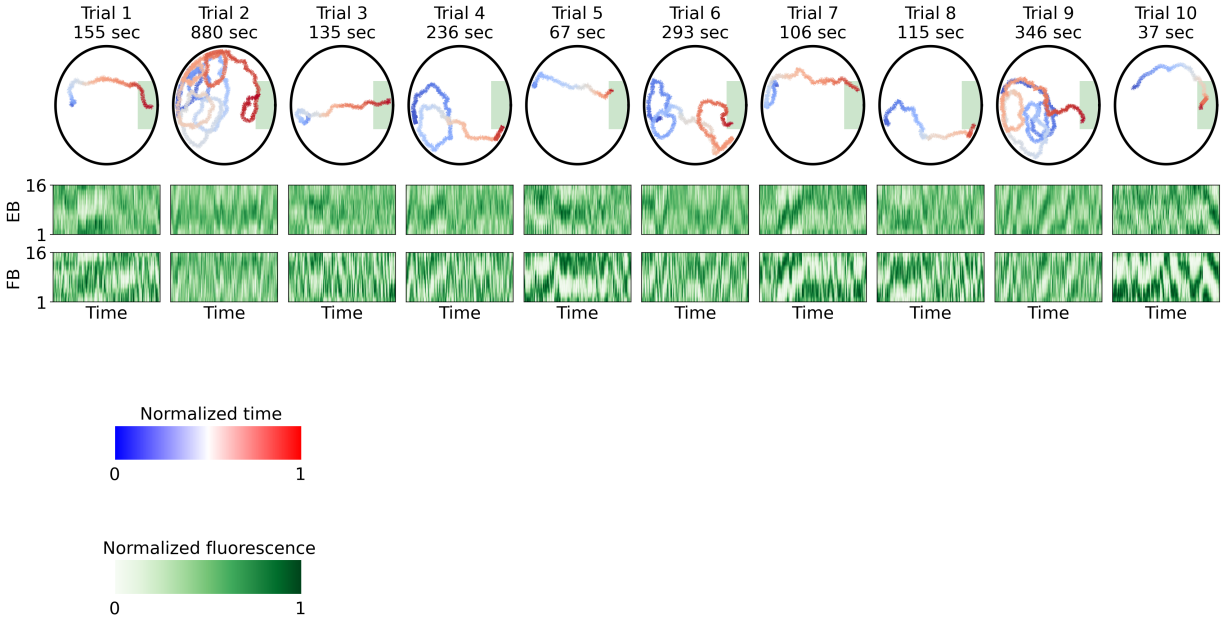
Supplementary Figure S6.2.2: Same as Supplementary Fig. S6.2.1 but for fly 2.



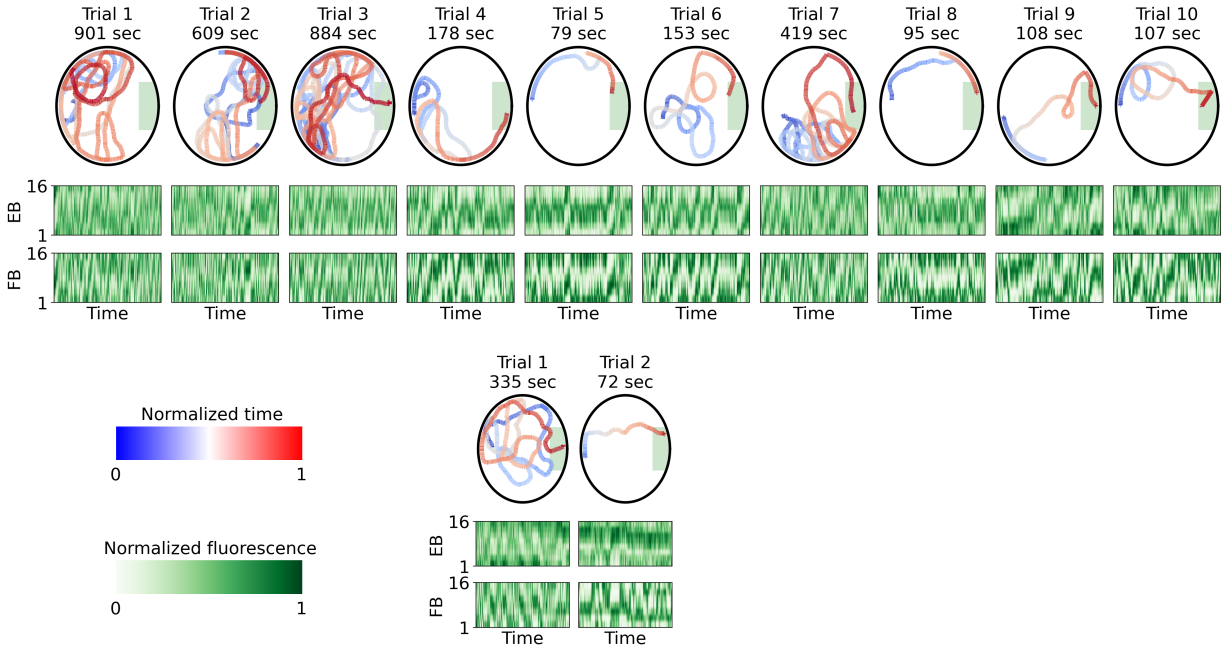
Supplementary Figure S6.2.3: Same as Supplementary Fig. S6.2.1 but for fly 3.



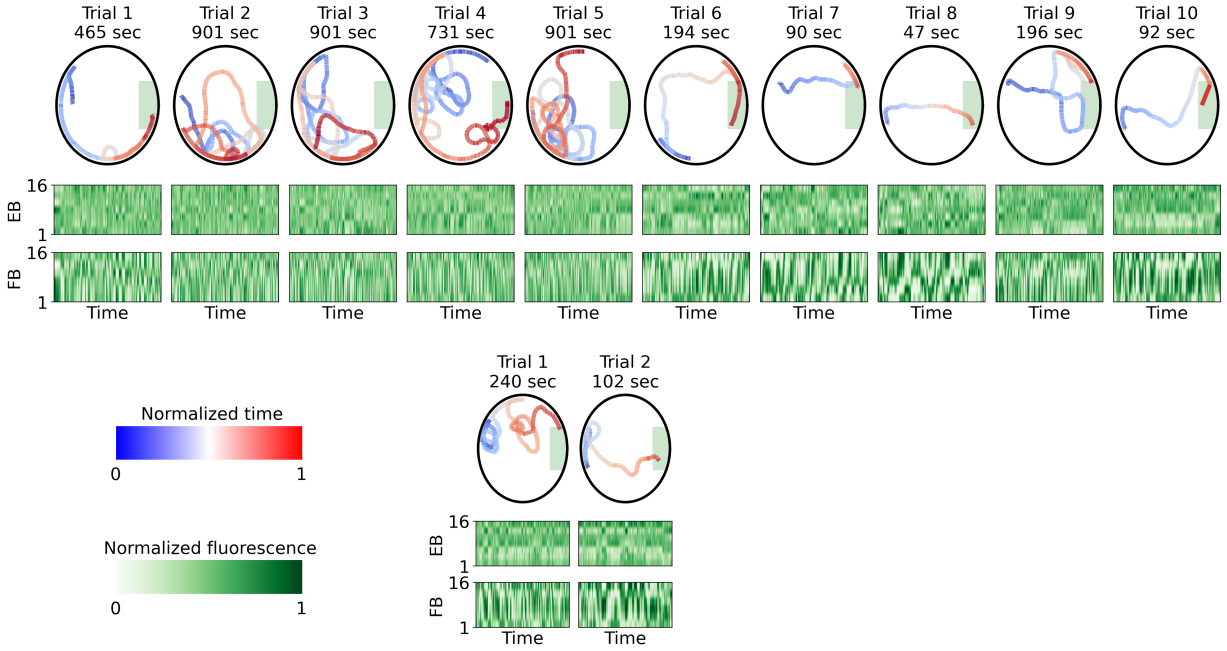
Supplementary Figure S6.2.4: Same as Supplementary Fig. S6.2.1 but for fly 4.



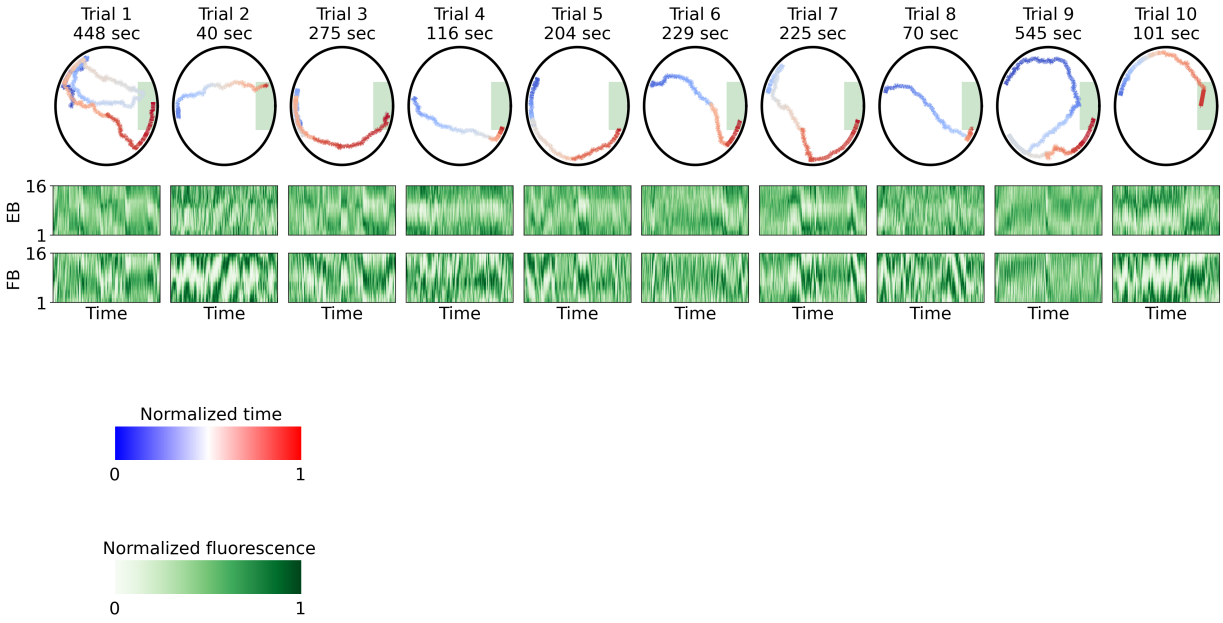
Supplementary Figure S6.2.5: Same as Supplementary Fig. S6.2.1 but for fly 5.



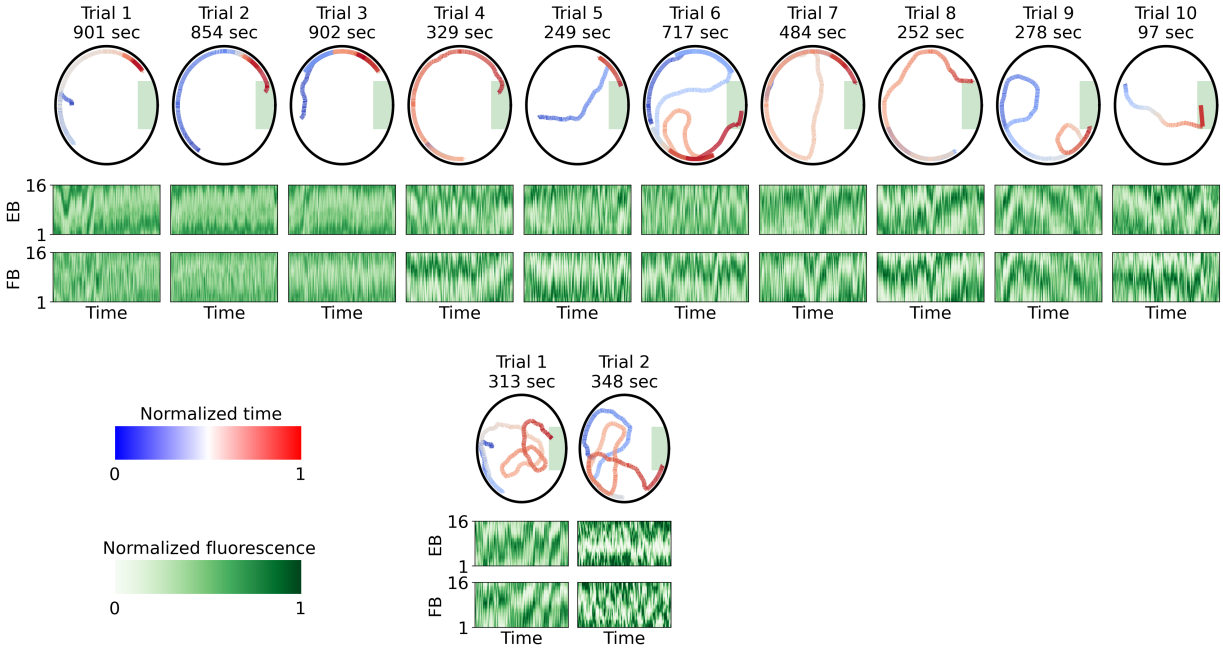
Supplementary Figure S6.2.6: Same as Supplementary Fig. S6.2.1 but for fly 6.



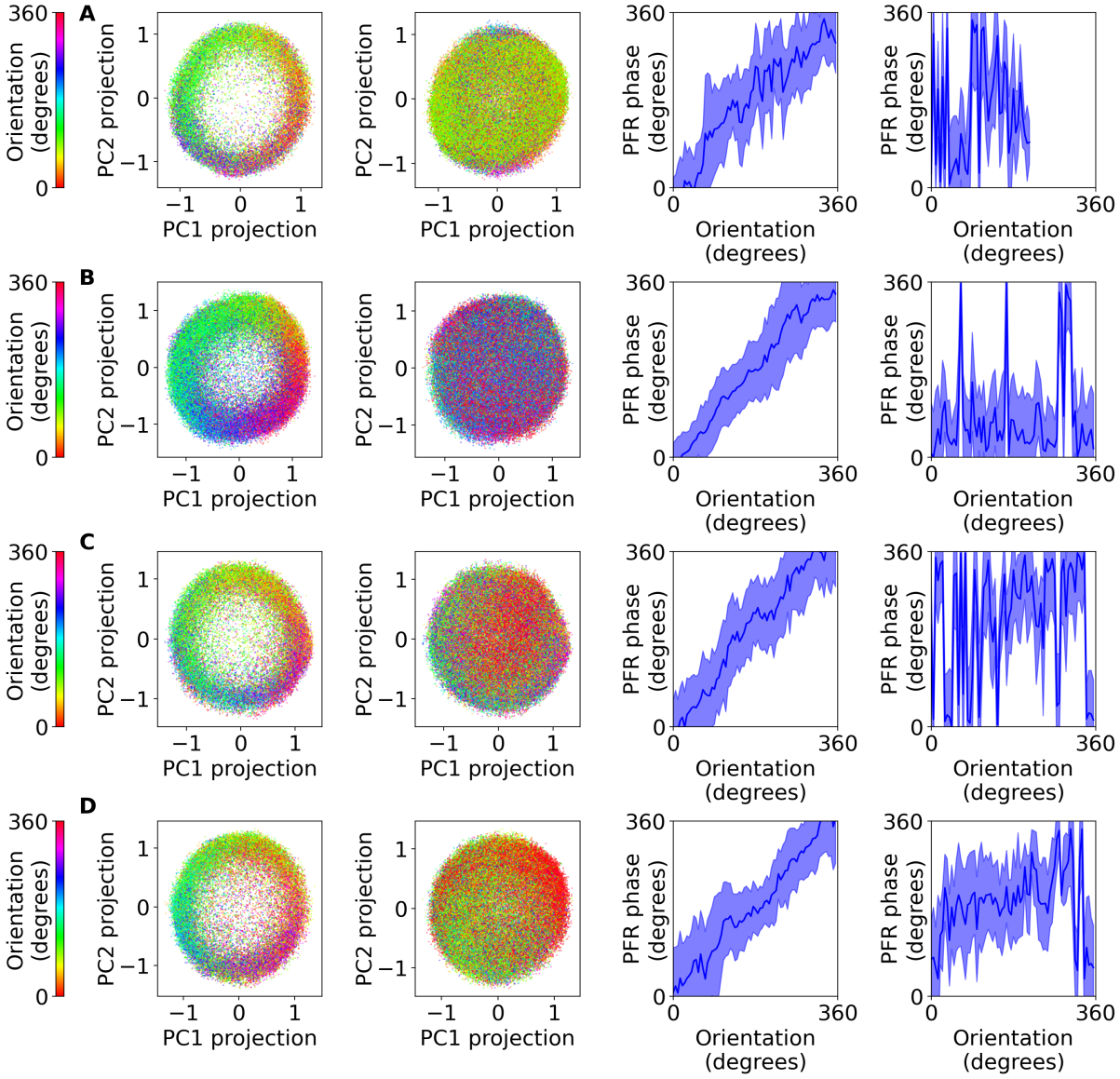
Supplementary Figure S6.2.7: Same as Supplementary Fig. S6.2.1 but for fly 7.



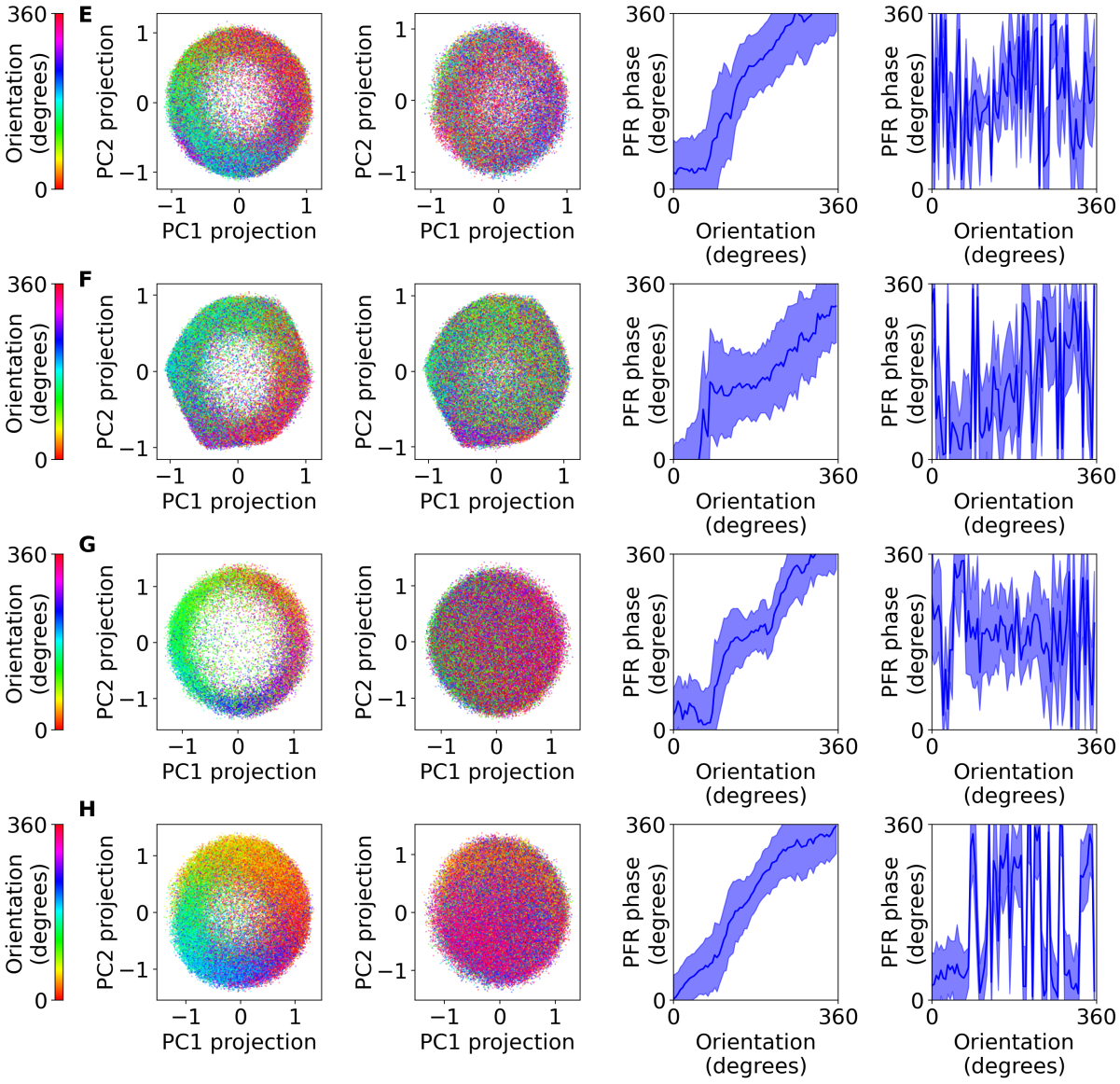
Supplementary Figure S6.2.8: Same as Supplementary Fig. S6.2.1 but for fly 8.



Supplementary Figure S6.2.9: Same as Supplementary Fig. S6.2.1 but for fly 9.



Supplementary Figure S6.2.10: Dimensionality reduction analysis for PFR neurons during rest and walking for flies 2-5. **A** First and second columns: normalized fluorescence projected along the first two principal components (PC1 and PC2) during walking and during rest, respectively, similarly to Fig. 6.2.4A. Third and fourth columns: PFR phase obtained from the embedded normalized fluorescence in the first two columns against the orientation of the fly for all times, during walking and rest, respectively, similarly to Fig. 6.2.4B. Blue lines represent mean value, while the blue region represents the standard deviation. **B-D** Same as A but for another three different flies.



Supplementary Figure S6.2.11: Same as Supplementary Fig. S6.2.10A, but for flies 5-9.

Chapter 7

Conclusions

The central complex of *Drosophila* is involved in sleep homeostasis and navigation. This thesis investigates these two different functionalities and their interaction in this brain area. To that end, this thesis used computational modeling, developed novel methods for imaging as well as for studying learning behavior, and applied some of these methods for recording neural activity in the fly brain over long timescales as well as during learning.

As a result of these experiments, the thesis characterizes calcium dynamics of a sleep homeostat encoded in ensheathing glia in the central brain. Ensheathing glia activity is also compared to that of populations of neurons that have been at the center of interest over the last years for the control of sleep homeostasis in the central complex. In the experiments described here, some of these neurons are in particular found to be modulated by feeding as well as behavioral activity.

Finally, autonomous or drift activity in neurons from the head direction system was observed in flies that were standing still or sleeping, similar to activity observed during active navigation. The dynamics during inactivity were additionally characterized and compared to the activity during behavior.

7.1 Methods for studying sleep in behaving flies

7.1.1 Theoretical approaches

The first model developed in Chapter 2 implements in mathematical terms a previously, only qualitatively, proposed circuit for sleep homeostasis in the central complex [125]. This computational model indeed shows cycles of sleep and wake phases, as qualitatively expected.

This chapter further explores why sleep need, encoded in R5 neurons, could be represented in neurons connected to the head direction system. For this purpose, another model is developed with plasticity introduced in compass (or EPG) neurons. Plasticity in these

neurons arises due to Hebbian plasticity between neighboring EPG neurons, which are typically active at the same time and therefore get more strongly connected. In the model, a sleep homeostat arises in R5 neurons, which act as the inhibitory component of the network, counteracting the detrimental effects of plasticity between EPG neurons.

The introduction of plasticity in the head direction system is motivated by the synaptic homeostasis hypothesis [265] (reviewed in section 1.4 and shown for example in Fig. 1.6) and the idea that autonomous activity during sleep, such as dreaming, serves as an unlearning mechanism [411, 414] (reviewed in section 1.8.2). This model captures the proposed dynamics of R5 neurons such as the increase of activity and synaptic strength during wakefulness and the reset during sleep [123, 125, 186].

The model makes several predictions for the integration of sleep homeostasis and head direction encoding, for example that the ring attractor network resets synaptic weights through autonomous drifting activity during sleep. The model also makes several assumptions that have not been proven experimentally, for example that connected compass neurons undergo plasticity. While such plasticity has so far not been observed, several other examples of plasticity in the head direction system have been reported. In particular, plasticity between R5 neurons and compass neurons, as also assumed in the model, was recently observed with electrophysiological experiments in brain explants [307]. Additionally, another type of plasticity between visual ring neurons and compass neurons underlies remapping of the visual scene to compass neurons [431, 432].

In the future, several additional neural populations could be included to obtain a more complete picture of activity in the head-direction system during wakefulness and sleep, such as visual ring neurons or other columnar neurons in the EB and FB. The population of R5 neurons, which were assumed to be inhibitory in the model, have recently been reported to be a mixture of inhibitory (GABAergic) and excitatory (cholinergic) neurons [307]. Nevertheless, blocking neurotransmission from only excitatory R5 neurons did not abolish sleep rebound after 12 hours of mechanical sleep deprivation. This implies that excitatory R5 neurons are not the only source of sleep homeostasis, but that also inhibitory R5 neurons contribute to homeostasis [307], as hypothesized in the model. Testing the predictions of this model motivated and guided the experiments described later in this thesis.

7.1.2 Long-term imaging

In this thesis, we developed an automated long-term imaging method that allows monitoring brain activity over short and long timescales, up to multiple days. This method relies on improved dissection of flies and on an automatic feeder that feeds the fly during imaging, without requiring any intervention from the experimenter. The improved dissection uses laser surgery and a motorized micro-robotic arm. These components make the dissections

more controlled and rely less on the skills of the experimenter, which also reduces training time.

Previous imaging techniques either allowed recording neural activity for a few hours [330, 331] or used intermittent imaging [363], while other long-term imaging approaches that characterize circadian brain dynamics used constrained flies for up to 24 hours without the possibility of identifying sleep bouts [294, 390]. In comparison, the method presented here routinely achieves recordings over multiple days in behaving animals.

During long-term imaging, flies sleep on the ball, as reflected by the increased arousal threshold after prolonged rest periods (Chapter 5, Fig. 5.2k). While the dissection is invasive, it did not impair visual place learning in the head-fixed paradigm developed in section 6.1. This, together with the fact that flies sleep on the ball and show circadian rhythms (Fig. 5.1k), indicates that a broad range of processes and behaviors can be investigated with this approach.

Methods for imaging through the cuticle, either by using light with longer wavelengths such as three-photon imaging, potentially combined with adaptive optics, can enable *in vivo* imaging in flies without dissection [364, 365]. However, with currently available indicators, imaging deeper in the brain is often close to the noise level, and likely will require the better imaging conditions provided by dissected flies in the foreseeable future.

Several future improvements of the developed techniques can be envisioned. For example, the developed dissection method offers the necessary hardware for completely automating fly brain dissections through computer vision and decision-making algorithms for robotic control.

Further, feeding during long-term imaging was implemented at defined times without taking into account the hunger state of the fly. The timing of feeding affects sleep and the circadian rhythm of flies, for example as observed when flies are fed every four hours. The feeder could alternatively run in closed loop, with flies triggering feeding by walking on the ball over a required distance. Finally, brain activity was recorded intermittently during long-term imaging since continuous recordings produce photobleaching and phototoxicity, eventually damaging the brain. The continued improvement of GCaMP sensors that minimize phototoxicity [344] is expected to further increase the recording time in the future.

Overall, this method opens up a range of possible experiments, and could for example be similarly applied for investigating other processes that evolve over longer timescales, such as feeding, drug testing, development, learning, immune response, or cancer development.

7.1.3 Development of imaging techniques

This thesis also includes the development of two novel methods for fluorescence microscopy (Chapter 4): a tomography approach for fast volume imaging using Bessel beams (section

4.1) and an approach for correcting brain motion (section 4.2).

Both the tomography and motion correction approaches make use of temporal multiplexing to record different projections or focal planes, respectively, at the same time in a single frame scan. Two simultaneous recorded slices of the sample can be used to estimate and correct motion using the algorithm described in section 4.2. The tomography approach uses four simultaneously recorded projections to reconstruct a volumetric sample in a single scan. Motion correction could also be achieved using tomography: thanks to the high volume rate, volumes could be aligned to a common reference to correct brain motion using standard correlation-based methods (section 4.1).

Although both methods were implemented in a two-photon fluorescence microscope, they can be adapted for other modalities as well. The tomography approach described in section 4.1 was for example also implemented for Raman imaging, which relies on intrinsic contrast of molecules with chemical specificity and therefore does not require labeling [600]. The method could also similarly be implemented with one- or three-photon fluorescence excitation.

The tomographic approach (section 4.1), was presented as a proof-of-concept using fluorescent beads and pollen grains. Since the laser power in a Bessel beam is distributed over a larger volume, it requires more power to excite fluorescence compared to a tightly focused Gaussian beam, therefore increasing sample heating. This approach was therefore not applied for *in vivo* imaging in flies. However, the method might potentially become attractive in the future as genetically encoded sensors become brighter. Further, using lasers with a lower repetition rate could ameliorate this problem as well as reduce cross-talk between the simultaneously recorded projections.

The axial motion correction method (section 4.2) requires at least two extended Gaussian beams that cover the entire range over which the sample moves. This also distributes the power along the z-axis and again requires more power for fluorescence excitation than a tightly focused beam. At the same time, an extended focus also excites a larger volume, thus exciting more fluorophores at the same time, which can increase the fluorescence signal. This approach was successfully used in the long-term imaging experiments described in Chapter 5 as well as in the experiments that combined learning with imaging described in section 6.1.

7.1.4 Place learning assay

In section 6.1 and section 6.2, an assay for spatial and visual learning based on a novel virtual reality setup was developed for tethered walking flies as well as during imaging, respectively.

This assay uses a cylindrical arena that rotates around the fly, similar to the flight simulator used in early experiments during visual learning [148, 149, 150, 151] (see 1.2.4),

but also translates, thus allowing 2D navigation. Despite recent developments in screen-based (that is, either using LED panels or projectors) virtual reality for flies [153, 154, 155, 156, 157, 160], visual place learning has not been investigated in head-fixed flies with these methods (section 6.1). The cylindrical arena presents a visual stimulus similar to what a freely moving fly would see from any corresponding position within such an environment, which is more difficult to achieve with screen-based virtual reality. Compared with LED screens or projectors, however, the lag between the motion onset of the animal and the response of the virtual reality is larger, although this could be improved with stronger and faster motors in the future. Compared with the place learning assay for freely moving flies, there are several additional differences, such as head fixation, different visual stimuli and field of view, different arena sizes, or methods for aversive conditioning. Nevertheless, the learning behavior in the developed assay is similar to the one observed in freely moving flies [146].

This assay has allowed monitoring neural activity during learning in neurons from the head direction system (section 6.2) and will therefore be useful to identify neural circuit dynamics underlying the acquisition, storage, and retrieval of spatial and visual memory. Furthermore, integrating this assay with the long-term imaging method developed in Chapter 3 should allow investigating how long-term memories in the context of visual and spatial learning are created, maintained, or degrade over time.

While an aversive stimulus was used here, an appetitive reward stimulus could potentially be used as well. This could be achieved, for example, by providing sucrose to the tethered flies when they reach the cool spot using the feeder developed in Chapter 3. Food or other physical objects could also be attached to the arena so that flies could approach them.

7.2 Sleep regulation in *Drosophila*

7.2.1 Ensheathing glia

Calcium activity in ensheathing glia shows the dynamics expected of a sleep homeostat, integrating time spent awake and resetting during rest or sleep, more reliably than other sleep-related neurons in the central complex.

These experiments provide the first characterization of the dynamics of a sleep homeostat at cellular resolution in a genetically identified cell type during wakefulness and sleep.

Calcium activity of ensheathing glia in the central complex completely resets to baseline after around 20-50 minutes of sleep. This suggests that sleep rebound after sleep deprivation should last for about the same time as the observed calcium resetting in ensheathing glia (assuming potentially similar homeostatic dynamics in other brain compartments with similar time constants). Indeed, methods that use gentle mechanical sleep deprivation (Fig.

1.2B) lead to sleep rebound in the expected time range based on the described calcium dynamics, even after 12 hours of sleep deprivation [134, 135] (see section 1.2.3).

Sleep deprivation through starvation does not lead to an observable sleep rebound using the *Drosophila* Activity Monitor (DAM) (see section 1.2.1) and it has therefore been suggested that starvation suppresses sleep homeostasis [113, 114, 115, 116]. However, the DAM has not the temporal resolution to identify sleep rebound in the order of minutes.

Sleep deprivation through starvation produced similar calcium dynamics in ensheathing glia imaging experiments as sleep deprivation through mechanical stimulation, suggesting that starvation does not inhibit the glia sleep homeostat reported here.

This however does not exclude more subtle differences between sleep deprivation through starvation and sleep deprivation by mechanical means. For example, since memory formation is metabolically expensive, lack of nutrients [601, 602] might affect the creation of long-term memories, which possibly could lead to a change in sleep homeostasis.

This thesis has focused on the regulation of sleep in the central complex. However, activity from ensheathing glia in the lateral accessory lobe, neuropil outside of the central complex, shows similar correlations with sleep and wake behavior. One could therefore speculate that corresponding ensheathing glia encode sleep need of each respective neuropil by integrating its activity, including for example the mushroom bodies (MB) where other neural populations have been identified for sleep regulation [128, 192, 297, 298, 299, 300].

Ensheathing glia calcium activity also showed circadian modulation, and could therefore potentially integrate sleep homeostasis and circadian activity similar to the two-process model [269]. Other glia types in *Drosophila* have not been monitored over long timescales, but calcium activity in astrocytes was suggested to encode sleep as well [246], however, rather by an increase in fluctuations than by an increase in overall activity, as expected of an integrator.

The discovery that ensheathing glia encode homeostatic signals for sleep can shed light on the function of sleep. What exactly glia are monitoring is unknown but the experiments performed in this thesis suggest that ensheathing glia could integrate overall neural activity within the neuropil by sensing the accumulation of extracellular glutamate. Indeed, ensheathing glia recycle extracellular glutamate, and impairing this process leads to increased sleep [251]. The accumulation of extracellular glutamate during wakefulness could reflect a net increase of neural activity over time, which could be the result of a net synaptic potentiation within the neuropil [265], as discussed in section 1.4.

Ensheathing glia create a diffusion barrier across the neuropil [247] but it is largely unknown how the trafficking of substances across this barrier is regulated [261]. Nevertheless, ensheathing glia could signal the accumulation of metabolites in the enclosed neuropil through calcium activity during wakefulness (as for example an increase in extracellular glutamate can give rise to an increase in intracellular calcium in mammalian astrocytes [603, 604]). Since the accumulation of metabolites likely depends on the activity or usage of

the enclosed neuropil, ensheathing glia are well-positioned to monitor the combined neural activity of a brain compartment.

Additionally, ensheathing glia could potentially also integrate neural activity by sensing dopamine, as dopamine activity is also tightly correlated with the animals walking activity [546, 605].

Consistent with the hypothesis of increased clearance of metabolites during sleep [218, 219] (see section 1.4), sleep could similarly support the removal of waste products in the fly brain, while ensheathing glia monitor the process by slowly decreasing calcium activity.

It is currently unknown how ensheathing glia promote sleep but it has been recently proposed that these cells release adenosine [216]. Extracellular accumulation in flies has not been reported during sleep and wake, but it is a marker for sleep homeostasis in mammals and is for example released by microglia to inhibit glutamatergic activity [543]. Alternatively, taurine feeding induces sleep in flies, and ensheathing glia expresses a taurine channel. Thus taurine could alternatively play a role in sleep homeostasis in the fly [252].

Overall, this thesis identifies a sleep homeostat in ensheathing glia of *Drosophila*, opening up new opportunities for studying the molecular and cellular mechanisms underlying sleep regulation in fruit flies.

7.2.2 dFB and R5 neurons for sleep homeostasis

Long-term imaging of dFB neurons revealed modulation due to feeding, but also due to behavioral activity, such as walking or pushing the ball (Chapter 5). While dFB and R5 neurons have been previously reported to regulate sleep homeostasis [123, 125, 186], their activity, recorded here for the first time during wakefulness and sleep over long timescales, does not show a simple correlation with sleep and wake episodes.

It however needs the be pointed out that both these GAL4 lines label multiple populations of neurons. For example, the GAL4 line typically used to target dFB neurons (23E10-GAL4, recorded in Chapter 5) is heterogeneous and contains different classes of neurons, including large neurons in the ventral nerve cord (VNC) [177, 606]. This suggests that activity recorded from this GAL4 line likely contains intermingled signals from different cell types, possibly deferentially correlated with sleep, feeding, or walking velocity. Thus, discrepancies with previously reported behavioral genetics experiments could be the result of recording a mixture of calcium signals from several populations.

Similar arguments also apply for R5 neurons labeled using 88F06-GAL4 or R58H05-GAL4 (recorded in Chapter 5). The R58H05-GAL4 line indeed labels a mixture of excitatory and inhibitory neurons [307]. The activity of R5 neurons in behaving flies does not increase with time spent awake, as previously suggested from experiments in brain explants [123].

A further caveat is the time resolution of calcium indicators, which does not allow for resolving single spikes in most fly neurons. Thus, faster dynamics such as oscillatory activity,

which have been observed in both R5 ring neurons [186] as well as dFB neurons [308] in some recordings, could encode additional information about sleep need. The analysis of such signals was however not included in the thesis.

dFB neurons innervate the 6th layer of the FB [305] and similar neurons in this layer, or potentially the same neurons, are modulated by food, as indicated by a drop in calcium activity after feeding [533]. Moreover, the magnitude of the drop in activity depends on the food type, suggesting that these neurons have a role in food preference [533]. Since these neurons are located in the navigation center of the fly, the central complex, they might potentially be involved in navigation strategies such as foraging, modulated by the fly's internal state [533, 607, 608].

Long-term imaging experiments not only reveal similar dynamics of dFB neurons after feeding but also steadily increasing activity before feeding. Moreover, the modulation of activity after feeding depends on the behavioral state, with resting, walking, or ball pushing respectively resulting in different resets of activity after feeding (Chapter 5). Additionally, the reset magnitude from dFB neurons was correlated with the amount of food ingested by the flies.

In contrast to these results, dFB neurons have been proposed to act as a sleep switch, with their activity being high during sleep and low during wakefulness [125, 308]. This role of dFB neurons is additionally supported by how artificial activation of dFB neurons produces immobility [176], which is often interpreted as sleep [176, 606].

As mentioned, possibly the sleep promoting cell type identified using optogenetics could not be visible in calcium imaging due to other neurons labeled in the same line dominating the signal. Nevertheless, it shows that the calcium activity observed in ensheathing glia does not simply mirror activity of the enclosed sleep-related neurons. For example, ensheathing glia showed a continued increase in calcium activity independent of fly activity after feeding, that is walking or ball-pushing, which was different from the activity observed in dFB neurons. Additionally, the activity from ensheathing glia was better characterized by a homeostat model, which exponentially increases over wakefulness and decreases during sleep, than the activity from either dFB or R5 neurons.

Since the central complex is at the center of sensory-motor integration, this brain area would be well-suited to disconnect sensory input from motor output during sleep. Thus for example the activity of dFB neurons could produce immobility in flies by disconnecting the link between sensory input and motor output, a question that could for example be addressed by imaging more specific GAL4 lines as introduced in [606].

7.3 Sleep and navigation

Long-term imaging in compass neurons over multiple days showed that these neurons track visual cues in the virtual reality as previously described based on recordings over short timescales, without showing any autonomous activity during sleep as hypothesized in the computational model (Chapter 3).

However, autonomous activity was identified in PFR neurons during learning (section 6.2), using the assay developed in section 6.1. PFR neurons encode head direction in a world-centered frame of reference during walking with a bump-like activity pattern. When flies were standing still or grooming, PFR neurons showed similar activity as during walking, with a bump of activity that drifted about two times faster than during navigation in the mechanical virtual reality.

After learning flies were left to rest for 20 minutes and displayed long bouts of immobility over 5 minutes. Such bouts of immobility during imaging show an increased arousal threshold (Fig. 5.2k), which supports the idea that flies sleep under imaging conditions. The autonomous activity of PFR neurons during sleep did not change or disappear, suggesting that this autonomous activity could persist during sleep. Interestingly, the observed autonomous activity was slightly slower during the first 5 seconds of immobility.

Autonomous activity during sleep has been observed in the head direction system of mammals. Autonomous activity has been studied in the context of learning and memory consolidation especially in place cells, suggesting that activity replays or predicts previous or future navigation behavior, respectively. On the other hand, computational models have hypothesized that autonomous activity serves as an unlearning mechanism (see section 1.8.2), including the model developed in Chapter 2. Although this model was proposed for different neurons in the ellipsoid body (EB), it could potentially be adapted to PFR neurons, for example with ensheathing glia acting as the inhibitory component as well as the sleep homeostat. Although the function of autonomous dynamics in PFR neurons is unknown, it might include the replay of previous navigation experiences, planning of future navigation strategies, or reorganization of memory and/or memory transfer [188].

In any case, these experiments characterize the first example of autonomous activity during rest and sleep in identified neural populations in the brain of *Drosophila* at high time resolution. Additionally, this is the first experiment that demonstrates the feasibility of combining spatial learning in tethered walking flies with calcium imaging. The developed setup and behavioral paradigm thus open up a range of experiments for investigating circuit dynamics underlying learning and memory in the fly, including over long timescales as well as sleep.

Although the activity of PFR neurons was recorded while flies displayed learning behavior, the autonomous activity of PFR neurons was not characterized in the context of learning, as this is an ongoing experiment at the time of the submission of this thesis. Fu-

ture work will include control experiments for learning as well as a more detailed analysis to assess whether autonomous activity in PFR neurons changes over learning. Moreover, we observed sleep bouts after learning in some of the flies, which will allow studying whether the observed drift dynamics play a role in memory consolidation. This analysis will provide more insights into the role of autonomous dynamics in the head direction system of the fly.

Bibliography

[1] Kandel, E. R., Schwartz, J. H., Jessell, T. M., et al. 2000, Principles of neural science, Vol. 4 (McGraw-hill New York)

[2] Barone, D. A. & Krieger, A. C., The function of sleep. 2015, AIMS Neuroscience, 2, 71

[3] Krueger, J. M., Frank, M. G., Wisor, J. P., & Roy, S., Sleep function: Toward elucidating an enigma. 2016, Sleep medicine reviews, 28, 46

[4] Siegel, J. M., Sleep function: an evolutionary perspective. 2022, The Lancet Neurology, 21, 937

[5] Jaggard, J. B., Wang, G. X., & Mourrain, P., Non-REM and REM/paradoxical sleep dynamics across phylogeny. 2021, Current Opinion in Neurobiology, 71, 44

[6] Siegel, J. M., Do all animals sleep? 2008, Trends in neurosciences, 31, 208

[7] Weiss, J. T. & Donlea, J. M., Roles for sleep in neural and behavioral plasticity: reviewing variation in the consequences of sleep loss. 2022, Frontiers in behavioral neuroscience, 15, 357

[8] Porkka-Heiskanen, T., Alanko, L., Kalinchuk, A., & Stenberg, D., Adenosine and sleep. 2002, Sleep medicine reviews, 6, 321

[9] Anafi, R. C., Kayser, M. S., & Raizen, D. M., Exploring phylogeny to find the function of sleep. 2019, Nature Reviews Neuroscience, 20, 109

[10] Diekelmann, S. & Born, J., The memory function of sleep. 2010, Nature Reviews Neuroscience, 11, 114

[11] Markow, T. A., The natural history of model organisms: the secret lives of Drosophila flies. 2015, elife, 4, e06793

[12] Raji, J. I. & Potter, C. J., The number of neurons in Drosophila and mosquito brains. 2021, PLoS One, 16, e0250381

[13] Kazama, H., Systems neuroscience in Drosophila: conceptual and technical advantages. 2015, Neuroscience, 296, 3

[14] Aimon, S. & Grunwald Kadow, I. C., Studying complex brain dynamics using Drosophila. 2020, Journal of Neurogenetics, 34, 171

[15] Simpson, J. H. & Looger, L. L., Functional imaging and optogenetics in Drosophila. 2018, Genetics, 208, 1291

[16] Jenett, A., Rubin, G. M., Ngo, T.-T., et al., A GAL4-driver line resource for Drosophila neurobiology. 2012, Cell reports, 2, 991

[17] Scheffer, L. K., Xu, C. S., Januszewski, M., et al., A connectome and analysis of the adult *Drosophila* central brain. 2020, eLife, 9, e57443

[18] Hendricks, J. C., Finn, S. M., Panckeri, K. A., et al., Rest in Drosophila is a sleep-like state. 2000, Neuron, 25, 129

[19] Shaw, P. J., Cirelli, C., Greenspan, R. J., & Tononi, G., Correlates of sleep and waking in Drosophila melanogaster. 2000, Science, 287, 1834

[20] Kirszenblat, L. & van Swinderen, B. 2019, in Handbook of Behavioral Neuroscience, Vol. 30 (Elsevier), 333–347

[21] Shafer, O. T. & Keene, A. C., The regulation of Drosophila sleep. 2021, Current Biology, 31, R38

[22] Artiushin, G. & Sehgal, A., The glial perspective on sleep and circadian rhythms. 2020, Annual review of neuroscience, 43, 119

[23] Donlea, J. M., Neuronal and molecular mechanisms of sleep homeostasis. 2017, Current opinion in insect science

[24] Honkanen, A., Adden, A., da Silva Freitas, J., & Heinze, S., The insect central complex and the neural basis of navigational strategies. 2019, Journal of Experimental Biology, 222, jeb188854

[25] Fisher, Y. E., Flexible navigational computations in the Drosophila central complex. 2022, Current Opinion in Neurobiology, 73, 102514

[26] Pfeiffer, K., The neuronal building blocks of the navigational toolkit in the central complex of insects. 2022, Current Opinion in Insect Science, 100972

[27] Flores-Valle, A., Gonçalves, P. J., & Seelig, J. D., Integration of sleep homeostasis and navigation in Drosophila. 2021, PLoS Computational Biology, 17, e1009088

[28] Flores-Valle, A., Honnef, R., & Seelig, J. D., Automated long-term two-photon imaging in head-fixed walking Drosophila. 2022, Journal of Neuroscience Methods, 368, 109432

[29] Valle, A. F. & Seelig, J. D., Two-photon Bessel beam tomography for fast volume imaging. 2019, Optics express, 27, 12147

[30] Flores-Valle, A. & Seelig, J. D., Axial motion estimation and correction for simultaneous multi-plane two-photon calcium imaging. 2022, Biomedical Optics Express, 13, 2035

[31] Flores-Valle, A. & Seelig, J. D., Dynamics of a sleep homeostat observed in glia during behavior. 2022, bioRxiv, 2022

[32] Flores-Valle, A. & Seelig, J. D., A place learning assay for tethered walking Drosophila. 2022, Journal of Neuroscience Methods, 378, 109657

[33] Banks, S. & Dinges, D. F., Behavioral and physiological consequences of sleep restriction. 2007, Journal of clinical sleep medicine, 3, 519

[34] Grandner, M. A., Sleep, health, and society. 2017, Sleep medicine clinics, 12, 1

[35] Kaur, J., Fahmy, L. M., Davoodi-Bojd, E., et al., Waste clearance in the brain. 2021, Frontiers in Neuroanatomy, 15, 665803

[36] Holst, S. C. & Landolt, H.-P., Sleep homeostasis, metabolism, and adenosine. 2015, Current Sleep Medicine Reports, 1, 27

[37] Williams, J. A. & Naidoo, N., Sleep and cellular stress. 2020, Current opinion in physiology, 15, 104

[38] Rico-Rosillo, M. G. & Vega-Robledo, G. B., Sleep and immune system. 2018, Revista Alergia Mexico, 65, 160

[39] Morgan, D. & Tsai, S. C., Sleep and the endocrine system. 2015, Critical care clinics, 31, 403

[40] Jiang, F., Sleep and early brain development. 2019, Annals of Nutrition and Metabolism, 75, 44

[41] Orzeł-Gryglewska, J., Consequences of sleep deprivation. 2010, International journal of occupational medicine and environmental health

[42] Bishir, M., Bhat, A., Essa, M. M., et al., Sleep deprivation and neurological disorders. 2020, BioMed research international, 2020

[43] Killgore, W. D., Effects of sleep deprivation on cognition. 2010, Progress in brain research, 185, 105

[44] Bolin, D. J., Sleep deprivation and its contribution to mood and performance deterioration in college athletes. 2019, Current sports medicine reports, 18, 305

[45] Hudson, A. N., Van Dongen, H. P., & Honn, K. A., Sleep deprivation, vigilant attention, and brain function: a review. 2020, Neuropsychopharmacology, 45, 21

[46] Al-Mekhlafi, A.-B. A., Isha, A. S. N., & Naji, G. M. A., The relationship between fatigue and driving performance: A review and directions for future research. 2020, J. Crit. Rev, 7, 134

[47] Suardiaz-Muro, M., Morante-Ruiz, M., Ortega-Moreno, M., et al., Sleep and academic performance in university students: a systematic review. 2020, Revista de Neurologia, 71, 43

[48] Fairholme, C. P. & Manber, R., Sleep, emotions, and emotion regulation: an overview. 2015, Sleep and affect, 45

[49] Cousins, J. N. & Fernández, G., The impact of sleep deprivation on declarative memory. 2019, Progress in brain research, 246, 27

[50] Freeman, D., Sheaves, B., Waite, F., Harvey, A. G., & Harrison, P. J., Sleep disturbance and psychiatric disorders. 2020, The Lancet Psychiatry, 7, 628

[51] Montagna, P., Gambetti, P., Cortelli, P., & Lugaresi, E., Familial and sporadic fatal insomnia. 2003, The Lancet Neurology, 2, 167

[52] Eugene, A. R. & Masiak, J., The neuroprotective aspects of sleep. 2015, MEDtube science, 3, 35

[53] Hill, V. M., O'Connor, R. M., & Shirasu-Hiza, M., Tired and stressed: Examining the need for sleep. 2020, European Journal of Neuroscience, 51, 494

[54] Steriade, M., Timofeev, I., & Grenier, F., Natural waking and sleep states: a view from inside neocortical neurons. 2001, Journal of neurophysiology, 85, 1969

[55] Vyazovskiy, V. V., Olcese, U., Lazimy, Y. M., et al., Cortical firing and sleep homeostasis. 2009, Neuron, 63, 865

[56] Massimini, M., Huber, R., Ferrarelli, F., Hill, S., & Tononi, G., The sleep slow oscillation as a traveling wave. 2004, Journal of Neuroscience, 24, 6862

[57] Buzsáki, G., Anastassiou, C. A., & Koch, C., The origin of extracellular fields and currents—EEG, ECoG, LFP and spikes. 2012, Nature reviews neuroscience, 13, 407

[58] Frank, M. G. 2018, in Sleep-Wake Neurobiology and Pharmacology (Springer), 83–96

[59] Krueger, J. M., Nguyen, J. T., Dykstra-Aiello, C. J., & Taishi, P., Local sleep. 2019, Sleep medicine reviews, 43, 14

[60] Loomis, A. L., Harvey, E. N., & Hobart, G. A., Cerebral states during sleep, as studied by human brain potentials. 1937, Journal of experimental psychology, 21, 127

[61] Lima, S. L., Rattenborg, N. C., Lesku, J. A., & Amlaner, C. J., Sleeping under the risk of predation. 2005, Animal Behaviour, 70, 723

[62] Aserinsky, E. & Kleitman, N., Regularly occurring periods of eye motility, and concomitant phenomena, during sleep. 1953, Science, 118, 273

[63] Dijk, D.-J., Regulation and functional correlates of slow wave sleep. 2009, Journal of Clinical Sleep Medicine, 5, S6

[64] Hilditch, C. J. & McHill, A. W., Sleep inertia: current insights. 2019, Nature and science of sleep, 11, 155

[65] Siclari, F., Bernardi, G., Cataldi, J., & Tononi, G., Dreaming in NREM sleep: a high-density EEG study of slow waves and spindles. 2018, Journal of Neuroscience, 38, 9175

[66] Tobler, I., Is sleep fundamentally different between mammalian species? 1995, Behavioural brain research, 69, 35

[67] Rattenborg, N. C., Van der Meij, J., Beckers, G. J., & Lesku, J. A., Local aspects of avian non-REM and REM sleep. 2019, Frontiers in Neuroscience, 13, 567

[68] Libourel, P.-A. & Barrillot, B., Is there REM sleep in reptiles? A key question, but still unanswered. 2020, Current Opinion in Physiology, 15, 134

[69] Libourel, P.-A. & Herrel, A., Sleep in amphibians and reptiles: a review and a preliminary analysis of evolutionary patterns. 2016, Biological Reviews, 91, 833

[70] Lyamin, O. I., Manger, P. R., Ridgway, S. H., Mukhametov, L. M., & Siegel, J. M., Cetacean sleep: an unusual form of mammalian sleep. 2008, Neuroscience & Biobehavioral Reviews, 32, 1451

[71] Mukhametov, L., Lyamin, O., & Polyakova, I., Interhemispheric asynchrony of the sleep EEG in northern fur seals. 1985, Experientia, 41, 1034

[72] Rattenborg, N. C., Voirin, B., Cruz, S. M., et al., Evidence that birds sleep in mid-flight. 2016, Nature communications, 7, 1

[73] Miyazaki, S., Liu, C.-Y., & Hayashi, Y., Sleep in vertebrate and invertebrate animals, and insights into the function and evolution of sleep. 2017, Neuroscience research, 118, 3

[74] Campbell, S. S. & Tobler, I., Animal sleep: a review of sleep duration across phylogeny. 1984, Neuroscience & Biobehavioral Reviews, 8, 269

[75] Rial, R. V., Akaârir, M., Gamundí, A., et al., Evolution of wakefulness, sleep and hibernation: from reptiles to mammals. 2010, Neuroscience & Biobehavioral Reviews, 34, 1144

[76] Keene, A. & Appelbaum, L. 2019, in Handbook of Behavioral Neuroscience, Vol. 30 (Elsevier), 363–374

[77] Zhdanova, I. V., Wang, S. Y., Leclair, O. U., & Danilova, N. P., Melatonin promotes sleep-like state in zebrafish. 2001, Brain research, 903, 263

[78] Yokogawa, T., Marin, W., Faraco, J., et al., Characterization of sleep in zebrafish and insomnia in hypocretin receptor mutants. 2007, PLoS biology, 5, e277

[79] Leung, L. C., Wang, G. X., Madelaine, R., et al., Neural signatures of sleep in zebrafish. 2019, Nature, 571, 198

[80] Tran, S. & Prober, D. A. 2022, in Circadian Clocks (Springer), 259–286

[81] Helfrich-Förster, C., Sleep in insects. 2018, Annual review of entomology, 63, 69

[82] Raizen, D. M., Zimmerman, J. E., Maycock, M. H., et al., Lethargus is a Caenorhabditis elegans sleep-like state. 2008, Nature, 451, 569

[83] Nath, R. D., Bedbrook, C. N., Abrams, M. J., et al., The jellyfish Cassiopea exhibits a sleep-like state. 2017, Current Biology, 27, 2984

[84] Kanaya, H. J., Park, S., Kim, J.-h., et al., A sleep-like state in Hydra unravels conserved sleep mechanisms during the evolutionary development of the central nervous system. 2020, Science advances, 6, eabb9415

[85] Konietzka, J., Fritz, M., Spiri, S., et al., Epidermal growth factor signaling promotes sleep through a combined series and parallel neural circuit. 2020, Current biology, 30, 1

[86] Foltenyi, K., Greenspan, R. J., & Newport, J. W., Activation of EGFR and ERK by rhomboid signaling regulates the consolidation and maintenance of sleep in Drosophila. 2007, Nature neuroscience, 10, 1160

[87] Lee, D. A., Liu, J., Hong, Y., et al., Evolutionarily conserved regulation of sleep by epidermal growth factor receptor signaling. 2019, Science advances, 5, eaax4249

[88] Kramer, A., Yang, F.-C., Snodgrass, P., et al., Regulation of daily locomotor activity and sleep by hypothalamic EGF receptor signaling. 2001, Science, 294, 2511

[89] Kushikata, T., Fang, J., Chen, Z., Wang, Y., & Krueger, J. M., Epidermal growth factor enhances spontaneous sleep in rabbits. 1998, American Journal of Physiology-Regulatory, Integrative and Comparative Physiology, 275, R509

[90] Ueno, T., Tomita, J., Tanimoto, H., et al., Identification of a dopamine pathway that regulates sleep and arousal in Drosophila. 2012, Nature neuroscience, 15, 1516

[91] Singh, K., Ju, J. Y., Walsh, M. B., DiIorio, M. A., & Hart, A. C., Deep conservation of genes required for both Drosophila melanogaster and Caenorhabditis elegans sleep includes a role for dopaminergic signaling. 2014, sleep, 37, 1439

[92] Monti, J. M. & Monti, D., The involvement of dopamine in the modulation of sleep and waking. 2007, Sleep medicine reviews, 11, 113

[93] Scheffer, L. K., Xu, C. S., Januszewski, M., et al., A connectome and analysis of the adult Drosophila central brain. 2020, Elife, 9

[94] Beckwith, E. J. & French, A. S., Sleep in Drosophila and its context. 2019, Frontiers in physiology, 10, 1167

[95] Saper, C. B. & Fuller, P. M., Wake–sleep circuitry: an overview. 2017, Current opinion in neurobiology, 44, 186

[96] Ly, S., Pack, A. I., & Naidoo, N., The neurobiological basis of sleep: Insights from Drosophila. 2018, Neuroscience & Biobehavioral Reviews, 87, 67

[97] Falup-Pecurariu, C., Diaconu, S., Tînț, D., & Falup-Pecurariu, O., Neurobiology of sleep. 2021, Experimental and Therapeutic Medicine, 21, 1

[98] Vaseghi, S., Arjmandi-Rad, S., Eskandari, M., et al., Modulating role of serotonergic signaling in sleep and memory. 2022, Pharmacological Reports, 1

[99] Wu, M. N., Ho, K., Crocker, A., et al., The effects of caffeine on sleep in Drosophila require PKA activity, but not the adenosine receptor. 2009, Journal of Neuroscience, 29, 11029

[100] Lin, F. J., Pierce, M. M., Sehgal, A., et al., Effect of taurine and caffeine on sleep–wake activity in Drosophila melanogaster. 2010, Nature and science of sleep, 221

[101] Rihel, J. & Schier, A. F., Sites of action of sleep and wake drugs: insights from model organisms. 2013, Current opinion in neurobiology, 23, 831

[102] Allada, R., Cirelli, C., & Sehgal, A., Molecular mechanisms of sleep homeostasis in flies and mammals. 2017, Cold Spring Harbor perspectives in biology, 9, a027730

[103] Gilestro, G. F., Video tracking and analysis of sleep in Drosophila melanogaster. 2012, Nature protocols, 7, 995

[104] Pfeiffenberger, C., Lear, B. C., Keegan, K. P., & Allada, R., Locomotor activity level monitoring using the Drosophila Activity Monitoring (DAM) System. 2010, Cold Spring Harbor Protocols, 2010, pdb

[105] Zimmerman, J. E., Raizen, D. M., Maycock, M. H., Maislin, G., & Pack, A. I., A video method to study Drosophila sleep. 2008, Sleep, 31, 1587

[106] Donelson, N., Kim, E. Z., Slawson, J. B., et al., High-resolution positional tracking for long-term analysis of Drosophila sleep and locomotion using the "tracker" program. 2012, PloS one, 7, e37250

[107] Dubowy, C. & Sehgal, A., Circadian rhythms and sleep in Drosophila melanogaster. 2017, Genetics, 205, 1373

[108] Garbe, D. S., Bollinger, W. L., Vigderman, A., et al., Context-specific comparison of sleep acquisition systems in Drosophila. 2015, Biology open, 4, 1558

[109] Geissmann, Q., Garcia Rodriguez, L., Beckwith, E. J., et al., Ethoscopes: An open platform for high-throughput ethomics. 2017, PLoS biology, 15, e2003026

[110] Parisky, K. M., Rivera, J. L. A., Donelson, N. C., Kotecha, S., & Griffith, L. C., Reorganization of sleep by temperature in Drosophila requires light, the homeostat, and the circadian clock. 2016, Current Biology, 26, 882

[111] Donlea, J. M., Ramanan, N., & Shaw, P. J., Use-dependent plasticity in clock neurons regulates sleep need in Drosophila. 2009, Science, 324, 105

[112] Keene, A. C., Duboué, E. R., McDonald, D. M., et al., Clock and cycle limit starvation-induced sleep loss in Drosophila. 2010, Current biology, 20, 1209

[113] Brown, E. B., Shah, K. D., Faville, R., Kottler, B., & Keene, A. C., Drosophila insulin-like peptide 2 mediates dietary regulation of sleep intensity. 2020, PLoS Genetics, 16, e1008270

[114] Thimgan, M. S., Suzuki, Y., Seugnet, L., Gottschalk, L., & Shaw, P. J., The perilipin homologue, lipid storage droplet 2, regulates sleep homeostasis and prevents learning impairments following sleep loss. 2010, PLoS biology, 8, e1000466

[115] Machado, D. R., Afonso, D. J., Kenny, A. R., et al., Identification of octopaminergic neurons that modulate sleep suppression by male sex drive. 2017, Elife, 6, e23130

[116] Beckwith, E. J., Geissmann, Q., French, A. S., & Gilestro, G. F., Regulation of sleep homeostasis by sexual arousal. 2017, Elife, 6, e27445

[117] Allada, R., White, N. E., So, W. V., Hall, J. C., & Rosbash, M., A mutant Drosophila homolog of mammalian Clock disrupts circadian rhythms and transcription of period and timeless. 1998, Cell, 93, 791

[118] Shaw, P. J., Tononi, G., Greenspan, R. J., & Robinson, D. F., Stress response genes protect against lethal effects of sleep deprivation in Drosophila. 2002, Nature, 417, 287

[119] Huber, R., Hill, S. L., Holladay, C., et al., Sleep homeostasis in Drosophila melanogaster. 2004, Sleep, 27, 628

[120] Gilestro, G. F., Tononi, G., & Cirelli, C., Widespread changes in synaptic markers as a function of sleep and wakefulness in Drosophila. 2009, science, 324, 109

[121] Seugnet, L., Suzuki, Y., Vine, L., Gottschalk, L., & Shaw, P. J., D1 receptor activation in the mushroom bodies rescues sleep-loss-induced learning impairments in Drosophila. 2008, Current Biology, 18, 1110

[122] Dissel, S., Angadi, V., Kirszenblat, L., et al., Sleep restores behavioral plasticity to Drosophila mutants. 2015, Current Biology, 25, 1270

[123] Liu, S., Liu, Q., Tabuchi, M., & Wu, M. N., Sleep drive is encoded by neural plastic changes in a dedicated circuit. 2016, Cell, 165, 1347

[124] Kayser, M. S., Mainwaring, B., Yue, Z., & Sehgal, A., Sleep deprivation suppresses aggression in Drosophila. 2015, Elife, 4, e07643

[125] Donlea, J. M., Pimentel, D., Talbot, C. B., et al., Recurrent Circuitry for Balancing Sleep Need and Sleep. 2018, Neuron

[126] Jin, X., Tian, Y., Zhang, Z. C., et al., A subset of DN1p neurons integrates thermosensory inputs to promote wakefulness via CNMa signaling. 2021, Current Biology, 31, 2075

[127] Weiss, J. T. & Donlea, J. M., Sleep deprivation results in diverse patterns of synaptic scaling across the Drosophila mushroom bodies. 2021, Current Biology, 31, 3248

[128] Joiner, W. J., Crocker, A., White, B. H., & Sehgal, A., Sleep in Drosophila is regulated by adult mushroom bodies. 2006, Nature, 441, 757

[129] Blum, I. D., Keleş, M. F., Baz, E.-S., et al., Astroglial calcium signaling encodes sleep need in Drosophila. 2021, Current Biology, 31, 150

[130] Donlea, J. M., Roles for sleep in memory: insights from the fly. 2019, Current opinion in neurobiology, 54, 120

[131] Marquand, K., Roselli, C., Cervantes-Sandoval, I., & Boto, T., Sleep benefits different stages of memory in Drosophila. 2023, Frontiers in Physiology, 14, 33

[132] Harbison, S. T. & Sehgal, A., Energy stores are not altered by long-term partial sleep deprivation in Drosophila melanogaster. 2009, PLoS One, 4, e6211

[133] Nollet, M., Wisden, W., & Franks, N. P., Sleep deprivation and stress: a reciprocal relationship. 2020, Interface focus, 10, 20190092

[134] Geissmann, Q., Beckwith, E. J., & Gilestro, G. F., Most sleep does not serve a vital function: Evidence from Drosophila melanogaster. 2019, Science advances, 5, eaau9253

[135] Chowdhury, B., Abhilash, L., Ortega, A., Liu, S., & Shafer III, O. T., Homeostatic control of deep sleep in Drosophila: Implications for Discovering Correlates of Sleep Pressure. 2022, bioRxiv, 2022

[136] Kahsai, L. & Zars, T., Learning and memory in Drosophila: behavior, genetics, and neural systems. 2011, International review of neurobiology, 99, 139

[137] Amin, H. & Lin, A. C., Neuronal mechanisms underlying innate and learned olfactory processing in Drosophila. 2019, Current Opinion in Insect Science, 36, 9

[138] Felsenberg, J., Changing memories on the fly: the neural circuits of memory re-evaluation in Drosophila melanogaster. 2021, Current Opinion in Neurobiology, 67, 190

[139] Dissel, S., Drosophila as a model to study the relationship between sleep, plasticity, and memory. 2020, Frontiers in physiology, 11, 533

[140] Perry, C. J., Barron, A. B., & Cheng, K., Invertebrate learning and cognition: relating phenomena to neural substrate. 2013, Wiley Interdisciplinary Reviews: Cognitive Science, 4, 561

[141] Boto, T., Stahl, A., & Tomchik, S. M., Cellular and circuit mechanisms of olfactory associative learning in Drosophila. 2020, Journal of neurogenetics, 34, 36

[142] Raun, N., Jones, S., & Kramer, J. M., Conditioned courtship suppression in Drosophila melanogaster. 2021, Journal of Neurogenetics, 35, 154

[143] Guo, A., Lu, H., Zhang, K., Ren, Q., & Wong, Y.-N. C. 2013, in Handbook of Behavioral Neuroscience, Vol. 22 (Elsevier), 378–394

[144] Liu, G., Seiler, H., Wen, A., et al., Distinct memory traces for two visual features in the Drosophila brain. 2006, Nature, 439, 551

[145] Pan, Y., Zhou, Y., Guo, C., et al., Differential roles of the fan-shaped body and the ellipsoid body in Drosophila visual pattern memory. 2009, Learning & Memory, 16, 289

[146] Ofstad, T. A., Zuker, C. S., & Reiser, M. B., Visual place learning in Drosophila melanogaster. 2011, Nature, 474, 204

[147] Artiushin, G. & Sehgal, A., The Drosophila circuitry of sleep–wake regulation. 2017, Current opinion in neurobiology, 44, 243

[148] Dill, M., Wolf, R., & Heisenberg, M., Visual pattern recognition in Drosophila involves retinotopic matching. 1993, Nature, 365, 751

[149] Heisenberg, M. & Wolf, R., Reafferent control of optomotor yaw torque in Drosophila melanogaster. 1988, Journal of Comparative Physiology A, 163, 373

[150] Ernst, R. & Heisenberg, M., The memory template in Drosophila pattern vision at the flight simulator. 1999, Vision research, 39, 3920

[151] Tang, S. & Guo, A., Choice behavior of Drosophila facing contradictory visual cues. 2001, Science, 294, 1543

[152] Tang, S., Wolf, R., Xu, S., & Heisenberg, M., Visual pattern recognition in Drosophila is invariant for retinal position. 2004, Science, 305, 1020

[153] Fry, S. N., Rohrseitz, N., Straw, A. D., & Dickinson, M. H., TrackFly: virtual reality for a behavioral system analysis in free-flying fruit flies. 2008, Journal of neuroscience methods, 171, 110

[154] Reiser, M. B. & Dickinson, M. H., A modular display system for insect behavioral neuroscience. 2008, Journal of neuroscience methods, 167, 127

[155] Seelig, J. D. & Jayaraman, V., Feature detection and orientation tuning in the Drosophila central complex. 2013, Nature, 503, 262

[156] Moore, R. J., Taylor, G. J., Paulk, A. C., et al., FicTrac: a visual method for tracking spherical motion and generating fictive animal paths. 2014, Journal of neuroscience methods, 225, 106

[157] Vishniakou, I., Plöger, P. G., & Seelig, J. D., Virtual reality for animal navigation with camera-based optical flow tracking. 2019, Journal of Neuroscience Methods, 327, 108403

[158] Dan, C., Hulse, B. K., Jayaraman, V., & Hermundstad, A. M., Flexible control of behavioral variability mediated by an internal representation of head direction. 2021, bioRxiv, 2021

[159] Grover, D., Chen, J.-Y., Xie, J., et al., Differential mechanisms underlie trace and delay conditioning in Drosophila. 2022, Nature, 603, 302

[160] Haberkern, H., Basnak, M. A., Ahanonu, B., et al., Visually guided behavior and optogenetically induced learning in head-fixed flies exploring a virtual landscape. 2019, Current Biology, 29, 1647

[161] Le Bourg, É. & Buecher, C., Learned suppression of photopositive tendencies in-Drosophila melanogaster. 2002, Animal learning & behavior, 30, 330

[162] Stern, U., Srivastava, H., Chen, H.-L., et al., Learning a spatial task by trial and error in Drosophila. 2019, Current Biology, 29, 2517

[163] Wustmann, G., Rein, K., Wolf, R., & Heisenberg, M., A new paradigm for operant conditioning of Drosophila melanogaster. 1996, Journal of Comparative Physiology A, 179, 429

[164] Foucaud, J., Burns, J. G., & Mery, F., Use of spatial information and search strategies in a water maze analog in Drosophila melanogaster. 2010, PLoS One, 5, e15231

[165] Vorhees, C. V. & Williams, M. T., Morris water maze: procedures for assessing spatial and related forms of learning and memory. 2006, Nature protocols, 1, 848

[166] Melnattur, K., Kirszenblat, L., Morgan, E., et al., A conserved role for sleep in supporting Spatial Learning in Drosophila. 2021, Sleep, 44, zsaa197

[167] Li, X., Yu, F., & Guo, A., Sleep deprivation specifically impairs short-term olfactory memory in Drosophila. 2009, Sleep, 32, 1417

[168] Glou, E. L., Seugnet, L., Shaw, P. J., Preat, T., & Goguel, V., Circadian modulation of consolidated memory retrieval following sleep deprivation in Drosophila. 2012, Sleep, 35, 1377

[169] Donlea, J. M., Pimentel, D., & Miesenböck, G., Neuronal machinery of sleep homeostasis in Drosophila. 2014, Neuron, 81, 860

[170] Ganguly-Fitzgerald, I., Donlea, J., & Shaw, P. J., Waking experience affects sleep need in Drosophila. 2006, Science, 313, 1775

[171] Seidner, G., Robinson, J. E., Wu, M., et al., Identification of neurons with a privileged role in sleep homeostasis in Drosophila melanogaster. 2015, Current Biology, 25, 2928

[172] Wiggin, T. D., Hsiao, Y., Liu, J. B., Huber, R., & Griffith, L. C., Rest Is Required to Learn an Appetitively-Reinforced Operant Task in Drosophila. 2021, Frontiers in behavioral neuroscience, 15, 681593

[173] Bushey, D., Huber, R., Tononi, G., & Cirelli, C., Drosophila Hyperkinetic mutants have reduced sleep and impaired memory. 2007, Journal of Neuroscience, 27, 5384

[174] Dissel, S., Seugnet, L., Thimgan, M. S., et al., Differential activation of immune factors in neurons and glia contribute to individual differences in resilience/vulnerability to sleep disruption. 2015, Brain, behavior, and immunity, 47, 75

[175] Seugnet, L., Suzuki, Y., Thimgan, M., et al., Identifying sleep regulatory genes using a Drosophila model of insomnia. 2009, Journal of Neuroscience, 29, 7148

[176] Donlea, J. M., Thimgan, M. S., Suzuki, Y., Gottschalk, L., & Shaw, P. J., Inducing sleep by remote control facilitates memory consolidation in Drosophila. 2011, Science, 332, 1571

[177] Dag, U., Lei, Z., Le, J. Q., et al., Neuronal reactivation during post-learning sleep consolidates long-term memory in Drosophila. 2019, Elife, 8, e42786

[178] Dissel, S., Morgan, E., Duong, V., et al., Sleep restores place learning to the adenylyl cyclase mutant rutabaga. 2020, Journal of neurogenetics, 34, 83

[179] Seugnet, L., Suzuki, Y., Donlea, J. M., Gottschalk, L., & Shaw, P. J., Sleep deprivation during early-adult development results in long-lasting learning deficits in adult Drosophila. 2011, Sleep, 34, 137

[180] Dissel, S., Klose, M., Donlea, J., et al., Enhanced sleep reverses memory deficits and underlying pathology in Drosophila models of Alzheimer's disease. 2017, Neurobiology of sleep and circadian rhythms, 2, 15

[181] Roselli, C., Ramaswami, M., Boto, T., & Cervantes-Sandoval, I., The making of long-lasting memories: a fruit fly perspective. 2021, Frontiers in behavioral neuroscience, 54

[182] Puentes-Mestril, C. & Aton, S. J., Linking network activity to synaptic plasticity during sleep: hypotheses and recent data. 2017, Frontiers in neural circuits, 11, 61

[183] Cirelli, C. & Tononi, G., Linking the need to sleep with synaptic function. 2019, Science, 366, 189

[184] Girardeau, G. & Lopes-Dos-Santos, V., Brain neural patterns and the memory function of sleep. 2021, Science, 374, 560

[185] Thomas, C. W., Guillaumin, M. C., McKillop, L. E., Achermann, P., & Vyazovskiy, V. V., Global sleep homeostasis reflects temporally and spatially integrated local cortical neuronal activity. 2020, Elife, 9, e54148

[186] Raccuglia, D., Huang, S., Ender, A., et al., Network-specific synchronization of electrical slow-wave oscillations regulates sleep drive in Drosophila. 2019, Current Biology, 29, 3611

[187] Dang-Vu, T. T., Schabus, M., Desseilles, M., et al., Spontaneous neural activity during human slow wave sleep. 2008, Proceedings of the National Academy of Sciences, 105, 15160

[188] Adamantidis, A. R., Gutierrez Herrera, C., & Gent, T. C., Oscillating circuitries in the sleeping brain. 2019, Nature Reviews Neuroscience, 20, 746

[189] Nitz, D. A., Van Swinderen, B., Tononi, G., & Greenspan, R. J., Electrophysiological correlates of rest and activity in Drosophila melanogaster. 2002, Current biology, 12, 1934

[190] Van Alphen, B., Yap, M. H., Kirszenblat, L., Kottler, B., & van Swinderen, B., A dynamic deep sleep stage in Drosophila. 2013, Journal of Neuroscience, 33, 6917

[191] van Swinderen, B. & Greenspan, R. J., Salience modulates 20–30 Hz brain activity in Drosophila. 2003, Nature neuroscience, 6, 579

[192] Bushey, D., Tononi, G., & Cirelli, C., Sleep-and wake-dependent changes in neuronal activity and reactivity demonstrated in fly neurons using in vivo calcium imaging. 2015, Proceedings of the National Academy of Sciences, 112, 4785

[193] Yap, M. H., Grabowska, M. J., Rohrscheib, C., et al., Oscillatory brain activity in spontaneous and induced sleep stages in flies. 2017, Nature communications, 8, 1815

[194] Tainton-Heap, L. A., Kirszenblat, L. C., Notaras, E. T., et al., A paradoxical kind of sleep in Drosophila melanogaster. 2021, Current Biology, 31, 578

[195] Van Alphen, B., Semenza, E. R., Yap, M., Van Swinderen, B., & Allada, R., A deep sleep stage in Drosophila with a functional role in waste clearance. 2021, Science advances, 7, eabc2999

[196] Buzsaki, G. & Draguhn, A., Neuronal oscillations in cortical networks. 2004, science, 304, 1926

[197] Siclari, F. & Tononi, G., Local aspects of sleep and wakefulness. 2017, Current Opinion in Neurobiology, 44, 222

[198] Lewis, P. A. & Bendor, D., How targeted memory reactivation promotes the selective strengthening of memories in sleep. 2019, Current Biology, 29, R906

[199] Findlay, G., Tononi, G., & Cirelli, C., The evolving view of replay and its functions in wake and sleep. 2020, Sleep Advances, 1, zpab002

[200] Ghandour, K. & Inokuchi, K., Memory reactivations during sleep. 2022, Neuroscience Research

[201] Hayes, T. L., Krishnan, G. P., Bazhenov, M., et al., Replay in deep learning: Current approaches and missing biological elements. 2021, Neural computation, 33, 2908

[202] Klinzing, J. G., Niethard, N., & Born, J., Mechanisms of systems memory consolidation during sleep. 2019, Nature neuroscience, 22, 1598

[203] Goto, A. & Hayashi, Y., Offline neuronal activity and synaptic plasticity during sleep and memory consolidation. 2022, Neuroscience Research

[204] Bellesi, M. & de Vivo, L., Structural synaptic plasticity across sleep and wake. 2020, Current Opinion in Physiology, 15, 74

[205] Sun, L., Zhou, H., Cichon, J., & Yang, G., Experience and sleep-dependent synaptic plasticity: from structure to activity. 2020, Philosophical Transactions of the Royal Society B, 375, 20190234

[206] Bushey, D., Tononi, G., & Cirelli, C., Sleep and synaptic homeostasis: structural evidence in Drosophila. 2011, Science, 332, 1576

[207] Huang, S., Piao, C., Beuschel, C. B., Götz, T., & Sigrist, S. J., Presynaptic active zone plasticity encodes sleep need in Drosophila. 2020, Current Biology, 30, 1077

[208] Wagh, D. A., Rasse, T. M., Asan, E., et al., Bruchpilot, a protein with homology to ELKS/CAST, is required for structural integrity and function of synaptic active zones in Drosophila. 2006, Neuron, 49, 833

[209] Holderith, N., Lorincz, A., Katona, G., et al., Release probability of hippocampal glutamatergic terminals scales with the size of the active zone. 2012, Nature neuroscience, 15, 988

[210] Weyhersmüller, A., Hallermann, S., Wagner, N., & Eilers, J., Rapid active zone remodeling during synaptic plasticity. 2011, Journal of Neuroscience, 31, 6041

[211] Modi, M. N., Shuai, Y., & Turner, G. C., The Drosophila mushroom body: from architecture to algorithm in a learning circuit. 2020, Annual review of neuroscience, 43, 465

[212] Peng, W., Wu, Z., Song, K., et al., Regulation of sleep homeostasis mediator adenosine by basal forebrain glutamatergic neurons. 2020, Science, 369, eabb0556

[213] Porkka-Heiskanen, T., Sleep homeostasis. 2013, Current opinion in neurobiology, 23, 799

[214] Holst, S. C. & Landolt, H.-P., Sleep-wake neurochemistry. 2018, Sleep medicine clinics, 13, 137

[215] Lazarus, M., Chen, J.-F., Huang, Z.-L., Urade, Y., & Fredholm, B. B., Adenosine and sleep. 2019, Sleep-wake neurobiology and pharmacology, 359

[216] Wang, F., Ruppell, K. T., Zhou, S., et al., Gliotransmission orchestrates neuronal type-specific axon regeneration. 2019, bioRxiv, 799635

[217] Jessen, N. A., Munk, A. S. F., Lundgaard, I., & Nedergaard, M., The glymphatic system: a beginner's guide. 2015, Neurochemical research, 40, 2583

[218] Xie, L., Kang, H., Xu, Q., et al., Sleep drives metabolite clearance from the adult brain. 2013, science, 342, 373

[219] Hauglund, N. L., Pavan, C., & Nedergaard, M., Cleaning the sleeping brain–the potential restorative function of the glymphatic system. 2020, Current Opinion in Physiology, 15, 1

[220] Zhang, S. L., Yue, Z., Arnold, D. M., Artiushin, G., & Sehgal, A., A circadian clock in the blood-brain barrier regulates xenobiotic efflux. 2018, Cell, 173, 130

[221] Artiushin, G., Zhang, S. L., Tricoire, H., & Sehgal, A., Endocytosis at the Drosophila blood–brain barrier as a function for sleep. 2018, Elife, 7, e43326

[222] Schirmeier, S. & Klämbt, C., The Drosophila blood-brain barrier as interface between neurons and hemolymph. 2015, Mechanisms of development, 138, 50

[223] Contreras, E. G. & Sierralta, J., The Fly Blood-Brain Barrier Fights Against Nutritional Stress. 2022, Neuroscience Insights, 17, 26331055221120252

[224] Kremer, M. C., Jung, C., Batelli, S., Rubin, G. M., & Gaul, U., The glia of the adult Drosophila nervous system. 2017, Glia, 65, 606

[225] Pogodalla, N., Kranenburg, H., Rey, S., et al., Drosophila ßHeavy-Spectrin is required in polarized ensheathing glia that form a diffusion-barrier around the neuropil. 2021, Nature communications, 12, 1

[226] Bittern, J., Pogodalla, N., Ohm, H., et al., Neuron–glia interaction in the Drosophila nervous system. 2021, Developmental neurobiology, 81, 438

[227] Frank, M. G., The role of glia in sleep regulation and function. 2019, Sleep-Wake Neurobiology and Pharmacology, 83

[228] Garofalo, S., Picard, K., Limatola, C., et al., Role of glia in the regulation of sleep in health and disease. 2020, Compr. Physiol, 10, 687

[229] Ingiosi, A. M. & Frank, M. G., Goodnight, astrocyte: Waking up to astroglial mechanisms in sleep. 2022, The FEBS Journal

[230] Sidoryk-Wegrzynowicz, M., Wegrzynowicz, M., Lee, E., Bowman, A. B., & Aschner, M., Role of astrocytes in brain function and disease. 2011, Toxicologic pathology, 39, 115

[231] Iliff, J. J., Wang, M., Liao, Y., et al., A paravascular pathway facilitates CSF flow through the brain parenchyma and the clearance of interstitial solutes, including amyloid β. 2012, Science translational medicine, 4, 147ra111

[232] Mestre, H., Hablitz, L. M., Xavier, A. L., et al., Aquaporin-4-dependent glymphatic solute transport in the rodent brain. 2018, Elife, 7, e40070

[233] Khakh, B. S. & Sofroniew, M. V., Diversity of astrocyte functions and phenotypes in neural circuits. 2015, Nature neuroscience, 18, 942

[234] Haydon, P. G., Astrocytes and the modulation of sleep. 2017, Current opinion in neurobiology, 44, 28

[235] Peng, W., Liu, X., Ma, G., et al., Adenosine-independent regulation of the sleep–wake cycle by astrocyte activity. 2023, Cell Discovery, 9, 16

[236] Ingiosi, A. M., Hayworth, C. R., Harvey, D. O., et al., A role for astroglial calcium in mammalian sleep and sleep regulation. 2020, Current Biology, 30, 4373

[237] Yildirim, K., Petri, J., Kottmeier, R., & Klämbt, C., Drosophila glia: Few cell types and many conserved functions. 2019, Glia, 67, 5

[238] Awasaki, T., Lai, S.-L., Ito, K., & Lee, T., Organization and postembryonic development of glial cells in the adult central brain of Drosophila. 2008, Journal of Neuroscience, 28, 13742

[239] Gerstner, J. R., Perron, I. J., Riedy, S. M., et al., Normal sleep requires the astrocyte brain-type fatty acid binding protein FABP7. 2017, Science advances, 3, e1602663

[240] Chen, W.-F., Maguire, S., Sowcik, M., et al., A neuron–glia interaction involving GABA transaminase contributes to sleep loss in sleepless mutants. 2015, Molecular psychiatry, 20, 240

[241] Fropf, R., Zhou, H., & Yin, J. C., The clock gene period differentially regulates sleep and memory in Drosophila. 2018, Neurobiology of learning and memory, 153, 2

[242] Luna, A. J. F., Perier, M., & Seugnet, L., Amyloid precursor protein in Drosophila glia regulates sleep and genes involved in glutamate recycling. 2017, Journal of Neuroscience, 37, 4289

[243] Vanderheyden, W. M., Goodman, A. G., Taylor, R. H., et al., Astrocyte expression of the Drosophila TNF-alpha homologue, Eiger, regulates sleep in flies. 2018, PLoS genetics, 14, e1007724

[244] Hindle, S. J. & Bainton, R. J., Barrier mechanisms in the Drosophila blood-brain barrier. 2014, Frontiers in neuroscience, 8, 414

[245] Li, Y., Haynes, P., Zhang, S. L., Yue, Z., & Sehgal, A., Ecdysone acts through cortex glia to regulate sleep in Drosophila. 2023, Elife, 12, e81723

[246] Vanderheyden, W. M., Van Dongen, H. P., Frank, M. G., & Gerstner, J. R., Sleep pressure regulates mushroom body neural-glial interactions in Drosophila. 2019, Matters select, 2019

[247] Otto, N., Marelja, Z., Schoofs, A., et al., The sulfite oxidase Shopper controls neuronal activity by regulating glutamate homeostasis in Drosophila ensheathing glia. 2018, Nature communications, 9, 3514

[248] Doherty, J., Logan, M. A., Taşdemir, Ö. E., & Freeman, M. R., Ensheathing glia function as phagocytes in the adult Drosophila brain. 2009, Journal of Neuroscience, 29, 4768

[249] Singh, P. & Donlea, J. M., Bidirectional regulation of sleep and synapse pruning after neural injury. 2020, Current Biology, 30, 1063

[250] Stanhope, B. A., Jaggard, J. B., Gratton, M., Brown, E. B., & Keene, A. C., Sleep regulates glial plasticity and expression of the engulfment receptor draper following neural injury. 2020, Current Biology, 30, 1092

[251] Kim, K., Lee, S.-G., Kegelman, T. P., et al., Role of excitatory amino acid transporter-2 (EAAT2) and glutamate in neurodegeneration: opportunities for developing novel therapeutics. 2011, Journal of cellular physiology, 226, 2484

[252] Stahl, B. A., Peco, E., Davla, S., et al., The taurine transporter Eaat2 functions in ensheathing glia to modulate sleep and metabolic rate. 2018, Current Biology, 28, 3700

[253] Brinkman, J. E., Reddy, V., & Sharma, S., Physiology of sleep. 2018

[254] Miletínová, E. & Bušková, J., Functions of Sleep. 2021, Physiological Research, 70, 177

[255] Chennaoui, M., Vanneau, T., Trignol, A., et al., How does sleep help recovery from exercise-induced muscle injuries? 2021, Journal of science and medicine in sport, 24, 982

[256] Zielinski, M. R., McKenna, J. T., & McCarley, R. W., Functions and mechanisms of sleep. 2016, AIMS neuroscience, 3, 67

[257] Benington, J. H. & Heller, H. C., Restoration of brain energy metabolism as the function of sleep. 1995, Progress in neurobiology, 45, 347

[258] Scharf, M. T., Naidoo, N., Zimmerman, J. E., & Pack, A. I., The energy hypothesis of sleep revisited. 2008, Progress in neurobiology, 86, 264

[259] Zimmerman, J. E., Mackiewicz, M., Galante, R. J., et al., Glycogen in the brain of Drosophila melanogaster: diurnal rhythm and the effect of rest deprivation. 2004, Journal of neurochemistry, 88, 32

[260] Mann, K., Deny, S., Ganguli, S., & Clandinin, T. R., Coupling of activity, metabolism and behaviour across the Drosophila brain. 2021, Nature, 593, 244

[261] De Backer, J.-F. & Kadow, I. C. G., A role for glia in cellular and systemic metabolism: insights from the fly. 2022, Current Opinion in Insect Science, 100947

[262] Rittschof, C. C. & Schirmeier, S., Insect models of central nervous system energy metabolism and its links to behavior. 2018, Glia, 66, 1160

[263] Tononi, G. & Cirelli, C., Sleep and synaptic homeostasis: a hypothesis. 2003, Brain research bulletin, 62, 143

[264] Tononi, G. & Cirelli, C., Sleep function and synaptic homeostasis. 2006, Sleep medicine reviews, 10, 49

[265] Cirelli, C. & Tononi, G. 2022, in Seminars in cell & developmental biology, Vol. 125, Elsevier, 91–100

[266] Seibt, J. & Frank, M. G., Primed to sleep: the dynamics of synaptic plasticity across brain states. 2019, Frontiers in systems neuroscience, 13, 2

[267] Borbély, A. A., A two process model of sleep regulation. 1982, Hum neurobiol, 1, 195

[268] Achermann, P., The two-process model of sleep regulation revisited. 2004, Aviation, space, and environmental medicine, 75, A37

[269] Borbély, A. A., Daan, S., Wirz-Justice, A., & Deboer, T., The two-process model of sleep regulation: a reappraisal. 2016, Journal of sleep research, 25, 131

[270] Saper, C. B., Fuller, P. M., Pedersen, N. P., Lu, J., & Scammell, T. E., Sleep state switching. 2010, Neuron, 68, 1023

[271] Scammell, T. E., Arrigoni, E., & Lipton, J. O., Neural circuitry of wakefulness and sleep. 2017, Neuron, 93, 747

[272] Wang, Y.-Q., Liu, W.-Y., Li, L., Qu, W.-M., & Huang, Z.-L., Neural circuitry underlying REM sleep: A review of the literature and current concepts. 2021, Progress in Neurobiology, 204, 102106

[273] Daan, S., Beersma, D., & Borbély, A. A., Timing of human sleep: recovery process gated by a circadian pacemaker. 1984, American Journal of Physiology-Regulatory, Integrative and Comparative Physiology, 246, R161

[274] Postnova, S., Sleep modelling across physiological levels. 2019, Clocks & sleep, 1, 166

[275] Achermann, P. & Borbély, A. A., Simulation of human sleep: ultradian dynamics of electroencephalographic slow-wave activity. 1990, Journal of biological rhythms, 5, 141

[276] Franken, P., Tobler, I., & Borbély, A. A., Sleep homeostasis in the rat: simulation of the time course of EEG slow-wave activity. 1991, Neuroscience letters, 130, 141

[277] Duhart, J. M., Inami, S., & Koh, K., Many faces of sleep regulation: beyond the time of day and prior wake time. 2021, The FEBS journal

[278] Benington, J. H., Sleep homeostasis and the function of sleep. 2000, Sleep, 23, 959

[279] Rosbash, M. & Hall, J. C., The molecular biology of circadian rhythms. 1989, Neuron, 3, 387

[280] Ray, S. & Reddy, A. B., Cross-talk between circadian clocks, sleep-wake cycles, and metabolic networks: Dispelling the darkness. 2016, Bioessays, 38, 394

[281] Albrecht, U. & Ripperger, J. A., Circadian clocks and sleep: impact of rhythmic metabolism and waste clearance on the brain. 2018, Trends in neurosciences, 41, 677

[282] Patke, A., Young, M. W., & Axelrod, S., Molecular mechanisms and physiological importance of circadian rhythms. 2020, Nature reviews Molecular cell biology, 21, 67

[283] Vansteensel, M. J., Michel, S., & Meijer, J. H., Organization of cell and tissue circadian pacemakers: a comparison among species. 2008, Brain research reviews, 58, 18

[284] Hastings, M. H., Maywood, E. S., & Brancaccio, M., Generation of circadian rhythms in the suprachiasmatic nucleus. 2018, Nature Reviews Neuroscience, 19, 453

[285] Hall, J. C., Genetics and molecular biology of rhythms in Drosophila and other insects. 2003

[286] Sheeba, V., Kaneko, M., Sharma, V. K., & Holmes, T. C., The Drosophila circadian pacemaker circuit: Pas de deux or tarantella? 2008, Critical reviews in biochemistry and molecular biology, 43, 37

[287] Nitabach, M. N. & Taghert, P. H., Organization of the Drosophila circadian control circuit. 2008, Current Biology, 18, R84

[288] Helfrich-Förster, C., The period clock gene is expressed in central nervous system neurons which also produce a neuropeptide that reveals the projections of circadian pacemaker cells within the brain of Drosophila melanogaster. 1995, Proceedings of the National Academy of Sciences, 92, 612

[289] Im, S. H. & Taghert, P. H., PDF receptor expression reveals direct interactions between circadian oscillators in Drosophila. 2010, Journal of Comparative Neurology, 518, 1925

[290] Emery, P., So, W. V., Kaneko, M., Hall, J. C., & Rosbash, M., CRY, a Drosophila clock and light-regulated cryptochrome, is a major contributor to circadian rhythm resetting and photosensitivity. 1998, Cell, 95, 669

[291] Stanewsky, R., Kaneko, M., Emery, P., et al., The cryb mutation identifies cryptochrome as a circadian photoreceptor in Drosophila. 1998, Cell, 95, 681

[292] Guo, F., Holla, M., Díaz, M. M., & Rosbash, M., A circadian output circuit controls sleep-wake arousal in Drosophila. 2018, Neuron, 100, 624

[293] Ni, J. D., Ogunmowo, T. H., Hackbart, H., et al., Coordinated activity of sleep and arousal neurons for stabilizing sleep/wake states in Drosophila. 2018, bioRxiv, 243444

[294] Liang, X., Ho, M. C., Zhang, Y., et al., Morning and evening circadian pacemakers independently drive premotor centers via a specific dopamine relay. 2019, Neuron, 102, 843

[295] Reinhard, N., Schubert, F. K., Bertolini, E., et al., The neuronal circuit of the dorsal circadian clock neurons in Drosophila melanogaster. 2022, Frontiers in physiology, 695

[296] Lawal, O., Ulloa Severino, F. P., & Eroglu, C., The role of astrocyte structural plasticity in regulating neural circuit function and behavior. 2022, Glia, 70, 1467

[297] Pitman, J. L., McGill, J. J., Keegan, K. P., & Allada, R., A dynamic role for the mushroom bodies in promoting sleep in Drosophila. 2006, Nature, 441, 753

[298] Aso, Y., Hattori, D., Yu, Y., et al., The neuronal architecture of the mushroom body provides a logic for associative learning. 2014, elife, 3, e04577

[299] Aso, Y., Sitaraman, D., Ichinose, T., et al., Mushroom body output neurons encode valence and guide memory-based action selection in Drosophila. 2014, elife, 3, e04580

[300] Sitaraman, D., Aso, Y., Jin, X., et al., Propagation of homeostatic sleep signals by segregated synaptic microcircuits of the Drosophila mushroom body. 2015, Current Biology, 25, 2915

[301] Turner-Evans, D. B. & Jayaraman, V., The insect central complex. 2016, Current Biology, 26, R453

[302] Homberg, U., Evolution of the central complex in the arthropod brain with respect to the visual system. 2008, Arthropod structure & development, 37, 347

[303] Strausfeld, N. J., Brain organization and the origin of insects: an assessment. 2009, Proceedings of the Royal Society B: Biological Sciences, 276, 1929

[304] Wolff, T., Iyer, N. A., & Rubin, G. M., Neuroarchitecture and neuroanatomy of the Drosophila central complex: A GAL4-based dissection of protocerebral bridge neurons and circuits. 2015, Journal of Comparative Neurology, 523, 997

[305] Hulse, B. K., Haberkern, H., Franconville, R., et al., A connectome of the Drosophila central complex reveals network motifs suitable for flexible navigation and context-dependent action selection. 2021, Biorxiv, 2020

[306] Hulse, B. K. & Jayaraman, V., Mechanisms underlying the neural computation of head direction. 2020, Annual review of neuroscience, 43, 31

[307] Ho, M. C., Tabuchi, M., Xie, X., et al., Sleep need-dependent changes in functional connectivity facilitate transmission of homeostatic sleep drive. 2022, Current Biology, 32, 4957

[308] Pimentel, D., Donlea, J. M., Talbot, C. B., et al., Operation of a homeostatic sleep switch. 2016, Nature, 536, 333

[309] Wegener, C. & Chen, J., Allatostatin A signalling: progress and new challenges from a paradigmatic pleiotropic invertebrate neuropeptide family. 2022, Frontiers in Physiology, 13

[310] Strauss, R. & Heisenberg, M., A higher control center of locomotor behavior in the Drosophila brain. 1993, Journal of Neuroscience, 13, 1852

[311] Green, J. & Maimon, G., Building a heading signal from anatomically defined neuron types in the Drosophila central complex. 2018, Current opinion in neurobiology, 52, 156

[312] Kim, S. S., Plasticity between visual input pathways and the head direction system. 2021, Current Opinion in Neurobiology, 71, 60

[313] Seelig, J. D. & Jayaraman, V., Neural dynamics for landmark orientation and angular path integration. 2015, Nature, 521, 186

[314] Green, J., Adachi, A., Shah, K. K., et al., A neural circuit architecture for angular integration in Drosophila. 2017, Nature, 546, 101

[315] Kim, S. S., Rouault, H., Druckmann, S., & Jayaraman, V., Ring attractor dynamics in the Drosophila central brain. 2017, Science, 356, 849

[316] Turner-Evans, D., Wegener, S., Rouault, H., et al., Angular velocity integration in a fly heading circuit. 2017, Elife, 6, e23496

[317] Skaggs, W., Knierim, J., Kudrimoti, H., & McNaughton, B., A model of the neural basis of the rat's sense of direction. 1994, Advances in neural information processing systems, 7

[318] Knierim, J. J. & Zhang, K., Attractor dynamics of spatially correlated neural activity in the limbic system. 2012, Annual review of neuroscience, 35, 267

[319] Okubo, T. S., Patella, P., D'Alessandro, I., & Wilson, R. I., A neural network for wind-guided compass navigation. 2020, Neuron, 107, 924

[320] Heinze, S. & Homberg, U., Maplike representation of celestial E-vector orientations in the brain of an insect. 2007, Science, 315, 995

[321] Homberg, U., Heinze, S., Pfeiffer, K., Kinoshita, M., & El Jundi, B., Central neural coding of sky polarization in insects. 2011, Philosophical Transactions of the Royal Society B: Biological Sciences, 366, 680

[322] Hardcastle, B. J., Omoto, J. J., Kandimalla, P., et al., A visual pathway for skylight polarization processing in Drosophila. 2021, Elife, 10, e63225

[323] Lu, J., Behbahani, A. H., Hamburg, L., et al., Transforming representations of movement from body-to world-centric space. 2022, Nature, 601, 98

[324] Pires, P. M., Abbott, L., & Maimon, G., Converting an allocentric goal into an egocentric steering signal. 2022, bioRxiv

[325] Westeinde, E. A., Kellogg, E., Dawson, P. M., et al., Transforming a head direction signal into a goal-oriented steering command. 2022, bioRxiv

[326] Pfeiffer, B. D., Jenett, A., Hammonds, A. S., et al., Tools for neuroanatomy and neurogenetics in Drosophila. 2008, Proceedings of the National Academy of Sciences, 105, 9715

[327] Pfeiffer, B. D., Ngo, T.-T. B., Hibbard, K. L., et al., Refinement of tools for targeted gene expression in Drosophila. 2010, Genetics, 186, 735

[328] Dionne, H., Hibbard, K. L., Cavallaro, A., Kao, J.-C., & Rubin, G. M., Genetic reagents for making split-GAL4 lines in Drosophila. 2018, Genetics, 209, 31

[329] Dombeck, D. A., Khabbaz, A. N., Collman, F., Adelman, T. L., & Tank, D. W., Imaging large-scale neural activity with cellular resolution in awake, mobile mice. 2007, Neuron, 56, 43

[330] Maimon, G., Straw, A. D., & Dickinson, M. H., Active flight increases the gain of visual motion processing in Drosophila. 2010, Nature neuroscience, 13, 393

[331] Seelig, J. D., Chiappe, M. E., Lott, G. K., et al., Two-photon calcium imaging from head-fixed Drosophila during optomotor walking behavior. 2010, Nature methods, 7, 535

[332] Neuser, K., Triphan, T., Mronz, M., Poeck, B., & Strauss, R., Analysis of a spatial orientation memory in Drosophila. 2008, Nature, 453, 1244

[333] Kuntz, S., Poeck, B., Sokolowski, M. B., & Strauss, R., The visual orientation memory of Drosophila requires Foraging (PKG) upstream of Ignorant (RSK2) in ring neurons of the central complex. 2012, Learning & memory, 19, 337

[334] Brand, A. H. & Perrimon, N., Targeted gene expression as a means of altering cell fates and generating dominant phenotypes. 1993, development, 118, 401

[335] Luan, H., Peabody, N. C., Vinson, C. R., & White, B. H., Refined spatial manipulation of neuronal function by combinatorial restriction of transgene expression. 2006, Neuron, 52, 425

[336] Kitamoto, T., Conditional modification of behavior in Drosophila by targeted expression of a temperature-sensitive shibire allele in defined neurons. 2001, Journal of neurobiology, 47, 81

[337] Hamada, F. N., Rosenzweig, M., Kang, K., et al., An internal thermal sensor controlling temperature preference in Drosophila. 2008, Nature, 454, 217

[338] Bernstein, J. G., Garrity, P. A., & Boyden, E. S., Optogenetics and thermogenetics: technologies for controlling the activity of targeted cells within intact neural circuits. 2012, Current opinion in neurobiology, 22, 61

[339] Klapoetke, N. C., Murata, Y., Kim, S. S., et al., Independent optical excitation of distinct neural populations. 2014, Nature methods, 11, 338

[340] Zhang, Y., Rózsa, M., Liang, Y., et al., Fast and sensitive GCaMP calcium indicators for imaging neural populations. 2021, Biorxiv, 2021

[341] Tian, L., Hires, S. A., Mao, T., et al., Imaging neural activity in worms, flies and mice with improved GCaMP calcium indicators. 2009, Nature methods, 6, 875

[342] Jayaraman, V. & Laurent, G., Evaluating a genetically encoded optical sensor of neural activity using electrophysiology in intact adult fruit flies. 2007, Frontiers in neural circuits, 3

[343] Nakai, J., Ohkura, M., & Imoto, K., A high signal-to-noise Ca2+ probe composed of a single green fluorescent protein. 2001, Nature biotechnology, 19, 137

[344] Zhang, Y., Rózsa, M., Bushey, D., et al., jGCaMP8 fast genetically encoded calcium indicators. 2020, Janelia Research Campus, 10, 13148243

[345] Lai, S.-L. & Lee, T., Genetic mosaic with dual binary transcriptional systems in Drosophila. 2006, Nature neuroscience, 9, 703

[346] Potter, C. J., Tasic, B., Russler, E. V., Liang, L., & Luo, L., The Q system: a repressible binary system for transgene expression, lineage tracing, and mosaic analysis. 2010, Cell, 141, 536

[347] Alivisatos, A. P., Chun, M., Church, G. M., et al., The brain activity map project and the challenge of functional connectomics. 2012, Neuron, 74, 970

[348] DeWeerdt, S., How to map the brain. 2019, Nature, 571, S6

[349] Bargmann, C. I. & Marder, E., From the connectome to brain function. 2013, Nature methods, 10, 483

[350] Scheffer, L. K. & Meinertzhagen, I. A., A connectome is not enough–what is still needed to understand the brain of Drosophila? 2021, Journal of Experimental Biology, 224, jeb242740

[351] Li, F., Lindsey, J. W., Marin, E. C., et al., The connectome of the adult Drosophila mushroom body provides insights into function. 2020, Elife, 9, e62576

[352] Kerr, J. N. & Denk, W., Imaging in vivo: watching the brain in action. 2008, Nature Reviews Neuroscience, 9, 195

[353] Yang, W. & Yuste, R., In vivo imaging of neural activity. 2017, Nature methods, 14, 349

[354] Minsky, M., Memoir on inventing the confocal scanning microscope. 1988, Scanning, 10, 128

[355] Denk, W., Strickler, J. H., & Webb, W. W., Two-photon laser scanning fluorescence microscopy. 1990, Science, 248, 73

[356] Wang, T. & Xu, C., Three-photon neuronal imaging in deep mouse brain. 2020, Optica, 7, 947

[357] Sanderson, J., Multi-Photon Microscopy. 2023, Current Protocols, 3, e634

[358] Helmchen, F. & Denk, W., Deep tissue two-photon microscopy. 2005, Nature methods, 2, 932

[359] Wilson, R. I., Turner, G. C., & Laurent, G., Transformation of olfactory representations in the Drosophila antennal lobe. 2004, Science, 303, 366

[360] Joesch, M., Plett, J., Borst, A., & Reiff, D. F., Response properties of motion-sensitive visual interneurons in the lobula plate of Drosophila melanogaster. 2008, Current Biology, 18, 368

[361] Turner, G. C., Bazhenov, M., & Laurent, G., Olfactory representations by Drosophila mushroom body neurons. 2008, Journal of neurophysiology, 99, 734

[362] Wang, J. W., Wong, A. M., Flores, J., Vosshall, L. B., & Axel, R., Two-photon calcium imaging reveals an odor-evoked map of activity in the fly brain. 2003, Cell, 112, 271

[363] Huang, C., Maxey, J. R., Sinha, S., et al., Long-term optical brain imaging in live adult fruit flies. 2018, Nature Communications, 9, 872

[364] Tao, X., Lin, H.-H., Lam, T., et al. 2017, in 2017 Conference on Lasers and Electro-Optics (CLEO), IEEE, 1–2

[365] Aragon, M. J., Mok, A. T., Shea, J., et al., Multiphoton imaging of neural structure and activity in Drosophila through the intact cuticle. 2022, Elife, 11, e69094

[366] Weisenburger, S. & Vaziri, A., A guide to emerging technologies for large-scale and whole-brain optical imaging of neuronal activity. 2018, Annual review of neuroscience, 41, 431

[367] Wu, J., Ji, N., & Tsia, K. K., Speed scaling in multiphoton fluorescence microscopy. 2021, Nature Photonics, 15, 800

[368] Ito, K. N., Isobe, K., & Osakada, F., Fast z-focus controlling and multiplexing strategies for multiplane two-photon imaging of neural dynamics. 2022, Neuroscience Research, 179, 15

[369] Amir, W., Carriles, R., Hoover, E. E., et al., Simultaneous imaging of multiple focal planes using a two-photon scanning microscope. 2007, Optics letters, 32, 1731

[370] Cheng, A., Gonçalves, J. T., Golshani, P., Arisaka, K., & Portera-Cailliau, C., Simultaneous two-photon calcium imaging at different depths with spatiotemporal multiplexing. 2011, Nature methods, 8, 139

[371] Beaulieu, D. R., Davison, I. G., Kılıç, K., Bifano, T. G., & Mertz, J., Simultaneous multiplane imaging with reverberation two-photon microscopy. 2020, Nature methods, 17, 283

[372] Chen, J. L., Voigt, F. F., Javadzadeh, M., Krueppel, R., & Helmchen, F., Long-range population dynamics of anatomically defined neocortical networks. 2016, Elife, 5, e14679

[373] Thériault, G., De Koninck, Y., & McCarthy, N., Extended depth of field microscopy for rapid volumetric two-photon imaging. 2013, Optics express, 21, 10095

[374] Lu, R., Sun, W., Liang, Y., et al., Video-rate volumetric functional imaging of the brain at synaptic resolution. 2017, Nature neuroscience, 20, 620

[375] Lu, R., Tanimoto, M., Koyama, M., & Ji, N., 50 Hz volumetric functional imaging with continuously adjustable depth of focus. 2018, Biomedical Optics Express, 9, 1964

[376] Fan, J. L., Rivera, J. A., Sun, W., et al., High-speed volumetric two-photon fluorescence imaging of neurovascular dynamics. 2020, Nature communications, 11, 6020

[377] Thériault, G., Cottet, M., Castonguay, A., McCarthy, N., & De Koninck, Y., Extended two-photon microscopy in live samples with Bessel beams: steadier focus, faster volume scans, and simpler stereoscopic imaging. 2014, Frontiers in cellular neuroscience, 8, 139

[378] Yang, Y., Yao, B., Lei, M., et al., Two-Photon Laser Scanning Stereomicroscopy for Fast Volumetric Imaging. 2016, PloS one, 11, e0168885

[379] Song, A., Charles, A. S., Koay, S. A., et al., Volumetric two-photon imaging of neurons using stereoscopy (vTwINS). 2017, Nature methods, 14, 420

[380] Guizar-Sicairos, M., Thurman, S. T., & Fienup, J. R., Efficient subpixel image registration algorithms. 2008, Optics letters, 33, 156

[381] Greenberg, D. S. & Kerr, J. N., Automated correction of fast motion artifacts for two-photon imaging of awake animals. 2009, Journal of neuroscience methods, 176, 1

[382] Miri, A., Daie, K., Burdine, R. D., Aksay, E., & Tank, D. W., Regression-based identification of behavior-encoding neurons during large-scale optical imaging of neural activity at cellular resolution. 2011, Journal of neurophysiology, 105, 964

[383] Pnevmatikakis, E. A. & Giovannucci, A., NoRMCorre: An online algorithm for piecewise rigid motion correction of calcium imaging data. 2017, Journal of neuroscience methods, 291, 83

[384] Stringer, C. & Pachitariu, M., Computational processing of neural recordings from calcium imaging data. 2019, Current opinion in neurobiology, 55, 22

[385] Griffiths, V. A., Valera, A. M., Lau, J. Y., et al., Real-time 3D movement correction for two-photon imaging in behaving animals. 2020, Nature methods, 17, 741

[386] Laffray, S., Pagès, S., Dufour, H., et al., Adaptive movement compensation for in vivo imaging of fast cellular dynamics within a moving tissue. 2011, PloS one, 6, e19928

[387] Chen, J. L., Pfäffli, O. A., Voigt, F. F., Margolis, D. J., & Helmchen, F., Online correction of licking-induced brain motion during two-photon imaging with a tunable lens. 2013, The Journal of physiology, 591, 4689

[388] Karagyozov, D., Skanata, M. M., Lesar, A., & Gershow, M., Recording neural activity in unrestrained animals with three-dimensional tracking two-photon microscopy. 2018, Cell reports, 25, 1371

[389] Ryan, T. M., Hinojosa, A. J., Vroman, R., Papasavvas, C., & Lagnado, L., Correction of z-motion artefacts to allow population imaging of synaptic activity in behaving mice. 2020, The Journal of physiology, 598, 1809

[390] Liang, X., Holy, T. E., & Taghert, P. H., Synchronous Drosophila circadian pacemakers display nonsynchronous Ca2+ rhythms in vivo. 2016, Science, 351, 976

[391] Dayan, P. & Abbott, L. F. 2005, Theoretical neuroscience: computational and mathematical modeling of neural systems (MIT press)

[392] Izhikevich, E. M. 2007, Dynamical systems in neuroscience (MIT press)

[393] Gerstner, W., Kistler, W. M., Naud, R., & Paninski, L. 2014, Neuronal dynamics: From single neurons to networks and models of cognition (Cambridge University Press)

[394] Héricé, C., Patel, A. A., & Sakata, S., Circuit mechanisms and computational models of REM sleep. 2019, Neuroscience research, 140, 77

[395] Rennó-Costa, C., da Silva, A. C. C., Blanco, W., & Ribeiro, S., Computational models of memory consolidation and long-term synaptic plasticity during sleep. 2019, Neurobiology of learning and memory, 160, 32

[396] Abel, J. H., Lecamwasam, K., St Hilaire, M. A., & Klerman, E. B., Recent advances in modeling sleep: from the clinic to society and disease. 2020, Current opinion in physiology, 15, 37

[397] Abhilash, L. & Shafer III, O. T., Circadian Regulation of Sleep in Drosophila: Insights from a Two-Process Model. 2022, bioRxiv, 2022

[398] Lazopulo, A. & Syed, S., A mathematical model provides mechanistic links to temporal patterns in Drosophila daily activity. 2016, BMC neuroscience, 17, 1

[399] Wiggin, T. D., Goodwin, P. R., Donelson, N. C., et al., Covert sleep-related biological processes are revealed by probabilistic analysis in Drosophila. 2020, Proceedings of the National Academy of Sciences, 117, 10024

[400] Saper, C. B., Chou, T. C., & Scammell, T. E., The sleep switch: hypothalamic control of sleep and wakefulness. 2001, Trends in neurosciences, 24, 726

[401] Behn, C. G. D., Brown, E. N., Scammell, T. E., & Kopell, N. J., Mathematical model of network dynamics governing mouse sleep–wake behavior. 2007, Journal of neurophysiology, 97, 3828

[402] Phillips, A. & Robinson, P. A., A quantitative model of sleep-wake dynamics based on the physiology of the brainstem ascending arousal system. 2007, Journal of Biological Rhythms, 22, 167

[403] Lu, J., Sherman, D., Devor, M., & Saper, C. B., A putative flip–flop switch for control of REM sleep. 2006, Nature, 441, 589

[404] Diniz Behn, C., Kopell, N., Brown, E. N., Mochizuki, T., & Scammell, T. E., Delayed orexin signaling consolidates wakefulness and sleep: physiology and modeling. 2008, Journal of neurophysiology, 99, 3090

[405] Rempe, M. J., Best, J., & Terman, D., A mathematical model of the sleep/wake cycle. 2010, Journal of mathematical biology, 60, 615

[406] Skeldon, A. C., Dijk, D.-J., & Derks, G., Mathematical models for sleep-wake dynamics: comparison of the two-process model and a mutual inhibition neuronal model. 2014, PloS one, 9, e103877

[407] Esser, S. K., Hill, S. L., & Tononi, G., Sleep homeostasis and cortical synchronization: I. Modeling the effects of synaptic strength on sleep slow waves. 2007, Sleep, 30, 1617

[408] Olcese, U., Esser, S. K., & Tononi, G., Sleep and synaptic renormalization: a computational study. 2010, Journal of neurophysiology, 104, 3476

[409] Nere, A., Hashmi, A., Cirelli, C., & Tononi, G., Sleep-dependent synaptic down-selection (I): modeling the benefits of sleep on memory consolidation and integration. 2013, Frontiers in neurology, 4, 143

[410] Singh, G., Astrocytic Sleep Homeostasis Model. 2022, bioRxiv, 2022

[411] Crick, F. & Mitchison, G., The function of dream sleep. 1983, Nature, 304, 111

[412] Hopfield, J. J., Feinstein, D. I., & Palmer, R. G., 'Unlearning'has a stabilizing effect in collective memories. 1983, Nature, 304, 158

[413] Hinton, G. E., Dayan, P., Frey, B. J., & Neal, R. M., The" wake-sleep" algorithm for unsupervised neural networks. 1995, Science, 268, 1158

[414] Thiele, J., Diehl, P., & Cook, M., A wake-sleep algorithm for recurrent, spiking neural networks. 2017, arXiv preprint arXiv:1703.06290

[415] Krishnan, G. P., Tadros, T., Ramyaa, R., & Bazhenov, M., Biologically inspired sleep algorithm for artificial neural networks. 2019, arXiv preprint arXiv:1908.02240

[416] Roscow, E. L., Chua, R., Costa, R. P., Jones, M. W., & Lepora, N., Learning offline: memory replay in biological and artificial reinforcement learning. 2021, Trends in neurosciences, 44, 808

[417] Wittkuhn, L., Chien, S., Hall-McMaster, S., & Schuck, N. W., Replay in minds and machines. 2021, Neuroscience & Biobehavioral Reviews, 129, 367

[418] Rolls, E. T., Attractor networks. 2010, Wiley Interdisciplinary Reviews: Cognitive Science, 1, 119

[419] Khona, M. & Fiete, I. R., Attractor and integrator networks in the brain. 2022, Nature Reviews Neuroscience, 1

[420] Barak, O. & Tsodyks, M., Working models of working memory. 2014, Current opinion in neurobiology, 25, 20

[421] Manohar, S. G., Zokaei, N., Fallon, S. J., Vogels, T. P., & Husain, M., Neural mechanisms of attending to items in working memory. 2019, Neuroscience & Biobehavioral Reviews, 101, 1

[422] Jaffe, R. J. & Constantinidis, C., Working memory: from neural activity to the sentient mind. 2021, Compr Physiol, 11, 1

[423] Laurens, J. & Angelaki, D. E., The brain compass: a perspective on how self-motion updates the head direction cell attractor. 2018, Neuron, 97, 275

[424] Angelaki, D. E. & Laurens, J., The head direction cell network: attractor dynamics, integration within the navigation system, and three-dimensional properties. 2020, Current opinion in neurobiology, 60, 136

[425] Petrucco, L., Lavian, H., Wu, Y. K., et al., Neural dynamics and architecture of the heading direction circuit in a vertebrate brain. 2022, bioRxiv, 2022

[426] Burak, Y. & Fiete, I. R., Fundamental limits on persistent activity in networks of noisy neurons. 2012, Proceedings of the National Academy of Sciences, 109, 17645

[427] Renart, A., Song, P., & Wang, X.-J., Robust spatial working memory through homeostatic synaptic scaling in heterogeneous cortical networks. 2003, Neuron, 38, 473

[428] Itskov, V., Hansel, D., & Tsodyks, M., Short-term facilitation may stabilize parametric working memory trace. 2011, Frontiers in computational neuroscience, 5, 40

[429] Seeholzer, A., Deger, M., & Gerstner, W., Stability of working memory in continuous attractor networks under the control of short-term plasticity. 2019, PLoS computational biology, 15, e1006928

[430] Ryu, L., Kim, S. Y., & Kim, A. J., From photons to behaviors: neural implementations of visual behaviors in Drosophila. 2022, Frontiers in Neuroscience, 16

[431] Fisher, Y. E., Lu, J., D'Alessandro, I., & Wilson, R. I., Sensorimotor experience remaps visual input to a heading-direction network. 2019, Nature, 576, 121

[432] Kim, S. S., Hermundstad, A. M., Romani, S., Abbott, L., & Jayaraman, V., Generation of stable heading representations in diverse visual scenes. 2019, Nature, 576, 126

[433] Krause, A. J., Simon, E. B., Mander, B. A., et al., The sleep-deprived human brain. 2017, Nature Reviews Neuroscience, 18, 404

[434] Tobaldini, E., Costantino, G., Solbiati, M., et al., Sleep, sleep deprivation, autonomic nervous system and cardiovascular diseases. 2017, Neuroscience & Biobehavioral Reviews, 74, 321

[435] Tononi, G. & Cirelli, C., Sleep and the price of plasticity: from synaptic and cellular homeostasis to memory consolidation and integration. 2014, Neuron, 81, 12

[436] Liu, D. & Dan, Y., A motor theory of sleep-wake control: arousal-action circuit. 2019, Annual review of neuroscience

[437] Xu, C. S., Januszewski, M., Lu, Z., et al., A connectome of the adult drosophila central brain. 2020, BioRxiv

[438] Omoto, J. J., Nguyen, B.-C. M., Kandimalla, P., et al., Neuronal constituents and putative interactions within the Drosophila ellipsoid body neuropil. 2018, Frontiers in neural circuits, 12, 103

[439] Skaggs, W. E., Knierim, J. J., Kudrimoti, H. S., & McNaughton, B. L. 1995, in Advances in neural information processing systems, 173–180

[440] Cope, A. J., Sabo, C., Vasilaki, E., Barron, A. B., & Marshall, J. A., A computational model of the integration of landmarks and motion in the insect central complex. 2017, PloS one, 12

[441] Stone, T., Webb, B., Adden, A., et al., An anatomically constrained model for path integration in the bee brain. 2017, Current Biology, 27, 3069

[442] Su, T.-S., Lee, W.-J., Huang, Y.-C., Wang, C.-T., & Lo, C.-C., Coupled symmetric and asymmetric circuits underlying spatial orientation in fruit flies. 2017, Nature communications, 8, 139

[443] Hulse, B. K., Haberkern, H., Franconville, R., et al., A connectome of the Drosophila central complex reveals network motifs suitable for flexible navigation and context-dependent action selection. 2020, bioRxiv

[444] Franconville, R., Beron, C., & Jayaraman, V., Building a functional connectome of the Drosophila central complex. 2018, Elife, 7, e37017

[445] Hulse, B. K. & Jayaraman, V., Mechanisms Underlying the Neural Computation of Head Direction. 2019, Annual Review of Neuroscience, 43

[446] Hanesch, U., Fischbach, K.-F., & Heisenberg, M., Neuronal architecture of the central complex in Drosophila melanogaster. 1989, Cell and Tissue Research, 257, 343

[447] Lin, C.-Y., Chuang, C.-C., Hua, T.-E., et al., A comprehensive wiring diagram of the protocerebral bridge for visual information processing in the Drosophila brain. 2013, Cell reports, 3, 1739

[448] Dayan, P. & Abbott, L. F., Theoretical neuroscience: computational and mathematical modeling of neural systems. 2001

[449] Gerstner, W. & Kistler, W. M., Mathematical formulations of Hebbian learning. 2002, Biological cybernetics, 87, 404

[450] Dana, H., Sun, Y., Mohar, B., et al., High-performance calcium sensors for imaging activity in neuronal populations and microcompartments. 2019, Nature Methods, 16, 649

[451] Faville, R., Kottler, B., Goodhill, G., Shaw, P., & Van Swinderen, B., How deeply does your mutant sleep? Probing arousal to better understand sleep defects in Drosophila. 2015, Scientific reports, 5, 8454

[452] Andretic, R. & Shaw, P. J., Essentials of sleep recordings in Drosophila: moving beyond sleep time. 2005, Methods in enzymology, 393, 759

[453] Peyrache, A., Lacroix, M. M., Petersen, P. C., & Buzsáki, G., Internally organized mechanisms of the head direction sense. 2015, Nature neuroscience, 18, 569

[454] Turner-Evans, D. B., Jensen, K., Ali, S., et al., The neuroanatomical ultrastructure and function of a biological ring attractor. 2019, bioRxiv, 847152

[455] Beyaert, L., Greggers, U., & Menzel, R., Honeybees consolidate navigation memory during sleep. 2012, Journal of Experimental Biology, 215, 3981

[456] Vorster, A. P. & Born, J., Sleep and memory in mammals, birds and invertebrates. 2015, Neuroscience & Biobehavioral Reviews, 50, 103

[457] Brzosko, Z., Mierau, S. B., & Paulsen, O., Neuromodulation of Spike-Timing-Dependent plasticity: past, present, and future. 2019, Neuron, 103, 563

[458] Pawlak, V., Wickens, J. R., Kirkwood, A., & Kerr, J. N., Timing is not everything: neuromodulation opens the STDP gate. 2010, Frontiers in synaptic neuroscience, 2, 146

[459] Cassenaer, S. & Laurent, G., Conditional modulation of spike-timing-dependent plasticity for olfactory learning. 2012, Nature, 482, 47

[460] Feldman, D. E., The spike-timing dependence of plasticity. 2012, Neuron, 75, 556

[461] Kahsai, L. & Winther, Å. M., Chemical neuroanatomy of the Drosophila central complex: distribution of multiple neuropeptides in relation to neurotransmitters. 2011, Journal of Comparative Neurology, 519, 290

[462] Liu, C., Meng, Z., Wiggin, T. D., et al., A serotonin-modulated circuit controls sleep architecture to regulate cognitive function independent of total sleep in Drosophila. 2019, Current Biology, 29, 3635

[463] Sejnowski, T. J., Neural networks: Sleep and memory. 1995, Current Biology, 5, 832

[464] Kirszenblat, L., Yaun, R., & van Swinderen, B., Visual experience drives sleep need in Drosophila. 2019, Sleep, 42, zsz102

[465] Shiozaki, H. M., Ohta, K., & Kazama, H., A Multi-regional Network Encoding Heading and Steering Maneuvers in Drosophila. 2020, Neuron

[466] Ni, J. D., Gurav, A. S., Liu, W., et al., Differential regulation of the Drosophila sleep homeostat by circadian and arousal inputs. 2019, Elife, 8, e40487

[467] Dunmyre, J. R., Mashour, G. A., & Booth, V., Coupled flip-flop model for REM sleep regulation in the rat. 2014, PloS one, 9, e94481

[468] Chen, C.-C., Wu, J.-K., Lin, H.-W., et al., Visualizing long-term memory formation in two neurons of the Drosophila brain. 2012, science, 335, 678

[469] Yang, G., Pan, F., Parkhurst, C. N., Grutzendler, J., & Gan, W.-B., Thinned-skull cranial window technique for long-term imaging of the cortex in live mice. 2010, Nature protocols, 5, 201

[470] Minocci, D., Carbognin, E., Murmu, M. S., & Martin, J.-R., In vivo functional calcium imaging of induced or spontaneous activity in the fly brain using a GFP-apoaequorin-based bioluminescent approach. 2013, Biochimica et Biophysica Acta (BBA)-Molecular Cell Research, 1833, 1632

[471] Aragon, M. J., Wang, M., Shea, J., et al., Non-invasive multiphoton imaging of neural structure and activity in Drosophila. 2019, bioRxiv, 798686

[472] Sinha, S., Liang, L., Ho, E. T., et al., High-speed laser microsurgery of alert fruit flies for fluorescence imaging of neural activity. 2013, Proceedings of the National Academy of Sciences, 110, 18374

[473] Hoover, E. E. & Squier, J. A., Advances in multiphoton microscopy technology. 2013, Nature photonics, 7, 93

[474] Pologruto, T. A., Sabatini, B. L., & Svoboda, K., ScanImage: flexible software for operating laser scanning microscopes. 2003, Biomedical engineering online, 2, 1

[475] Martin, J. L., Sanders, E. N., Moreno-Roman, P., et al., Long-term live imaging of the Drosophila adult midgut reveals real-time dynamics of division, differentiation and loss. 2018, Elife, 7, e36248

[476] Tainton-Heap, L. A., Kirszenblat, L. C., Notaras, E. T., et al., A Paradoxical Kind of Sleep in Drosophila melanogaster. 2020, Current Biology

[477] Flores-Valle, A. & Seelig, J. D., Axial motion estimation and correction for simultaneous multi-plane two-photon calcium imaging. 2021, bioRxiv

[478] Li, X., Zhang, G., Wu, J., et al., Reinforcing neuron extraction and spike inference in calcium imaging using deep self-supervised denoising. 2021, Nature Methods, 1

[479] Reiff, D. F., Plett, J., Mank, M., Griesbeck, O., & Borst, A., Visualizing retinotopic half-wave rectified input to the motion detection circuitry of Drosophila. 2010, Nature neuroscience, 13, 973

[480] Renninger, S. L. & Orger, M. B., Two-photon imaging of neural population activity in zebrafish. 2013, Methods, 62, 255

[481] Van der Walt, S., Schönberger, J. L., Nunez-Iglesias, J., et al., scikit-image: image processing in Python. 2014, PeerJ, 2, e453

[482] Virtanen, P., Gommers, R., Oliphant, T. E., et al., SciPy 1.0: Fundamental Algorithms for Scientific Computing in Python. 2020, Nature Methods, 17, 261

[483] Benjamini, Y. & Hochberg, Y., Controlling the false discovery rate: a practical and powerful approach to multiple testing. 1995, Journal of the Royal statistical society: series B (Methodological), 57, 289

[484] Seabold, S. & Perktold, J. 2010, in 9th Python in Science Conference

[485] Keller, P. J. & Ahrens, M. B., Visualizing whole-brain activity and development at the single-cell level using light-sheet microscopy. 2015, Neuron, 85, 462

[486] Calarco, J. A. & Samuel, A. D., Imaging whole nervous systems: insights into behavior from worms to fish. 2019, Nat. Methods, 16, 14

[487] Hillman, E. M., Voleti, V., Patel, K., et al., High-speed 3D imaging of cellular activity in the brain using axially-extended beams and light sheets. 2018, Curr. Opin. Neurobiol., 50, 190

[488] Kazemipour, A., Novak, O., Flickinger, D., et al., Kilohertz frame-rate two-photon tomography. 2018, bioRxiv, 357269

[489] Nylk, J. & Dholakia, K. 2019, in Neurophotonics and Biomedical Spectroscopy (Elsevier), 477–501

[490] Fahrbach, F. O., Simon, P., & Rohrbach, A., Microscopy with self-reconstructing beams. 2010, Nat. Photonics, 4, 780

[491] Feeman, T. G. 2010, The mathematics of medical imaging (Springer)

[492] Sharpe, J., Ahlgren, U., Perry, P., et al., Optical projection tomography as a tool for 3D microscopy and gene expression studies. 2002, Science, 296, 541

[493] Rieckher, M., Birk, U. J., Meyer, H., Ripoll, J., & Tavernarakis, N., Microscopic optical projection tomography in vivo. 2011, PLOS ONE, 6, e18963

[494] Ma, X. F., Fukuhara, M., & Takeda, T., Neural network CT image reconstruction method for small amount of projection data. 2000, NUCL INSTRUM METH A, 449, 366

[495] Thaler, F., Payer, C., & Štern, D. 2018, in Proc. of the OAGM Workshop, 13–19

[496] Goy, A., Roghoobur, G., Li, S., et al., High-Resolution Limited-Angle Phase Tomography of Dense Layered Objects Using Deep Neural Networks. 2018, arXiv preprint arXiv:1812.07380

[497] Nguyen, T. C., Bui, V., & Nehmetallah, G., Computational optical tomography using 3-D deep convolutional neural networks. 2018, Opt. Eng., 57, 043111

[498] Pelt, D., Batenburg, K., & Sethian, J., Improving Tomographic Reconstruction from Limited Data Using Mixed-Scale Dense Convolutional Neural Networks. 2018, J. Imaging, 4, 128

[499] Ronneberger, O., Fischer, P., & Brox, T. 2015, in Med. Image. Comput. Comput. Assist. Interv., Springer, 234–241

[500] Çiçek, Ö., Abdulkadir, A., Lienkamp, S. S., Brox, T., & Ronneberger, O. 2016, in Med. Image. Comput. Comput. Assist. Interv., Springer, 424–432

[501] Weigert, M., Schmidt, U., Boothe, T., et al., Content-aware image restoration: pushing the limits of fluorescence microscopy. 2018, Nat. Methods, 15, 1090

[502] Chollet, F., Keras. 2015, https://keras.io

[503] Soulet, D., Paré, A., Coste, J., & Lacroix, S., Automated filtering of intrinsic movement artifacts during two-photon intravital microscopy. 2013, PLoS One, 8, e53942

[504] Aghayee, S., Winkowski, D. E., Bowen, Z., et al., Particle tracking facilitates real time capable motion correction in 2D or 3D two-photon imaging of neuronal activity. 2017, Frontiers in neural circuits, 11, 56

[505] Weisenburger, S., Tejera, F., Demas, J., et al., Volumetric Ca2+ Imaging in the Mouse Brain Using Hybrid Multiplexed Sculpted Light Microscopy. 2019, Cell, 177, 1050

[506] Wu, J., Liang, Y., Chen, S., et al., Kilohertz two-photon fluorescence microscopy imaging of neural activity in vivo. 2020, Nature methods, 17, 287

[507] Flores-Valle, A., Honnef, R., & Seelig, J. D., Automated long-term two-photon imaging in head-fixed walking Drosophila. 2021, Journal of neuroscience methods, 109432

[508] Perillo, E. P., Liu, Y.-L., Huynh, K., et al., Deep and high-resolution three-dimensional tracking of single particles using nonlinear and multiplexed illumination. 2015, Nature communications, 6, 1

[509] Liu, C., Liu, Y.-L., Perillo, E., et al., Improving z-tracking accuracy in the two-photon single-particle tracking microscope. 2015, Applied physics letters, 107, 153701

[510] Hou, S., Johnson, C., & Welsher, K., Real-time 3D single particle tracking: towards active feedback single molecule spectroscopy in live cells. 2019, Molecules, 24, 2826

[511] Kuglin, C. D. 1975, in Proc. Int. Conference Cybernetics Society, 163–165

[512] Liu, R., Ball, N., Brockill, J., et al., Aberration-free multi-plane imaging of neural activity from the mammalian brain using a fast-switching liquid crystal spatial light modulator. 2019, Biomedical Optics Express, 10, 5059

[513] Grewe, B. F., Voigt, F. F., van't Hoff, M., & Helmchen, F., Fast two-layer two-photon imaging of neuronal cell populations using an electrically tunable lens. 2011, Biomedical optics express, 2, 2035

[514] Díaz-Francés, E. & Rubio, F. J., On the existence of a normal approximation to the distribution of the ratio of two independent normal random variables. 2013, Statistical Papers, 54, 309

[515] Frank, M. G., Challenging sleep homeostasis. 2021, Neurobiology of Sleep and Circadian Rhythms, 10, 100060

[516] Heller, C. 2021, in Oxford Research Encyclopedia of Neuroscience

[517] Borbély, A., The two-process model of sleep regulation: Beginnings and outlook. 2022, Journal of Sleep Research, e13598

[518] Borb, A. A. & Achermann, P., Sleep homeostasis and models of sleep regulation. 1999, Journal of biological rhythms, 14, 559

[519] Sulaman, B. A., Wang, S., Tyan, J., & Eban-Rothschild, A., Neuro-orchestration of sleep and wakefulness. 2022, Nature Neuroscience, 1

[520] Bojarskaite, L., Bjørnstad, D. M., Pettersen, K. H., et al., Astrocytic Ca 2+ signaling is reduced during sleep and is involved in the regulation of slow wave sleep. 2020, Nature communications, 11, 1

[521] Tsunematsu, T., Sakata, S., Sanagi, T., Tanaka, K. F., & Matsui, K., Region-specific and state-dependent astrocyte Ca2+ dynamics during the sleep-wake cycle in mice. 2021, Journal of Neuroscience, 41, 5440

[522] Vaidyanathan, T. V., Collard, M., Yokoyama, S., Reitman, M. E., & Poskanzer, K. E., Cortical astrocytes independently regulate sleep depth and duration via separate GPCR pathways. 2021, Elife, 10, e63329

[523] Hastings, M. H., Brancaccio, M., Gonzalez-Aponte, M. F., & Herzog, E. D., Circadian Rhythms and Astrocytes: The Good, the Bad, and the Ugly. 2022, Annual Review of Neuroscience, 46

[524] Borbély, A. A. & Achermann, P., Concepts and models of sleep regulation: an overview. 1992, Journal of sleep research, 1, 63

[525] Lee, G. & Park, J. H., Hemolymph sugar homeostasis and starvation-induced hyperactivity affected by genetic manipulations of the adipokinetic hormone-encoding gene in Drosophila melanogaster. 2004, Genetics, 167, 311

[526] Isabel, G., Martin, J.-R., Chidami, S., Veenstra, J. A., & Rosay, P., AKH-producing neuroendocrine cell ablation decreases trehalose and induces behavioral changes in Drosophila. 2005, American Journal of Physiology-Regulatory, Integrative and Comparative Physiology, 288, R531

[527] Pool, A.-H. & Scott, K., Feeding regulation in Drosophila. 2014, Current opinion in neurobiology, 29, 57

[528] Aimon, S., Cheng, K. Y., Gjorgjieva, J., & Grunwald Kadow, I. C., Global change in brain state during spontaneous and forced walk in Drosophila is composed of combined activity patterns of different neuron classes. 2023, eLife, 12, e85202

[529] Richter, F. G., Fendl, S., Haag, J., Drews, M. S., & Borst, A., Glutamate signaling in the fly visual system. 2018, Iscience, 7, 85

[530] Marvin, J. S., Borghuis, B. G., Tian, L., et al., An optimized fluorescent probe for visualizing glutamate neurotransmission. 2013, Nature methods, 10, 162

[531] Bohnslav, J. P., Wimalasena, N. K., Clausing, K. J., et al., DeepEthogram, a machine learning pipeline for supervised behavior classification from raw pixels. 2021, Elife, 10, e63377

[532] Liu, Q., Tabuchi, M., Liu, S., et al., Branch-specific plasticity of a bifunctional dopamine circuit encodes protein hunger. 2017, Science, 356, 534

[533] Sareen, P. F., McCurdy, L. Y., & Nitabach, M. N., A neuronal ensemble encoding adaptive choice during sensory conflict in Drosophila. 2021, Nature communications, 12, 4131

[534] Dissel, S., Klose, M. K., van Swinderen, B., et al., Sleep-promoting neurons remodel their response properties to calibrate sleep drive with environmental demands. 2022, PLoS biology, 20, e3001797

[535] Walker, S. J., Goldschmidt, D., & Ribeiro, C., Craving for the future: the brain as a nutritional prediction system. 2017, Current Opinion in Insect Science, 23, 96

[536] Northeast, R. C., Vyazovskiy, V. V., & Bechtold, D. A., Eat, sleep, repeat: the role of the circadian system in balancing sleep–wake control with metabolic need. 2020, Current Opinion in Physiology, 15, 183

[537] Oesch, L. T. & Adamantidis, A. R., Sleep and metabolism: Implication of lateral hypothalamic neurons. 2021, The Orexin System. Basic Science and Role in Sleep Pathology, 45, 75

[538] Rector, D. M., Schei, J. L., Van Dongen, H. P., Belenky, G., & Krueger, J. M., Physiological markers of local sleep. 2009, European Journal of Neuroscience, 29, 1771

[539] Lyu, C., Abbott, L., & Maimon, G., Building an allocentric travelling direction signal via vector computation. 2022, Nature, 601, 92

[540] Araque, A., Carmignoto, G., Haydon, P. G., et al., Gliotransmitters travel in time and space. 2014, Neuron, 81, 728

[541] Katz, M., Corson, F., Iwanir, S., Biron, D., & Shaham, S., Glia modulate a neuronal circuit for locomotion suppression during sleep in C. elegans. 2018, Cell reports, 22, 2575

[542] Nagai, J., Yu, X., Papouin, T., et al., Behaviorally consequential astrocytic regulation of neural circuits. 2021, Neuron, 109, 576

[543] Badimon, A., Strasburger, H. J., Ayata, P., et al., Negative feedback control of neuronal activity by microglia. 2020, Nature, 586, 417

[544] Pfeiffer, T. & Attwell, D. 2020, Brain's immune cells put the brakes on neurons

[545] Wang, F., Ruppell, K. T., Zhou, S., et al., Gliotransmission orchestrates neuronal type-specific axon regeneration. 2022, bioRxiv, 799635

[546] Berry, J. A., Cervantes-Sandoval, I., Chakraborty, M., & Davis, R. L., Sleep facilitates memory by blocking dopamine neuron-mediated forgetting. 2015, Cell, 161, 1656

[547] Virtanen, P., Gommers, R., Oliphant, T. E., et al., SciPy 1.0: Fundamental Algorithms for Scientific Computing in Python. 2020, Nature Methods, 17, 261

[548] Zwietering, M., Jongenburger, I., Rombouts, F., & Van't Riet, K., Modeling of the bacterial growth curve. 1990, Applied and environmental microbiology, 56, 1875

[549] Lisman, J., Buzsáki, G., Eichenbaum, H., et al., Viewpoints: how the hippocampus contributes to memory, navigation and cognition. 2017, Nature neuroscience, 20, 1434

[550] Eichenbaum, H., The role of the hippocampus in navigation is memory. 2017, Journal of neurophysiology, 117, 1785

[551] Chaaya, N., Battle, A. R., & Johnson, L. R., An update on contextual fear memory mechanisms: Transition between Amygdala and Hippocampus. 2018, Neuroscience & Biobehavioral Reviews, 92, 43

[552] Aso, Y. & Rubin, G. M., Toward nanoscale localization of memory engrams in Drosophila. 2020, Journal of neurogenetics, 34, 151

[553] Putz, G. & Heisenberg, M., Memories in Drosophila heat-box learning. 2002, Learning & memory, 9, 349

[554] Sitaraman, D., Zars, M., LaFerriere, H., et al., Serotonin is necessary for place memory in Drosophila. 2008, Proceedings of the National Academy of Sciences, 105, 5579

[555] Ostrowski, D., Kahsai, L., Kramer, E. F., Knutson, P., & Zars, T., Place memory retention in Drosophila. 2015, Neurobiology of learning and memory, 123, 217

[556] Mishra, A., Cronley, P., Ganesan, M., Schulz, D. J., & Zars, T., Dopaminergic neurons can influence heat-box place learning in Drosophila. 2020, Journal of neurogenetics, 34, 115

[557] Morris, R., Developments of a water-maze procedure for studying spatial learning in the rat. 1984, Journal of neuroscience methods, 11, 47

[558] Foucaud, J., Philippe, A.-S., Moreno, C., & Mery, F., A genetic polymorphism affecting reliance on personal versus public information in a spatial learning task in Drosophila melanogaster. 2013, Proceedings of the Royal Society B: Biological Sciences, 280, 20130588

[559] Wolf, R. & Heisenberg, M., Basic organization of operant behavior as revealed in Drosophila flight orientation. 1991, Journal of Comparative Physiology A, 169, 699

[560] Liu, L., Wolf, R., Ernst, R., & Heisenberg, M., Context generalization in Drosophila visual learning requires the mushroom bodies. 1999, Nature, 400, 753

[561] Brembs, B. & Heisenberg, M., The operant and the classical in conditioned orientation of Drosophila melanogaster at the flight simulator. 2000, Learning & Memory, 7, 104

[562] Guo, J. & Guo, A., Crossmodal interactions between olfactory and visual learning in Drosophila. 2005, Science, 309, 307

[563] Nuwal, N., Stock, P., Hiemeyer, J., et al., Avoidance of heat and attraction to optogenetically induced sugar sensation as operant behavior in adult Drosophila. 2012, Journal of neurogenetics, 26, 298

[564] Götz, K. G., Optomotorische untersuchung des visuellen systems einiger augenmutanten der fruchtfliege Drosophila. 1964, Kybernetik, 2, 77

[565] Guo, A., Li, L., Xia, S., et al., Conditioned visual flight orientation in Drosophila: dependence on age, practice, and diet. 1996, Learning & Memory, 3, 49

[566] Buchner, E., Elementary movement detectors in an insect visual system. 1976, Biological cybernetics, 24, 85

[567] Warren, T. L., Giraldo, Y. M., & Dickinson, M. H., Celestial navigation in Drosophila. 2019, Journal of Experimental Biology, 222, jeb186148

[568] Schuster, S., Strauss, R., & Götz, K. G., Virtual-reality techniques resolve the visual cues used by fruit flies to evaluate object distances. 2002, Current Biology, 12, 1591

[569] Grabowska, M. J., Steeves, J., Alpay, J., et al., Innate visual preferences and behavioral flexibility in Drosophila. 2018, Journal of Experimental Biology, 221, jeb185918

[570] El Jundi, B. & Dacke, M., Insect Orientation: The Drosophila Wind Compass Pathway. 2021, Current Biology, 31, R83

[571] Kim, I. S. & Dickinson, M. H., Idiothetic path integration in the fruit fly Drosophila melanogaster. 2017, Current Biology, 27, 2227

[572] Corfas, R. A., Sharma, T., & Dickinson, M. H., Diverse food-sensing neurons trigger idiothetic local search in Drosophila. 2019, Current Biology, 29, 1660

[573] Webb, B., The internal maps of insects. 2019, Journal of Experimental Biology, 222, jeb188094

[574] Sun, X., Yue, S., & Mangan, M., A decentralised neural model explaining optimal integration of navigational strategies in insects. 2020, Elife, 9, e54026

[575] Berkes, P., Orbán, G., Lengyel, M., & Fiser, J., Spontaneous cortical activity reveals hallmarks of an optimal internal model of the environment. 2011, Science, 331, 83

[576] Kenet, T., Bibitchkov, D., Tsodyks, M., Grinvald, A., & Arieli, A., Spontaneously emerging cortical representations of visual attributes. 2003, Nature, 425, 954

[577] Pezzulo, G., Zorzi, M., & Corbetta, M., The secret life of predictive brains: what's spontaneous activity for? 2021, Trends in cognitive sciences, 25, 730

[578] Sutherland, G. R. & McNaughton, B., Memory trace reactivation in hippocampal and neocortical neuronal ensembles. 2000, Current opinion in neurobiology, 10, 180

[579] Ólafsdóttir, H. F., Bush, D., & Barry, C., The role of hippocampal replay in memory and planning. 2018, Current Biology, 28, R37

[580] Hunt, L., Daw, N., Kaanders, P., et al., Formalizing planning and information search in naturalistic decision-making. 2021, Nature neuroscience, 24, 1051

[581] Miller, K. J. & Venditto, S. J. C., Multi-step planning in the brain. 2021, Current Opinion in Behavioral Sciences, 38, 29

[582] Mattar, M. G. & Lengyel, M., Planning in the brain. 2022, Neuron

[583] Buzsáki, G., McKenzie, S., & Davachi, L., Neurophysiology of remembering. 2022, Annual review of psychology, 73, 187

[584] Tang, W. & Jadhav, S. P., Multiple-Timescale Representations of Space: Linking Memory to Navigation. 2022, Annual review of neuroscience, 45, 1

[585] Jones, E. A. A. & Giocomo, L. M., Neural ensembles in navigation: From single cells to population codes. 2023, Current Opinion in Neurobiology, 78, 102665

[586] Brodt, S., Inostroza, M., Niethard, N., & Born, J., Sleep—A brain-state serving systems memory consolidation. 2023, Neuron, 111, 1050

[587] Chaudhuri, R., Gerçek, B., Pandey, B., Peyrache, A., & Fiete, I., The intrinsic attractor manifold and population dynamics of a canonical cognitive circuit across waking and sleep. 2019, Nature neuroscience, 22, 1512

[588] Ajabi, Z., Keinath, A. T., Wei, X.-X., & Brandon, M. P., Population dynamics of head-direction neurons during drift and reorientation. 2023, Nature, 1

[589] Malvache, A., Reichinnek, S., Villette, V., Haimerl, C., & Cossart, R., Awake hippocampal reactivations project onto orthogonal neuronal assemblies. 2016, Science, 353, 1280

[590] Chang, N., Huang, H.-P., & Lo, C.-C., Global inhibition in head-direction neural circuits: a systematic comparison between connectome-based spiking neural circuit models. 2023, Journal of Comparative Physiology A, 1

[591] Robins, A. & McCALLUM, S., Catastrophic forgetting and the pseudorehearsal solution in Hopfield-type networks. 1998, Connection Science, 10, 121

[592] Robins, A. & McCallum, S., The consolidation of learning during sleep: comparing the pseudorehearsal and unlearning accounts. 1999, Neural Networks, 12, 1191

[593] Johnson, A. & Redish, A. D., Neural ensembles in CA3 transiently encode paths forward of the animal at a decision point. 2007, Journal of Neuroscience, 27, 12176

[594] Redish, A. D., Vicarious trial and error. 2016, Nature Reviews Neuroscience, 17, 147

[595] Mattar, M. G. & Daw, N. D., Prioritized memory access explains planning and hippocampal replay. 2018, Nature neuroscience, 21, 1609

[596] Eckstein, M. K., Wilbrecht, L., & Collins, A. G., What do reinforcement learning models measure? Interpreting model parameters in cognition and neuroscience. 2021, Current opinion in behavioral sciences, 41, 128

[597] Botvinick, M., Wang, J. X., Dabney, W., Miller, K. J., & Kurth-Nelson, Z., Deep reinforcement learning and its neuroscientific implications. 2020, Neuron, 107, 603

[598] Momennejad, I., Learning structures: predictive representations, replay, and generalization. 2020, Current Opinion in Behavioral Sciences, 32, 155

[599] Matsuo, Y., LeCun, Y., Sahani, M., et al., Deep learning, reinforcement learning, and world models. 2022, Neural Networks

[600] Lin, P., Li, C., Flores-Valle, A., et al., Tilt-angle stimulated Raman projection tomography. 2022, Optics Express, 30, 37112

[601] Plaçais, P.-Y. & Preat, T., To favor survival under food shortage, the brain disables costly memory. 2013, Science, 339, 440

[602] Placais, P.-Y., de Tredern, É., Scheunemann, L., et al., Upregulated energy metabolism in the Drosophila mushroom body is the trigger for long-term memory. 2017, Nature communications, 8, 15510

[603] Wang, T.-f., Zhou, C., Tang, A.-h., Wang, S.-q., & Chai, Z., Cellular mechanism for spontaneous calcium oscillations in astrocytes. 2006, Acta Pharmacologica Sinica, 27, 861

[604] Poskanzer, K. E. & Yuste, R., Astrocytes regulate cortical state switching in vivo. 2016, Proceedings of the National Academy of Sciences, 113, E2675

[605] Fisher, Y. E., Marquis, M., D'Alessandro, I., & Wilson, R. I., Dopamine promotes head direction plasticity during orienting movements. 2022, Nature, 1

[606] Jones, J. D., Holder, B. L., Eiken, K. R., et al., A Split-GAL4 screen identifies novel sleep-promoting neurons in the ventral nerve cord of Drosophila. 2022, bioRxiv, 2022

[607] Miroschnikow, A., Schlegel, P., & Pankratz, M. J., Making feeding decisions in the Drosophila nervous system. 2020, Current Biology, 30, R831

[608] Münch, D., Ezra-Nevo, G., Francisco, A. P., Tastekin, I., & Ribeiro, C., Nutrient homeostasis—translating internal states to behavior. 2020, Current Opinion in Neurobiology, 60, 67